BULLETIN OF RUSSIAN STATE MEDICAL UNIVERSITY

BIOMEDICAL JOURNAL OF PIROGOV RUSSIAN NATIONAL RESEARCH MEDICAL UNIVERSITY

EDITOR-IN-CHIEF Denis Rebrikov, DSc

DEPUTY EDITOR-IN-CHIEF Alexander Oettinger, DSc

EDITORS Valentina Geidebrekht, Liliya Egorova

TECHNICAL EDITOR Nina Tyurina

TRANSLATORS Ekaterina Tretiyakova, Vyacheslav Vityuk

DESIGN AND LAYOUT Marina Doronina

EDITORIAL BOARD

Belousov VV, DSc, professor (Moscow, Russia)
Bogomilskiy MR, corr. member of RAS, DSc, professor (Moscow, Russia)
Bozhenko VK, DSc, CSc, professor (Moscow, Russia)
Bylova NA, CSc, docent (Moscow, Russia)
Gainetdinov RR, CSc (Saint-Petersburg, Russia)
Ginter EK, member of RAS, DSc (Moscow, Russia)
Gudkov AV, PhD, DSc (Buffalo, USA)
Gulyaeva NV, DSc, professor (Moscow, Russia)
Gusev EI, member of RAS, DSc, professor (Moscow, Russia)
Danilenko VN, DSc, professor (Moscow, Russia)
Zatevakhin II, member of RAS, DSc, professor (Moscow, Russia)
Kzyshkowska YuG, DSc, professor (Heidelberg, Germany)
Kotelevtsev YuV, CSc (Moscow, Russia)
Lebedev MA, PhD (Darem, USA)
Manturova NE, DSc (Moscow, Russia)
Moshkovskii SA, DSc, professor (Moscow, Russia)
Munblit DB, MSc, PhD (London, Great Britain)
Negrebetsky VV, DSc, professor (Moscow, Russia)
Novikov AA, DSc (Moscow, Russia)
Polunina NV, corr. member of RAS, DSc, professor (Moscow, Russia)
Poryadin GV, corr. member of RAS, DSc, professor (Moscow, Russia)
Savelieva GM, member of RAS, DSc, professor (Moscow, Russia)
Semiglazov VF, corr. member of RAS, DSc, professor (Saint-Petersburg, Russia)
Slavyanskaya TA, DSc, professor (Moscow, Russia)
Spallone A, DSc, professor (Rome, Italy)
Starodubov VI, member of RAS, DSc, professor (Moscow, Russia)
Stepanov VA, corr. member of RAS, DSc, professor (Tomsk, Russia)
Takhchidi KhP, corr.member of RAS, DSc (medicine), professor (Moscow, Russia)
Suchkov SV, DSc, professor (Moscow, Russia)
Trufanov GE, DSc, professor (Saint-Petersburg, Russia)
Favorova OO, DSc, professor (Moscow, Russia)
Filipenko ML, CSc, leading researcher (Novosibirsk, Russia)
Khazipov RN, DSc (Marsel, France)
Shimanovskii NL, corr. member of RAS, Dsc, professor (Moscow, Russia)
Shishkina LN, DSc, senior researcher (Novosibirsk, Russia)
Yakubovskaya RI, DSc, professor (Moscow, Russia)

SUBMISSION http://vestnikrgmu.ru/login?lang=en
CORRESPONDENCE editor@vestnikrgmu.ru
COLLABORATION manager@vestnikrgmu.ru
ADDRESS ul. Ostrovityanova, d. 1, Moscow, Russia, 117997

Indexed in Scopus since 2017

Indexed in WoS since 2018

Five-year h-index is 3

Indexed in RSCI. IF 2017: 0,326

Listed in HAC 27.01.2016 (no. 1760)

Open access to archive

Issue DOI: 10.24075/brsmu.2018–06
The mass media registration certificate no. 012769 issued on July 29, 1994
Founder and publisher is Pirogov Russian National Research Medical University (Moscow, Russia)
The journal is distributed under the terms of Creative Commons Attribution 4.0 International License www.creativecommons.org

Approved for print 10.01.2019
Circulation: 100 copies. Printed by Print.Formula
www.print-formula.ru

ВЕСТНИК РОССИЙСКОГО ГОСУДАРСТВЕННОГО МЕДИЦИНСКОГО УНИВЕРСИТЕТА

НАУЧНЫЙ МЕДИЦИНСКИЙ ЖУРНАЛ РНИМУ ИМ. Н. И. ПИРОГОВА

ГЛАВНЫЙ РЕДАКТОР Денис Ребриков, д. б. н.

ЗАМЕСТИТЕЛЬ ГЛАВНОГО РЕДАКТОРА Александр Эттингер, д. м. н.

РЕДАКТОРЫ Валентина Гейдебрехт, Лилия Егорова

ТЕХНИЧЕСКИЙ РЕДАКТОР Нина Тюрина

ПЕРЕВОДЧИКИ Екатерина Третьякова, Вячеслав Витюк

ДИЗАЙН И ВЕРСТКА Марина Доронина

РЕДАКЦИОННАЯ КОЛЛЕГИЯ

В. В. Белоусов, д. б. н., профессор (Москва, Россия)
М. Р. Богомильский, член-корр. РАН, д. м. н., профессор (Москва, Россия)
В. К. Боженко, д. м. н., к. б. н., профессор (Москва, Россия)
Н. А. Былова, к. м. н., доцент (Москва, Россия)
Р. Р. Гайнетдинов, к. м. н. (Санкт-Петербург, Россия)
Е. К. Гинтер, академик РАН, д. б. н. (Москва, Россия)
А. В. Гудков, PhD, DSc (Буффало, США)
Н. В. Гуляева, д. б. н., профессор (Москва, Россия)
Е. И. Гусев, академик РАН, д. м. н., профессор (Москва, Россия)
В. Н. Даниленко, д. б. н., профессор (Москва, Россия)
И. И. Затевахин, академик РАН, д. м. н., профессор (Москва, Россия)
Ю. Г. Кжышковска, д. б. н., профессор (Гейдельберг, Германия)
Ю. В. Котелевцев, к. х. н. (Москва, Россия)
М. А. Лебедев, PhD (Дарем, США)
Н. Е. Мантурова, д. м. н. (Москва, Россия)
С. А. Мошковский, д. б. н., профессор (Москва, Россия)
Д. Б. Мунблит, MSc, PhD (Лондон, Великобритания)
В. В. Негребецкий, д. х. н., профессор (Москва, Россия)
А. А. Новиков, д. б. н. (Москва, Россия)
Н. В. Полунина, член-корр. РАН, д. м. н., профессор (Москва, Россия)
Г. В. Порядин, член-корр. РАН, д. м. н., профессор (Москва, Россия)
Г. М. Савельева, академик РАН, д. м. н., профессор (Москва, Россия)
В. Ф. Семиглазов, член-корр. РАН, д. м. н., профессор (Санкт-Петербург, Россия)
Т. А. Славянская, д. м. н., профессор (Москва, Россия)
А. Спаллоне, д. м. н., профессор (Рим, Италия)
В. И. Стародубов, академик РАН, д. м. н., профессор (Москва, Россия)
В. А. Степанов, член-корр. РАН, д. б. н., профессор (Томск, Россия)
С. В. Сучков, д. м. н., профессор (Москва, Россия)
Х. П. Тахчиди, член-корр. РАН, д. м. н., профессор (Москва, Россия)
Г. Е. Труфанов, д. м. н., профессор (Санкт-Петербург, Россия)
О. О. Фаворова, д. б. н., профессор (Москва, Россия)
М. Л. Филипенко, к. б. н., в. н. с. (Новосибирск, Россия)
Р. Н. Хазипов, д. м. н. (Марсель, Франция)
Н. Л. Шимановский, член-корр. РАН, д. м. н., профессор (Москва, Россия)
Л. Н. Шишкина, д. б. н., с. н. с. (Новосибирск, Россия)
Р. И. Якубовская, д. б. н., профессор (Москва, Россия)

ПОДАЧА РУКОПИСЕЙ http://vestnikrgmu.ru/login
ПЕРЕПИСКА С РЕДАКЦИЕЙ editor@vestnikrgmu.ru
СОТРУДНИЧЕСТВО manager@vestnikrgmu.ru
АДРЕС РЕДАКЦИИ ул. Островитянова, д. 1, г. Москва, 117997

Журнал включён в Scopus с 2017 года

Журнал включён в WoS с 2018 года

Индекс Хирша (h^{5}) журнала по оценке Google Scholar: 3

Журнал включён в РИНЦ. IF 2017: 0,326

Журнал включён в Перечень 27.01.2016 (№ 1760)

Здесь находится открытый архив журнала

DOI выпуска: 10.24075/vrgmu.2018–06

Свидетельство о регистрации средства массовой информации № 012769 от 29 июля 1994 г.

Учредитель и издатель — Российский национальный исследовательский медицинский университет имени Н. И. Пирогова (Москва, Россия)

Журнал распространяется по лицензии Creative Commons Attribution 4.0 International www.creativecommons.org

Подписано в печать 10.01.2018
Тираж 100 экз. Отпечатано в типографии Print.Formula
www.print-formula.ru

Contents
Содержание

TARGETED NANOMEDICINES FOR APPLICATIONS IN PRECLINICAL CANCER MODELS

Serena Marchiò[1,2] ✉, Federico Bussolino[1,2]

[1] Department of Oncology; University of Turin; Candiolo, Italy

[2] Candiolo Cancer Institute-FPO-IRCCS; Candiolo, Italy

Despite substantial advancements in cancer management, a considerable proportion of patients cannot yet be cured. Strategies to address this open medical need are actively pursued and include two main approaches: 1) optimizing diagnostic protocols to detect tumors at early stages, and 2) designing personalized therapies to increase efficiency and selectivity of clinical interventions. Our recent work has been directed to a rationally-designed implementation of both approaches. Particularly, we have contributed to the development of nanomedicines that can be targeted to diseased tissues for theranostic purposes in preclinical models of human cancers. Such modular nanoscale systems proved to be versatile platforms to combine imaging and drug delivery for applications in the oncological field and could be a basis for future improvements.

Keywords: theranostic, cancer, targeted nanomedicines, preclinical models

✉ **Correspondence should be addressed:** Serena Marchiò
Institute for Cancer Research and Treatment, University of Torino, 142 Km 3.95, Candiolo, Italy, 10060; serena.marchio@ircc.it

Received: 29.06.2018 **Accepted:** 21.08.2018

DOI: 10.24075/brsmu.2018.081

АДРЕСНАЯ ДОСТАВКА ЛЕКАРСТВЕННЫХ НАНОПРЕПАРАТОВ В ПРИМЕНЕНИИ К МОДЕЛЯМ РАКА НА ДОКЛИНИЧЕСКОМ ЭТАПЕ ИССЛЕДОВАНИЙ

С. Марчио[1,2] ✉, Ф. Буссолино[1,2]

[1] Кафедра онкологии, Туринский университет, Кандиоло, Италия

[2] Институт онкологии (FPO-IRCCS), Кандиоло, Италия

Несмотря на значительные успехи в терапии рака, большое число пациентов пока не может быть излечено. Представленные в обзоре стратегии преодоления этой проблемы активно разрабатываются по двум направлениям: 1) оптимизация диагностических протоколов для обнаружения опухолей на ранних стадиях; 2) разработка персонализированных средств терапии для увеличения эффективности и селективности лечения. Проводимые в последнее время исследования были направлены на рациональное внедрение обоих подходов, а их результаты внесли вклад в разработку нанопрепаратов, которые можно адресно доставлять к пораженным тканям в целях тераностики опухолей на доклинических моделях. Эти модульные наносистемы достаточно гибки и позволяют объединить визуализацию и таргетирование лекарств для применения в онкологии. Они могут служить базой для дальнейшего усовершенствования методов лечения рака.

Ключевые слова: наночастицы, адресная доставка лекарств, доклинические исследования, нанофармакология, онкология, тераностика

✉ **Для корреспонденции:** Серена Марчио
Институт исследований и лечения рака, Университет Турина, 142 Km 3.95, Кандиоло, Италия, 10060; serena.marchio@ircc.it

Статья получена: 29.06.2018 **Статья принята к печати:** 21.08.2018

DOI: 10.24075/vrgmu.2018.081

Early diagnosis and effective treatment of cancer are essential to minimize morbidity and mortality. These goals can be achieved by combining 1) disease-specific molecules that may serve as both diagnostic markers and therapeutic targets with 2) imaging and drug delivery tools capable of providing high-performance intervention on diseased sites without (or only marginally) affecting nearby or distant healthy tissues. Despite this broadly accepted assumption, progress in patient-tailored approaches has been relatively slow, particularly due to the paucity of suitable molecular markers. For example, of the ~1,500 proteins proposed as new cancer biomarkers in the decade 2000-2010, only < 20 have been approved by the Food and Drug Administration (FDA) to be used in routine testing [1]. On the other hand, applications of nanotechnology to medicine (collectively defined as nanomedicine) are experiencing a tremendous impact on next-generation cancer management, as demonstrated by the number of ongoing clinical trials and advanced preclinical studies [2, 3]. A nanomedicine is a therapeutic, diagnostic or combined (theranostic = therapeutic + diagnostic) agent embedded in, or otherwise associated to, a nanoparticle to provide better biodistribution, improve the efficacy and/or reduce the toxicity of the agent itself. In our studies, we identified new biomarkers and explored preclinical applications of targeted nanomedicines for cancer imaging (targeted fluorescent nanoparticles) and treatment (targeted drug-loaded liposomes). In this minireview, we outline the principal findings of these studies.

Targeted molecular imaging of metastatic colorectal cancer

Our research group has described a previously unknown complex of α_6 integrin and E-cadherin, which is present on the surface of colon cancer cells but not of normal colon cells

[4]. We have also identified a specific ligand to this receptor complex, namely angiopoietin-like 6, a factor secreted in high amounts by normal liver and physiologically involved in lipid metabolism. We have demonstrated that this receptor/ligand circuit is operative in secondary tumor spreading: colon cancer cells expose the receptor, normal liver cells secrete the ligand, and their mutual recognition allows cancer cells to colonize the liver and eventually produce a metastatic mass in this site [4].

In addition, we have characterized two angiopoietin-like-6 mimicking peptides that bind the α_6 integrin/E-cadherin complex. These peptides, of sequence CGIYRLRS and CGVYSLRS (single letter amino acid code), besides competing with angiopoietin-like 6 for binding the receptor complex (and therefore inhibiting hepatic metastasis), represent potential tools to flag tumor cells that expose both α_6 integrin and E-cadherin [4]. So, we have exploited their binding properties to design nanomedicines for cancer imaging [5]. This study was based on silica nanoparticles, which exhibit favorable toxicological profile and biocompatibility *in vivo* coupled to ease of manipulation *in vitro* [6, 7]. We produced modular nanosystems to obtain an imaging platform consisting of fluorescent silica-polyethylene glycol (PEG) nanoparticles (SPNs) that expose either the CGIYRLRS or CGVYSLRS peptide on their surface. These SPNs have a silica nucleus associated to one or more alkoxysilane-derivatized fluorescent dyes, included in a micelle of the copolymer Pluronic®F127. In other words, they consist of a PEG shell incorporating a dye-doped silica core. The external PEG provides a standard of stealth polymer for stable dispersion in physiological conditions and for prevention of uptake by the phagocyte system. Moreover, the PEG tails can be derivatized to allow covalent attachment of targeting peptides. Our SPNs have a core diameter of 11 ± 3 nm, a hydrodynamic diameter of 23 nm and are doped with either Rhodamine A (Rhod), Cyanine 5 (Cy5) (single-color), or both (dual-color). Their specificity was first investigated *ex-vivo* on patient-derived specimens of hepatic metastasis, compared to normal liver and to primary colon cancer (Fig. 1). Sections of frozen human tissues were incubated with control (untargeted) and dual-color peptide-targeted (Rhod+Cy5)-SPNs. Nanoparticle selectivity was evaluated by confocal microscopy (imaging; Fig. 1 A–D, quantification; Fig. 1 E), revealing specific binding of CGIYRLRS- and CGVYSLRS-(Rhod+Cy5)-SPNs on hepatic metastasis (Fig. 1 B) compared to normal liver (Fig. 1 A) and colon (Fig. 1 C), and to the primary tumor (Fig. 1 D).

The SPNs were also tested *in vivo* in a mouse model of pseudo-metastatic tumor (human colon cancer cells implanted into the spleen of non-obese diabetic/severe combined immunodeficient mice, NOD/SCID; Fig. 2). Tumor-bearing mice were injected with control and targeted SPNs and signal was detected after increasing circulation times starting at 1 hour. At 6 hours, we observed a substantial reduction in background fluorescence and this signal-to-background ratio remained consistent at 16 and 24 hours. This suggests that clearance of untargeted nanoparticles is accompanied by accumulation of targeted SPNs in metastatic foci, providing a large timeframe for applications to be translated to the clinics. Fluorescence imaging by stereomicroscopy and confocal microscopy confirmed a metastasis-specific accumulation of (Rhod)-CGIYRLRS-SNPs (Fig. 2 A, D, G, H), (Cy5)-CGIYRLRS-SNPs (Fig. 2 B, E, I, J) and (Rhod-Cy5)-CGIYRLRS-SNPs (Fig. 2 C, F, K, L, M, N). A tridimensional reconstruction of several confocal microphotographs showed that the targeted SNPs localize in close proximity of tumor blood vessels (Fig. 2 O, P).

The intra-operative use of fluorescence tracers is starting to emerge in prostate, gastric, urinary and ovarian cancers [8–11]. Fluorescent imaging of externally accessible human cancers, namely nonmelanoma skin tumors can be achieved [12] and endoscopic fluorescence imaging systems have also been developed for applications in colon cancer [13]. All these systems are based on untargeted fluorescent tracers, while our SPNs have the additional feature of being molecularly targeted, providing further proof of feasibility for translational consideration.

Targeted drug delivery in metastatic neuroblastoma

In the past years, we and our collaborators have also identified peptides with unique targeting features for applications in tumor treatment. Among these, CPRECES [14] and CNGRC [15] (single letter amino acid code) bind with high selectivity to the tumor endothelial/perivascular markers aminopeptidase A (APA) and N (APN), respectively, so they are optimal for *in vivo* applications of drug delivery *via* the circulation.

These two peptides were exploited in a first study aimed to define the preclinical feasibility of targeted nanomedicines for doxorubicin (DXR) delivery to models of infantile neuroblastoma [16]. For this purpose, a synthetic version of each peptide was produced as fusion with human tumor necrosis factor (TNF) and the short linker KY (single letter amino acid code), and then coupled to the PEG tails of stealth liposomes (SL) composed of distearoyl phosphatidylethanolamine (DSPE)-PEG, hydrogenated soy phosphatidylcholine (HSPC) and cholesterol. These SLs were loaded with DXR to obtain the targeted

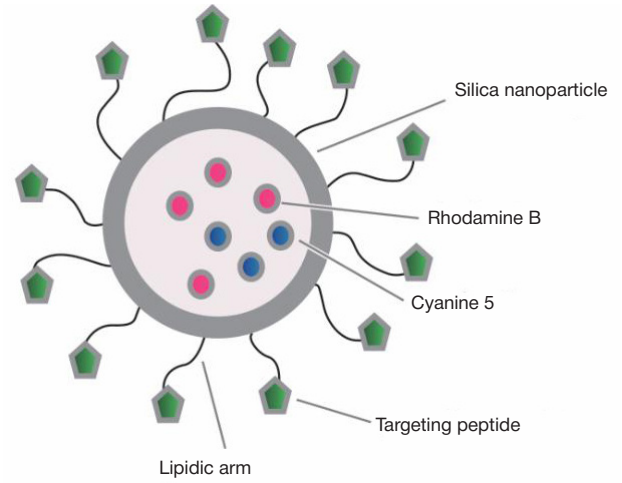

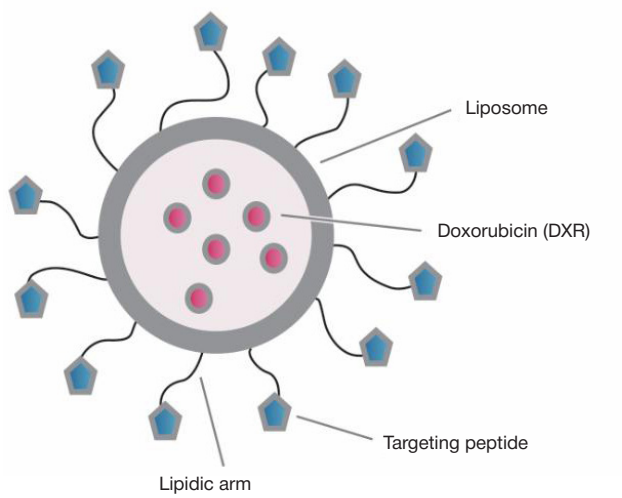

nanosystems CPRECES-SL[DXR] and CNGRC-SL[DXR], respectively, with a size of 90–115 nm, drug entrapment of 95% and peptide coupling of 4 μg/μmol of SL. For pharmacokinetic studies, these SLs were dual-labeled by incorporation of ^{3}H and ^{14}C in cholesterol and DXR, respectively, demonstrating suitable stability and long circulation times (up to 24 hours) [16]. The efficacy of such formulations, either as a single agent or in combination regimens (COMBO), was evaluated in orthotopic models derived by implant of human neuroblastoma cells into the left adrenal gland of nude mice. Starting 21 days after tumor cell implant, mice were treated once a week for 5 weeks with 5 mg/kg DXR (free or liposome-incapsulated), showing that administration of CPRECES-SL[DXR], CNGRC-SL[DXR] and COMBO provided a consistent lifespan extension vs. the free drug (up to 17, 37 and 66 days, respectively; Fig. 3) [16].

This work demonstrates that targeting a drug to the tumor microenvironment increases its efficacy and can therefore be exploited for the development of innovative medicines.

Based on these encouraging results, in a successive study we performed combined *in vitro/ex-vivo* screenings of

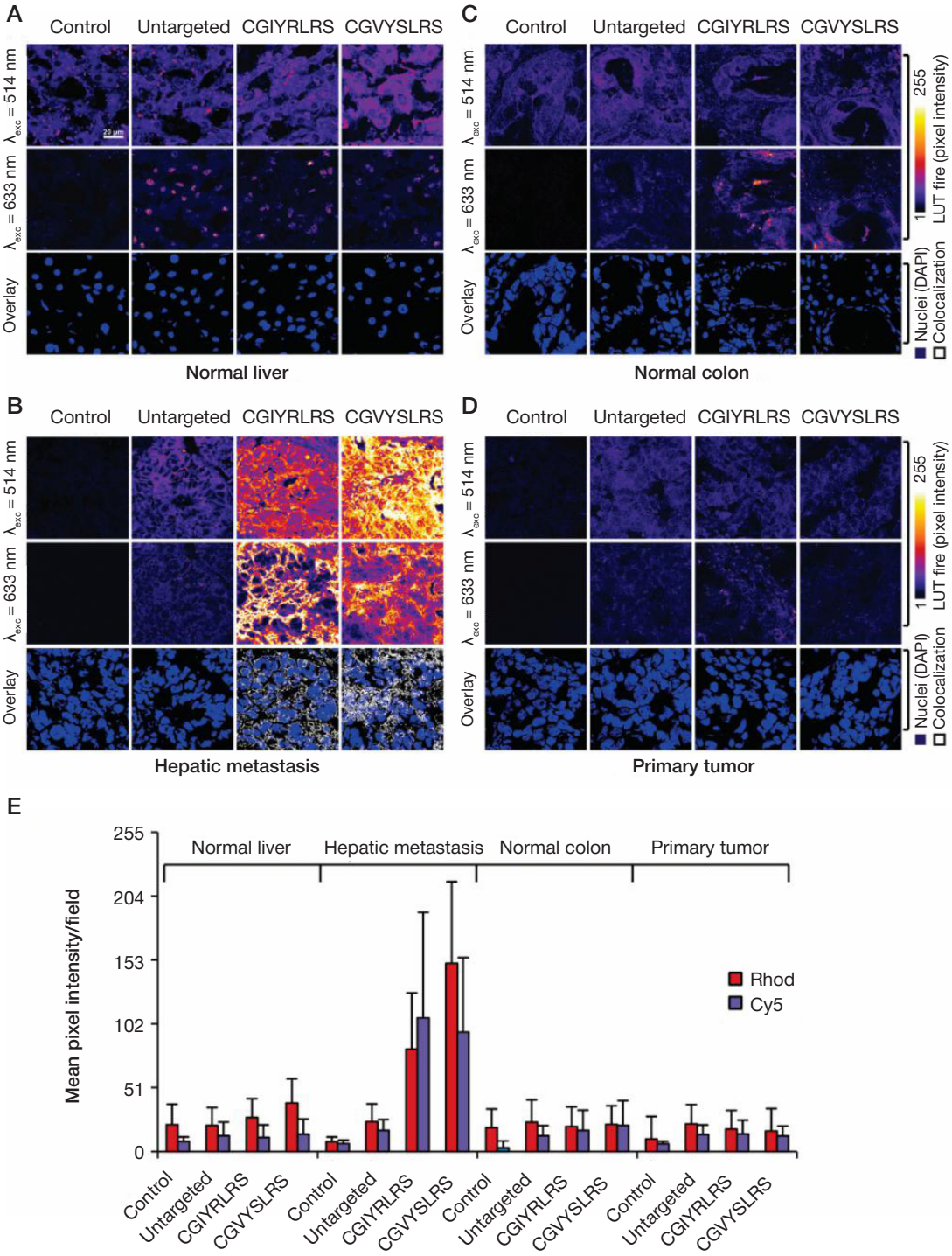

Fig. 1. Frozen sections of (**A**) normal liver, (**B**) hepatic metastasis, (**C**) normal colon and (**D**) primary tumor were fixed in 4% formaldehyde, before incubation with untargeted, CGIYRLRS-, or CGVYSLRS-(Rhod+Cy5)-SPNs for 4 hours at room temperature. After washing, SPN-emitted fluorescence was analyzed by confocal microscopy and the output was converted into the false-color LUT Fire scale for prompt visualization. Nuclei were stained with 4′,6-diamidino-2-phenylindole (DAPI). Colocalized pixels were identified by ImageJ software. Experiments were performed with similar results on specimens from 10 patients with metastatic CRC; exemplary images from tissues of patient #P85 are shown. (**E**) Quantification of SPN binding is expressed as the intensity of emitted pixel following excitation at 514 nm (Rhod) and 633 nm (Cy5), and represents a mean value of 5 images for each tissue. From Soster et al. [5]

phage-displayed peptide libraries to identify novel peptide motifs with high specificity for human neuroblastoma [16]. These experiments were designed to isolate peptides capable of binding the whole primary tumor (*n* = 26 motifs retrieved) or metastatic mass (*n* = 15 motifs), the primary tumor microenvironment (ME) (*n* = 57 motifs) or the metastasis ME (*n* = 23 motifs). The specificity of 5 peptides targeting the metastatic mass (phage clone #14, peptide sequence KSFFLSH), the primary tumor ME (#1, YEGLISR) and the metastasis ME (#5, HSYWLRS; #8, WSWPREL; #10, ALAAHKL) was confirmed *ex vivo* by binding assays on sections of human stage IV neuroblastoma and *in vivo* in mouse models. These peptides were therefore synthetized with the addition of an *N*-terminal (YSHS, single letter amino acid code) and a *C*-terminal (GGG, single letter amino acid code) linkers and coupled to SLs as described above [16]. The potential efficacy of these nanosystems was tested in an orthotopic model derived from implant of luciferase-transduced human neuroblastoma cells; in addition, a pseudo-metastatic model was obtained by tumor cell injection in the tail vein of nude mice. Orthotopically-implanted

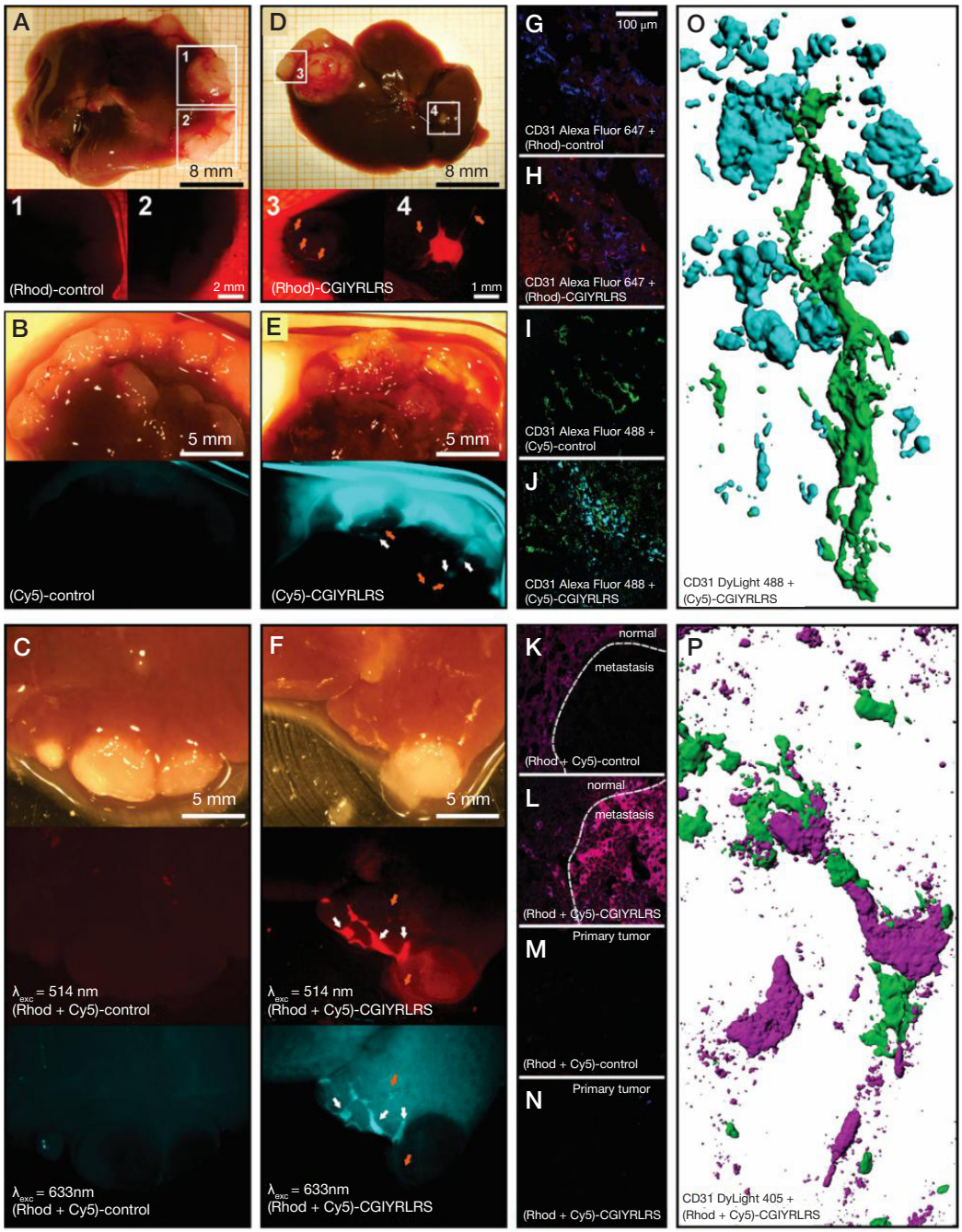

Fig. 2. NOD/SCID mice bearing a primary tumor and multiple liver metastases were injected with single- [control (**A**, Rhod; **B**, Cy5) or CGIYRLRS- (**D**, Rhod; **E**, Cy5)] or dual-color [control (**C**) or CGIYRLRS (**F**)] SPNs. After 16 hours, mice were euthanized and explanted organs were photographed with a high-resolution digital camera connected to a fluorescence stereomicroscope. In **D**, **E**, and **F**, orange arrows indicate blood vessels crossing the hepatic metastasis; in **E** and **F**, white arrows indicate sub-millimetric metastatic foci. Samples of the same tissues were OCT-frozen, cut into 10-μm slices, and evaluated by confocal analysis of single- [control (**G**, Rhod; **I**, Cy5), CGIYRLRS (**H**, Rhod; J, Cy5)] or dual-color [control (**K**), CGIYRLRS (**L**)] fluorescence. To visualize blood vessels, staining for CD31 was superimposed to the SPNs signal and visualized by the secondary antibodies Alexa Fluor®647 (**G**–**H**), Alexa Fluor®488 (**I**–**J**) and DyLight™405 (**K**–**N**), for overlay with (Rhod)-SPNs, (Cy5)-SPNs and dual-color SPNs, respectively. In the case of dual-color SPNs, samples of primary tumors from mice injected with either control (**M**) or CGIYRLRS (**N**) SPNs are visualized as a further negative control. In **O** (detail of the field in **J**) and **P** (detail of the field in **L**), tridimensional models of 50–80 confocal image series were reconstructed with IMARIS software. From Soster et al. [5]

mice were treated once a week for 3 weeks starting 21 days after tumor cell implant, and intravenously-implanted mice were treated with the same schedule but starting 4 hours after tumor cell implant. In a first series of experiments, growth of luciferase-expressing orthotopic tumors was monitored by bioluminescence imaging (BLI) at days 26, 33, 40 after implant (5 days after each treatment) showing that 5-SL[DXR] and 10-SL[DXR] were the most efficient in delaying tumor progression, as also confirmed by a whole-body X-ray scan performed one month after the end of treatments (Fig. 4 A). Successively, the capacity of targeted formulations to prolong the lifespan of tumor-bearing mice was evaluated in both the pseudo-metastatic (Fig. 4 B) and the orthotopic (Fig. 4 C) model. Again, treatment with 5-SL[DXR] or 10-SL[DXR] provided a survival advantage to neuroblastoma-bearing mice when compared to control animals or even to animals treated with DXR, either free or included in untargeted liposomal formulations [16].

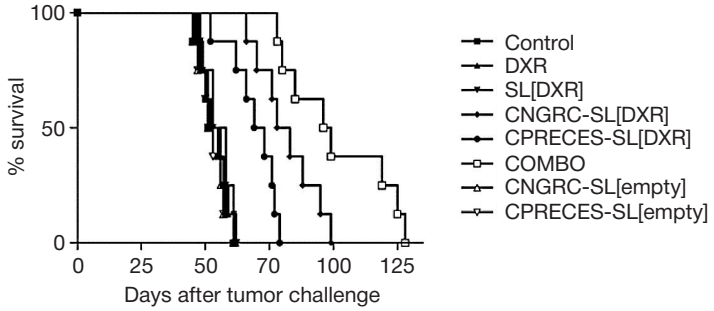

Fig. 3. Therapeutic efficacy of APN- and APA-targeted liposomal formulations in mouse models of neuroblastoma. Nude mice (8/group) implanted orthotopically with human neuroblastoma cells were treated (starting 21 days after tumor implant) by intravenous administration of HEPES-buffered saline (control), CNGRC-SL[empty], CPRECES-SL[empty] or 5 mg/kg of DXR, either free (DXR) or encapsulated in untargeted (SL[DXR]), APN- (CNGRC-SL[DXR]) or APA-targeted (CNGRC-SL[DXR]) liposomes or an equimolar mixture of CNGRC-SL[DXR] and CNGRC-SL[DXR] (COMBO), once-a-week for a total of 5 weeks. The efficacy of each formulation was evaluated in terms of survival and is expressed in a Kaplan–Maier graph as % of alive mice at different timepoints. From Loi et al. [18]

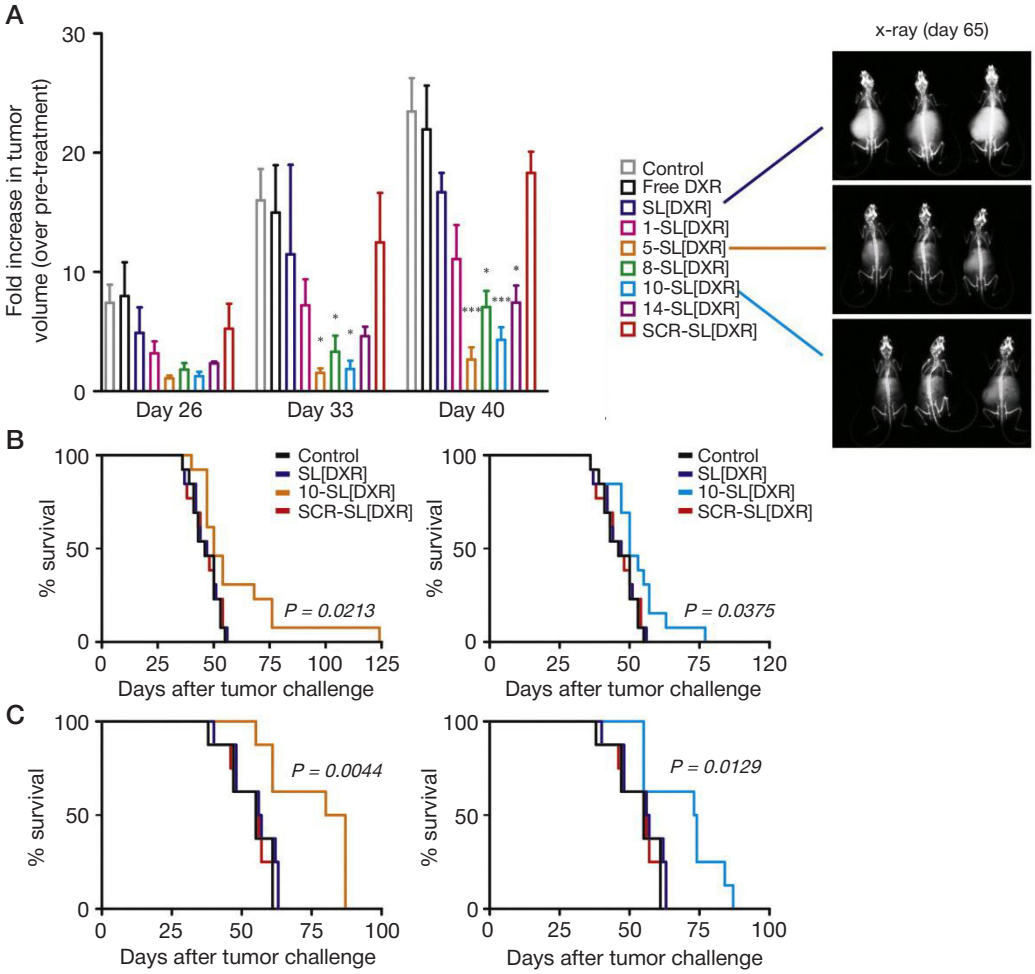

Fig. 4. (**A**) Therapeutic efficacy of peptide-targeted liposomal formulations in mouse models obtained by orthotopic implant of luciferase-expressing human neuroblastoma cells. Treatments started 21 days after tumor implant. Mice (5/group) were administered intravenous with HEPES-buffered saline (control), or 5 mg/kg of DXR, either free (DXR) or encapsulated in untargeted (SL[DXR]), scramble peptide- (SCR-SL[DXR] or targeting peptide-functionalized (1-, 5-, 8-, 10-, 14-SL[DRX]) liposomes, once-a-week for a total of 3 weeks. Tumor growth was monitored by BLI 5 days after each treatment (days 26, 33, 40 from tumor implant). Values are reported as fold increase in tumor volume compared to pre-treatment (day 20). Exemplary pictures of X-ray acquisitions one month after the end of treatment (day 65), relative to mice treated with SL[DXR], 5-SL[DXR] or 10-SL[DXR], are shown. (**B**–**C**) Therapeutic effect of the targeted formulations evaluated in terms of overall survival in both the pseudo-metastatic model (13 animals/ group, **B**) and the orthotopic model (8 animals/group, **C**). Statistical analysis: **A**, *p vs*. SL[DXR]; **B**–**C**, *p vs*. control, SL[DXR] and SCR-SL[DXR]. From Loi et al. [16].

These preliminary findings were complemented by a successive in-depth characterization of the HSYWLRS peptide (#5 of the previous study) as a targeting moiety in preclinical applications [17]. Binding and internalization specificity was confirmed on additional cell lines and tissue specimens from animal models and human stage IV neuroblastoma. DXR-loaded, peptide-targeted SLs (HSWYLRS-SL[DXR]) were therefore produced and tested as *in vivo* drug delivery nanosystems. Vascular permeability was evaluated by administration of Evans Blue in neuroblastoma-bearing mice treated with HSYWLRS-SL[DXR], observing a specific increase in dye extravasation and accumulation in orthotopic tumors, but not in non-tumor tissues (Fig. 5 A). Treatment with HSYWLRS-SL[DXR] also increased perfusion of tumor blood vessels, as determined by intravenous injection of fluorescein isothiocyanate (FITC)-lectin and analysis of emitted fluorescence by confocal microscopy (Fig. 5 B). These phenomena were accompanied by (1) enhanced tumor accumulation of HSYWLRS-SL[DXR], but not of DRX included into an untargeted liposomal formulation, and (2) prolonged animal survival (Fig. 5 C) in the absence of toxicity signs such as weight loss (Fig. 5 C, inset). Additionally, the therapeutic efficacy of HSYWLRS-SL[DXR] was compared to that of free DXR by monitoring the *in vivo* growth of orthotopically-implanted, luciferase-expressing human neuroblastoma cells with BLI, revealing that only the targeted liposomal formulation elicits effective antitumor responses (Fig. 6 A–B) and prolongs the lifespan of tumor-bearing mice (Fig. 6 C). The effect was also validated by positron emission tomography (PET) coupled with glucose consumption measurement. This analysis revealed that treatment with HSYWLRS-SL[DXR] led to a substantial inhibition not only of primary tumor growth but also of secondary tumor spreading (Fig. 7 A), which was confirmed by animal autopsy in terms of both metastatic foci number (Fig. 7 C) and overall metastasis volume (Fig. 7 C).

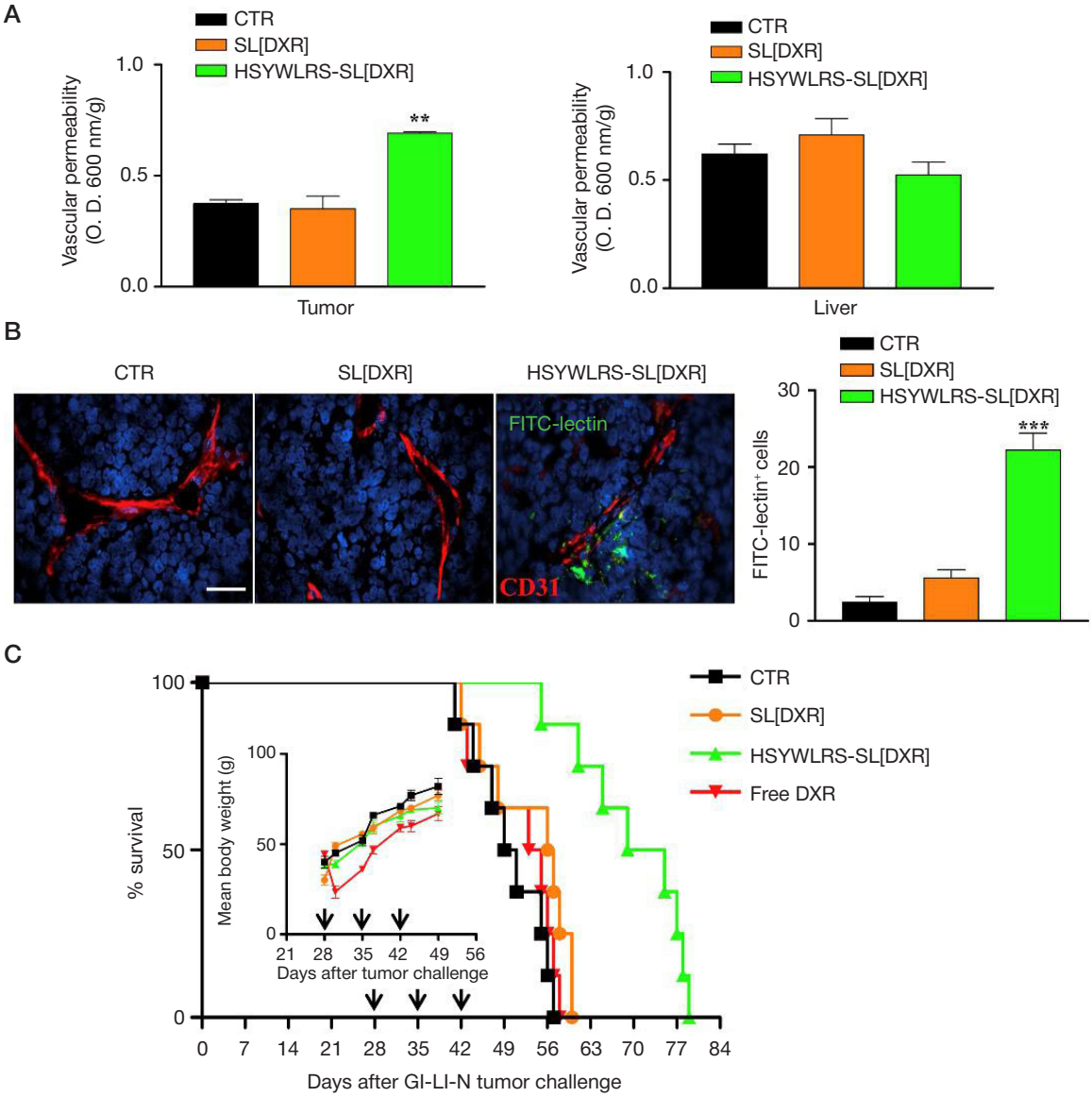

Fig. 5. (**A**) *In vivo* systemic permeability. Mice (3/group) bearing orthotopic tumors were treated, 28 days after, with a single bolus of DXR (5 mg/kg), encapsulated into untargeted (SL[DXR]) or HSYWLRS-targeted (HSYWLRS-SL[DXR]) liposomes, in combination with 1 mg of Evans Blue dye. Control mice (CTR) received HEPES-buffered saline only. One hour after, mice were perfused, tumors and livers collected and Evans Blue extracted and quantified (O.D. 600 nm). Results are expressed as Evans Blue dye per g of tissue. **, $p < 0.01$: HSYWLRS-SL[DXR] *vs*. CTR and SL[DXR]. (**B**) Exemplary tumor sections from control mice or from mice treated with SL[DXR] or HSYWLRS-SL[DXR] and inoculated with FITC-lectin (green). Red: CD31. Blue: cell nuclei (DAPI). Scale bar: 40 μm. Graph on the right, numbers of FITC-lectin positive cells. ***, $p < 0.001$, HSYWLRS-SL[DXR] *vs*. CTR and SL[DXR]. (**C**) Potentiated therapeutic efficacy of HSYWLRS-SL[DXR]. Mice (8/group) bearing orthotopic tumors were treated intravenous with 5 mg/kg of DXR, either free (free DXR) or encapsulated into SL[DXR] or HSYWLRS-SL[DXR] liposomes, once-a-week for 3 weeks (arrows). Control mice received HEPES buffer only (CTR). Survival: $p < 0.0008$: HSYWLRS-SL[DXR] *vs*. SL[DXR]). Insert: mean body weight at different timepoints. From Cossu et al. [17]

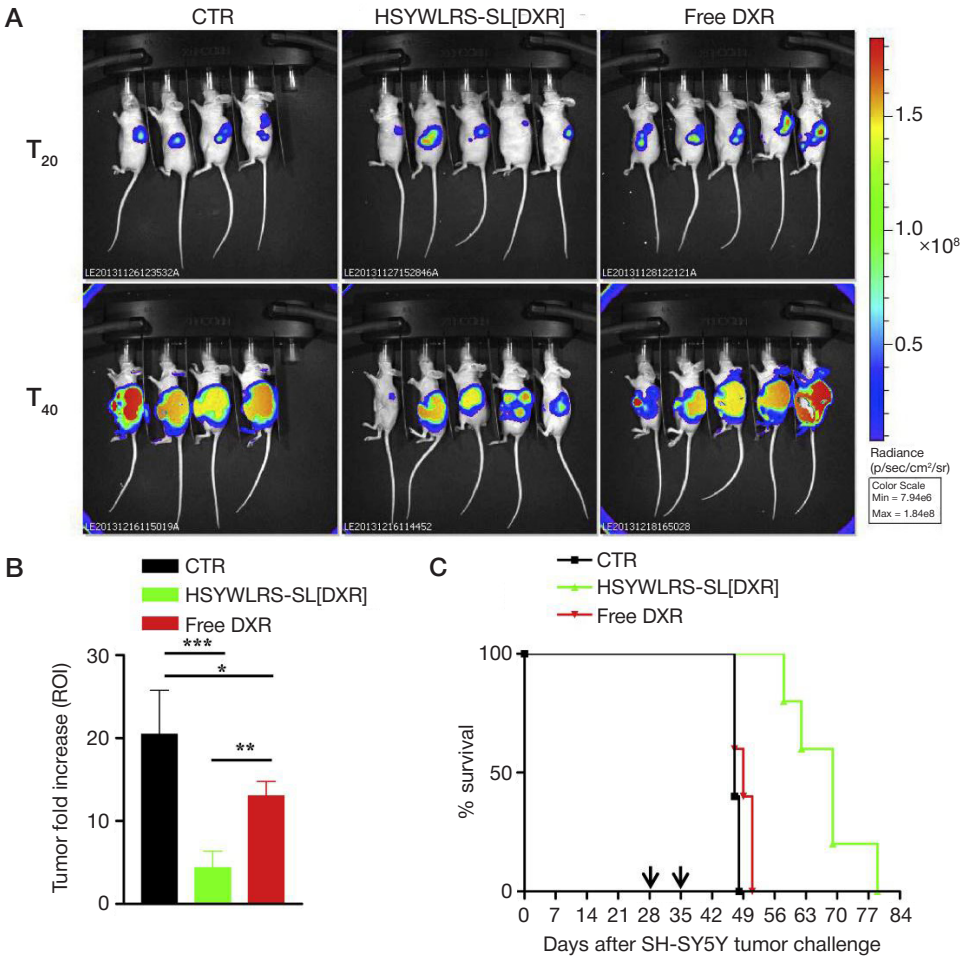

Fig. 6. (**A**) Lateral (tumor side) images from mice orthotopically implanted with luciferase-expressing human neuroblastoma cells. Animals were treated intravenously, once a week for 2 weeks (arrows), with 5 mg/kg of DXR, either free (free DXR) or encapsulated into HSYWLRS-targeted liposomes (HSYWLRS-SL[DXR]). CTR mice received HEPES-buffered saline. Tumor growth was monitored by BLI at day 20 (before treatment) and 40 (end of treatments) after tumor challenge. (**B**) Antitumor effects at the end of treatments; values are reported as fold increase in tumor volume at day 40 over day 20. *, $p < 0.05$: free DXR *vs*. CTR; **, $p < 0.01$: HSYWLRS-SL[DXR] *vs*. free DXR; ***, $p < 0.001$: HSYWLRS-SL[DXR] *vs*. CTR; (**C**) HSYWLRS-SL[DXR] show potentiated therapeutic efficacy. Survival: $p < 0.0025$: HSYWLRS-SL[DXR] *vs*. CTR and free DXR. From Cossu et al. [17]

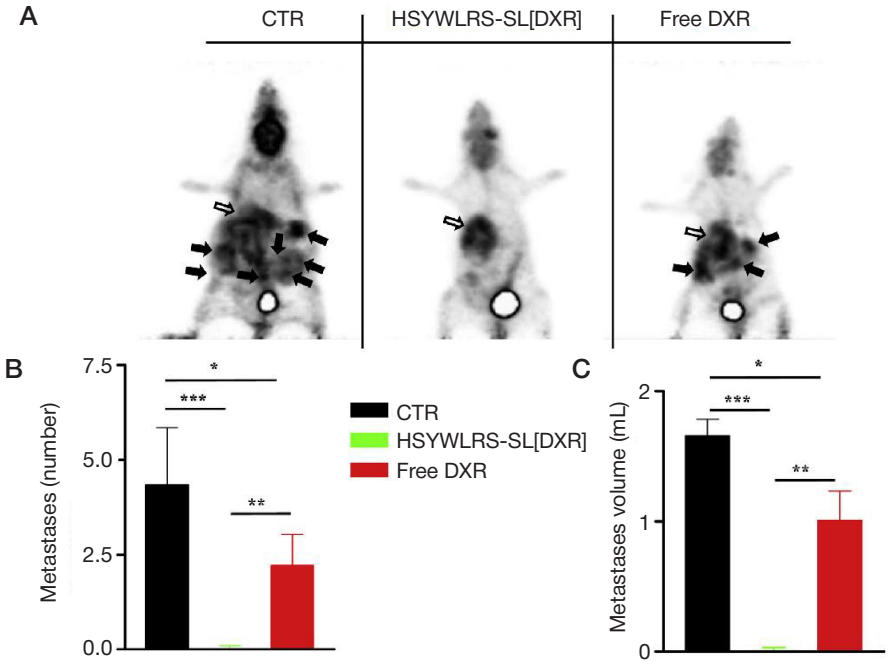

Fig. 7. Treatment with HSYWLRS-SL[DXR] inhibits secondary tumor spreading. Mice (4/CTR, 5/treatments) orthotopically implanted with luciferase-expressing human neuroblastoma cells were treated as reported in the legend of Figure 6 and tumor extension was evaluated by PET after 41 days (**A**). Glucose consumption maps (white arrows: primary tumor; black arrows: metastases). (**B**) Number and (**C**) volume of metastases following treatments. *, $p < 0.05$: free DXR *vs*. CTR; **, $p < 0.01$: HSYWLRS-SL[DXR] *vs*. free DXR; ***, $p < 0.001$: HSYWLRS-SL [DXR] *vs*. CTR

Together, these data support the development of the neuroblastoma-targeting peptide HSYWLRS as a powerful tool for therapeutic applications.

CONCLUSIONS

Early tumor diagnosis and efficient treatment (namely, a treatment that reaches max antitumor efficacy while sparing normal tissues) remain an open medical need. The advent of nanomedicine is delivering new tools that could revolutionize our approach to cancer monitoring and therapy, provided that we identify biomarkers with suitable properties. In fact, while the development of nanomaterials is rapidly expanding, we still need more selective targets to allow patient-tailored approaches. In this perspective, our recent work contributed a number of targets and targeting moieties that were validated preclinically and could be exploited to develop clinical tools.

References

1. Arap W, Pasqualini R, Montalti M, Petrizza L, Prodi L, Rampazzo E et al. Luminescent silica nanoparticles for cancer diagnosis. Curr Med Chem. 2013; 20 (17): 2195–211.
2. Bobo D, Robinson KJ, Islam J, Thurecht KJ, Corrie SR. Nanoparticle-based medicines: a review of FDA-approved materials and clinical trials to date. Pharm Res. 2016; 33 (10): 2373–87.
3. Caster JM, Patel AN, Zhang T, Wang A. Investigational nanomedicines in 2016: a review of nanotherapeutics currently undergoing clinical trials. Rev Nanomed Nanobiotechnol. 2017; 9 (1): e1456.
4. Marchiò S, Soster M, Cardaci S, Muratore A, Bartolini A, Barone V et al. A complex of alpha(6) integrin and E-cadherin drives liver metastasis of colorectal cancer cells through hepatic angiopoietin-like 6. EMBO Mol Med. 2012 Nov; 4 (11): 1156–75.
5. Soster M, Juris R, Bonacchi S, Genovese D, Montalti M, Rampazzo E et al. Targeted dual-color silica nanoparticles provide univocal identification of micrometastases in preclinical models of colorectal cancer. Int J Nanomed. 2012; (7): 4797–807.
6. Bonacchi S, Genovese D, Juris R, Montalti M, Prodi L, Rampazzo E et al. Luminescent chemosensors based on silica nanoparticles. Top Curr Chem. 2011; (300): 93–138.
7. Bonacchi S, Genovese D, Juris R, Montalti M, Prodi L, Rampazzo E et al. Luminescent silica nanoparticles: extending the frontiers of brightness. Angew Chem Int Ed Engl. 2011; 50 (18): 4056–66.
8. D'Hallewin MA, Kamuhabwa AR, Roskams T, De Witte PA, Baert L. Hypericin-based fluorescence diagnosis of bladder carcinoma. BJU Int. 2002; 89 (7): 760–3.
9. Miyashiro I, Miyoshi N, Hiratsuka M, Kishi K, Yamada T, Ohue M et al. Detection of sentinel node in gastric cancer surgery by indocyanine green fluorescence imaging: comparison with infrared imaging. Ann Surg Oncol. 2008; 15 (6): 1640–3.
10. van Dam GM, Themelis G, Crane LM, Harlaar NJ, Pleijhuis RG, Kelder W et al. Intraoperative tumor-specific fluorescence imaging in ovarian cancer by folate receptor-alpha targeting: first in-human results. Nat Med. 2011; 17 (10): 1315–9.
11. van der Poel HG, Buckle T, Brouwer OR, Valdes Olmos RA, van Leeuwen FW. Intraoperative laparoscopic fluorescence guidance to the sentinel lymph node in prostate cancer patients: clinical proof of concept of an integrated functional imaging approach using a multimodal tracer. Eur Urol. 2011; 60 (4): 826–33.
12. de Leeuw J, van der Beek N, Neugebauer WD, Bjerring P, Neumann HA. Fluorescence detection and diagnosis of non-melanoma skin cancer at an early stage. Lasers Surg Med. 2009; 41 (2): 96–103.
13. Atlamazoglou V, Yova D, Kavantzas N, Loukas S. Microscopical examination of the localisation patterns of two novel rhodamine derivatives in normal and neoplastic colonic mucosa. Lasers Med Sci. 2001; 16 (4): 253–9.
14. Marchiò S, Lahdenranta J, Schlingemann RO, Valdembri D, Wesseling P, Arap MA et al. Aminopeptidase A is a functional target in angiogenic blood vessels. Cancer Cell. 2004; 5 (2): 151–62.
15. Pasqualini R, Koivunen E, Kain R, Lahdenranta J, Sakamoto M, Stryhn A. Aminopeptidase N is a receptor for tumor-homing peptides and a target for inhibiting angiogenesis. Cancer Res. 2000; 60 (3): 722–7.
16. Loi M, Di Paolo D, Soster M, Brignole C, Bartolini A, Emionite L et al. Novel phage display-derived neuroblastoma-targeting peptides potentiate the effect of drug nanocarriers in preclinical settings. J Control Release. 2013; 170 (2): 233–41.
17. Cossu I, Bottoni G, Loi M, Emionite L, Bartolini A, Di Paolo D et al. Neuroblastoma-targeted nanocarriers improve drug delivery and penetration, delay tumor growth and abrogate metastatic diffusion. Biomaterials. 2015; (68): 89–99.
18. Loi M, Marchiò S, Becherini P, Di Paolo D, Soster M, Curnis F et al. Combined targeting of perivascular and endothelial tumor cells enhances anti-tumor efficacy of liposomal chemotherapy in neuroblastoma. J Control Release. 2010; 145 (1): 66–73.

Литература

1. Arap W, Pasqualini R, Montalti M, Petrizza L, Prodi L, Rampazzo E et al. Luminescent silica nanoparticles for cancer diagnosis. Curr Med Chem. 2013; 20 (17): 2195–211.
2. Bobo D, Robinson KJ, Islam J, Thurecht KJ, Corrie SR. Nanoparticle-based medicines: a review of FDA-approved materials and clinical trials to date. Pharm Res. 2016; 33 (10): 2373–87.
3. Caster JM, Patel AN, Zhang T, Wang A. Investigational nanomedicines in 2016: a review of nanotherapeutics currently undergoing clinical trials. Rev Nanomed Nanobiotechnol. 2017; 9 (1): e1456.
4. Marchiò S, Soster M, Cardaci S, Muratore A, Bartolini A, Barone V et al. A complex of alpha(6) integrin and E-cadherin drives liver metastasis of colorectal cancer cells through hepatic angiopoietin-like 6. EMBO Mol Med. 2012 Nov; 4 (11): 1156–75.
5. Soster M, Juris R, Bonacchi S, Genovese D, Montalti M, Rampazzo E et al. Targeted dual-color silica nanoparticles provide univocal identification of micrometastases in preclinical models of colorectal cancer. Int J Nanomed. 2012; (7): 4797–807.
6. Bonacchi S, Genovese D, Juris R, Montalti M, Prodi L, Rampazzo E et al. Luminescent chemosensors based on silica nanoparticles. Top Curr Chem. 2011; (300): 93–138.
7. Bonacchi S, Genovese D, Juris R, Montalti M, Prodi L, Rampazzo E et al. Luminescent silica nanoparticles: extending the frontiers of brightness. Angew Chem Int Ed Engl. 2011; 50 (18): 4056–66.
8. D'Hallewin MA, Kamuhabwa AR, Roskams T, De Witte PA, Baert L. Hypericin-based fluorescence diagnosis of bladder carcinoma. BJU Int. 2002; 89 (7): 760–3.
9. Miyashiro I, Miyoshi N, Hiratsuka M, Kishi K, Yamada T, Ohue M et al. Detection of sentinel node in gastric cancer surgery by indocyanine green fluorescence imaging: comparison with infrared imaging. Ann Surg Oncol. 2008; 15 (6): 1640–3.
10. van Dam GM, Themelis G, Crane LM, Harlaar NJ, Pleijhuis RG, Kelder W et al. Intraoperative tumor-specific fluorescence imaging

in ovarian cancer by folate receptor-alpha targeting: first in-human results. Nat Med. 2011; 17 (10): 1315–9.
11. van der Poel HG, Buckle T, Brouwer OR, Valdes Olmos RA, van Leeuwen FW. Intraoperative laparoscopic fluorescence guidance to the sentinel lymph node in prostate cancer patients: clinical proof of concept of an integrated functional imaging approach using a multimodal tracer. Eur Urol. 2011; 60 (4): 826–33.
12. de Leeuw J, van der Beek N, Neugebauer WD, Bjerring P, Neumann HA. Fluorescence detection and diagnosis of non-melanoma skin cancer at an early stage. Lasers Surg Med. 2009; 41 (2): 96–103.
13. Atlamazoglou V, Yova D, Kavantzas N, Loukas S. Microscopical examination of the localisation patterns of two novel rhodamine derivatives in normal and neoplastic colonic mucosa. Lasers Med Sci. 2001; 16 (4): 253–9.
14. Marchiò S, Lahdenranta J, Schlingemann RO, Valdembri D, Wesseling P, Arap MA et al. Aminopeptidase A is a functional target in angiogenic blood vessels. Cancer Cell. 2004; 5 (2): 151–62.
15. Pasqualini R, Koivunen E, Kain R, Lahdenranta J, Sakamoto M, Stryhn A. Aminopeptidase N is a receptor for tumor-homing peptides and a target for inhibiting angiogenesis. Cancer Res. 2000; 60 (3): 722–7.
16. Loi M, Di Paolo D, Soster M, Brignole C, Bartolini A, Emionite L et al. Novel phage display-derived neuroblastoma-targeting peptides potentiate the effect of drug nanocarriers in preclinical settings. J Control Release. 2013; 170 (2): 233–41.
17. Cossu I, Bottoni G, Loi M, Emionite L, Bartolini A, Di Paolo D et al. Neuroblastoma-targeted nanocarriers improve drug delivery and penetration, delay tumor growth and abrogate metastatic diffusion. Biomaterials. 2015; (68): 89–99.
18. Loi M, Marchiò S, Becherini P, Di Paolo D, Soster M, Curnis F et al. Combined targeting of perivascular and endothelial tumor cells enhances anti-tumor efficacy of liposomal chemotherapy in neuroblastoma. J Control Release. 2010; 145 (1): 66–73.

A NOVEL SPHEROID MODEL FOR PRECLINICAL INTERCELLULAR NANOPHOTOSENSITIZER-MEDIATED TUMOR STUDY

Maklygina YuS[1] ✉, Romanishkin ID[1], Ryabova AV[1], Yakavets IV[2,3], Bolotin L[2], Loschenov VB[1,4]

[1] Prokhorov General Physics Institute of the Russian Academy of Sciences, Moscow

[2] Centre de Recherche en Automatique de Nancy (CRAN), Université de Lorraine, France

[3] Belarusian State University, Minsk, Belarus

[4] National Research Nuclear University «MEPhI», Moscow

Aluminum phthalocyanine nanoparticles (NP AlPc) possess the features that make them a promising photosensitizer. In particular, AlPc NPs do not fluoresce in free nanoform, fluoresce weakly in normal tissue, strongly in tumors and very strongly in macrophages. Also, such particles fluoresce and become phototoxic when contacting certain biocomponents. The type of biocomponents that bind to AlPc NPS defines intensity, lifetime, and spectral distribution of the fluorescence. This study aimed to investigate the peculiarities of nanophotosensitizer capturing in 3D models of cell cultures. The data obtained demonstrate that AlPc NPs are captured by cells inside the spheroid in the course of the first hour, as the fluorescent signal's growth shows. Having analyzed the fluctuations of the fluorescence signal of AlPc NPs inside a spheroid, we have also discovered that the cellular 3D models are heterogeneous. Laser irradiation (two-photon excitation at λ = 780/390 nm) resulted in photobleaching of fluorescence, which is probably associated with AlPc NP deactivation. Thus, the created model comprised of a 3D cell culture and AlPc NPs provides a better insight into metabolic processes in cells than monolayer 2D cell cultures. Besides, the model allows to evaluate the photodynamic effect depending on phenotypic properties of various areas in the heterogeneous 3D-structure.

Keywords: aluminum phthalocyanine, nanoparticles, nanophotosensitizer, multicellular tumor spheroid, laser scanning microscopy

Funding: the study was supported by the Ministry of Education and Science of the Russian Federation (Agreement RFMEFI61618X0096 #14.616.21.0096 of February 12, 2018).

✉ **Correspondence should be addressed:** Yuliya S. Maklygina
Vavilova 38, Moscow, 119991; us.samsonova@physics.msu.ru

Received: 26.06.2018 **Accepted:** 23.10.2018

DOI: 10.24075/brsmu.2018.079

ИССЛЕДОВАНИЕ СВОЙСТВ ТРЕХМЕРНОЙ КЛЕТОЧНОЙ МОДЕЛИ ОПУХОЛИ С ИСПОЛЬЗОВАНИЕМ НАНОФОТОСЕНСИБИЛИЗАТОРА В КАЧЕСТВЕ НОВОЙ ПРЕДКЛИНИЧЕСКОЙ МОДЕЛИ

Ю. С. Маклыгина[1] ✉, И. Д. Романишкин[1], А. В. Рябова[1], И. В. Яковец[2,3], Л. Болотин[2], В. Б. Лощенов[1,4]

[1] Институт общей физики имени А. М. Прохорова Российской академии наук, Москва

[2] Научно-исследовательский центр автоматики университета Лотарингии, Нанси, Франция

[3] Белорусский государственный университет, Минск, Белоруссия

[4] Национальный исследовательский ядерный университет «МИФИ», Москва

Ввиду своих особенностей наночастицы (НЧ), состоящие из фталоцианина алюминия (НЧ AlPc), являются перспективным фотосенсибилизатором. НЧ AlPc не флуоресцируют в свободной наноформе, слабо флуоресцируют в нормальной ткани, сильно — в опухолях и очень сильно — в макрофагах. НЧ AlPc обладают уникальной особенностью приобретать способность к флуоресценции и фототоксичности в контакте с некоторыми биокомпонентами. При этом тип биокомпонентов, связывающихся с НЧ AlPc, влияет на интенсивность, время жизни и спектральное распределение флуоресценции. Целью работы было исследовать особенности захвата нанофотосенсибилизатора в 3D-моделях клеточных культур. Полученные данные демонстрируют захват НЧ AlPc клетками внутри сфероида в течение первого часа по росту флуоресцентного сигнала. Обнаружена гетерогенность клеточных 3D-моделей по анализу изменения сигнала флуоресценции НЧ AlPc внутри сфероида. В результате лазерного облучения (двухфотонного возбуждения с λ = 780/390 нм) наблюдали фотобличинг флуоресценции, который, вероятно, связан с деактивацией НЧ AlPc. Таким образом, созданная модель, состоящая из клеточной 3D-культуры с НЧ AlPc, позволяет лучше оценивать метаболитические процессы в клетках, чем монослойные клеточные 2D-культуры. Кроме того, модель позволяет оценивать фотодинамический эффект в зависимости от фенотипичных свойств различных областей в гетерогенной 3D-структуре.

Ключевые слова: фталоцианин алюминия, наночастицы, нанофотосенсибилизатор, многоклеточный опухолевый сфероид, лазерная сканирующая микроскопия

Финансирование: работа поддержана Министерством образования и науки Российской Федерации (соглашение RFMEFI61618X0096 № 14.616.21.0096 от 12.02.2018).

✉ **Для корреспонденции:** Юлия Сергеевна Маклыгина
ул. Вавилова, д. 38, г. Москва, 119991; us.samsonova@physics.msu.ru

Статья получена: 26.06.2018 **Статья принята к печати:** 23.10.2018

DOI: 10.24075/vrgmu.2018.079

Nanoparticles (NPs), which are based on molecular nanocrystals of photosensitizer (PS), are promising agents for the fluorescence diagnostics (FD) and treatment by the photodynamic therapy (PDT). Aluminium phthalocyanine (AlPc) nanocrystals have an advantage over the molecular PS used in clinic settings due to the significantly higher accumulation selectivity of nanoscale materials [1–4]. Moreover, they are able to fluoresce only in monomeric form upon the interaction of nanocrystals with biological structures, hereby providing appropriate FD detection efficiency [1, 2]. The type of interaction, the intensity, the lifetime and the spectrum of fluorescence depends on phenotype of the interacting cells. Fluorescence intensity of AlPc NPs in pathological tissue (inflammation, malignancy) significantly exceeds that in normal tissue [1, 2]. Moreover, AlPc NPs can be considered as theranostic probes providing both fluorescence for FD and photosensitizing activity for PDT treatment.

The *in vitro* screening of novel anti-cancer agents, particularly PSs, is mainly relied on photocytotoxicity assays using established cancer cell lines. Conventional two-dimensional (2D) 2D cell cultures exhibit a rapid, uncontrolled growth phenotype and are not able to mimic the complexity and heterogeneity of *in vivo* tumors. Evidently, *in vivo* tumors grow in a three-dimensional conformation with a specific organization and architecture that a 2D monolayer cell culture cannot reproduce [5–7]. Three-dimensional (3D) cell cultures are considered as a more accurate and reproducible model for performing *in vitro* drug screening. This model displays several features of *in vivo* tumor tissues such as presence of extracellular matrix, intercellular interaction, hypoxia, drug penetration and resistance [8–10]. Therefore, *in vitro* spheroid model is an intermediate stage between conventional 2D *in vitro* testing and animal models. The sphe [11–13].

Thereby, we have chosen 3D multicellular spheroids as a model to study accumulation, distribution and PDT efficiency of AlPc NPs in HeLa cells.

METHODS

Multicellular spheroids were initiated by seeding 10^4 HeLa cells into 96-well plate previously coated with 1% Agarose. Spheroid culture medium was changed every 2–3 days. When spheroids reached 140 ± 20 μm in diameter after 7 days, they were used for experiments. In this study, aluminium phthalocyanine nanoparticles (AlPc NPs, d ~ 100 nm, c = 10 μg/ml) were used as the PS. The investigations of AlPc fluorescence after different incubation intervals were performed using laser scanning confocal microscopy. For microscopy the spheroids were finally washed twice with pre-warmed phosphate buffered saline (PBS). The images were acquired with laser scanning microscope LSM-710-NLO (Zeiss; Germany). The 20× Plan-Apochromat objective with numerical aperture (NA) of 1.4 was used. The novel PS Aluminum phthalocyanine (AlPc) (synthesized by Organic Intermediates & Dyes Institute (NIOPIK), Russia) was prepeared and studied using the spheroid model. The polycrystalline powder was added to distilled water to a concentration of 1 mg/ml. The resulting suspension was dispersed in Bandelin SONOPLUS HD2070 ultrasonic homogenizer with KE76 attachment (20 kHz, the amplitude of 165 microns) [2]. Using Photocor Complex (Russia) multi-angle spectrometer of the dynamic light scattering, allowing obtaining the nanoparticles distribution by size via the analysis of correlation function of the scattered light intensity fluctuations, it was found that the average particle diameter in the aqueous colloid was 100–150 nm. AlPc colloid (c = 10 μg/ml) was added to the medium of the spheroid model to mimic conditions of tumor cells interaction with PS NPs. The main AlPc NPs feature is the photoactivation ability. The primary AlPc colloid did not luminesce upon the laser excitation into the absorption band (at the wavelengths 633 nm and 780 nm by two-photon ex.) i.e. the PS nanocrystals in a free form showed no photoactivity. So, the nanoparticles colloid of AlPc was not initially photoactive and did not display fluorescent properties. However, during interaction of AlPc NPs with cells, the NPs are involving into metabolic cells processes and become photoactive (λ_{fl} ~ 670 nm at the excitation λ_{ex} ~ 633 nm and 780 nm by two-photon ex.).

Thus, the experiment protocol consisted of the following steps (Fig. 1.):

1) At the beginning of experiments, 10 spheroids have been transferred to separate Petri dish. After that the AlPc NPs colloid was added to a set of 10 spheroids at the concentration 10 μg/ml each. PS incubation was performed at 37 °C for 15 min in the dark.

2) During futher incubation the cells autofluorescence was excited with 488 nm laser and simultaneously the AlPc NPs fluorescence was excited with 633 nm laser under the laser scanning microscope. After 1 hour of AlPs NPs accumulation the fluorescence signal stopped rising.

3) After that, the spheroids were washed twice with PBS and directly observed on an upright fluorescence microscope. Fluorescence images were recorded using 20× objective from the spheroid surface. After PS NPs interaction with biocomponents the NPs photoactivity was sufficient for the FD and PDT. Therefore, the detected interest zones were exposed to laser radiation with wavelength 780/390 nm (by two-photon excitation) after analysis of PS accumulation.

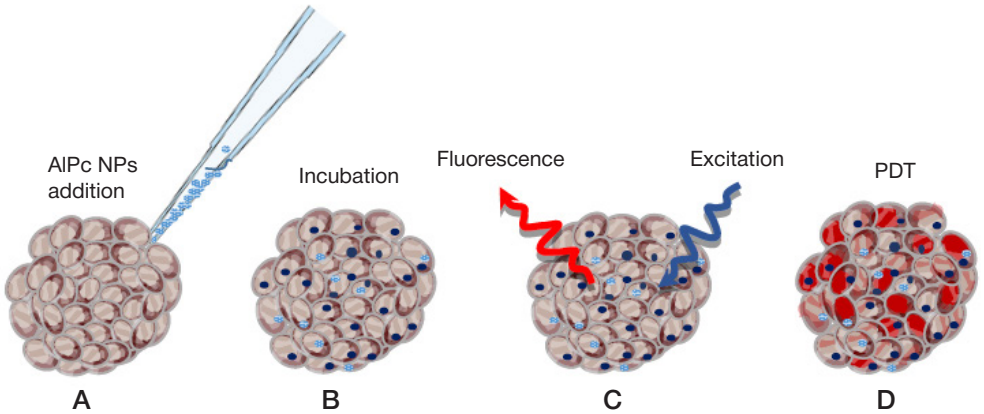

Fig. 1. The stepwise scheme of experiment with spheroid model and AlPc NPs

4) Laser irradiations were performed at 780/390 nm (by two-photon excitation). The irradiation times were adapted for each irradiation. The assessement of photodynamic effect was realized analyzing the fluorescent signal after staining with acridine orange (for healthy cells detection — green; AO, MolecularProbes®) and ethidium bromide (for dead cells detection — red; EB, MolecularProbes®). For staining, the spheroids in PBS, previously washed from the culture medium, were incubated in the presence of working solution of dyes for 5 minutes. Stained spheroids from the 96-well plates for *in vitro* culture have been transferred to Petri dishes with a 0.17 mm glasse's thick in PBS solution. AO/EB fluorescence signals distribution was studied using confocal microscopy. Excitation of fluorescent AO was performed with a 488 nm laser, fluorescence was recorded in the range of 495–545 nm. Excitation of fluorescent EB was performed with a 561 nm laser, fluorescence was recorded in the range of 580–690 nm. As a result, fluorescence images of AO (green) and EB (red) were obtained in the transmitted light mode. Thus, this stepwise approach enabled mimicing the conditions of tumor cells interaction with PS NPs at the first hour and the processes of FD and PDT with AlPc NPs *in vivo*.

RESULTS

AlPc NPs uptake in spheroids was evaluated at different times during 1 hour. An intense accumulation was observed during the first 30 minutes (Fig. 2 A–C). After 40 minutes of incubation the fluorescence signal reached a plateau without considerable further changes (Fig. 2 D–F). AlPc NPs fluorescence flaring up visualization in space and time allowed tracking of PS distribution. It was observed that after first 15 minutes AlPc NPs were accumulated in the peculiar regions at the periphery. Peripherical cells of spheroids had access to the NPs and could be primarly involved into endocytosis. It needed at least 15 minutes of incubation for the first uptake regions to be separated into irregularly shaped areas. Over the time these areas have rapidly grown directionlessly into the spheroid core (Fig. 2 C, D). After that, the nominal regions have shrunk into the single zone with minimal NPs uptake in the center (Fig. 2 E). The time and spatial dynamic of AlPc NPs uptake described above could be explained by the heterogeneity of cells in 3D model in temrs of different metabolic processes and phenotypes. Otherwise, the AlPc NPs uptake would have been observed as uniform at the periphery and slightly decreasing towards the spheroid core concentrically.

The numerical estimation of PS uptake in various areas was obtained by recording fluorescence spectra (Fig. 3). Before starting the analysis it is worth introducing the equivalent diameter, needed in the presence of a non-perfect sphericity, and defined as the diameter of a circle with 150 μm, corresponding to the average spheroid's size and having the same area as the spheroid section being imaged. Thus, the total fluorescent signal from the single area was digitized and divided into the auto- and AlPc NPs fluorescent contributions (Fig. 3 A, B). Autofluorescence signal was in the spectral range of 430–630 nm, excited by the λ_{ex} ~ 488 nm. AlPc NPs fluorescence maximum was about 670 nm, excited by the λ_{ex} ~ 633 nm (Fig. 3). Analysis of spectra from the concentric regions had shown that the AlPc NPs uptake decreased with the autofluorescence increasing from the periphery to the center of spheroid (Fig. 3 C).

At the same time the PS NPs uptake distribution was represented by the spheroid's sections of 4 projections to simplify visual perception, considering PS NPs fluorescence signal alone (Fig. 4). This also demonstrates the maximum of PS uptake in the periphery with local minimum in the center.

DISCUSSION

The penetration ability and phototoxicity of AlPc NPs was tested by the confocal laser scanning microscopy. Endocytosis was assumed to be the kind of uptake of NPs. The NPs penetration into the depth of the spheroid was observed over the first hour. However, under the assumption that the multicellular 3D model is homogeneous, NPs should be able to penetrate deep

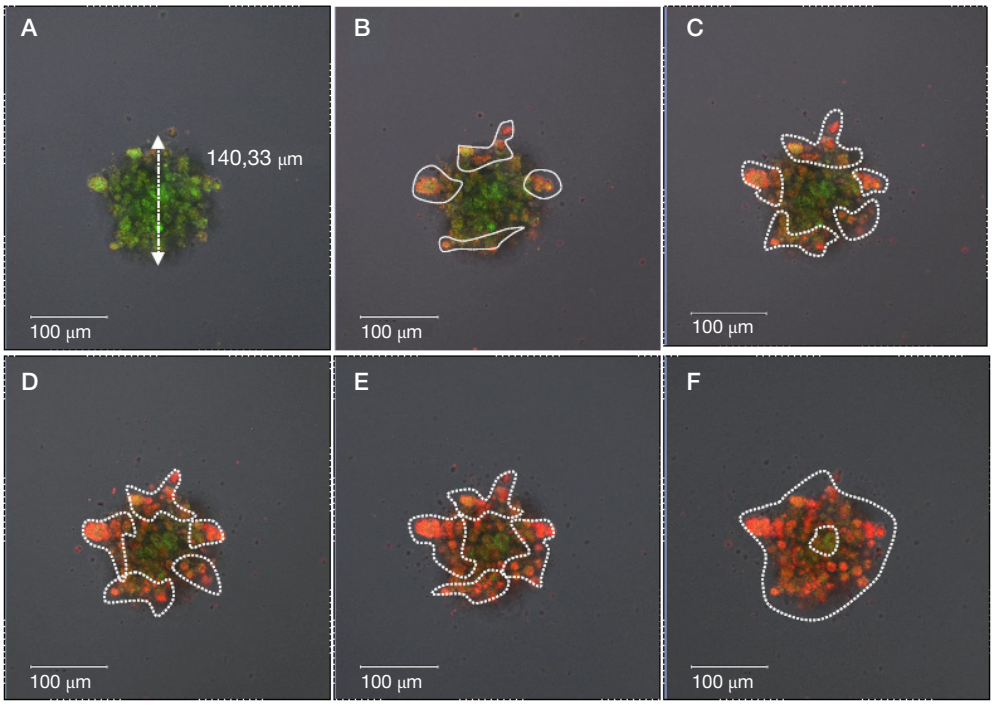

Fig. 2. Image of AlPc NP fluorescence flaring up over the time. Autofluorescence (green) excitation at λ_{ex} ~ 488 nm, AlPc NPs fluorescence (red) excitation at λ_{ex} ~ 633 nm: 15 min (**A**); 20 min (**B**); 30 min (**C**); 40 min (**D**); 50 min (**E**); 1 h (**F**)

into the spheroids with a uniform volume distribution, which was not observed. So, likely, the uptake diversity in different spheroid's areas is due to the heterogeneity of spheroid model containing the cells of different phenotypes. This assumption is confirmed by the variety of the phototoxicity effect in the different spheroid's regions, depending on the presense of oxygen.

Therefore, the tumor model oxygenation was estimated indirectly. In this way, this model for investigating the uptake and photoinduced toxicity of AlPc NPs closely resembles *in vivo* tumors [14–15].

This result could be explained by the difference in the cells metabolic processes. Indeed, previous studies reported that an apoptotic core begins forming in spheroids of approximately 150–200 μm in diameter [16]. Similar to *in vivo* tumors, multicellular spheroids include hypoxic and apoptotic/necrotic areas, developing as a consequence of the formation of oxygen and nutrient gradients. Remarkably, in spheroids, hypoxia occurs gradually over time, with the increase of the spheroid size [17]. Thus, the AlPc NPs uptake gradient could be explained by nutrient gradients and phenotype differences in the cells of 3D model. The degree of the molecular oxygen avalaibility in the different regions can be estimated by the rate of fluorescence signal decrease during the photodynamic irradiation upon the condition that phototoxicity depends on the presence of molecular oxygen. Phototreatment induces the energy transfer as a consecuence of PS fluorescence parching and also a production of active oxygen forms leading to cell death. The areas with a strong photodynamic effect were identified by a comparison of AlPc NPs fluorescence

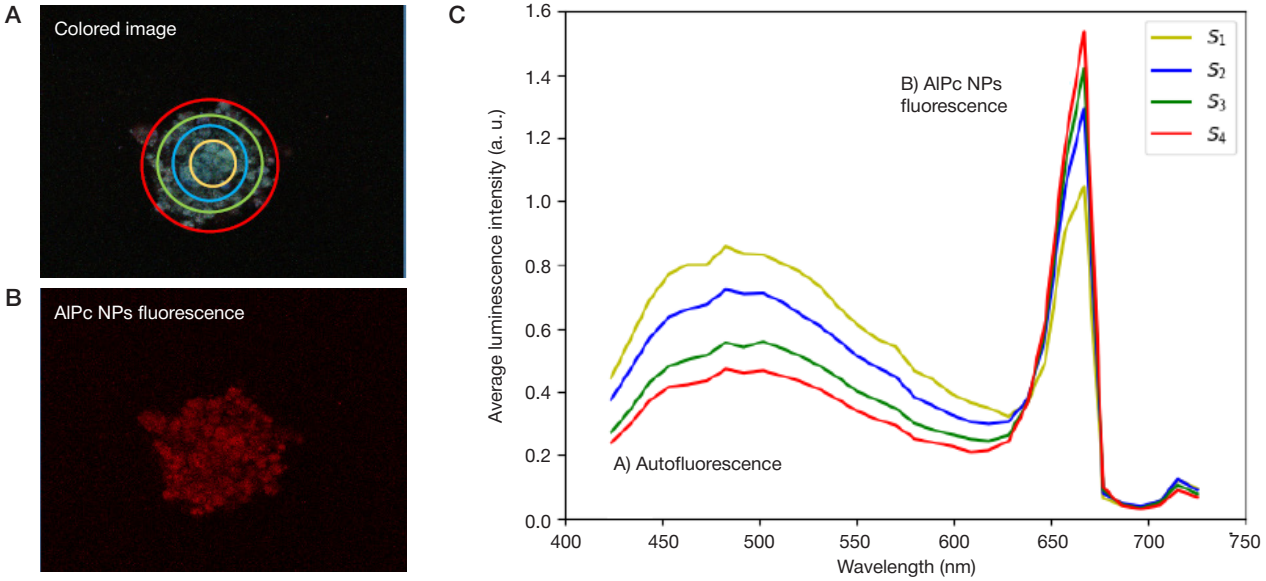

Fig. 3. The imaging of digital separation signals of (**A**) spectral image converted to RGB colors and (**B**) AlPc NPs fluorescence distribution. **C**. The fluorescence spectra recorded with the curve color corresponding to the highlighted areas. The spectra are normalized on each area's surface

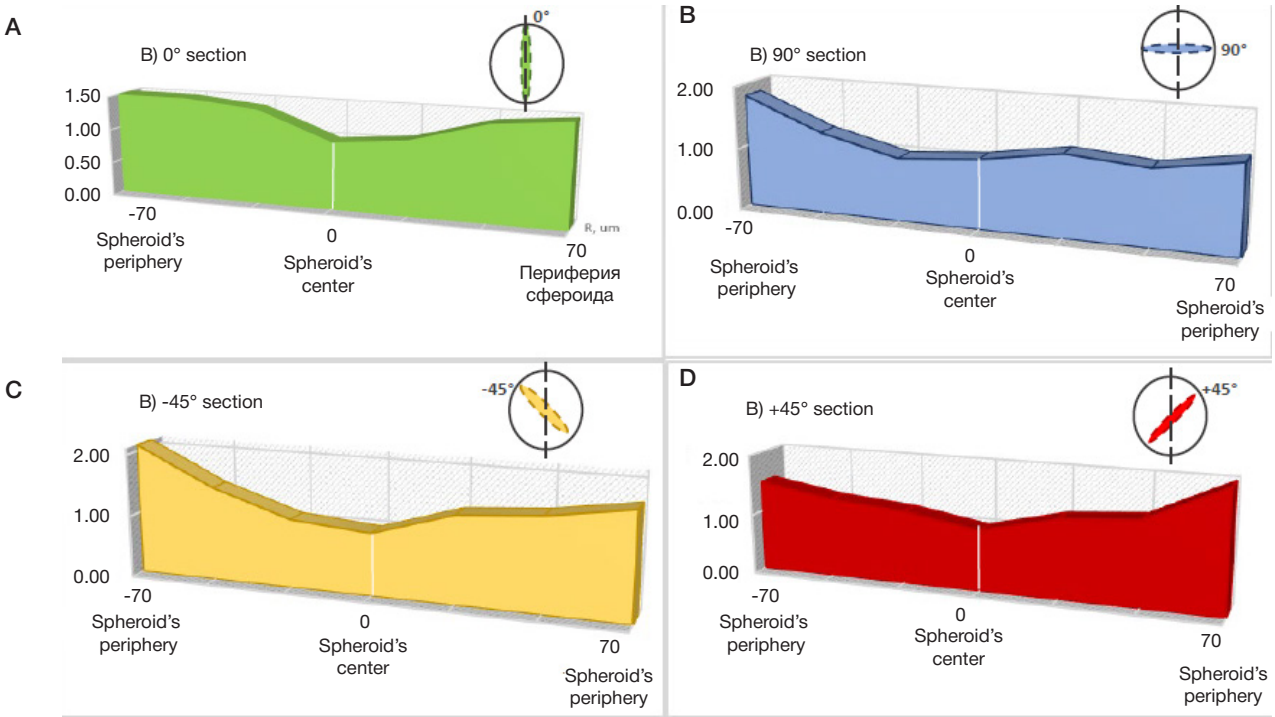

Fig. 4. The graphic representation of AlPc NPs uptake in the 4 spheroid sections: (**A**) 0°; (**B**) 90°; (**C**) 45°; (**D**) –45°. It was calculated only from the PS fluorescence λ_{fl} ~ 670 nm (λ_{ex} ~ 633 nm), excluding cell's autofluorescnence

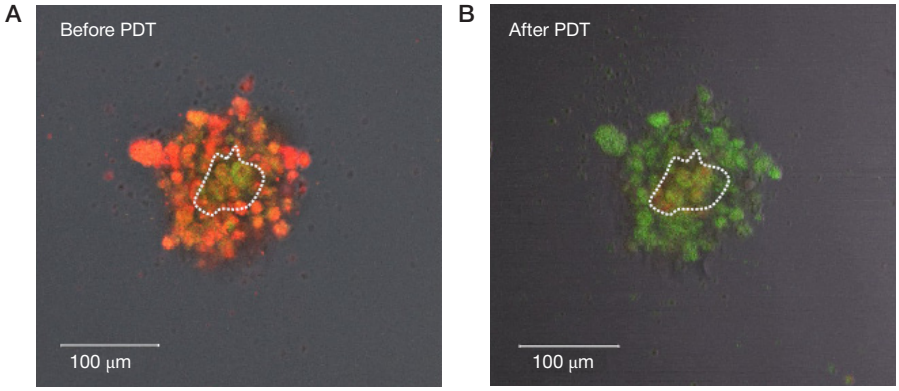

Fig. 5. Comparison of AlPc fluorescence before PDT (**A**) vs after PDT (**B**). Autofluorescence excitation λ ~ 488 nm, AlPc NPs fluorescence excitation λ ~ 633 nm.

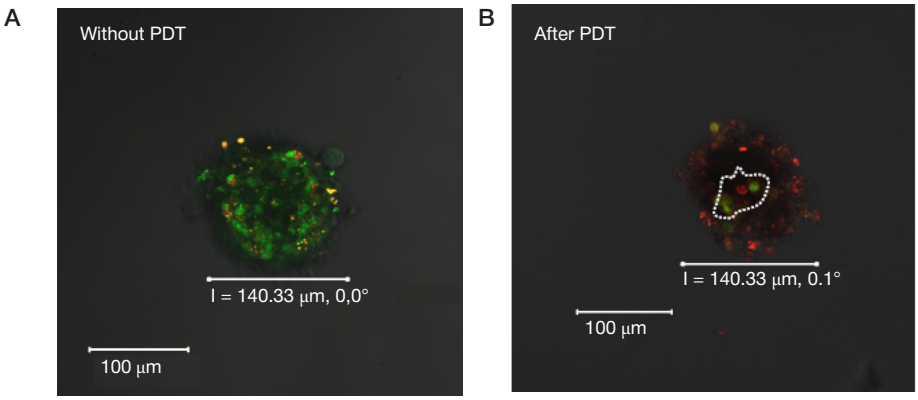

Fig. 6. Cell viability analysis after PDT, stained with acridine orange (AO) (green — living cells) (**A**) and propidium iodide (PI) (red — dead cells) (**B**). Excitation of AO fluorescence with 488 nm laser, excitation of 561 nm laser

before and after PDT. Analysing spheroid regions, the residual PS fluorescence signal was observed only in the core, while elsewhere the PS fluorescence was absent (Fig. 5). It can be related to the heterogeneous structure of spheroid with the various accessibility of deep layers to irradiation light and with different cells proliferation activity. In particular, this means that molecular oxygen is absent in the cental spheroid area, leading to limited photodynamic effect with partial fluorescence decline. Thus, the oxygen gradient in spheroids could be indirectly estimated analysing PS phototoxicity effects. That is also inherent to *in vivo* features of tumors such as hypoxia.

Finally, the photoxicity was estimated by analysing the spheroid cells viability using the living and dead cells staining. It was shown in comparison with staining of primary spheroid with green marked living cells (Fig. 6 A). This evidence consists in the detection of green marking living cells only in the spheroid's core after PDT (Fig. 6 B). At the same time red marked dead cells constitute the main bulk (Fig. 6 B). It should be noted that the distribution of standard dye is homogeneous due the staining of cells viability only.

High PS accumulation and penetration are the most important characteristics responsible for anti-tumor efficiency. These characteristics must be carefully considered for novel PS screening. Furthermore, the main factor of incomplete tumor eradication is the PS heterogeneous distribution into the tumor. That is why the complex spatial and temporal distribution processes in tissues are especially important. The spheroid models allow simulating the penetration and intratumor transport of photosensitizer nanoparticles. Nowadays numerous nanoparticles have been studied for efficient and targeted PS delivery. The negative feature of some nanocarriers is the limited penetration, but presumably the size of nanoparticles matters significantly [18–19]. Summarazing the research results, the AlPc NPs are the promising PS with high phototoxicity and, more importantly, AlPc NPs are the probe for the inderect analysis of oxygen distribution, phenotype and metabolic cell processes. At the same time by the AlPc fluorescence estimation it was observed that the 3D multicellular model possesses primary *in vivo* features of tumors such as intercellular interaction, heterogeneity, hypoxia, oxygen and nutrient gradients. Thus, we suggest that *in vitro* spheroid model is a good predictive platform for studying the nanosized drugs, including the PS, prior to the animal models.

CONCLUSION

Our investigation clearly demonstrated an advantage of using AlPc nanoparticles as photosensitizer and multifunctional fluorescence probe. AlPc NPs have the sufficient capacity to accumulate, diffuse and penetrate into the spheroids. Microscopy techniques demonstrated that besides sufficient accumulation, AlPc NPs have the dynamic photoactivity depending on the bioenvironment. Particularly, AlPc NPs were used to evaluate the heterogeneity and to indirectly estimate the oxygen concentration, phenotype and metabolic cell processes. These are the most important parameters for the specific local nanophototheranostics. Received results should be useful for the other sighting studies of cell models, for example using the co-culture spheroids, which are taken into the account the immune response [20–24].

References

1. Breymayer J, Rück A, Ryabova AV, Loschenov VB, Steiner RW. Fluorescence Investigation of the Effect of Monocytes/ Macrophages and Skin Cells on Aluminium Phthalocyanine Nanoparticles. Journal Photodiagnosis and Photodynamic Therapy. 2014; 11(3): 380–90.
2. Vasilchenko SYu, Volkova AI, Ryabova AV, Loschenov VB, Konov VI, Mamedov AA et al. Application of aluminum phthalocyanine nanoparticles for fluorescent diagnostics in dentistry and skin autotransplantology. J Biophoton. 2010; 3 (5–6): 336–46.
3. Chiarante N, García Vior MC, Awruch J, Marino J, Roguin LP. Phototoxic action of a zinc (II) phthalocyanine encapsulated into poloxamine polymeric micelles in 2D and 3D colon carcinoma cell cultures. J Photochem Photobiol B. 2017; 170: 140–51.
4. Waite CL, Roth CM. Nanoscale drug delivery systems for enhanced drug penetration into solid tumors: current progress and opportunities. Crit Rev Biomed Eng. 2012; 40: 21–41.
5. Kumari P, Jain S, Ghosh B, Zorin V, Biswas S. Polylactide-Based Block Copolymeric Micelles Loaded with Chlorin e6 for Photodynamic Therapy: In Vitro Evaluation in Monolayer and 3D Spheroid Models. Mol Pharm. 2017 Nov 6; 14 (11): 3789–800.
6. Patel NR, Aryasomayajula B, Abouzeid AH, Torchilin VP. Cancer cell spheroids for screening of chemotherapeutics and drug-delivery systems. Ther Deliv. 2015; (6): 509–20.
7. Khanna S, Bhatt AN, Dwarakanath BS. Chapter 11 — multicellular spheroid: 3-D tissue culture model for cancer research A2. In: Ashish S Verma, Singh A, editors. Animal Biotechnology. San Diego: Academic Press, 2014; 195–210.
8. Kimlin LC, Casagrande G, Virador VMю In vitro three-dimensional (3D) models in cancer research: an update. Mol Carcinog. 2013; (52): 167–82.
9. Baker BM, Chen CS. Deconstructing the third dimension: how 3D culture microenvironments alter cellular cues. J Cell Sci. 2012; (125): 3015–24.
10. Wartenberg M et al. Regulation of the multidrug resistance transporter P-glycoprotein in multicellular tumor spheroids by hypoxia-inducible factor (HIF-1) and reactive oxygen species. FASEB J. 2003; (17): 503–5.
11. Evans CL. Three-dimensional in vitro cancer spheroid models for photodynamic therapy: strengths and opportunities. Front Phys. 2015; 3 (15): 1–7.
12. Yakavets I, Yankovsky I, Millard M, Lamy L, Lassalle HP, Wiehe A et al. The alteration of temoporfin distribution in multicellular tumor spheroids by β-cyclodextrins. Int J Pharm. 2017; 529 (1–2): 568–75.
13. Ricketts KP, Cheema U, Nyga A, Castoldi A, Guazzoni C, Magdeldin T et al. A 3D in vitro cancer model as a platform for nanoparticle uptake and imaging investigations. 2014; 10 (19): 3954–61.
14. Kapinus VN, Kaplan MA, Yaroslavtseva-Isayeva EV, Spichenkova IS. Photodynamic therapy for head and neck basal cell skin cancer with additional interstitial laser irradiation. Biomedical Photonics. 2017; 6 (4): 20–6.
15. Abraham JA, Golubnitschaja O. Time for paradigm change in management of hepatocellular carcinoma: is a personalized approach on the horizon? Per Med. 2016; 13 (5): 455–67.
16. Hirschhaeuser F, Menne H, Dittfeld C, West J, Mueller-Klieser W, Kunz-Schughart LA. Multicellular tumor spheroids: an underestimated tool is catching up again. J Biotechnol. 2010; (148): 3–15.
17. Josef LB, Boyle RW. Unique diagnostic and therapeutic roles of porphyrins and phthalocyanines in photodynamic therapy, imaging and theranostics. Theranostics. 2012; (2): 916–66.
18. Franken NAP, Rodermond HM, Stap J, Haveman J, van Bree C. Clonogenic assay of cells in vitro. Nat Protoc. 2006; (1): 2315–9.
19. Dreher MR, Liu W, Michelich CR, Dewhirst MW, Yuan F, Chilkoti A. Tumor vascular permeability, accumulation, and penetration of macromolecular drug carriers. J Natl Cancer Inst. 2006; (98): 335–44.
20. Dobiasova M, Urbanova Z, Samanek M Relations between particle size of HDL and LDL lipoproteins and cholesterol esterification rate. Physiol Res Acad Sci Bohemoslov. 2005; (54): 159–65.
21. Kitamura T, Qian BZ, Pollard JW. Immune cell promotion of metastasis. Nat Rev Immunol. 2015; 15 (2): 73–86.
22. Kumar V, Patel S, Tcyganov E, Gabrilovich DI. The Nature of Myeloid-Derived Suppressor Cells in the Tumor Microenvironment. Trends Immunol. 2016; 37 (3): 208–20.
23. Long L, Yin M, Min W. 3D Co-culture System of Tumor-associated Macrophages and Ovarian Cancer. Cells Bio Protoc. 2018; 8 (8).
24. Sherman H, Gitschier HJ, Rossi AE. A novel three-dimensional immune oncology model for high-throughput testing of tumoricidal activity. Front Immunol. 2018 Apr 23; (9): 857.

Литература

1. Breymayer J, Rück A, Ryabova AV, Loschenov VB, Steiner RW. Fluorescence Investigation of the Effect of Monocytes/ Macrophages and Skin Cells on Aluminium Phthalocyanine Nanoparticles. Journal Photodiagnosis and Photodynamic Therapy. 2014; 11(3): 380–90.
2. Vasilchenko SYu, Volkova AI, Ryabova AV, Loschenov VB, Konov VI, Mamedov AA et al. Application of aluminum phthalocyanine nanoparticles for fluorescent diagnostics in dentistry and skin autotransplantology. J Biophoton. 2010; 3 (5–6): 336–46.
3. Chiarante N, García Vior MC, Awruch J, Marino J, Roguin LP. Phototoxic action of a zinc (II) phthalocyanine encapsulated into poloxamine polymeric micelles in 2D and 3D colon carcinoma cell cultures. J Photochem Photobiol B. 2017; 170: 140–51.
4. Waite CL, Roth CM. Nanoscale drug delivery systems for enhanced drug penetration into solid tumors: current progress and opportunities. Crit Rev Biomed Eng. 2012; 40: 21–41.
5. Kumari P, Jain S, Ghosh B, Zorin V, Biswas S. Polylactide-Based Block Copolymeric Micelles Loaded with Chlorin e6 for Photodynamic Therapy: In Vitro Evaluation in Monolayer and 3D Spheroid Models. Mol Pharm. 2017 Nov 6; 14 (11): 3789–800.
6. Patel NR, Aryasomayajula B, Abouzeid AH, Torchilin VP. Cancer cell spheroids for screening of chemotherapeutics and drug-delivery systems. Ther Deliv. 2015; (6): 509–20.
7. Khanna S, Bhatt AN, Dwarakanath BS. Chapter 11 — multicellular spheroid: 3-D tissue culture model for cancer research A2. In: Ashish S Verma, Singh A, editors. Animal Biotechnology. San Diego: Academic Press, 2014; 195–210.
8. Kimlin LC, Casagrande G, Virador VMю In vitro three-dimensional (3D) models in cancer research: an update. Mol Carcinog. 2013; (52): 167–82.
9. Baker BM, Chen CS. Deconstructing the third dimension: how 3D culture microenvironments alter cellular cues. J Cell Sci. 2012; (125): 3015–24.
10. Wartenberg M et al. Regulation of the multidrug resistance transporter P-glycoprotein in multicellular tumor spheroids by hypoxia-inducible factor (HIF-1) and reactive oxygen species. FASEB J. 2003; (17): 503–5.
11. Evans CL. Three-dimensional in vitro cancer spheroid models for photodynamic therapy: strengths and opportunities. Front Phys. 2015; 3 (15): 1–7.
12. Yakavets I, Yankovsky I, Millard M, Lamy L, Lassalle HP, Wiehe A et al. The alteration of temoporfin distribution in multicellular tumor spheroids by β-cyclodextrins. Int J Pharm. 2017; 529 (1–2): 568–75.
13. Ricketts KP, Cheema U, Nyga A, Castoldi A, Guazzoni C, Magdeldin T et al. A 3D in vitro cancer model as a platform for nanoparticle uptake and imaging investigations. 2014; 10 (19): 3954–61.
14. Kapinus VN, Kaplan MA, Yaroslavtseva-Isayeva EV, Spichenkova IS. Photodynamic therapy for head and neck basal cell skin cancer

with additional interstitial laser irradiation. Biomedical Photonics. 2017; 6 (4): 20–6.
15. Abraham JA, Golubnitschaja O. Time for paradigm change in management of hepatocellular carcinoma: is a personalized approach on the horizon? Per Med. 2016; 13 (5): 455–67.
16. Hirschhaeuser F, Menne H, Dittfeld C, West J, Mueller-Klieser W, Kunz-Schughart LA. Multicellular tumor spheroids: an underestimated tool is catching up again. J Biotechnol. 2010; (148): 3–15.
17. Josef LB, Boyle RW. Unique diagnostic and therapeutic roles of porphyrins and phthalocyanines in photodynamic therapy, imaging and theranostics. Theranostics. 2012; (2): 916–66.
18. Franken NAP, Rodermond HM, Stap J, Haveman J, van Bree C. Clonogenic assay of cells in vitro. Nat Protoc. 2006; (1): 2315–9.
19. Dreher MR, Liu W, Michelich CR, Dewhirst MW, Yuan F, Chilkoti A. Tumor vascular permeability, accumulation, and penetration of macromolecular drug carriers. J Natl Cancer Inst. 2006; (98): 335–44.
20. Dobiasova M, Urbanova Z, Samanek M Relations between particle size of HDL and LDL lipoproteins and cholesterol esterification rate. Physiol Res Acad Sci Bohemoslov. 2005; (54): 159–65.
21. Kitamura T, Qian BZ, Pollard JW. Immune cell promotion of metastasis. Nat Rev Immunol. 2015; 15 (2): 73–86.
22. Kumar V, Patel S, Tcyganov E, Gabrilovich DI. The Nature of Myeloid-Derived Suppressor Cells in the Tumor Microenvironment. Trends Immunol. 2016; 37 (3): 208–20.
23. Long L, Yin M, Min W. 3D Co-culture System of Tumor-associated Macrophages and Ovarian Cancer. Cells Bio Protoc. 2018; 8 (8).
24. Sherman H, Gitschier HJ, Rossi AE. A novel three-dimensional immune oncology model for high-throughput testing of tumoricidal activity. Front Immunol. 2018 Apr 23; (9): 857.

MAGNETIC RESONANCE IMAGING FOR PREDICTING PERSONALIZED ANTITUMOR NANOMEDICINE EFFICACY

Naumenko VA[1] ✉, Garanina AS[1,2], Vodopyanov SS[1], Nikitin AA[1,2], Prelovskaya AO[1], Demikhov EI[4], Abakumov MA[1,3], Majouga AG[1,2,5], Chekhonin VP[3]

[1] Biomedical Nanomaterials Laboratory, National University of Science and Technology MISIS, Moscow
[2] Tissue-specific Ligands Research Laboratory, Faculty of Chemistry, Lomonosov Moscow State University, Moscow
[3] Pirogov Russian National Research Medical University, Moscow
[4] Lebedev Physical Institute, Russian Academy of Sciences, Moscow
[5] Mendeleyev University of Chemical Technology of Russia, Moscow

Magnetic resonance imaging (MRI) is widely used to diagnose cancer and study patterns and effectiveness of nanocarrier delivery of anticancer drugs. Accumulation of nanoparticles in a tumor varies widely in a given population; it is also highly dependent on biological factors, which remain largely unstudied. In recent years, there was developed a hypothesis that suggests that MRI can be used to predict response to nanoformulations-based anticancer therapy since it provides data on accumulation of MRI contrast agents in the tumor. Pilot tests prove feasibility of the approach based on this hypothesis, however, there is a number of conceptual and technical problems and limitations that hamper its introduction into the routine clinical practice. This article discusses the advantages and disadvantages of methods to stratify tumors by level of nanoparticles accumulation. Further research in this field would facilitate development of effective algorithms of personalized treatment with anticancer drugs delivered by nanoparticles.

Keywords: anticancer therapy, magnetic resonance imaging, nanoparticles, personalized medicine

Funding: the study was financially supported by the Ministry of Education and Science of the Russian Federation under the Federal Targeted Programme for Research and Development in Priority Areas of Development of the Russian Scientific and Technological Complex for 2014–2020, Agreement #14.575.21.0147 of 27.09.2017 (Agreement ID RFMEFI57517X0147).

✉ **Correspondence should be addressed:** Victor A. Naumenko
Leninsky 4, Moscow, 119049; naumenko.vict@gmail.com

Received: 30.08.2018 **Accepted:** 25.09.2018

DOI: 10.24075/brsmu.2018.086

МАГНИТНО-РЕЗОНАНСНАЯ ТОМОГРАФИЯ ДЛЯ ПЕРСОНАЛИЗИРОВАННОЙ ОЦЕНКИ И ПРОГНОЗИРОВАНИЯ ЭФФЕКТИВНОСТИ ДОСТАВКИ НАНОФОРМУЛЯЦИЙ ПРОТИВООПУХОЛЕВЫХ ПРЕПАРАТОВ

В. А. Науменко[1] ✉, А. С. Гаранина[1,2], С. С. Водопьянов[1], А. А. Никитин[1,2], А. О. Преловская[1], Е. И. Демихов[4], М. А. Абакумов[1,3], А. Г. Мажуга[1,2,5], В. П. Чехонин[3]

[1] Лаборатория биомедицинских наноматериалов, Национальный исследовательский технологический университет «МИСиС», Москва
[2] Научно-исследовательская лаборатория тканеспецифических лигандов, Химический факультет, Московский государственный университет имени М. В. Ломоносова, Москва
[3] Российский национальный исследовательский медицинский университет имени Н. И. Пирогова, Москва
[4] Физический институт имени П. Н. Лебедева Российской академии наук, Москва
[5] Российский химико-технологический университет имени Д. И. Менделеева, Москва

Магнитно-резонансная томография (МРТ) широко используется для диагностики онкологических заболеваний, а также для исследования доставки препаратов на магнитных наноносителях. Накопление наночастиц в опухоли высоко вариабельно в популяции и зависит от биологических факторов, которые во многом остаются неизученными. В последние годы было высказано предположение о возможности использования МРТ для предсказания ответа на терапию наноформулированными препаратами на основе скрининговых данных о накоплении в опухоли магнитно-контрастных диагностикумов. Несмотря на то что пилотные испытания указывают на принципиальную возможность предложенного подхода, существует ряд концептуальных проблем и технических ограничений для внедрения технологии в клинику. В статье обсуждаются преимущества и недостатки методов, позволяющих стратифицировать опухоли по степени накопления наночастиц. Дальнейшие исследования в данной области позволят разработать эффективные алгоритмы индивидуального лечения противоопухолевыми препаратами, доставляемыми на наночастицах.

Ключевые слова: противоопухолевая терапия, магнитно-резонансная томография, наночастицы, персонализированная медицина

Финансирование: работа выполнена при финансовой поддержке Министерства образования и науки РФ в рамках ФЦП «Исследования и разработки по приоритетным направлениям развития научно-технологического комплекса России на 2014–2020 годы», соглашение от 27.09.2017 г. № 14.575.21.0147 (уникальный идентификатор соглашения RFMEFI57517X0147).

✉ **Для корреспонденции:** Виктор Алексеевич Науменко
Ленинский проспект, д. 4, г. Москва, 119049; naumenko.vict@gmail.com

Статья получена: 30.08.2018 **Статья принята к печати:** 25.09.2018

DOI: 10.24075/vrgmu.2018.086

Oncological diseases are a major cause of death, disabilities, poor quality of life of the patients and the associated economic loss. Traditional cancer treatment methods, which include radical surgery, chemo and radiation therapy, are not highly effective, which makes the search for new therapeutic approaches to the problem an urgent task. Current cancer diagnostics and treatment trends seen worldwide are 1) introduction of the highly sensitive diagnostic methods, 2) development of the new drugs and methods to deliver them into tumors; 3) transition to personalized medicine.

All these trends and the underlying concepts benefit from the use of nanoparticles (NPs) [1]. Firstly, magnetic NPs (MNPs) allow using MRI for cancer detection. Secondly, there is a number of nanoformulations capable of delivering chemotherapeutic drugs to the tumor (liposomes, polymeric micelles, albumin-based NPs) that have already been approved for clinical use. Diagnostic and therapeutic potential of NPs enables their use in the context of personalized prediction of treatment efficacy. Picture 1 depicts the main idea of using MRI in the personalized MNP-based therapeutic algorithms. Screening tumors to register accumulation of nanocarriers therein aides the selection of the appropriate treatment strategy. MRI-assisted estimation of the level of contrast agents accumulation in a tumor allows predicting accumulation of the selected anticancer drug. The hypothesis is that the tumors with higher levels of contrast agent accumulation will respond better to MNP-based therapy.

There is a number of reasons behind the need for personalized treatment effectiveness prediction. Firstly, nanoformulations should be prescribed when the EPR-effect (higher blood vessels permeability and weaker lymphatic drainage) ensures sufficient drug accumulation in the tumor. Otherwise, nanoformulations-based therapy should be preceded by treatments increasing permeability of the tumor's vessels, e.g., local vasodilation through heating, injecting nitric oxide, prostaglandins (Fig. 1). Increasing arterial pressure with the help of angiotensin II or breaking the tumor matrix with collagenase can also facilitate delivery of drugs to the tumor [2]. Yet another method to counter insufficient accumulation of anticancer agent in the tumor is to deliver it on NPs conjugated with cancer specific ligands [3, 4]. Secondly, there are purely economic reasons to pick the latter when considering nanoformulations and regular anticancer drugs: for example, the cost of 20 mg doxorubicin is 540 rubles while that of Doxil is 42,300 rubles.

Methods and strategies for individual prognosis of nanodrug delivery to tumors

Currently, there are no routinely applied clinical algorithms allowing to evaluate the EPR-effect and the related efficacy of nanoformulated drug in a given patient. The issue is being addressed, however: a number of research teams conduct respective preclinical and clinical studies.

One of such studies examined the possibility of using magnetic particles (ferumoxytol) to estimate the efficacy of treatment with paclitaxel nanoformulation. The animals (this was an animal model study) were divided into groups by the MRI-registered level of EPR effect intensity; subsequent treatment with nanoformulated drug showed significant differences in the tumor cells death rates and response to therapy among those groups [5]. In 2017, researchers published the first results of a clinical study that implied using MRI to register the magnetic nanoparticles (ferumoxytol) delivery data and subsequently evaluate the effectiveness of treatment of 13 solid tumor patients with irinotecan nanoformulation. High ferumoxytol accumulation levels (within 1 to 24 hours) were shown to correlate with the therapy-induced tumor involution [6]. The suggested approach, however, has a major drawback: the difference in physical properties of diagnostic and therapeutic NPs was significant; their sizes, in particular, were 23 nm and 110 nm, respectively. It is well-known that delivery of NPs to a tumor depends on their hydrodynamic size: the smaller the particle, the more effective its extravasation and penetration into the tumor tissues [7]. Intravital microscopy conducted to determine pharmacokinetics of ferumoxytol and PGLA-PEG revealed the differences in speed and patterns of accumulation for these two NP types [5].

Mammography allowed predicting efficacy of breast cancer treatment in rats with doxorubicin incapsulated into 100 nm iodine-containing liposomes [8]. Contrast agent accumulation data was used to identify animals that were supposed to respond well to anticancer therapy, a prediction that fulfilled later. However, the efficacy of this approach was shown only in one tumor model. The method proposed is based on X-ray

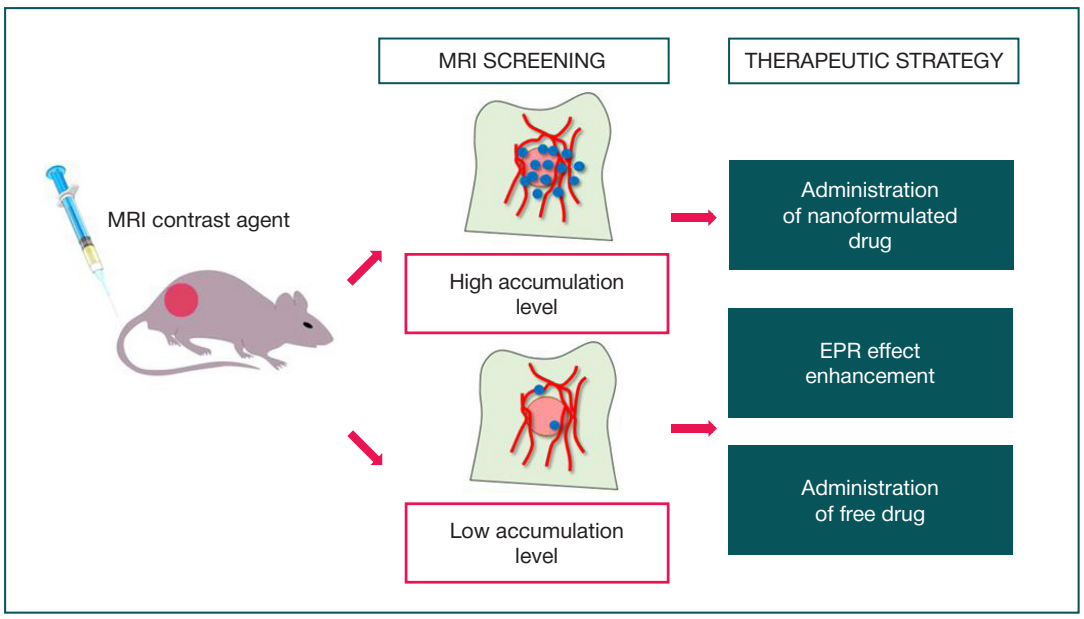

Fig. 1. Algorithm of personalized evaluation and antitumor nanodrug delivery efficacy prediction in an animal model

examination, which is less sensitive and safe than MRI, the factors that limit its adoption in the routine clinical practice.

Another interesting clinical study investigated the correlation between accumulation of doxorubicin-containing ^{64}Cu-labeled HER2-directed PEG-modified liposomes in tumor and efficacy of therapy in 19 patients with HER2-positive metastatic breast cancer. Positron emission tomography and computed tomography was applied to detect the radioactively labeled NPs. The researchers found a positive correlation between the high level of accumulation of labeled NPs and positive response to therapy [9]. The original aim of this study was to evaluate the effectiveness of breast cancer treatment with a combination of liposomal doxorubicin, trastuzumab and cyclophosphamide. In this connection, it is difficult to interpret contribution of the concomitant factors to the data obtained. Besides, the study focused on one tumor type only, so further investigations are needed to arrive at a valid conclusion.

A series of studies that researched doxorubicin nanoformulations labeled with radioactive technetium yielded similar data. In an animal model, researchers revealed a correlation between intensity of signal from the tumor (registered with the help of a single photon emission computed tomography) and accumulation of the drug in extracted tumors [10]. The efficacy of this approach was confirmed in a clinical trial, where $^{(99m)}$Tc-labeled liposomal doxorubicin was administered to 35 patients with mesothelioma. There was a correlation between the level of the drug accumulation in tumors and antitumor response [11]. However, due to safety concerns radioactive materials are not widely used in clinics, which limits applicability of the approach.

Gene, protein and cellular predictive markers were suggested as alternatives to the *in vivo* visualization methods used to assess the EPR effect. For example, liposome accumulation can be predicted based on the MMP9 (metalloproteinase 9) to TIMP1 (metaloproteinase 1 tissue inhibitor) ratio [12, 13]. In addition, growth factors of endothelial cells (VEGFA) and fibroblasts (FGF2), interleukins (IL6, IL8), peptides (endostatin), as well as endothelial cells and their precursors [14, 15] are being researched as potential EPR markers.

MRI in personalized MNP-based cancer therapy: problems and prospects

In our opinion, the approaches based on *in vivo* imaging, confirmed in animal models and being researched in the context of clinical trials, are the most promising. Unlike biomarkers analysis, these non-invasive methods make use of equipment and contrast agents available in the majority of hospitals. Besides, compared to the radiological and X-ray examination methods, MRI is safer and more widely spread. However, there is a number of conceptual problems and technical constraints that hamper development of a technology to evaluate and predict the effectiveness of nanodrug delivery in a given patient, namely:

1) different properties of the NPs used as diagnostic and therapeutic agents [5];

2) lack of data on the potential effect the first (diagnostic) dose has on biodistribution of the second (therapeutic) dose;

3) lack of data describing the time-related change, if any, of the EPR effect in the same tumor (the change that may determine differences in accumulation of the first and second NP doses);

4) retrospective character of the majority of studies delivering the data, as well as their focus on one model of tumor only and small samples;

5) lack of studies where investigating the correlation between EPR effect and antitumor response to nanodrugs is a primary goal and there are no concominant factors such as combination therapy

A comprehensive assessment of the EPR effect heterogeneity and its determinants requires studying different tumor models (allografts and xenografts, orthotopic and heterotopic) and types. The analysis of differences in NPs accumulation in different animals within the same tumor model allows intra-group heterogeneity assessment. We have recently performed a number of experiments with MNPs and the results clearly demonstrate that MRI can be used to assess the EPR effect in different tumor models and various animals (Fig. 2). Based on the data obtained, it is possible to rank animals into prognostic groups and subsequently assess therapeutic efficacy of the nanodrugs. Heterogeneity of the NPs accumulation can also be associated with evolution of tumor vessels and changes in the tissues architecture, which dictates the need for studying EPR effect at the different stages of tumor growth.

An important step in the process of introducing personalized nanodrug therapy to routine clinical practice is comparison of accumulation of the first and the second doses of NPs. Firstly, physicochemical properties of diagnostic and therapeutic NPs should be the same. Secondly, there is a possibility that the first dose affects subsequent NP administrations. For example, earlier studies have shown that first intravenous injection of

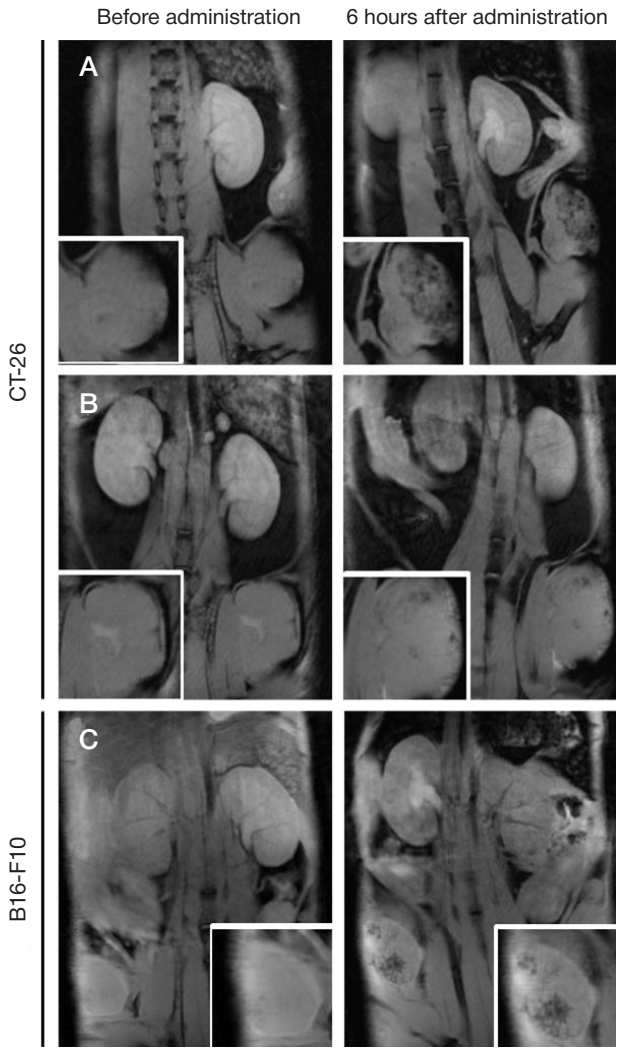

Fig. 2. EPR effect heterogeneity: intragroup (**A**–**B**); between different tumor models (**A**–**C**)

oncolytic viruses activates subsequent doses capturing by monocytes/macrophages. The same phenomenon may be peculiar to multiple dosing of NPs. Finally, the EPR effect can change dynamically within the same tumor, a factor that should be taken into account when assessing predictive power of the first dose. NPs conjugated with different dyes can be used to model biodistribution of the two doses. Intravital microscopy allows evaluating extravasation, diffusion and accumulation dynamics of the first and the second doses, as well as target cells in the tumor microenvironment. A combination of MRI and intravital microscopy also shows promise. The first method allows screening and ranking tumors into high and low NP accumulation groups, while the second enables investigation of the cellular mechanisms defining the differences in the EPR effect.

CONCLUSIONS

The concept of applying non-invasive methods and MNPs to develop individual therapeutic algorithms in oncology seems promising and realistic. The use of novel methods studying EPR determinants, as well as validation of MRI as a screening method in animal models will facilitate introduction of the personalized cancer nanotherapy technology to the routine clinical practice.

References

1. Shi J et al. Cancer nanomedicine: progress, challenges and opportunities. Nat Rev Cancer. NIH Public Access, 2017; 17 (1): 20–37.
2. Prabhakar U et al. Challenges and key considerations of the enhanced permeability and retention effect for nanomedicine drug delivery in oncology. Cancer Res. 2013; 73 (8): 2412–17.
3. Davis ME et al. Evidence of RNAi in humans from systemically administered siRNA via targeted nanoparticles. Nature. 2010; 464 (7291): 1067–70.
4. Hrkach J et al. Preclinical development and clinical translation of a PSMA-targeted docetaxel nanoparticle with a differentiated pharmacological profile. Sci Transl Med. 2012; 4 (128): 128ra39.
5. Miller MA et al. Predicting therapeutic nanomedicine efficacy using a companion magnetic resonance imaging nanoparticle. Sci Transl Med. 2015; 7 (314): 314ra183.
6. Ramanathan RK et al. Correlation between Ferumoxytol Uptake in Tumor Lesions by MRI and Response to Nanoliposomal Irinotecan in Patients with Advanced Solid Tumors: A Pilot Study. Clin Cancer Res. 2017; 23 (14): 3638–48.
7. Wilhelm S et al. Analysis of nanoparticle delivery to tumours. Nat Rev Mater. 2016; 1 (5): 16014.
8. Karathanasis E et al. Imaging nanoprobe for prediction of outcome of nanoparticle chemotherapy by using mammography. Radiology. 2009; 250 (2): 398–406.
9. Lee H et al. 64Cu-MM-302 Positron Emission Tomography Quantifies Variability of Enhanced Permeability and Retention of Nanoparticles in Relation to Treatment Response in Patients with Metastatic Breast Cancer. Clin Cancer Res. 2017; 23 (15): 4190–02.
10. Head HW et al. Combination radiofrequency ablation and intravenous radiolabeled liposomal Doxorubicin: imaging and quantification of increased drug delivery to tumors. Radiology. 2010; 255 (2): 405–14.
11. Arrieta O et al. A phase II trial of prolonged, continuous infusion of low-dose gemcitabine plus cisplatin in patients with advanced malignant pleural mesothelioma. Cancer Chemother Pharmacol. 2014; 73 (5): 975–82.
12. Yokoi K et al. Capillary-Wall Collagen as a Biophysical Marker of Nanotherapeutic Permeability into the Tumor Microenvironment. Cancer Res. 2014; 74 (16): 4239–46.
13. Yokoi K et al. Serum biomarkers for personalization of nanotherapeutics-based therapy in different tumor and organ microenvironments. Cancer Lett. 2014; 345 (1): 48–55.
14. Sessa C et al. Biomarkers of angiogenesis for the development of antiangiogenic therapies in oncology: tools or decorations? Nat Clin Pract Oncol. 2008; 5 (7): 378–91.
15. Sherwood LM, Parris EE, Folkman J. Tumor Angiogenesis: Therapeutic Implications. N Engl J Med. 1971; 285 (21): 1182–6.

Литература

1. Shi J et al. Cancer nanomedicine: progress, challenges and opportunities. Nat Rev Cancer. NIH Public Access, 2017; 17 (1): 20–37.
2. Prabhakar U et al. Challenges and key considerations of the enhanced permeability and retention effect for nanomedicine drug delivery in oncology. Cancer Res. 2013; 73 (8): 2412–17.
3. Davis ME et al. Evidence of RNAi in humans from systemically administered siRNA via targeted nanoparticles. Nature. 2010; 464 (7291): 1067–70.
4. Hrkach J et al. Preclinical development and clinical translation of a PSMA-targeted docetaxel nanoparticle with a differentiated pharmacological profile. Sci Transl Med. 2012; 4 (128): 128ra39.
5. Miller MA et al. Predicting therapeutic nanomedicine efficacy using a companion magnetic resonance imaging nanoparticle. Sci Transl Med. 2015; 7 (314): 314ra183.
6. Ramanathan RK et al. Correlation between Ferumoxytol Uptake in Tumor Lesions by MRI and Response to Nanoliposomal Irinotecan in Patients with Advanced Solid Tumors: A Pilot Study. Clin Cancer Res. 2017; 23 (14): 3638–48.
7. Wilhelm S et al. Analysis of nanoparticle delivery to tumours. Nat Rev Mater. 2016; 1 (5): 16014.
8. Karathanasis E et al. Imaging nanoprobe for prediction of outcome of nanoparticle chemotherapy by using mammography. Radiology. 2009; 250 (2): 398–406.
9. Lee H et al. 64Cu-MM-302 Positron Emission Tomography Quantifies Variability of Enhanced Permeability and Retention of Nanoparticles in Relation to Treatment Response in Patients with Metastatic Breast Cancer. Clin Cancer Res. 2017; 23 (15): 4190–02.
10. Head HW et al. Combination radiofrequency ablation and intravenous radiolabeled liposomal Doxorubicin: imaging and quantification of increased drug delivery to tumors. Radiology. 2010; 255 (2): 405–14.
11. Arrieta O et al. A phase II trial of prolonged, continuous infusion of low-dose gemcitabine plus cisplatin in patients with advanced malignant pleural mesothelioma. Cancer Chemother Pharmacol. 2014; 73 (5): 975–82.
12. Yokoi K et al. Capillary-Wall Collagen as a Biophysical Marker of Nanotherapeutic Permeability into the Tumor Microenvironment. Cancer Res. 2014; 74 (16): 4239–46.
13. Yokoi K et al. Serum biomarkers for personalization of nanotherapeutics-based therapy in different tumor and organ microenvironments. Cancer Lett. 2014; 345 (1): 48–55.
14. Sessa C et al. Biomarkers of angiogenesis for the development of antiangiogenic therapies in oncology: tools or decorations? Nat Clin Pract Oncol. 2008; 5 (7): 378–91.
15. Sherwood LM, Parris EE, Folkman J. Tumor Angiogenesis: Therapeutic Implications. N Engl J Med. 1971; 285 (21): 1182–6.

MOLECULAR ORIGIN OF SURFACE-ENHANCED RAMAN SPECTRA OF *E. COLI* SUSPENSIONS EXCITED AT 532 AND 785 NM USING SILVER NANOPARTICLE SOLS AS SERS SUBSTRATES

Durovich EA[1], Evtushenko EG[1,2] ✉, Senko OV[1], Stepanov NA[1], Efremenko EN[1], Eremenko AV[2], Kurochkin IN[1,2]

[1] Faculty of Chemistry, Lomonosov Moscow State University, Moscow

[2] Emanuel Institute of Biochemical Physics of RAS, Moscow

Research into the molecular origin of surface-enhanced Raman spectra (SERS) of bacteria is a crucial step in assessing the future of SERS-based discrimination and identification of bacteria in clinical analysis, food quality control, etc. Previous studies have revealed that at 785 nm excitation wavelength SERS of bacterial cells placed on a solid surface functionalized with *in-situ* grown aggregated gold nanoparticles covered with SiO_2 originate from a mixture of 6 purine derivatives (adenine, guanine, AMP, hypoxanthine, xanthine, and uric acid) that are released by the cells into the medium. The aim of the present work was to investigate whether such interpretation is possible with a different class of SERS substrates: silver nanoparticle sols at excitation wavelengths of 785 and 532 nm. The suspension of the *Escherichia coli* DH5α strain was used as a model bacterium. Sols of silver nanoparticles were obtained by reducing silver nitrate in the presence of alkaline hydroxylamine hydrochloride. Number-weighted mean hydrodynamic diameter of the particles was 43±2 nm. We confirm that at both excitation wavelengths the spectra can be best described as a superposition of 4 purine derivatives: adenine, guanine, hypoxanthine, and xanthine. Importantly, we have discovered that 1) the spectra of the purine mixture are characteristic of viable cells only; 2) due to the variations in the concentrations of purine metabolites released by the cells into the surrounding medium the spectra of a bacterial strain can vary significantly when a silver nanoparticle sol is used as a SERS substrate.

Keywords: SERS of bacteria, *E. coli*, silver nanoparticles, purines

✉ **Correspondence should be addressed:** Evgeniy G. Evtushenko
Leninskie gory 1, bl. 3, Moscow, 119991; evtushenko@enzyme.chem.msu.ru

Received: 15.08.2018 **Accepted:** 09.09.2018

DOI: 10.24075/brsmu.2018.088

МОЛЕКУЛЯРНАЯ ПРИРОДА ГКР-СПЕКТРОВ СУСПЕНЗИИ *E. COLI* ПРИ ДЛИНАХ ВОЛН ВОЗБУЖДЕНИЯ 532 И 785 НМ С ИСПОЛЬЗОВАНИЕМ ЗОЛЕЙ НАНОЧАСТИЦ СЕРЕБРА В КАЧЕСТВЕ ГКР-СУБСТРАТОВ

Е. А. Дурович[1], Е. Г. Евтушенко[1,2] ✉, О. В. Сенько[1], Н. А. Степанов[1], Е. Н. Ефременко[1], А. В. Еременко[2], И. Н. Курочкин[1,2]

[1] Химический факультет, Московский государственный университет имени М. В. Ломоносова, Москва

[2] Институт биохимической физики имени Н. М. Эмануэля РАН, Москва

Вопрос о молекулярной природе спектров гигантского комбинационного рассеяния (ГКР) бактерий является ключевым для оценки перспектив их дискриминации и идентификации данным методом в целях клинической диагностики, обеспечения безопасности пищевых продуктов и др. Ранее было показано, что при использовании в качестве ГКР-субстрата агрегированных и покрытых слоем SiO_2 золотых наночастиц на твердой поверхности источником спектра при длине волны возбуждения 785 нм является смесь шести пуриновых производных (аденина, гуанина, АМФ, гипоксантина, ксантина и мочевой кислоты), выделяемая клетками в раствор. Целью настоящей работы было показать применимость данной интерпретации спектров на примере суспензии клеток *Escherichia coli* штамма DH5α для другого класса ГКР-субстратов — золей наночастиц серебра при длинах волн возбуждения 785 и 532 нм. Золи получали восстановлением нитрата серебра хлоридом гидроксиламина в щелочной среде, среднечисловой размер частиц составил 43 ± 2 нм. Выявлены две важные особенности: во-первых, спектр пуриновых метаболитов регистрируется только при наличии живых клеток; во-вторых, при использовании золей наночастиц серебра в качестве ГКР-субстрата спектрам даже одного и того же штамма присуща значительная вариативность вследствие изменения соотношения концентраций пуриновых метаболитов, выделяемых клетками в раствор.

Ключевые слова: ГКР-спектры бактерий, *E. coli*, наночастицы серебра, пуриновые производные

✉ **Для корреспонденции:** Евгений Геннадиевич Евтушенко
Ленинские горы, д. 1, стр. 3, г. Москва, 119991; evtushenko@enzyme.chem.msu.ru

Статья получена: 15.08.2018 **Статья принята к печати:** 09.09.2018

DOI: 10.24075/vrgmu.2018.088

Surface-enhanced Raman spectroscopy (SERS) is an optical technique that relies on the amplification of the weak Raman signal emitted by a molecule located in close proximity to a metal surface with nanoscale roughness. Dating back a few decades, SERS still has not lost its appeal as a powerful detection technique. It is rapid and simple in instrumentation; it can be optimized to achieve a very high sensitivity and measure multiple analytes. SERS can also be employed for local analysis. Metal nanostructures used for signal enhancement are referred to as SERS substrates and fall into two major categories: nanostructures on solid supports and colloidal sols of metal nanoparticles.

SER spectra of bacteria were first recorded at a 514.5 nm laser excitation wavelength (EW) from *Escherichia coli* and *Bacillus megaterium* [1]. It was soon discovered that excitation at 488 or 514.5 nm results in almost identical SER spectra from gram-positive and gram-negative bacteria, as well as their isolated cell membranes: all acquired spectra originated from reduced or oxidized riboflavin (RF) [2–4]. The RF extinction band overlaps with 488 and 514.5 nm EWs, which induces resonant enhancement of the RF spectrum [3]. RF is a component of cofactors of redox enzymes and electron transport proteins found in cell membranes. If a bacterial cell is applied onto the surface of a solid SERS substrate or, alternatively, metal nanoparticles are synthesized or absorbed onto the cell, RF will come to occur in close proximity to the metal surface [3, 4]. From a bioanalytical standpoint, it means that laser sources with short wavelengths of 488 and 514.5 nm cannot be used for the identification of or discrimination between different bacteria.

At the same time, bacterial cells excited at long incident EW (785 nm) have SER spectra that do not contain the bands characteristic of riboflavin. Moreover, SER spectra vary between bacterial species and sometimes strains, not to mention intact and inactivated samples of the same strain [5–7]. This inspired a hypothesis in the early 21st century about the feasibility of SERS for the identification of bacterial species and strains excited at 785 nm wavelength. If adopted, this approach would have sped up pathogen detection in patients' samples, food products, and environmental objects. However, the molecular origin of bacterial SER spectra at long EWs was vague. According to a proposed hypothesis, such spectra could originate from the molecules localized in the bacterial glycocalyx (a slime layer or a capsule) or bacterial envelope (a cell wall or a membrane), as was the case with short wavelength lasers. Some authors speculated that the spectra might originate from N-acetyl-D-glucosamine [6], amino acid residues, peptides, protein prosthetic groups, phospholipids, metabolites (such as glucose or acetoacetic acid), or DNA and its constituents (guanine and adenine) [5, 7–13]. However, the proposed hypotheses lacked substance: they interpreted the origin of individual bands only ignoring the full spectra. As a result, this area of science was long dominated by a formal mathematical approach that combined the method of principal component analysis (PCA) used to reduce the dimensionality of experimental data and discriminant or cluster analysis aimed to prove the feasibility of discrimination between bacterial genera, species and strains based on their SER spectra [6, 12–15].

But then a study published in 2016 demonstrated convincingly that it was 6 purine metabolites released into the medium by the bacterial cell that were the source of SER spectra at 785 nm EW for 10 investigated samples [16]. The purine derivatives included adenine, guanine, adenosine monophosphate, hypoxanthine, xanthine, and uric acid. The suggested interpretation imposes a dramatic limitation on the use of bacterial SER spectra for the identification/discrimination of pathogens because the differences between their spectra are caused by only 6 secreted purine derivatives and not the whole diversity of molecules on the cell surface. For example, a hypoxanthine-free *E. coli* mutant with a silent adenosine deaminase gene was closer in its SER spectrum to *Staphylococcus aureus* than to the parent strain. The EW used in that experiment was 785 nm. Aggregated gold nanoparticles grown on a solid surface and coated with a thin silica layer were used as a SERS substrate. The aim of our study was to verify the authors' conclusions using a principally different type of SERS substrates (silver nanoparticle sols) and to investigate the molecular origin of bacterial SER spectra at 532 nm EW lying between riboflavin-dominated (488 and 514.5 nm) and infrared (785 and 1,064 nm) spectral regions.

METHODS

E. coli DH5α (Thermo Fisher Scientific; USA) was used as a model strain. The cells were cultivated in a liquid culture medium consisting of 10.0 g/l tryptone (Difco; USA), 5.0 g/l yeast extract (Difco; USA) and 10.0 g/l chemically pure NaCl (pH 6.8) (Chimmed; Russia) at 37 °C for 14–16 h until the stationary phase was reached. According to the literature [17], the cultured cells should be washed thoroughly to remove the residual components of the culture medium. Bearing that in mind, we applied the following protocol. Briefly, the cells were pelleted in the Beckman J-2-21 centrifuge (Beckman Coulter; USA) at 8,000 rpm for 7 min. The pellet was washed in an equivalent volume of 0.9% NaCl. The procedure was repeated twice. The obtained biomass was diluted with 0.9% NaCl taken at a volume sufficient for obtaining a suspension of $1 \cdot 10^8$ cells per ml. The final concentration was determined spectrophotometrically at 540 nm.

For the experiments with partially inactivated bacteria, the suspensions were placed into a water bath preheated to 70 °C or 90 °C and kept at this temperature for 1 h. The degree of inactivation was inferred from the concentration of intracellular ATP measured by the luciferase-luciferin assay using the reagent kit and calibration standards by Lumtek; Russia.

A sol of Ag nanoparticles (AgNPs) was used as SERS substrate. The sol was prepared by reducing silver nitrate with hydroxylamine hydrochloride in the presence of sodium hydroxide using $AgNO_3$ (ASC reagent, ≥ 99.0%; Sigma-Aldrich; USA), $NH_2OH \cdot HCl$ (purified; Prime Chemicals Group; Russia), and NaOH (reagent grade; Mosreaktiv; Russia). Following the original protocol [18], the silver nitrate solution was poured into the alkaline hydroxylamine solution. The final concentrations of the reagents in the mixture were 1 mM $AgNO_3$, 1.5 mM $NH_2OH \cdot HCl$, and 3 mM NaOH. Sols older than 3 days were not used in the experiment.

The absorption spectra of the synthesized nanoparticles were measured in a UV-visible region (300–750 nm) with the cuvette spectrophotometer UV-1800 (Shimadzu; Japan). The size and concentration of AgNPs were measured by nanoparticle tracking analysis (NTA) using the Nanosight LM10 HS-BF system (Nanosight Ltd; UK).

The SER spectra of both intact and inactivated bacteria were recorded on the day of sample preparation. Until then, the samples were stored at +4 °C. Immediately before the measurement, a sample aliquot was centrifuged twice at 3,700 rpm for 5 min in the Biofuge A centrifuge (Heraeus Sepatech; Germany) and washed in an equivalent volume of deionized water. The obtained cell suspension in water was mixed with the AgNP sol at a ratio of 1:1 and incubated for 1 min. Then, the NaCl solution taken at a final concentration of 40 mM was introduced into the mixture to stimulate particle aggregation and enhance the signal. An aliquot of this mixture (260 µl) was transferred into a well of an aluminum well-plate to minimize the background signal and improve heat dissipation. The spectra were measured in 3 to 4 replicates per sample; the samples were stirred by pipetting between measurements.

To study the changes in the SER spectra over time, 5 ml of the *E. coli* suspension were transferred to deionized water following the procedure described above. The obtained water suspension was stored at +4 °C and its aliquots were picked

to register SER spectra over the course of 4 h.The filtrate was prepared by filtering the *E. coli* water suspension slowly using a syringe filter SFNY030022S (Membrane Solutions; USA) with a diameter of 30 mm and a pore size of 0.22 μm.

At 785 nm EW, SER spectra were recorded using the innoRam BWS445(B)-785S spectrometer (BWTek; USA) with a 785 nm diode laser source and a ×20 PL L 20/0.40 objective. The instrument was operated at a measuring range of 64–3,011 cm^{-1} and resolution of 4 cm^{-1}. The spectra were recorded using the incident beam power of 42 mW, 5 s signal accumulation time, and averaging over 20 repeated scans. At 532 nm EW, SER spectra were recorded using the iRaman BWS415-532S spectrometer (BWTek; USA) with a 532 nm diode laser source and a ×20 PL L 20/0.40 objective. The instrument was operated at a measuring range of 174–4,001 cm^{-1} and resolution of 4 cm^{-1}. The spectra were recorded using the incident beam power of 20 mW; 5 s signal accumulation time, and averaging over 20 repeated scans.

Table. The table shows all spectral bands observed in the SER spectra of *E. coli* including the filtrates of cell suspensions and their assignment to the purine metabolites whose spectra were characterized in [16]. A — adenine, G — guanine, Hx — hypoxanthine, X — xanthine

785 nm		532 nm		Assignment
Peak position, cm^{-1}	Band frequency in the spectra, %	Peak position, cm^{-1}	Band frequency in the spectra, %	
502–515	75	502–512	50	X, G
522–540	100	526	75	G
		549–550	25	Hx, A
561–574	100			X, G, A
621–633	50	617–623 (sh)	100	Hx, A, G
653–667	100	648–651	100	G, X, A
680–683	38			X, A
724–735	100	721–728	100	A, Hx
780–792	63	770	25	Hx
		788	25	A
838–842	38	833	25	Tyrosine (?)
		848–850	50	
867–883	63	875–878	25	G, X
925–930	38			Hx
958–966	100	952–955	100	X, G, Hx, A
1002–1008	88	1000–1006	100	Phenylalanine (?), A+Hx+X interaction (?)
1027–1033	25	1024–1027	100	G, A, Hx
		1043–1045	75	G, X
1084–1096	50	1085–1095	100	Hx
1115–1130	38	1129–1140	100	X, G, A
1157–1160	25	1154	25	Hx
1175–1189	63			G, A
1213–1215	25	1215–1233	100	G, Hx, A
1245–1251	50	1242	25	X
1267–1276	25	1276	25	G, A
1310–1315	25			X, A
1324–1334	63	1322–1325	75	Hx
		1330–1331	50	Hx
		1341	25	A
1362–1380	63	1371–1379	100	G, X, Hx, A
1389–1390	13	1399	25	X, Hx
1444–1453	88	1444	25	Hx, G, A
1464–1473	75	1457–1468	100	Hx, G, X, A
1508	13	1506	25	A+Hx+X interaction (?)
1528–1534	25	1532–1538	100	G, Hx, K
1568–1578	63	1567–1575	50	G, A
1582–1591	25	1584–1595	25	X, Hx
1630–1721 (broad)	75	1646	25	G, A
		1692–1698	100	X, Hx, G

The recorded spectra were processed in OPUS 7.0 (Bruker Optik GmbH; Germany). The data outside the 500–1,800 cm^{-1} range was discarded, and the baseline was subtracted using the Background correction tool. Smoothing was not applied to determine peak positions and intensity. However, SERS data for plots was smoothened using the Smooth tool with a frame width of 9 cm^{-1}. The spectra were processed using vector normalization for a clear visual representation of qualitative differences. Normalization was not performed when the intensities of the spectra were compared.

RESULTS

The popular hydroxylamine technique for the synthesis of AgNP sols [18] is simple and reproducible; the sols it yields significantly enhance the spectra emitted by various analytes, including bacterial cells [19–21]. The AgNP sols we prepared were transparent, deep yellowish-brown in color and did not contain any precipitate. They had a broad and intense absorption band in the near UV-blue region corresponding to the localized surface plasmon resonance of AgNPs with a maximum at 407–409 nm and absorption at this wavelength ranging from 16.5 to 18 (this accounts for 30-fold dilution with deionized water). The number-weighted mean hydrodynamic diameter of the particles measured by nanoparticle tracking analysis was 43 ± 2 nm in three independent AgNP batches. The total particle concentration was (8.0 ± 1.7) • 10^{11} particles per ml. The synthesized AgNS sols aggregated in 40 mM NaCl did not have their own SER spectra at both EW except for a broad low-intensity band contributed by aluminum (the material of the plate) in the region between 1,200 and 1,700 cm^{-1}. This band can be totally subtracted during data processing.

The reproducibility of intact *E. coli* SER spectra at 785 nm EW was tested in a series of different experiment. First, we repeatedly measured the spectra of the same mixture of *E. coli* + AgNPs + NaCl. Second, we measured the spectra of different aliquots of bacterial sample using the same and different AgNP batches. Third, we measured the spectra of independently cultured and isolated *E. coli* applied onto one and the same AgNP substrate. Repeatedly measured bacterial samples demonstrated good repeatability (Fig. 1A). The SER spectra of independently cultured bacterial samples varied considerably (Fig. 1B). The most significant variations were observed in the following spectral regions: 508–532; 655; 730–734; 958; 1,450; 1,570–1,576 cm^{-1}.

E. coli stored in water at +4 °C for 4 h (Fig. 1C) demonstrated a gradual increase in the total intensity of the SER spectrum over time accompanied by a change in the intensity ratio of its individual bands. For example, the ratio I_{730} / I_{655} = 1.2 remained constant at all time points, but the ratio I_{1325} / I_{655} monotonously declined from its initial value of 1.6 to 1.0 over the course of 4 h.

The spectra of the intact *E. coli* suspension in water were compared to its filtrate (0.22 μm) in order to locate the molecules giving rise to the SER spectra (Fig. 1D). Considering the slow dynamics, the spectra of aliquots of the initial bacterial suspension were recorded before and after filtration. All spectral

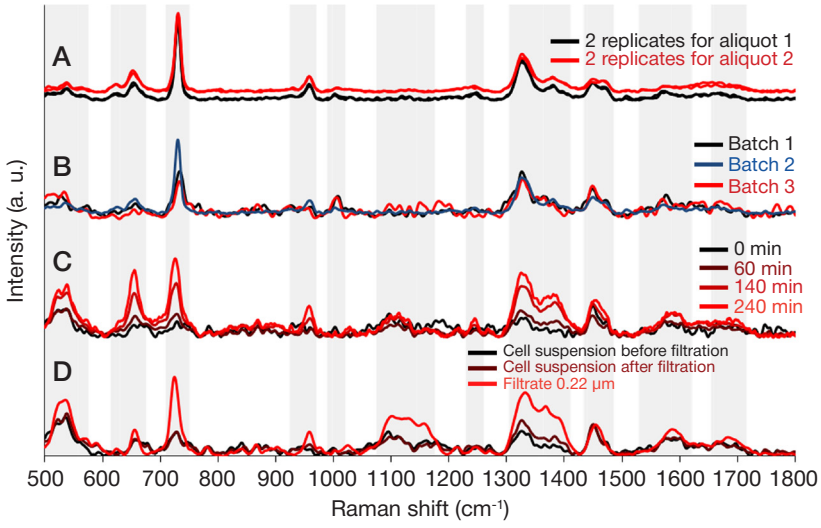

Fig. 1. SER spectra of *E. coli* suspensions at 785 nm excitation wavelength. **A**. Repeatability of measurements for one aliquot and one cell batch. **B**. Reproducibility of the spectra for different batches of cell suspensions. **C**. Dynamics of SER spectra over time observed in cells stored in water at +4 °C. **D**. Comparison of the spectra of the cell suspension and the filtrate (0.22 μm) of the same suspension. Vector normalization was applied to the spectra (**A**, **B**); the spectra (**C**, **D**) were not normalized to demonstrate the difference in their intensity. Ranges of spectral differences are shown in gray

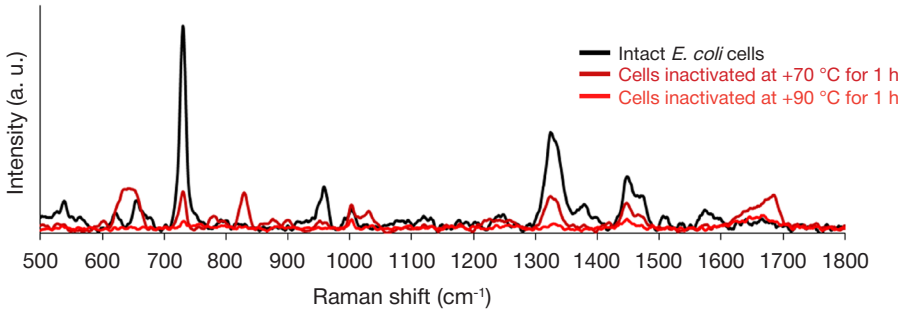

Fig. 2. Changes in the SER spectra of *E. coli* suspensions (785 nm) following inactivation by heating. The spectra were not normalized to demonstrate the difference in their intensity

bands observed for the cell suspension were present in the spectra of the filtrate. Moreover, the total intensity of the filtrate spectrum was significantly higher.

The SER spectra of intact cells and those inactivated at 70 °C or 90 °C for 60 min were compared in an attempt to understand whether the observed SER spectra can indicate the presence of viable *E. coli* or whether they come from an inactivated bacterial biomass (Fig. 2). The residual concentration of intracellular ATP was also measured in all three sample types (intact bacteria and cells inactivated at 70 °C and 90 °C) as it is indicative of cell viability. The ATP concentrations were $1 \cdot 10^{-9}$, $5.6 \cdot 10^{-12}$ and $4.1 \cdot 10^{-12}$ mol per 1 ml of cell suspension, respectively. On the whole, considerable variability was observed in the number and position of spectral bands. However, the total intensity of the spectrum tended to decrease. The spectra of inactivated bacteria (90 °C) contained only 4 very low-intensity bands characteristic of intact *E. coli* (730; 1,002; 1,325, and 1,450 cm^{-1}) and two low-intensity bands of the amide III (1,230–1,270 cm^{-1}) and amide I (1,640–1.680 cm^{-1}) regions.

The reproducibility of the SER spectra of intact *E. coli* was also tested at 532 nm EW. In this case, the intensity of the spectra was twice as high as that observed at 785 nm, resulting in a higher number of informative spectral bands and a better accuracy in locating their position. Similar to 785 nm EW, at 532 nm the high repeatability of the spectra was observed for one and the same aliquot of one and the same bacterial sample (Fig. 3A). But the SER spectra of independently cultured and isolated bacteria varied considerably (Fig. 3B).

DISCUSSION

Measurements conducted at EW 785 nm demonstrate that the SER spectra of *E. coli* stored in water are not determined by a single compound, but rather by a mixture of a few different components. This becomes clear when we look at the array of all recorded spectra that contains a fixed set of spectral bands (see the Table). The ratios of the mixture components slowly change over time when cells are stored in water (Fig. 1C) and differ significantly between independently cultured batches of intact cells (Fig. 1B). Comparison of the spectra of the intact bacterial preparation and its filtrate (Fig. 1D) shows that the components of the mixture do not originate from the cell surface but are present in the solution. Moreover, the cell itself can be seen as interfering with the recording of SER spectra, as it adsorbs particles on its surface. This is suggested by a significant increase in the total intensity of the filtrate spectrum in comparison with that of the cell suspension.

Inactivation of bacterial cells demonstrates that the mixture of the compounds in question bears connection to cell viability (Fig. 2) but is not a product of passive desorption from the surface of inactivated cells.

The Table features a list of spectral bands observed in all acquired SER spectra of intact *E. coli*, including the filtrates.

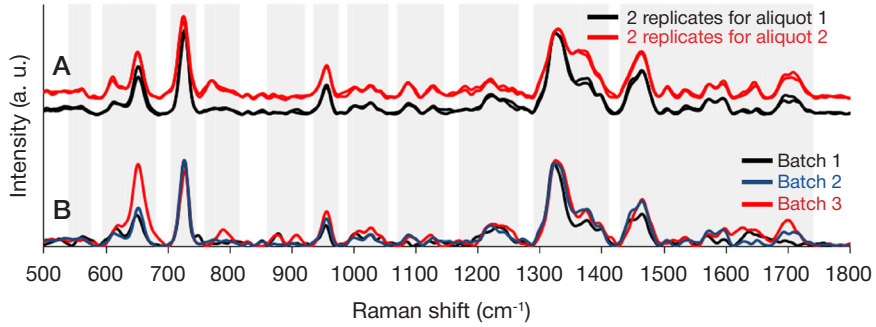

Fig. 3. SER spectra of *E. coli* suspensions at 532 nm excitation wavelength **A**. Repeatability of measurements for one aliquot and one cell batch. **B**. Reproducibility of the spectra for different batches of cell suspensions. Vector normalization was applied to the spectra. Ranges of spectral differences are shown in gray

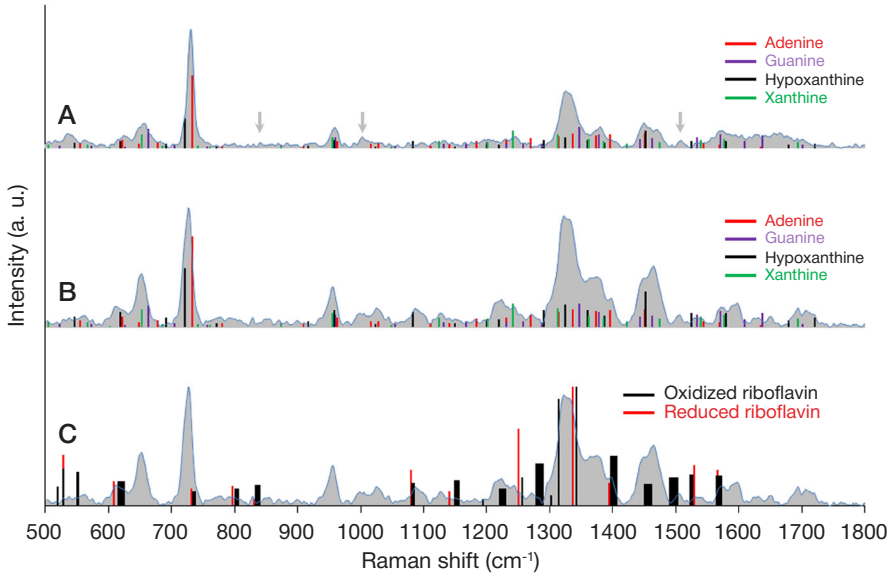

Fig. 4. Overlay of SER spectra corresponding to purine derivatives [16] and riboflavin [4, 24, 25] on the SER spectra of *E. coli* suspension **A**. Spectral bands of purine derivatives in the spectra of *E. coli* at 785 nm EW. Arrows mark uncharacterized low-intensity bands. **B**. Spectral bands of purine derivatives in the spectra of *E. coli* at 532 nm EW. **C**. Overlay of spectral bands of riboflavin on the spectra of *E. coli* at 532 nm EW. The width of riboflavin bands on the graph reflects the variability of their positions in literature sources

Upon analyzing the literature, we concluded that at 785 nm EW almost all spectral bands are a product of superposition of spectra originating from 4 purine derivatives (adenine, guanine, hypoxanthine, and xanthine). This conclusion is consistent with [16]. Besides, for every individual SER spectrum, the intensity and positions of bands correspond to such superposition as well. (Fig. 4A). Unlike the authors of [16] who exploited aggregated gold nanoparticles on a solid surface, we used sols of silver nanoparticles. Considering the possibility of slight variations in the relative intensity of the spectral bands associated with the use of different SER substrates and an increase in intensity following overlay of spectral bands of individual compounds, our description is quite accurate.

Only 3 low-intensity bands remain uncharacterized: 838–842, 1,002–1,008 and 1,508 cm^{-1}. On the one hand, there is a chance that low-intensity bands can be lost during digital conversion of the spectra from literature sources. On the other hands, it is possible that those bands have never been present in the spectra of individual purine derivatives. Then, their origin can be explained by two hypotheses. First, the bands can result from the interactions between the components of the mixture. For example, a SER spectrum of a mixture consisting of adenine, hypoxanthine and xanthine contains two bands (1,000 and 1,510 cm^{-1}) absent in the individual spectra of its constituents [22]. Besides, the presence of 838–842 and 1,002 cm^{-1} bands can be explained by minor presence of tyrosine (the most intense spectral bands are 824; 847; 928; 1,046; 1,389 and 1,583 cm^{-1} [23]) and phenylalanine (the most intense spectral bands are 930; 1,002; 1,031; 1,394; and 1,602 cm^{-1} [23]).

The suggested origin of bacterial SER spectra explains a considerable variation in the position of peaks observed for some bands within *E. coli* spectra. Thus, the variability in the position of the peak of a broad multicomponent band ranging from 502 to 574 cm^{-1} can be explained by an overlap of the following bands: xanthine (508 cm^{-1}), guanine (526 cm^{-1}), hypoxanthine (550 cm^{-1}), adenine (558 cm^{-1}), and guanine (577 cm^{-1}). For the band in the region between 653 and 667 cm^{-1}, the contributing bands are 652 cm^{-1} (adenine), 657 cm^{-1} (xanthine) and 667 cm^{-1} (guanine); for the 724–735 cm^{-1} band, 725 cm^{-1} (hypoxanthine) and 734 cm^{-1} (adenine); for the broad double band with peaks at 1,444–1,452 cm^{-1} and 1,464–1,473 cm^{-1}, the contribution is made by guanine (1447 cm^{-1}), adenine (1455 cm^{-1}), hypoxanthine (1456 cm^{-1}), guanine (1466 cm^{-1}), and xanthine (1478 cm^{-1}).

The SER spectra of *E. coli* are very similar at 785 and 532 nm EW (Fig. 4A, 4B) with regards to the position and intensity of some of their constituting bands (Fig. 1B, 3B). This finding encouraged us to describe the acquired SER spectra at EW 532 nm as representing a mixture of 4 purine metabolites (adenine, guanine, hypoxanthine, and xanthine) as well. The reference spectra characterized in [16] differ from the acquired *E. coli* spectra in the type of the SER substrate used and EW, resulting in slight shifts in band positions. Considering that, our description of the experimental SER spectra of *E.coli* at EW 532 nm can be characterized as satisfactory.

We also explored a possibility of ascribing the bands in the SER spectra of *E. coli* at 532 nm EW to reduced or oxidized riboflavin and FAD whose reference spectra were borrowed from some early works [4, 24, 25] (Fig. 4C). A few high and medium intensity bands of *E. coli* are absent in the SER spectra of RF including 650, 725–733, 955, and 1,365 cm^{-1}. In turn, the SER spectra of *E. coli* either miss a number of RF bands or include the bands with a strongly different intensity: 528–529, 834–839, 1,149–1,156, 1,279–1,289, 1,491–1,502, and 1,523–1,527 cm^{-1} for oxidized RF and 528, 1,251, 1,501 and 1,530 cm^{-1} for reduced RF. Nevertheless, the contribution of the RF to the *E. coli* spectra at 532 nm EW cannot be ruled out. It could additionally increase the intensity of a broad band in the region between 1,300 and 1,350 cm^{-1} in comparison with the mixture of purine derivatives. However, RF does not dominate the spectrum. This somewhat contradicts the early conclusions about its dominance in the spectra of *Pseudomonas aeruginosa*, *Bacillus subtilis*, and *Geobacillus stearothermophilus* at 532 nm [25]. Such discrepancy can be explained by the difference in the used bacteria species.To sum up, the SER spectra of *E. coli* at 532 nm EW can be best described as a superposition of the spectra of purine derivatives. Similarly to 785 EW, the variability of the spectra of bacterial samples from different batches at 532 nm EW results from the difference in the concentrations of these compounds released by the cells into the solution.

CONCLUSIONS

The SER spectra of *E. coli* excited at 785 and 532 nm originate from a mixture of purine derivatives released by the cells into the solution, given that a silver nanoparticle sol synthesized following the hydroxylamine technique is used as a SERS substrate. For both excitation wavelengths, the acquired spectra are best described as originating from adenine, guanine, hypoxanthine, and xanthine. Riboflavin may slightly contribute to the spectra excited at 532 nm. The acquired spectra are characteristic of viable bacteria cells only. Their variability results from the differences in the ratio of the contributing components. Such molecular origin of bacterial SER spectra imposes serious limitations on the use of SERS for bacterial identification and discrimination.

References

1. Efrima S, Bronk BV. Silver Colloids Impregnating or Coating Bacteria. J Phys Chem B. 1998; 102 (31): 5947–50.
2. Zeiri L, Bronk BV, Shabtai Y, Czégé J, Efrima S. Silver metal induced surface enhanced Raman of bacteria. Colloids Surfaces A Physicochem Eng Asp. 2002; 208 (1): 357–62.
3. Picorel R, Lu T, Holt RE, Cotton TM, Seibert M. Surface-Enhanced Resonance Raman Scattering (SERRS) Spectroscopy of Bacterial Membranes: The Flavoproteins. In: Baltscheffsky M, editor. Current Research in Photosynthesis: Proceedings of the VIIIth International Conference on Photosynthesis; 1989 Aug 6–11; Stockholm, Sweden. Dordrecht: Springer Netherlands, 1990; p. 1867–70.
4. Zeiri L, Bronk BV, Shabtai Y, Eichler J, Efrima S. Surface-Enhanced Raman Spectroscopy as a Tool for Probing Specific Biochemical Components in Bacteria. Appl Spectrosc. 2004; 58 (1): 33–40.
5. Guzelian AA, Sylvia JM, Janni JA, Clauson SL, Spencer KM. SERS of whole-cell bacteria and trace levels of biological molecules. Proc. SPIE, Vibrational Spectroscopy-Based Sensor Systems. 2002; (4577): 183–92.
6. Jarvis RM, Goodacre R. Discrimination of Bacteria Using Surface-Enhanced Raman Spectroscopy. Anal Chem. 2004; 76 (1): 40–7.
7. Premasiri WR, Moir DT, Klempner MS, Krieger N, Jones G, Ziegler LD. Characterization of the Surface Enhanced Raman Scattering (SERS) of Bacteria. J Phys Chem B. 2005; 109 (1): 312–20.

8. Luo BS, Lin M. A Portable Raman System for the Identification of Foodborne Pathogenic Bacteria. J Rapid Methods Autom Microbiol. 2008; 16 (3): 238–55.
9. Kahraman M, Keseroğlu K, Çulha M. On sample preparation for surface-enhanced Raman scattering (SERS) of bacteria and the source of spectral features of the spectra. Appl Spectrosc. 2011; 65 (5): 500–6.
10. Feng J, de la Fuente-Núñez C, Trimble MJ, Xu J, Hancock REW, Lu X. An in situ Raman spectroscopy-based microfluidic "lab-on-a-chip" platform for non-destructive and continuous characterization of *Pseudomonas aeruginosa* biofilms. Chem Commun. 2015; 51 (43): 8966–9.
11. Su L, Zhang P, Zheng D, Wang Y, Zhong R. Rapid detection of *Escherichia coli* and *Salmonella typhimurium* by surface-enhanced Raman scattering. Optoelectron Lett. 2015; 11 (2): 157–160.
12. Mosier-Boss AP. Review on SERS of Bacteria. Biosensors. 2017; 7 (4): 51–76.
13. Witkowska E, Korsak D, Kowalska A, Janeczek A, Kamińska A. Strain-level typing and identification of bacteria — a novel approach for SERS active plasmonic nanostructures. Anal Bioanal Chem. 2018; 410 (20): 5019–31.
14. Patel IS, Premasiri WR, Moir DT, Ziegler LD. Barcoding bacterial cells: a SERS-based methodology for pathogen identification. J Raman Spectrosc. 2008; 39 (11): 1660–72.
15. Sundaram J, Park B, Hinton A, Lawrence KC, Kwon Y. Detection and differentiation of *Salmonella* serotypes using surface enhanced Raman scattering (SERS) technique. J Food Meas Charact. 2013; 7 (1): 1–12.
16. Premasiri WR, Lee JC, Sauer-Budge A, Théberge R, Costello CE, Ziegler LD. The biochemical origins of the surface-enhanced Raman spectra of bacteria: a metabolomics profiling by SERS. Anal Bioanal Chem. 2016; 408 (17): 4631–47.
17. Marotta NE, Bottomley LA. Surface-Enhanced Raman Scattering of Bacterial Cell Culture Growth Media. Appl Spectrosc. 2010; 64 (6): 601–6.
18. Leopold N, Lendl B. A New Method for Fast Preparation of Highly Surface-Enhanced Raman Scattering (SERS) Active Silver Colloids at Room Temperature by Reduction of Silver Nitrate with Hydroxylamine Hydrochloride. J Phys Chem B. 2003; 107 (24): 5723–7.
19. Cañamares MV, Garcia-Ramos JV, Sanchez-Cortes S, Castillejo M, Oujja M. Comparative SERS effectiveness of silver nanoparticles prepared by different methods: A study of the enhancement factor and the interfacial properties. J Colloid Interface Sci. 2008; 326 (1): 103–9.
20. Knauer M, Ivleva NP, Niessner R, Haisch C. Optimized Surface-enhanced Raman Scattering (SERS) Colloids for the Characterization of Microorganisms. Anal Sci. 2010; 26 (7): 761–6.
21. Félix-Rivera H, González R, Rodríguez GDM, Primera-Pedrozo OM, Ríos-Velázquez C, Hernández-Rivera SP. Improving SERS Detection of Bacillus thuringiensis Using Silver Nanoparticles Reduced with Hydroxylamine and with Citrate Capped Borohydride. Int J Spectrosc. 2011; Article ID 989504.
22. Ranc V, Hruzikova J, Maitner K, Prucek R, Milde D, Kvítek L. Quantification of purine basis in their mixtures at femto-molar concentration levels using FT-SERS. J Raman Spectrosc. 2011; 43 (8): 971–6.
23. Kim SK, Kim MS, Suh SW. Surface-enhanced Raman scattering (SERS) of aromatic amino acids and their glycyl dipeptides in silver sol. J Raman Spectrosc. 1987; 18 (3): 171–5.
24. Kazanci M, Schulte JP, Douglas C, Fratzl P, Pink D, Smith-Palmer T. Tuning the Surface-Enhanced Raman Scattering Effect to Different Molecular Groups by Switching the Silver Colloid Solution pH. Appl Spectrosc. 2009; 63 (2): 214–3.
25. Smith-Palmer T, Douglas C, Fredericks P. Rationalizing the SER spectra of bacteria. Vib Spectrosc. 2010; 53 (1): 103–6.

Литература

1. Efrima S, Bronk BV. Silver Colloids Impregnating or Coating Bacteria. J Phys Chem B. 1998; 102 (31): 5947–50.
2. Zeiri L, Bronk BV, Shabtai Y, Czégé J, Efrima S. Silver metal induced surface enhanced Raman of bacteria. Colloids Surfaces A Physicochem Eng Asp. 2002; 208 (1): 357–62.
3. Picorel R, Lu T, Holt RE, Cotton TM, Seibert M. Surface-Enhanced Resonance Raman Scattering (SERRS) Spectroscopy of Bacterial Membranes: The Flavoproteins. In: Baltscheffsky M, editor. Current Research in Photosynthesis: Proceedings of the VIIIth International Conference on Photosynthesis; 1989 Aug 6–11; Stockholm, Sweden. Dordrecht: Springer Netherlands, 1990; p. 1867–70.
4. Zeiri L, Bronk BV, Shabtai Y, Eichler J, Efrima S. Surface-Enhanced Raman Spectroscopy as a Tool for Probing Specific Biochemical Components in Bacteria. Appl Spectrosc. 2004; 58 (1): 33–40.
5. Guzelian AA, Sylvia JM, Janni JA, Clauson SL, Spencer KM. SERS of whole-cell bacteria and trace levels of biological molecules. Proc. SPIE, Vibrational Spectroscopy-Based Sensor Systems. 2002; (4577): 183–92.
6. Jarvis RM, Goodacre R. Discrimination of Bacteria Using Surface-Enhanced Raman Spectroscopy. Anal Chem. 2004; 76 (1): 40–7.
7. Premasiri WR, Moir DT, Klempner MS, Krieger N, Jones G, Ziegler LD. Characterization of the Surface Enhanced Raman Scattering (SERS) of Bacteria. J Phys Chem B. 2005; 109 (1): 312–20.
8. Luo BS, Lin M. A Portable Raman System for the Identification of Foodborne Pathogenic Bacteria. J Rapid Methods Autom Microbiol. 2008; 16 (3): 238–55.
9. Kahraman M, Keseroğlu K, Çulha M. On sample preparation for surface-enhanced Raman scattering (SERS) of bacteria and the source of spectral features of the spectra. Appl Spectrosc. 2011; 65 (5): 500–6.
10. Feng J, de la Fuente-Núñez C, Trimble MJ, Xu J, Hancock REW, Lu X. An in situ Raman spectroscopy-based microfluidic "lab-on-a-chip" platform for non-destructive and continuous characterization of *Pseudomonas aeruginosa* biofilms. Chem Commun. 2015; 51 (43): 8966–9.
11. Su L, Zhang P, Zheng D, Wang Y, Zhong R. Rapid detection of *Escherichia coli* and *Salmonella typhimurium* by surface-enhanced Raman scattering. Optoelectron Lett. 2015; 11 (2): 157–160.
12. Mosier-Boss AP. Review on SERS of Bacteria. Biosensors. 2017; 7 (4): 51–76.
13. Witkowska E, Korsak D, Kowalska A, Janeczek A, Kamińska A. Strain-level typing and identification of bacteria — a novel approach for SERS active plasmonic nanostructures. Anal Bioanal Chem. 2018; 410 (20): 5019–31.
14. Patel IS, Premasiri WR, Moir DT, Ziegler LD. Barcoding bacterial cells: a SERS-based methodology for pathogen identification. J Raman Spectrosc. 2008; 39 (11): 1660–72.
15. Sundaram J, Park B, Hinton A, Lawrence KC, Kwon Y. Detection and differentiation of *Salmonella* serotypes using surface enhanced Raman scattering (SERS) technique. J Food Meas Charact. 2013; 7 (1): 1–12.
16. Premasiri WR, Lee JC, Sauer-Budge A, Théberge R, Costello CE, Ziegler LD. The biochemical origins of the surface-enhanced Raman spectra of bacteria: a metabolomics profiling by SERS. Anal Bioanal Chem. 2016; 408 (17): 4631–47.
17. Marotta NE, Bottomley LA. Surface-Enhanced Raman Scattering of Bacterial Cell Culture Growth Media. Appl Spectrosc. 2010; 64 (6): 601–6.
18. Leopold N, Lendl B. A New Method for Fast Preparation of Highly Surface-Enhanced Raman Scattering (SERS) Active Silver Colloids at Room Temperature by Reduction of Silver Nitrate with Hydroxylamine Hydrochloride. J Phys Chem B. 2003; 107 (24): 5723–7.
19. Cañamares MV, Garcia-Ramos JV, Sanchez-Cortes S, Castillejo M, Oujja M. Comparative SERS effectiveness of silver nanoparticles prepared by different methods: A study of the enhancement factor and the interfacial properties. J Colloid Interface Sci. 2008;

326 (1): 103–9.
20. Knauer M, Ivleva NP, Niessner R, Haisch C. Optimized Surface-enhanced Raman Scattering (SERS) Colloids for the Characterization of Microorganisms. Anal Sci. 2010; 26 (7): 761–6.
21. Félix-Rivera H, González R, Rodríguez GDM, Primera-Pedrozo OM, Ríos-Velázquez C, Hernández-Rivera SP. Improving SERS Detection of Bacillus thuringiensis Using Silver Nanoparticles Reduced with Hydroxylamine and with Citrate Capped Borohydride. Int J Spectrosc. 2011; Article ID 989504.
22. Ranc V, Hruzikova J, Maitner K, Prucek R, Milde D, Kvítek L. Quantification of purine basis in their mixtures at femto-molar concentration levels using FT-SERS. J Raman Spectrosc. 2011; 43 (8): 971–6.
23. Kim SK, Kim MS, Suh SW. Surface-enhanced Raman scattering (SERS) of aromatic amino acids and their glycyl dipeptides in silver sol. J Raman Spectrosc. 1987; 18 (3): 171–5.
24. Kazanci M, Schulte JP, Douglas C, Fratzl P, Pink D, Smith-Palmer T. Tuning the Surface-Enhanced Raman Scattering Effect to Different Molecular Groups by Switching the Silver Colloid Solution pH. Appl Spectrosc. 2009; 63 (2): 214–3.
25. Smith-Palmer T, Douglas C, Fredericks P. Rationalizing the SER spectra of bacteria. Vib Spectrosc. 2010; 53 (1): 103–6.

DEVELOPMENT OF LIPOSOMAL DRUG FORMULATIONS: QUALITY ATTRIBUTES AND METHODS FOR QUALITY CONTROL

Melnikova EV, Goryachev DV, Chaplenko AA ✉, Vodyakova MA, Sayfutdinova AR, Merkulov VA

Scientific Centre for Expert Evaluation of Medicinal Products
of the Ministry of Health of the Russian Federation, Moscow

The use of nanostructured components in drug manufacturing and, more specifically, targeted drug delivery has recently become a major pharmacy trend. Nanodrugs encompass a wide range of pharmaceutical agents containing dendrimers, nanocrystals, micelles, liposomes, and polymer nanoparticles. Liposomes are the most well-studied nanoparticles and effective drug carriers. However, the more complex their structure is, the more process controls are needed and the more quality attributes have to be monitored, including the chemical properties of the liposomal fraction such as the shape, size and charge of the nanoparticle, conjugation efficacy, and distribution of the active ingredient. We believe that quality control of key liposome characteristics can be carried out using dynamic and laser light scattering coupled with electrophoresis, differential scanning calorimetry, cryo-electron microscopy, nuclear magnetic resonance, laser diffraction analysis, and gel filtration chromatography.

Keywords: liposomes, nanodrugs, quality control, guidance documents

✉ **Correspondence should be addressed:** Alexander A. Chaplenko
Schukinskaya 6, bl. 1, Moscow, 127051; chaplenko@Expmed.ru

Received: 29.06.2018 **Accepted:** 02.09.2018

DOI: 10.24075/brsmu.2018.092

РАЗРАБОТКА ЛИПОСОМАЛЬНЫХ ФОРМ ЛЕКАРСТВЕННЫХ ПРЕПАРАТОВ: МЕТОДЫ ОЦЕНКИ И ПОКАЗАТЕЛИ КАЧЕСТВА

Е. В. Мельникова, Д. В. Горячев, А. А. Чапленко ✉, М. А. Водякова, А. Р. Сайфутдинова, В. А. Меркулов

Федеральное государственное бюджетное учреждение «Научный центр экспертизы средств медицинского применения»
Министерства здравоохранения Российской Федерации, Москва

Одним из трендов фармации на сегодняшний день является применение наноструктурных компонентов для производства лекарств, в частности для направленной доставки лекарственных средств в заданную область организма, органа или клетки. К нанопрепаратам авторы относят средства, содержащие дендримеры, нанокристаллы, мицеллы, липосомы, а также полимерные наночастицы. В настоящее время липосомы — одни из наиболее исследованных наночастиц, которые рассматривают как современные и эффективные средства доставки различных препаратов. Однако увеличение сложности структуры препарата неизбежно приводит к увеличению числа критических точек производства, а также к расширению списка показателей качества. Наряду с классическими показателями качества авторы считают необходимым оценивать также физико-химические свойства липосомной фракции: форму, размер и заряд частиц; эффективность конъюгации маркеров; равномерность распределения действующего вещества. Мы полагаем, что для контроля ключевых параметров липосом целесообразно использовать динамическое и лазерное светорассеяние в сочетании с электрофорезом, дифференциальную сканирующую калориметрию, криорасщепляющую электронную микроскопию, ядерный магнитный резонанс, лазерную дифракцию и гель-фильтрацию.

Ключевые слова: липосомы, нанопрепараты, контроль качества, нормативные документы

✉ **Для корреспонденции:** Александр Андреевич Чапленко
ул. Щукинская, д. 6, корп. 1, г. Москва, 127051; chaplenko@Expmed.ru

Статья получена: 29.06.2018 **Статья принята к печати:** 02.09.2018

DOI: 10.24075/vrgmu.2018.092

Some of the major current challenges before the pharmaceutical industry are regulation of all pharmacokinetic parameters of a drug (absorption, distribution, clearance and biotransformation), ensuring its safety and selective action on target organs and other targets, minimization of undesirable reactions and side effects. Using nanostructured components in general and to deliver drugs to a given body part, organ or cell in particular is one of the trends that sees development today. Russian legislation does not describe the concepts of “nanopreparations” or “nanodrugs”; in reality, all drugs that are nanoparticles or contain them are considered to be such. This definition mainly applies to the drugs based on liposomes and micelles, where nanostructures enable transportation of the active pharmaceutical ingredient inside the body, prolong its absorption, increase stability, etc. Another case are drugs considered to be nanostructured due to the physicochemical characteristics of their active ingredients, an example of which are antianemic iron preparations that may contain iron (III) atoms stabilized by a carbohydrate complex, which defines their nanocolloidal structure. Currently, we are developing quality assessment and research guidelines applicable to drugs based on liposomes and micelles, as well as containing nanoparticles.

Features of the nanodrugs' compositions define the individual approaches to assessing their quality. For example, quality of liposomal preparations largely depends on their individual specific attributes (size of nanoparticles, surface morphology, surface charge), which can affect the following pharmacokinetic and pharmacodynamic properties *in vivo*:

• rate of release of the active ingredient from liposomes, a factor that has an effect on pharmacokinetics (PK) and pharmacodynamics (PD) and, consequently, drug's safety profile and efficacy;

• bioavailability of the active pharmaceutical ingredient in liposome, its biotransformation and clearance.

PK of the encapsulated active ingredient depends on that of the carrier, which is determined by the physicochemical properties of the nanoparticle material; interactions between the nanoparticle's components, active ingredient and biological environment (body) should also be taken into account.

We define nanodrugs as drugs that contain dendrimers, nanocrystals, micelles, liposomes and polymeric nanoparticles. Currently, liposome is one of the best-studied nanoparticles among those considered as effective carriers for various drugs. In the recent years, global pharmaceutical industry has developed and released over 20 liposomal drugs primarily used to treat cancer (Dauno Xome (Gilead, NeXstar), Doxil (Alza, Sequus), Couloux (Schering-Plow), Muocet (Elan, TLS)) and fungal infections (AmBisome, ABELSET (Gilead, NeXstar)) [1]. Specific capabilities related to transportation, translocation through histohematogenous barriers and cell membranes, as well as metabolic transformations, provide liposome-based drugs with unique properties that improve their PK.

This article summarizes and analyzes the data describing the use of various types of liposomes for drug delivery and defines the specifics of the liposome-based nanodrugs quality assessment.

Varieties of liposomes and their use by pharmaceutical industry

Liposomes are vesicles with a lipid bilayer built of amphiphilic molecules enclosing their contents. Recently, liposomes have evolved from a simple model that mimics cell membranes into an object of active research and practical application [2]. In the context of drug delivery, liposomes enable selective accumulation of the active ingredient in pathological lesions (tumors, inflamed tissues) due to their passive targeting ability. This ability is the results of the difference in distance between capillary cells in lesions/tumors and normal tissue: the former, which is 210 to 1000 nm, is significantly greater than the latter, which is approximately 40 nm. Thus, liposomes less than 200 nm in size cannot escape the bloodstream anywhere except the lesions (with the exception of the brain, where tumors typically have pores of 7–100 nm [3, 4]), and the active pharmaceutical ingredient, which can be toxic, is unlikely to contaminate anything but the target. For example, liposomal doxorubicin is 2–3 times less toxic than the solution of this drug [5].

Using target (endothelial) protein antibodies, which are specific to vessels of various organs, allows manifold improvement of precision of the nanoparticle-enabled delivery of active pharmaceutical ingredients and DNA [6–9].

To date, various researchers have described liposome-based preparations carrying a plethora of active ingredients, X-ray and scintigraphic tracers, toxins, peptides, proteins and nucleic acids. The overwhelming majority of studies in this field has to do with anticancer drugs (most often, anthracycline-based) [8]. There are five types of liposomes, different in composition and action *in vivo*, that the researchers preferred, namely: simple liposomes; sterically stabilized liposomes; directed liposomes (immunoliposomes); cationic liposomes; liposomes sensitive to physical and chemical stimuli, such as temperature, light, and changes in pH [2, 10] (Table 1).

When progress in biotechnology and genetic engineering allowed developing a new generation of drugs, such as recombinant proteins, peptides (biotechnological drugs), drugs based on nucleic acids (gene therapy drugs), liposomes acquired a special significance due to the susceptibility of these medicines to chemical and enzymatic hydrolysis [8, 39–41]. In gene therapy, liposome nanocontainers may carry a plasmid with a therapeutic gene sequence, antisense oligonucleotides or small interfering RNAs [42-44]. The volume of the liposomes allows them to contain genes of various sizes [45]. Vector molecules attached to the outer surface of the liposomes target delivery, a mechanism similar to that used for cytotoxic drugs and paramagnetic contrast agents.

When liposomes are used as DNA vaccines, they hold the antigen in their capsule and double as an immunomodulator [46, 47]. In one of the studies, S-antigen sequence of HBV (pRc / CMV HBS) enclosed in cationic liposomes was used as a DNA vaccine [47]. Balb/c mice received a vaccine of 10 μg of plasmid DNA (i.m., per mouse) twice on days 0 and 21. After administration of the native HBsAg, the levels of detectable cytokines in spleens of mice immunized with the liposome-based preparation were 4 times higher than those registered in intact mice and animals vaccinated with DNA, which suggests a possibility of using this liposomal construct as a Hepatitis B vaccine.

Both cationic or anionic liposomes and those with a neutral surface charge can be loaded with DNA. Neutral liposomes circulate in the bloodstream for a much longer period of time than the charged ones; moreover, their advantages are lesser toxicity and non-specific persorption in organs and tissues. However, it is much harder to load them with DNA. In case of passive loading, which is a plain emulsification of lipid components in the presence of DNA, only 10% of the total amount of DNA gets into the liposomes. There are special techniques that allow increasing the number to 40%, but, as a rule, they also increase the size of the liposomes [45]. Charged liposomes can be loaded with more DNA, which is their key advantage. However, cationic and anionic liposomes have higher levels toxicity and non-specific penetration into organs and tissues than neutral liposomes.

Specifics of the liposome-based drugs quality and production control

The main stages of production of liposomal drug formulations and the controlled parameters thereof are listed below [48].

1) Lipid film production and its dispersion/degradation. Controlled parameters: amount of residual organic solvents in the lipid film; active pharmaceutical ingredient integration rate and size of the liposomes after lipid film dispersion; stability; pH value.

2) Production of liposomes of the required size, separating the non-integrated active ingredient, sterilization by filtration. Controlled parameters: amount of the integrated active pharmaceutical ingredient; size of the liposomes; concentration of the lipid components; stability; pH value.

3) Lyophilization. Controlled parameters: residual moisture; stability and percentage of drug integration into the liposomes after lyophilisate rehydration.

The above-listed stages of the technological process allow a conclusion that the critical liposome-based drug quality checks imply determination of its crucial physicochemical properties; therefore, state registration applications for such formulations should provide the following information (Fig. 1).

Table 1. Use of different types of liposomes for drug delivery

Types of liposomes	Simple	Sterically stabilized	Immunoliposomes	Cationic (lipoplexes)	Thermosensitive and photosensitive
Composition specifics	Phospholipids (neutral and/or negatively charged) and/or cholesterol	Phospholipids + polyethylene glycol (PEG)	Modified PEG-vesicles conjugated with monoclonal antibodies or their fragments, peptides, growth factors, glycoproteins, etc.	Positively charged lipids	Phospholipids the phase transition temperature of which exceeds body temperature (thermosensitive). 1,2-Bis(4-(n-butyl)phenylazo-4'-phenylbutyroyl)phosphatidylcholine (Bis-Azo PC) in low concentrations is part of the vesicles of the photoisomerized lipid molecule. May be conjugated with PEG or antibodies (AB)
Route of administration	Oral, injection, inhalation, local, endovitreal	Injection, oral	Injection	Injection, intranasal	Injection
Half-life	Several minutes to 2-3 hours	6–8 hours to several days		Several minutes to 4-6 hours	Several days
Key accumulation sites	Liver, spleen, lungs		Determined by the attached ligands, liver, lungs	Liver, lungs	Tumor cells
Mode of action	Passive targeting	Passive targeting	Directed transport	Passive targeting	Directed transport
Examples of use	– part of the virus, antibacterial, parasitic infection vaccines [11]; – delivery of immunomodulators, cytotoxic and antimicrobial compounds to macrophages; – treatment of metastases after surgical removal of primary tumors [12, 13]; – delivery of drugs against intracellular pathogens [14], systemic fungal infection, HIV, mycobacterial infection [13]; – carrying radioisotopes and contrast agents for visualization purposes [12, 13]; – carrying antigens [12, 15]	– accumulation of drugs in solid tumors [16–18]; – treatment of small cell lung cancer and cutaneous melanoma [19], leukemia and lung carcinoma [20, 21]	– delivery of drug to the tumor [10, 22–26]; – treatment of chronic B-lymphocytic leukemia and acute T-cell leukemia [23], various lymphomas [27]; – treatment of breast, thyroid gland, ovarian cancer, that of uterus, lung, esophagus, stomach, colon and rectum, kidney [23, 26, 28]	– delivery of the genetic material to the liver, cell therapy of endothelial pulmonary tumors [2, 29, 30]; – antiangiogenic therapy; – treatment of tumors of neck and head, melanomas [30]	– delivery of drug to the tumor [2, 31]
Key advantages	Penetrate into the relatively inaccessible lesions (e.g., in the brain) due to their negative charge [32, 33]	Contain PEG, which prevents liposome opsonization, hinders their recognition by the reticuloendothelial system cells and increases the time of their persistence in the bloodstream [34, 35]	Antibodies allow modulating distribution of the liposomes in organs and tissues. Optimization of the drug's therapeutic properties. Correction of the effective dose	Penetrate into the tumor's vessels (as opposed to neutral or negatively charged liposomes) [36]	Offer greater selectivity of action compared to the free drug [31, 37, 38]

The behavior of the active pharmaceutical ingredient in a physiological environment is one of the main parameters influencing the liposome-based drug's PK and PD. Therefore, for the purposes listed below it is necessary to develop reliable, validated methods of assessment of the active ingredient release *in vitro*.

– Monitoring of imitation of the active ingredient release from liposomes in the body; a test for "leakage" *in vitro* in the relevant environment under various conditions (e.g., in a certain range of temperatures and pH) can be conducted given there are grounds for that.

– Monitoring of stability in storage to ensure consistency of lots;

– Investigation of stability and review of the production process in the intended conditions of use.

Table 2 provides an example of the certificate data (key parameters and quality indicators) describing liposomes [49, 50] used for delivery of the therapeutic genes' DNA.

We believe that, depending on the specific function of the liposomes (e.g., modification of the active ingredient's distribution by encapsulation in order to improve the safety profile), the following additional parameters should also be evaluated in the development of the drug:

– maintaining the integrity of the liposomal formulation in plasma;

– characteristics of the lipid bilayer phase transition process (transition temperature and enthalpy);

– determination of the surface charge of the liposomes;

– pH of the inner chamber of the liposomes filled by the pH gradient;

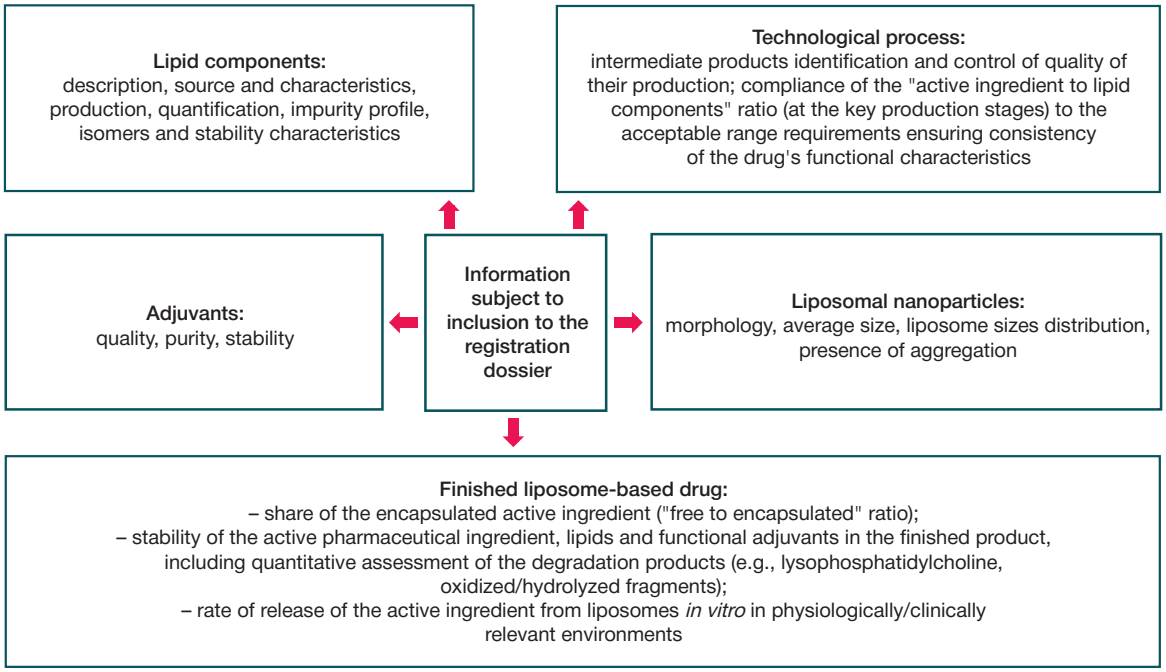

Fig. 1. Information about the quality characteristics of liposomal drug formulations

– if significant, determination of characteristics of the active pharmaceutical ingredient's physical state inside the liposome (e.g., formation of a precipitate for doxorubicin);

– distribution of the active ingredient (e.g., on the surface of liposomes, in the bilayer, internal environment, etc.);

– for conjugated (eg, pegylated) liposome-based preparations: the quality and purity of the pegylated starting material, molecular weight of the conjugated lipid and size distribution (dispersion), location of PEG on the surface, stability of the conjugate.

It is necessary to compile a list of tests each lot should routinely be subjected to. This list should be based on the parameters used to characterize the drug in accordance with the requirements described above.

Legal regulation of liposome-based drugs in the world

Table 3 provides the examples of requirements regulator bodies from various countries of the world impose on the production, quality control, preclinical and clinical studies of liposome-based forms of drugs.

CONCLUSIONS

Liposome-based drug delivery systems give a drug designer control over the active ingredient's absorption and release parameters. As a rule, liposome-based drugs are less toxic, pose a lower risk of adverse reactions and allow delivering

Table 2. Liposome-based drugs characteristics

Parameters		Analytical/instrumental methods
Physical characteristics		
1	Vesicle size and surface morphology	Electron microscopy
2	Distribution of the vesicles sizes (submicron and micron ranges)	Dynamic and laser light scattering, exclusion chromatography (gel filtration)
3	Surface charge	Dynamic light scattering
4	Surface pH	pH sensitive samples
5	Integrated DNA/free preparation percentage	Methanol-chloroform extraction and centrifugation in separation columns, ion exchange chromatography, spectrophotometry, radioactive labeling
Chemical characteristics		
1	Phospholipid concentration	Extraction and centrifugation in separation columns
2	Cholesterol concentration	Extraction and centrifugation in separation columns
3	Osmolality	Osmometry
Biological characteristics		
1	Sterility	Pharmacopoeial sterility test
2	Pyrogenicity	LAL test (Limulus amebocyte lysate test)
3	Toxicity	*In vitro* and *in vivo* monitoring, histology

Table 3. Regulatory documents containing requirements to liposomal drug

State	Document	Selected aspects
EU countries	Reflection paper on the data requirements for intravenous liposomal products developed with reference to an innovator liposomal product/21 February 2013 EMA/CHMP/806058/2009/Rev. 02, Committee for Human Medicinal Products (CHMP)	Quality control specifics: – composition and authenticity of the components (lipids, adjuvants); – active pharmaceutical ingredient to lipids ratio; – liposomes morphology, average size and size distribution, aggregation; – fraction of the encapsulated active ingredient (free/integrated amount); – stability of the active ingredient, lipids, adjuvants, critical decomposition products; – *in vitro* rate of release of the ingredient from liposomes in physiologically/clinically significant environments; – stability; – recovery; – maintaining integrity of the liposomal formulation in plasma
	Recommendations. Commission recommendation of 18 October 2011 on the definition of nanomaterial (Text with EEA relevance) (2011/696/EU)	Definition of nanomaterials
	Reflection paper on surface coatings: general issues for consideration regarding parenteral administration of coated nanomedicine products/22 May 2013, EMA/325027/2013, Committee for Medicinal Products for Human Use (CHMP)	Key critical quality indicators, as well as the requirements for clinical and preclinical studies, are included. Special attention is paid to the following aspects: – presence of a coating can affect the critical properties of the nanodrugs from the points of view of their safety and efficacy. The physico-chemical nature of the coating, uniformity of its surface coating and stability (both in terms of attachment and in terms of degradation) will determine the drug's PK and biodistribution; – in some cases, the coating material may cause new biological reactions that are not observed either for the coating material or for the active pharmaceutical ingredients separately
USA	Guidance for Industry. Liposome Drug Products Chemistry, Manufacturing, and Controls; Human Pharmacokinetics and Bioavailability; and Labeling Documentation. — U.S. Department of Health and Human Services Food and Drug Administration Center for Drug Evaluation and Research, 2002	Brief description of the liposomes, critical stages of their production and quality control, recommendations for conducting research on PK and bioavailability of liposome-based drugs and labeling requirements. The guideline contains general principles and recommendations for registration of the drugs of this class.
	USP41-NF36 <1> Injections and implanted drug products (parenterals)-product quality tests	Contains definition of liposomes and liposome-based drugs and states that in the case of liposomes, quality control implies both general and special tests.
China	Pharmacopoeia of the Peoples Republic of China. Beijing: People's Medical Publishing Hous. 2010; (2). p. A244–245	Definitions of various nanoparticles, requirements, nanodrugs quality control criteria and methods are provided. The attributes that should be monitored in production and storage of the drugs (e.g., residual amounts of organic solvents, shape, particle size and distribution, encapsulation rate and amount of drugs in liposomes, liposome oxidation degree, etc.) are listed.

the active ingredient to the target part of the body. Innovative drugs containing liposomes conjugated with antibodies can be targeted with maximum effectiveness and release the active ingredient where needed. However, the more complex the drug's structure becomes, the more crucial stages its production acquires. Moreover, the list of parameters to control, those that determine the quality of the drug, grows. Evaluation of the liposomal fraction's physicochemical properties is added to the classic quality control methods: the shape, size, and charge of the particles are being assessed, as well as marker conjugation effectiveness and uniformity of distribution of the active ingredient. Key methods for estimating the liposome parameters make use of the optical effects: dynamic and laser light scattering, electron microscopy.

References

1. Krasnopolsky YuM, Stepanov AE, Shvets VI. Technological aspects of production of liposomal preparations under GMP conditions. Biofarm J. 2009; 3: 18–29.
2. Baryshnikov AYu. Nanostructured liposomal systems as a means of delivery of anticancer drugs. Vestnik RAMS. 2012; 3: 23–31.
3. Hobbs SK, Monsky WL, Yuan F. et al. Regulation of transport pathways in tumor vessels: role of tumor type and microenvironment. Proc Natl Acad Sci USA. 1998; 95: 4607–4612.
4. Shvets IV, Kaplun AP, Krasnopolsky YuM. et al. From liposome seventies to nanobiotechnology XXI century. Ross nanotechnologies. 2008; 3 (11–12): 6–20.
5. Love WG, Amos N, Kellaway IW, Williams BD. Specific accumulation of cholesterol-rich liposomes in the inflammatory tissue of rats with adjuvant arthritis. Ann Rheum Dis. 1990; 49 (8): 611–614.
6. Chekhonin VP, Baklaushev VP, Yusubalieva GM. et al. Modeling and immunohistochemical analysis of glioma C6. Cell technol in biol and med. 2007; 2: 65–73.
7. Chekhonin VP, Zhirkov YuA, Gurina OI. et al. The Pegylated immunoliposome specific to astrocytes. Dokl. RAN. 2003; 391 (6): 1–7.
8. Chekhonin VP, Gurina OI, Dmitrieva TB. Monoclonal antibodies to neurospecific proteins. M.: Medicine, 2007; 344.
9. Errede M, Benagiano V, Girolamo F et al. Differential expression of connexin43 in foetal, adult and tumour-associated human brain endothelial cells. Histochem J. 2002; 34: 265–271.
10. Immordino ML, Dosio F, Cattel L. Stealth liposomes: review of the basic science, rationale and clinical applications, existing and potential. Int J Nanomedicine. 2006; 1 (3): 297–315.
11. Felnerova D, Viret J-F, Gluck R, Moser C. Liposomes and virosomes as delivery systems for antigens, nucleic acids and drugs. Curr Opin Biotechnol. 2004; 15: 518–529.

12. Barenholz Y. Liposome application: problems and prospects. Curr Opin Colloid Interface Sci. 2001; 6: 66–77.
13. Vasir JK, Reddy MK, Labhasetwar VD. Nanosystems in drug targeting: opportunities and challenges. Curr Nanoscience. 2005; 1 (1): 47–64.
14. Basu MK. Liposomal delivery of antileishmanial agents. J Applied Research. 2005; 5 (1): 221–236.
15. Zurbriggen R, Amacker M, Krammer AR. Immunopotentiating reconstituted influenza virosomes. In: G. Gregoriadis eds. Liposome technology. 3rd edn. Vol. I. Liposome preparation and related techniques. New York: Informa Healthcare USA, 2007; 85–96.
16. Fang J, Sawa T, Maeda H. Factors and mechanism of «epr» effect and the enhanced antitumor effects of macromolecular drugs including smancs. Adv Exp Med Biol. 2003; 519: 29–49.
17. Greish K, Fang J, Inutsuka T. et al. Macromolecular therapeutics: advantages and prospects with special emphasis on solid tumour targeting. Clin Pharmacokinet. 2003; 42: 1089–1105.
18. Maeda H. The enhanced permeability and retention (epr) effect in tumor vasculature: the key role of tumor-selective macromolecular drug targeting. Adv Enzyme Regul. 2001; 41: 189–207.
19. Haley B, Frenkel E. Nanoparticles for drug delivery in cancer treatment. Urologic Oncology: Seminars and Original Investigations. 2008; 26: 57–64.
20. Lantsova AV. Creation and biopharmaceutical study of liposomal dosage forms of anticancer drugs derived from nitrosourea. Abstract dis kand farm. sciences. Moscow, 2006; 173.
21. Lantsova AV, Oborotova NA, Peretolchina NM et al. Comparative study of the antitumor activity of the liposomal dosage forms of drugs, derivatives of nitrozomocevina. Sibirs oncologist J. 2005; 2 (14): 25–29.
22. Allen TM. Ligand-targeted therapeutics in anticancer therapy. Nat Rev Cancer. 2002; 2 (10): 750–763.
23. Tolcheva EV. Design of immunoliposomes and study of immunoliposomal form of anticancer drug doxorubicin. Abstract dis kand Biol sciences. M., 2007; 109 p.
24. Sokolova DV, Tazina EV, Kortava MA. et al. Anti-CD40 and anti-HLA-DR immunoliposomal form doxorubicin: technology of production and antigen specificity in vivo. Ross biotherapeutic J. 2010; 9 (2): 90.
25. Sokolova DV, Tazina EV, Kortava MA et al. Anti-MUC1 immunoliposomal form of doxorubicin: technology of production and antigen specificity in vitro. Ross biotherapeutic J. 2010; 9 (3): 21.
26. Khugaeva OV, Kortava MA, Sokolova DV et al. Receiving liposomal mitoxantrone/materials of the IX all-Russian. scientific.-prakt. Conf. "Domestic anticancer drugs". Ross biotherapeutic J. 2010; 9 (2): 91.
27. Nasonov EL. Prospects of rituximab use in autoimmune diseases of a person. Rus Med J. 2007; 15 (26): 1–6.
28. Sokolova DV. Immunoliposomal constructions of doxorubicin and models for their preclinical study. Abstract dis kand Biol sciences. M., 2011; 122.
29. Kawakami S, Fumoto S, Nishikawa M et al. In vivo gene delivery to the liver using novel galactosylated cationic liposomes. Pharmaceuttic Research. 2000; 17 (3): 306–313.
30. Dass CR, Choong PFM. Targeting of small molecule anticancer drugs to the tumor and its vasculature using cationic liposomes: lessons from gene therapy. Cancer Cell Int. 2006; 6 (17): 1–9.
31. Ponce AM, Wright A, Dewhirst MW, Needham D. Targeted bioavailability of drugs by triggered release from liposomes. Future Lipidol. 2006; 1 (1): 25–34.
32. Jain S, Mishra V, Singh P et al. RGD-anchored magnetic liposomes for monocytes/neutrophils-mediated brain targeting. Int J Pharm. 2003; 261 (1–2): 43–55.
33. Qin J, Chen D, Hu H et al. Surface modification of RGD-liposomes for selective drug delivery to monocytes/Neutrophils in brain. Chem Pharm Bull. 2007; 55 (8): 1192–1197.
34. Campbell RB, Fukumura D, Brown EB et al. Cationic charge determines the distribution of liposomes between the vascular and extravascular compartments of tumors. Cancer Res. 2002; 62: 6831–6836.
35. Ambegia E, Ansell S, Cullis P et al. Stabilized plasmid-lipid particles containing PEG-diacylglycerols exhibit extended circulation lifetimes and tumor selective gene expression. Biochim Biophys Acta. 2005; 1669 (2): 155–163.
36. Dass CR. Improving anti-angiogenic therapy via selective delivery of cationic liposomes to tumor vasculature. Int J Pharm. 2003; 267 (1–2): 1–12.
37. Tazina EV, Mescheryakova VV, Ignatieva EV et al. Biopharmaceutical studies of temperature-sensitive liposomal formulations of doxorubicin. Ross biotherapeutic J. 2009; 1 (8): 40–47.
38. Huang Z, Szoka FC. Bioresponsive liposomes and their use for macromolecular delivery. In: G. Gregoriadis eds. Liposome technology. 3rd edn. Vol. I. Liposome preparation and related techniques. New York: Informa Healthcare USA, 2007; 165–196.
39. Chekhonin VP, Zhirkov YuA, Aglow NV et al. Directed transport of drugs using liposomes. Vestn RAMS. 2004; 5: 42–47.
40. Wu D, Pardridge WM. Neuroprotection with noninvasive neurotrophin delivery to the brain. Proc Natl Acad Sci USA. 1999; 96: 254–259.
41. Shi N, Pardridge WM. Noninvasive gene targeting to the brain. Proc Natl Acad Sci USA. 2000; 97 (13): 7567–7572.
42. Pal A, Ahmad A, Khan S et al. Systemic delivery of RafsiRNA using cationic liposomes silences Raf in xenograft model of human prostate cancer. Int J Oncol. 2005; 26 (4): 1087–1091.
43. Omidi Y, Barar J, Akhtar S. Toxicogenomics of cationic lipid-based vectors for gene therapy: impact of microarray. Curr Drug Del. 2005; 2 (4): 429–441.
44. Oliveira S, Storm G, Schiffelers. Targeted delivery of siRNA. J Biomed Biotechnol. 2006; 2006: 1–7.
45. Miyazaki M, Obata Y, Abe K et al. Gene transfer using nonviral delivery systems. Perit Dial Int. 2006; 26: 633–640.
46. Aguilar JC. Vaccine adjuvants revisited. Vaccine. 2007; 25: 3752–3762.
47. Perrie Y, Frederik PM, Gregoriadis G. Liposome-mediated DNA vaccination: the effect of vesicle composition. Vaccine. 2001; 19: 3301–3310.
48. Pharmaceutical development: concept and practical recommendations. Scientific-practical guide for the pharmaceutical industry / ed. by Bykov SN, Vasilenko IA, Demina NB, Shokhin IE, Novojilov OV, Meshkovsky AP, Spitskov ORM. Pero, 2015; 472 p.
49. Lu D, Hickey AJ. Liposomal dry powders as aerosols for pulmonary delivery of proteins. AAPS Pharm Sci Tech. 2005; 6 (4): 641–648.
50. De Lima MCP, Simoes S, Pires P et al. Cationic lipid-DNA complexes in gene delivery: from biophysics to biological applications. Adv Drug Del Rev. 2001; 47: 277–294.

Литература

1. Краснопольский Ю. М., Степанов А. Е., Швец В. И. Технологические аспекты получения липосомальных препаратов в условиях GMP. Биофарм журнал. 2009; (3): 18–29.
2. Барышников А. Ю. Наноструктурированные липосомальные системы как средство доставки противоопухолевых препаратов. Вестник РАМН. 2012; (3): 23–31.
3. Hobbs SK, Monsky WL, Yuan F et al. Regulation of transport pathways in tumor vessels: role of tumor type and microenvironment. Proc Natl Acad Sci USA. 1998; (95): 4607–12.
4. Швец В. И., Каплун А. П., Краснопольский Ю. М., Степанов А. Е., Чехонин В. П. От липосом семидесятых к нанобиотехнологии XXI века. Российские нанотехнологии. 2008; 3 (11–12): 6–20.
5. Love WG, Amos N, Kellaway IW, Williams BD. Specific accumulation of cholesterol-rich liposomes in the inflammatory tissue of rats with adjuvant arthritis. Ann Rheum Dis. 1990; 49 (8): 611–14.
6. Чехонин В. П., Баклаушев В. П., Юсубалиева Г. М. Моделирование и иммуногистохимический анализ глиомы С6

in vivo. Клеточные технологии в биологии и медицине. 2007; (2): 65–73.
7. Чехонин В. П., Жирков Ю. А., Гурина О. И. ПЭГилированные иммуннолипосомы, специфичные к астроцитам. Доклады Академии наук. 2003; 391 (6): 1–7.
8. Чехонин В. П., Гурина О. И., Дмитриева Т. В. Моноклональные антитела к нейроспецифическим белкам. М.: Медицина, 2007; 344 с.
9. Errede M, Benagiano V, Girolamo F et al. Differential expression of connexin43 in foetal, adult and tumour-associated human brain endothelial cells. Histochem J. 2002; (34): 265–71.
10. Immordino ML, Dosio F, Cattel L. Stealth liposomes: review of the basic science, rationale and clinical applications, existing and potential. Int J Nanomedicine. 2006; 1 (3): 297–315.
11. Felnerova D, Viret J-F, Gluck R, Moser C. Liposomes and virosomes as delivery systems for antigens, nucleic acids and drugs. Curr Opin Biotechnol. 2004; (15): 518–29.
12. Barenholz Y. Liposome application: problems and prospects. Curr Opin Colloid Interface Sci. 2001; (6): 66–77.
13. Vasir JK, Reddy MK, Labhasetwar VD. Nanosystems in drug targeting: opportunities and challenges. Curr Nanoscience. 2005; 1 (1): 47–64.
14. Basu MK. Liposomal delivery of antileishmanial agents. J Applied Research. 2005; 5 (1): 221–36.
15. Zurbriggen R, Amacker M, Krammer AR. Immunopotentiating reconstituted influenza virosomes. In: G. Gregoriadis, editor. Liposome technology. 3rd edn. Vol. I. Liposome preparation and related techniques. New York: Informa Healthcare USA, 2007; 85–96.
16. Fang J, Sawa T, Maeda H. Factors and mechanism of «epr» effect and the enhanced antitumor effects of macromolecular drugs including smancs. Adv Exp Med Biol. 2003; (519): 29–49.
17. Greish K, Fang J, Inutsuka T et al. Macromolecular therapeutics: advantages and prospects with special emphasis on solid tumour targeting. Clin Pharmacokinet. 2003; (42): 1089–105.
18. Maeda H. The enhanced permeability and retention (epr) effect in tumor vasculature: the key role of tumor-selective macromolecular drug targeting. Adv Enzyme Regul. 2001; (41): 189–207.
19. Haley B, Frenkel E. Nanoparticles for drug delivery in cancer treatment. Urologic Oncology: Seminars and Original Investigations. 2008; (26): 57–64.
20. Ланцова А. В. Создание и биотерапевтическое изучение липосомальных лекарственных форм противоопухолевых препаратов производных нитрозомочевины [диссертация]. М., 2006; 173 с.
21. Ланцова А. В., Оборотова Н. А. Перетолчина Н. М. Сравнительное изучение противоопухолевой активности липосомальных лекарственных форм препаратов производных нитрозоалкилмочевины. Сибирский онкологический журнал. 2005; 2 (14): 25–9.
22. Allen TM. Ligand-targeted therapeutics in anticancer therapy. Nat Rev Cancer. 2002; 2 (10): 750–63.
23. Толчева Е. В. Создание конструкции иммунолипосомы и изучение иммунолипосомальной формы противоопухолевого препарата доксорубицин [диссертация]. М., 2007; 109 с.
24. Соколова Д. В., Тазина Е. В., Кортава М. А. Анти-CD40 и анти-HLA-DR иммунолипосомальные формы доксорубицина: технология получения и антигенспецифичность in vivo. Российский биотерапевтический журнал. 2010; 9 (2): 90.
25. Соколова Д. В., Тазина Е. В., Кортава М. А. и др. Анти-MUC1 иммунолипосомальная форма доксорубицина: технология получения и антигенспецифичность in vitro. Российский биотерапевтический журнал. 2010; 9 (3): 21.
26. Хугаева О. В., Кортава М. А., Соколова Д. В. и др. Получение липосомального митоксантрона. Материалы IX Всеросс. науч.-практ. конф. «Отечественные противоопухолевые препараты». Российский биотерапевтический журнал. 2010; 9 (2): 91.
27. Насонов Е. Л. Перспективы применения ритуксимаба при аутоиммунных заболеваниях человека. Российский медицинский журнал. 2007; 15 (26): 1–6.
28. Соколова Д. В. Иммунолипосомальные конструкции доксорубицина и модели для их доклинического исследования [диссертация]. М., 2011; 122 с.
29. Kawakami S, Fumoto S, Nishikawa M et al. In vivo gene delivery to the liver using novel galactosylated cationic liposomes. Pharmaceuttic Research. 2000; 17 (3): 306–13.
30. Dass CR, Choong PFM. Targeting of small molecule anticancer drugs to the tumor and its vasculature using cationic liposomes: lessons from gene therapy. Cancer Cell Int. 2006; 6 (17): 1–9.
31. Ponce AM, Wright A, Dewhirst MW, Needham D. Targeted bioavailability of drugs by triggered release from liposomes. Future Lipidol. 2006; 1 (1): 25–34.
32. Jain S, Mishra V, Singh P et al. RGD-anchored magnetic liposomes for monocytes/neutrophils-mediated brain targeting. Int J Pharm. 2003; 261 (1–2): 43–55.
33. Qin J, Chen D, Hu H et al. Surface modification of RGD-liposomes for selective drug delivery to monocytes/Neutrophils in brain. Chem Pharm Bull. 2007; 55 (8): 1192–7.
34. Campbell RB, Fukumura D, Brown EB et al. Cationic charge determines the distribution of liposomes between the vascular and extravascular compartments of tumors. Cancer Res. 2002; (62): 6831–6.
35. Ambegia E, Ansell S, Cullis P et al. Stabilized plasmid-lipid particles containing PEG-diacylglycerols exhibit extended circulation lifetimes and tumor selective gene expression. Biochim Biophys Acta. 2005; 1669 (2): 155–63.
36. Dass CR. Improving anti-angiogenic therapy via selective delivery of cationic liposomes to tumor vasculature. Int J Pharm. 2003; 267 (1–2): 1–12.
37. Тазина Е. В., Мещерикова В. В., Игнатьева Е. В. и др. Биофармацевтические исследования термочувствительной липосомальной лекарственной формы доксорубицина. Российский биотерапевтический журнал. 2009; 1 (8): 40–7.
38. Huang Z, Szoka FC. Bioresponsive liposomes and their use for macromolecular delivery. In: G. Gregoriadis, editor. Liposome technology. 3rd edn. Vol. I. Liposome preparation and related techniques. New York: Informa Healthcare USA, 2007; p. 165–96.
39. Березов Т. Т., Яглова Н. В., Дмитриева Т. Б. и др. Направленный транспорт лекарственных средств с помощью липосом. Вестник РАМН. 2004; 5: 42–7.
40. Wu D, Pardridge WM. Neuroprotection with noninvasive neurotrophin delivery to the brain. Proc Natl Acad Sci USA. 1999; (96): 254–9.
41. Shi N, Pardridge WM. Noninvasive gene targeting to the brain. Proc Natl Acad Sci USA. 2000; 97 (13): 7567–72.
42. Pal A, Ahmad A, Khan S et al. Systemic delivery of RafsiRNA using cationic liposomes silences Raf in xenograft model of human prostate cancer. Int J Oncol. 2005; 26 (4): 1087–91.
43. Omidi Y, Barar J, Akhtar S. Toxicogenomics of cationic lipid-based vectors for gene therapy: impact of microarray. Curr Drug Del. 2005; 2 (4): 429–41.
44. Oliveira S, Storm G, Schiffelers. Targeted delivery of siRNA. J Biomed Biotechnol. 2006; (2006): 1–7.
45. Miyazaki M, Obata Y, Abe K et al. Gene transfer using nonviral delivery systems. Perit Dial Int. 2006; (26): 633–40.
46. Aguilar JC. Vaccine adjuvants revisited. Vaccine. 2007; (25): 3752–62.
47. Perrie Y, Frederik PM, Gregoriadis G. Liposome-mediated DNA vaccination: the effect of vesicle composition. Vaccine. 2001; (19): 3301–10.
48. Фармацевтическая разработка: концепция и практические рекомендации. В книге: Быковский С. Н., Василенко И. А., Демина Н. Б., Шохин И. Е., Новожилов О. В., Мешковский А. П., Спицкий О. Р., редакторы. Научно-практическое руководство для фармацевтической отрасли. М.: Перо, 2015; 472 с.
49. Lu D, Hickey AJ. Liposomal dry powders as aerosols for pulmonary delivery of proteins. AAPS Pharm Sci Tech. 2005; 6 (4): 641–8.
50. De Lima MCP, Simoes S, Pires P et al. Cationic lipid-DNA complexes in gene delivery: from biophysics to biological applications. Adv Drug Del Rev. 2001; (47): 277–94.

LIPIDOID IRON OXIDE NANOPARTICLES ARE A PLATFORM FOR NUCLEIC ACID DELIVERY TO THE LIVER

Uvarova VI[1,3] ✉, Nizamov TR[1], Abakumov MA[1], Vodopyanov SS[1], Abakumova TO[2], Saltykova IV[3], Mogilnikov PS[4], Shchetinin IV[4], Majouga AG[1,5]

[1] Laboratory of Biomedical Nanomaterials, National University of Science and Technology MISiS, Moscow

[2] Center of Life Science, Skolkovo Institute of Science and Technology, Moscow

[3] Laboratory of Tissue Specific Ligands Investigation, Lomonosov Moscow State University, Moscow

[4] Department of Physical Materials Science, National University of Science and Technology MISiS, Moscow

[5] Mendeleev University of Chemical Technology of Russia, Moscow

Targeted delivery of antisense drugs is a promising technology which can provide a platform for the development of highly effective therapeuticals against a broad range of diseases. Insufficient stability of RNA in biological media coupled with hydrophilicity that prevents the molecule from penetrating cell membranes considerably limit RNA application in clinical practice. The aim of this work was to design a system for antisense drug delivery to liver hepatocytes using lipidoid magnetic nanoparticles (LNP). Nanocubes (NC) with average sizes of 16 and 27 nm were synthesized through decomposition of iron (III) oleate under high temperature conditions and functionalized with a cationic lipidoid C12-200. Magnetic NC demonstrated good MR-contrasting properties. Biodistribution of LNP was studied *in vivo* in BALB/c mice using the MR scanner. Additionally, liver sections obtained from the mice were subjected to histological examination. Nanoparticles of smaller size did not have a cytotoxic effect on HepG2 and Huh7 cell lines, whereas for larger NC, IC_{50} was 21.5 μg/ml and 126 μg/ml for HepG2 and Huh7 cells, respectively. Smaller particles tended to accumulate in hepatocytes. Bigger NC mainly accumulated in the spleen but also ended up in liver macrophages. This fact can be explained by a bigger hydrodynamic size of nanoparticles with a bigger magnetic core. Particles with smaller cores are a more effective platform for the delivery of antisense drugs to hepatocytes.

Keywords: magnetic nanoparticles, MRI, lipids, targeted delivery

Funding: the study was funded by the Ministry of Science and Higher Education of the Russian Federation. Project 14.578.21.0201 (ID RFMEFI57816X0201).

✉ **Correspondence should be addressed:** Victoria I. Uvarova
Leninsky 4, Moscow, 119049; uvarova_viktoriya@bk.ru

Received: 26.06.2018 **Accepted:** 25.08.2018

DOI: 10.24075/brsmu.2018.080

ЛИПИДОПОДОБНЫЕ НАНОЧАСТИЦЫ ОКСИДА ЖЕЛЕЗА КАК ПЛАТФОРМА ДЛЯ ДОСТАВКИ НУКЛЕИНОВЫХ КИСЛОТ В ПЕЧЕНЬ

В. И. Уварова[1,3] ✉, Т. Р. Низамов[1], М. А. Абакумов[1], С. С. Водопьянов[1], Т. О. Абакумова[2], И. В. Салтыкова[3], П. С. Могильников[4], И. В. Щетинин[4], А. Г. Мажуга[1,5]

[1] Лаборатория биомедицинских наноматериалов, Национальный исследовательский технологический университет «МИСиС», Москва

[2] Центр наук о жизни, Сколковский институт науки и технологий, Москва

[3] Лаборатория тканеспецифических лигандов, Московский государственный университет имени М. В. Ломоносова, Москва

[4] Кафедра физического материаловедения, Национальный исследовательский технологический университет «МИСиС», Москва

[5] Российский химико-технологический университет имени Д. И. Менделеева, Москва

Адресная доставка антисмысловых препаратов является перспективной технологией, на основе которой возможна разработка высокоэффективных лекарственных средств для терапии широкого спектра заболеваний. Однако недостаточная стабильность РНК в биологических средах и гидрофильность, ограничивающая проникновение через клеточные мембраны, существенно сужают их использование в клинической практике. Целью исследования была разработка средств доставки антисмысловых препаратов в гепатоциты печени с помощью липидоподобных магнитных наночастиц (ЛНЧ). Кубические магнитные наночастицы (НЧ) со средними размерами 16 и 27 нм синтезировали методом высокотемпературного разложения прекурсора — олеата железа (III) и химически модифицировали формуляцией, включающей катионный липидоид С12-200. Магнитные НЧ обладают хорошими МРТ-контрастными свойствами, биораспределение ЛНЧ исследовали *in vivo* на линейных мышах BALB/c с помощью МР-томографа. С этой же целью провели последующее гистологическое исследование срезов печени. Наночастицы меньшего размера не продемонстрировали цитотоксического действия по отношению к клеточным линиям HepG2 и Huh7, а для НЧ кубической формы большего размера IC_{50} составила 21,5 мкг/мл для HepG2 и 126 мкг/мл для Huh7. Выявлено, что НЧ меньшего размера аккумулируются преимущественно в гепатоцитах печени, а НЧ большего размера — в селезенке, в печени же они накапливаются главным образом в макрофагах. Такая разница может быть вызвана большим гидродинамическим размером НЧ, которые имеют больший размер магнитного ядра. Образец с ядром меньшего размера является наиболее эффективной платформой для доставки антисмысловых препаратов в гепатоциты.

Ключевые слова: магнитные наночастицы, МРТ, липиды, адресная доставка

Финансирование: работа выполнена при поддержке Министерства образования и науки РФ, соглашение № 14.578.21.0201 (уникальный идентификатор RFMEFI57816X0201).

✉ **Для корреспонденции:** Виктория Игоревна Уварова
ул. Ленинский проспект, д. 4, г. Москва, 119049; uvarova_viktoriya@bk.ru

Статья получена: 26.06.2018 **Статья принята к печати:** 25.08.2018

DOI: 10.24075/vrgmu.2018.080

The term “hyperlipidemia” describes abnormally elevated levels of low-density lipoproteins and their metabolites in blood serum. Hyperlipidemia is a significant contributing factor in the risk of atherosclerosis and cardiovascular disorders [1], which, in turn, are a leading cause of death worldwide [2]. One of the approaches to treating this pathological condition is the silencing of genes responsible for elevated lipoproteins levels in plasma. [3, 4]. For example, lipoprotein levels can be lowered by inhibiting the synthesis of proteins participating in lipoprotein metabolism, such as angiopoietin-like protein 3 or apolipoproteins B and C3 produced by liver hepatocytes [5]. The major obstacles to safe and effective gene therapy aimed at reducing lipoprotein levels arise from the difficulties that complicate targeted delivery of antisense therapeutic agents to hepatocytes and the release of therapeutic agents from endocytic vesicles [6, 7].

Platforms for the delivery of antisense drugs are traditionally classified into viral and nonviral [8, 9]. Viruses effectively transport foreign genetic material to cells. However, intense debate is continuing about the safety of viral carriers: adenoviral vectors can induce a strong immune response and their retroviral counterparts pose a risk of insertional mutagenesis [10]. Nonviral delivery systems comprise vectors based on inorganic nanoparticles (NP) [11], liposomes [12, 13], and complexes with cationic lipids or polymers [14, 15].

Lipidoids are lipid-like materials holding great promise for effective targeted drug delivery. They can be used both as drug carriers and NP surface coatings for the subsequent loading of nucleic acids. RNA delivery systems based on the C12–200 lipidoid exhibit high efficacy in laboratory animals, including rodents and nonhuman primates [16]. Lipid nanoparticles need auxiliary components for better performance. Those include fusogenic phospholipids (DSPC), which improve transfection efficacy of the system by destabilizing the lipid bilayer of cell membranes, PEG lipids (mPEG2000-DMG), which reduce immune response by stabilizing LNP and protecting them from macrophages, and cholesterol, which fills the space between the lipid molecules on the NP surface and enhances the activity of cationic lipids [17].

Transfection methods vary greatly in their efficacy determined by the accuracy of drug delivery to a target cell, interactions between the carrier and the cell membrane and the release of the carrier from endosomes. Once endocytosed, nonviral vectors can get trapped by the endosomal compartment of the cell, suffering subsequent degradation of the therapeutic gene they carry [18]. New strategies are being sought to facilitate release of viral vectors from endosomes, which will naturally improve the efficacy of transfection.

Magnetic iron oxide NP offer a solution to the problem of poor transfection efficacy of nonviral vectors. Magnetite and maghemite nanoparticles have a few attractive properties beneficial for such biomedical applications as targeted drug delivery, magnetic hyperthermia, and contrast-enhanced MRI [19]. Importantly, magnetic NP can be used to attain controlled drug release in biological objects, including cells and experimental animals, made possible by the effect of Brownian relaxation, which in essence is intense oscillations of magnetic particles induced by a low-frequency magnetic field. This approach can significantly improve the efficacy of therapeutic agents: some researchers report that magnetic liposomes (liposomes enriched with magnetic NP) demonstrate better performance in the targeted delivery of doxorubicin and paclitaxel than their conventional counterparts [20, 21].

The functional properties of drug delivery systems based on magnetic NP are largely determined by their magnetic properties. For example, their suitability as contrast agents is influenced by their size and geometry [22].

In this study we attempted to design a platform for targeted delivery of antisense nucleic acids based on iron oxide nanocubes functionalized with a lipid formulation and to test the obtained carrier for the efficacy of drug delivery into hepatocytes *in vivo*.

METHODS

The following reagents were used: 1-octadecene, trioctylamine, dibenzyl ether, oleic acid, sodium oleate, iron oleate (III), anhydrous sodium acetate, cholesterol, 1,2-distearoyl-sn-glycero-3-phosphocholine (DSPC), 1,2-dimyristoyl-sn-glycero-3-methoxypolyethylene glycol monomethyl ether (DMG-mPEG), N-methyl-2-pyrrolidone (Sigma-Aldrich; USA), hydrochloric acid, nitric acid, ethanol, butanol-1, chloroform (SigmaTec; Russia), 1,1’-(2-(4-(2-((2-(bis(2-hydroxydodecyl)amino)ethyl)(2-hydroxydodecyl)amino)ethyl)piperazine-1-yl) ethylazanediyl) didodecane-2-ol (C12-200), DMEM and DMEM/F12, deionized water.

Cell cultures

The initial stock of Huh7 cells was provided by the Department of RNA Structure and Functions of A.N.Belozersky Research Institute of Physico-Chemical Biology. HepG2 cells were purchased from a cell bank (ATCC, HB-8065). Manipulations with the cells were carried out in the SafeFAST Elite 212 S sterile class II microbiological safety cabinet (Faster; Italy). The cells were cultured in the MCO-18AIC CO_2 Incubator (Sanyo; Japan) at 37 °C in 5% CO_2 environment. The culture medium for Huh7 cells was DMEM (Corning, catalog number 10-013-CV) supplemented with 4.5 g/l glucose, 10% fetal bovine serum and 4 mM L-glutamine. HepG2 cells were cultured in DMEM/F12 (Gibco™, catalog number 21331020) containing 10% fetal bovine serum and 4 mM L-glutamine.

Animal model

The experiments were carried out in adult female BALB/c mice (age of 6–7 weeks, weight of 19–20 g) purchased from the Central breeding nursery of the Academy of Medical Sciences (Andreevka; Russia) and kept in individually ventilated cages. The study was approved by the Ethics Committee of Pirogov Russian National Research Medical University (Protocol 1/2016 dated February 3, 2016).

Synthesis of lipidoid nanocubes

Precursor iron (III) oleate was synthesized following a protocol described in [23]. Magnetite nanocubes with an average size of 16 nm (CbS) were obtained through thermal decomposition of the precursor in a high-boiling organic solvent. The detailed description of the procedure is available in [24].

Nanocubes with an average size of 27 nm (CbB) were synthesized in two steps. In the first step, magnetic nuclei (seeds) were obtained as described above. In the second step, the precursor was introduced into the reaction mixture to stimulate NP growth. Briefly, 37.5 mg of the seeds, 0.35 g of sodium oleate and 0.32 g of oleic acid were loaded into a three-neck flask equipped with a mercury thermometer. Then, a solvent mix was added consisting of 2.85 g trioctylamine and 3.13 g of dibenzyl ether. The resulting mixture was heated to 110 °C under vigorous stirring under argon flow and maintained

under such conditions for 1 h. After that, the mixture was heated to a boiling temperature at a rate of 5 °C/min. Subsequently, 20 ml of 0.2 M iron (III) oleate solution in dibenzyl ether were added dropwise to the mixture at 3 ml/h, which was then left to boil for 20 min and cooled down to room temperature. The synthesized NP were separated from the reaction mixture by magnetic decantation in the presence of butanol-1. The precipitate was redispersed in chloroform and sonicated for 5-10 min.

The nanoparticles were coated with a lipidoid formulation using the phase transfer approach [25]. The coating consisted of the C12–200 lipidoid [26], cholesterol, DSPC and DMG-mPEG taken at a mass ratio of 75 : 15 : 7 : 3. The mass percent of the lipid formulation used to coat CbB and CbS was 0.9 and 1% (relative to magnetite), respectively.

Characterization of physical and chemical properties of the obtained nanoparticles

Transmission electron microscopy (TEM)

The obtained nanoparticles were imaged under the JEOL 1200-EX II transmission electron microscope (JEOL; Japan) operating at an accelerating voltage of 100 kV. Samples for TEM were prepared by applying 1–2 µl of the NP solution onto a formvar-coated copper mesh (d = 3.05 mm) that was subsequently left to air-dry. Further manipulations with images necessary to determine the distribution of NP sizes and characterize NP morphology was done in ImageJ ver. 1.50d (Wayne Rasband (NIH); USA).

X-ray diffraction analysis (XRD)

The crystalline structure of the particles was studied by X-ray diffraction on the DRON-4 diffractometer (Burevestnik; Russia) with the following settings: CoKα radiation with λ = 0.179 nm, tube voltage of 40 kV, and current of 30 mA. The samples were scanned through a range of diffraction angles 2θ from 20° to 120° by increments of 0.1°. Exposure time was 3 seconds per frame. Phases were identified by comparing the obtained data to the database of about 200,000 X-ray spectra in PHAN software.

Thermal gravimetric analysis and differential scanning calorimetry (TGA/DSC)

TGA and DSC were performed using the simultaneous thermal analyzer Netzsch STA 449 F3 (NETZSCH; Germany). The samples were placed into alundum crucibles and heated in the temperature range from 50 to 800 °C at 10 °C/min under argon flow. Before the analysis, solvents were removed from the samples by evaporation using a rotary evaporator.

Vibrating-sample magnetometry

Static magnetic properties of the nanoparticles were profiled by applying a range of magnetic fields from –20 to 20 kOe at 300 K. Measurements were done using the Quantum Design Physical Property Measurement System (PPMS; Germany) equipped with a vibrating sample magnetometer with an oscillation amplitude of 2 mm and frequency of 40 Hz. The sensitivity of the system was 10^{-6} emu.

Photon correlation spectroscopy (PCS)

The hydrodynamic sizes and ζ-potential (charge) of the particles coated with a lipid formulation were measured by PCS in 0.5 mg/ml LNP solutions in phosphate-buffered saline (1×PBS) or distilled water. The solutions were poured into plastic or glass cuvettes. The analysis was carried out at 25 °C using Zetasizer Nano ZS (Malvern; Germany). The ζ-potential of the particles was measured in distilled water using disposable capillary cuvettes for ζ-potential measurements.

Cytotoxicity of lipidoid nanoparticles *in vitro*

LNP cytotoxicity was assessed by the MTS-assay (3-(4,5-dimethylthiazol-2-yl)-5-(3-carboxymethoxyphenyl)-2-(4-sulfophenyl)-2H-tetrazolium) [27]. Human hepatocellular carcinoma cells (Huh7 and HepG2) were seeded onto 96-well plates at 5,000 cells per well and cultured at 37 °C in 5% CO_2 environment until 70% confluence of the monolayer was achieved, which took 48 hours. Then, CbS and CbB were introduced into the wells at magnetite concentrations of 370, 187, 94, 47, 23, 12, and 6 µg/ml and 420, 210, 105, 52, 26, 13, and 6 µg/ml, respectively. After that, the cells were incubated at 37 °C in 5% CO_2 for 24 h and washed. Then, the MTS reagent was added to the wells. Cells incubated in a culture medium supplemented with equivalent volumes of phosphate buffered saline (1×PBS) were used for control. Optical density was measured using the plate reader VictorX3 (PerkinElmer; USA) at λ = 490 nm. The proportion of the survived cells was calculated as a ratio of optical density of cells treated with nanoparticles to the optical density of untreated controls. Graphs were constructed and IC_{50} (half-maximal inhibitory concentration) was calculated in GraphPad Prism 8.0.0 (GraphPad Software; USA).

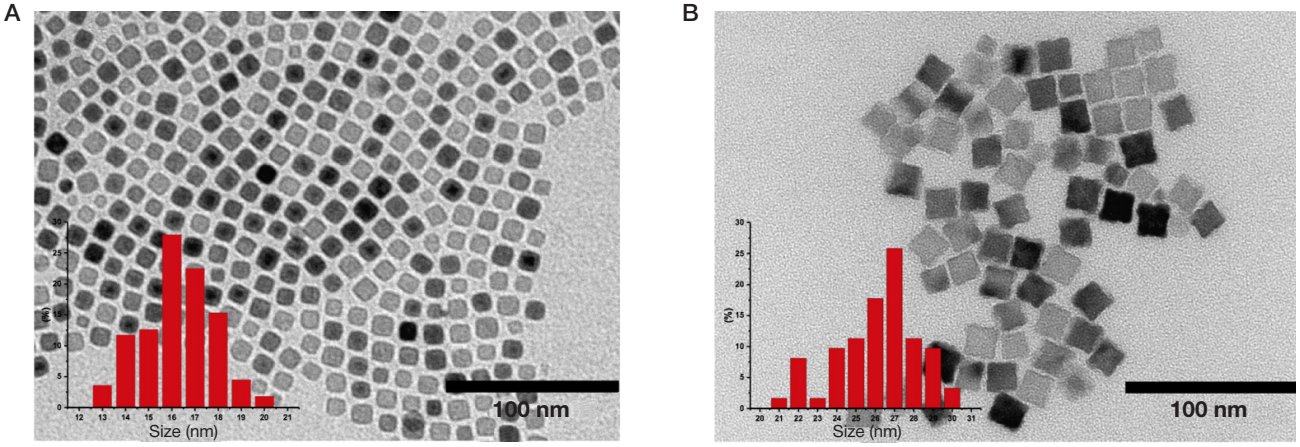

Fig. 1. A TEM image and a size distribution histogram of the magnetite nanoparticles: size range of 10 to 20 nm (**A**); size range of 20 to 30 nm (**B**)

Study of biodistribution of nanoparticles

Biodistribution of LNP was studied in BALB/c mice divided into 3 groups of 3. The animals from the experimental group received 120 µl of the LNP solution (an iron concentration of 720 µg/ml) intravenously. The control group did not receive any injections.

Studying the dynamics of LNP accumulation by MRI

The animals were scanned by the 7T animal MRI scanner ClinScan (Bruker Biospin; USA). Transverse T2-weighted images were obtained in the fat-suppression mode with the following Turbo Spin Echo (TSE) parameters: TR/TE = 2000/42 ms, slice thickness = 1 mm, matrix = 380 x 640, FOV = 34 x 60 mm. To assess the dynamics of NP accumulation, scans were performed before the LNP injection and 1, 12, 24, and 48 hours after it.

Histological examination

Forty-eight hours after the LNP injection, the animals were euthanized with a lethal dose of Zoletil® injected intraperitoneally. After the reflexes were gone, the abdominal cavity was opened by a midline incision. The rib cage was cut laterally on both sides, perpendicular to the rib bones. The right atrium was dissected and perfused with 40 ml of PBS. The solution was supplied through a needle introduced into the left ventricle and attached to a Janet's syringe via a cannula. Then the cervical vertebrae were dislocated and the organs were excised, including the liver, spleen, kidneys, and lungs. The removed organs were submerged in 4% paraformaldehyde and stored at 4 °C until further analysis. Sixty-µm-thick slices were prepared using the Thermo Scientific Microm HM 650 V Vibration system (Thermo Fisher Scientific; USA) and Perls-stained using the Iron Stain Kit (Sigma-Aldrich; USA). Perls staining involves treating histological slices with a mixture of hydrochloric acid and potassium hexacyanoferrate (II). The reaction between the mixture and the deposits of iron compounds in a histological slice produces a Prussian blue pigment. Its granules of different shades of blue can be seen under a light microscope. The samples were washed in distilled water twice, incubated in 70% glycerol and imaged under a light microscope by Carl Zeiss (Germany) equipped with Axioplan 2 Imaging camera.

Biodistribution of iron in the internal organs of mice assessed by inductively coupled plasma atomic emission spectroscopy (AES)

Paraformaldehyde-fixed organ fragments (one-third of the liver and spleen, one kidney, one lung and a half of the heart) were dissolved in 2 ml of a freshly prepared mix consisting of 1,500 µl of concentrated hydrochloric acid (HCl) and 500 µl of nitric acid (HNO_3). The fragments were incubated in the acid mix for 24 h. Then, water was added to bring the volume of the dissolved liver and spleen to 20 ml and of the heart, kidney and lung, to 10 ml. After the calibration curve was constructed, iron concentrations were measured in the obtained solutions using the 4200 MP–AES machine (Agilent Technologies; USA).

RESULTS

TEM images of monodisperse nanocubes with an average size of 16 nm (CbS) and histograms of their size distribution are presented in Fig. 1A. TEM images of bigger nanocubes (CbB) sized 20–30 nm show that CbB samples have distinct morphology and a well-faceted cubic shape (Fig. 1 B).

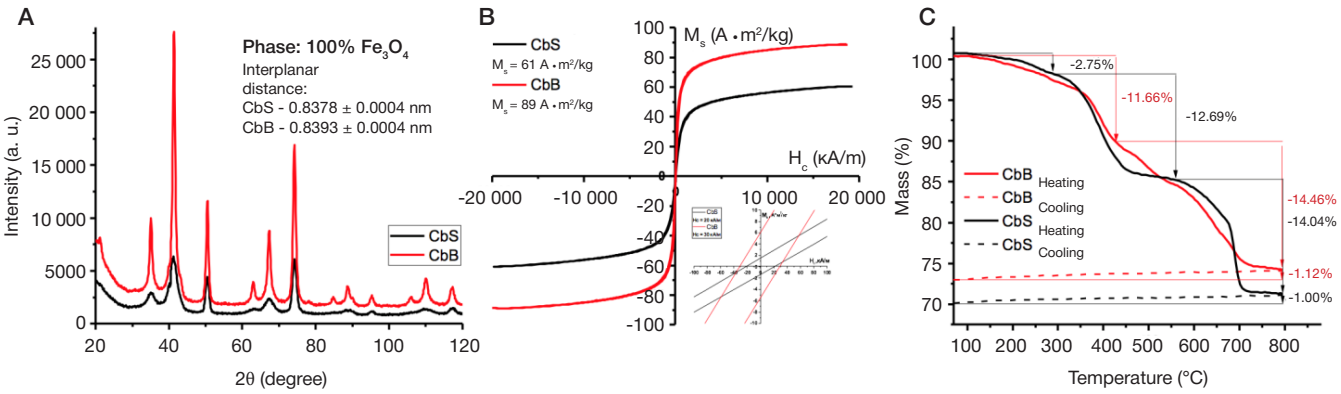

Fig. 2. Physical and chemical properties of nanocubes: X-ray diffraction analysis (**A**); hysteresis loops (**B**); TGA/DSC (**C**)

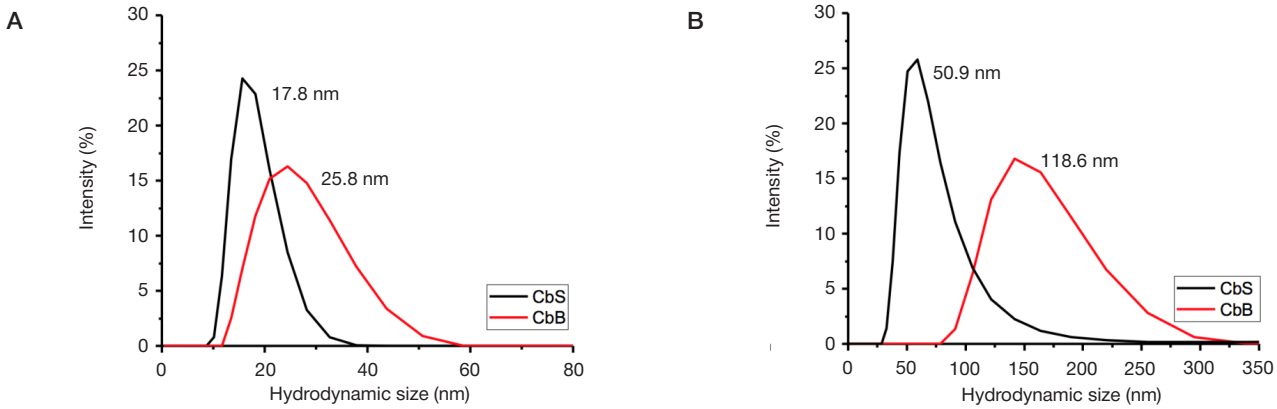

Fig. 3. A. Hydrodynamic size of uncoated nanocubes in chloroform. **B**. Hydrodynamic size of lipid-coated nanoclusters in water

X-ray diffraction analysis yielded very similar results for both CbS and CbB samples: the positions of diffraction peaks in the diffraction pattern correspond to the inverse spinel structure of magnetite with lattice constants of 0.838 nm and 0.839 nm for CbS and CbB, respectively (Fig. 2A). Hysteresis loops (Fig. 2 B) indicate that CbS and CbB are ferrimagnetic materials with coercivity of 20–30 kA/m. Magnetic saturation (Ms) of CbS is 61 A • m^2/kg. Large nanocubes (CbB) have Ms of 89 A • m^2/kg. In our study, magnetic saturation was normalized to the amount of the iron oxide phase (minus the mass of organic stabilizers) determined by TGA/DSC (Fig. 2C).

The TG curve constructed for CbS has three regions indicating abrupt weight loss: the first recorded at 150–300 °C corresponds to the desorption of organic compounds noncovalently bound to the surface of NP; the second recorded at 300–450 °C corresponds to the desorption of covalently bound stabilizers; the third recorded over a temperature range of 600–700 °C occurs when magnetite undergoes phase transition. The region of the CbB TG curve showing desorption of covalently and noncovalently bound organic molecules looks smoother; phase transition is observed at temperatures over 500 °C.

Nanocubes with hydrophobic residues of oleic acid on their surface can be dispersed in nonpolar organic solvents (chloroform, hexane) and can be regarded as a colloid system resistant to sedimentation. The average hydrodynamic size of CbS and CbB in chloroform is shown in Fig. 3A. The polydispersity index (PdI) is 0.113 and 0.151 for NP with an actual average sample of 16 and 27 nm, respectively. To stimulate the phase transfer of magnetite NP to an aqueous phase, the particles were coated with a lipid formulation consisting of the lipidoid C12-200, cholesterol, DSPC, and 1,2-DMG-mPEG taken at a mass ratio of 75 : 15 : 7 : 3. The average hydrodynamic size of the coated CbS in the aqueous phase increased to 50.9 nm (PdI = 0.119) (Fig. 3B). Based on the size distribution pattern, we inferred that the majority of CbS nanocubes were present in the solution as individual particles, while the minority tended to aggregate into clusters. The pattern of CbB size distribution was completely opposite: the average hydrodynamic size of CbB particles was 118.6 nm (PdI = 0.201) (Fig. 3B), which is 4 times bigger than their actual size, suggesting more vigorous aggregation of nanocubes functionalized with lipids. The value of the ζ-potential of magnetite-based LNP in water was positive and equaled +20.5 mV and +34.3 mV for CbB and CbS, respectively.

The survival of HepG2 and Huh7 cells incubated with CbS and CbB is shown in Fig.4. Using the MTS assay, we calculated IC50 for CbB: it was 21.5 μkg/ml (magnetite concentration) for HepG2 and 126 μkg/ml, which is 6 times higher, for Huh7. CbS did not exhibit any cytotoxic activity at studied concentrations.

Fig. 5A features representative T2-weighted coronal images that clearly show that the most pronounced NP accumulation could be observed in the liver and spleen of the experimental mice 0–48 h after the intravenous injection of the formulation. The accumulation of both CbS and CbB was noticeable as early as 1 hour after the injection and its level remained stable for the next 48 hours. This suggests that intravenously injected NP are readily taken up by the liver and spleen. It should be born in mind, though, that MRI is a semi-quantitative modality and cannot be used to conclusively distinguish between the accumulation patterns of different NP types in different organs. Therefore, we additionally employed AES to study iron accumulation in the internal organs of the experimental mice (Fig. 5B). AES revealed that LNP tended to be sequestered mostly by the liver and spleen, which was consistent with MRI findings (Fig. 5A). LNP deposition in other organs was negligible. The CbS sample accumulated in the liver most effectively: the liver retained 84% of the injected LNP amount, whereas CbB

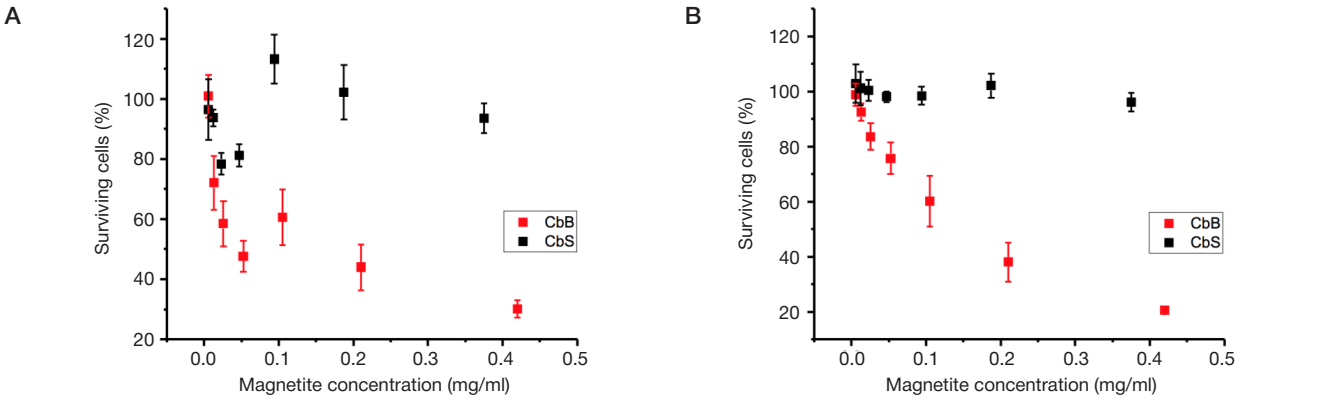

Fig. 4. Cytotoxicity of different concentrations of lipidoid-coated CbS and CbB nanoclusters with magnetic core against HepG2 (**A**) and Huh7 (**B**) cell lines

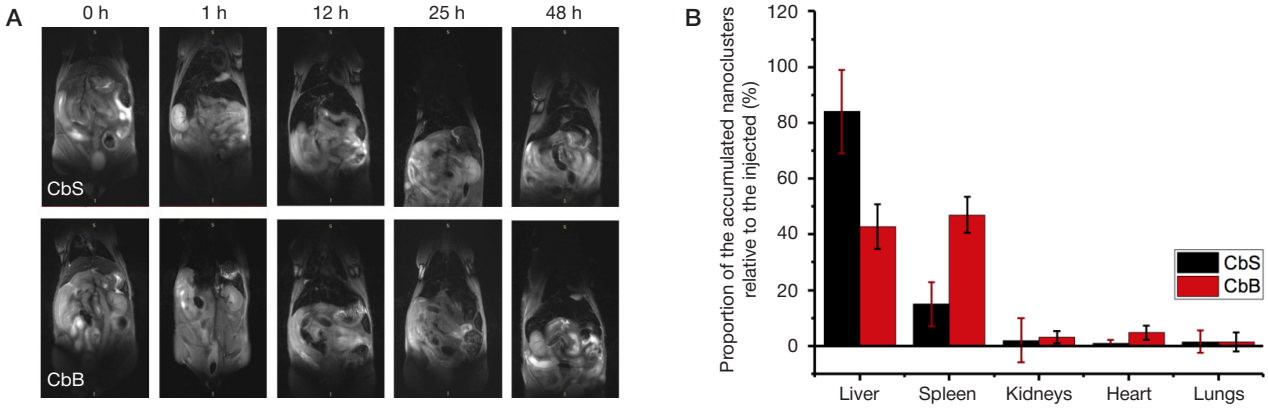

Fig. 5. Distribution of magnetic core CbS and CbB nanoclusters in the liver and spleen visualized by MRI (**A**); in all studied internal organs measured by AES (**B**)

Fig. 6. Distribution of magnetic core CbS and CbB nanoclusters in liver cells (Perls reaction)

showed poor accumulation in this organ (only 43% of the injected LNP amount).

The images of Perls-stained liver slices clearly demonstrate that both types of iron-based NP increasingly build up in the liver in comparison with the controls (Fig. 6). There was a difference in the pattern of iron accumulation between the CbS and CbB samples. CbS diffusely spread in the liver parenchyma (presumably, depositing in hepatocytes), whereas CbB exhibited a mixed discoloration pattern: some of the particles deposited in irregular-shaped cells (presumably, macrophages) lying at the border between the sinusoids and the parenchyma, and some produced diffuse discoloration evident of their buildup in hepatocytes.

DISCUSSION

The classic process of NP growth can be broken down into 3 stages: in the first stage, the precursor — iron (III) oleate — decomposes producing unstable iron-organic intermediates until their critical concentration is reached necessary for nucleation. In the second stage, the concentration of the intermediates declines as these molecules attach to the surface of magnetic seeds stimulating their growth. In the last stage, the concentration of the intermediates drops to thermodynamically stable levels, and the generated NP undergo Ostwald ripening. A steady rate of NP growth can be maintained by the controlled addition of a precursor, making NP expand in size while retaining their monodispersity. Using this approach, one can synthesize NP with a programmed size (as large as required) characterized by low polydispersity, which is particularly important for the particles with dimensions over 20 nm. When added to the reaction mixture, a stabilizer (potassium oleate) that can be specifically adsorbed onto the plane (111) promotes formation of cube-shaped nanoparticles (Fig. 1B). In our study, the rate at which the precursor was supplied to the mixture in the second stage of synthesis, its concentration and duration of its addition were determined experimentally. At low rates, NP underwent Ostwald ripening: the mass was transferred from small particles to large, promoting polydispersity. At high rates, the concentration of intermediates in the reaction mixture surged triggering the mechanism of primary nucleation and increasing NP polydispersity.

For both samples, the results of the conducted X-ray diffraction analysis are consistent with the literature [28].

For CbS, magnetic saturation (Ms) agrees with the values reported for average-sized magnetite NP comparable in their dimensions with CbS particles [23, 29]. The Ms of large cube-shaped NP (CbB) was very high and comparable to that of a massive sample [30] or huge NP [31].

According to the results of the TGA/DSC analysis (Fig. 2C), the amount of the organic phase adsorbed onto the surface of iron oxide NP constitutes 15.5% of the total CbS and 11.7% of the total CbB masses. For samples with similar masses, an increase in the average size of NP entails an increase in the ratio of their surface area to their volume. The process yields more stabilizing molecules that can be adsorbed onto the NP surface. This significantly affects the stability of the studied colloidal system largely determined by 2 factors: steric stabilization ensured by the presence of long hydrophobic residues of oleic acid adsorbed onto the surface of NP and the aggregation of those residues caused by mutual magnetism. As the magnetic core grows, the PdI of the CbB sample increases (as demonstrated by PCS) and the peak of its hydrodynamic size broadens, as compared to CbS, suggesting more vigorous clusterization of the particles resulting from the magnetic core growth, which, in turn, is caused by intense magnetic interactions.

The hydrodynamic size of NP and the physical and chemical properties of their surface largely determine the pattern of intercellular interactions, endocytic routes and the efficacy of NP uptake by the cell [32, 33]. The internalization of NP into cells causes disorganization of the cytoskeleton [34, 35]. When accumulated in abundance, NP induce disruption of the actin and microtubule networks in neural progenitor cells of mice and primary endothelial cells of human blood vessels [36]. We hypothesized that the mere physical presence of sufficient amounts of NP captured by large lysosomal structures normally found near the nucleus sterically impairs the function of the cytoskeleton and causes reorganization of the actin network. The results of cytotoxicity tests correlate well with a hypothesis that establishes a link between the disruption of the cytoskeleton and NP toxicity: the studied concentrations of the CbB sample, whose actual size was 1.7 bigger than that of CbS, were toxic against the used cell lines, unlike CbS, whose phase composition, coating and morphology were similar.

The initial characteristics of magnetic NP, including size and shape homogeneity, resistance to aggregation, and stability of the coating, are key to the pharmacokinetics and biodistribution of the particles. It is well known that NP with the hydrodynamic size of less than 20–30 nm are filtered by renal glomeruli and those over 200 nm in size build up in the liver [37]. Nanoparticles with the dimensions between 30 and 200 nm are normally sequestered in the liver: they can be easily captured by endocytic vesicles with an average diameter of 40-60 nm. However, particles over 150 nm in size (the upper limit for entering the cell through caveolae) are engulfed by macrophages. Therefore, an ideal hydrodynamic LNP size to be taken up by the liver would be 30 to 150 nm. The histological examination and the analysis of NP biodistribution in the organs of mice reveal that the CbB particles are mainly accumulated in the reticuloendothelial system, which explains the even distribution of NP between the liver and spleen. These findings correlate well with other studies [38]. In contrast, the CbS sample is not sequestered in macrophages but is caught by hepatocytes instead, leading to its buildup in the liver. This fact is consistent with the literature describing the behavior of

NP with a magnetic core of a comparable size [39]. Perhaps, larger nanocubes (CbB) grow in size when introduced into the bloodstream of a mouse because they adsorb serum proteins on the surface which form a crown of biomolecules [40], thereby increasing the hydrodynamic size of NP; as a result, the latter accumulate in the spleen.

CONCLUSIONS

The proposed platform for the delivery of antisense drugs into liver hepatocytes has proved to be effective both *in vivo* and *in vitro*. The synthesized CbS lipid-coated nanoparticles exhibit low toxicity against Huh7 and HepG2 cell lines. The analysis of *in vivo* biodistribution of differently sized LNP with magnetic cores reveals significant accumulation of the particles in the liver as early as 1 hour after the injection. The level of accumulation remained stable for 48 hours following the injection. Nanocubes with magnetic iron oxide cores sized 10 to 20 nm and a hydrodynamic size of <100 nm increasingly accumulated in hepatocytes (>80% of the injected dose) whereas larger NP were readily taken up by Kupffer cells and other components of the reticuloendothelial system.

References

1. Wouters K, Shiri-Sverdlov R, van Gorp PJ, van Bilsen M, Hofker MH. Understanding hyperlipidemia and atherosclerosis: lessons from genetically modified apoe and ldlr mice. Clin Chem Lab Med [Internet]. 2005 [cited 2017 Oct 28]; 43 (5): 470–9. Available from: http://www.ncbi.nlm.nih.gov/pubmed/15899668.
2. Pagidipati NJ, Gaziano TA. Estimating Deaths From Cardiovascular Disease: A Review of Global Methodologies of Mortality Measurement. Circulation. 2013; 127 (6): 749–56.
3. Sullenger BA, Nair S. From the RNA world to the clinic. Science 17. 2016; 352 (6292): 1417–20.
4. McClorey G, Wood MJ. An overview of the clinical application of antisense oligonucleotides for RNA-targeting therapies. Curr Opin Pharmacol. 2015; (24): 52–8.
5. Kulkarni JA, Cullis PR, van der Meel R. Lipid Nanoparticles Enabling Gene Therapies: From Concepts to Clinical Utility. Nucleic Acid Ther. 2018; 28 (3): 146–57.
6. Mahajan UM, Teller S, Sendler M, Palankar R, van den Brandt C, Schwaiger T et al. Tumour-specific delivery of siRNA-coupled superparamagnetic iron oxide nanoparticles, targeted against PLK1, stops progression of pancreatic cancer. Gut. 2016; 65 (11): 1838–49.
7. Kim M-C, Lin MM, Sohn Y, Kim J-J, Kang BS, Kim DK. Polyethyleneimine-associated polycaprolactone-Superparamagnetic iron oxide nanoparticles as a gene delivery vector. J Biomed Mater Res Part B Appl Biomater. 2017; 105 (1): 145–54.
8. Nayerossadat N, Ali P, Maedeh T. Viral and nonviral delivery systems for gene delivery. Adv Biomed Res. 2012; 1 (1): 27.
9. Yang N. An overview of viral and nonviral delivery systems for microRNA. Int J Pharm Investig. 2015; 5 (4): 179.
10. Nayak S, Herzog RW. Progress and prospects: immune responses to viral vectors. Gene Ther. 2010; 17 (3): 295–304.
11. Qiu J, Kong L, Cao X, Li A, Wei P, Wang L et al. Enhanced Delivery of Therapeutic siRNA into Glioblastoma Cells Using Dendrimer-Entrapped Gold Nanoparticles Conjugated with β-Cyclodextrin. Nanomaterials. 2018; 8 (3): 131.
12. Singh Y, Tomar S, Khan S, Meher JG, Pawar VK, Raval K et al. Bridging small interfering RNA with giant therapeutic outcomes using nanometric liposomes. J Control Release. 2015; (220): 368–87.
13. Leung AK, Tam YY, Cullis PR. Lipid Nanoparticles for Short Interfering RNA Delivery. Adv Genet. 2014; (88): 71–110.
14. Nakamura T, Yamada K, Fujiwara Y, Sato Y, Harashima H. Reducing the Cytotoxicity of Lipid Nanoparticles Associated with a Fusogenic Cationic Lipid in a Natural Killer Cell Line by Introducing a Polycation-Based siRNA Core. Mol Pharm. 2018; 15 (6): 2142–50.
15. Jin M, Jin G, Kang L, Chen L, Gao Z, Huang W. Smart polymeric nanoparticles with pH-responsive and PEG-detachable properties for co-delivering paclitaxel and survivin siRNA to enhance antitumor outcomes. Int J Nanomedicine. 2018; (13): 2405.
16. Novobrantseva TI, Borodovsky A, Wong J, Klebanov B, Zafari M, Yucius K et al. Systemic RNAi-mediated Gene Silencing in Nonhuman Primate and Rodent Myeloid Cells. Mol Ther Nucleic Acids. 2012; (1): e4.
17. Kumar V, Qin J, Jiang Y, Duncan RG, Brigham B, Fishman S et al. Shielding of Lipid Nanoparticles for siRNA Delivery: Impact on Physicochemical Properties, Cytokine Induction, and Efficacy. Mol Ther Nucleic Acids. 2014; (3): e210.
18. Alshehri A, Grabowska A, Stolnik S. Pathways of cellular internalisation of liposomes delivered siRNA and effects on siRNA engagement with target mRNA and silencing in cancer cells. Sci Rep. 2018; 8 (1): 3748.
19. Soenen SJ, Hodenius M, De Cuyper M. Magnetoliposomes: versatile innovative nanocolloids for use in biotechnology and biomedicine. Nanomedicine. 2009; 4 (2): 177–91.
20. Dobson J. Magnetic nanoparticles for drug delivery. Drug Dev Res [Internet]. 2006 [cited 2017 Sep 18]; 67(1): 55–60. Available from: http://onlinelibrary.wiley.com/doi/10.1002/ddr.20067/abstract.
21. Zhang JQ, Zhang ZR, Yang H, Tan QY, Qin SR, Qiu XL. Lyophilized paclitaxel magnetoliposomes as a potential drug delivery system for breast carcinoma via parenteral administration: in vitro and in vivo studies. Pharm Res [Internet]. 2005 [cited 2017 Sep 18]; 22 (4): 573–83. Available from: http://www.ncbi.nlm.nih.gov/pubmed/15846465.
22. Yang L, Wang Z, Ma L, Li A, Xin J, Wei R et al. The Roles of Morphology on the Relaxation Rates of Magnetic Nanoparticles. ACS Nano. 2018; 12 (5): 4605–14.
23. Bronstein LM, Huang X, Retrum J, Schmucker A, Pink M, Stein BD et al. Influence of Iron Oleate Complex Structure on Iron Oxide Nanoparticle Formation. 2007 [cited 2017 Dec 16]; 19 (15): 3624–32. Available from: http://pubs.acs.org/doi/abs/10.1021/cm062948j.
24. Hai HT, Yang HT, Kura H, Hasegawa D, Ogata Y, Takahashi M et al. Size control and characterization of wustite (core)/spinel (shell) nanocubes obtained by decomposition of iron oleate complex. J Colloid Interface Sci [Internet]. 2010; 346 (1): 37–42. Available from: http://dx.doi.org/10.1016/j.jcis.2010.02.025.
25. Jiang S, Eltoukhy A, Love K, Langer R, Anderson D. Lipidoid-Coated Iron Oxide Nanoparticles for Efficient DNA and siRNA delivery. Nano Lett [Internet]. 2013; 1–6. Available from: citeulike-article-id:12014954%5Cnhttp://dx.doi.org/10.1021/nl304287a.
26. Love KT, Mahon KP, Levins CG, Whitehead KA, Querbes W, Dorkin JR et al. Lipid-like materials for low-dose, in vivo gene silencing. Proc Natl Acad Sci. 2010; 107 (5): 1864–9.
27. Mosmann T. Rapid colorimetric assay for cellular growth and survival: Application to proliferation and cytotoxicity assays. J Immunol Methods. 1983; 65 (1–2): 55–63.
28. Mamani JB, Costa-Filho AJ, Cornejo DR, Vieira ED, Gamarra LF. Synthesis and characterization of magnetite nanoparticles coated with lauric acid. Mater Charact. 2013; (81): 28–36.
29. Nemati Z, Das R, Alonso J, Clements E, Phan MH, Srikanth H. Iron Oxide Nanospheres and Nanocubes for Magnetic Hyperthermia Therapy: A Comparative Study. J Electron Mater [Internet]. 2017 [cited 2017 Dec 16]; 46 (6): 3764–9. Available from: http://link.springer.com/10.1007/s11664-017-5347-6.
30. Cullity BD, Graham CD. Introduction to magnetic materials. 2nd ed. Hoboken, NJ: IEEE/Wiley, 2009; 544 p.
31. Marciello M, Connord V, Veintemillas-Verdaguer S, Vergés MA, Carrey J, Respaud M, et al. Large scale production of biocompatible

magnetite nanocrystals with high saturation magnetization values through green aqueous synthesis. J Mater Chem B. 2013; 1 (43): 5995–6004.
32. Verma A, Stellacci F. Effect of Surface Properties on Nanoparticle–Cell Interactions. Small. 2010; 6 (1): 12–21.
33. Adler AF, Leong KW. Emerging links between surface nanotechnology and endocytosis: Impact on nonviral gene delivery. Nano Today. 2010; 5 (6): 553–69.
34. Gupta AK, Gupta M. Cytotoxicity suppression and cellular uptake enhancement of surface modified magnetic nanoparticles. Biomaterials [Internet]. 2005 [cited 2017 Jun 9]; 26 (13): 1565–73. Available from: http://www.ncbi.nlm.nih.gov/pubmed/15522758.
35. Gupta AK, Curtis AS. Lactoferrin and ceruloplasmin derivatized superparamagnetic iron oxide nanoparticles for targeting cell surface receptors. Biomaterials. 2004; 25 (15): 3029–40.
36. Soenen SJH, Nuytten N, De Meyer SF, De Smedt SC, De Cuyper M. High Intracellular Iron Oxide Nanoparticle Concentrations Affect Cellular Cytoskeleton and Focal Adhesion Kinase-Mediated Signaling. Small. 2010; 6 (7): 832–42.
37. Berry CC. Progress in functionalization of magnetic nanoparticles for applications in biomedicine. J Phys D Appl Phys. 2009; 42 (22): 224003.
38. Zhang J, Ring HL, Hurley KR, Shao Q, Carlson CS, Idiyatullin D et al. Quantification and biodistribution of iron oxide nanoparticles in the primary clearance organs of mice using T1 contrast for heating. Magn Reson Med [Internet]. 2017 [cited 2017 Dec 22]; 78 (2): 702–12. Available from: http://www.ncbi.nlm.nih.gov/pubmed/27667655.
39. Bargheer D, Giemsa A, Freund B, Heine M, Waurisch C, Stachowski GM et al. The distribution and degradation of radiolabeled superparamagnetic iron oxide nanoparticles and quantum dots in mice. Beilstein J Nanotechnol. 2015; (6): 111–23.
40. Ruiz A, Hernández Y, Cabal C, González E, Veintemillas-Verdaguer S, Martínez E, et al. Biodistribution and pharmacokinetics of uniform magnetite nanoparticles chemically modified with polyethylene glycol. Nanoscale. 2013; 5 (23): 11400–8.

Литература

1. Wouters K, Shiri-Sverdlov R, van Gorp PJ, van Bilsen M, Hofker MH. Understanding hyperlipidemia and atherosclerosis: lessons from genetically modified apoe and ldlr mice. Clin Chem Lab Med [Internet]. 2005 [cited 2017 Oct 28]; 43 (5): 470–9. Available from: http://www.ncbi.nlm.nih.gov/pubmed/15899668.
2. Pagidipati NJ, Gaziano TA. Estimating Deaths From Cardiovascular Disease: A Review of Global Methodologies of Mortality Measurement. Circulation. 2013; 127 (6): 749–56.
3. Sullenger BA, Nair S. From the RNA world to the clinic. Science 17. 2016; 352 (6292): 1417–20.
4. McClorey G, Wood MJ. An overview of the clinical application of antisense oligonucleotides for RNA-targeting therapies. Curr Opin Pharmacol. 2015; (24): 52–8.
5. Kulkarni JA, Cullis PR, van der Meel R. Lipid Nanoparticles Enabling Gene Therapies: From Concepts to Clinical Utility. Nucleic Acid Ther. 2018; 28 (3): 146–57.
6. Mahajan UM, Teller S, Sendler M, Palankar R, van den Brandt C, Schwaiger T et al. Tumour-specific delivery of siRNA-coupled superparamagnetic iron oxide nanoparticles, targeted against PLK1, stops progression of pancreatic cancer. Gut. 2016; 65 (11): 1838–49.
7. Kim M-C, Lin MM, Sohn Y, Kim J-J, Kang BS, Kim DK. Polyethyleneimine-associated polycaprolactone-Superparamagnetic iron oxide nanoparticles as a gene delivery vector. J Biomed Mater Res Part B Appl Biomater. 2017; 105 (1): 145–54.
8. Nayerossadat N, Ali P, Maedeh T. Viral and nonviral delivery systems for gene delivery. Adv Biomed Res. 2012; 1 (1): 27.
9. Yang N. An overview of viral and nonviral delivery systems for microRNA. Int J Pharm Investig. 2015; 5 (4): 179.
10. Nayak S, Herzog RW. Progress and prospects: immune responses to viral vectors. Gene Ther. 2010; 17 (3): 295–304.
11. Qiu J, Kong L, Cao X, Li A, Wei P, Wang L et al. Enhanced Delivery of Therapeutic siRNA into Glioblastoma Cells Using Dendrimer-Entrapped Gold Nanoparticles Conjugated with β-Cyclodextrin. Nanomaterials. 2018; 8 (3): 131.
12. Singh Y, Tomar S, Khan S, Meher JG, Pawar VK, Raval K et al. Bridging small interfering RNA with giant therapeutic outcomes using nanometric liposomes. J Control Release. 2015; (220): 368–87.
13. Leung AK, Tam YY, Cullis PR. Lipid Nanoparticles for Short Interfering RNA Delivery. Adv Genet. 2014; (88): 71–110.
14. Nakamura T, Yamada K, Fujiwara Y, Sato Y, Harashima H. Reducing the Cytotoxicity of Lipid Nanoparticles Associated with a Fusogenic Cationic Lipid in a Natural Killer Cell Line by Introducing a Polycation-Based siRNA Core. Mol Pharm. 2018; 15 (6): 2142–50.
15. Jin M, Jin G, Kang L, Chen L, Gao Z, Huang W. Smart polymeric nanoparticles with pH-responsive and PEG-detachable properties for co-delivering paclitaxel and survivin siRNA to enhance antitumor outcomes. Int J Nanomedicine. 2018; (13): 2405.
16. Novobrantseva TI, Borodovsky A, Wong J, Klebanov B, Zafari M, Yucius K et al. Systemic RNAi-mediated Gene Silencing in Nonhuman Primate and Rodent Myeloid Cells. Mol Ther Nucleic Acids. 2012; (1): e4.
17. Kumar V, Qin J, Jiang Y, Duncan RG, Brigham B, Fishman S et al. Shielding of Lipid Nanoparticles for siRNA Delivery: Impact on Physicochemical Properties, Cytokine Induction, and Efficacy. Mol Ther Nucleic Acids. 2014; (3): e210.
18. Alshehri A, Grabowska A, Stolnik S. Pathways of cellular internalisation of liposomes delivered siRNA and effects on siRNA engagement with target mRNA and silencing in cancer cells. Sci Rep. 2018; 8 (1): 3748.
19. Soenen SJ, Hodenius M, De Cuyper M. Magnetoliposomes: versatile innovative nanocolloids for use in biotechnology and biomedicine. Nanomedicine. 2009; 4 (2): 177–91.
20. Dobson J. Magnetic nanoparticles for drug delivery. Drug Dev Res [Internet]. 2006 [cited 2017 Sep 18]; 67(1): 55–60. Available from: http://onlinelibrary.wiley.com/doi/10.1002/ddr.20067/abstract.
21. Zhang JQ, Zhang ZR, Yang H, Tan QY, Qin SR, Qiu XL. Lyophilized paclitaxel magnetoliposomes as a potential drug delivery system for breast carcinoma via parenteral administration: in vitro and in vivo studies. Pharm Res [Internet]. 2005 [cited 2017 Sep 18]; 22 (4): 573–83. Available from: http://www.ncbi.nlm.nih.gov/pubmed/15846465.
22. Yang L, Wang Z, Ma L, Li A, Xin J, Wei R et al. The Roles of Morphology on the Relaxation Rates of Magnetic Nanoparticles. ACS Nano. 2018; 12 (5): 4605–14.
23. Bronstein LM, Huang X, Retrum J, Schmucker A, Pink M, Stein BD et al. Influence of Iron Oleate Complex Structure on Iron Oxide Nanoparticle Formation. 2007 [cited 2017 Dec 16]; 19 (15): 3624–32. Available from: http://pubs.acs.org/doi/abs/10.1021/cm062948j.
24. Hai HT, Yang HT, Kura H, Hasegawa D, Ogata Y, Takahashi M et al. Size control and characterization of wustite (core)/spinel (shell) nanocubes obtained by decomposition of iron oleate complex. J Colloid Interface Sci [Internet]. 2010; 346 (1): 37–42. Available from: http://dx.doi.org/10.1016/j.jcis.2010.02.025.
25. Jiang S, Eltoukhy A, Love K, Langer R, Anderson D. Lipidoid-Coated Iron Oxide Nanoparticles for Efficient DNA and siRNA delivery. Nano Lett [Internet]. 2013; 1–6. Available from: citeulike-article-id:12014954%5Cnhttp://dx.doi.org/10.1021/nl304287a.
26. Love KT, Mahon KP, Levins CG, Whitehead KA, Querbes W, Dorkin JR et al. Lipid-like materials for low-dose, in vivo gene silencing. Proc Natl Acad Sci. 2010; 107 (5): 1864–9.
27. Mosmann T. Rapid colorimetric assay for cellular growth and

survival: Application to proliferation and cytotoxicity assays. J Immunol Methods. 1983; 65 (1–2): 55–63.
28. Mamani JB, Costa-Filho AJ, Cornejo DR, Vieira ED, Gamarra LF. Synthesis and characterization of magnetite nanoparticles coated with lauric acid. Mater Charact. 2013; (81): 28–36.
29. Nemati Z, Das R, Alonso J, Clements E, Phan MH, Srikanth H. Iron Oxide Nanospheres and Nanocubes for Magnetic Hyperthermia Therapy: A Comparative Study. J Electron Mater [Internet]. 2017 [cited 2017 Dec 16]; 46 (6): 3764–9. Available from: http://link.springer.com/10.1007/s11664-017-5347-6.
30. Cullity BD, Graham CD. Introduction to magnetic materials. 2nd ed. Hoboken, NJ: IEEE/Wiley, 2009; 544 p.
31. Marciello M, Connord V, Veintemillas-Verdaguer S, Vergés MA, Carrey J, Respaud M, et al. Large scale production of biocompatible magnetite nanocrystals with high saturation magnetization values through green aqueous synthesis. J Mater Chem B. 2013; 1 (43): 5995–6004.
32. Verma A, Stellacci F. Effect of Surface Properties on Nanoparticle–Cell Interactions. Small. 2010; 6 (1): 12–21.
33. Adler AF, Leong KW. Emerging links between surface nanotechnology and endocytosis: Impact on nonviral gene delivery. Nano Today. 2010; 5 (6): 553–69.
34. Gupta AK, Gupta M. Cytotoxicity suppression and cellular uptake enhancement of surface modified magnetic nanoparticles. Biomaterials [Internet]. 2005 [cited 2017 Jun 9]; 26 (13): 1565–73. Available from: http://www.ncbi.nlm.nih.gov/pubmed/15522758.
35. Gupta AK, Curtis AS. Lactoferrin and ceruloplasmin derivatized superparamagnetic iron oxide nanoparticles for targeting cell surface receptors. Biomaterials. 2004; 25 (15): 3029–40.
36. Soenen SJH, Nuytten N, De Meyer SF, De Smedt SC, De Cuyper M. High Intracellular Iron Oxide Nanoparticle Concentrations Affect Cellular Cytoskeleton and Focal Adhesion Kinase-Mediated Signaling. Small. 2010; 6 (7): 832–42.
37. Berry CC. Progress in functionalization of magnetic nanoparticles for applications in biomedicine. J Phys D Appl Phys. 2009; 42 (22): 224003.
38. Zhang J, Ring HL, Hurley KR, Shao Q, Carlson CS, Idiyatullin D et al. Quantification and biodistribution of iron oxide nanoparticles in the primary clearance organs of mice using T1 contrast for heating. Magn Reson Med [Internet]. 2017 [cited 2017 Dec 22]; 78 (2): 702–12. Available from: http://www.ncbi.nlm.nih.gov/pubmed/27667655.
39. Bargheer D, Giemsa A, Freund B, Heine M, Waurisch C, Stachowski GM et al. The distribution and degradation of radiolabeled superparamagnetic iron oxide nanoparticles and quantum dots in mice. Beilstein J Nanotechnol. 2015; (6): 111–23.
40. Ruiz A, Hernández Y, Cabal C, González E, Veintemillas-Verdaguer S, Martínez E, et al. Biodistribution and pharmacokinetics of uniform magnetite nanoparticles chemically modified with polyethylene glycol. Nanoscale. 2013; 5 (23): 11400–8.

NANOPARTICLES GUIDED PRECISE TRANSPLANTATION OF VARYING NUMBERS OF MESENCHYMAL STEM CELLS INTO POST–TRAUMATIC SYRINX IN SPINAL CORD INJURY RAT

Chao Zhang[1,2,3,4] ✉, Morozova AY[4], Baklaushev VP[3], Gubsky IL[2], Melnikov PA[4], Gabashvily AN[6], Guowen Wang[1], Lili Li[1], Haixiao Wu[1], Xin Wang[5], Chekhonin VP[2,4]

[1] Department of Bone and Soft Tissue Tumors, Tianjin Medical University Cancer Institute and Hospital, National Clinical Research Center for Cancer, Key Laboratory of Cancer Prevention and Therapy, Tianjin's Clinical Research Center for Cancer, Tianjin, China

[2] Department of Medicinal Nanobiotechnology, Pirogov Russian National Research Medical University, Moscow

[3] Federal Research and Clinical Center, Moscow

[4] Federal Medical Research Center for Psychiatry and Narcology, Moscow

[5] Department of Epidemiology and Biostatistics, First Affiliated Hospital, Army Medical University, Chongqing, China

[6] Vavilov Institute of General Genetics Russian Academy of Sciences, Moscow

Spinal cord injury (SCI) is a traumatic injury to the spinal cord which is not a consequence of the disease. Mesenchymal stem cells (MSCs) have gradually become one of the most used stem cells in research and clinic trial. Based on the previous reports employed the cells ranged from $4 \cdot 10^5$ to $1 \cdot 10^6$, the present study was performed to figure out the best number of MSCs for transplantation of the chronic SCI. Magnetic nanoparticles were used for proving the precise transplantation strategy. Using magnetic resonance imaging (MRI), diffusion tensor imaging (DTI), diffusion tensor tractography (DTT), and behavior testing evaluations, we focused the effect of varying numbers of MSCs on reducing lesion cavity and post–traumatic syrinx formation, suppressing glial scar formation, enhancing neuronal fibers remodeling, promoting axonal regeneration and sprouting, improving vascularization, ameliorating the neuronal factors expressional level, and function improvement. Magnetic nanoparticles were precisely transplanted into the post–traumatic syrinx (PTS). MSCs can restore function after chronic SCI through stimulating the regeneration and sprouting of the axons, reducing the formation of PTS. The effect of MSCs on PTS management and functional improvement post chronic SCI was cell number–dependent, and within the range of $4 \cdot 10^5$ to $1 \cdot 10^6$, $1 \cdot 10^6$ cells were proved to be the best dose.

Keywords: mesenchymal stem cells; spinal cord injury; cell transplantation; nanoparticles

Funding: the present study was sponsored by China Scholarship Council (201406940004), and Russian Scientific Foundation (16–15–10432).

✉ **Correspondence should be addressed:** Chao Zhang
Huanhu Xi Road, Hexi Area, Tianjin, China, 300060; drzhangchao@tmu.edu.cn

Received: 26.08.2018 **Accepted:** 25.09.2018

DOI: 10.24075/brsmu.2018.084

НАНОЧАСТИЦЫ СПОСОБНЫ НАПРАВЛЯТЬ ТРАНСПЛАНТИРОВАННЫЕ МЕЗЕНХИМАЛЬНЫЕ СТВОЛОВЫЕ КЛЕТКИ В ПОСТТРАВМАТИЧЕСКИЙ СВИЩ У КРЫС С ПОВРЕЖДЕНИЯМИ СПИННОГО МОЗГА

Чао Чжан[1,2,3,4] ✉, А. Ю. Морозова[4], В. П. Баклаушев[3], И. Л. Губский[2], П. А. Мельников[4], А. Н. Габашвили[6], Гуовен Ванг[1], Лили Ли[1], Хайсяо У[1], Ксин Ванг[5], В. П. Чехонин[2,4]

[1] Кафедра опухолей костей и мягких тканей, Онкологический институт и госпиталь Тяньцзиньского медицинского университета, Национальный клинический исследовательский центр рака, Главная лаборатория профилактики и лечения рака, Тяньцзиньский клинический исследовательский центр рака, Тяньцзинь, Китай

[2] Кафедра медицинской нанобиотехнологии, Российский национальный исследовательский медицинский университет имени Н. И. Пирогова, Москва

[3] Федеральное медико-биологическое агентство, Москва

[4] Национальный медицинский исследовательский центр психиатрии и наркологии имени В. П. Сербского, Москва

[5] Кафедра эпидемиологии и биостатистики, Первая больница медицинского университета Сухопутных войск, Чунцин, Китай

[6] Институт общей генетики имени Н. И. Вавилова РАН, Москва

Травма спинного мозга (ТСМ) — это травматическое повреждение, не являющееся следствием заболевания. Мезенхимальные стволовые клетки (МСК) становятся одним из наиболее используемых типов стволовых клеток как в научных исследованиях, так и в клинических испытаниях. С учетом предыдущих работ, в которых использовали от $4 \cdot 10^5$ до $1 \cdot 10^6$ кл., целью данного исследования было определить количество МСК, оптимальное для трансплантации при хронической ТСМ. Магнитные наночастицы (НЧ) использовали для доказательства точности проведенной трансплантации. С помощью магнитно-резонансной томографии (МРТ), диффузионно-тензорной визуализации (DTI), диффузионно-тензорной трактографии (DTT) и поведенческих тестов мы проверили влияние различного количества МСК на уменьшение пораженной полости и посттравматического свища, подавление формирования глиального рубца, усиление ремоделирования нейронных волокон, содействие регенерации и прорастанию аксонов, улучшение васкуляризации, повышение уровня экспрессии нейронных факторов и улучшение функционирования системы. Магнитные НЧ были точно трансплантированы в посттравматический свищ (ПТС). МСК могут восстанавливать функцию после хронической ТСМ посредством стимуляции регенерации и прорастания аксонов, уменьшая образование ПТС. Таким образом, влияние МСК на ПТС и функциональное улучшение после хронической ТСМ зависит от количества клеток, и в диапазоне от $4 \cdot 10^5$ до $1 \cdot 10^6$ наилучшей дозой является $1 \cdot 10^6$.

Ключевые слова: мезенхимальные стволовые клетки; травма спинного мозга; трансплантация клеток; наночастицы

Финансирование: исследование поддержано Китайским стипендиальным советом (№ 201406940004) и Российским научным фондом (№ 16-15-10432).

✉ **Для корреспонденции:** Чао Чжан
ул. Хуанху Си, Район Хэси, Тяньцзинь, Китай, 300060; drzhangchao@tmu.edu.cn

Статья получена: 26.08.2018 **Статья принята к печати:** 25.09.2018

DOI: 10.24075/vrgmu.2018.084

Previous epidemiological research suggested the annual incidence in China of spinal cord injury (SCI) reached 23.7 cases per million people [1]. The global annual incidence was recently reported range from 9.2 to 246 cases per million [2]. Almost half of the cases result in complete loss of function below the injury level. First–year medical costs for a high tetraplegic patient and a paraplegic patient are estimated at over $800,000 and $300,000 respectively [3]. In the past decades, the mortality rate in the first year has been successfully reduced. However, SCI is still regarded as untreatable condition [4].

The pathophysiology of SCI can be defined as a biphasic process: (1) the primary phase which involves the initial mechanical injury and (2) the delayed secondary phase which is characterized by inflammation activation, vascular disruption, ischemia, oxidative stress, and excitotoxicity [5–6]. The secondary phase is divided into the immediate, acute, intermediate, and chronic stages of SCI [5]. The main features of chronic SCI are glial scar and cavity formation following function loss [7–8].

Stem cell transplantation has become a widely accepted treatment for overcoming SCI. The first description of mesenchymal stem cells (MSCs) occurred in 1991 [9]. MSCs have gradually become one of the most utilized methods in research and surgery. A number of studies on MSCs transplantation for SCI were conducted [11–16]. The increasing number of the clinical trials employing MSCs for treating SCI indicates that MSCs are considered to be potentially beneficial for translational studies despite several questions which still need to be examined basic and preclinical research level [10].

In order to promote the MSCs transplantation into formal clinical application, the following issues must be addressed, optimal transplantation timing, the most effective transplantation method and the optimal number of stem cells. Our previous research focused on the benefits of employing mesenchymal stem cells in the acute and subacute phase of the contusion rat model [17]. After a broad literature review, we found that the chronic phase could also be considered a potential time to perform cell transplantation [11–16]. Two main reasons are given: (1) globally, there are many chronic SCI patients eagerly waiting for an effective treatment; (2) the microenvironment is continuously changing during the acute/subacute phase, while it is relatively stable during the chronic stage, which will affect the survival or differentiation of transplanted cells. Considering the transplanted cell survival, migration and safety, intralesional transplantation is preferable, compared with intrathecal transplantation and intravenous transplantation [18–19]. Across the current studies and clinical trials, the number of employed MSCs are not uniform. The number of cells used ranged from $4 \cdot 10^5$ to $1 \cdot 10^6$ in the animal studies [19–22], and $7 \cdot 10^5$ to $2 \cdot 10^7$ in the clinical trials [12, 14, 15, 23].

This experiment was designed to determine: (1) to verify our strategy for MSCs precise transplantation; (2) to explore the best number of MSCs transplantation ranged from $4 \cdot 10^5$ to $1 \cdot 10^6$ for improvement of chronic SCI.

METHODS

Nanoparticles transplantation

Nanoparticles were designed and generated as we reported [24]. Transplantation was performed under the guidance of MRI, as we previously reported [25]. Generally, the rats were anesthetized throughout the whole procedure with the E–Z Anesthesia system EZ–7000 330 (PA, USA). The fur over T10 was carefully shaved and the exposed skin was sterilize. The skin and the superfcial fascia were opened along the initial laminectomy incision. Two silver acupuncture needles (Kazan medical instruments plant JSC; Russia) were inserted through the erector spinae. The needles were positioned parallel to the ground and at a 40–degree angle to the spine with 1 needle on both sides of the animal. The tips the needles were passed through the muscle and intersected each other, creating a cross–like shape.

The MRI was conducted to calculate both the volume of PTS and the 3–dimensionl (3D) coordinates using the crossed needles as a reference point. Both the lateral and the longitudinal distances between PTS and the crossed needles were measured with software MultiVox Dicom Viewer (R3.0 SP13; USA). The depth of PTS was also calculated.

Animals group allocation

In order to prove the precise intra–PTS transplantation strategy, adult Sprague–Dawley rats (n = 3) weighted 180–220 g were used to create the chronic SCI models. To evaluate the effect of MSCs transplantation, another adult Sprague–Dawley rats (n = 24) weighted 180–220 g were used to create the chronic SCI models. Rats were randomly divided into four groups with 6 rats in each group): (1) DMEM group (the cell culture medium group); (2) the $4 \cdot 10^5$ cells group; (3) the $8 \cdot 10^5$ cells group; (4) the $1 \cdot 10^6$ cells group.

Experiments were carried out in compliance with the principles of International Laboratory Animal Care, and the European Communities Council Directive of 24 November 1986 (86/609/EEC). All efforts were made to minimize the number of animals used and their suffering.

Isolation, Culture, and Characterization of MSCs

MSCs were collected from the bone marrow of 4–6–month–old SD rats. Generally, in a ficoll density gradient 1.077 g/ml (Sigma-Aldrich; USA), we centrifuged to isolate the fraction of mononuclear cells (300 rpm, 30 min). The cells were cultured in RPMI 1640 (Gibco; USA), supplemented with 2 mM glutamine, 100 U/ml penicillin, 0.1 mg/ml streptomycin (Gibco; USA) and 15% FBS (Biowest; USA) at 37 °C, 5% CO_2. Passage 2–4 MSCs were used in the present research. The presence of positive specific MSCs markers (CD105, CD90, and CD44) and negative hematopoietic markers (CD45, CD34) was verified by flow cytometry (MoFlo sorter; Beckman Coulter; USA) with the appropriate primary–labeled antibodies (Miltenyi Biotec GmbH; Germany).

MSC cells were trypsinized (trypsin–EDTA, 0.25%) (Invitrogen; Russia) and counted. Then 4 aliquots of medium with the composition of serum free DMEM (Gibco; USA), supplemented with 2 mM glutamine, 100 U/ml penicillin, 0.1 mg/ml streptomycin (Gibco; USA) were prepared. Three of them were randomly selected to prepare the cell suspension in different concentrations: $1 \cdot 10^5$, $2 \cdot 10^5$ and $2.5 \cdot 10^5$ cells/μl.

Chronic spinal cord injury model

The surgery was performed as we previously reported [17]. After intraperitoneal anesthetization with ketamine (50 mg/kg), animals were placed on a warm pad in the prone position and the dorsal fur was shaved. The surgical area was sterilized. The laminectomy at T9–10 segment was performed to expose the spinal cord. Then a force of 200 kilodynes was induced an impact injury to the spinal cord using the PSI–IH Impactor, which has sensors to accurately measure the impact force. (Precision Systems and Instrumentation LLC, Fairfax, VA; USA).

After flushing the wound with ice saline, the surgical site was sutured. A subcutaneous injection of Baytril (2.5 mg/kg/d) (Bayer; USA) was administered on the rats. After surgery, the animals were returned to their home cages and received manual bladder expression twice daily until the recovery of spontaneous urinary function.

Stereotactic MSCs transplantation

Cell transplantation was performed at 4w post injury [11]. After the induction of general anesthesia, the cell transplantation was performed through the skin guided by MRI. MRI was employed to locate the injured area of each rat prior to the transplantation procedure. Using a Hamilton syringe and a 33–gauge, 45 degree–beveled needle (Hamilton, Reno; USA), 4 μl of liquid was directly transplanted into the injury area with the assistance of the microinjection unit and Razel Syringe Pump (NE–1002X) (Razel Scientific; USA) in 2 min. The needle was held at the injection site for 2 min and was withdrawn slowly for another minute.

MRI and DTI scan

All rats were anesthetized throughout the whole procedure by inhalation of isoflurane (5DG9621, BAXTER; USA) with the E–Z Anesthesia system (EZ–7000 330, PA; USA). MRI and DTI scans were performed using 7 Tesla animal MRI scanners (ClinScan, Bruker BioSpin; USA) on the first and the fourth week after SCI to evaluate the injury area, and the eighth week after SCI to determine the effect of MSCs transplantation. For coronal images: T2-weighted images in coronal plane were acquired by Turbo Spin Echo sequence with the following parameters: FOV 120 • 59.2 mm, base resolution 320 • 158, TR = 3850 ms, TE = 39 ms, slice thickness 1 mm, number of acquisition = 1, echo train length = 9. For sagittal images: T2-weighted imaged in sagittal plane were acquired by Turbo Spin Echo sequence with following parameters: FOV 100 • 49.2 mm, base resolution 256 • 126, TR = 3850 ms, TE = 42 ms, slice thickness 1 mm, number of acquisition = 3, echo train length = 9.

DTI images were acquired with identical geometry as the anatomical images using single shot spin–echo planar imaging (EPI) sequence with TR/TE of 4000 ms/88 ms, slice thickness of 3 mm, b factor of 1000 s/mm2, bandwidth of 200 kHz, 25 gradient encoding directions, acquisition matrix of 64 • 64, and field of view 10 • 10 mm. To calculate the DTI indices, the collected images were analyzed on an independent workstation. DTT of the spinal cord was generated using the FACT algorithm implemented in Volume–One software, and fractional anisotropy (FA) threshold < 0.2 and stopping angle of > 25° were used as parameters.

Macroscopic assessment of injury area

Macroscopic assessment was performed 8 w post cell transplantation in each rat. All rats were humanely euthanized with the same aforementioned process. Intracardial perfusion with saline and then 4% paraformaldehyde was performed to flush possible blood components from the sample. The spinal cords form the injury level were collected. The images of spinal cords from each group were generated by the digital camera (Leica Co.; Germany). With Image J software (Basics 1.38; USA), the macroscopic injury sites on the surface of spinal cords were selected and the injury areas were auto–calculated. The average injury area of each group was gained and quantitatively compared.

Hematoxylin-eosin (H & E) staining

After macroscopic assessment, rats were deeply anesthetized with ketamine and xylazine, and perfused with saline and 4% paraformaldehyde in 0.1 M phosphate buffer. Three spinal cord samples from each group were randomly selected. The samples were dehydrated gradually in 70%, 80%, 90%, 100% ethanol, and embedded in xylene and paraffin. 10 μm longitudinal slices were made on the microtome (Rotary microtome) (Microm HM 650V; USA).

For hematoxylin eosin staining, slices were hydrated in 100%, 90%, 80%, 70% ethanol and water, stained in hematoxylin for 1 minute, washed in water for 5 minutes, followed by staining in eosin for 1 minute. After coversliping with entelan, the slices were sent to the light microscope for the evaluation of the injured area. Three slices from each group were collected, the mean injured area was calculated. With Image J software, the injury sites of the slices were selected and the injury areas were auto-calculated. The average injury area of each group was gained and quantitatively compared.

Immunohistochemistry (IHC)

Three spinal cords from each group were randomly selected. The samples were embedded in PBS, 50μm longitudinal slices were made on the vibratome HM 650V (Thermo Scientific; USA). Three slices from each sample were collected and analyzed. The slices were incubated with anti-microtubule Associated Protein 2 (MAP2; mouse anti–rat; 1 : 400) (Abcam; UK), anti–β3–tubulin (β3-tubulin; rabbit anti–rat; 1 : 400) (Sigma; USA), anti-glial fibrillary acidic protein (GFAP; rabbit anti–rat; 1 : 500) (Abcam; UK), Nestin (1 : 400, rabbit anti–rat) (Abcam; UK), brain derived neurotrophic factor (BDNF; mouse anti–rat; 1 : 400) (Abcam; UK) and vascular ecndothelial growth factor (VEGF; mouse anti-rat; 1 : 200) (Abcam; UK) overnight at 4 °C, followed by TRITC-conjugated goat anti-mouse or FITC-conjugated anti-rabbit IgG (1 : 200; ZSGB–BIO) for one hour at 37 °C. The slices were examined using confocal microscopy (Nikon, A1+MP) (Nikon; Japan).

3D surface plot was employed for evaluating fluorescence measurements semi–quantitatively. The sample's heatmap of each slice was generated based on the fluorescence intensity in different fluorescence channels. The sample's heatmap, which is simply a three–column matrix colored from light blue to bright red, illustrated the different expressional levels of positive proteins.

Behavioral analysis

Basso, Beattie, and Bresnahan (BBB) locomotor test was performed based on the principle of double blind before injury and weekly post injury to evaluate the hindlimb motor behavior recovery. To assess motor coordination, a rotarod test was conducted before the rats were killed (at 8 w post transplantation). All rats were placed on a standard Rotarod (Med Associates, Inc.; USA) to determine their motor performances. The test was not conducted throughout all the experimental period because falling from the rod might lead to further injuries. Each animal was placed on a 10 cm diameter, 15 cm long rod, rotating at constant speed. Impairment of motor coordination was defined as the inability of rats to remain on the rotating rod for a 60 s test period. Animals were pre-trained on the rotating track before the injury and re-trained 24 h before the test. The testing protocol comprised of one 60 s test period every 24 hours for 72 hours. On these continuous

days of testing at 4, 8, and 12 rpm on, respectively, 1st, 2nd, and 3rd day, with a 10 min interval between each trial.

Statistical analysis

All statistical analyses were performed by SPSS 17.0 software package (SPSS Inc.; USA). Results were considered to be statistically significant with $p < 0.05$. All data are presented as mean ± standard error of the mean (SEM), and repeated measures ANOVA (RANOVA) was employed.

RESULTS

Precise transplantation into PTS

The nanoparticles showed low signal change in T2-weighted MRI scanning (Fig. 1). Nanoparticle transplantation was repeatedly conducted in the rats with PTS. As shown in Figure, the PTS volume showed a significant decrease from (5.71 ± 0.21) mm^3 to (3.23 ± 0.364) mm^3 post first transplantation ($p < 0.05$), the volume further decreased from (3.23 ± 0.364) mm^3 to (1.48 ± 0.722) mm^3 post sect transplantation ($p < 0.05$). Thus, our transplantation strategy was proved to be precise by nanoparticle.

General situation and motor functional recovery

All the rats involved in the present research showed no signs of complications or died unexpectedly, during the whole experimental procedure.

Preoperatively, the rat BBB scores were 21 points in all rats. Immediately after SCI, all rats demonstrated significant loss of motor function of the hind limbs and the BBB scores were reduced to 0 points (Fig. 2). Gradually, BBB score increased in all groups, and reached 5.85 ± 0.83 (DMEM group), 5.94 ± 0.74 ($4 \cdot 10^5$ group), 6.08 ± 0.75 ($8 \cdot 10^5$ group) and 6.02 ± 0.84 ($1 \cdot 10^6$ group) at four weeks after injury. Differences in the BBB scores among the four groups were not statistically significant before cell transplantation.

One week post transplantation, compared with the DMEM group, the differences were found to be statistically significant in cell transplanted groups (Fig. 2 M). Compared with the DMEM group, the behavior ability also suggested the better outcome in the cell transplanted groups. Among all the groups, $1 \cdot 10^6$ group showed the best outcome (Fig. 2 M). Eight–week post transplantation, BBB score reached 7.02 ± 1.36 (DMEM group), 8.14 ± 1.12 ($4 \cdot 10^5$ group), 10.25 ± 1.02 ($8 \cdot 10^5$ group) and 11.07 ± 1.44 ($1 \cdot 10^6$ group). The rats showed different behavior abilities on weight support, plantar placement, and plantar stepping (Fig. 2 A–M).

The Reduction of PTS

MRI was performed on the first week and fourth week post injury, and eighth week post MSCs transplantation. The formation of post–traumatic syrinx (PTS) was evaluated. As shown in the Table 1, the cases of the animal with PTS on different weeks were listed.

As shown in the Fig. 4, the PTS volumes were calculated based on the MRI. The volume of PTS decreased in the cell transplant groups when evaluated 8 w post transplantation. Among all the groups, $1 \cdot 10^6$ group showed the best improvement (Fig. 3 S–Y).

The visible injured area was caluated in order to evaluate the effect of MSCs on preventing scar formation post chronic SCI. As shown in the Figure 4, compared with the DMEM group, the differences were statistically significant in cell transplanted groups (Fig. 4 E). Among all the groups, $1 \cdot 10^6$ group showed the best outcome (Fig. 4 A–E).

The promotion of neural restoration

In order to evaluate the effect of MSCs on promoting the neural regeneration and sprouting, DTI and DTT were conducted on eighth week post cell transplantation. As shown in the Fig. 4 and Table 2, the dorsal columns tracts of lesion site from each group were evaluated. Compared with the DMEM group, the continuity and density of neural fibers were found to be improved in cell transplanted groups (Fig. 4 B–D). Among all the groups, $1 \cdot 10^6$ group showed the best neural fibers with complete continuity and high density (Fig. 4 D). As shown in the Table 2, compared with other groups, ADC showed significant decrease and FA showed significant increase in the $1 \cdot 10^6$ MSCs group, the effect showed the cell–dose dependent manner.

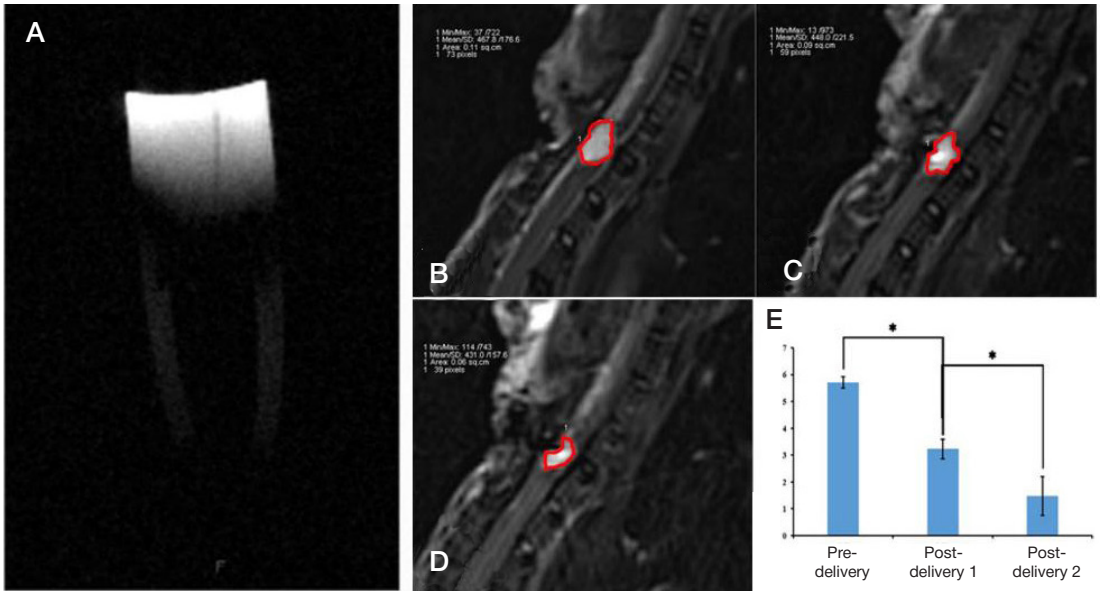

Fig. 1. Nanoparticles transplantation and MRI analysis. **A**. Nanoparticles showed low signal change in T2–weighted scanning. **B**–**E**. The volume change of PTS post nanoparticle transplantation. PTS volume decreased after the first transplantation, and further decreased after the second transplantation ($p < 0.05$)

DISCUSSION

Based on the present research and the previous reports, it was suggested that the beneficial effect of MSCs transplantation is dose–dependent [26]. The research into the optimal dose is desirable. The optimize number of cells ranged from $4 \cdot 10^5$ to $1 \cdot 10^6$ was studied in the present research. In order to avoid producing additional damage to the spinal cord, high concentrations of cells were employed. In the present research, $1 \cdot 10^5$, $2 \cdot 10^5$ and $2.5 \cdot 10^5$ cells/μl were employed [19–22]. As observed, $2.5 \cdot 10^5$ cells/μl is the maximum concentration for preparing MSCs. The higher concentration exerted the negative influences on cells survival, and required the larger caliber of the injection needle, which led to additional damage. The smallest possible volume 4μl of cell suspension was used due to the volume of the rat spinal cord and the adequate cell suspension medium for cells survival [19–22].

Varying strategies for transplantation into the spinal cord were reported, including lesion site delivery, single-point with various intervals delivery, multi–target point delivery, and twice separately delivery [26–28]. Four factors should be considered when planning an administration route: (1) a greater number of cells could be administered into lesion site and fewer cells could be administered into normal tissue; (2) higher rates of cell survival; (3) the approach that can be repeated accurately in each individual; (4) less added damage. Thus, based on our previous reports, the local lesion site delivery was employed in the present research [25].

Several studies reported that MSCs transplantation was able to positively improve the outcome post SCI [19–22]. Based on the present study, MSCs transplantation can stimulate the regeneration and sprouting of the axons, improve the motor function recovery, reduce the formation of PTS and glial scar, promote vascularization and neuro–trophic factor expression. In the present research, the effect suggested the cell number–dependent manner, $1 \cdot 10^6$ cells showed the best outcome among all groups. The hypothesis can be drawn that the more employed cells, the better gained effect. It was reported that one of the main mechanisms of MSCs transplantation on treating chronic SCI is MSCs' paracrine effect [11]. Thus,

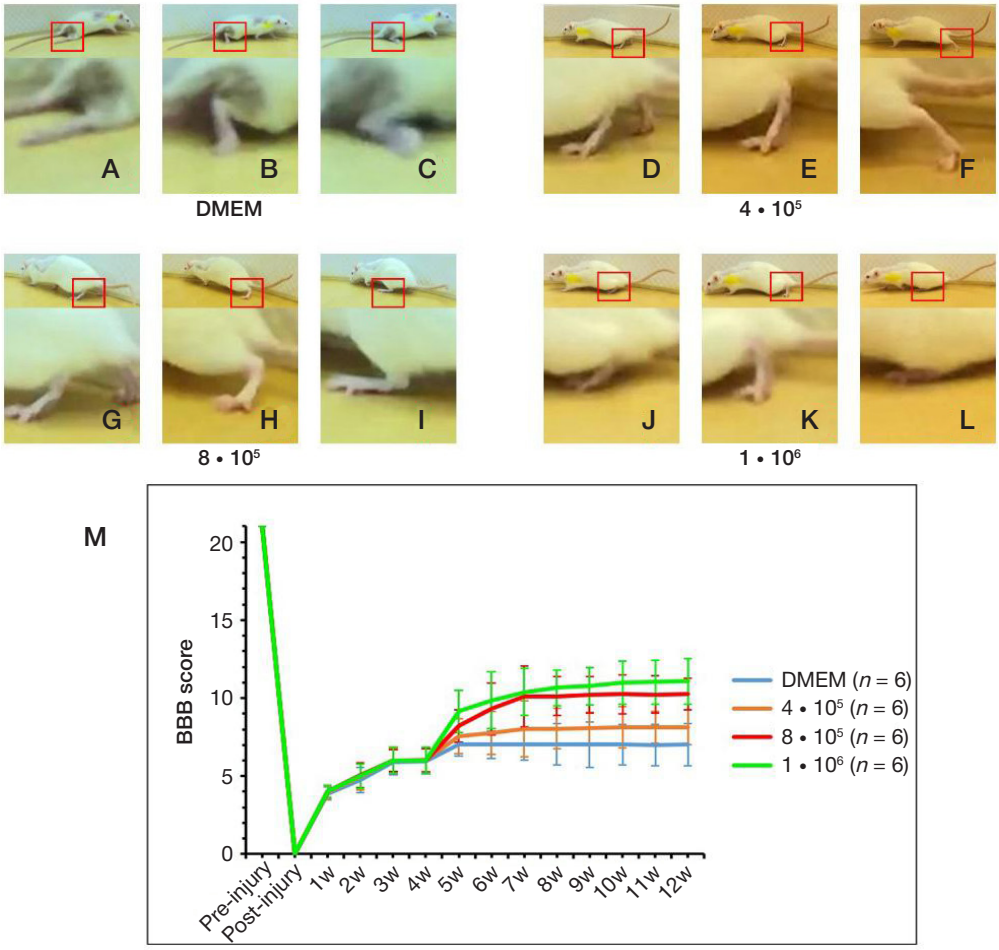

Fig. 2. Motor function recovery evaluated by BBB score. Differences in the BBB scores among the four groups were not statistically significant before cell transplantation. One–week post transplantation, compared with the DMEM group, the differences were found to be statistically significant in cell transplanted groups (**M**). Compared with the DMEM group, the behavior ability suggested the better outcome in the cell transplanted groups. Among all the groups, $1 \cdot 10^6$ group showed the best outcome (**M**). Eight–week post transplantation, the rats showed different abilities on weight support (**A**, **D**, **G**, **J**), plantar placement (**B**, **E**, **H**, **K**), and plantar stepping (**C**, **F**, **I**, **L**)

Table 1. The cases counting of PTS formation

	1 w post injury	4 w post injury	8 w post transplantation
DMEM group	0	3	3
$4 \cdot 10^5$ group	0	3	3
$8 \cdot 10^5$ group	0	4	4
$1 \cdot 10^6$ group	0	4	3

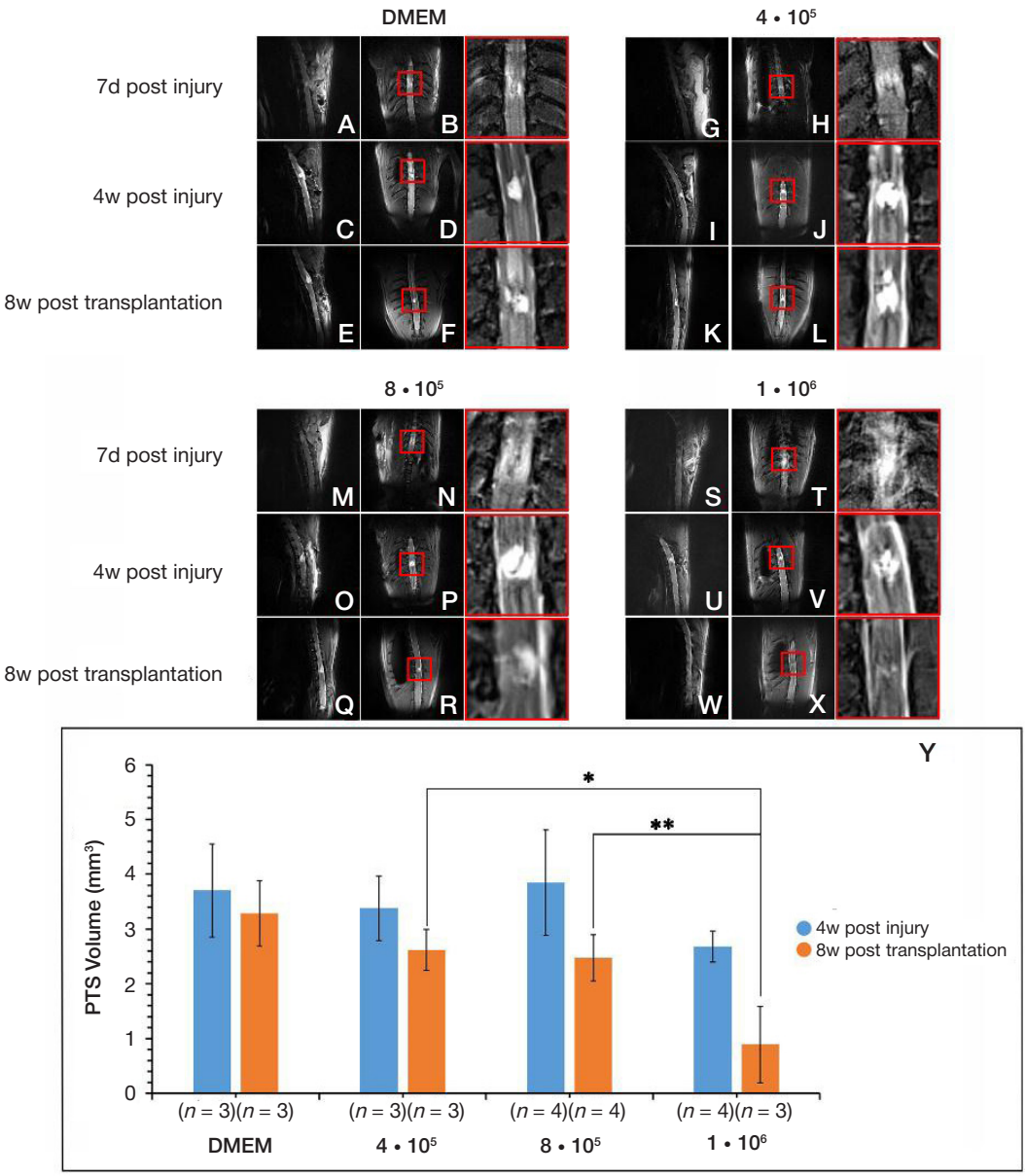

Fig. 3. The Reduction of post-traumatic syrinx. Lateral and horizontal MRI scanning was performed in all groups to evaluate the situation of post-traumatic syrinx pre- and post- transplantation (**A**–**X**). The volume of PTS decreased in the cell transplant groups when evaluated 8 w post transplantation. Among all the groups, 1 • 10^6 group showed the best improvement (**S**–**Y**). The areas in the red box were magnified in the figures with red frame

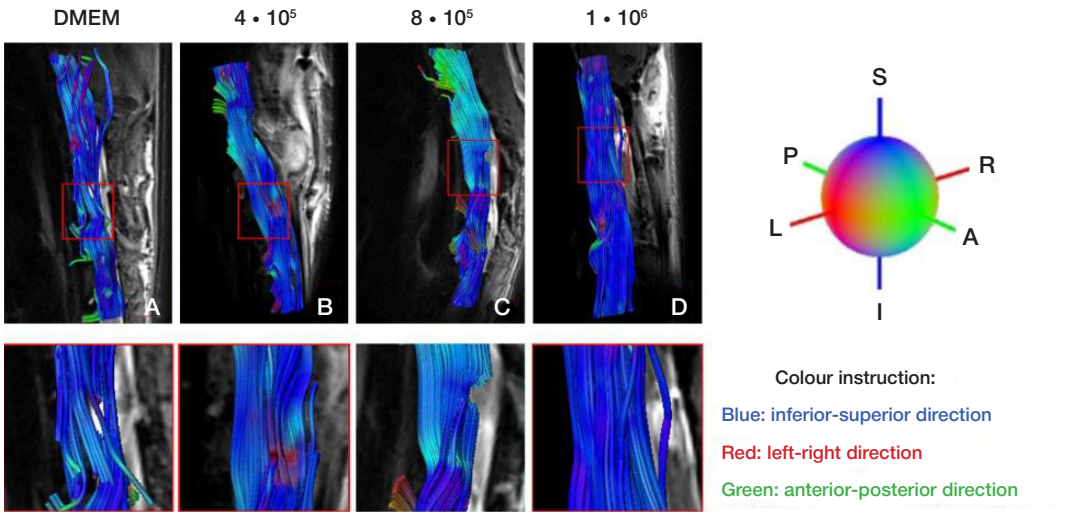

Fig. 4. Tractography images of the spinal cords in all the groups at 8w post cell transplantation. Tractography image of the spinal cord in DMEM group showed the fracture of neural fibers (**A**). All cell transplanted groups showed the repairing sign of spinal neural fibers (**B**–**D**). 1 • 10^6 group showed the best outcome (**D**)

Table 2. The situation of ADC and FA in the injury area

Group	DMEM		$4 \cdot 10^5$ MSCs		$8 \cdot 10^5$ MSCs		$1 \cdot 10^6$ MSCs	
	ADC	FA	ADC	FA	ADC	FA	ADC	FA
8w post transplantation	(1792.64 ± 719.28) $\cdot 10^{-6}$ mm^2/s	0.34 ± 0.08	(1483.52 ± 924.91) $\cdot 10^{-6}$ mm^2/s	0.41 ± 0.10	(1351.77 ± 1024.55) $\cdot 10^{-6}$ mm^2/s	0.45 ± 0.09	(1276.39 ± 1214.84) $\cdot 10^{-6}$ mm^2/s	0.51 ± 0.12

we hypothesized that the more employed cells, the more gained trophic factors. As proved in the present research with immunohistochemistry, the expressional levels of BDNF and VEGF in the lesion site were the highest after the transplantation of $1 \cdot 10^6$ cells among all groups, while after transplanting $4 \cdot 10^5$ cells and $8 \cdot 10^5$ cells, the BDNF and VEGF expressions were also improved compared with DMEM group. Currently, there has been no quantitative study looking into the changing of trophic factors post chronic SCI, or looking into the detailed number of desired trophic factors for treating SCI. Our study suggested the more employed cells, the higher expressional trophic factors, the better gained behavioral recovery. However, prudent planning should be employed when increasing cell volume and/or concentration to ensure additional damage.

It is a limitation of the present research that the survival rates of the transplanted MSCs were not evaluated. Further studies on the evaluation of survival rates and cell apoptosis would be performed.

CONCLUSIONS

MSCs transplantation therapy for chronic SCI is a safe strategy with the concentration of $1 \cdot 10^5$, $2 \cdot 10^5$ and $2.5 \cdot 10^5$ cells/μl, and with the cells number of $4 \cdot 10^5$, $8 \cdot 10^5$, and $1 \cdot 10^6$. In the present basic study in vivo, MSCs can restore function after chronic SCI through stimulating the regeneration and sprouting of the axons, improving the motor function recovery, reducing the formation of PTS and glial scar, promoting vascularization and neuro-trophic factor expression. The effect was cell number-dependent, and $1 \cdot 10^6$ cells were proved to be the best dose. At the same time, the combined application of DTI and DTT could be the quantitative strategy for evaluating PTS situation post chronic SCI.

References

1. Ning GZ, Yu TQ, Feng SQ, Zhou XH, Ban DX, Liu Y et al. Epidemiology of traumatic spinal cord injury in Tianjin, China. Spinal Cord. 2011; (49): 386–90.
2. Furlan JC, Sakakibara BM, Miller WC, Krassioukov AV. Global incidence and prevalence of traumatic spinal cord injury. Can J Neurol Sci. 2014; (40): 456–64.
3. Oliveri RS, Bello S, Biering-Sørensen F. Mesenchymal stem cells improve locomotor recovery in traumatic spinal cord injury: systematic review with meta-analyses of rat models. Neurobiol Dis. 2014; (62): 338–53.
4. Devivo M. Epidemiology of traumatic spinal cord injury: Trends and future implications. Spinal Cord. 2012; (50): 365–72.
5. Siddiqui AM, Khazaei M, Fehlings MG. Translating mechanisms of neuroprotection, regeneration, and repair to treatment of spinal cord injury. Prog Brain Res. 2015; (218): 15–54.
6. Salewski RP, Mitchell RA, Li L, Shen C, Milekovskaia M, Nagy A et al. Transplantation of Induced Pluripotent Stem Cell-Derived Neural Stem Cells Mediate Functional Recovery Following Thoracic Spinal Cord Injury Through Remyelination of Axons. Stem Cells Transl Med. 2015; (4): 743–54.
7. Raspa A, Pugliese R, Maleki M, Gelain F. Recent therapeutic approaches for spinal cord injury. Biotechnol Bioeng. 2016; (113): 253–9.
8. Boido M, Garbossa D, Fontanella M, Ducati A, Vercelli A. Mesenchymal stem cell transplantation reduces glial cyst and improves functional outcome after spinal cord compression. World Neurosurg. 2014; (81): 183–90.
9. Caplan AI. Mesenchymal stem cells. J Orthop Res. 1991; (9): 641–50.
10. U.S. National Institutes of Health. Clinical trials. Available from: https://clinicaltrials.gov/.
11. de Almeida FM, Marques SA, Ramalho Bdos S, Massoto TB, Martinez AM. Chronic spinal cord lesions respond positively to tranplants of mesenchymal stem cells. Restor Neurol Neurosci. 2015; (33): 43–55.
12. Mendonça MV, Larocca TF, de Freitas Souza BS, Villarreal CF, Silva LF, Matos AC et al. Safety and neurological assessments after autologous transplantation of bone marrow mesenchymal stem cells in subjects with chronic spinal cord injury. Stem Cell Res Ther. 2014; (5): 126.
13. Lee SH, Kim Y, Rhew D, Kuk M, Kim M, Kim WH et al. Effect of the combination of mesenchymal stromal cells and chondroitinase ABC on chronic spinal cord injury. Cytotherapy. 2015; (17): 1374–83.
14. Amr SM, Gouda A, Koptan WT, Galal AA, Abdel-Fattah DS, Rashed LA et al. Bridging defects in chronic spinal cord injury using peripheral nerve grafts combined with a chitosan-laminin scaffold and enhancing regeneration through them by co-transplantation with bone-marrow-derived mesenchymal stem cells: case series of 14 patients. J Spinal Cord Med. 2014; (37): 54–71.
15. Dai G, Liu X, Zhang Z, Yang Z, Dai Y, Xu R. Transplantation of autologous bone marrow mesenchymal stem cells in the treatment of complete and chronic cervical spinal cord injury. Brain Res. 2013; (1533): 73–9.
16. Hodgetts SI, Simmons PJ, Plant GW. A comparison of the behavioral and anatomical outcomes in sub-acute and chronic spinal cord injury models following treatment with human mesenchymal precursor cell transplantation and recombinant decorin. Exp Neurol. 2013; (248): 343–9.
17. Ning G, Tang L, Wu Q, Li Y, Li Y, Zhang C et al. Human umbilical cord blood stem cells for spinal cord injury: early transplantation results in better local angiogenesis. Regen Med. 2013; (8): 271–81.
18. Takahashi Y, Tsuji O, Kumagai G, Hara CM, Okano HJ, Miyawaki A et al. Comparative study of methods for administering neural stem/progenitor cells to treat spinal cord injury in mice. Cell Transplant. 2011; (20): 727–39.
19. Kim JW, Ha KY, Molon JN, Kim YH. Bone marrow-derived mesenchymal stem cell transplantation for chronic spinal cord injury in rats: comparative study between intralesional and intravenous transplantation. Spine (Phila Pa 1976). 2013; (38): E1065–74.
20. Amemori T, Jendelová P, Růzicková K, Arboleda D, Syková E. Co-transplantation of olfactory ensheathing glia and mesenchymal stromal cells does not have synergistic effects after spinal cord injury in the rat. Cytotherapy. 2010; (12): 212–25.
21. Kang KN, Kim DY, Yoon SM, Lee JY, Lee BN, Kwon JS et al. Tissue engineered regeneration of completely transected spinal cord using human mesenchymal stem cells. Biomaterials. 2012; (33): 4828–35.
22. Kumagai G, Tsoulfas P, Toh S, McNiece I, Bramlett HM, Dietrich WD. Genetically modified mesenchymal stem cells (MSCs) promote axonal regeneration and prevent hypersensitivity after spinal cord injury. Exp Neurol. 2013; (248): 369–80.
23. Karamouzian S, Nematollahi-Mahani SN, Nakhaee N, Eskandary H. Clinical safety and primary efficacy of bone marrow mesenchymal

cell transplantation in subacute spinal cord injured patients. Clin Neurol Neurosurg. 2012; (114): 935–9.
24. Abakumov MA, Nukolova NV, Sokolsky-Papkov M, et al. VEGF-targeted magnetic nanoparticles for MRI visualization of brain tumor. Nanomedicine. 2015; 11 (4): 825–33.
25. Zhang C, Morozova AY, Abakumov MA, Gubsky IL, Douglas P, Feng S et al. Precise Delivery Into Chronic Spinal Cord Injury Syringomyelic Cysts with Magnetic Nanoparticles MRI Visualization. Med Sci Monit. 2015; (21): 3179–85.
26. Cigognini D, Satta A, Colleoni B, Silva D, Donegà M, Antonini S et al. Evaluation of early and late effects into the acute spinal cord injury of an injectable functionalized self-assembling scaffold. PLoS One. 2011; (6): e1978.
27. Mannoji C, Koda M, Kamiya K, Dezawa M, Hashimoto M, Furuya T et al. Transplantation of human bone marrow stromal cell-derived neuroregenrative cells promotes functional recovery after spinal cord injury in mice. Acta Neurobiol Exp (Wars). 2014; (74): 479–88.
28. Rao YJ, Zhu WX, Du ZQ, Jia CX, Du TX, Zhao QA et al. Effectiveness of olfactory ensheathing cell transplantation for treatment of spinal cord injury. Genet Mol Res. 2014; (13): 4124–9.

Литература

1. Ning GZ, Yu TQ, Feng SQ, Zhou XH, Ban DX, Liu Y et al. Epidemiology of traumatic spinal cord injury in Tianjin, China. Spinal Cord. 2011; (49): 386–90.
2. Furlan JC, Sakakibara BM, Miller WC, Krassioukov AV. Global incidence and prevalence of traumatic spinal cord injury. Can J Neurol Sci. 2014; (40): 456–64.
3. Oliveri RS, Bello S, Biering-Sørensen F. Mesenchymal stem cells improve locomotor recovery in traumatic spinal cord injury: systematic review with meta-analyses of rat models. Neurobiol Dis. 2014; (62): 338–53.
4. Devivo M. Epidemiology of traumatic spinal cord injury: Trends and future implications. Spinal Cord. 2012; (50): 365–72.
5. Siddiqui AM, Khazaei M, Fehlings MG. Translating mechanisms of neuroprotection, regeneration, and repair to treatment of spinal cord injury. Prog Brain Res. 2015; (218): 15–54.
6. Salewski RP, Mitchell RA, Li L, Shen C, Milekovskaia M, Nagy A et al. Transplantation of Induced Pluripotent Stem Cell-Derived Neural Stem Cells Mediate Functional Recovery Following Thoracic Spinal Cord Injury Through Remyelination of Axons. Stem Cells Transl Med. 2015; (4): 743–54.
7. Raspa A, Pugliese R, Maleki M, Gelain F. Recent therapeutic approaches for spinal cord injury. Biotechnol Bioeng. 2016; (113): 253–9.
8. Boido M, Garbossa D, Fontanella M, Ducati A, Vercelli A. Mesenchymal stem cell transplantation reduces glial cyst and improves functional outcome after spinal cord compression. World Neurosurg. 2014; (81): 183–90.
9. Caplan AI. Mesenchymal stem cells. J Orthop Res. 1991; (9): 641–50.
10. U.S. National Institutes of Health. Clinical trials. Available from: https://clinicaltrials.gov/.
11. de Almeida FM, Marques SA, Ramalho Bdos S, Massoto TB, Martinez AM. Chronic spinal cord lesions respond positively to tranplants of mesenchymal stem cells. Restor Neurol Neurosci. 2015; (33): 43–55.
12. Mendonça MV, Larocca TF, de Freitas Souza BS, Villarreal CF, Silva LF, Matos AC et al. Safety and neurological assessments after autologous transplantation of bone marrow mesenchymal stem cells in subjects with chronic spinal cord injury. Stem Cell Res Ther. 2014; (5): 126.
13. Lee SH, Kim Y, Rhew D, Kuk M, Kim M, Kim WH et al. Effect of the combination of mesenchymal stromal cells and chondroitinase ABC on chronic spinal cord injury. Cytotherapy. 2015; (17): 1374–83.
14. Amr SM, Gouda A, Koptan WT, Galal AA, Abdel-Fattah DS, Rashed LA et al. Bridging defects in chronic spinal cord injury using peripheral nerve grafts combined with a chitosan-laminin scaffold and enhancing regeneration through them by co-transplantation with bone-marrow-derived mesenchymal stem cells: case series of 14 patients. J Spinal Cord Med. 2014; (37): 54–71.
15. Dai G, Liu X, Zhang Z, Yang Z, Dai Y, Xu R. Transplantation of autologous bone marrow mesenchymal stem cells in the treatment of complete and chronic cervical spinal cord injury. Brain Res. 2013; (1533): 73–9.
16. Hodgetts SI, Simmons PJ, Plant GW. A comparison of the behavioral and anatomical outcomes in sub-acute and chronic spinal cord injury models following treatment with human mesenchymal precursor cell transplantation and recombinant decorin. Exp Neurol. 2013; (248): 343–9.
17. Ning G, Tang L, Wu Q, Li Y, Li Y, Zhang C et al. Human umbilical cord blood stem cells for spinal cord injury: early transplantation results in better local angiogenesis. Regen Med. 2013; (8): 271–81.
18. Takahashi Y, Tsuji O, Kumagai G, Hara CM, Okano HJ, Miyawaki A et al. Comparative study of methods for administering neural stem/progenitor cells to treat spinal cord injury in mice. Cell Transplant. 2011; (20): 727–39.
19. Kim JW, Ha KY, Molon JN, Kim YH. Bone marrow-derived mesenchymal stem cell transplantation for chronic spinal cord injury in rats: comparative study between intralesional and intravenous transplantation. Spine (Phila Pa 1976). 2013; (38): E1065–74.
20. Amemori T, Jendelová P, Růzicková K, Arboleda D, Syková E. Co-transplantation of olfactory ensheathing glia and mesenchymal stromal cells does not have synergistic effects after spinal cord injury in the rat. Cytotherapy. 2010; (12): 212–25.
21. Kang KN, Kim DY, Yoon SM, Lee JY, Lee BN, Kwon JS et al. Tissue engineered regeneration of completely transected spinal cord using human mesenchymal stem cells. Biomaterials. 2012; (33): 4828–35.
22. Kumagai G, Tsoulfas P, Toh S, McNiece I, Bramlett HM, Dietrich WD. Genetically modified mesenchymal stem cells (MSCs) promote axonal regeneration and prevent hypersensitivity after spinal cord injury. Exp Neurol. 2013; (248): 369–80.
23. Karamouzian S, Nematollahi-Mahani SN, Nakhaee N, Eskandary H. Clinical safety and primary efficacy of bone marrow mesenchymal cell transplantation in subacute spinal cord injured patients. Clin Neurol Neurosurg. 2012; (114): 935–9.
24. Abakumov MA, Nukolova NV, Sokolsky-Papkov M, et al. VEGF-targeted magnetic nanoparticles for MRI visualization of brain tumor. Nanomedicine. 2015; 11 (4): 825–33.
25. Zhang C, Morozova AY, Abakumov MA, Gubsky IL, Douglas P, Feng S et al. Precise Delivery Into Chronic Spinal Cord Injury Syringomyelic Cysts with Magnetic Nanoparticles MRI Visualization. Med Sci Monit. 2015; (21): 3179–85.
26. Cigognini D, Satta A, Colleoni B, Silva D, Donegà M, Antonini S et al. Evaluation of early and late effects into the acute spinal cord injury of an injectable functionalized self-assembling scaffold. PLoS One. 2011; (6): e1978.
27. Mannoji C, Koda M, Kamiya K, Dezawa M, Hashimoto M, Furuya T et al. Transplantation of human bone marrow stromal cell-derived neuroregenrative cells promotes functional recovery after spinal cord injury in mice. Acta Neurobiol Exp (Wars). 2014; (74): 479–88.
28. Rao YJ, Zhu WX, Du ZQ, Jia CX, Du TX, Zhao QA et al. Effectiveness of olfactory ensheathing cell transplantation for treatment of spinal cord injury. Genet Mol Res. 2014; (13): 4124–9.

PROMISING METHODS FOR NONINVASIVE MEDICAL DIAGNOSIS BASED ON THE USE OF NANOPARTICLES: SURFACE-ENHANCED RAMAN SPECTROSCOPY IN THE STUDY OF CELLS, CELL ORGANELLES AND NEUROTRANSMITTER METABOLISM MARKERS

Goodilin EA[1,2]✉, Semenova AA[2], Eremina OE[1], Brazhe NA[3], Goodilina EA[4], Danzanova TYu[4], Maksimov GV[3], Veselova IA[1]

[1] Faculty of Chemistry, Lomonosov Moscow State University, Moscow
[2] Faculty of Materials Science, Lomonosov Moscow State University, Moscow
[3] Faculty of Biology, Lomonosov Moscow State University, Moscow
[4] Blokhin Russian Cancer Research Center, Moscow

Application of advances in nanomedicine and materials science to medical diagnostics is a promising area of research. Surface-enhanced Raman spectroscopy (SERS) is an innovative analytical method that exploits noble metal nanoparticles to noninvasively study cells, cell organelles and protein molecules. Below, we summarize the literature on the methods for early clinical diagnosis of some neurodegenerative and neuroendocrine diseases. We discuss the specifics, advantages and limitations of different diagnostic techniques based on the use of low- and high molecular weight biomarkers. We talk about the prospects of optical methods for rapid diagnosis of neurotransmitter metabolism disorders. Special attention is paid to new approaches to devising optical systems that expand the analytical potential of SERS, the tool that demonstrates remarkable sensitivity, selectivity and reproducibility of the results in determining target analytes in complex biological matrices.

Keywords: medical diagnostics, nanomaterials, noble metal nanoparticles, surface-enhanced Raman spectroscopy, mitochondria, erythrocytes, neurotransmitter markers, nanomedicine

Funding: this work was supported by the Russian Science Foundation (Grant 14-13-00871).

Acknowledgments: the authors wish to thank Professor Chekhonin VP, who graciously agreed to collaborate on this project, Nickelsparg E. for her assistance in preparing the figures for the manuscript, and Professor Sinukova GT for the fruitful discussion of contrast-enhanced ultrasound diagnostics.

✉ **Correspondence should be addressed:** Eugene A. Goodilin
Leninskie gory 1, bl. 3, Moscow, 119992; goodilin@yandex.ru

Received: 20.07.2018 **Accepted:** 19.08.2018

DOI: 10.24075/brsmu.2018.077

ПЕРСПЕКТИВНЫЕ МЕТОДЫ НЕИНВАЗИВНОЙ МЕДИЦИНСКОЙ ДИАГНОСТИКИ С ИСПОЛЬЗОВАНИЕМ НАНОМАТЕРИАЛОВ: СПЕКТРОСКОПИЯ ГИГАНТСКОГО КОМБИНАЦИОННОГО РАССЕЯНИЯ В ИССЛЕДОВАНИИ КЛЕТОК, КЛЕТОЧНЫХ ОРГАНЕЛЛ, МАРКЕРОВ НЕЙРОМЕДИАТОРНОГО ОБМЕНА

Е. А. Гудилин[1,2]✉, А. А. Семенова[2], О. Е. Еремина[1], Н. А. Браже[3], Е. А. Гудилина[4], Т. Ю. Данзанова[4], Г. В. Максимов[3], И. А. Веселова[1]

[1] Химический факультет, Московский государственный университет имени М. В. Ломоносова, Москва
[2] Факультет наук о материалах, Московский государственный университет имени М. В. Ломоносова, Москва
[3] Биологический факультет, Московский государственный университет имени М. В. Ломоносова, Москва
[4] Национальный медицинский исследовательский центр онкологии имени Н. Н. Блохина, Москва

Использование достижений наномедицины и материаловедения в диагностике заболеваний является перспективным направлением научных исследований. Спектроскопия гигантского комбинационного рассеяния (ГКР) — инновационный метод анализа, связанный с применением наноматериалов на основе благородных металлов для неинвазивного исследования клеток, клеточных органелл, белковых молекул. В работе обобщены литературные данные по методам ранней клинической диагностики ряда нейродегенеративных и нейроэндокринных заболеваний. Обсуждены особенности, достоинства и ограничения различных методов диагностики по низкомолекулярным и высокомолекулярным маркерам указанных заболеваний. Продемонстрированы перспективы применения оптических методов для экспресс-диагностики нарушений нейромедиаторного обмена. Особое внимание уделено новым подходам при создании универсальных оптических индикаторных систем, расширяющих аналитические возможности спектроскопии ГКР, обладающей уникально высокой чувствительностью, селективностью и воспроизводимостью результатов анализа при определении целевых аналитов в биологических матрицах сложного состава.

Ключевые слова: медицинская диагностика, наноматериалы, наночастицы благородных металлов, гигантское комбинационное рассеяние, митохондрии, эритроциты, маркеры нейромедиаторного обмена, наномедицина

Финансирование: работа поддержана Российским научным фондом (грант 14-13-00871).

Благодарности: авторы благодарны академику В. П. Чехонину за возможность творческого сотрудничества и Э. Никельшпарг за помощь в подготовке иллюстраций к обзору, а также профессору Г. Т. Синюковой за плодотворное обсуждение результатов ультразвуковой диагностики с использованием контрастных агентов.

✉ **Для корреспонденции:** Евгений Алексеевич Гудилин
Ленинские горы, д. 1, стр. 3, г. Москва, 119992; goodilin@yandex.ru

Статья получена: 20.07.2018 **Статья принята к печати:** 19.08.2018

DOI: 10.24075/vrgmu.2018.077

In the past 10–15 years, the evolution of nanomedicine and materials science made possible by the findings of interdisciplinary studies at the interface of chemistry, physics and biology has been driven by the challenges of medical diagnosis [1–3]. Hopes are high for research into targeted drug delivery, theranostics, discovery of therapeutic nanoparticles and diagnostic nanomaterials, including contrasting agents for scintigraphy, CT, MRI and ultrasonography (Fig. 1). Some of them have already been launched onto the market and set a new standard for medical imaging. Yet, there is a lot to be done, including creation of next-generation biosensing systems [1, 2, 4–11].

Surface-enhanced Raman scattering (or spectroscopy, SERS) holds an important place among actively evolving noninvasive diagnostic techniques. It is an optical analytical modality with record-breaking sensitivity that can be applied to the study of nature objects; it is also a unique approach to rapid detection assays [12–15]. Because of its underlying physical principles, SERS urges development of novel silver- and gold-derived nanomaterials with programmable properties. Noble metal nanoparticles are highly inert, both chemically and biologically, and allow effective control over surface plasmon resonance and distribution of externally induced local electromagnetic fields (Fig. 2). Among prioritized applications of SERS are nondestructive analysis of biological objects, cells or cell fragments [16–22], including red blood cells [16, 17, 23–25], bacteria [26–28], viruses [29, 30], stem cells [31, 32], human tissue cells in general [33], and cancer cells in particular[34–37]; quality control in the pharmaceutical and food industries [38, 39]; detection and quantification of proteins, peptides, and DNA molecules [9, 15, 19–21], low molecular weight biomarkers of pathological conditions, and toxic agents [9–11, 36, 40–42]. Most research works on SERS conducted recently sought the way to introduce SERS into routine practice, proving that SERS has a big future in biological and medical diagnostics.

SERS has been around since 1974 [43]. However, it was not until 2010–2012 that it gradually came to be extensively used for noninvasive analysis of living cells and cell organelles, which was dictated by the need for novel nanomaterials and instrumental approaches [9, 13, 16–20]. SERS can be successfully combined with *in vivo* bioimaging [44] or microfluidic systems [45] that significantly expand the scope of its application. SERS has remarkable sensitivity crucial for the detection and quantification of trace amounts of analytes, down to the level of single molecules. Much anticipated is the adoption of SERS for multiplex detection of analytes in complex matrices. Indeed, SERS has the necessary potential because Raman spectra are determined by the molecular composition of an analyte. It means that SERS is capable of identifying analytes in complex mixtures based on their molecular fingerprints and determining molecular conformations.

Although SERS demonstrates exceptional sensitivity in detecting the presence of ultralow concentrations (from nM to fM) of analytes in complex matrices, it may not be that successful at analyte quantitation. SERS is a spatially localized analytical technique: signal enhancement occurs at distances less than 10–15 nm from a nanostructured surface and largely depends on its texture, condition, size, anisotropy, specifics of analyte sorption by nanoparticles, their mutual orientation and tendency to aggregate [9]. Therefore, the functional properties

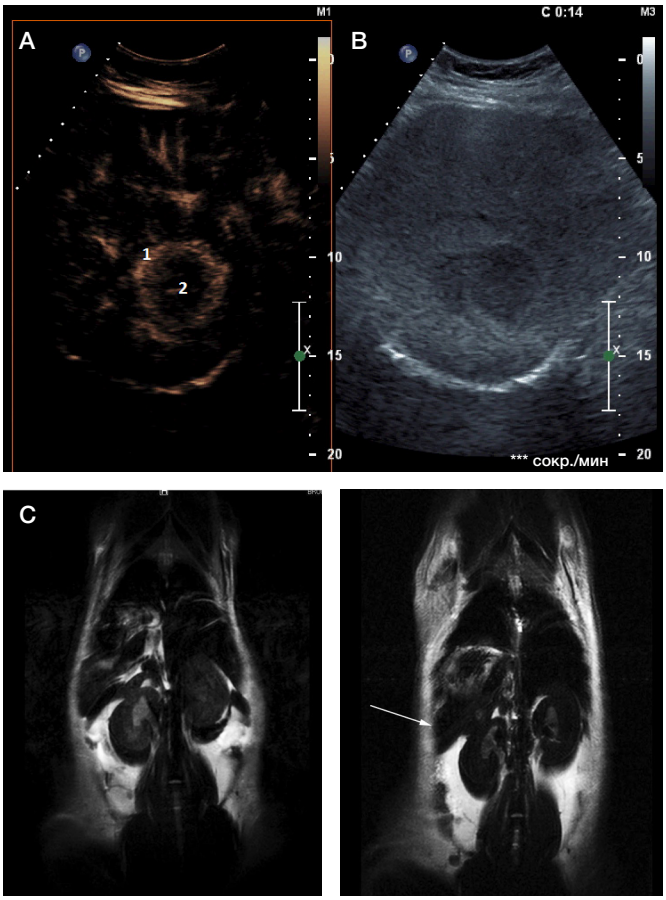

Fig. 1. Contrasting agents in medical imaging (photos are provided by the authors of this article). **A**, **B**. A contrast-enhanced ultrasound scan of the liver with a metastatic lesion: **A** — the arterial phase (14 seconds after the injection of SonoVue), 1 — peripheral enhancement; 2 — no enhancement in the central region; **B** — the gray-scale B-mode. **C**. A contrast-enhanced MR image of a rat's spleen (enhancement with iron oxide PEG-shell nanoparticles)

of a synthetic nanomaterial are determined by its morphology, microstructure and a wide range of physical and chemical properties.

SERS modifications tailored to suit specific needs can be further refined to improve the reproducibility, sensitivity and selectivity of the method and solve the problem of quantitative analysis. Here, an important contribution has been made by the study of hot spots — areas of a very strong electromagnetic field in the crevices between nanoparticles [9]. Hot spots play a significant role in the SERS effect because10^7–10^8-fold signal enhancement is registered in these particular regions.

Currently existing approaches to chemical synthesis are capable of producing high yields of silver nanoparticles (AgNP) different in their size and shape (spheres, tetrahedra, decahedra, triangular and hexagonal plates, discs, rods, threads, more complex shapes) [9, 46–51]. Physical methods of AgNP synthesis include laser ablation, thermal evaporation, arc discharge, electron-beam deposition, ion-beam sputtering, ion implantation, and different types of radiation. Interestingly, AgNP can be synthesized using naturally occurring compounds [52–55]. Planar structures are traditionally obtained using lithography, electrochemical approaches, vapor phase synthesis, chemical precipitation, Langmuir–Blodgett films, copolymer micelles, inoculation of microsphere surface functionalized with amino or thiol groups with preformed nanoparticles, and spraying of nanoparticles onto scaffolds, such as cellulose carriers, replica surfaces, etc. [9, 11, 13, 16, 17, 25]. The listed trends in SERS research aimed at designing reliable SERS-active surfaces, sensors and analytical techniques are paving the way for SERS applications in biomedical diagnostics.

Noninvasive diagnostic modalities for biological objects

Among the most interesting SERS applications that are being explored at the moment is early detection of trace amounts of bioactive molecules in physiological solutions (blood, saliva and cerebrospinal fluid). One of the recent advances in this field is a method that utilizes a combination of SERS and immunoassays exploiting the principle of specific antigen binding by a complementary antibody [56]. The use of SERS labels in combination with composite materials based on microbeads and metal nanoparticles facilitates development of targeted immunoassays for highly sensitive detection of biomolecules [56–58]. Another important field of SERS application is biosensors for analyte quantitation that rely on plasmon particles with chemically modified surfaces. As a rule, such modifications are achieved by coating the surface with a monolayer of functional thiol groups and are necessary for the subsequent sorption of analytes and preconcentration [59]. This approach enables real-time measurement of glucose levels (> 25 Mm, which is close to typical glucose concentrations occurring in some physiological fluids) in the presence of model plasma proteins (bovine serum albumin) or following a long (up to 3 days) contact of a sensor with electrolytes taken at physiological concentrations. When subcutaneously implanted in experimental animals, SERS-based sensors stably demonstrate high accuracy and reproducibility of the results over the course of at least 2 weeks; this suggests that such sensors have a good potential to be used for *in situ* monitoring of biological processes in living organisms [59]. The use of nanostructured surfaces for the study of biological objects may have an advantage over other methods because nanomaterials ensure the reproducibility of signal enhancment and allow integration of SERS-active substrates into a lab-on-a-chip or a microfluidic device. No matter what nanostructures are used to study biological objects, there are a few requirements they must satisfy, including zero toxicity against cells, chemical and morpholoigcal stability in biological fluids and solutions, an ability to reliably enhance the SERS signal as much as possible, zero interference with biological processes inside the cell and confirmations of molecules a sensor has a direct contact with.

Surface-enhanced Raman spectroscopy is also employed in cancer research [60, 61]. SERS-based sensors are capable of measuring intracellular redox potential. One of them was designed to study oxidative stress in cells; the sensor is composed of gold nanobeads enriched in quinones that act as redox-sensitive molecules and operates in a range between –400 and +100 mV exceeding the capacity of fluorescent probes [62]. Another example of a SERS-based sensor is a highly selective hybrid nanosensor made of silver nanoparticles coated with cytochrome *c*. It was designed to measure concentrations of a superoxide anion radical inside the cell and has a detection threshold of 10 nM [63]. Its underlying principle is as follows: when an electron is transferred from a superoxide anion radical to cytochrome *c*, the band representing oxidized cytochrome *c* in SERS spectra undergoes a shift to the position typical of reduced cytochrome *c*.

Of interest is the approach based on the use of nanostructures functionalized with molecules that do not produce an intense SERS spectrum but can specifically bind to a biological object whose SERS spectrum is recorded instead. This approach can be exemplified by a highly sensitive sensor that detects the presence of bacteria in blood [64]. The authors of the invention coated gold and silver-gold nanostructured composites with vancomycin that can specifically bind to gram-positive bacteria. Vancomycin causes deformation of the bacterial cell wall promoting aggregation of nanoparticles and thereby enhancing the SERS signal. Such nanostructured substrates can be used in multifunctional biochips: vancomycin can be replaced with other glycopeptides, which will expand the range of microorganisms and viruses the system can detect. Another team of researchers conducted a number of experiments involving the use of glass microcapillaries coated with gold nanoparticles that was introduced into the cell [65]. Depending on where the capillary was located inside the cell, signal enhancement occurred in the nucleus or cytoplasm; the emitted spectra reflected the functional state of the cell. Another novel method is based on the use of surfaces coated with gold nanoparticles and serves to detect a secondary messenger — an intracellular molecule released in response to stimulation of cell receptors and activation of primary effector proteins in Ca^{2+}-signaling of NADP [66]. A new approach based on the use of gold nanomaterials has been devised to perform highly sensitive detection of conformational changes in nucleic acids and proteins, as well as cell visualization *in vivo* [9, 19, 20]. Another team of researchers suggest that functionalized gold nanoparticles can be used to discriminate between different types of lymphocytes and detect leukemic cells [67].

One of the most important areas of SERS research covers the possibility of highly selective enhancement of the SERS signal from those intracellular molecules whose conformation and properties are indicators of their functional state and the state of the entire cell in general and individual organelles in particular. Among the biomolecules that can be conveniently used in basic and applied research are heme proteins: hemoglobin (Hb) and cytochromes. It is known that heme porphyrins and heme proteins produce a strong and highly specific SERS effect [68] determined by the redox state of the iron atom, heme conformation and conformation of its protein microenvironment. This fact makes it possible

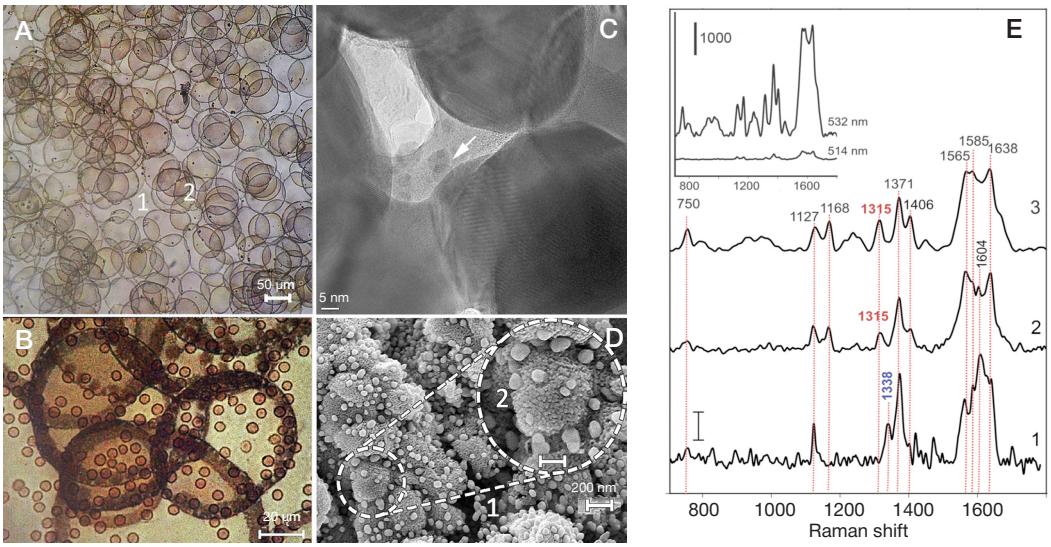

Fig. 2. The Ag nanostructured surface for SERS-based analysis. **A**. An optical microphotograph of silver rings. **B**. Living red blood cells on the nanostructured surface. **C**. Nanostructured elements of the surface (Ag nanoparticles in the substrate channels, TEM). **D**. "Sesame seeds" on the nanostructured substrate (SEM). **E**. SERS spectra of red blood cells (1) and mitochondria (2 and 3) on the $Ag@SiO_2$ nanocomposite at laser excitation wavelength of 532 nm (1 and 3) and 514 nm (2). For convenience, the spectra were normalized to their total intensity. Figures above the spectra indicate the position of peak maxima. The inset plot shows unnormalized SERS spectra of mitochondria on the $Ag@SiO_2$ nanocomposite at laser excitation wavelength of 514 and 532 nm

to study mitochondrial cytochromes in cells or organs [9] and hemoglobin in whole blood, isolated red blood cells or vascular erythrocytes *in vivo*. There are, however, a few limitations to the use of traditional spectroscopy in the study of heme porphyrins. For example, oxidized cytochromes produce weak and therefore undetectable scattering effects. When studying red blood cells, one should bear in mind that SERS spectra can be obtained only from cytoplasmic Hb (Hb_{cyt}), which constitutes the largest proportion of total Hb, but not from membrane-bound Hb (Hb_{mb}) whose conformation can change in patients with blood diseases, hereditary or endocrine disorders (thalassemia, hemoglobinopathy, etc.) [69], intoxication, or under extreme conditions [70]. In those cases, signal enhancement is caused by Hb_{mb} located in close proximity to silver nanostructures. Thus, the use of SERS-active nanostructures is indispensable in the study of heme proteins and can serve as a basis for rapid noninvasive medical testing and screening.

The authors of the present article have proposed a novel methodological approach, developed and synthesized nanostructured materials with planar architecture and Ag_2SiO_2 nanocomposites, which allowed them to attain highly reproducible and selective enhancement of the SERS signal from cytochrome *c* of a respiratory chain (electron transport chain, ETC) of intact, normally functioning mitochondria (Fig. 2 D). Using the original method, the authors were able to study conformational changes and redox properties of cytochrome *c* in intact, normally functioning mitochondria under the conditions of modulated ETC activity [9, 18]. The study also demonstrated changes in the redox state and conformation of cytochrome *c* heme molecules induced by the inhibition of ATP synthase and introduction of protonophore FCCP, which causes the uncoupling of electron transport and ATP synthesis. The SERS-based analyis involving the use of planar silver plasmon structures allowed the authors to estimate the changes in the relative concentrations of reduced cytochrome *c* in mitochondria and the conformational mobility of cytochrome *c* heme both inside mitochondria and in its isolated state (Fig. 2 D). Using intact mitochondria, the authors demonstrated that the FCCP protonophore capable of uncoupling electron transport and ATP synthesis and oligomycin, which inhibits the ATP synthase, produce opposite effects on relative cytochrome *c* concentrations and the mobility of methine bridges in heme molecules [18], whereas mutant cytochrome *c* whose heme molecules exhibit increased rigidity enjoys lower conformational mobility and functional activity of heme. It is hypothesized that conformational changes that cytochrome *c* undergoes might be employed by mitochondria to vary the rate of electron acceptance from ETC complex III and electron transfer to complex IV. The proposed methodological approach is a promising tool for further study of ETC in intact mitochondria. Application of SERS-active nanostructures to biomedicine necessitates discovery of novel analytical methods for integrating nanostructures into a lab-on-a-chip.

Rapid diagnosis of neurotransmission disorders

Neurotransmission is a cornerstone of neural mediation in both peripheral and central nervous systems [71]. Among the key neurotransmitters are 3 catecholamines (CA): dopamine, adrenaline (epinephrine) and noradrenaline (norepinephrine), and their metabolites, including vanillylmandelic, homovanillic and 5-hydroxyindoleacet acids, metanephrine and normetanephrine. CA metabolism is a crucial regulator of mental and physical activities: through dopaminergic and adrenergic receptors, CA control stress response, psychomotor activity, emotions, learning, sleep, and memory [72]. Because CA are involved in the pathogenesis of many diseases, they are extensively used in pharmacology [73]. Neurotransmission disorders are divided into two major groups: neurodegenerative diseases accompanied by the progressive loss of neural cells and the decline in CA levels (and, naturally, the levels of their metabolites) and neuroendocrine diseases characterized by increased CA synthesis induced by organic pathology or genetic defects of the hypothalamus. Among the most important neurodegenerative disorders are Alzheimer's and Parkinson's diseases. The most common neuroendocrine catecholamine-producing tumors are pheochromocytoma, paraganglioma, and neuroblastoma.

Neuroendocrine tumors pose a serious diagnostic challenge: the malignancy is often diagnosed retrospectively, in its advanced metastatic stages or during a relapse episode. In Russia, over 90% of neurodegenerative disorders are

misdiagnosed because their symptoms are confused with the signs of aging. Many neurodegenerative disorders are alike in their clinical manifestations, which also complicates the diagnosis [74]. The most dangerous neuroendocrine diseases accompanied by increased CA levels are pheochromocytoma and paraganglioma — benign and malignant catecholamine-producing tumors, respectively. They arise from chromaffin cells of the sympathoadrenal system and in 90% of cases occur in the adrenal medulla [75]. Carcinoid tumors constitute less than 1% of all malignancies and are formed by the cells of the diffuse neuroendocrine system; these cells are derived from the neural crest during fetal development and later migrate to other organs [76]. Another malignant tumor, neuroblastoma, produces multiple metastases. The majority of these tumors occur in the retroperitoneal space, most commonly in the suprarenal glands, mediastinum or neck [77].

Dopamine, noradrenaline and their metabolites can be used as molecular markers to facilitate the diagnosis of Alzheimer's and Parkinson's diseases: the onset of the disease can be inferred from the decline in their concentrations in biological fluids. It has been shown that as the symptoms of Parkinson's progress, the ratio of dopamine to dioxy phenylacetic acid (DOPAA) in urine decreases and production of dopamine and dioxyphenylalanine (DOPA) declines. The patient develops pronounced deficit of catecholamine neurotransmitters (dopamine, noradrenaline and serotonin) in the early stages of the disease, accompanied by dopamine catabolism which results from increased oxidative deamination of this neurotransmitter. However, early manifestations of Parkinson's occur in the backdrop of increased dopamine turnover compensating for neural loss. As cell degeneration progresses, DOPA levels dwindle, as does the dopamine/DOPAA ratio, indicating neurotransmission pathology and the lack of monoamine oxidase activity, which suggests depletion of resources for CA synthesis. Thus, decreasing concentrations of CA in Parkinson's and their relatively simple molecular structure make CA promising biological markers of this disease.

In healthy individuals CA levels are very low (about 1 nM), shrinking further in pathology (Alzheimer's and Parkinson's). In blood, CA are quickly oxidized by platelet monoamine oxidases. Therefore, CA tests should take no longer than 15 to 30 minutes. This poses a certain difficulty and necessitates development of rapid specific and sensitive assays for determining CA and their metabolites in biological fluids.

At present, early diagnosis of neurodegenerative disorders is facilitated by a variety of neuroimaging modalities, including MRI, CT, PET (positron emission tomography), SPECT (single-photon emission computed tomography), ^{1}H-MRS (proton magnetic resonance spectroscopy), EEG (electroencephalography), etc. [10, 11]. In recent years, PET and SPECT have been adopted to clinical practice to aid the diagnosis of Alzheimer's and Parkinson's diseases. However, the availability of these radionuclide-based imaging techniques is largely determined by an arsenal of available labeled compounds referred to as radiopharmaceuticals (RP) that are administered to the patient before the scan. As a rule, RP used in PET are based on bioactive short- (^{18}F) and ultrashort-lived (^{11}C, ^{13}N, ^{15}O) positron-emitting radionuclides [10]. SPECT, another imaging modality, is instrumental in assessing the functional state of brain regions. SPECT can help to differentiate between neurodegenerative diseases that have similar clinical manifestations but affect different parts of the brain. But although neuroimaging is an accurate diagnostic tool for early diagnosis of neurodegenerative and neuroendocrine conditions, it has no prognostic value in patients with neurotransmission disorders. Besides, neuroimaging equipment and consumables are expensive, and a patient may not have clear indications for the procedure. In spite of high prevalence of neurotransmission disorders, neuroimaging is often available only to the residents of big cities. Therefore, novel approaches are needed to create a rapid, cheap, simple and sensitive system for multiplex detection of biomarkers associated with neurological pathology.

Traditional immunoassays are a simple and available diagnostic tool for suspected Alzheimer's or Parkinson's. Neurotransmission biomarkers determined by such assays comprise a number of high molecular weight compounds, such as β-amyloid, the tau protein, and the phosphorylated tau protein, in the first place. Patients with Parkinson's disease accumulate synuclein, whereas patients with Alzheimer's develop senile plagues (protein deposits of β-amyloid). A lot of effort has been channeled into the development of novel techniques for β-amyloid determination in recent years. Distribution of β-amyloid in the body can be studied by radioisotope-based instrumental modalities, as well as by immunoassays of cerebrospinal fluid [10, 11]. The procedure of sample preparation for such assays, however, is too complicated and time-consuming. On the whole, even though immunoassays for measuring concentrations of biomarkers associated with neurodegenerative disorders hold certain promise, they have limitations related to the object of analysis itself and the structure of diagnostic molecules. Besides, concentrations of protein biomarkers can vary depending on the age and sex of a patient [10] causing the assay to yield false results. Neuroendocrine diseases have their own protein biomarkers. For example, chromogranin A (CgA) present in chromaffin granules of neuroendocrine cells is a biomarker of pheochromocytoma, paraganglioma, neuroblastoma, and carcinoid tumors [10, 11]. However, this method cannot reliably discriminate between the listed pathologies. Therefore, patients with suspected neuroblastoma are tested not only for the traditional biochemical markers, but also for neuron-specific enolase, ferritin, lactate dehydrogenase, and γ-glutamyl transferase [10, 11]. High on the agenda are the search for and the study of nonprotein biomarkers, such as CA and their metabolites, as well as development of simple selective and highly sensitive methods for measuring their concentrations that will ensure accurate and reliable diagnosis early in pathology.

The process of neurotransmission involves inactivation of CA and their metabolism. CA are methoxylated in the presence of catechol-o-methyl transferase; the reaction produces metanephrine and normetanephrine. Besides, CA undergo oxidative deamination in the presence of monoamine oxidase; the end products of this reaction are vanillylmandelic and homovanillic acids [10, 11]. Because the levels of CA and their metabolites are different in health and pathology, these catecholamines can be used as diagnostic markers in basic research and clinical tests. Among the methods aiding neuroendocrine or neurodegenerative diagnosis based on blood or urine levels of CA or their metabolites, chromatography combined with electrochemical detection or mass spectrometry (MS) is the most popular [11]. In spite of high selectivity, sensitivity and availability of electrochemical detectors, its results are poorly reproducible, it is sensitive to fluctuations of the mobile phase flow rate, is not free of electrode contamination, and imposes strict requirements on the origin of the mobile phase. High-performance liquid chromatography with electrochemical detection (HPLC-ED) suffers high levels of background noise (in comparison with a useful signal), does not always have sufficient sensitivity and demonstrates low separation efficacy. HPLC-MS is significantly more sensitive

to CA and their metabolites but at the same time insufficiently rapid and has a few limitations related to the elution of certain compounds in dead time, high levels of background noise and difficulties with peak resolution [11]. In spite of the vast body of accumulated knowledge and the extensive arsenal of methods for measuring CA in blood plasma and urine, poor reproducibility and resolution coupled with time required for the procedure produce a whole lot of diagnostic errors leading to ineffective treatment. The solution to this problem may lie in the development of electrochemical sensors [78]. In the majority of such sensors, indicator electrodes are functionalized with pre-synthesized compounds with a certain structure ensuring selective detection of CA. These compounds comprise DNA fingerprints, polymers, synthetic receptors, nanotubes and nanocores modified with organic molecules (polyethyleneimine, cyclodextrin, metal complexes) [79–81]. Electrochemical methods for CA/CA metabolite determination have average sensitivity in the range between 0.01 and 1 μM. Unfortunately, the majority of electrochemical analytical methods cannot be multiplexed, which limits their application in clinical practice.

An alternative to the methods described above is spectroscopy, its primary advantages being the rate of analysis, simplicity, low costs, and in some cases higher sensitivity, as compared to its electrochemical or chromatography-based counterparts. Fluorescence-based modalities capable of detecting CA or their metabolites also hold some promise as diagnostic techniques. In the presence of enzymes, such as peroxidase [82], CA is oxidized by hydrogen peroxide; the end product of their oxidation is a compound capable of quenching fluorescence of water-soluble synthetic poly(2,5-bis(3-sulfonatopropoxy)-1,4-phenylene, disodium salt-alt-1,4-phenylene). The method exhibits low sensitivity towards individual CA types (about 0.1 μM), but can be multiplexed to selectively detect catecholamines over other molecules [83]. There are detection methods that utilize nanoparticles, including F_e3O_4-based ones. These nanoparticles are used instead of horse radish peroxidase. The principle underlying this approach exploits the inhibition of *Amplex UltraRed* reagent (peroxidase substrate) oxidation by CA in the presence of hydrogen peroxide and Fe_3O_4 nanoparticles. The oxidized *Amplex UltraRed* emits an intense fluorescence signal with 587 nm wavelength at 567 nm excitation. CA covalently binds to the surface of iron oxide (III) nanoparticles and quenches fluorescence of the oxidized *Amplex UltraRed*. Although the sensitivity of the method is high (detection threshold of 3 nM), it can only selectively distinguish between catecholamines and other molecules but cannot be multiplexed [84]. Unfortunately, the sensitivity of the majority of similar methods is insufficient to allow quantitation of nanomolar concentrations of catecholamine, which limits the application of such biosensing systems to the analysis of biological objects [10, 11].

SERS-based methods are more or less free of the major drawbacks associated with other analytical modalities employed for the detection of CA and their metabolites, such as low sensitivity and low rate of analysis. Unoptimized SERS-based methods can detect neurotransmitters at concentrations ranging from 0.1 to 0.5 M [85], which obviously does not satisfy the requirements set for the analysis of biological fluids. A solution can be offered by highly sensitive and selective optical biosensing SERS-based systems, in which enhancement of the SERS signal is achieved through the effect of plasmon resonance occurring on a nanostructured surface of a noble metal, as described above. In such systems, specificity is ensured by capturing SERS signals with 1,500–650 cm^{-1} wavelength that provide valuable information about individual components of complex matrices. SERS is very sensitive even to minor changes in the structure and orientation of molecules. Considering its characteristics listed above and a weak SERS signal of water, SERS seems to be a promising analytical method with very little sample preparation that can be applied to complex matrices. Importantly, Raman spectroscopy ensures signal enhancement at a broad range of excitation frequencies, which allows selecting an excitation source that has minimal background autofluorescence and causes no damage to the sample. Nevertheless, today SERS is only making its first steps into clinical practice as a tool for the detection of neurotransmitters [9–11, 86]. Recently, SERS has been shown to be a feasible method for dopamine detection at concentrations between 1 and 10 mM [87, 88]. Some authors have attained better sensitivity of 0.01–0.1 fM. SERS-based methods have demonstrated selectivity towards dopamine in the presence of ascorbic acid, glucose, L-cysteine, tyrosine, catechol, phenylethylamine, and serum albumin [89]. SERS can be easily combined with other modalities and improve their results. For example, selectivity exhibited by electrochemical methods for the detection of neurotransmitters in biological fluids is limited in the presence of ascorbic acid whose redox potential almost coincides with dopamine potential [90]. Using colloidal silver solutions, researchers were able to achieve a lower detection threshold of 5 nM [91]. Other authors report formation of complexes accompanied by charge transfer that can help to attain a stable and intense SERS signal [92, 93]. There is no doubt that the approaches discussed in this article can be optimized further to reach pico- and femtomolar detection thresholds, promoting the use of SERS in biomedical diagnostics.

CONCLUSIONS

SERS has a very good potential as a biomedical analytical modality that can be applied to complex multicomponent matrices. It combines high sensitivity and high selectivity and requires little sample preparation. It also breaks ground for novel noninvasive multiplex detection of analytes in biological matrices. Further evolution of SERS depends on a number of factors. Those include research into SERS-active nanostructures focusing on their application in the clinical setting and comprehensive investigation of properties exhibited by such nanostructures in biological fluids and in contact with cells. Development of analytical methods with little sample preparation for simple, sensitive and selective multiplex detection of neurotransmitters, their metabolites or other biological markers in living cells or cell organelles holds promise for early diagnosis of various pathologies. The authors believe that optical systems for multiplex detection of pathology-associated biomarkers in biological fluids and cells constitute one of the most promising areas of research in clinical diagnostics and can significantly improve diagnostic accuracy.

References

1. Semkina A, Abakumov M, Grinenko N, Abakumov A, Skorikov A, Mironova E et al. Core-shell-corona doxorubicin-loaded superparamagnetic Fe3O4 nanoparticles for cancer theranostics. Colloids Surf B Biointerfaces. 2015; (136): 1073–80.
2. Chekhonin VP, Baklaushev VP, Yusubalieva GM, Belorusova AE, Gulyaev MV, Tsitrin EB et al. Targeted delivery of liposomal nanocontainers to the peritumoral zone of glioma by means of monoclonal antibodies against GFAP and the extracellular loop of Cx43 Nanomedicine. 2012; 8 (1): 63–70.
3. Nukolova NV, Aleksashkin AD, Abakumova TO, Morozova AY, Gubskiy IL, Kirzhanova EA et al. Multilayer polyion complex nanoformulations of superoxide dismutase 1 for acute spinal cord injury. J Control Release. 2018; (270): 226–36.
4. Kovaleva EV, Sinyukova GT, Danzanova TY, Lepedatu PI, Gidulina EA, Vozmozhnosti UZI s primeneniyem contrastnogo usileniya v diagnostike metastazov v pecheni u bolnih kolorectalnim rakom. Koloproktologiya. 2018; 1 (63): 36–42.
5. Bednikov SN, Sholokhov VN, Sinyukova GT, Goodilina EA, Abgaryan MG, Kalinin AE i dr. Differentsialnaya diagnostika ochagovih giperekhogennih orazovaniy v pecheni. Koloproktologiya. 2017; 2 (60): 19–25.
6. Nirmala D. Review: Medical image contrast enhancement techniques, Research Journal of Pharmaceutical Biological and Chemical Sciences. 2015; 6 (3): 321–9.
7. Chen F, Hableel G, Zhao ER, Jokerst JV. Multifunctional nanomedicine with silica: Role of silica in nanoparticles for theranostic, imaging and drug monitoring. J Colloid and Interface Science. 2018; (521): 261–79.
8. Balthazar P, Shinagare AB, Tirumani SH, Jagannathan JP, Ramaiya NH, Khorosani R. Gastroenteropancreatic neuroendocrine tumors: impact of consistent contrast agent selection on radiologists' confidence in hepatic lesion assessment on restarding MRIs. Abdominal Radiology. 2018; 6 (43): 1386–92.
9. Eremina OE, Semenova AA, Sergeeva EA, Brazhe NA, Maksimov GV, Shekhovtsova TN, Goodilin EA, Veselova IA, Surface enhanced Raman spectroscopy in modern chemical analysis: achievements and prospects. Russ Chem Rev. 2018; 87 (8): 741–70, DOI: doi.org/10.1070/RCR4804.
10. Vatsadze SZ, Eremina OE, Veselova IA, Kalmykov SN, Nenajdenko VG. 18F-Labelled catecholamine type radiopharmaceuticals in the diagnosis of neurodegenerative diseases and neuroendocrine tumours: approaches to synthesis and development prospects. Russ Chem Rev. 2018; 87 (4): 350–73, DOI: doi.org/10.1070/RCR4752/
11. Veselova IA, Sergeeva EA, Makedonskaya MI, Eremina OE, Kalmykov SN, Shekhovtsova TN. Metodi opredeleniya markerov neyromediatornogo obmena v celyah klinicheskoy diagnostiki. Russian Journal of Analytical chemistry. 2016; 71 (12): 1235–49.
12. Kneipp K, Wang Y, Kneipp H, Perelman LT, Itzkan I, Dasari RR et al. Single molecule detection using surface-enhanced Raman scattering (SERS). Phys Rev Lett. 1997; (78): 1667–70.
13. Olenin AY, Lisichkin GV. Metal nanoparticles in condensed media: preparation and the bulk and surface structural dynamics. Russ Chem Rev. 2011; (80): 605–35.
14. Cialla D, März A, Böhme R, Theil F, Weber K, Schmitt M et al. Surface-enhanced Raman spectroscopy (SERS): Progress and trends. Anal Bioanal Chem. 2012; (403): 27–54.
15. Laing S, Gracie K, Faulds K. Multiplex in vitro detection using SERS. Chem Soc Rev. 2016; (45): 1901–18.
16. Semenova AA, Goodilin EA, Brazhe NA, Ivanov VK, Baranchikov AE, Lebedev VA et al. Planar SERS nanostructures with stochastic silver ring morpholgy for biosensor chips. J Mater Chem. 2012; (22): 24530–44.
17. Semenova AA, Brazhe NA, Parshina EY, Sarycheva AS, Maksimov GV, Goodilin EA. A new route for SERS analysis of intact erythrocytes using polydisperse silver nanoplatelets on biocompatible scaffolds. RSC Adv. 2016; (6): 85156–63.
18. Brazhe NA, Evlyukhin AB, Goodilin EA, Semenova AA, Novikov SM, Bozhevolnyi SI et al. Probing cytochrome c in living mitochondria with surface-enhanced Raman spectroscopy. Sci Rep. 2015; (5): 13793(1)–13793(13).
19. Durmanov NN, Guliev RR, Eremenko AV, Boginskaya IA, Ryzhikov IA, Trifonova EA et al. Non-labeled selective virus detection with novel SERS-active porous silver nanofilms fabricated by Electron Beam Physical Vapor Deposition. Sens Actuators B. 2018; (257): 37–47.
20. Nechaeva N, Prokopkina T, Makhaeva G, Rudakova E, Boltneva N, Dishovsky et al. Quantitative butyrylcholinesterase activity detection by surface-enhanced Raman spectroscopy. Sens Actuators B. 2018; (259): 75–82.
21. Kneipp J, Kneipp H, Wittig B, Kneipp K. One- and two-photon excited optical ph probing for cells using surface-enhanced Raman and hyper-Raman nanosensors. Nano Lett. 2007; (7): 2819–23.
22. Drescher D, Kneipp J. Nanomaterials in complex biological systems: insights from Raman spectroscopy. Chem Soc Rev. 2012; (41): 5780–99.
23. Wood BR, Caspers P, Puppels GJ, Pandiancherri S, McNaughton D. Resonance Raman spectroscopy of red blood cells using near-infrared laser excitation. Anal Bioanal Chem. 2007; (387): 1691–703.
24. Brazhe NA, Parshina EY, Khabatova VV, Semenova AA, Brazhe AR, Yusipovich AI et al. Tuning SERS for living erythrocytes: Focus on nanoparticle size and plasmon resonance position. J Raman Spectrosc. 2013; (44): 686–94.
25. Semenova AA, Brazhe NA, Parshina EY, Ivanov VK, Maksimov GV, Goodilin EA. Aqueous diaminsilver hydroxide as a precursor of pure silver nanoparticles for SERS probing of living erythrocytes. Plasmonics. 2013; (9): 227–35.
26. Jarvis RM, Goodacre R. Discrimination of bacteria using surface-enhanced Raman spectroscopy. Anal Chem. 2004; (76): 40–7.
27. Wang P, Pang S, Chen J, McLandsborough L, Nugen SR, Fan M et al. Label-free mapping of single bacterial cells using surface-enhanced Raman spectroscopy. Analyst. 2016; (141): 1356–62.
28. Granger JH, Schlotter NE, Crawford AC, Porter MD. Prospects for point-of-care pathogen diagnostics using surface-enhanced Raman scattering (SERS). Chem Soc Rev. 2016; (45): 3865–82.
29. Hoang V, Tripp RA, Rota P, Dluhy RA. Identification of individual genotypes of measles virus using surface enhanced Raman spectroscopy. Analyst. 2010; (135): 3103–9.
30. Luo S-C, Sivashanmugan K, Liao J-D, Yao C-K, Peng H-C. Nanofabricated SERS-active substrates for single-molecule to virus detection in vitro: A review. Biosens Bioelectron. 2014; (61): 232–40.
31. El-Said WA, Kim SU, Choi J-W. Monitoring in vitro neural stem cell differentiation based on surface-enhanced Raman spectroscopy using a gold nanostar array. J Mater Chem C. 2015; (3): 3848–59.
32. Han J, Qian X, Wu Q, Jha R, Duan J, Yang Z et al. Novel surface-enhanced Raman scattering-based assays for ultra-sensitive detection of human pluripotent stem cells. Biomaterials. 2016; (105): 66–76.
33. Howes PD, Rana S, Stevens MM. Plasmonic nanomaterials for biodiagnostics. Chem Soc Rev. 2014; (43): 383–8.
34. McAughtrie S, Faulds K, Graham D. Surface enhanced Raman spectroscopy (SERS): potential applications for disease detection and treatment. J Photochem Photobiol C. 2014; (21): 40–53.
35. Puppels GJ, de Mul FFM, Otto C, Greve J, Robert-Nicoud M, Arndt-Jovin DJ et al. Studying single living cells and chromosomes by confocal Raman microspectroscopy. Nature. 1990; (347): 301–3.
36. Alvarez-Puebla RA, Liz-Marzán LM. SERS-based diagnosis and biodetection. Small. 2010; (6): 604–10.
37. März A, Mönch B, Rösch P, Kiehntopf M, Henkel T, Popp J. Detection of thiopurine methyltransferase activity in lysed red blood cells by means of lab-on-a-chip surface enhanced Raman spectroscopy (LOC-SERS). Anal Bioanal Chem. 2011; (400): 2755–61.
38. Jahn IJ, Žukovskaja O, Zheng X-S, Weber K, Bocklitz TW, Cialla-May D et al. Surface-enhanced Raman spectroscopy and microfluidic platforms: challenges, solutions and potential applications. Analyst. 2017; (142): 1022–47.
39. Kumar S, Goel P, Singh JP. A facile method for fabrication of buckled PDMS silver nanorod arrays as active 3D SERS cages for

bacterial sensing. Sens Actuators B. 2017; (241): 577–83.
40. Polavarapu L, Perez-Juste J, Xu Q, Liz-Marzán LM. Optical sensing of biological, chemical and ionic species through aggregation of plasmonic nanoparticles. J Mater Chem C. 2014; (2): 7460–76.
41. Dhillon A, Nair M, Kumar D. Analytical methods for sensing of health-hazardous arsenic from biotic and abiotic natural resources. Anal Methods. 2015; (7): 10088–108.
42. Xiao L, Zhang M, Liu Z, Bian W, Zhang X, Zhan J. Hydrophobic silver nanowire membrane for swabbing extraction and in situ SERS detection of polycyclic aromatic hydrocarbons on toys. Anal Methods. 2017; (9): 1816–24.
43. Fleischmann M, Hendra PJ, McQuillan AJ. Raman spectra of pyridine adsorbed at a silver electrode. Chem Phys Lett. 1974; (26): 163–6.
44. Wachsmann-Hogiu S, Weeks T, Huser T. Chemical analysis in vivo and in vitro by Raman spectroscopy — From single cells to humans. Curr Opin Biotechnol. 2009; (20): 63–73.
45. Yazdi SH, White IM. A nanoporous optofluidic microsystem for highly sensitive and repeatable surface enhanced Raman spectroscopy detection. Biomicrofluidics. 2012; (6): 14105–59.
46. Sharma VK, Yngard RA, Lin Y. Green synthesis and their antimicrobial activities. Adv Colloid Interface Sci. 2009; (145): 83–96.
47. Sun Y. Shape-controlled synthesis of gold and silver nanoparticles. Science. 2002; (298): 2176–9.
48. Guerrero-Martínez A, Barbosa S, Pastoriza-Santos I, Liz-Marzán LM. Nanostars shine bright for you: colloidal synthesis, properties and applications of branched metallic nanoparticles. Curr Opin Colloid Interface Sci. 2011; (16): 118–27.
49. Lim B, Xia Y. Metal nanocrystals with highly branched morphologies. Angew Chem Int Ed. 2011; (50): 76–85.
50. Pietrobon B, Kitaev V. Photochemical synthesis of monodisperse size-controlled silver decahedral nanoparticles and their remarkable optical properties. Chem Mater. 2008; (20): 5186–90.
51. Phan-Quang GC, Lee HK, Phang IY, Ling XY. Plasmonic colloidosomes as three-dimensional SERS platforms with enhanced surface area for multiphase sub-microliter toxin sensing. Angew Chem Int Ed. 2015; (54): 9691–5.
52. Tien D-C, Liao C-Y, Huang J-C, Tseng K-H, Lung J-K, Tsung T-T et al. Novel technique for preparing a nano-silver water suspension by the arc-discharge method. Rev Adv Mater Sci. 2008; (18): 750–6.
53. Gongalsky MB, Osminkina LA, Pereira A, Manankov AA, Fedorenko AA, Vasiliev AN et al. Laser-synthesized oxide-passivated bright Si quantum dots for bioimaging. Sci Rep. 2016; (6): 24732(1)–24732(8).
54. Nadagouda MN, Varma RS. Green synthesis of silver and palladium nanoparticles at room temperature using coffee and tea extract. Green Chem. 2008; (10): 859–62.
55. Moulton MC, Braydich-Stolle LK, Nadagouda MN, Kunzelman S, Hussain SM, Varma RS. Synthesis, characterization and biocompatibility of "green" synthesized silver nanoparticles using tea polyphenols. Nanoscale. 2010; (2): 763–70.
56. Hwang H, Chon H, Choo J, Park JK. Optoelectrofluidic sandwich immunoassays for detection of human tumor marker using surface-enhanced Raman scattering. Analyt Chem. 2010; (82): 7603–10.
57. Li J-M, Ma W-F, Wei C, Guo J, Hu J, Wang C-C. Poly(styrene-co-acrylic acid) core and silver nanoparticle/silica shell composite microspheres as high performance surface-enhanced Raman spectroscopy (SERS) substrate and molecular barcode label. J Mater Chem. 2011; (21): 5992–98.
58. Chen J-W, Lei Y, Liu X-J, Jiang J-H, Shen G-L, Yu R-Q. Immunoassay using surface-enhanced Raman scattering based on aggregation of reporter-labeled immunogold nanoparticles. Anal Bioanal Chem. 2008; (392): 187–93.
59. Ma K, Yuen JM, Shah NC, Walsh JT, Glucksberg MR, Van Duyne RP. In Vivo, transcutaneous glucose sensing using surface-enhanced spatially offset Raman spectroscopy: multiple rats, improved hypoglycemic accuracy, low incident power, and continuous monitoring for greater than 17 days. Anal Chem. 2011; (83): 9146–52.
60. Pînzaru SC, Andronie LM, Domsa I, Cozar O, Astilean S. Bridging biomolecules with nanoparticles: surface-enhanced Raman scattering from colon carcinoma and normal tissue. J Raman Spectrosc. 2008; (39): 331–4.
61. Wang X, Qian X, Beitler JJ, Chen ZG, Khuri FR, Lewis MM et al. Detection of circulating tumor cells in human peripheral blood using surface-enhanced Raman scattering nanoparticles. Cancer Res. 2011; (71): 1526–32.
62. Thomson PIT, Camus VL, Hu Y, Campbell CJ. Series of quinone-containing nanosensors for biologically relevant redox potential determination by surface-enhanced Raman spectroscopy. Anal Chem. 2015; 87 (9): 4719–35.
63. Qu L-L, Li D-W, Qin L-X, Mu J, Fossey JS, Long Y-T. Selective and sensitive detection of intracellular O2(•-) using Au NPs/cytochrome c as SERS nanosensors. Anal Chem. 2013; 85 (20): 9549–55.
64. Sivanesan A, Witkowska E, Adamkiewicz W, Dziewit Ł, Kamińska A, Waluk J. Nanostructured silver-gold bimetallic SERS substrates for selective identification of bacteria in human blood. Analyst. 2013; 139 (5): 1037–43.
65. Vitol EA, Orynbayeva Z, Bouchard MJ, Azizkhan-Clifford J, Friedman G, Gogotsi Y. In situ intracellular spectroscopy with surface enhanced Raman spectroscopy (SERS)-enabled nanopipettes. ACS Nano. 2009; 3 (11): 3529–36.
66. Vitol EA, Brailoiu E, Orynbayeva Z, Dun NJ, Friedman G, Gogotsi Y. Surface-enhanced Raman spectroscopy as a tool for detecting Ca2+ mobilizing second messengers in cell extracts. Anal Chem. 2010; 8 (16): 6770–4.
67. Zhang Q, Lu X, Tang P, Zhang D, Tian J, Zhong L. Gold nanoparticle (AuNP)-based surface-enhanced Raman scattering (SERS) probe of leukemic lymphocytes. Plasmonics. 2016; (11): 1361–8.
68. Berezhna S, Wohlrab H, Champion PM. Resonance Raman investigations of cytochrome c conformational change upon interaction with the membranes of intact and Ca2+-exposed mitochondria. Biochemistry. 2003; (42): 6149–58.
69. Pankratova MS, Baizhumanov AA, Yusipovich AI, Faassen M, Shiryaeva TYu, Peterkova VA et al. Imbalance in the blood antioxidant systemin growth hormone-deficient children before and after 1 year of recombinant growth hormone therapy. Peer J. 2015; (3): e1055(1)–e1055(12).
70. Brazhe NA, Baizhumanov AA, Parshina EYu, Yusipovich AI, Akhalaya MYa, Yarlykova YuV et al. Studies of the blood antioxidant system and oxygen-transporting properties of human erythrocytes during 105-day isolation. Human physiology. 2014; (40): 804–9.
71. Rodan LH, Gibson KM, Pearl PL. Clinical Use of CSF Neurotransmitters J Pediatr Neurol. 2015; 53 (4): 277–86.
72. Eisenhofer G, Kopin IJ, Goldstein DS. Catecholamine metabolism: a contemporary view with implications for physiology and medicine. Pharmacol Rev. 2004; 56 (3): 331–49.
73. Goldstein DS, Kopin IJ, Sharabi Y. Catecholamine autotoxicity. Implications for pharmacology and therapeutics of Parkinson disease and related disorders. Pharmacol Ther. 2014; 144 (3): 268–82.
74. Postuma RB, Gagnon JF, Vendette M, Montplaisir JY. Markers of neurodegeneration in idiopathic rapid eye movement sleep behaviour disorder and Parkinson's disease. Brain. 2009; 132 (12): 3298–307.
75. Subramaniam R. Pheochromocytoma — current concepts in diagnosis and management. Trends Anaesth Crit Care. 2011; 1 (2): 104–10.
76. Yangong H, Shi C, Shahbaz M, Zhengchuan N, Wang J, Liang B et al. Diagnosis and treatment experience of rectal carcinoid (a report of 312 cases). Int J Surg. 2014; 12 (5): 408–11.
77. Sadilkova K, Dugaw K, Benjamin D, Jack RM. Analysis of vanillylmandelic acid and homovanillic acid by UPLC-MS/MS in serum for diagnostic testing for neuroblastoma. Clin Chim Acta. 2013; (424): 253–7.
78. Rodriguez MC, Rubianes MD, Rivas GA. Highly selective determination of dopamine in the presence of ascorbic acid and serotonin at glassy carbon electrodes modified with carbon nanotubes dispersed in polyethylenimine. J Nanosci Nanotechnol. 2008; 8 (11): 6003–9.
79. Mazloum-Ardakani M, Khoshroo A. High performance electrochemical sensor based on fullerene-functionalized carbon nanotubes/ionic liquid: Determination of some catecholamines. Electrochem Comm. 2014; (42): 9–12.

80. Rezaei B, Boroujeni MK, Ensafi AA. Fabrication of DNA, o-phenylenediamine, and gold nanoparticle bioimprinted polymer electrochemical sensor for the determination of dopamine. Biosens. Bioelectron. 2015; (66): 490–6.
81. Gao N, Xu Z, Wang F, Dong SJ. Sensitive biomimetic sensor based on molecular imprinting at functionalized indium tin oxide electrodes. Electroanalisis. 2007; (19): 1655–60.
82. Poliakov AE, Dumshakova AV, Muginova SV, Shekhovtsova TN. A peroxidase-based method for the determination of dopamine, adrenaline, and α-methyldopa in the presence of thyroid hormones in pharmaceutical forms. Talanta. 2011; 84 (3): 710–6.
83. Huang H, Gao Y, Shi F, Wang G, Shah SM, Su X. Determination of catecholamine in human serum by a fluorescent quenching method based on a water-soluble fluorescent conjugated polymer-enzyme hybrid system. Analyst. 2012; 137 (6): 1481–6.
84. Liu CH, Yu CJ, Tseng WL. Fluorescence assay of catecholamines based on the inhibition of peroxidase-like activity of magnetite nanoparticles. Anal Chim Acta. 2012; (745): 143–8.
85. Schulze HG, Blades MW, Bree AV, Gorzalka BB, Greek LS, Turner RFB. Characteristics of backpropagation neural networks employed in the identification of neurotransmitter Raman spectra. Appl Spectrosc. 1994; (48): 50–7.
86. Sharma B, Frontiera RR, Henry AI, Ringe E, Van Duyne RP. SERS: Materials, applications, and the future. Mater Today. 2012; (15): 16–25.
87. Lim JW, Kang IJ. Fabrication of chitosan-gold nanocomposites combined with optical fiber as SERS substrates to detect dopamine molecules. Bull Korean Chem Soc. 2014; (35): 25–9.
88. Lim JW, Kang IJ. Chitosan-gold nano composite for dopamine analysis using Raman scattering. Bull Korean Chem Soc. 2013; (34): 237–42.
89. Tang L, Li S, Han F, Liu L, Xu L, Ma W et al. SERS-active Au@Ag nanorod dimers for ultrasensitive dopamine detection. Biosens Bioelectron. 2015; (71): 7–12.
90. Lee NS, Hsieh YZ, Paisley RF, Morris MD. Surface enhanced Raman spectroscopy of the catecholamine neurotransmitters and related compounds. Anal Chem. 1998; (60): 442–6.
91. Kneipp K, Wang Y, Dasari RR, Feld MS. Near-infrared surface-enhanced Raman scattering (NIR-SERS) of neurotransmitters in colloidal silver solutions. Spectrochim Acta. 1995; (51A): 481–7.
92. Volkan M, Stokes DL, Vo-Dinh T. Surface-Enhanced Raman of dopamine and neurotransmitters using sol-gel substrates and polymer-coated fiber-optic probes. Appl Spectrosc. 2000; 54 (12): 1842–8.
93. Barreto WJ, Barreto SRG, Ando RA, Santos PS, DiMauro E, Jorge T. Raman, IR, UV–vis and EPR characterization of two copper dioxolene complexes derived from L-DOPA and dopamine. Spectrochim. Acta Part A. 2008; 71 (4): 1419–24.

Литература

1. Semkina A, Abakumov M, Grinenko N, Abakumov A, Skorikov A, Mironova E et al. Core-shell-corona doxorubicin-loaded superparamagnetic Fe3O4 nanoparticles for cancer theranostics. Colloids Surf B Biointerfaces. 2015; (136): 1073–80.
2. Chekhonin VP, Baklaushev VP, Yusubalieva GM, Belorusova AE, Gulyaev MV, Tsitrin EB et al. Targeted delivery of liposomal nanocontainers to the peritumoral zone of glioma by means of monoclonal antibodies against GFAP and the extracellular loop of Cx43. Nanomedicine. 2012; 8 (1): 63–70.
3. Nukolova NV, Aleksashkin AD, Abakumova TO, Morozova AY, Gubskiy IL, Kirzhanova EA et al. Multilayer polyion complex nanoformulations of superoxide dismutase 1 for acute spinal cord injury. J Control Release. 2018; (270): 226–36.
4. Ковалева Е. В., Синюкова Г. Т., Данзанова Т. Ю., Лепэдату П. И., Гудилина Е. А., Возможности УЗИ с применением контрастного усиления в диагностике метастазов в печени у больных колоректальным раком. Колопроктология. 2018; 1 (63): 36–42.
5. Бердников С. Н., Шолохов В. Н., Синюкова Г. Т., Гудилина Е. А., Абгарян М. Г., Калинин А. Е. и др. Дифференциальная диагностика очаговых гиперэхогенных образований в печени. Колопроктология. 2017; 2 (60): 19–25.
6. Nirmala D. Review: Medical image contrast enhancement techniques, Research Journal of Pharmaceutical Biological and Chemical Sciences. 2015; 6 (3): 321–9.
7. Chen F, Hableel G, Zhao ER, Jokerst JV. Multifunctional nanomedicine with silica: Role of silica in nanoparticles for theranostic, imaging and drug monitoring. J Colloid and Interface Science. 2018; (521): 261–79.
8. Balthazar P, Shinagare AB, Tirumani SH, Jagannathan JP, Ramaiya NH, Khorosani R. Gastroenteropancreatic neuroendocrine tumors: impact of consistent contrast agent selection on radiologists' confidence in hepatic lesion assessment on restarding MRIs. Abdominal Radiology. 2018; 6 (43): 1386–92.
9. Еремина О. Е., Семенова А. А., Сергеева Е. А., Браже Н. А., Максимов Г. В., Шеховцова Т. Н. и др. Спектроскопия гигантского комбинационного рассеяния в современном химическом анализе: достижения и перспективы использования. Успехи химии. 2018; 87 (8): 741–70.
10. Вацадзе С. З., Еремина О. Е., Веселова И. А., Калмыков С. Н., Ненайденко В. Г., Радиофармпрепараты группы катехоламинов, меченные 18F, в диагностике нейродегенеративных заболеваний и нейроэндокринных опухолей: подходы к синтезу и перспективы развития. Успехи Химии. 2018; 87 (4): 350–73.
11. Веселова И. А., Сергеева Е. А., Македонская М. И., Еремина О. Е., Калмыков С. Н., Шеховцова Т. Н., Методы определения маркеров нейромедиаторного обмена в целях клинической диагностики. Журнал аналитической химии. 2016; 71 (12): 1235–49.
12. Kneipp K, Wang Y, Kneipp H, Perelman LT, Itzkan I, Dasari RR et al. Single molecule detection using surface-enhanced Raman scattering (SERS). Phys Rev Lett. 1997; (78): 1667–70.
13. Оленин А. Ю., Лисичкин Г. В. Получение, динамика структуры объема и поверхности металлических наночастиц в конденсированных средах. Успехи химии. 2011; 80: 605–35.
14. Cialla D, März A, Böhme R, Theil F, Weber K, Schmitt M et al. Surface-enhanced Raman spectroscopy (SERS): Progress and trends. Anal Bioanal Chem. 2012; (403): 27–54.
15. Laing S, Gracie K, Faulds K. Multiplex in vitro detection using SERS. Chem Soc Rev. 2016; (45): 1901–18.
16. Semenova AA, Goodilin EA, Brazhe NA, Ivanov VK, Baranchikov AE, Lebedev VA et al. Planar SERS nanostructures with stochastic silver ring morpholgy for biosensor chips. J Mater Chem. 2012; (22): 24530–44.
17. Semenova AA, Brazhe NA, Parshina EY, Sarycheva AS, Maksimov GV, Goodilin EA. A new route for SERS analysis of intact erythrocytes using polydisperse silver nanoplatelets on biocompatible scaffolds. RSC Adv. 2016; (6): 85156–63.
18. Brazhe NA, Evlyukhin AB, Goodilin EA, Semenova AA, Novikov SM, Bozhevolnyi SI et al. Probing cytochrome c in living mitochondria with surface-enhanced Raman spectroscopy. Sci Rep. 2015; (5): 13793(1)–13793(13).
19. Durmanov NN, Guliev RR, Eremenko AV, Boginskaya IA, Ryzhikov IA, Trifonova EA et al. Non-labeled selective virus detection with novel SERS-active porous silver nanofilms fabricated by Electron Beam Physical Vapor Deposition. Sens Actuators B. 2018; (257): 37–47.
20. Nechaeva N, Prokopkina T, Makhaeva G, Rudakova E, Boltneva N, Dishovsky et al. Quantitative butyrylcholinesterase activity detection by surface-enhanced Raman spectroscopy. Sens Actuators B. 2018; (259): 75–82.
21. Kneipp J, Kneipp H, Wittig B, Kneipp K. One- and two-photon excited optical ph probing for cells using surface-enhanced Raman and hyper-Raman nanosensors. Nano Lett. 2007; (7): 2819–23.
22. Drescher D, Kneipp J. Nanomaterials in complex biological systems: insights from Raman spectroscopy. Chem Soc Rev.

2012; (41): 5780–99.
23. Wood BR, Caspers P, Puppels GJ, Pandiancherri S, McNaughton D. Resonance Raman spectroscopy of red blood cells using near-infrared laser excitation. Anal Bioanal Chem. 2007; (387): 1691–703.
24. Brazhe NA, Parshina EY, Khabatova VV, Semenova AA, Brazhe AR, Yusipovich AI et al. Tuning SERS for living erythrocytes: Focus on nanoparticle size and plasmon resonance position. J Raman Spectrosc. 2013; (44): 686–94.
25. Semenova AA, Brazhe NA, Parshina EY, Ivanov VK, Maksimov GV, Goodilin EA. Aqueous diaminsilver hydroxide as a precursor of pure silver nanoparticles for SERS probing of living erythrocytes. Plasmonics. 2013; (9): 227–35.
26. Jarvis RM, Goodacre R. Discrimination of bacteria using surface-enhanced Raman spectroscopy. Anal Chem. 2004; (76): 40–7.
27. Wang P, Pang S, Chen J, McLandsborough L, Nugen SR, Fan M et al. Label-free mapping of single bacterial cells using surface-enhanced Raman spectroscopy. Analyst. 2016; (141): 1356–62.
28. Granger JH, Schlotter NE, Crawford AC, Porter MD. Prospects for point-of-care pathogen diagnostics using surface-enhanced Raman scattering (SERS). Chem Soc Rev. 2016; (45): 3865–82.
29. Hoang V, Tripp RA, Rota P, Dluhy RA. Identification of individual genotypes of measles virus using surface enhanced Raman spectroscopy. Analyst. 2010; (135): 3103–9.
30. Luo S-C, Sivashanmugan K, Liao J-D, Yao C-K, Peng H-C. Nanofabricated SERS-active substrates for single-molecule to virus detection in vitro: A review. Biosens Bioelectron. 2014; (61): 232–40.
31. El-Said WA, Kim SU, Choi J-W. Monitoring in vitro neural stem cell differentiation based on surface-enhanced Raman spectroscopy using a gold nanostar array. J Mater Chem C. 2015; (3): 3848–59.
32. Han J, Qian X, Wu Q, Jha R, Duan J, Yang Z et al. Novel surface-enhanced Raman scattering-based assays for ultra-sensitive detection of human pluripotent stem cells. Biomaterials. 2016; (105): 66–76.
33. Howes PD, Rana S, Stevens MM. Plasmonic nanomaterials for biodiagnostics. Chem Soc Rev. 2014; (43): 383–8.
34. McAughtrie S, Faulds K, Graham D. Surface enhanced Raman spectroscopy (SERS): potential applications for disease detection and treatment. J Photochem Photobiol C. 2014; (21): 40–53.
35. Puppels GJ, de Mul FFM, Otto C, Greve J, Robert-Nicoud M, Arndt-Jovin DJ et al. Studying single living cells and chromosomes by confocal Raman microspectroscopy. Nature. 1990; (347): 301–3.
36. Alvarez-Puebla RA, Liz-Marzán LM. SERS-based diagnosis and biodetection. Small. 2010; (6): 604–10.
37. März A, Mönch B, Rösch P, Kiehntopf M, Henkel T, Popp J. Detection of thiopurine methyltransferase activity in lysed red blood cells by means of lab-on-a-chip surface enhanced Raman spectroscopy (LOC-SERS). Anal Bioanal Chem. 2011; (400): 2755–61.
38. Jahn IJ, Žukovskaja O, Zheng X-S, Weber K, Bocklitz TW, Cialla-May D et al. Surface-enhanced Raman spectroscopy and microfluidic platforms: challenges, solutions and potential applications. Analyst. 2017; (142): 1022–47.
39. Kumar S, Goel P, Singh JP. A facile method for fabrication of buckled PDMS silver nanorod arrays as active 3D SERS cages for bacterial sensing. Sens Actuators B. 2017; (241): 577–83.
40. Polavarapu L, Perez-Juste J, Xu Q, Liz-Marzán LM. Optical sensing of biological, chemical and ionic species through aggregation of plasmonic nanoparticles. J Mater Chem C. 2014; (2): 7460–76.
41. Dhillon A, Nair M, Kumar D. Analytical methods for sensing of health-hazardous arsenic from biotic and abiotic natural resources. Anal Methods. 2015; (7): 10088–108.
42. Xiao L, Zhang M, Liu Z, Bian W, Zhang X, Zhan J. Hydrophobic silver nanowire membrane for swabbing extraction and in situ SERS detection of polycyclic aromatic hydrocarbons on toys. Anal Methods. 2017; (9): 1816–24.
43. Fleischmann M, Hendra PJ, McQuillan AJ. Raman spectra of pyridine adsorbed at a silver electrode. Chem Phys Lett. 1974; (26): 163–6.
44. Wachsmann-Hogiu S, Weeks T, Huser T. Chemical analysis in vivo and in vitro by Raman spectroscopy — From single cells to humans. Curr Opin Biotechnol. 2009; (20): 63–73.
45. Yazdi SH, White IM. A nanoporous optofluidic microsystem for highly sensitive and repeatable surface enhanced Raman spectroscopy detection. Biomicrofluidics. 2012; (6): 14105–59.
46. Sharma VK, Yngard RA, Lin Y. Green synthesis and their antimicrobial activities. Adv Colloid Interface Sci. 2009; (145): 83–96.
47. Sun Y. Shape-controlled synthesis of gold and silver nanoparticles. Science. 2002; (298): 2176–9.
48. Guerrero-Martínez A, Barbosa S, Pastoriza-Santos I, Liz-Marzán LM. Nanostars shine bright for you: colloidal synthesis, properties and applications of branched metallic nanoparticles. Curr Opin Colloid Interface Sci. 2011; (16): 118–27.
49. Lim B, Xia Y. Metal nanocrystals with highly branched morphologies. Angew Chem Int Ed. 2011; (50): 76–85.
50. Pietrobon B, Kitaev V. Photochemical synthesis of monodisperse size-controlled silver decahedral nanoparticles and their remarkable optical properties. Chem Mater. 2008; (20): 5186–90.
51. Phan-Quang GC, Lee HK, Phang IY, Ling XY. Plasmonic colloidosomes as three-dimensional SERS platforms with enhanced surface area for multiphase sub-microliter toxin sensing. Angew Chem Int Ed. 2015; (54): 9691–5.
52. Tien D-C, Liao C-Y, Huang J-C, Tseng K-H, Lung J-K, Tsung T-T et al. Novel technique for preparing a nano-silver water suspension by the arc-discharge method. Rev Adv Mater Sci. 2008; (18): 750–6.
53. Gongalsky MB, Osminkina LA, Pereira A, Manankov AA, Fedorenko AA, Vasiliev AN et al. Laser-synthesized oxide-passivated bright Si quantum dots for bioimaging. Sci Rep. 2016; (6): 24732(1)–24732(8).
54. Nadagouda MN, Varma RS. Green synthesis of silver and palladium nanoparticles at room temperature using coffee and tea extract. Green Chem. 2008; (10): 859–62.
55. Moulton MC, Braydich-Stolle LK, Nadagouda MN, Kunzelman S, Hussain SM, Varma RS. Synthesis, characterization and biocompatibility of "green" synthesized silver nanoparticles using tea polyphenols. Nanoscale. 2010; (2): 763–70.
56. Hwang H, Chon H, Choo J, Park JK. Optoelectrofluidic sandwich immunoassays for detection of human tumor marker using surface-enhanced Raman scattering. Analyt Chem. 2010; (82): 7603–10.
57. Li J-M, Ma W-F, Wei C, Guo J, Hu J, Wang C-C. Poly(styrene-co-acrylic acid) core and silver nanoparticle/silica shell composite microspheres as high performance surface-enhanced Raman spectroscopy (SERS) substrate and molecular barcode label. J Mater Chem. 2011; (21): 5992–98.
58. Chen J-W, Lei Y, Liu X-J, Jiang J-H, Shen G-L, Yu R-Q. Immunoassay using surface-enhanced Raman scattering based on aggregation of reporter-labeled immunogold nanoparticles. Anal Bioanal Chem. 2008; (392): 187–93.
59. Ma K, Yuen JM, Shah NC, Walsh JT, Glucksberg MR, Van Duyne RP. In Vivo, transcutaneous glucose sensing using surface-enhanced spatially offset Raman spectroscopy: multiple rats, improved hypoglycemic accuracy, low incident power, and continuous monitoring for greater than 17 days. Anal Chem. 2011; (83): 9146–52.
60. Pînzaru SC, Andronie LM, Domsa I, Cozar O, Astilean S. Bridging biomolecules with nanoparticles: surface-enhanced Raman scattering from colon carcinoma and normal tissue. J Raman Spectrosc. 2008; (39): 331–4.
61. Wang X, Qian X, Beitler JJ, Chen ZG, Khuri FR, Lewis MM et al. Detection of circulating tumor cells in human peripheral blood using surface-enhanced Raman scattering nanoparticles. Cancer Res. 2011; (71): 1526–32.
62. Thomson PIT, Camus VL, Hu Y, Campbell CJ. Series of quinone-containing nanosensors for biologically relevant redox potential determination by surface-enhanced Raman spectroscopy. Anal Chem. 2015; 87 (9): 4719–35.
63. Qu L-L, Li D-W, Qin L-X, Mu J, Fossey JS, Long Y-T. Selective and sensitive detection of intracellular O2(•-) using Au NPs/cytochrome c as SERS nanosensors. Anal Chem. 2013; 85 (20): 9549–55.
64. Sivanesan A, Witkowska E, Adamkiewicz W, Dziewit Ł, Kamińska A, Waluk J. Nanostructured silver-gold bimetallic SERS substrates for selective identification of bacteria in human blood. Analyst. 2013; 139 (5): 1037–43.

65. Vitol EA, Orynbayeva Z, Bouchard MJ, Azizkhan-Clifford J, Friedman G, Gogotsi Y. In situ intracellular spectroscopy with surface enhanced Raman spectroscopy (SERS)-enabled nanopipettes. ACS Nano. 2009; 3 (11): 3529–36.
66. Vitol EA, Brailoiu E, Orynbayeva Z, Dun NJ, Friedman G, Gogotsi Y. Surface-enhanced Raman spectroscopy as a tool for detecting Ca2+ mobilizing second messengers in cell extracts. Anal Chem. 2010; 8 (16): 6770–4.
67. Zhang Q, Lu X, Tang P, Zhang D, Tian J, Zhong L. Gold nanoparticle (AuNP)-based surface-enhanced Raman scattering (SERS) probe of leukemic lymphocytes. Plasmonics. 2016; (11): 1361–8.
68. Berezhna S, Wohlrab H, Champion PM. Resonance Raman investigations of cytochrome c conformational change upon interaction with the membranes of intact and Ca2+-exposed mitochondria. Biochemistry. 2003; (42): 6149–58.
69. Pankratova MS, Baizhumanov AA, Yusipovich AI, Faassen M, Shiryaeva TYu, Peterkova VA et al. Imbalance in the blood antioxidant systemin growth hormone-deficient children before and after 1 year of recombinant growth hormone therapy. Peer J. 2015; (3): e1055(1)–e1055(12).
70. Brazhe NA, Baizhumanov AA, Parshina EYu, Yusipovich AI, Akhalaya MYa, Yarlykova YuV et al. Studies of the blood antioxidant system and oxygen-transporting properties of human erythrocytes during 105-day isolation. Human physiology. 2014; (40): 804–9.
71. Rodan LH, Gibson KM, Pearl PL. Clinical Use of CSF Neurotransmitters J Pediatr Neurol. 2015; 53 (4): 277–86.
72. Eisenhofer G, Kopin IJ, Goldstein DS. Catecholamine metabolism: a contemporary view with implications for physiology and medicine. Pharmacol Rev. 2004; 56 (3): 331–49.
73. Goldstein DS, Kopin IJ, Sharabi Y. Catecholamine autotoxicity. Implications for pharmacology and therapeutics of Parkinson disease and related disorders. Pharmacol Ther. 2014; 144 (3): 268–82.
74. Postuma RB, Gagnon JF, Vendette M, Montplaisir JY. Markers of neurodegeneration in idiopathic rapid eye movement sleep behaviour disorder and Parkinson's disease. Brain. 2009; 132 (12): 3298–307.
75. Subramaniam R. Pheochromocytoma — current concepts in diagnosis and management. Trends Anaesth Crit Care. 2011; 1 (2): 104–10.
76. Yangong H, Shi C, Shahbaz M, Zhengchuan N, Wang J, Liang B et al. Diagnosis and treatment experience of rectal carcinoid (a report of 312 cases). Int J Surg. 2014; 12 (5): 408–11.
77. Sadilkova K, Dugaw K, Benjamin D, Jack RM. Analysis of vanillylmandelic acid and homovanillic acid by UPLC-MS/MS in serum for diagnostic testing for neuroblastoma. Clin Chim Acta. 2013; (424): 253–7.
78. Rodriguez MC, Rubianes MD, Rivas GA. Highly selective determination of dopamine in the presence of ascorbic acid and serotonin at glassy carbon electrodes modified with carbon nanotubes dispersed in polyethylenimine. J Nanosci Nanotechnol. 2008; 8 (11): 6003–9.
79. Mazloum-Ardakani M, Khoshroo A. High performance electrochemical sensor based on fullerene-functionalized carbon nanotubes/ionic liquid: Determination of some catecholamines. Electrochem Comm. 2014; (42): 9–12.
80. Rezaei B, Boroujeni MK, Ensafi AA. Fabrication of DNA, o-phenylenediamine, and gold nanoparticle bioimprinted polymer electrochemical sensor for the determination of dopamine. Biosens Bioelectron. 2015; (66): 490–6.
81. Gao N, Xu Z, Wang F, Dong SJ. Sensitive biomimetic sensor based on molecular imprinting at functionalized indium tin oxide electrodes. Electroanalisis. 2007; (19): 1655–60.
82. Poliakov AE, Dumshakova AV, Muginova SV, Shekhovtsova TN. A peroxidase-based method for the determination of dopamine, adrenaline, and α-methyldopa in the presence of thyroid hormones in pharmaceutical forms. Talanta. 2011; 84 (3): 710–6.
83. Huang H, Gao Y, Shi F, Wang G, Shah SM, Su X. Determination of catecholamine in human serum by a fluorescent quenching method based on a water-soluble fluorescent conjugated polymer-enzyme hybrid system. Analyst. 2012; 137 (6): 1481–6.
84. Liu CH, Yu CJ, Tseng WL. Fluorescence assay of catecholamines based on the inhibition of peroxidase-like activity of magnetite nanoparticles. Anal Chim Acta. 2012; (745): 143–8.
85. Schulze HG, Blades MW, Bree AV, Gorzalka BB, Greek LS, Turner RFB. Characteristics of backpropagation neural networks employed in the identification of neurotransmitter Raman spectra. Appl Spectrosc. 1994; (48): 50–7.
86. Sharma B, Frontiera RR, Henry AI, Ringe E, Van Duyne RP. SERS: Materials, applications, and the future. Mater Today. 2012; (15): 16–25.
87. Lim JW, Kang IJ. Fabrication of chitosan-gold nanocomposites combined with optical fiber as SERS substrates to detect dopamine molecules. Bull Korean Chem Soc. 2014; (35): 25–9.
88. Lim JW, Kang IJ. Chitosan-gold nano composite for dopamine analysis using Raman scattering. Bull Korean Chem Soc. 2013; (34): 237–42.
89. Tang L, Li S, Han F, Liu L, Xu L, Ma W et al. SERS-active Au@Ag nanorod dimers for ultrasensitive dopamine detection. Biosens Bioelectron. 2015; (71): 7–12.
90. Lee NS, Hsieh YZ, Paisley RF, Morris MD. Surface enhanced Raman spectroscopy of the catecholamine neurotransmitters and related compounds. Anal Chem. 1998; (60): 442–6.
91. Kneipp K, Wang Y, Dasari RR, Feld MS. Near-infrared surface-enhanced Raman scattering (NIR-SERS) of neurotransmitters in colloidal silver solutions. Spectrochim Acta. 1995; (51A): 481–7.
92. Volkan M, Stokes DL, Vo-Dinh T. Surface-Enhanced Raman of dopamine and neurotransmitters using sol-gel substrates and polymer-coated fiber-optic probes. Appl Spectrosc. 2000; 54 (12): 1842–8.
93. Barreto WJ, Barreto SRG, Ando RA, Santos PS, DiMauro E, Jorge T. Raman, IR, UV–vis and EPR characterization of two copper dioxolene complexes derived from L-DOPA and dopamine. Spectrochim. Acta Part A. 2008; 71 (4): 1419–24.

TOWARDS A COMPUTATIONAL PREDICTION FOR THE TUMOR SELECTIVE ACCUMULATION OF PARAMAGNETIC NANOPARTICLES IN RETINOBLASTOMA CELLS

Johansen RJ[1,2], Bukhvostov AA[3], Ermakov KV[3], *Kuznetsov DA[2,3] ✉

[1] Department of Mathematics and Computer Science, University of Southern Denmark, Odense, DK-5230, Denmark

[2] N. N. Semenov Institute of Chemical Physics, Russian Academy of Sciences, Moscow

[3] Department of Medical Nanobiotechnologies, N. I. Pirogov Russian National Research Medical University, Moscow

Retinoblastoma is a malignant growth affecting retina. An original combination of modified Non-Markov and Gompertzian computational approaches is proven of being a reliable tool for prediction of tumor selective accumulation of the bivalent metal isotopes (^{25}Mg, ^{43}Ca, ^{60}Co, ^{67}Zn, …) — releasing nanoparticles in human retinoblastoma cells. This mathematical model operates with a starting point of the discriminative drug uptake caused by a gap-like distinction between the neighboring malignant and normal cell proliferation rates. This takes into account both pharmacokinetic and pharmacodynamic peculiarities of PMC16, fullerene-C_{60} based nanoparticles, known for their unique capabilities for a cancer-targeted delivery of paramagnetic metal isotopes followed by an essential chemotherapeutic effect. Being dependent on a tumor growth rate but not on the neoplasm steady state mass, a randomized level of drug accumulation in retinoblastoma cells has been formalized as a predictive paradigm suitable to optimize an ongoing PMC16 preclinical research.

Keywords: retinoblastoma, paramagnetic cytostatics, nanocationites, tumor selective nanoparticles uptake, drug accumulation mathematical model

Acknowledgments: this work was performed due to an exceptional technical assistance kindly provided by Erasmus-Plus DK06811/2020 Program associates affiliated with the Southern Denmark University at Odense, Denmark, and, most specifically, by Ms. Patricia Wladyczewski, SDU Erasmus chief supervising officer.

✉ **Correspondence should be addressed:** Dmitry A. Kuznetsov
Ostrovityanova 1, Moscow, 117997; kuznano@mail.ru

Received: 27.06.2018 **Accepted:** 18.08.2018

DOI: 10.24075/brsmu.2018.078

МАТЕМАТИЧЕСКОЕ ПРОГНОЗИРОВАНИЕ ПАРАМЕТРОВ ОПУХОЛЬ-СЕЛЕКТИВНОГО НАКОПЛЕНИЯ ПАРАМАГНИТНЫХ НАНОЧАСТИЦ КЛЕТКАМИ РЕТИНОБЛАСТОМЫ

Р. Дж. Йохансен[1,2], А. А. Бухвостов[3], К. В. Ермаков[3], Д. А. Кузнецов[2,3] ✉

[1] Кафедра математики и компьютерных наук, Университет Южной Дании, Оденсе, Дания

[2] Институт химической физики имени Н. Н. Семенова РАН, Москва

[3] Кафедра медицинских нанобиотехнологий, Российский национальный исследовательский медицинский университет имени Н. И. Пирогова, Москва

Ретинобластома — злокачественное новообразование, поражающее сетчатку глаза. Целью работы было разработать вычислительный подход к прогнозированию опухоль-специфического накопления наночастиц, высвобождающих катионы изотопов двухвалентных металлов (^{25}Mg, ^{43}Ca, ^{60}Co, ^{67}Zn, …) в клетках ретинобластомы человека. Предложена математическая модель, основанная на применении уравнения Гомперца и оригинальной версии немарковской популяционной динамики. Она основана на факте ярко выраженного дискриминационного распределения препарата между злокачественными и «соседствующими» с ними нормальными клетками и различиях в параметрах их клеточных циклов. Учтены как фармакокинетические, так и фармакодинамические особенности наночастиц PMC16 — порфирин-производных фуллерена C_{60}, известных благодаря их уникальным возможностям в отношении направленной доставки парамагнитных изотопов металлов в раковые клетки, сопровождающейся существенным химиотерапевтическим эффектом. Демонстрируя зависимость от скорости роста опухоли, но не от ее массы в стационарной фазе, рандомизированный уровень накопления препарата в клетках ретинобластомы формализован как ценный в прогностическом отношении расчетный метод, пригодный для оптимизации проводимых в настоящее время доклинических исследований катионообменных наночастиц PMC16.

Ключевые слова: ретинобластома, парамагнитные цитостатики, нанокатиониты, опухоль-селективное накопление наночастиц, математическая модель накопления препарата

Благодарности: эта работа была бы невозможна без помощи в технических вопросах, которую нам оказали сотрудники Университета Южной Дании в Оденсе в рамках программы Erasmus-Plus DK06811/2020. Авторы выражают особую благодарность Патриции Владычевской, главному руководителю SDS Erasmus.

✉ **Для корреспонденции:** Дмитрий Анатольевич Кузнецов
ул. Островитянова, д. 1, г. Москва, 117997; kuznano@mail.ru

Статья получена: 27.06.2018 **Статья принята к печати:** 18.08.2018

DOI: 10.24075/vrgmu.2018.078

Human retinoblastoma (RB) is found to be very sensitive to some metal paramagnetic isotopes due their ability to promote a so called *magnetic isotope effects* which, in turn, promotes a sharp inhibition of DNA repair in malignant cells along with a formation of shorted, and hence DNA repair inconsistent, DNA sequences [1–4]. This might be taken as a "hopeful pullout" for coming up with a new element in RB chemotherapy based on administration of $^{25}Mg^{2+}$, $^{43}Ca^{2+}$, $^{60}Co^{2+}$, $^{67}Zn^{2+}$ carrying/releasing nanoparticles (NPs) once the RB cell does indeed overexpresses the DNA Polymerase Beta, a target enzyme for the nuclear spin selective DNA repair [1, 5, 6].

These complexes of paramagnetic isotopes with PMC16 (Fig. 1), a peculiar type of amphiphilic low-toxic NPs, were in fact deliberately developed to face a requirement for ion transporter applicable in both tumor cell targeting and a subsequent intracellular controlled drug release [1, 5]. As a sign of such paramagnetic impacts, a significant decrease of proliferation rates has been observed in Y79 and WERI-RB-1 retinoblastoma cell strains [2–4].

According to PubMed statistics, the amount of publications on nanoparticles (NPs) for a passive targeted drug delivery has been increased in the past 15 years from about 40 (year 2000) up to nearly 1,800 (2015) taking the solid tumors research only [7]. As per the PMC16 passive targeting which would presumably take place in RB engaging preclinical studies, a tumor selectivity of anticipated NPs uptake looks rather obscure and unpredictable owing to a number of the RB-marking epigenetic factors [8–10].

A reliable prediction on the rate and extent of NP (PMC16) — RB selective accumulation would be no doubt a sort of beneficial supplement to anti-RB chemotherapeutic strategies proposed for a preclinical trial program. This work is an attempt to solve this task by employing a certain arsenal of mathematical modeling tools.

Noteworthy, an autonomous trend of computational approach has already made an essential contribution to preclinical and clinical trial scenaria in oncology and related areas [11–17].

METHODS

To proceed the simulation data, the most common drug (NP) — cell distribution and the RB/RT cell proliferation patterns (Table) [8, 9, 15, 18] were treated using a Sigma QXL600 software algorithm in HP9107 (Hewlett-Packard, Inc; USA) and Olivetti Riccetta SL110 (Ing. C. Olivetti & Co.; Италия) analytical units adopting a slightly modified Penman–Dalbreaux probabilistic approximation technique [14, 16] to harmonize the output with the population dynamics platforms based on both non-Markov [12, 14] and Gompertz [11] equation systems.

RESULTS

Drug toxicity to normal tissues and the emergence of drug-resistance along with a tumor selectivity in drug (NP) targeting/accumulation processes are no doubt the major limiting barriers on a path to chemotherapy of cancer [5, 6, 8]. A computational modeling of cell population dynamics in harshly varying object-surrounding environment could be applied to chemotherapeutic paradigm [7, 14, 17, 18]. In several cases, this approach might make a difference for improving responsiveness to the phase-specific drugs (NPs) taking into account their non-discriminative, vector-free ("passive"), distribution within a cell pool consisting of neighboring slow and fast proliferating populations.

Non-Markov population dynamics

The dynamics under various drug regimens of populations that differ in life-cycle parameters is simulated using a computer model whose simplest form is given in:

$$x(t) = \lambda\, x\,(t-\tau)[1 - \mathrm{D}(t)]\,,$$

where $x(t)$ is population density at time t, λ is the cell birth rate, τ is generation time, and $D(t)$ denotes the environmental process, so that $D(t) > 0$ corresponds to the occurrence of effective concentration of the drug in the system. Using this model the elimination time of malignant population (T_m) and that of the limiting host population (T_h) were estimated, and the elimination coefficient, Z, measuring the treatment efficacy, was calculated according to:

$$Z = 1 - T_m/T_h.$$

The treatment efficacy is a nonmonotonic function of the relation between the cell generation time and the period of drug administration, with maximal occurring when the limiting host cell cycle length is a multiple of the chemotherapeutic period. Analytical results further show that in fully periodic systems elimination time, T, is given for $\tau > \delta > \tau/2$:

$$T = \tau\omega/|\tau - (\delta + \omega)|\,.$$

Here, δ is the duration of the period in which the drug effective, and ω is the period in which the drug dosage is below efficiency. The point, $\tau = \delta + \omega$, is a singular point with T being infinite.

This makes possible to assume that a classical non-Markovian model of population dynamics [12, 14] is indeed an appropriate tool to simulate the NP (PMC16) distribution between malignant (fast expanding compartment) and the hostile normal cell (slow expanding compartment) pools. The above mentioned amphiphilic pharmacophore (PMC16, cyclohexyl(C_{60})porphyne-based bivalent metal isotopes nanocarrier; Fig. 1) is a suitable probe for our non-Markovian simulation since this type of NPs was found capable to manifest a clear and sharp cytostatic mode in acute myeloblast leukemia and RB cell cultures [1, 5, 6].

A two-compartment model we proposed is fitted to the following non-Markovian compatible pharmacokinetics data with both inter-specimen and randomized effects on CL, V, Q, and V2 corrected to an error best described the pattern of residual error [12, 13, 16]. So this our model works out for both PMC16 tumor uptake selectivity (fast proliferation caused

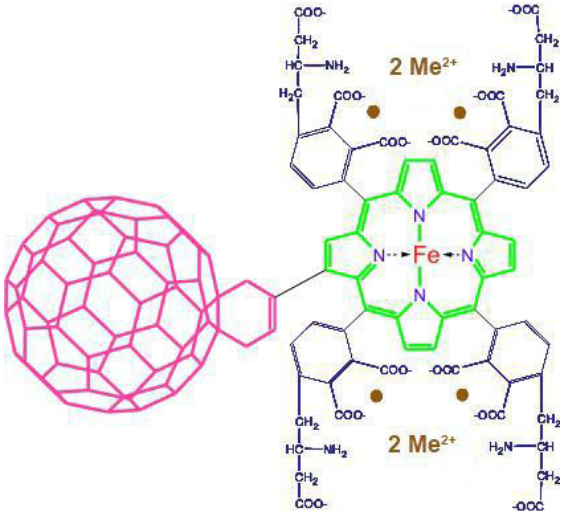

Fig. 1. Structure of PMC16 (cyclohexyl(C60)porphyrin), Me^{2+} — carrying and releasing nanoparticles with the marked membranotropic/amphiphilic properties [1]

Table 1. Population turnover in Y79 and WERI-RB-1 cell lines

Parameter	Meaning	T, hr	Ref
TG_1	Duration of G_1 phase	8.0	[9, 15]
T_S	Duration of S phase	7.5	[8, 15]
T_{G_2M}	Duration of G_2M phase	2.0	[8, 18]
T_{G_0}	Duration of G_0 phase	3.0	[9, 15]
$T_{Apoptosis}$	Duration of the apoptotic phase	4.0	[8, 9]

phenomenon) and a routine pharmacokinetic key points prediction.

Inter-specimen covariant models

A. Pharmacokinetic model

$$C = D/V \bullet \left[\frac{(\alpha - k_{21})}{(\alpha - \beta)} exp - (\alpha \bullet t) + \frac{(k_{21} - \beta)}{(\alpha - \beta)} \bullet exp - (\beta \bullet t) \right]$$

B. Non-vectoral covariative model

$$CL_j = [\theta_3 \bullet OCC1 + \theta_4 (WT - 75)] \bullet exp\ (\eta_{CL_j})$$

$$V_{cj} = [\theta_1 - (GFR - 80) \bullet \theta_2] \bullet exp\ (\eta_{V_j})$$

$$k_{12_j} = (\theta_5) \bullet exp\ (\eta_{k12_j})$$

C. Population dynamics model

$$C_{ij} = \frac{D_{iv}}{\theta_1 \bullet OCC_1 + \theta_2 \bullet (WT - 75) \bullet exp\ (\eta_{V_j})} \begin{cases} \frac{k_{21} - \frac{CL_j}{V_{vj}} \bullet exp - \left(\frac{CL_j}{V_{cj}} t\right)}{\beta - \frac{CL_j}{V_{cj}}} \\ + \frac{k_{21} - k_{12}}{\frac{CL_j}{V_{cj}} - \beta} \bullet exp - (k_{12} f) \end{cases} \bullet exp\ (\varepsilon_y)$$

D. Population parameters

$$\theta_1 = 19.5$$
$$\theta_2 = 0.198$$

Gompertzian model

The Gompertz equation based models were already used to describe cancer growth dynamics [7, 11, 14], these formalisms have been also applied to optimize some therapeutic strategies dealing with antiangiogenic [11, 12] and radiation treatment [11, 13].

The model is fully deterministic. Cell cycle phases durations τ_φ have been discretized in several elementary age intervals $\alpha \in \{1,\ldots, N_\phi\}$ where N_ϕ is an integer such as $\tau_\phi = dt \bullet N_\phi$. Here dt is the time step of the cell cycle model. The cell density $n_{\alpha,\phi}$ at age α in phase ϕ is governed by:

$$\frac{\partial n_{\alpha,\varphi}}{\partial t} + \nabla \bullet (v n_{\alpha,\varphi}) = P_{\alpha,\varphi}\ .$$

In this equation, $\phi \in \{G_1, S, G_2 M, G_0$, Apoptosis and $\alpha \in \{1,\ldots,N_\phi\}$. $P_{\alpha,\phi}$ is the cell density proliferation term in phase at age retrieved from the cell cycle model. In these simulations, the intracellular and extracellular conditions were identified for cells at the end of G_1 phase.

Furthermore, noting that $\sum_{\alpha,\phi} n_{\alpha,\phi}$ is constant, so we can sum to obtain an expression for the pressure field of the form:

$$-\nabla \bullet (k \nabla p) = \sum_{\alpha,\varphi} P_{\alpha,\varphi}\ .$$

The computer program starts from an initial distribution of neighboring RB and RT cells in each state $\{\alpha, \phi\}$. The compupations are performed using a splitting technique. We run the cell cycle model for one time-step dt, then retrieve new values for $n_{\alpha,\phi}$ and compute $P_{\alpha,\phi}$. This drives to a system:

$$\begin{cases} \frac{\partial n_{\alpha,\varphi}}{\partial t} + \nabla \bullet (\upsilon n_{\alpha,\varphi}) = 0 \\ \frac{\partial n_{\alpha,\varphi}}{\partial t} + \upsilon \bullet \nabla n_{\alpha,\varphi} = \left(\sum_{\alpha',\varphi'} P_{\alpha',\varphi'} \right) n_{\alpha,\varphi} \end{cases}$$

Applied to the cell division cycle key patterns (Table) represented as a non-Markov population dynamics model organized in a merry-go-round of subpopulations biologically identified as phase (G_1, S, G_2 and M), this might be re-formalized as:

$$\begin{cases} \frac{\partial n_i(t,x)}{\partial t} + \frac{\partial n_i(t,x)}{\partial t} + d_\tau(t,x) n_\tau(t,x) + K_{i \to i+1}(t,x) n_i(t,x) = 0 \\ n_{\tau+1}(t,0) = \int_0^\infty K_{i \to i+1}(t,x) n_i(t,x) dx \\ n_1(t,0) = 2 \int_0^\infty K_{I \to 1}(t,x) n_I(t,x) dx\ . \end{cases}$$

along with the initial conditions $(n_i = 0)_{1 \le i \le I}$.

Cell death rates in phases are noted d_ϕ and transition rates between phases, assumed to be time-periodic. $K_{i \to i+1}$. Phase i ($1 \le i \le I$) may be one of the classical four G_1, S, G_2 and M, but also an aggregated phase such as S-G_2, or even a single proliferating phase G_1-S-G_2-M, or, on the contrary, a subdivision inside a phase, e.g., pre- or post-restriction point in G_1; the equation describes the evolution of the densities $n_i(t, x)$ of cells having age x at time t in phase i.

The above stated two systems that represent two neighboring, fast and slow growing, cell populations are physically apart from each other. Hence, in this system of equations, function g, which represents anti-tumor drug efficacy, is assumed, as is function f for cytotoxicity:

$$g(D,t) = ll\left(1 + \cos(2\pi \frac{(t - \varphi_B)}{24})\right) \bullet \frac{(D^{\Upsilon,B})}{D_{50}^{\Upsilon,B} + D^{\Upsilon,B}},$$

whereas λ, ν, ε_D, α, B_{max}, H, φ_B, Υ_B, D_{50} are positive constants, identified on tumor growth curves or from literature data [8, 15, 18], or else estimated.

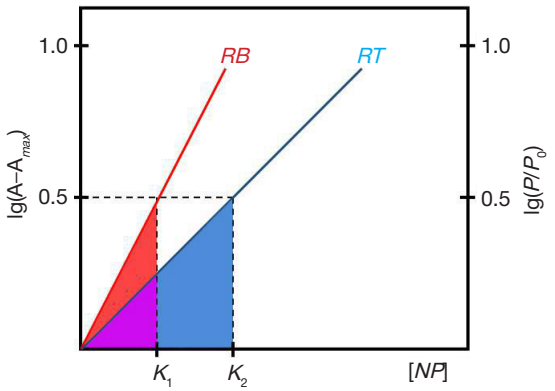

Fig. 2. The *NP* uptake selectivity prediction in a complete accessibility of intracellular ligands. P — [*NP*] uptaken, units per cell; P_0 — intracellular initial concentration of NP-ligands; K_S — Gompertz equation vectoral K; K_1 — an *NP* uptake steady state constant; K_2 — an efficient constant of saturation of a cellular ligand pool at [*NP*] → 0.5 P_{max}

The difference of behaviors between these two populations of cells (RB-RT pair) with respect to drug response is coded as $\varphi_A - \varphi_B = 13$ hours.

Turning back to the roots, a damped harmonic approximation stands for healthy (RT) cell population dynamics:

$$\begin{cases} \frac{dP}{dt} = -\lambda P + \frac{i(t)}{V_{dist}}\phi(t) \\ \frac{dC}{dt} = -\mu C + \varepsilon_C P \\ \frac{dP}{dt} = \{-\alpha - f(C,t)\}Z - \beta A + \Upsilon \\ \frac{dA}{dt} = Z - Z_{eq}, \end{cases}$$

where

$$f(C,t) = F\left(1 + \cos(2\pi\frac{t-\varphi_A}{24})\right)\frac{C^{\gamma,A}}{C_{50}^{\gamma,A} + C^{\gamma,A}},$$

and λ, μ, ε_C, α, β, Υ, Z_{eq}, F, φ_A, Υ_A, C_{50} are positive constants, which, again, were identified on tumor growth curves or from literature data [7, 10, 15], or else estimated.

These equations represent drug diffusion and elimination by first order pharmacokinetics for concentrations in the plasmatic and target cell compartments (P and C), from infusion in the general circulation according to the instantaneous drug delivery flow i (t) (Φ representing a "tap on-tap off" function), and health tissue homeostasis by a linear system showing a stable focus at Z_{eq}, $A_{eq} = \beta^{-1}(\Upsilon - \alpha Z_{eq})$, perturbed by the drug cytotoxicity function which comes to strengthen the natural self-regulation coefficient α.

So our model, as derived from a Gompertz equations row, is completely adequate to the tumor cell population dynamics:

$$\begin{cases} \frac{dP}{dt} = -\lambda P + \frac{i(t)}{V_{dist}}\phi(t) \\ \frac{dD}{dt} = -\nu D + \varepsilon_D P \\ \frac{dB}{dt} = -\alpha B \ln\left(\frac{B}{B_{max}} - g(D,t)B\right). \end{cases}$$

Clearly, this is nothing but the way to represent exchanges with quiescent population in a still linear model which normally means to exclude feedback from quiescence to proliferation, considering quiescence only as a sideway expansion cell tank:

$$\begin{cases} \frac{\partial}{\partial t}p(t,x) + \frac{\partial}{\partial x}p(t,x) + \{\mu + K(x)\}p(t,x) = 0 \\ p(t,x=0) = 2(1-f)\int_{\varepsilon\geq 0} K(\varepsilon)\,p(t,\varepsilon)\,d\varepsilon \\ p(t,x=0) = p_0(x) \\ \frac{d}{dt}Q(t) = 2f\int_{\varepsilon\geq 0} K(\varepsilon)\,p(t,\varepsilon)\,d\varepsilon - \nu Q(t) \\ Q(0) = Q_0 \end{cases}$$

To emphasize a perspective proclaimed, this our model is to reveal the action of a cytostatic drug enhancing the way out of proliferating cells with density $p(t, x)$ to quiescent cells with density Q (t), the drug target here is f, rate of escape at mitosis towards the siding phase Q, f to be enhanced by a cytostatic drug.

DISCUSSION

Tumor selective NP uptake. Probability and prediction

As seen from above, a probabilistic prognosis for the RB-selective NP uptake relates predominantly on a ratio between malignant and normal cell proliferation rates while the mass of a cancer tissue *per se* (amount of RB cells) might be practically neglected (Fig. 2). This derives from a predictive cell response to a rapidly *in situ* diffusing probe (PMC16) once these Me^{2+}-nanocarriers arrive to the RB/RT frontier area. In this stochastic scenario, however, a cellular lattice is nothing but a peculiarity reflecting the target cell specific energy landscape [16, 19] which makes the drug trapping probability dependent on the EL motion and, therefore, on expanding dynamics of a most rapidly growing compartment within a given RB/RT pair (Fig. 3).

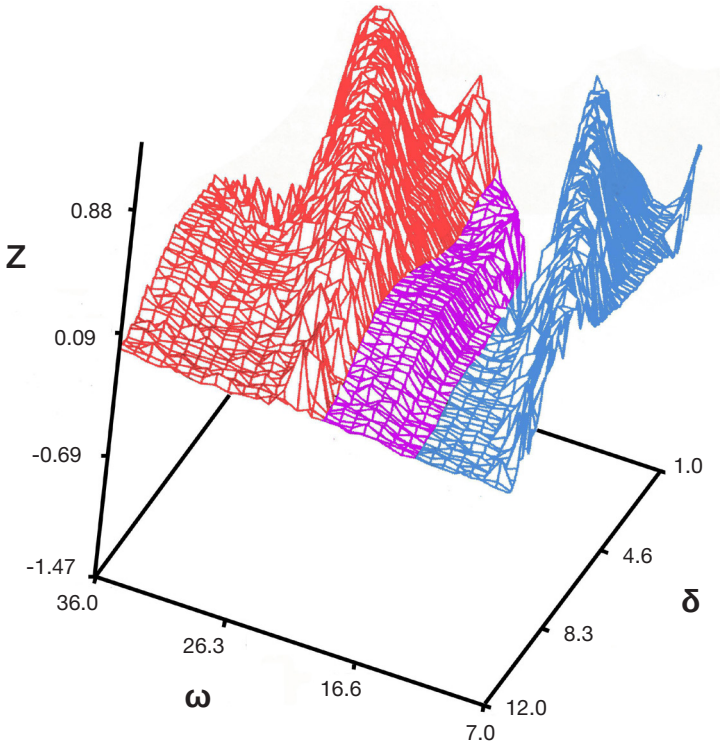

Fig. 3. Probabilistic model for NPs distribution between RB and the neighboring RT cells as a function of the discriminative cell cycle turnover. Z-elimination coefficient for malignant and the RB-surrounding normal cells (RT) estimated for the drug efficiency duration time (σ) and the drug-free cell functioning time interval (ω). σ is normally distributed within a variation range of $\sigma = \sigma/10$, where remain constant while the inner rate of the "newborn" cell appearance is $\lambda = 2$, for a starting population size $x(0) = 5$

A symbolic blue-red shift in Figures 2 and 3 marks a trend to predominant accumulation of NPs in the most faster expanding cell tank, RT.

So turning back to a background proceeding probabilistic approach [12, 14], a tumor selective accumulation of the PMC16-specific probe become predictable due to enormous difference between RB and RT growth rates [8–10, 12]. This allows a rate–discriminative RT–PMC16 uptake described by our model (Fig. 2) working in accordance with:

$$A_C = Kd[\mathrm{tg}\alpha_{RB}/(\mathrm{tg}\alpha_{RB} - \mathrm{tg}\alpha_{RT})],$$

where K_d is an Arnauld-Pitot disclaimer approximation constant [16,19].

Paul Ehrlich's "magic bullet": dream or nightmare?

Meaning the end of a long lasting post–Virchowian era, a truly prophetic outlook stated by Paul Ehrlich back in 1908–1913, now well-known as a hope for an infamous *magic bullet* in cellular pathology and pharmacology [8, 17], has been eventually adopted within a contemporary drug targeted delivery concept [5, 7, 19]. The latter requires a broad variety of nanodevices, all sorts of the *magic bullets*, designed to conduct both the towards-a-target navigated drug transfer and a consequent *in situ* controlled drug release [1, 5, 17].

However, a new unclear horizon appears straight in front of a marksman equipped with the *magic bullet* loaded "cartridge". Suppose a reasonable amount of the active drug molecules or ions have reached the tumor location border due to a perfect delivery performed by some nanocarrier. A good shot with the *bullet* though. Then a tumor selective intralization of a drug becomes a rather obscure step in a whole pharmacokinetic scenario. Indeed, no matter how precise the *bullet's* trajectory is, a further distribution of NPs between the neighboring malignant and normal tissue compartments is the case.

That's why a predictive model we proposed is in fact a promising tool the one might need to come up with the trustworthy path/dose/exposition plan to follow and a strategic roadmap to observe upfront of experiment.

After all, a direct Schlemm channel drug influx and/or the intraocular administration paths, often applicable to RB particular case [8], would make this approach not only possible but even preferable as well. A numerous holistic impacts, ineluctable when the routine parenteral administration paths involved, should be therefore minimized or merely neglected as long as the RB chemotherapy is in a focus.

CONCLUSIONS

A mathematical model proposed is found sustainable to predict a quantitative extent of tumor selective accumulation of medicinal nanoparticles in human retinoblastoma cells as long as these NPs are amphiphilic and membranotropic agents with a marked mode for permeability into the target cell.

The C_{60}-fullerene based Me^{2+} — carrying-n-releasing members of PMC16 family fit the above specified requirements. So our RB/RT proliferation "rate gap" focused computational technique might make a difference in optimization of the preclinical research program for these and related pharmacophores.

References

1. Buchachenko AL. Magneto-Biology and Medicine. New York: Nova Biomedical Publ., 2015.
2. Bukhvostov AA, Dvornikov AS, Ermakov KV, Kurapov PB, Kuznetsov DA. Retinoblastoma: magnetic isotope effects might make a differece in the current anti-cancer research strategy. Acta Medica (Prague). 2017; 60 (2): 93–6.
3. Bukhvostov AA, Dvornikov AS, Ermakov KV, Kuznetsov DA. Retinoblastoma case: shall we get a paramagnetic trend in chemotherapy? Arch Cancer Res. 2017; 5 (4): 158–62.
4. Bukhvostov AA, Pavlov KA, Ermakov KV, Sidoruk KN, Rybakova IV, Kuznetsov DA, Roumiantsev SA. An atypical β-like DNA Polymerase of retinoblastoma cells as a target for spin-selective inhibitory cytostatics. J Fund Med Biol (Russian). 2018; 7 (2): 50–3.
5. Orlova MA, Osipova EY, Roumiantsev SA. Effect of ^{67}Zn-nanoparticles on leukemic cells and normal lymphocytes. Brit J Med Med Res. 2012; 2 (1): 21–30.
6. Orlov AP, Orlova MA, Trofimova TP, Kalmykov SN, Kuznetsov DA. The role of zinc and its compounds in leukemia. J Biol Inorg Chem. 2018; 23 (3): 347–62.
7. Siccardi M, Owen A. Towards a computational prediction of nanoparticle pharmakokinetics and distribution. J In Silico & In Vitro Pharmacol. 2016; 2 (1): 8–11.
8. Augsburger JJ, Chow CML, Dyer V, Roussel MF. Translating science into survival. In: Cajjar A, Pappo A, editors. St. Jude's Children's Research Hospital Report. St. Judes CRH Publ.: Memphis, TN — Cincinnati, OH. 2016; 6–55.
9. Zhang J, Benavente CA, McEvoy J, Flores-Otero J, Ding L, Chen X, Ulyanov A. A novel retinoblastoma therapy from genomic and epigenetic analyses. Nature. 2012; 481 (7381): 329–34.
10. Bozic I, Nowak MA. Resisting resistance. Ann Rev Cancer Biol. 2017; 1 (1): 203–21.
11. Bassukas ID. Comparative Gompertzian analysis of alterations of tumor growth patterns. Cancer Res. 1994; 54 (16): 4385–92.
12. Byrne H, Prezidosi L. Modelling solid tumor growth using the theory of mixtures. Math Med Biol. 2003; 20 (4): 341–66.
13. Komarova NL. Mathematical modelling of tumorigenesis: mission possible. Curr Opinion Oncol. 2005; 17 (1): 39–43.
14. Trapp S, Horobin RW. A predictive model for the selective accumulation of chemicals in tumor cells. Eur Biophys J. 2005; 34 (7): 959–66.
15. Udvardi L, Lakatos J, Loewenhaupt RK. Dividing Cell. In Vitro–In Silico Models. Szeged, Budapest: Alba Regia, 2017.
16. Lehman RJ, Waugh TS, Rattenau KR, Bielka H. An expanding compartment mode to implement a guest probe diffusion input adopted by the comprehensive Gunault muxtures theory. In: Sieliwanowicz B, Martell SJ, edsitors.Combinational Dynamics in Systems Theory. Sydney—Melbourne—Perth: Adler & Adler Publ., 2018; 116–37.
17. Lamprecht A, Pellecker J. Anti-cancer nano-size agents: targeting paths and pharmacokinetics. In: Lamprecht A, editor. Nanotherapeutics. Drug Delivery Concepts in Nanoscience. NY—London—Singapore: Pan Stanford Publ., 2018; 92–101.
18. Altinok A, Gonze D, Levi F, Goldbeter A. An Automaton model for the cell cycle. Interface Focus. 2011; 1 (1): 36–47.
19. Delbreaux J, Pitot CA. Mathematical model in a new drug preclinical trial. Predictive power and limitations. Leuven—Ghent—Antwerp: Leuven University Press, 2018.

Литература

1. Buchachenko AL. Magneto-Biology and Medicine. New York: Nova Biomedical Publ., 2015.
2. Bukhvostov AA, Dvornikov AS, Ermakov KV, Kurapov PB, Kuznetsov DA. Retinoblastoma: magnetic isotope effects might make a differece in the current anti-cancer research strategy. Acta Medica (Prague). 2017; 60 (2): 93–6.
3. Bukhvostov AA, Dvornikov AS, Ermakov KV, Kuznetsov DA. Retinoblastoma case: shall we get a paramagnetic trend in chemotherapy? Arch Cancer Res. 2017; 5 (4): 158–62.
4. Bukhvostov AA, Pavlov KA, Ermakov KV, Sidoruk KN, Rybakova IV, Kuznetsov DA, Roumiantsev SA. An atypical β-like DNA Polymerase of retinoblastoma cells as a target for spin-selective inhibitory cytostatics. J Fund Med Biol (Russian). 2018; 7 (2): 50–3.
5. Orlova MA, Osipova EY, Roumiantsev SA. Effect of ^{67}Zn-nanoparticles on leukemic cells and normal lymphocytes. Brit J Med Med Res. 2012; 2 (1): 21–30.
6. Orlov AP, Orlova MA, Trofimova TP, Kalmykov SN, Kuznetsov DA. The role of zinc and its compounds in leukemia. J Biol Inorg Chem. 2018; 23 (3): 347–62.
7. Siccardi M, Owen A. Towards a computational prediction of nanoparticle pharmakokinetics and distribution. J In Silico & In Vitro Pharmacol. 2016; 2 (1): 8–11.
8. Augsburger JJ, Chow CML, Dyer V, Roussel MF. Translating science into survival. In: Cajjar A, Pappo A, editors. St. Jude's Children's Research Hospital Report. St. Judes CRH Publ.: Memphis, TN — Cincinnati, OH. 2016; 6–55.
9. Zhang J, Benavente CA, McEvoy J, Flores-Otero J, Ding L, Chen X, Ulyanov A. A novel retinoblastoma therapy from genomic and epigenetic analyses. Nature. 2012; 481 (7381): 329–34.
10. Bozic I, Nowak MA. Resisting resistance. Ann Rev Cancer Biol. 2017; 1 (1): 203–21.
11. Bassukas ID. Comparative Gompertzian analysis of alterations of tumor growth patterns. Cancer Res. 1994; 54 (16): 4385–92.
12. Byrne H, Prezidosi L. Modelling solid tumor growth using the theory of mixtures. Math Med Biol. 2003; 20 (4): 341–66.
13. Komarova NL. Mathematical modelling of tumorigenesis: mission possible. Curr Opinion Oncol. 2005; 17 (1): 39–43.
14. Trapp S, Horobin RW. A predictive model for the selective accumulation of chemicals in tumor cells. Eur Biophys J. 2005; 34 (7): 959–66.
15. Udvardi L, Lakatos J, Loewenhaupt RK. Dividing Cell. In Vitro–In Silico Models. Szeged, Budapest: Alba Regia, 2017.
16. Lehman RJ, Waugh TS, Rattenau KR, Bielka H. An expanding compartment mode to implement a guest probe diffusion input adopted by the comprehensive Gunault muxtures theory. In: Sieliwanowicz B, Martell SJ, edsitors.Combinational Dynamics in Systems Theory. Sydney—Melbourne—Perth: Adler & Adler Publ., 2018; 116–37.
17. Lamprecht A, Pellecker J. Anti-cancer nano-size agents: targeting paths and pharmacokinetics. In: Lamprecht A, editor. Nanotherapeutics. Drug Delivery Concepts in Nanoscience. NY—London—Singapore: Pan Stanford Publ., 2018; 92–101.
18. Altinok A, Gonze D, Levi F, Goldbeter A. An Automaton model for the cell cycle. Interface Focus. 2011; 1 (1): 36–47.
19. Delbreaux J, Pitot CA. Mathematical model in a new drug preclinical trial. Predictive power and limitations. Leuven—Ghent—Antwerp: Leuven University Press, 2018.

NANOSTRUCTURED PHOTOSENSITIZER BASED ON A TETRACATIONIC DERIVATIVE OF BACTERIOCHLORIN FOR ANTIBACTERIAL PHOTODYNAMIC THERAPY

Meerovich GA[1,2] ✉, Akhlyustina EV[2], Tiganova IG[3], Makarova EA[4], Philipova NI[3], Romanishkin ID[1], Alekseeva NV[3], Lukyanets EA[4], Romanova YuM[3], Loschenov VB[1,2]

[1] Prokhorov General Physics Institute of the Russian Academy of Sciences, Moscow

[2] Institute of engineering physics for biomedicine, National Research Nuclear University "MEPHI", Moscow

[3] Gamaleya National Research Center of Epidemiology and Microbiology, Moscow

[4] Organic Intermediates and Dyes Institute, Moscow

Making antibacterial PDT more effective is a task that calls for the development of photosensitizers (PS) based on polycationic synthetic bacteriochlorins and subsequent analysis of properties of such photosensitizers. This study aimed to explore photophysical and antibacterial properties of the nanostructured PS based on 3-$Py_4BSHp_4Br_4$, tetracationic amphiphilic derivative of synthetic bacteriochlorin. The PS was solubilized in a 4% Kolliphor ELP to obtain its nanostructured dispersion. We researched the absorption and fluorescence spectra intensity and profiles, studying concentrations from 0.001 to 0.2 mM, and found that the aggregation level of the PS in question is low throughout the range investigated while the *S. aureus* (gram-positive) and *P. aeruginosa* and *K. pneumoniae* (gram-negative) PD inactivation effectiveness is high.

Keywords: photosensitizer, cationic bacteriochlorin, aggregation, nanostructured dispersion, fluorescence, antibacterial photodynamic therapy

✉ **Correspondence should be addressed:** Gennady A. Meerovich
Vavilova 38, Moscow, 119991; meerovich@mail.ru

Received: 31.08.2018 **Accepted:** 27.09.2018

DOI: 10.24075/brsmu.2018.087

НАНОСТРУКТУРИРОВАННЫЙ ФОТОСЕНСИБИЛИЗАТОР НА ОСНОВЕ ТЕТРАКАТИОННОГО ПРОИЗВОДНОГО БАКТЕРИОХЛОРИНА ДЛЯ АНТИБАКТЕРИАЛЬНОЙ ФОТОДИНАМИЧЕСКОЙ ТЕРАПИИ

Г. А. Меерович[1,2] ✉, Е. В. Ахлюстина[2], И. Г. Тиганова[3], Е. А. Макарова[4], Н. И. Филипова[3], И. Д. Романишкин[1], Н. В. Алексеева[3], Е. А. Лукьянец[4], Ю. М. Романова[3], В. Б. Лощенов[1,2]

[1] Институт общей физики имени А. М. Прохорова РАН, Москва

[2] Инженерно-физический институт биомедицины, Национальный исследовательский ядерный университет «МИФИ», Москва

[3] Национальный исследовательский центр эпидемиологии и микробиологии имени Н. Ф. Гамалеи, Москва

[4] Научно-исследовательский институт органических полупродуктов и красителей, Москва

Задача повышения эффективности антибактериальной ФДТ делает актуальными создание и исследование фотосенсибилизаторов (ФС) на основе поликатионных синтетических бактериохлоринов. Целью работы было изучить в широком диапазоне концентраций фотофизические и антибактериальные свойства наноструктурированного ФС на основе тетракатионного амфифильного производного синтетического бактериохлорина 3-$Py_4BCHp_4Br_4$. Наноструктурированную дисперсию ФС получили путем его солюбилизации в 4%-м Kolliphor ELP. Исследование интенсивности и формы спектров поглощения и флуоресценции в диапазоне концентраций от 0,001 до 0,2 мМ продемонстрировало низкую агрегацию этого ФС во всем диапазоне и высокую эффективность фотодинамической инактивации грамположительных бактерий *S. aureus* и грамотрицательных бактерий *P. aeruginosa* и *K. pneumoniae*.

Ключевые слова: фотосенсибилизатор, катионный бактериохлорин, агрегация, наноструктурированная дисперсия, флуоресценция, антибактериальная фотодинамическая терапия

✉ **Для корреспонденции:** Геннадий Александрович Меерович
ул. Вавилова, д. 38, г. Москва, 119991; meerovich@mail.ru

Статья получена: 31.08.2018 **Статья принята к печати:** 27.09.2018

DOI: 10.24075/vrgmu.2018.087

Antibacterial photodynamic therapy (APDT) is a promising mode of treatment of localized infection sites: surgical and burn wounds, trophic and diabetic ulcers, etc [1, 2]. Unlike antibiotic therapy, APDT destroys cells of bacteria without promoting their resistance to the treatment [3–6]. Most pathogens, including antibiotic-resistant strains of bacteria, are susceptible to APDT [7].

Localized infection sites, infected wounds in particular, most often contain *Staphylococcus aureus* (*S. aureus*) Gram-positive bacteria, *Pseudomonas aeruginosa* (*P. aeruginosa*) and *Klebsiella pneumoniae* (*K. pneumoniae*) Gram-negative bacteria, the strains of which may be resistant to many types of antibiotics, cause chronic infections and various dangerous consequences for the patients [8].

Gram-positive and Gram-negative bacteria are fundamentally different in their structure and sensitivity to drug exposure. The cell wall of Gram-positive bacteria is just a minor obstacle for most photosensitizers (PS). In Gram-negative bacteria, it

has an additional structural element, a 10–15 nm thick outer membrane, which is heterogeneous and consists of porin proteins, lipopolysaccharide trimers and lipoproteins that build an external pseudo-surface of densely packed negative charges [9–11]. Such a system prevents the humoral protective factors from penetrating and enables resistance to many drugs: only relatively hydrophilic compounds with a molecular weight below 700 Da diffuse through the porin channels, and as the size and weight of the molecules grow, the probability of their diffusion into Gram-negative bacteria decreases. Only cationic PSs effectively interact with Gram-negative bacteria [10, 11]. Cationic PS have another advantage: their highly concentrated aqueous compositions (solutions or nanodispersions) can be used for sensitization, since the Coulomb repulsion of molecules of cationic bacteriochlorins negatively affects their aggregation [12] and thus improves the efficacy of the photodynamic processes.

While selecting PS for APDT, it is necessary to take in account that some bacteria, e.g., *P. aeruginosa*, can infect the tissue up to the depth of 12–15 mm [13], which renders conventional antibacterial agents (solutions, ointments, gels) and PSs phototoxic only when excited with visible range light ineffective. Therefore, proper photodynamic treatment of such infected sites requires PSs excited by the light in near infrared spectral range, at the wavelengths of 720–850 nm, which cover the "biological tissue transparency window". In this connection, derivatives of cationic bacteriochlorins are being actively investigated for their potential to be PS in APDT. A number of studies are dedicated to researching the properties of polycationic derivatives of synthetic bacteriochlorins with a molecular weight of 1500–1800 Da; according to their results, such PSs are capable of inactivating both Gram-positive *S. aureus* bacteria and Gram-negative *P. aeruginosa* bacteria, but the minimum bactericidal concentrations of such photosensitizers are quite high (> 6 μM for *S. aureus* and about 25 μM for *P. aeruginosa*) [14].

Increasing the efficacy of APDT is a problem that requires development of PSs based on polycationic synthetic bacteriochlorins having smaller molecular size and mass. This study is aimed at exploring photophysical and antibacterial properties of the nanostructured PSs based on 3-$Py_4BCHp_4Br_4$, tetracationic amphiphilic derivative of synthetic bacteriochlorin meso-tetra-(1 heptyl-3-pyridyl)-bacteriochlorin tetrabromide.

METHODS

Compared to a derivative described in an earlier study [14], tetracathionic amphiphilic derivative of synthetic bacteriochlorin meso-tetra-(1-heptyl-3-pyridyl)-bacteriochlorin tetrabromide 3-$Py_4BCHp_4Br_4$, is less lipophilic and has the molecule of a smaller radius. The derivative was synthesized by meso-tetra-(3-pyridyl)-bacteriochlorin alkylation with heptyl bromide in nitromethane in an inert atmosphere. The nanostructured dispersion of 3-$Py_4BCHp_4Br_4$ was obtained through its solubilization in 4% Kolliphor ELP (BASF; Germany). Measurements taken with Zetasizer Nano Series ZS 3600 (Malvern Panalitical; UK) put the hydrodynamic size of nanoparticles within 12–14 nm.

We used Hitachi U-3410 dual-beam spectrophotometer (Hitachi; Japan) to study PS absorption in the concentration range of 0.001–0.1 mM and LESA-01-Biospec spectrum analyzer (BIOSPEC; Russia) to study the spectral-fluorescent properties. 532 nm laser was used to excite the fluorescence; this wavelength belongs to the bacteriochlorin derivative's Q2 band. To study the features of the spectral band shape we investigated spectral-fluorescent properties of the PS in cuvettes of various lengths (1 mm and 10 mm) and normalized its fluorescence spectral intensity to the fluorescence band maximum (reduced spectral maximum to 1). Thus, when analyzing the spectra, we could separate changes associated with reabsorption from those resulting from aggregation.

To measure the luminescence lifetime of aqueous compositions of the studied PSs, we used a time-resolved spectrometer. The spectrometer consisted of Picosecond Light Pulser PLP-10 (Hamamatsu; Japan), a fiber output pulse laser emitting 65 ps pulses at 637 nm; Jarrell-Ash fiber input polychromator (Division of Fisher Co; USA); Semrock LD01-785/10-12.5 optical filter (Semrock Inc; USA) at the input, which filtered out light outside of the bacteriochlorin derivatives luminescence band and minimized background noise. The resulting signal was approximated by the sum of several exponentials.

We used *S. aureus* 15, *P. aeruginosa* 32, *K. pneumoniae* 1556 clinical isolates to study the process of photoinactivation of planktonic bacteria. The bacteria were grown in LB nutrient broth or on 1% LB agar (Difco; USA). To determine the minimal bactericidal concentration (MBC) of PS applicable to plankton cultures, we incubated them with PS for 30 minutes and irradiated at the light energy density of 20 J/cm^2 (standard conditions). The initial titer of bacteria was $1 \cdot 10^8$ CFU/ml (Colony Forming Units per ml). The PS dilution pattern was double, starting at 1 mM. After incubation, the bacterial suspension was centrifuged for 5 min at 7000 rpm in the Eppendorf laboratory centrifuge (Eppendorf; Germany), PS removed, bacteria resuspended in saline; then the suspensions of each concentration, as well as the PS-free control samples, were poured into wells of the two 96-well flat-bottomed plates, 100 μl in each well. One plate was used for the irradiation experiment, the other served as a dark control.

SFD-M-760 LED source (ANO MIKEL; Russia) emitting at 760 nm (wavelength at maximum) and 35 nm FWHM was used for irradiation purposes. The power density was 22–25 mW/cm^2; irradiation lasted for 20 minutes. To control the power density, we used Coherent labmax (Coherent; USA) diaphragm laser power meter.

After irradiation, 50 μl of suspension from each well were added to LB agar Petri dishes, then incubated in the dark at 37 °C for 20 h. Examining the dishes, we looked for the samples that gave no growth, registered the corresponding PS concentrations and took the smallest of them as MBC.

RESULTS

By studying the dependence of 3-$Py_4BCHp_4Br_4$ absorption on its concentration in the nanodispersion, we aimed to evaluate the severity of the aggregation process. The operating absorption band of 3-$Py_4BCHp_4Br_4$ has a narrow spectral contour; its FWHM is about 22 nm, maximum at approximately 760 nm. According to the research, in contrast to polycationic phthalocyanines, there are no expressed signs of aggregation in the absorption spectra of the 3-$Py_4BCHp_4Br_4$ dispersion [15]: the shape of the absorption spectrum does not change as the concentration grows; the dependence of optical density on molar concentration is linear (Bouguer law satisfied) and consistent with the extinction values determined at low concentrations (Fig. 1).

To confirm the assumption that the studied PS shows low aggregation capabilities, we studied the spectral-fluorescent properties of its nanodispersion, focusing on the shape and intensity of fluorescence spectra, as well as radiative lifetime of the excited 3-$Py_4BCHp_4Br_4$ at high and low concentrations.

The analysis of the PS fluorescence spectra shows that increasing the cuvette length from 1 to 10 mm at low (0.005 mM) concentrations does not affect the shape of the spectral contour (Fig. 2, spectra 1, 2) and leads only to an insignificant (0.3 nm) shift of the spectrum maximum due to reabsorption. The fluorescence band remains narrow (27 nm).

At high (0.05 mM) concentrations that approximately correspond to the PS concentrations in blood plasma 1 hour after intravenous administration, reabsorption causes a long wavelength shift of the fluorescence band spectrum maximum that depends on the length of the cuvette: 1.5 nm in the cuvette 1 mm long, 3.4 nm — in a cuvette 10 mm long. The half-width of the fluorescence band also grows (by 1.1 nm in a 1 mm cuvette, by 4.3 nm in a 10 mm cuvette), but the shape of the spectral contour does not change, no additional bathochromically and hypsochromically shifted peaks appear there.

Studying the radiative lifetime with the help of the approach described earlier [16], we discovered two components. In water-based experiments, the dominant component has the average lifetime of 2.8 ns; its share is approximately 86%. In

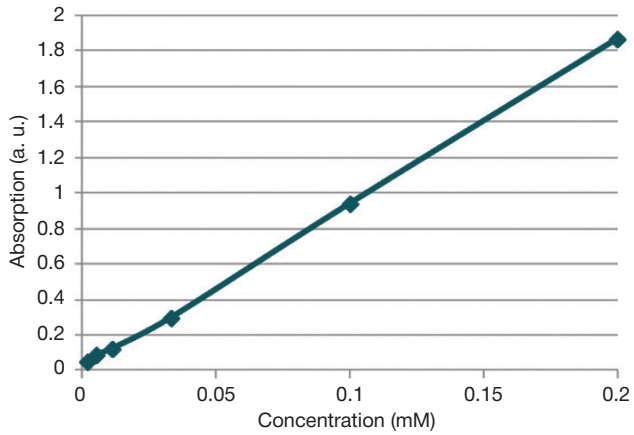

Fig. 1. Dependence of 4% Kolliphor ELP 3-$Py_4BCHp_4Br_4$ dispersion absorption on its concentration

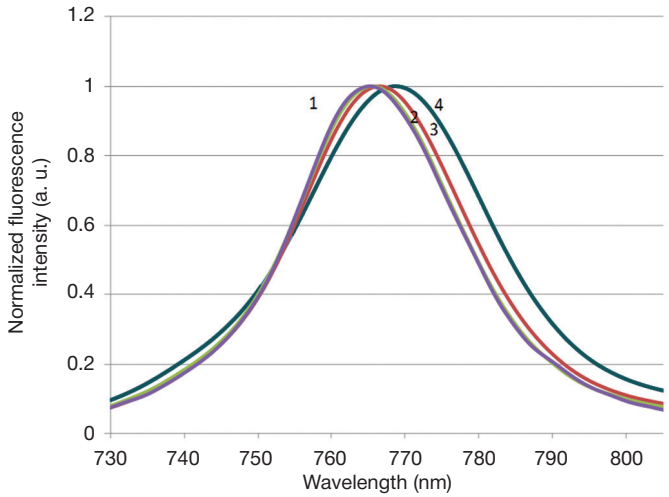

Fig. 2. Normalized fluorescence spectra of 3-$Py_4BCHp_4Br_4$ dispersions, various concentrations (spectra 1, 2 — 0.005 mM; spectra 3, 4 — 0.05 mM) and lengths of cuvettes (spectra 1, 3 — 1 mm; spectra 2, 4 — 10 mm)

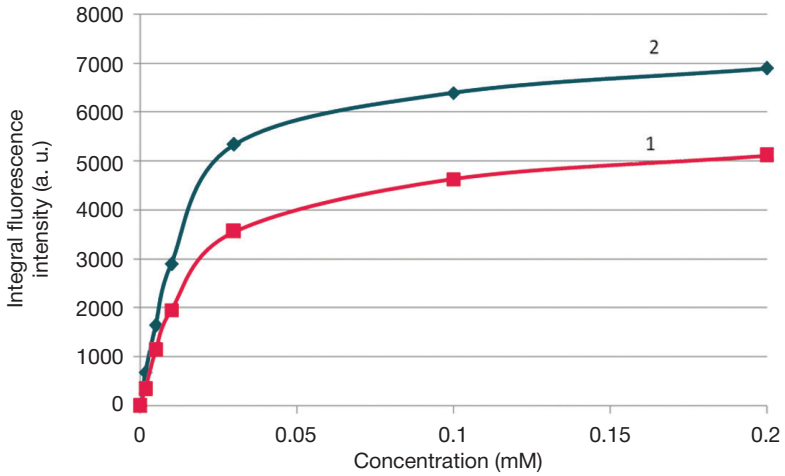

Fig. 3. Dependence of integral fluorescence intensity of 3-$Py_4BCHp_4Br_4$ aqueous compositions on their molar concentration: 1 — in water; 2 — in blood plasma

experiments with blood plasma, where aggregation is reduced, the dominant component has the average lifetime of about 2.9 ns, and its share is almost 100%.

The dependence of dispersion's integral fluorescence intensity on PS concentration is close to being linear up to 0.03 mM (Fig. 3); at higher concentrations, it becomes sublinear. The dependence pattern is the same for the 3-$Py_4BCHp_4Br_4$ composition in blood plasma. Furthermore, the shape of the curves remains almost unchanged, although the fluorescence intensity in blood plasma is 1.3–1.4 times higher than that in water.

Table below contains the discovered MBCs of 3-$Py_4BCHp_4Br_4$ at standard conditions.

DISCUSSION

Investigating absorption of the studied PS, we found that its aggregation values are low in the considered range of concentrations [15], shape and half-width of the absorption band spectrum therein do not change, and the absorption itself linearly depends on the concentration.

Analysis of the fluorescence band shape changes associated with increased concentrations and cuvette lengths allows an assumption that the main reason behind the phenomenon observed at higher concentrations of the researched PS is reabsorption, and contribution of aggregation, which also occurs, is insignificant. This is also backed by the investigation of radiative lifetime of the excited PS based on 3-$Py_4BCHp_4Br_4$ and dependence of the fluorescence intensity on concentration of 3-$Py_4BCHp_4Br_4$ in dispersion, especially in blood plasma [17–21].

These data lead to a conclusion that the efficacy of photodynamic processes at high concentrations of 3-$Py_4BCHp_4Br_4$ will not deteriorate, which allows using 3-$Py_4BCHp_4Br_4$ nanodispersions of such concentrations as sensitizers in APDT.

Compared to the previously described PSs based on cationic bacteriochlorins [14], 3-$Py_4BCHp_4Br_4$ offers significantly lower MBC values for Gram-positive *S. aureus* bacteria and Gram-negative *P. aeruginosa* bacteria in plankton state. The MBC for Gram-negative *K. pneumoniae* bacteria are also low.

CONCLUSIONS

The results of the research show that tetracationic PS based on the synthetic amphiphilic derivative of 3-$Py_4BCHp_4Br_4$ bacteriochlorin, the molecular size and weight of which are smaller, can photodynamically inactivate Gram-positive *S. aureus*, Gram-negative *P. aeruginosa* and *K. pneumoniae* bacteria. Investigation of photophysical properties of the PS in a wide range of concentrations revealed its low aggregation capability in water and blood plasma. The studies conducted allow a conclusion that the PS based on a nanostructured 3-$Py_4BCHp_4Br_4$ is promising as a component of protocols of photodynamic treatment of localized infections by Gram-positive and Gram-negative bacteria.

Table. 3-$Py_4BCHp_4Br_4$ MBC values, standard conditions (incubation time 0.5 h, exposure dose 20 J/cm^2)

Bacteria	*S. aureus*	*P. aeruginosa*	*K. pneumoniae*
MBC, μM	0.2	6.2	3.1

References

1. Park YS, Lee HB, Chin S et al. Acquisition of extensive drug-resistant *Pseudomonas aeruginosa* among hospitalized patients: risk factors and resistance mechanisms to carbapenems. Hosp Infect. 2011; 79 (1): 54–8. DOI: 10.1016/j.jhin.2011.05.014.
2. Bertoloni G, Rossi F, Valduga G, Jori et al. Photosensitising activity of water- and lipid-soluble phthalocyanines on prokaryotic and eukaryotic microbial cells. Microbios. 1992; 71 (286): 33–46.
3. Nakonieczna J, Michta E, Rybicka M et al. Superoxide dismutase is upregulated in Staphylococcus aureus following protoporphyrin-mediated photodynamic inactivation and does not directly influence the response to photodynamic treatment. BMC Microbiol. 2010; (10): 323. https://DOI.org/10.1186/1471-2180-10-323.
4. Tavares A, Carvalho CMB, Faustino MA et al. Antimicrobial photodynamic therapy: study of bacterial recovery viability and potential development of resistance after treatment. Marine Drugs. 2010; 8 (1): 91–105. DOI: 10.3390/md8010091.
5. Hamblin MR, Hasan T. Photodynamic therapy: a new antimicrobial approach to infectious disease. Photochem Photobiol Sci. 2004; 3 (5): 436–50.
6. Vera DM, Haynes MH, Ball AR et al. Strategies to potentiate antimicrobial photoinactivation by overcoming resistant phenotypes. Photochem Photobiol. 2012; 88 (3): 499–511. DOI: 10.1111/j.1751-1097.2012.01087.x.
7. Maisch T. Resistance in antimicrobial photodynamic inactivation of bacteria. Photochem Photobiol. 2015; 14 (8): 1518–26. DOI: 10.1039/c5pp00037h.
8. Almeida A, Cunha A, Faustino MAF et al. Porphyrins as antimicrobial photosensitizing agents. In: Photodynamic Inactivation of Microbial Pathogens: Medical and Environmental Applications. Hamblin MR, Jori G, editors. London: RSC Publishing, 2011; p. 83–160.
9. Wainwright M. Photodynamic antimicrobial chemotherapy. Antimicrob Chemother. 1998; 42 (1): 13–28.
10. Friedrich CL, Moyles D, Beveridge TJ, Hancock RE. Antibacterial action of structurally diverse cationic peptides on Gram-positive bacteria. Antimicrob Agents Chemother. 2000; 44 (8): 2086–92.
11. Nikaido H. Prevention of drug access to bacterial targets: Permeability barrier and active efflux. Science. 1994; 264 (5157): 382–8.
12. Moan J. Photochemistry and Photobiology. The photochemical yield of singlet oxygen from porphyrins in different states of aggregation. 1984; (39): 445–9. Available from: https://DOI.org/10.1111/j.1751-1097.1984.tb03873.x.
13. Bjarnsholt Th, Jensen PO, Moser C, Hoiby N. Biofilm infections. Heidelberg: Springer, 2011.
14. Tiganova IG, Makarova EA, Meerovich GA, Alekseeva NV, Tolordava ER, Zhizhimova YS et al. Photodynamic inactivation of pathogenic bacteria in biofilms using new synthetic bacteriochlorin derivatives. Biomedical Photonics. 2017; 6 (4): 27–36. Russian. Available from: https://DOI.org/10.24931/2413-9432-2017-6-4-27-36.
15. Makarov DA, Kuznetsova NA, Yuzhakova OA, Savina LP, Kaliya OL, Lukyanets EA et al. Effects of the degree of substitution on the physicochemical properties and photodynamic activity of zinc and aluminum phthalocyanine polycations. Russian Journal of Physical Chemistry A. 2009; 83 (6): 1044–50.
16. Bystrov FG, Makarov VI, Pominova DV, Ryabova AV, Loschenov VB. Analysis of photoluminescence decay kinetics of aluminum phthalocyanine nanoparticles interacting with immune cells. Biomedical Photonics. 2016; 5 (1): 3–8. Russian. Available from: https://DOI.org/10.24931/2413-9432-2016-5-1-3-8.

17. Juzenas P, Juzeniene A, Rotomskis R, Moan J. Spectroscopic evidence of monomeric aluminium phthalocyanine tetrasulphonate in aqueous solutions. Journal of Photochemistry and Photobiology B: Biology. 2004; 75 (1–2): 107–10. DOI: 10.1016/j.jphotobiol.2004.05.011.
18. Dhami S, Phillips D. Comparison of the photophysics of an aggregating and non-aggregating aluminium phthalocyanine system incorporated into unilamellar vesicles. Journal of Photochemistry and Photobiology A: Chemistry. 1996; 100 (1–3): 77–84.
19. Reddi E, Jori G. Reviews of Chemical Intermediates. 1988; (10): 241–68. Available from: https://DOI.org/10.1007/BF03155995.
20. Tominaga TT, Yusbmanov VE, Borissevitch IE, Imasato H, Tabak M. Aggregation phenomena in the complexes of iron tetraphenylporphine sulfonate with bovine serum albumin. Journal of Inorganic Biochemistry. 1997; (65): 235–44.
21. Changenet-Barret P, Gustavsson T, Markovitsi D, Manet I, Monti S. Unravelling molecular mechanisms in the fluorescence spectra of doxorubicin in aqueous solution by femtosecond fluorescence spectroscopy. Physical Chemistry Chemical Physics. 2013; 15 (8): 2937–44.

Литература

1. Park YS, Lee HB, Chin S et al. Acquisition of extensive drug-resistant *Pseudomonas aeruginosa* among hospitalized patients: risk factors and resistance mechanisms to carbapenems. Hosp Infect. 2011; 79 (1): 54–8. DOI: 10.1016/j.jhin.2011.05.014.
2. Bertoloni G, Rossi F, Valduga G, Jori et al. Photosensitising activity of water- and lipid-soluble phthalocyanines on prokaryotic and eukaryotic microbial cells. Microbios. 1992; 71 (286): 33–46.
3. Nakonieczna J, Michta E, Rybicka M et al. Superoxide dismutase is upregulated in Staphylococcus aureus following protoporphyrin-mediated photodynamic inactivation and does not directly influence the response to photodynamic treatment. BMC Microbiol. 2010; (10): 323. https://DOI.org/10.1186/1471-2180-10-323.
4. Tavares A, Carvalho CMB, Faustino MA et al. Antimicrobial photodynamic therapy: study of bacterial recovery viability and potential development of resistance after treatment. Marine Drugs. 2010; 8 (1): 91–105. DOI: 10.3390/md8010091.
5. Hamblin MR, Hasan T. Photodynamic therapy: a new antimicrobial approach to infectious disease. Photochem Photobiol Sci. 2004; 3 (5): 436–50.
6. Vera DM, Haynes MH, Ball AR et al. Strategies to potentiate antimicrobial photoinactivation by overcoming resistant phenotypes. Photochem Photobiol. 2012; 88 (3): 499–511. DOI: 10.1111/j.1751-1097.2012.01087.x.
7. Maisch T. Resistance in antimicrobial photodynamic inactivation of bacteria. Photochem Photobiol. 2015; 14 (8): 1518–26. DOI: 10.1039/c5pp00037h.
8. Almeida A, Cunha A, Faustino MAF et al. Porphyrins as antimicrobial photosensitizing agents. In: Photodynamic Inactivation of Microbial Pathogens: Medical and Environmental Applications. Hamblin MR, Jori G, editors. London: RSC Publishing, 2011; p. 83–160.
9. Wainwright M. Photodynamic antimicrobial chemotherapy. Antimicrob Chemother. 1998; 42 (1): 13–28.
10. Friedrich CL, Moyles D, Beveridge TJ, Hancock RE. Antibacterial action of structurally diverse cationic peptides on Gram-positive bacteria. Antimicrob Agents Chemother. 2000; 44 (8): 2086–92.
11. Nikaido H. Prevention of drug access to bacterial targets: Permeability barrier and active efflux. Science. 1994; 264 (5157): 382–8.
12. Moan J. Photochemistry and Photobiology. The photochemical yield of singlet oxygen from porphyrins in different states of aggregation. 1984; (39): 445–9. Available from: https://DOI.org/10.1111/j.1751-1097.1984.tb03873.x.
13. Bjarnsholt Th, Jensen PO, Moser C, Hoiby N. Biofilm infections. Heidelberg: Springer, 2011.
14. Тиганова И. Г., Макарова Е. А., Меерович Г. А., Алексеева Н. В., Толордава Э. Р., Жижимова Ю. С. и др. Фотодинамическая инактивация патогенных бактерий в биопленках с использованием новых синтетических производных бактериохлорина. Biomedical Photonics. 2017; 6 (4): 27–36. Доступно по ссылке: https://DOI.org/10.24931/2413-9432-2017-6-4-27-36.
15. Макаров Д. А., Кузнецова Н. А., Южакова О. А., Савина Л. П., Калия О. Л., Лукьянец Е. А. и др. Поликатионные фталоцианины цинка и алюминия: синтез, влияние степени замещения на физико-химические свойства и фотодинамическую активность в водной среде. Журнал физической химии. 2009; 83 (6): 1183–90.
16. Быстров Ф. Г., Макаров В. И., Поминова Д. В., Рябова А. В., Лощенов В. Б. Исследование кинетики затухания фотолюминесценции молекулярных нанокристаллов фталоцианина алюминия при взаимодействии с иммунокомпетентными клетками. Biomedical Photonics. 2016; 5 (1): 3–8. Доступно по ссылке: https://DOI.org/10.24931/2413-9432-2016-5-1-3-8.
17. Juzenas P, Juzeniene A, Rotomskis R, Moan J. Spectroscopic evidence of monomeric aluminium phthalocyanine tetrasulphonate in aqueous solutions. Journal of Photochemistry and Photobiology B: Biology. 2004; 75 (1–2): 107–10. DOI: 10.1016/j.jphotobiol.2004.05.011.
18. Dhami S, Phillips D. Comparison of the photophysics of an aggregating and non-aggregating aluminium phthalocyanine system incorporated into unilamellar vesicles. Journal of Photochemistry and Photobiology A: Chemistry. 1996; 100 (1–3): 77–84.
19. Reddi E, Jori G. Reviews of Chemical Intermediates. 1988; (10): 241–68. Available from: https://DOI.org/10.1007/BF03155995.
20. Tominaga TT, Yusbmanov VE, Borissevitch IE, Imasato H, Tabak M. Aggregation phenomena in the complexes of iron tetraphenylporphine sulfonate with bovine serum albumin. Journal of Inorganic Biochemistry. 1997; (65): 235–44.
21. Changenet-Barret P, Gustavsson T, Markovitsi D, Manet I, Monti S. Unravelling molecular mechanisms in the fluorescence spectra of doxorubicin in aqueous solution by femtosecond fluorescence spectroscopy. Physical Chemistry Chemical Physics. 2013; 15 (8): 2937–44.

GOLD NANOPARTICLES IN THE DIAGNOSIS AND TREATMENT OF CANCER

Kurapov PB[1] ✉, Bakhtenko EYu[2]

[1] Pirogov Russian National Research Medical University, Moscow
[2] Vologda State University, Vologda

Due to chemical stability, low toxicity, and relative simplicity of synthesis/modification techniques, gold nanoparticles (NP) enjoy a wide range of biomedical applications, including *in vitro* diagnostics, targeted drug delivery, contrast-enhanced radiation therapy, and photothermal therapy. The high ratio of the gold NP surface area to their volume facilitates design of complex nanoplatforms for various therapeutic and diagnostic purposes. Unique electrical and optical properties of gold NP known as surface plasmon resonance assist medical diagnosis. In this work we look at the basic methods for gold NP synthesis and modification, including the so-called green chemistry, talk about the pharmacological aspects of their application and highlight their potential as diagnostic agents. We believe that due to their unique properties, gold-based nanoplatforms for targeted drug delivery and theranostics have indisputable advantages over other nanoparticles.

Keywords: gold nanoparticles, nanodiagnostics, nanotherapy, targeted drug delivery, theranostics, cancer research

✉ **Correspondence should be addressed:** Pavel B. Kurapov
Ostrovityanova 1, Moscow, 117997; kurapoff@mail.ru

Received: 29.11.2018 **Accepted:** 18.12.2018

DOI: 10.24075/brsmu.2018.090

НАНОЧАСТИЦЫ ЗОЛОТА ДЛЯ ДИАГНОСТИКИ И ТЕРАПИИ ОНКОЛОГИЧЕСКИХ ЗАБОЛЕВАНИЙ

П. Б. Курапов[1] ✉, Е. Ю. Бахтенко[2]

[1] Российский национальный исследовательский медицинский университет имени Н. И. Пирогова, Москва
[2] Вологодский государственный университет, Вологда

Химическая стабильность, низкая токсичность, относительная простота методов синтеза и модификации наночастиц (НЧ) золота способствуют их использованию в различных областях биомедицины, таких как диагностика *in vitro*, адресная доставка лекарств, фототермическая и фотодинамическая терапия. Высокое соотношение площади поверхности к объему этих НЧ существенно облегчает создание на их основе комплексных наноплатформ, используемых сразу в нескольких терапевтических и диагностических направлениях. Уникальные электрические и оптические свойства НЧ золота, известные как локализованный поверхностный плазмонный резонанс особенно актуальны для диагностики различных заболеваний. Рассмотрены основные методы синтеза и модификации НЧ золота, в частности методами «зеленой химии», фармакологические аспекты их применения и использования в качестве диагностических агентов. По нашему мнению, именно благодаря своим уникальным свойствам наноплатформы для адресной доставки лекарственных препаратов и тераностики, созданные на основе НЧ золота, имеют неоспоримые преимущества перед другими типами наночастиц.

Ключевые слова: наночастицы золота, нанодиагностика, нанотерапия, адресная доставка лекарственных средств, тераностика, онкология

✉ **Для корреспонденции:** Павел Борисович Курапов
ул. Островитянова, д. 1, г. Москва, 117997; kurapoff@mail.ru

Статья получена: 29.11.2018 **Статья принята к печати:** 18.12.2018

DOI: 10.24075/vrgmu.2018.090

The use of gold nanoparticles (NP) in biomedicine was pioneered in the study investigating the possibility of direct microscopic visualization of Salmonella surface antigens using antibodies conjugated to colloidal gold [1]. That study gave rise to an independent field of scientific knowledge focusing on the applications of gold NP in biomedical research, diagnostics, biosensors, photothermal and photodynamic therapy, as well as targeted delivery of pharmaceutical drugs or genetic material [2].

The interest in gold NP has been growing ever since, yielding an increasing number of publications every year (Fig. 1).

Gold NP can be categorized into two major groups based on their structure and application. The first group comprises NP conjugated to molecules that have various functions and properties. Such platforms are employed in the targeted delivery and controlled release of tumoricidal agents [3], locally induced hyperthermia against cancer [4], medical imaging, and sensor design [5]. It is important that methods for gold NP synthesis should be robust and reliable and the surface of the synthesized particles could be effortlessly modified. Today, gold NP from this group can be functionalized with oligonucleotides, peptides and polyethylene glycol.

The second group consists of hollow NP with a dielectric or magnetic core and a gold shell. These are used to encapsulate therapeutic agents. The size of gold NP varies from 20 to 500 nm, which facilitates their biodistribution following passive targeted delivery. Advantageously, these multilayer particles are polyfunctional: their functions are distributed between the core and the shell.

Gold NP are characterized by increased absorption and scattering cross-sections; their absorption spectra depend on their shape and size. Au^0 nanospheres of 10–25 nm in diameter

absorb light at 520 nm, whereas gold nanorods absorb in the near infrared region of the spectrum. This can assist *in vivo* diagnosis and further treatment.

Modified gold NP are lowly immunogenic and highly biocompatible. Particles sized 10–22 nm can serve as carriers for vaccine delivery [6]. It has been demonstrated that Au^0 NP enhance the immune response *in vivo*, especially against viral infections, such as tick-borne encephalitis, HIV and hepatitis B.

Unique electrical and optical properties of gold NP and their ability to form stable complexes with biomolecules are actively exploited in biosensor design. For example, Au^0 nanoparticles encapsulated in graphene oxide were used to design a DNA biosensor for the detection of biomarkers, including proteins found on the surface of breast cancer cells.

It is known that inflammation causes elevated blood plasma levels of C-reactive protein of humans. In clinical practice, this protein serves as a marker of many pathologies, including cardiovascular disorders [7, 8]. A novel sensor for the electrochemical detection of troponin I (a specific biomarker of myocardial tissue injury) in the blood plasma is based on capturing the signal emitted by Au^0 NP localized on the electrode surface [9].

Methods for gold NP synthesis

Gold NP can be synthesized using two major techniques: dispersion and condensation. Dispersion occurs as a result of applying a high-voltage electrical current or a similar destructive physical force to the metal. Condensed gold NP are synthesized from ions of gold salts by chemical reduction or following mild physical stress (radiolysis, sonication, etc.) [2]. Dispersion yields heterogeneously sized particles. Because of this major drawback, condensation remains the preferred method for gold NP synthesis.

Au^0 NP obtained through condensation are colloidal particles of 5 to 20 nm in diameter derived from gold halides, such as hydrogen tetrachloroaurate produced as gold is dissolved in aqua regia. Among the chemical reducing agents used for condensation are sodium citrate and borohydride, ascorbic and ethylenediaminetetraacetic acids, and alkaline solutions of hydrogen peroxide. Ultra-dispersed sols of 2–3 nm in diameter are synthesized from sodium or potassium thiocyanates.

The rate of NP synthesis depends on the concentration of the reagents and the chemical composition of the reducing agent. A low rate of nucleation and a high rate of particle condensation yield relatively small quantities of big particles. At a low rate of condensation, small particles are likely to form in large quantities.

Gold 8–120 nm-sized NP for medical applications are usually synthesized by reducing hydrogen tetrachloroaurate in the presence of sodium citrate; the method was originally proposed to fabricate NP of 20 ± 1.5 nm in diameter [10]. Large gold NP of > 80 nm in size can be synthesized by condensation using isoascorbic acid as a reducing agent and gum arabic as a protective colloid.

Monodisperse gold NP sols are sometimes synthesized using two-phase techniques. In the first step, metal-containing reagents are transferred from an aqueous to an organic phase (hexane, toluene); in the second step, solutions of surfactants and a reducing agent (butanol) are added to the reaction mixture. The surface of nanoclusters is capped with hexadecylamine. Its amino groups interact with the metal surface in such a way that nonpolar hydrocarbon tails remain outside the surface [11].

The size and shape of gold nanoparticles are affected, among other things, by the type of a reducing agent used for their synthesis. For example, sodium citrate and hydrogen peroxide will yield spheres, whereas hydroxylamine will produce cubic crystals with well-shaped facets [12].

NP are stabilized with thiols and disulfides. High affinity of sulfur to gold promotes formation of a gold thiolate monolayer on the surface of the particles. Gold halides can be reduced using both chemical and physical methods; the latter include exposure to ultrasound, ultraviolet and infrared ionizing radiation, laser photolysis and electrochemistry. The NP yielded by these methods do not have any trace amounts of chemical reagents of their surface.

The use of microorganisms, cells of plants, animal or humans has given rise to a unique, advanced biotechnological approach to the synthesis of gold NP relying on the principles of "green chemistry" [13, 14]. Interestingly, green chemistry techniques are hardly ever used for the synthesis of other NP types.

A recently published review takes a close look at the application of plant extracts in the synthesis of metal NP [15]. Plants contain bioactive compounds, such as flavonoids, phenols, citric and ascorbic acids, polyphenols, terpenes, alkaloids, and reductases, that can act as reducing agents [16]. Biotechnological production of NP has certain advantages over chemical methods due to the ability of plant extracts to play the role of both reducing and stabilizing/isolating agents (see the Table).

Plants produce NP intra- and extracellularly [23]. To stimulate intracellular biosynthesis of NP, plants should be grown in organic media or on metal-enriched soils (cell/tissue engineering, hydroponics) [24]. Extracellular methods of NP synthesis rely on leaf extracts [25]. Biotechnologically produced

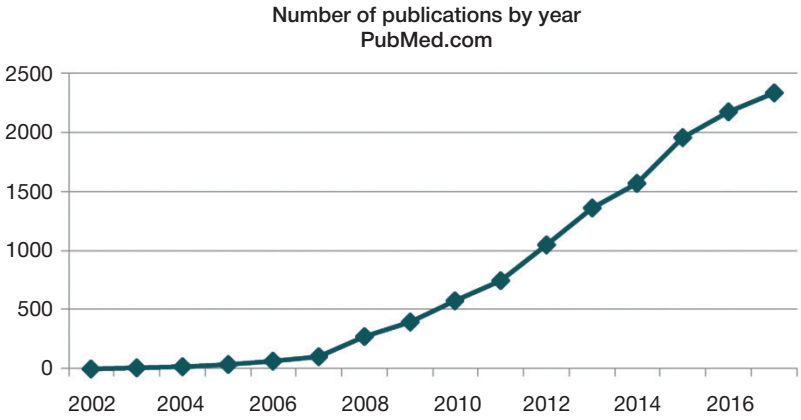

Fig. 1. The number of research articles on the use of gold NP in biomedicine published between 2002 and 2017 (figures provided by PubMed.com)

gold NP have various sizes and shapes: spheres, rods, cubes, and triangles.

A simple, cost-effective and reproducible technique for the synthesis of almost monodisperse gold nanocubes of 20 nm in diameter is based on the use of extracts derived from fresh or dried mango (*Mangifera indica*) leaves. It takes only 2 minutes to fabricate such NP by adding the leaf extract to the solution of $HAuCl_4 \bullet 3H_2O$; importantly, the colloid remains stable for over 5 months. Smaller and uniformly distributed particles can be obtained from a dried leaf extract of the same plant [26].

The size of NP synthesized by green chemistry techniques depends on what extract is employed as a reducing and stabilizing agent. The olive leaf extract yields Au^0 NP of 50–100 nm in size; the geranium extract, about 12 nm; white willow seeds, 50–80 nm [26]. Production of gold NP can be assisted by pollen, seed, flower, bark, and root extracts [27]. Another method of NP synthesis relies on chitosan that acts as a reducing and stabilizing agent. Positively charged chitosan-containing particles help to mitigate the adverse effects of the chemotherapy drug 5-fluorouracil [28].

Au^0 nanospheres are a product of $HAuCl_4$ reduction in colloidal solutions. At the first stage of synthesis, the rapid reduction of hydrogen tetrachloroaurate results in a supersaturated gold solution. Then reduction slows abruptly and the new phase condensates producing very small NP nuclei of less than 2 nm in diameter. The rate of nucleation in the new phase is determined by the degree of saturation of the solution and the concentrations and chemical structure of the reducing agent. At a low rate of nucleation and a high rate of condensation, a small amount of relatively large particles is produced. Higher rates of nucleation and smaller rates of condensation are more likely to yield large quantities of small NP.

Nonspherical colloidal gold NP are synthesized on hard silica or aluminum oxide matrices under artificially created anisotropic conditions by electrochemical methods [29]. Nanorods are synthesized on soft matrices (micellar solutions of surface-active agents) through chemical reduction.

The last few years have witnessed a rapid evolution of nanomedicine involving the use of ultra-small NP with a diameter of less than 6 nm. Gold nanorods with a diameter of < 6 nm have the same electrical and optical properties as their large counterparts, but are devoid of their flaws which is important for biomedical applications [30]. Gold nanothreads are thermally derived from gold NP adsorbed on the surface of nanotubes. Tubular gold nanothreads with an external diameter of 10 nm can be obtained by thermally removing residual nanotubes. DNA molecules can also be used as a matrix for nanothread synthesis.

Spherical gold nanoshells consist of a dielectric nucleus of 100 nm in diameter coated with a thin layer of gold. The optical properties of such particles can be tuned by varying the diameter of the nucleus and the thickness of the shell. Gold nanoshells hold great promise for biomedical research, diagnosis and therapy. One of the methods for nanoshell fabrication consists of 4 major steps: first, spherical silica cores are synthesized and then their surface is functionalized with amino groups onto which gold particles are absorbed [31].

The physical and chemical properties of synthesized NP and their average diameter and shape are traditionally controlled and measured by electron microscopy and spectrophotometry. The NP size can also be assessed by laser correlation spectroscopy (dynamic light scattering). Differential centrifugation, scanning/atomic force microscopy, small/wide X-ray scattering, X-ray diffraction analysis, mass spectroscopy, and other methods are less common.

Methods for gold NP surface modification

Adsorption and hemadsorption are two major methods for Au^0 NP surface modification. Adsorption of biomolecules onto the NP surface facilitated by hydrophobic and electrostatic interactions stabilizes nanoparticles. A strong negative charge of the gold NP surface ensures stable adsorption of a wide range of high molecular weight compounds.

Biocompatibility of Au^0 NP can be improved by functionalizing their surface with coatings, layers, and linkers. The same strategy is employed for creating diagnostic or therapeutic platforms. At the molecular level, surface modifications are required to confer specificity, sensitivity and biological compatibility to the nanoparticles.

Gold NP are capable of interacting with immunoglobulins, lectins, enzymes, hormones, lipoproteins, etc. As carriers, they have numerous advantages over other platforms. Gold NP improve the solubility of therapeutic agents and protect them from deterioration on the way to the target. Gold NP can actively or passively accumulate in the target organ and enable controlled release of the carried drug. Their magnetic and photothermal properties expand the arsenal of therapeutic techniques that can be applied to a patient and reduce the toxicity of a carried drug ensuring the desired therapeutic effect at lower drug doses.

Methods for Au^0 NP surface modifications can be covalent and noncovalent. Advantageously, noncovalent methods do not require a therapeutic agent to be modified, too, and ensure easy release of the drug from a carrier, which is a prerequisite for successful therapy. Charged or hydrophilic groups accumulated on the surface of nanostructures increase their solubility and facilitate interactions with biomolecules. Amphiphilic polymer coatings also improve the solubility of the complex, promote nonspecific interactions with biological

Table. Plant extracts for the synthesis of gold NP

Common name of plant	Latin name of plant	Part of plant used for extract preparation	Gold NP diameter, nm	References
Rose geranium	*Pelargonium graveolens*	Leaves	45	[17]
Lemon verbena	*Lippia citriodora*	Leaves	36	[17]
Garden sage	*Salvia officinalis*	Leaves	29	[17]
Pomegranate	*Punica granatum*	Fruit	32	[17]
Dragonhead	*Dracocephalum kotschyi*	Leaves	11	[18]
Cinnamon	*Cinnamomum zeylanicum*	Leaves	25	[19]
Pomelo	*Citrus maxima*	Fruit	15–35	[20]
Black cherry	*Prunus serotina*	Flowers	10–20	[21]
Date palm	*Phoenix dactylifera*	Pollen	20–50	[22]

macromolecules, increase compatibility of the nanostructures with proteins and their affinity to cell membranes. Polyethylene glycol coatings enhance the efficacy of NP uptake by body cells, prevent NP aggregation in the medium characterized by high ionic strength and increase their circulation time in the blood stream.

Surface-modified Au^0 NP demonstrate an improved ability to penetrate blood vessel walls and cell membranes. Nanoparticles interact with therapeutic agents and reduce their cytotoxicity. The most common method for gold NP surface modification is thiolation by bifunctional thiols, whose additional functional group allows them to conjugate to biomolecules. The surface of gold NP can be stabilized with modified dextran. The appeal of such structures is grounded in their ability to reversibly change their properties depending on the temperature or pH of the environment.

Modification of gold nanostructures by self-assembled monolayers or complex molecular aggregates is described in detail in a number of works [32]. Also, there is a plethora of functional molecular linkers, including aryl diazonium salts, that can be used to modify the surface of gold NP [33, 34].

Gold nanoparticles in diagnostics and therapy

Aurotherapy of arthritis was first attempted in 1929. Its underlying mechanism is based on the ability of gold compounds to inhibit macrophages *in vivo* and suppress pathological immune response.

Gold nanorods actively absorb in the near infrared spectrum for which the human body is relatively transparent. Therefore, they are ideal for photothermal therapy (selective destruction of pathogens by heating). For example, gold NP complexes with antibodies can kill intracellular *Toxoplasma gondii* that causes toxoplasmosis. Antibodies allow NP to selectively bind the target. Exposed to laser radiation, NP get heated inducing death of up to 83% of toxoplasma cells.

Until recently, gold NP were not used in cancer research. An increased interest in these particles is evoked by their unique optical and electronic properties (surface plasmon resonance) that can revolutionize the approaches to the diagnostics and treatment of cancer. Theranostic platforms combining diagnostic and therapeutic functions enable control over patients' response to treatment [35].

The epidermal growth factor receptor (EFGR) expressed on the surface of many cancer cells can be exploited as a diagnostic marker in the treatment of malignancies. The selective effect of gold NP on tumor tissue may be explained by the specifics of tumor architecture and growth. Cancer cells grow rapidly forming gaps between each other and fenestrations on their surfaces. This phenomenon is referred to as enhanced permeability and retention, EPR. It allows NP to easily penetrate a cancer cell. Increased acidity inside the cancer cell is also a beneficial factor aiding targeted and timely release of therapeutic agents into the lesion.

Once gold NP have bound to their target, the affected organ is irradiated with low-energy infrared laser beams. This energy is absorbed by the nanoparticles, which emit ultrasound and thermal waves in response. The emitted ultrasound waves lay the basis for the photoacoustic imaging of malignancies whereas the produced heat kills cancer cells (photothermal therapy). Locally induced hyperthermia stimulates targeted release of drugs entrapped in a gold capsule [36].

Photoacoustic imaging can be performed with gold nanorods. But the best therapeutic effect is achieved by using star-shaped gold NP sized 25 nm with 5–10 sharp-tipped branches. Owing to the large surface area of such NP, increased amounts of a therapeutic agent can be loaded onto the "star" whose shape stimulates light absorption and ensures targeted drug delivery.

Biocompatible gold NP functionalized with molecules that can selectively interact with cancer cells are an ideal tool for hyperthermia-based therapy against cancer [37].

Inhibition of metastases with gold nanoparticles by increasing the rigidity of nuclear membranes of cancer cells

As the tumor grows, its cells migrate to neighboring tissues and organs forming metastases. Therefore, curbing their metastatic spread is a critical clinical task. Au^0 HP modified with ligands consisting of L-arginine, glycine and L-aspartic acid (RGD peptide) and nuclear localization signal (NLS) peptides were used to design a drug that increased the rigidity of nuclear cancer cell membranes. It stimulated overexpression of A/C lamin proteins and reduced the ability of cancer cells to metastasize. Free RGD peptide is often employed in cell biology research and biotechnology as it is capable of inhibiting intercellular interactions [38]. Inhibiting the spread of metastases leaves a doctor and a patient more time to fight cancer [39].

Gold NP as platforms for molecular diagnostics and therapy of cancer

In clinical practice, diagnosis and treatment do not take place simultaneously. Theranostics is a combination of the two comprising an entire range of medical services from early diagnosis to therapy to follow-up observation. Theranostics involves the use of targeted therapy and diagnostic tests based on the so-called nanoplatforms and has an important role in oncology.

Au^0 NP-based platforms have certain advantages over other carriers due to their unique optical characteristics, high efficiency of photothermal conversion and a high value of X-ray absorption coefficient. The energy absorbed by the particle is partly emitted as scattered light and partly turns to heat. Thus, gold NP find their application in both diagnostics and treatment based on optical hyperthermia. By tuning the shape of NP, one can vary their analytical and therapeutic parameters.

Some authors have demonstrated that gold NP sized about 13 nm are ideal for theranostics. They are potent contrasting agents for CT and X-ray modalities and can be successfully used to create theranostic platforms [40–42].

Photothermal therapy

Conventional chemotherapy is a systemic treatment that affects every organ. Chemotherapy drugs have serious adverse effects. Au^0 NP are a suitable material for biocompatible and highly effective photothermal platforms that can absorb and convert near infrared light to heat causing a local rise in temperature, which destroys cancer cells. This phenomenon is known as optical hyperthermia [43].

Chinese researchers have designed unique theranostic nanoplatforms capable of simultaneous detection and killing of cancer cells. The hollow gold NP components of the platforms contain iron oxide that has paramagnetic properties; the surface of these NP is functionalized with antibodies against some cancer cells. The NP are administered to a patient by injection. Their migration to organs and tissues can be monitored by CT thanks to the properties of iron oxide. Heated by infrared

light, the NP localized in the tumor destroy cancer cells (the phenomenon of optical hyperthermia, see above) [44].

Another type of nanoplatforms was created based on the traditional anticancer drug doxorubicin and gold NP encapsulated in heat-sensitive liposomes. This nanoplatform combines a thermal tumoricidal effect with the effect produced by doxorubicin that is released directly into cancer cells following their irradiation with infrared light. The concentration of the drug in the tumor increases as the liposome membrane degrades [45].

So far, two gold-based intravenous drugs (AurImmune™ and AuroLase™) have been approved for clinical use [46, 47].

The therapeutic effect of Au^0 NP is based on the narrowing of blood vessels that supply nutrients to the tumor and inhibiting angiogenesis in the affected organs and tissues. Normally, angiogenesis is moderately intensive. It is stimulated when tissue needs regenerating, in thrombosis and inflammation, scarring and other regenerative processes; it is also vital for the growth and development of an individual. In cancer tissues angiogenesis is very vigorous; therefore, cancer cells are continuously supplied with sufficient amounts of blood and nutrients boosting their growth.

The majority of existing angiogenesis inhibitors are represented by antibodies against VEGF. (vascular endothelial growth factor) and cause serious adverse reactions. Unlike most of them, gold NP suppress VEGF function without producing a toxic effect on the cells [48].

Radioactive gold and its application in cancer research

Colloidal solutions of radioactive gold are used as tumoricidal agents. Au^0 has found its medical application in oncology in the form of a radioactive isotope ^{198}Au obtained through the irradiation of the naturally occurring Au^0 with neutrons. The half-life of ^{198}Au does not exceed 3 days. It emits β- and γ-rays that help to locate the isotope inside the body. Radioactive gold colloids selectively accumulate in the cells of the mononuclear phagocyte system and connective tissue and therefore can be used for diagnostic and therapeutic purposes. Radionuclide-based diagnostic procedures utilize colloidal solutions with Au^0 NP concentrations of 3–6 mg/ml and a particle size of 10–30 nm.

Mono- and polydisperse colloidal Au^0 NP solutions produce a therapeutic effect on cancer patients. Radioactive concentration of the drug must not exceed 4 mCi/ml; it is achieved by diluting the initial drug with 0.25—0.5% solutions of novocain or sodium chloride.

CONCLUSIONS

Rapid evolution of technologies for the synthesis of gold NP has yielded an abundance of diversely shaped, sized and structured nanoparticles with various optical properties. Modification of NP surfaces with specific molecules is critical for the biomedical application of NP, as it improves their stability *in vivo* and specificity to a biological target. At present, thiolated derivatives of polyethylene glycol and some other molecules are considered to be the best NP stabilizers. Particles modified with polyethylene glycol circulate in the blood stream longer and are better protected against immune cells. Gold NP conjugates are potent biomarkers of cancer, Alzheimer's disease, AIDS, hepatitis, TB, diabetes mellitus, and other disorders. Plasmonic photothermal laser therapy is now being tested in the clinical setting. The success of this technology is determined by how fast researchers will be able to develop reliable methods for *in vivo* targeted drug delivery and to improve control over photothermolysis *in situ*. We believed that diagnostic and therapeutic targeted drug delivery platforms based on gold NP and synthesized by green chemistry techniques hold the best promise for nanobiomedicine.

References

1. Faulk WP, Taylor GM. An immunocolloid method for the electron microscope. Immunochemistry. 1971; 8 (11): 1081–3.
2. Dykman L, Khlebtsov N. Gold Nanoparticles in Biomedical Applications. CRS Press, 2018; 331 p.
3. Sukhorukov GB, Rogach AL, Zebli B, Liedl T, Skirtach AG, Köhler K et al. Nanoengineered polymer capsules: tools for detection, controlled delivery, and site-specific manipulation. Small. 2005; 1 (2): 194–200.
4. Xia Y, Li W, Cobley CM, Chen J, Xia X, Zhang Q et al. Gold nanocages: from synthesis to theranostic applications. Acc Chem Res. 2011; 44 (10): 914–24.
5. Zharov VP, Kim JW, Curiel DT, Everts M. Self-Assembling Nanoclusters in Living Systems: Application for Integrated Photothermal Nanodiagnostics and Nanotherapy. Nanomed Nanotechnol Biology and Medicine. 2005; 1 (4): 326–45.
6. Kang S, Ahn S, Lee J, Kim JY, Choi M, Gujrati V et al. Effects of gold nanoparticle-based vaccine size on lymph node delivery and cytotoxic T-lymphocyte responses. J Control Release. 2017; (256): 56–67.
7. Fan L, Fang L, Yongtao Y, Yu W, Weiqun T. Strategies on Nanodiagnostics and Nanotherapies of the Three Common Cancers. Nanomaterials. 2018; 8 (4): 202.
8. Antonio M, Nogueira J, Vitorino R, Daniel-da-Silva AL. Functionalized Gold Nanoparticles for the Detection of C-Reactive Protein. Nanomaterials. 2018; 8 (4): 200.
9. Shumkov AA, Suprun EV, Shumyanceva VV, Archakov AI. Sensornyj ehlement na osnove nanochastic zolota dlya opredeleniya kardiomarkyorov. Biomedicina. 2011; (3): 46–9.
10. Turkevich J, Stevenson PC, Hiller JA. Study of the nucleation and growth processes in the synthesis of colloidal gold. Discuss Faraday Soc. 1951; (11): 55–75.
11. Hirai H, Aizawa H. Preparation of stable dispersions of colloidal gold in hexanes by phase transfer. J Colloid Interface Sci. 1993; (161): 471–4.
12. Mihajlov MD. Himicheskie metody polucheniya nanochastic i nanomaterialov. Sankt-Peterburg, 2012; 260 s.
13. Anshup A, Venkataraman JS et al. Growth of gold nanoparticles in human cells. Langmuir. 2006; 21 (25): 11562–7.
14. Santhoshkumar J, Rajeshkumar S, Venkat KS. Phyto-assisted synthesis, characterization and applications of gold nanoparticles. Biochemistry and Biophysics Reports. 2017; (11): 46–57.
15. Makarov VV, Lav A, Sinicyna OV, Makarova SS, Yaminskij IV i dr. «Zelenye» nanotexnologii: sintez metallicheskix nanochastic s ispol'zovaniem rastenij. Acta Naturae. 2014; 6 (1): 37–47.
16. Kurapov PB, Baxtenko EYu. Mnogoobrazie vtorichnyx metabolitov vysshix rastenij i ix lechebnye svojstva. M.: Izd-vo RNIMU, 2012; 200 s.
17. Elia P, Zach R, Hazan S, Kolusheva S, Porat Z, Zeiri Y. Green synthesis of gold nanoparticles using plant extracts as reducing agents. Int J Nanomedicine. 2014; 9 (1): 4007–21.
18. Dorosti N, Jamshidi F. Plant-mediated gold nanoparticles by Dracocephalum kotschyi as anticholinesterase agent: Synthesis, characterization, and evaluation of anticancer and antibacterial activity. Journal of Applied Biomedicine. 2016; 14 (3): 235–45.
19. Smitha SL, Philip D, Gopchandran KG Green synthesis of gold nanoparticles using Cinnamomum zeylanicum leaf broth. Spectrochim Acta Part A Mol Biomol Spectrosc. 2009; 74 (3): 735–9.

20. Yu J, Xu D, Guan HN, Wang C, Huang LK, Chi DF. Facile one-step green synthesis of gold nanoparticles using Citrus maxima aqueous extracts and its catalytic activity. Mater Lett. 2016; (166): 110–2.
21. Teimuri-Mofrad R, Hadi R, Tahmasebi B, Farhoudian S, et al. Green synthesis of gold nanoparticles using plant extract. Nanochem Res. 2017; 2 (1): 8–19.
22. Banu H, Renuka N, Faheem SM, Ismail R, Singh V et al. Gold and silver nanoparticles biomimetically synthesized using date palm pollen extract-induce apoptosis and regulate P53 and BCL-2 expression in human breast adenocarcinoma cells. Biol Trace Elem Res. 2018; 18 (3): 12011–8.
23. Rai M, Yadav A. Plants as potential synthesiser of precious metal nanoparticles: progress and prospects. IET Nanobiotechnol. 2013; 7 (3): 117–24.
24. Masumeh N. Biosynthesis of gold nanoparticles using plant extracts. Bioprocess and Biosystems Engineering. 2015; 38 (1): 1–14.
25. Ankamwar B. Biosynthesis of gold nanoparticles (Green-gold) using leaf extract of Terminalia catappa. E J Chem. 2010; 7 (4): 1334–9.
26. Philip D. Rapid green synthesis of spherical gold nanoparticles using Mangifera indica leaf. Spectrochim Acta Part A Mol Biomol Spectrosc. 2010; 77 (4): 807–10.
27. Vadlapudi V, Kaladhar DS. Review: green synthesis of silver and gold nanoparticles. Middle-East J Sci Res. 2014; 19 (6): 834–42.
28. Salem DS, Sliem MA, El-Sesy M, Shouman SA, Badr Y. Improved chemo-photothermal therapy of hepatocellular carcinoma using chitosan-coated goldnanoparticles. Journal of photochemistry and photobiology B Biology. 2018; 182 (5): 92–9.
29. Zhivkov A, van der Zande BMI., Stoylov S. Electro-optics of metal particles: electric birefringence of gold rods. Coll Surf A. 2002; 209 (2–3): 299–303.
30. Lu An, Yuanyuan W, Qiwei T, Shiping Y. Small gold nanorods: recent advances in synthesis, biological imaging, and cancer therapy. Materials. 2017; 10 (12): 1372.
31. Oldenburg SJ, Averitt RD, Westcott SL, Halas N. Nanoengineering of optical resonances. Chem Phys Lett. 1998; 288 (2): 243–7.
32. Love JC, Estroff LA, Kriebel JK, Nuzzo RG, and Whitesides GM. Self-assembled monolayers of thiolates on metals as a form of nanotechnology. Chem Rev. 2005; 105 (4): 1103–69.
33. Marchenkov NS, Marchenko NV. Nanochasticy zolota i ix primenenie dlya teranostiki zabolevanij cheloveka. Medicinskaya fizika. 2014; 4 (64): 64–77.
34. Silva SM, Tavallaie R, Sandiford L, Tilley RD, Gooding J. Gold coated magnetic nanoparticles: from preparation to surface modification for analytical and biomedical applications. Chem Commun. 2016; 52 (48): 7528–40.
35. Guo J, Rahme K, He Y, Li LL, Holmes JD, O'Driscoll CM. Gold nanoparticles enlighten the future of cancer theranostics. International Journal of Nanomedicine. 2017; 12: 6131–52.
36. Dykman LA, Xlebcov NG. Zolotye nanochasticy v biologii i medicine: dostizheniya poslednix let i perspektivy. Acta Naturae. 2011; 3 (2): 36–58.
37. Marchenko NV, Marchenkov NS. Nanochasticy zolota — ot cerkovnyx vitrazhej k nanomedicine. Uspexi v ximii i ximicheskoj texnologii. 2012; 26 (6): 104–9.
38. Ali MRK, Wu Y, Ghosh D, Do BH, Chen K, Dawson MR et al. Nuclear membrane-targeted gold nanoparticles inhibit cancer cell migration and invasion. ACS Nano. 2017; 11 (4): 3716–26.
39. Fan L, Fang L, Yongtao Y, Yu W, Weiqun T. Strategies on Nanodiagnostics and Nanotherapies of the Three Common Cancers. Nanomaterials. 2018; 8 (4): 202.
40. Garcia CP, Chambrier I, Cook MJ, Haines AH, Field RA, Russell DA. Targeted photodynamic therapy of breast cancer cells using lactose-phthalocyanine functionalized gold nanoparticles. J Colloid Interface Sci. 2018; 512: 249–59.
41. Chen Y, Xianyu Y, Jiang, X. Surface modification of gold nanoparticles with small molecules for biochemical analysis. Acc Chem Res. 2017; 50 (2): 310–9.
42. Deng H, Zhong Y, Du M, Liu Q, Fan Z, Dai F, et al. Theranostic self-assembly structure of gold nanoparticles for nir photothermal therapy and x-ray computed tomography imaging. Theranostics. 2014; 4 (9): 904–18.
43. Deev SM, Lebedenko EN. Supramolekulyarnye agenty dlya teranostiki. Bioorganicheskaya ximiya. 2015; 41 (5): 539–52.
44. Hwang S, Nam J, Jung S, Song J, Doh H, Kim S. Gold nanoparticle-mediated photothermal therapy: current status and future perspective. Nanomedicine Lond. 2014; 9 (13): 2003–22.
45. Li Y, He D, Tu J, Wang R, Zu C, Chen Y et al. The comparative effect of wrapping solid gold nanoparticles and hollow gold nanoparticles with doxorubicin-loaded thermosensitive liposomes for cancer thermo-chemotherapy. Nanoscale. 2018; 10 (18): 8628–41.
46. Boisselier E, Astruc D. Gold nanoparticles in nanomedicine: preparations, imaging, diagnostics, therapies and toxicity. Chem Rev. 2009; 38 (6): 1759–82.
47. Dykman LA, Bogatyrev VA, Shhegolev SYu, Xlebcov NG. Zolotye nanochasticy: sintez, svojstva, biomedicinskoe primenenie. M.: Nauka, 2008; 319 c.
48. Sumbayev VV, Yasinska IM, Gibbs BF. Biomedical Applications of Gold Nanoparticles Recent Advances in Circuits. Communications and Signal Processing. Athens: WSEAS Press, 2013; p. 342–48.

Литература

1. Faulk WP, Taylor GM. An immunocolloid method for the electron microscope. Immunochemistry. 1971; 8 (11): 1081–3.
2. Dykman L, Khlebtsov N. Gold Nanoparticles in Biomedical Applications. CRS Press, 2018; 331 p.
3. Sukhorukov GB, Rogach AL, Zebli B, Liedl T, Skirtach AG, Köhler K et al. Nanoengineered polymer capsules: tools for detection, controlled delivery, and site-specific manipulation. Small. 2005; 1 (2): 194–200.
4. Xia Y, Li W, Cobley CM, Chen J, Xia X, Zhang Q et al. Gold nanocages: from synthesis to theranostic applications. Acc Chem Res. 2011; 44 (10): 914–24.
5. Zharov VP, Kim JW, Curiel DT, Everts M. Self-Assembling Nanoclusters in Living Systems: Application for Integrated Photothermal Nanodiagnostics and Nanotherapy. Nanomed Nanotechnol Biology and Medicine. 2005; 1 (4): 326–45.
6. Kang S, Ahn S, Lee J, Kim JY, Choi M, Gujrati V et al. Effects of gold nanoparticle-based vaccine size on lymph node delivery and cytotoxic T-lymphocyte responses. J Control Release. 2017; (256): 56–67.
7. Fan L, Fang L, Yongtao Y, Yu W, Weiqun T. Strategies on Nanodiagnostics and Nanotherapies of the Three Common Cancers. Nanomaterials. 2018; 8 (4): 202.
8. Antonio M, Nogueira J, Vitorino R, Daniel-da-Silva AL. Functionalized Gold Nanoparticles for the Detection of C-Reactive Protein. Nanomaterials. 2018; 8 (4): 200.
9. Шумков А. А., Супрун Е. В., Шумянцева В. В., Арчаков А. И. Сенсорный элемент на основе наночастиц золота для определения кардиомаркеров. Биомедицина. 2011; (3): 46–9.
10. Turkevich J, Stevenson PC, Hiller JA. Study of the nucleation and growth processes in the synthesis of colloidal gold. Discuss Faraday Soc. 1951; (11): 55–75.
11. Hirai H, Aizawa H. Preparation of stable dispersions of colloidal gold in hexanes by phase transfer. J Colloid Interface Sci. 1993; (161): 471–4.
12. Михайлов М. Д. Химические методы получения наночастиц и наноматериалов. Санкт-Петербург, 2012; 260 с.
13. Anshup A, Venkataraman JS et al. Growth of gold nanoparticles in human cells. Langmuir. 2006; 21 (25): 11562–7.
14. Santhoshkumar J, Rajeshkumar S, Venkat KS. Phyto-assisted synthesis, characterization and applications of gold nanoparticles. Biochemistry and Biophysics Reports. 2017; (11): 46–57.
15. Макаров В. В., Лав А., Синицына О. В., Макарова С. С.,

Яминский И. В. и др. «Зеленые» нанотехнологии: синтез металлических наночастиц с использованием растений. Acta Naturae. 2014; 6 (1): 37–47.
16. Курапов П. Б., Бахтенко Е. Ю. Многообразие вторичных метаболитов высших растений и их лечебные свойства. М.: Изд-во РНИМУ, 2012; 200 с.
17. Elia P, Zach R, Hazan S, Kolusheva S, Porat Z, Zeiri Y. Green synthesis of gold nanoparticles using plant extracts as reducing agents. Int J Nanomedicine. 2014; 9 (1): 4007–21.
18. Dorosti N, Jamshidi F. Plant-mediated gold nanoparticles by Dracocephalum kotschyi as anticholinesterase agent: Synthesis, characterization, and evaluation of anticancer and antibacterial activity. Journal of Applied Biomedicine. 2016; 14 (3): 235–45.
19. Smitha SL, Philip D, Gopchandran KG Green synthesis of gold nanoparticles using Cinnamomum zeylanicum leaf broth. Spectrochim Acta Part A Mol Biomol Spectrosc. 2009; 74 (3): 735–9.
20. Yu J, Xu D, Guan HN, Wang C, Huang LK, Chi DF. Facile one-step green synthesis of gold nanoparticles using Citrus maxima aqueous extracts and its catalytic activity. Mater Lett. 2016; (166): 110–2.
21. Teimuri-Mofrad R, Hadi R, Tahmasebi B, Farhoudian S, et al. Green synthesis of gold nanoparticles using plant extract. Nanochem Res. 2017; 2 (1): 8–19.
22. Banu H, Renuka N, Faheem SM, Ismail R, Singh V et al. Gold and silver nanoparticles biomimetically synthesized using date palm pollen extract-induce apoptosis and regulate P53 and BCL-2 expression in human breast adenocarcinoma cells. Biol Trace Elem Res. 2018; 18 (3): 12011–8.
23. Rai M, Yadav A. Plants as potential synthesiser of precious metal nanoparticles: progress and prospects. IET Nanobiotechnol. 2013; 7 (3): 117–24.
24. Masumeh N. Biosynthesis of gold nanoparticles using plant extracts. Bioprocess and Biosystems Engineering. 2015; 38 (1): 1–14.
25. Ankamwar B. Biosynthesis of gold nanoparticles (Green-gold) using leaf extract of Terminalia catappa. E J Chem. 2010; 7 (4): 1334–9.
26. Philip D. Rapid green synthesis of spherical gold nanoparticles using Mangifera indica leaf. Spectrochim Acta Part A Mol Biomol Spectrosc. 2010; 77 (4): 807–10.
27. Vadlapudi V, Kaladhar DS. Review: green synthesis of silver and gold nanoparticles. Middle-East J Sci Res. 2014; 19 (6): 834–42.
28. Salem DS, Sliem MA, El-Sesy M, Shouman SA, Badr Y. Improved chemo-photothermal therapy of hepatocellular carcinoma using chitosan-coated goldnanoparticles. Journal of photochemistry and photobiology B Biology. 2018; 182 (5): 92–9.
29. Zhivkov A, van der Zande BMI., Stoylov S. Electro-optics of metal particles: electric birefringence of gold rods. Coll Surf A. 2002; 209 (2–3): 299–303.
30. Lu An, Yuanyuan W, Qiwei T, Shiping Y. Small gold nanorods: recent advances in synthesis, biological imaging, and cancer therapy. Materials. 2017; 10 (12): 1372.
31. Oldenburg SJ, Averitt RD, Westcott SL, Halas N. Nanoengineering of optical resonances. Chem Phys Lett. 1998; 288 (2): 243–7.
32. Love JC, Estroff LA, Kriebel JK, Nuzzo RG, and Whitesides GM. Self-assembled monolayers of thiolates on metals as a form of nanotechnology. Chem Rev. 2005; 105 (4): 1103–69.
33. Марченков Н. С., Марченко Н. В. Наночастицы золота и их применение для тераностики заболеваний человека. Медицинская физика. 2014; 4 (64): 64–77.
34. Silva SM, Tavallaie R, Sandiford L, Tilley RD, Gooding J. Gold coated magnetic nanoparticles: from preparation to surface modification for analytical and biomedical applications. Chem Commun. 2016; 52 (48): 7528–40.
35. Guo J, Rahme K, He Y, Li LL, Holmes JD, O'Driscoll CM. Gold nanoparticles enlighten the future of cancer theranostics. International Journal of Nanomedicine. 2017; 12: 6131–52.
36. Дыкман Л. А., Хлебцов Н. Г. Золотые наночастицы в биологии и медицине: достижения последних лет и перспективы. Acta Naturae. 2011; 3 (2): 36–58.
37. Марченко Н. В., Марченков Н. С. Наночастицы золота — от церковных витражей к наномедицине. Успехи в химии и химической технологии. 2012; 26 (6): 104–9.
38. Ali MRK, Wu Y, Ghosh D, Do BH, Chen K, Dawson MR et al. Nuclear membrane-targeted gold nanoparticles inhibit cancer cell migration and invasion. ACS Nano. 2017; 11 (4): 3716–26.
39. Fan L, Fang L, Yongtao Y, Yu W, Weiqun T. Strategies on Nanodiagnostics and Nanotherapies of the Three Common Cancers. Nanomaterials. 2018; 8 (4): 202.
40. Garcia CP, Chambrier I, Cook MJ, Haines AH, Field RA, Russell DA. Targeted photodynamic therapy of breast cancer cells using lactose-phthalocyanine functionalized gold nanoparticles. J Colloid Interface Sci. 2018; 512: 249–59.
41. Chen Y, Xianyu Y, Jiang, X. Surface modification of gold nanoparticles with small molecules for biochemical analysis. Acc Chem Res. 2017; 50 (2): 310–9.
42. Deng H, Zhong Y, Du M, Liu Q, Fan Z, Dai F, et al. Theranostic self-assembly structure of gold nanoparticles for nir photothermal therapy and x-ray computed tomography imaging. Theranostics. 2014; 4 (9): 904–18.
43. Деев С. М., Лебеденко Е. Н. Супрамолекулярные агенты для тераностики. Биоорганическая химия. 2015; 41 (5): 539–52.
44. Hwang S, Nam J, Jung S, Song J, Doh H, Kim S. Gold nanoparticle-mediated photothermal therapy: current status and future perspective. Nanomedicine Lond. 2014; 9 (13): 2003–22.
45. Li Y, He D, Tu J, Wang R, Zu C, Chen Y et al. The comparative effect of wrapping solid gold nanoparticles and hollow gold nanoparticles with doxorubicin-loaded thermosensitive liposomes for cancer thermo-chemotherapy. Nanoscale. 2018; 10 (18): 8628–41.
46. Boisselier E, Astruc D. Gold nanoparticles in nanomedicine: preparations, imaging, diagnostics, therapies and toxicity. Chem Rev. 2009; 38 (6): 1759–82.
47. Дыкман Л. А., Богатырев В. А., Щеголев С. Ю., Хлебцов Н. Г. Золотые наночастицы: синтез, свойства, биомедицинское применение. М.: Наука, 2008; 319 с.
48. Sumbayev VV, Yasinska IM, Gibbs BF. Biomedical Applications of Gold Nanoparticles Recent Advances in Circuits. Communications and Signal Processing. Athens: WSEAS Press, 2013; p. 342–48.

HYDROXYAPATITE AND PORPHYRIN-FULLERENE NANOPARTICLES FOR DIAGNOSTIC AND THERAPEUTIC DELIVERY OF PARAMAGNETIC IONS AND RADIONUCLIDES

Orlova MA[1,2] ✉, Nikolaev AL[1], Trofimova TP[1,3], Orlov AP[1], Severin AV[1], Kalmykov SN[1]

[1] Faculty of Chemistry, Lomonosov Moscow State University, Moscow

[2] Department of Biochemistry and Pharmacology,
Dmitry Rogachev National Medical Research Centre of Hematology, Oncology and Immunology, Moscow

[3] Institute of Physiological Active Compounds of RAS, Chernogolovka

Nanoparticles for drug delivery are the subject of extensive research. Importantly, they can transform in size during synthesis or actual use, thereby changing their cytotoxic properties. The aim of the present work was to study the tendency of [^{67}Zn] porphyrin-fullerene nanoparticles (BFNP) to aggregate over time and to compare the properties of hydroxyapatite (HAP) nanoparticles obtained through 3 different techniques. We found that aggregation of BFNP nanoparticles does not affect their function but attenuates their cytotoxicity against leukemia cells. We were also able to obtain HAP nanoparticles with programmable properties (such as size, shape or the capacity to adsorb metal ions, ligands and chemical complexes) through enzymatic synthesis by varying its conditions. The synthesized HAP nanoparticles contain short-lived isotopes of zinc and copper (in the form of ions and complexes with pyrimidine or thiazine derivatives). These tumoricidal components (a radionuclide and a ligand or a complex) determine the diagnostic and therapeutic potential of the obtained radiopharmaceutical agents.

Keywords: hydroxyapatite, porphyrin-fullerene, thiazine and pyrimidine derivatives, HL-60, K-562, MOLT-4, zinc and copper radionuclides

✉ **Correspondence should be addressed:** Marina A. Orlova
Leninskie gory 1, bl. 3, Moscow, 119992; orlova.radiochem@mail.ru

Received: 27.06.2018 **Accepted:** 20.09.2018

DOI: 10.24075/brsmu.2018.075

НАНОЧАСТИЦЫ НА ОСНОВЕ ГИДРОКСИАПАТИТА И ПОРФИРИНФУЛЛЕРЕНА ДЛЯ ДИАГНОСТИЧЕСКОГО И ТЕРАПЕВТИЧЕСКОГО ПРИМЕНЕНИЯ ПАРАМАГНИТНЫХ ИОНОВ И РАДИОНУКЛИДОВ

М. А. Орлова[1,2] ✉, А. Л. Николаев[1], Т. П. Трофимова[1,3], А. П. Орлов[1], А. В. Северин[1], С. Н. Калмыков[1]

[1] Химический факультет, Московский государственный университет имени М. В. Ломоносова, Москва

[2] Отдел биохимии и фармакологии,
Национальный медицинский исследовательский центр детской гематологии, онкологии и иммунологии имени Д. Рогачева, Москва

[3] Институт физиологически активных веществ РАН, Черноголовка

Использование наночастиц как носителей лекарственных средств широко изучается. Одним из важных вопросов остается изменение размеров и цитотоксических свойств частиц в процессе их получения и применения. Целью работы было исследовать возможную агрегацию [^{67}Zn]порфиринфуллерен-наночастиц (BFNP) в зависимости от времени и провести сравнительный анализ свойств наночастиц гидроксиапатита (HAP), полученных различными способами. Оказалось, что агрегация BFNP качественно не влияет на функцию наночастиц, но количественно уменьшает их воздействие на лейкемические клетки. Варьирование способов получения и обработки наночастиц HAP позволяет менять их форму, размеры и сорбционную способность по отношению к ионам металлов, а также лигандам и комплексам. Используя ферментативный метод, мы получили HAP с заранее заданными свойствами путем варьирования условий синтеза. Полученные наночастицы HAP представляют собой радиопрепараты, содержащие короткоживущие изотопы цинка и меди (в виде ионов и соединений — производных тиазина и пиримидина). Эти наноконструкции содержат два антиопухолевых компонента (радионуклид и лиганд или комплекс), что определяет их фармакологический потенциал для диагностики и лучевой терапии.

Ключевые слова: гидроксиапатит, порфиринфуллерен, производные тиазина и пиримидина, HL-60, K-562, MOLT-4, радионуклиды цинка и меди

✉ **Для корреспонденции:** Марина Алексеевна Орлова
Ленинские горы, д. 1, стр. 3, г. Москва, 119992; orlova.radiochem@mail.ru

Статья получена: 27.06.2018 **Статья принята к печати:** 20.09.2018

DOI: 10.24075/vrgmu.2018.075

The evolution of contemporary medicine prompts researchers to seek new approaches to drug design and administration, especially when it comes to highly toxic tumoricidal agents whose delivery to a biological target must be strictly precise. Attention is increasingly paid to monoclonal antibodies [1], biological transporters [2], nanostructures and nanoplatforms. Especially worth mentioning are such carriers as fullerenes [3], nanodiamonds [4], inorganic nanoparticles of different nature

[5, 6], liposomes [7], nanoporous silicon [8], and hydroxyapatites (HAP) [9]. There are a few important goals that novel drug delivery systems are intended to achieve. First, they are expected to reduce the toxic effect of a carried drug on healthy organs and tissues. A good example here is doxil, the liposomal formulation of doxorubicin [10], Second, they can enhance the tumoricidal effect through the synergy of the drug/carrier complex [11]. For example, synthetic Buckminsterfullerene (C_{60})-2-(butadiene-1-yl)-tetra(*o*-γ-aminobutyryl-*o*-phthalyl) porphyrin (BFNP) nanoparticles can be used to deliver magnetic isotopes ^{25}Mg and ^{67}Zn, which have a biological activity of their own. Such complexes can alleviate metabolic acidosis induced by post-chemotherapy hypoxia [12]. Third, drug delivery systems aim to increase the bioavailability of the drug (which can be done by using, say, albumin as a carrier), ensure its sustained release (nanofullerenes, HAP) and enhance the tumoricidal effect by binding to the target specifically (monoclonal antibodies). Fourth, a carrier and a drug constituting a delivery system can have different tumoricidal effects. For example, fullerene derivatives capable of killing cancer cells are used as carriers of magnetic isotopes or radionuclides [13]. This principle is employed in designing radiopharmaceuticals for anticancer radiation therapy.

HAP nanoparticles are attractive drug and radionuclide carriers due to their biodegradability, biocompatibility and bioresorbability. These qualities are determined by their calcium-phosphate origin, which mimics the chemical composition of the human bone mineral fraction [14, 15].

The aim of this work was to study the properties of HAP obtained through different methods of synthesis (and therefore exhibiting different properties) and BFNP in relation to their use as bioactive metal ion carriers, including radionuclides, and ligands with tumoricidal activity.

METHODS

Zinc complexes

The N(5,6-dihydro-4*H*-1,3-thiazine-2-yl)benzamide (L^1) ligand in the form of L^1HBr was synthesized following a previously described technique [16]. To obtain the L^1ZnCl_2 (C^1) complex, L^1HBr in the aqueous solution was converted to its basic form in the presence of NaOH (Fig. 1). A solution of zinc chloride in diethyl ether at a ratio of 1 : 1 was gradually added to the L^1 base in diethyl ether. The solution was stirred for 0.5 h. The white crystalline precipitate was separated and washed with ether. The reaction yield was 64%. Ligand L^2 was 2-aminopyrimidine (Sigma; USA), ligand L^3 was 2-aminopyrimidine salicylate. Their complexes with zinc $Zn(L^2)_2Cl_2$ (C^2) and $Zn(L^3)_2$ (C^3) were obtained as described in [17]. The composition of all complexes was characterized by element analysis and ^{1}H-NMR (Bruker CXP-200 spectrometer; Germany).

Spectrophotometry

Spectrophotometry was performed using the UV-1280 spectrophotometer (Shimadzu; Japan). Calibration curves were constructed for the ligands and the complexes in the aqueous, physiological saline and alcohol solutions.

Protonation and stability constants

The constants were determined by potentiometry using the automatic titrator Metrohm 848 Titrino plus (Metrohm AG; Switzerland). The stability constant was measured using the glass electrode. Computations were done in Hyperquad 2013.

HAP synthesis

Coprecipitation. There are different methods of HAP synthesis [18–20] producing end products with different parameters. We synthesized HAP_1 at room temperature using the stoichiometric Ca/P molar ratio of 1.67 [21]. All reagents were taken in the amount sufficient to produce a 5% (solid mass content) suspension [22]. Trace amounts of calcium and zinc in the residual liquid were determined by inductively coupled plasma atomic emission spectroscopy (ICP-AES) on Optima 100 DV (Perkin Elmer; USA). To obtain HAP_2, the suspension was continuously heated to 90 °C without boiling for 4 h.

Enzymatic hydrolysis. HAP_E was synthesized through the enzymatic hydrolysis of calcium glycerophosphate in the presence of alkaline phosphatase (Merck; Germany). Reaction

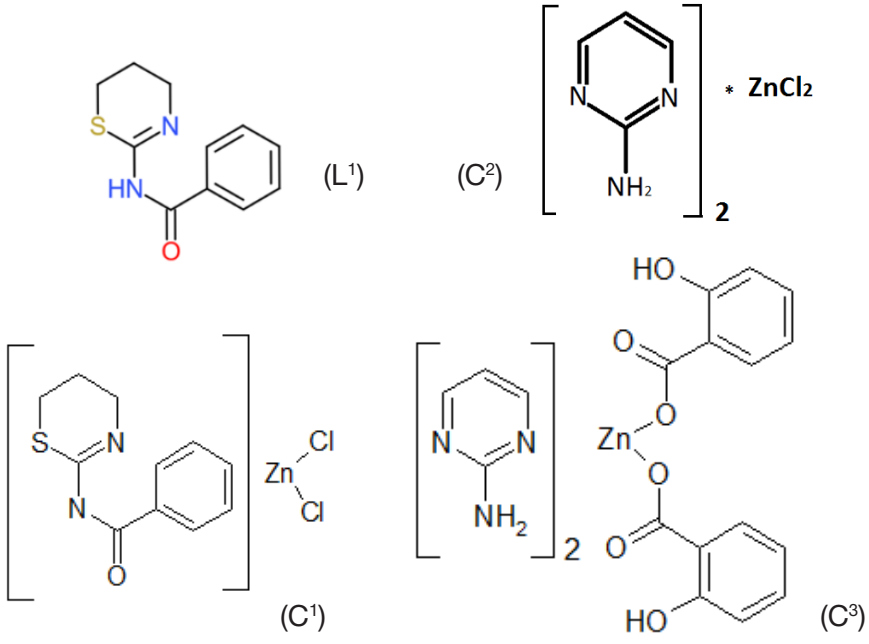

Fig. 1. The structural formula of the compounds used in the present study

conditions were varied, including the enzyme concertation, the medium (water, glycerol buffer, tris buffer), pH (7 to 10), calcium concentration and the reaction time. The glycerophosphate hydrolysis reaction was triggered by adding the enzyme solution to the calcium glycerophosphate solution taken at a concentration of 0.02 mol/l. Working concentrations of the enzyme ranged from 0.02 to 0.4 μg/ml. Depending on the conditions, the reaction time was varied between a few hours and a few days.

Introduction of zinc and copper ions during HAP synthesis. Weighted amounts of zinc or copper oxides (chemically pure, C. P.) corresponding to the anticipated Zn(Cu)/Ca molar ratio of 5 (15 mol%) were dissolved in H_3PO_4. The obtained solution was introduced dropwise to the suspension of $Ca(OH)_2$ under continuous stirring. The samples of HAP_{Zn1}, HAP_{Zn2} and HAP_{Cu} were obtained. Some of those samples were dried, annealed in a muffle furnace in air at 900 °C for 3 h and subsequently studied with XPA (*see below*).

Electron microscopy of HAP samples

Some of the samples were sonicated in a sonic bath for 30 s at 22 kHz frequency and 50 W power. The samples were prepared for microscopy using a standard technique and then inspected under the JSM-6380LA microscope (JEOL; Japan) at the accelerating voltage of 20 kV.

Metal nuclides

^{69m}Zn ($T_{1/2}$ = 13.7 h; E_γ = 438.7 keV) was produced by the photonuclear reaction $^{71}Ga(\gamma, np)^{69m}Zn$ as described in [21]. To obtain a labeled compound, a reaction of isotope exchange was carried out between the C^1 complex in physiological saline and ethanol solutions (1 : 1) and a concentrated solution of carrier-free ^{69m}Zn eluted from a chromatography column. To obtain labeled C^2 and C^3 complexes, the ligands in the basic form were treated with $^{69m}ZnCl_2$ solution under continuous stirring and heating.

$^{64,67}Cu$ ($T_{1/2}$ = 12.7 h and 61.8 h, respectively; $E_\gamma(^{64}Cu)$ = 1345.8 keV, $E_\gamma(^{67}Cu)$ = 184.5 keV) was produced by the reaction $^{nat}Zn(\gamma,np)^{64}Cu$; $^{nat}Zn(n,\beta)^{67}Cu$. Copper was separated from zinc by extraction in the 0.001% dithizone solution in CCl_4 followed by re-execration in 6M HCl and ion-exchange chromatography in the column with Cu-Resin (Triskem; France). Radioactivity of the reaction products was measured using a gamma-ray spectrometer with the GC 3020 HPGE detector (Canberra; USA). ^{67}Zn and ^{25}Mg (Isotope; Russia) are stable isotopes with s of –5/2 and +5/2, respectively (enrichment in ^{67}Zn is 94.5%, isotope ^{25}Mg frequency is 99.9%).

Size of nanoparticles

Nanoparticle sizes were measured by dynamic light scattering.

Thin-layer chromatography (TLC)

For TLC we used Silufol plates with different eluents. The plates were developed with iodine vapors.

Autoradiography (ARG)

After TLC, the plates with the obtained radioactive compounds were analyzed using Cyclone Plus, the storage phosphor system

Table 1. Lethal concentrations (LC_{50}) of Zn-BFNP and ^{67}Zn-BFNP complexes for leukemic cell lines and healthy lymphocytes depending on the nanoparticle size

Complex	LC_{50}, μg/ml		
	B-ALL	AML	HD*
Zn- BFNP	60 ± 8	64 ± 3	81 ± 9
^{67}Zn- BFNP	16 ± 3	63 ± 8	79 ± 9
Average size of nanoparticles and LC_{50}			
Zn- BFNP	25 nm	55 nm	
^{67}Zn- BFNP	37 ± 3 μg/ml	78 ± 6, μg/ml	
Average size of nanoparticles and LC_{50}			
Zn- BFNP	50 nm	80 nm	
^{67}Zn- BFNP	10 ± 2 μg/ml	23 ± 3 μg/ml	

Note: *HD — lymphocytes obtained from healthy donors.

Table 2. Survival (LC_{50}) of different cells in the presence of the studied zinc salts, chelators and HAPs

Compounds	LC_{50}, μmol/ml					
	HD cells	K-562	MOLT-4	MOLT-4 (res)	HL-60	B-ALL*
$ZnCl_2$ **	1.6 ± 0.3	0.52 ± 0.05				
$ZnSal_2(H_2O)_2$ **	0.68 ± 0.06	0.41 ± 0.05				
C^3	1.0 ± 0.2	0.25 ± 0.04				
L^1	10.6 ± 0.5	1.0 ± 0.3				
C^1	4.5 ± 0.4	1.1 ± 0.2				
C^2	0.24 ± 0.04	0.12 ± 0.02	0.062 ± 0.008	0.040 ± 0.009	0.039 ± 0.009	0.061 ± 0.007
HAP_1	>> 5 • 10^{-3} mol/l		3.5 • 10^{-3} mol/l	> 5 • 10^{-3} mol/l		
HAP_2	>> 5 • 10^{-3} mol/l		4 • 10^{-3} mol/l	> 5 • 10^{-3} mol/l		
HAP_{Zn1}	>> 5 • 10^{-3} mol/l		>> 5 • 10^{-3} mol/l	> 5 • 10^{-3} mol/l		
HAP_{Zn2}	>> 5 • 10^{-3} mol/l		>> 5 • 10^{-3} mol/l	6,5 • 10^{-3} mol/l		
HAP_{Cu}	>> 5 • 10^{-3} mol/l		>> 5 • 10^{-3} mol/l	5 •10^{-3} mol/l		

Note: * — B-ALL designates BM cells of patients with B-cell acute lymphoblastic leukemia; ** — according to [17].

for digital ARG (Perkin Elmer; USA), and storage phosphor screens coated with BaFBr:Eu by the same manufacturer.

X-ray diffraction phase analysis (XPA)

The analysis was performed on the automated X-Ray diffractometer DRON-3 (Innoscope; Russia) with a Cu-K_α anode using the software supplied by the manufacturer. The size *D* of crystallites was determined by the Sherrer equation:

$$D_{HKL} = \frac{\lambda}{\beta \cos\theta}$$

Measurements of adsorption

Measurements were done using the ASAP 2000 analyzer (Micromeritics; USA). The specific surface area was calculated in the Micromeritics software supplied by the manufacturer.

MTT-assay

The protocol of the assay is described in [13]. The cell lines used in the present study included HL-60, K-562, MOLT-4, and MOLT-4 (res) (res. means the cells were resistant to asparaginase, one of the main drugs used in children with acute leukemia). The cells were cultured following the standard protocol. Statistical analysis included the Mann Whitney U test. Each series of measurements consisted of at least 5 tests carried out in 3 replicates.

Isolation of mononuclear cells from bone marrow and peripheral blood

Bone marrow (BM) cells collected from patients with B-cell acute lymphoblastic leukemia (B-ALL), acute myeloid leukemia (AML) and T-cell acute lymphoblastic leukemia (TALL) were kindly provided by D.Rogachev National Research Center of Pediatric Hematology, Oncology and Immunology. Blood tests demonstrated that the proportion of blast cells in the peripheral blood mononuclear fraction was at least 80%.

Cell morphology was inspected under the fluorescence microscope LEICA DM6000B (Leica Microsystems; Germany) or the confocal laser scanning microscope LSM 710 (Carl Zeiss; Germany). The images were captured and saved by a digital camera.

RESULTS

Relationship between the size of porphyrin-fullerene nanoparticles and their cytotoxicity

Some findings suggest that increased aggregation of nanoparticles (in particular, fullerene-based) promotes survival leading to a rise in LC_{50}, i.e. attenuates the cytotoxic effect of a drug [23–26]. However, there is counterevidence to that, mainly for $nanoC_{60}$. So, we decided to study the effect of aggregation in BFNP.

Table 1 presents data on the survival of leukemia cell lines and BM cells of untreated patients with acute leukemias in the presence of BFNP loaded with a naturally occurring zinc isotope or enriched in magnetic ^{67}Zn. The table demonstrates the relationship between LC_{50} and the nanoparticle size. In all cases, cell survival improved with increased nanoparticle aggregation, but the specificity of the studied complexes did not change.

Sonication caused the average nanoparticle size to shrink to 15–20 nm. However, a week after the average nanoparticle size reached 20–30 nm; 2 weeks after, 30–40 nm; one month after it was as big as 50–60 nm.

Morphological examination revealed that not only nanoparticles but also cells treated with ^{67}Zn-loaded BFNP tended to aggregate increasingly (these data are not provided in the table).

Effect of ligands and HAP-ligand compositions on the cells

Both ligands and their complexes with metal ions, such as zinc or copper (which can be substituted with radionuclides to produce a radiopharmaceutical), can be regarded as potential tumoricidal chelating agents and used for HAP doping. Ligands

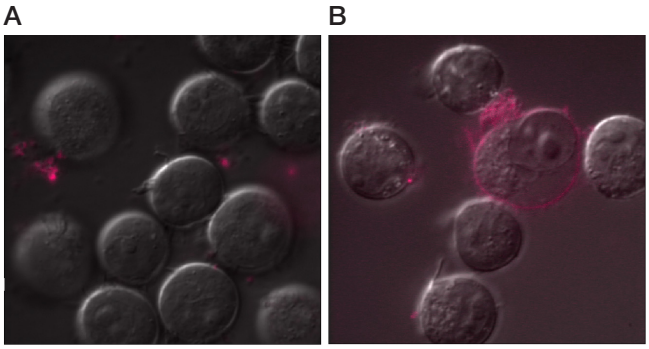

Fig. 2. MOLT-4 cells treated with L^3 (**A**) and C^3 (**B**) under the confocal laser scanning microscope

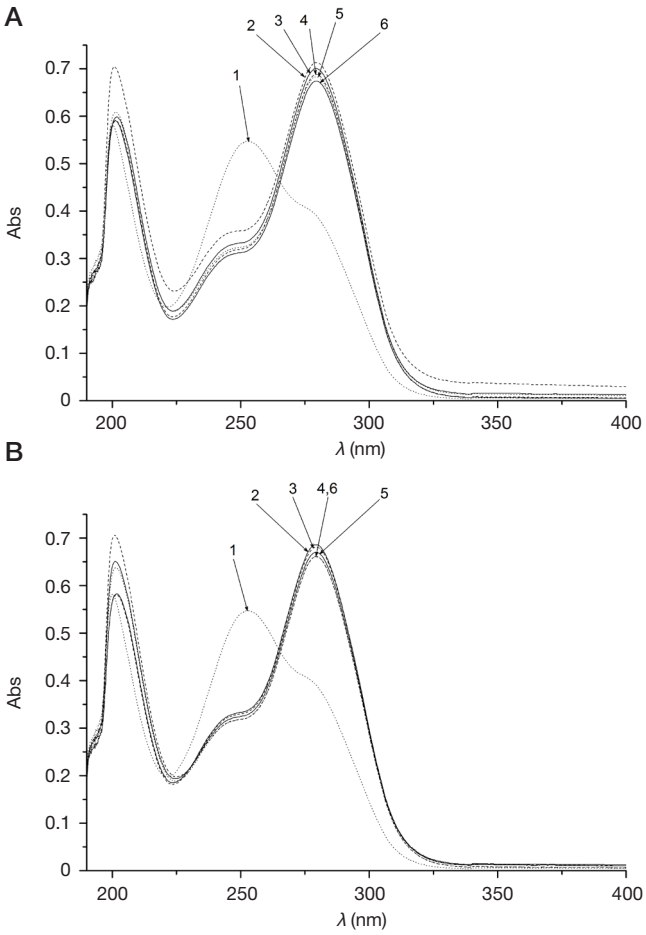

Fig. 3. Absorption spectra of 10–2 mg/ml L^1 solution that was in contact with HAP_2 (**A**) and HAP_1 (**B**) for 0 min (1), 5 min (2), 10 min (3), 15 min (4), 30 min (5), and 60 min (6)

and metal ions can be loaded to HAP together as complexes or separately. In both cases, the complex and its components will produce either synergistic or independent effects.

Table 2 compares the survival of K-562 cells and lymphocytes of healthy donors (HD) in the presence of L^1 and complexes. Both healthy lymphocytes and MOLT-4 и MOLT-4 (res) cells demonstrated very high survival rates when treated with different HAP samples, including those that contained zinc and copper ions.

The studied chelators and complexes displayed a tendency to increased (decreased) toxicity against healthy lymphocytes and cancer cells. The lymphocytes of healthy donors demonstrated the following pattern of survival rate decline: $L^1 > C^1 > ZnCl_2 > C^3 > ZnSal_2(H_2O)_2 > C^2$. With chronic myeloid leukemia cells (K-562), the pattern changed: $C^1 > L^1 > ZnCl_2 > ZnSal_2(H_2O)_2 > C^3 > C^2$. The therapeutic window (or the therapeutic index $TI = LC_{50}$ (HD)/LC_{50} (leukemia cells)) declined in the following fashion: $L^1 > C^3 \sim C^1 > ZnCl_2 > C^2 > ZnSal_2(H_2O)_2$. This leads us to conclude that all 3 studied complexes have a potential to be considered as tumoricidal agents.

When comparing the toxic effects of C^2 on leukemia cell lines and BM cells obtained from patients with B-ALL, we observed the following pattern: HD cells > K-562 > HL-60 ~ MOLT-4 > MOLT-4(res) ~ BM (B-ALL). Importantly, C^2 exhibited higher toxicity towards MOLT-4 (res) than to MOLT-4 cells, meaning it has specificity to the cells with the most resistance to chemotherapy. The complexes tended to exhibit higher cytotoxicity than the ligands, perhaps due to the development of necrosis in addition to apoptosis (Fig. 2).

Stability of ligands and their complexes in aqueous/physiological saline solutions is their important property. Unfortunately, much more common are bioactive chelating ligands and complexes that are poorly soluble. They need a special shell or a carrier to be delivered to a target. HAP meets this requirement only partly.

Spectrophotometric measurements of stability of the studied complexes in water, ethanol and physiological saline solutions revealed that C^1 was the least stable complex: it tended to hydrolyze over time producing thiazine that, however, has mild tumoricidal and strong radioprotective properties. Other complexes were quite stable when dissolved, which makes them more suitable for clinical purposes.

As determined by the potentiometric titration of the ligand L^1 performed in aqueous and physiological saline solutions with varying pH (at C (L^1) = 1 • 10^{-3} mol/l, I = 0.15 NaCl (0.1 mol/l KNO_3)), the values of protonation constants (log K) were 5.1 ± 0.1 (aqueous solutions) and 5.3 ± 0.2 (physiological solutions). Attempts to potentiometrically determine the stability constant of C^1 failed. This might have been due to the production of zinc hydroxide that interfered with titration. For C^2 the stability constant logK (C^2) was 10.4 ± 0.5.

Behavior of nanoHAP doped with ligands, metal ions and/or complexes

Fig. 3 (A, B) shows sorption of the ligand L^1 by HAP_1 and HAP_2. Changes occur when sorption starts and are probably due to the interaction with calcium released as nanoHAP dissolves. It means that the ligand L^1 does not bind to hydroxyapatite. The same behavior was observed for L^2 and L^3.

The morphology of nanocrystals can be visualized using electron microscopy, while the composition of the solid phase (biohydroxyapatite) can be inferred from the results of X-ray diffraction phase analysis. For HAP_1, results of these analytical modalities are presented in Fig. 4. When subjected to heating, both zinc-loaded and "pure" nanoparticles shrank in size. This transformation was considerable for "pure" samples and almost insignificant for those doped with zinc (Table 3).

The major phase of HAP_E (Fig. 5A) was hydroxyapatite (Fig. 5B); HAP_E nanoparticles tended to have a spherical shape and formed aggregates. The specific surface area of the studied sample determined by nitrogen absorption was 300 m^2/g. Pore sizes varied considerably (2–300 nm). The size of crystallites in the samples with crystal structure was calculated using the Sherrer equation (12–14 nm). Crystallites and aggregates significantly varied in size; their average dimensions are shown in Fig. 6.

We synthesized 6 different types of HAP: 3 without metal ions (HAP_1, HAP_2, HAP_E) and 3 with metal ions (HAP_{Zn1}, HAP_{Zn2}, HAP_{Cu}). HAP_E were big-sized hollow spheres that

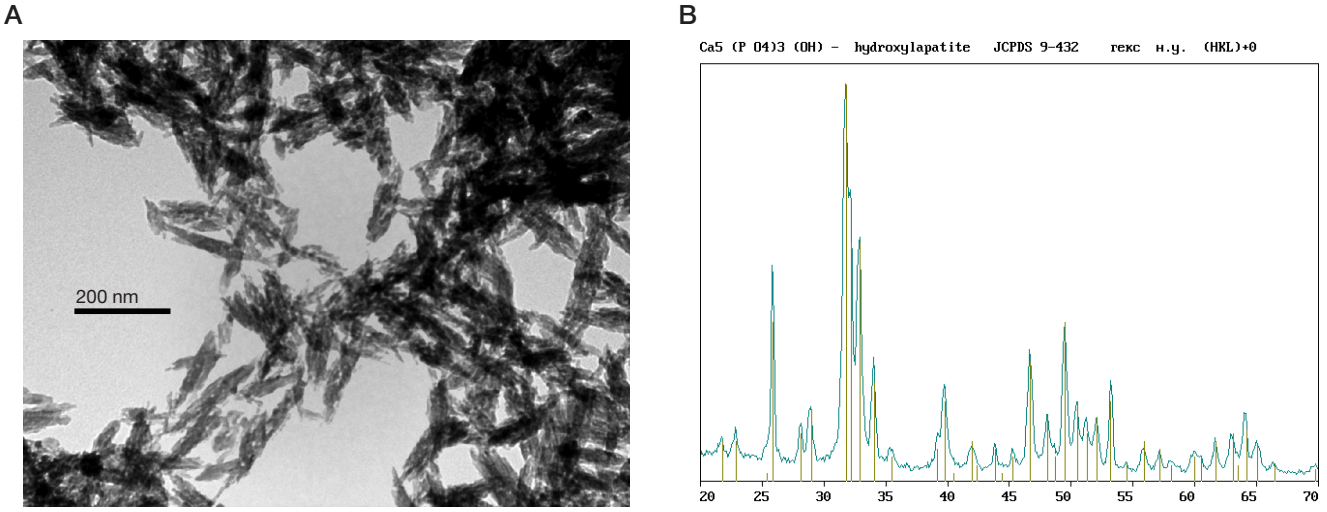

Fig. 4. Electron microscopy (**A**) and X-ray diffraction phase analysis (**B**) of HAP_1 synthesized from the suspension of calcium oxide and phosphorus acid

Table 3. Average sizes of HAP nanoparticles obtained through precipitation and HAP nanoparticles doped with zinc

Parameter	HAP_1	HAP_{Zn1}	HAP_{Zn2}	HAP_2
Length, nm	120 ± 5	110 ± 5	98 ± 4	56 ± 2
Width, nm	36 ± 3	23 ± 2	26 ± 2	19 ± 1

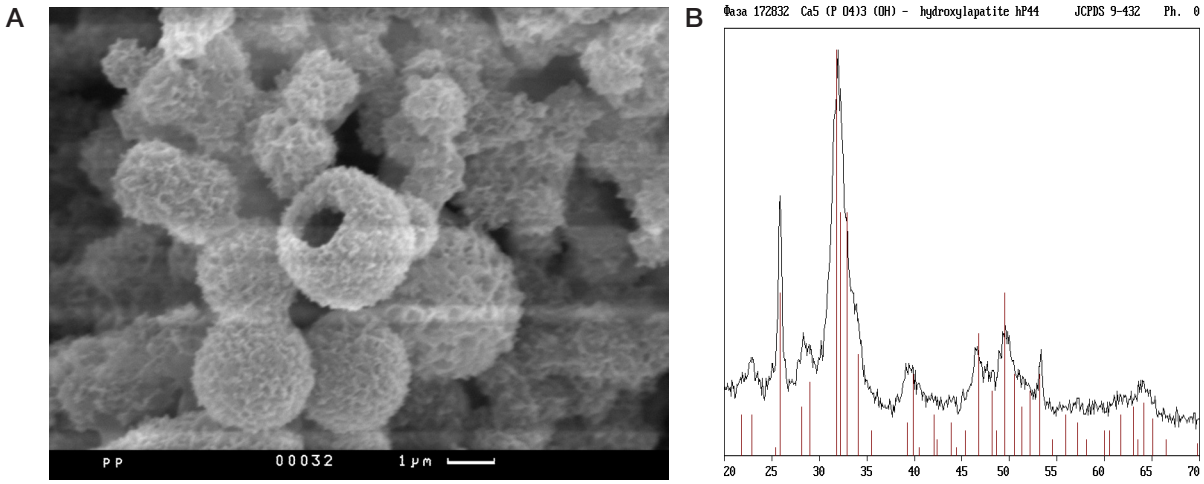

Fig. 5. Laser scanning electron microscopy (**A**) and X-ray diffraction phase analysis (**B**) of HAP_E synthesized from the aqueous solution of calcium glycerophosphate (0.2 mol/l) at the alkaline phosphatase concertation of 0.1 μg/ml

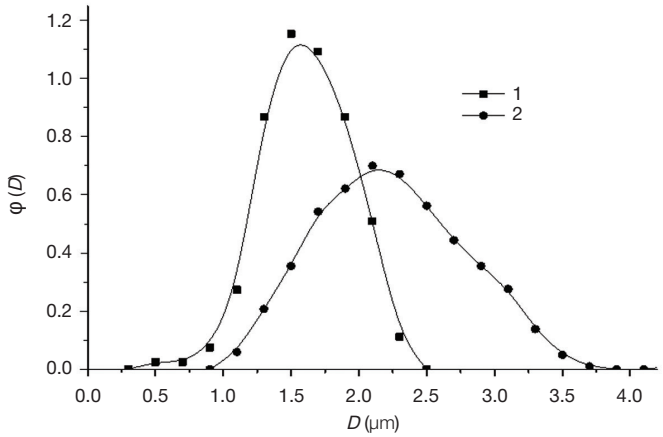

Fig. 6. Differential function of nanoparticle diameter distribution in the sample synthesized in the tris buffer (pH = 9.2) in the presence of alkaline phosphatase taken at a concentration of: 1) 0.02 μg/ml (the average nanoparticle size was 1.57 μm); 2) 0.1 μg/ml (the average nanoparticle size was 2.22 μm)

exhibited increased sorption capacity. Averages sizes of other nanoparticles were as follows: HAP_1 > HAP_{Zn1} > HAP_{Zn2} ~ HAP_{Cu} > HAP_2.

We measured specific adsorption of zinc/copper ions by HAP_1 and HAP_E and calculated adsorption isotherm constants using Langmuir and Freundlich methods. Adsorption of copper ions corresponded to the Langmuir model, while adsorption of zinc ions (with equal correlation coefficients) could be described by both Langmuir and Freundlich models.

The sorption capacity of HAP towards copper ions was significantly higher than towards zinc ions. Introduction of zinc into the reaction during HAP synthesis did not seriously affect the size of nanoparticles. However, average sizes of a thermally processed HAP_2 were smaller than those of HAP_1. HAP_2 particles acquired a more regular isometric shape growing in thickness, as compared to HAP_1, and therefore had a smaller specific surface area. As a result, the maximum sorption capacity of HAP_2 decreased.

Complexes with zinc and copper radionuclides

Complexes $^{69m}ZnC_1$ (I), $^{69m}ZnC_3$ (II) and $[(L^2)_2{}^{64,67}CuCl_4]$ (III) were obtained through isotope exchange and analyzed by TLC, ARG and γ-spectroscopy. The time of isotope exchange was selected experimentally to be sure that the R_f values of radioactive complexes and those that did not contain a radionuclide were the same and also to prevent formation of side products. The obtained compounds were sorbed onto HAP and physical and chemical measurements were then repeated. The ready pharmaceuticals had similar properties, but the copper complex disintegrated during HAP_1 doping. HAP_1 absorbed only copper ions. Perhaps, this problem can be solved by loading HAP with the copper complex during HAP synthesis.

DISCUSSION

Previously, it was demonstrated that the magnetic isotope ^{25}Mg (amounting to 11% in the natural isotope mixture) hyper-activates magnesium-dependent regulation of ATP synthesis, which makes the delivery of this isotope to hypoxic tissues/cells an ambitious pharmacological task [12]. Here, BFNP nanoparticles capable of sustained release of Mg^{2+} and Zn^{2+} ions can be used as carriers. However, the major constraint for the clinical application of fullerene derivatives is their possible uncontrolled aggregation accompanied by changes in their initial cytotoxicity and physiological properties. Our study demonstrates that size transformations do not lead to critical changes in the properties of nanoparticles but attenuate their cytotoxic effect. The fundamental finding of this study is that survival of BM cells of untreated patients with B-ALL decreases 6–7-fold in the presence of ^{67}Zn-BFNP, as compared to ^{nat}Zn-BFNP. Aggregation of nanoparticles can be slowed down by sonication.

HAP nanoparticles have good prospects as drug delivery systems. There are a lot of methods for their synthesis that

produce particles of different sizes, shapes and sorption capacity. HAP nanoparticles are also lowly toxic. Introduction of ligands and complexes into the reaction during HAP synthesis is a clever trick that helps the components of the complex to retain their properties. Enzymatic synthesis seems to be especially promising as it allows varying reaction conditions and, therefore, the parameters of the end product. This significantly expands the area of the potential application of nanoparticles.

Zinc and copper are essential micronutrients [27, 28]. They are cofactors for the majority of regulatory and antioxidant enzymes; they also are involved in DNA repair and the work of transcription factors. Complexes of short-lived zinc and copper radionuclides can be used to solve a number of diagnostic and therapeutic tasks, either simultaneously or consecutively. HAP can serve as a scaffold for a drug ensuring a synergistic sustained effect. To achieve it, a vector is needed, monoclonal antibodies being the most optimal. Importantly, HAP itself has an ability to integrate into bone tissue and become a vector. This matters in the therapy of bone and blood cancers aimed at eliminating malignant stem cells.

In our experiments, the specific activity of the obtained radioactive agents was not high, because the experiments were preliminary and aimed to demonstrate that such complexes can be synthesized in reasonable time for the use in the clinical setting. We have sufficient resources to improve their specific activity.

CONCLUSIONS

Transformation of ^{67}Zn-BFNP sizes following their aggregation does not affect their function but attenuates their cytotoxicity against leukemic cells. By applying different methods of HAP synthesis and processing, one can alter the sorption capacity of HAP towards metal ions, ligands and complexes. HAP_E with preprogrammed properties can be synthesized by varying reaction conditions. We have synthesized HAP nanoparticles containing short-lived zinc/copper isotopes in the form of ions and compounds. These nanostructures have a good potential to solve a number of diagnostic and therapeutic tasks in patients with cancer.

References

1. Karachunskie AI, Rumyantseva YuV, fon Shtakelberg A. Anti-CD19 monoclonal antibody in acute lymphoblastic leukemia in children. Russ J Pediatric Hematol Oncol. 2016; 3 (4): 60–72. DOI: 10.21682/2311-1267-2016-3-4-60-72.
2. Lee Y, Lin Y, Lima C. Factors Controlling the Role of Zn and Reactivity of Zn-bound Cysteines in Proteins: Application to Drug Target Discovery. J Chin Chem Soc. 2014; 61 (1): 142–50. DOI: 10.1002/jccs.201300392.
3. Chen Z, Ma L, Liu Y, Chen C. Applications of Functionalized Fullerenes in Tumor Theranostics. Theranostics. 2012; 2 (3): 238–50. DOI: 10.7150/thno.3509.
4. Mochalin VN, Shenderova O, Ho D, Gogotsi Y. The properties and applications of nanodiamonds. Nature Nanotechnol. 2011; 7 (1): 11–23. DOI: 10.1038/nnano.2011.209.
5. Meshalkin YP, Bgatova NP. Prospects and problems of using inorganic nanoparticles in oncology. J Siber Fed Univ Biol. 2008; 3 (1): 248–68.
6. Nunes C, Estevez SV, Chantada MP. Inorganic nanoparticles in diagnosis and treatment of breast cancer. J Biol Inorg Chem. 2018; (23): 331–45. DOI: org/10.1007/s00775-018-1542-z.
7. Lasis DD, Papahadjopoulos D, editors. Medical Applications of Liposomes. USA: Elsevier Sci, 2007; 779 p. DOI: 1016/B978-0-444-82917-7.X5000-5.
8. Haidary SM, Corcoles EP, Ali NK. Nanoporous Silicon as Drug Delivery Systems for Cancer Therapies. J Nanomater. 2012; ID 830503:15. DOI: 10.1155/2012/830503.
9. Ferraz MP, Monteiro FJ, Manuel CM. Hydroxyapatite nanoparticles: A review of preparation methodologies. J Appl Biomater Biomechanics. 2004; 2 (2): 74–80.
10. Zhao Y, Alakhova DY, Kim JO, Bronich TK, Kabanov AV. A simple way to enhance Doxil therapy: Drug release from liposomes at the tumor site by amphiphilic block copolymer. J Control Release. 2013; 168 (1): 61–9. DOI: 10.1016/j.jconrel.2013.02.026.
11. Liu JH, Cao L, Luo PG et al. Fullerene-conjugated doxorubicin in cells. Acs Appl Mater Interf. 2010; (2): 1384–9.
12. Buchachenko AL, Kouznetsov DA, Breslavskaya NN, Orlova MA. Magnesium Isotope Effect in Enzymatic Phosphorylation. J Phys Chem. 2008; (112): 2548–56.
13. Orlova MA, Osipova EY, Roumiantsev SA. Effect of 67Zn-Nanoparticles on Leukemic Cells and Normal Lymphocytes. Br J Med Med Res. 2012; 2 (1): 21–30. DOI: 10.9734/BJMMR/2012/783.
14. Sun F, Zhou H, Lee J. Various preparation methods of highly porous hydroxyapatite/polymer nanoscale biocomposites for bone regeneration. Acta Biomaterialia. 2011; 7 (11): 3813–28. DOI: 10.1016/j.actbio.2011.07.002.
15. Hutmacher DW, Schantz JT, Lam CXF, Tan KC, Lim TC. State of the art and future directions of scaffold-based bone engineering from a biomaterials perspective. J Tissue Eng Regenerative Med. 2007; 1 (4): 245–60. DOI: 10.1002/term.24.
16. Orlova MA, Trofimova TP, Aliev RA, Orlov AP, Nikulin SV, Kalmykov SN et al. 69mZn-containing radiopharmaceuticals. A novel approach to molecular design. J Radioanal Nucl Chem. 2017; 311 (2): 1177–83. DOI: 10.1007/s10967-016-5076-y.
17. Orlov AP, Orlova MA, Trofimova TP, Osipova EY, Proshin AN. Effect of salicylates and zinc salts on leukemic cells. Russ Chem Bull. 2016; 65 (7): 1879–81. DOI: 10.1007/s11172-016-1525-6.
18. Safronova EV, Putlyaev VI, Sergeeva AI, Kunenkov EV, Tretyakov YD. Synthesis of Nanocrystalline Calcium Hydroxyapatite from Calcium Saccharates and Ammonium Hydrogen Phosphate. Doklady Chem. 2009; 426 (2): 118–23. DOI: 10.1134/S0012500809060020.
19. Thian ES, Konishi T, Kawanobe Y, Lim PN, Choong C, Ho B, Aizawa M. Zinc-substituted hydroxyapatite: a biomaterial with enhanced bioactivity and antibacterial properties. J Mater Sci: Mater Med. 2013; 24 (2): 437–45. DOI: 10.1007/s10856-012-4817-x.
20. Tang Y, Chappell HF, Dove MT, Reeder RJ, Lee YJ. Zinc incorporation into hydroxylapatite. Biomaterials. 2009; 30 (15): 2864–2872. DOI: 10.1016/j.biomaterials.2009.01.043.
21. Severin AV, Pankratov DA. Synthesis of nanohydroxyapatite in the presence of iron (III) ions. Russ J Inorg Chem. 2016; 61 (1): 265–72.
22. Xu Y, Schwartz FW, Traina SJ. Sorption of Zn2+ and Cd2+ on Hydroxyapatite Surfaces. Envir Sci Technol. 1994; 28 (8): 1472–80.
23. Markovic Z, Trajkovic V. Biomedical potential of the reactive oxygen species generation and quenching by fullerenes (C60). Biomaterials, 2008; (29): 3561–73.
24. Fortner JD, Lyon DY, Sayes CM, Boyd AM, Falkner JC, Hotze EM et al. C-60 in water: nanocrystal formation and microbial response. Environ Sci Technol. 2005; (39): 4307–16.
25. Colvin VL. The potential environmental impact of engineered nanomaterials. Nat Biotechnol. 2003; (21): 1166–70.
26. Sayes CM, Gobin AM, Ausman KD, Mendez J, West J, Colvin VL. Nano-C60 cytotoxicity is due to lipid peroxidation. Biomaterials. 2005; (26): 7587–95.
27. Colvin RA, Holmes WR, Fontainea CP, Maret W. Cytosolic zinc buffering and muffling: their role in intracellular zinc homeostasis. Metallomics. 2010; 2 (2): 306–17.
28. Du Y, Guo D, Wu Q, Liu D, Bi H. Zinc Chloride Inhibits Human Lens Epithelial Cell Migration and Proliferation Involved in TGF-β1 and TNF-α Signaling Pathways in HLE B-3 Cells. Biol Trace Elem Res. 2014; 159 (4): 425–43. DOI: 10.1007/s12011-014-9979-6.

Литература

1. Karachunskie AI, Rumyantseva YuV, fon Shtakelberg A. Anti-CD19 monoclonal antibody in acute lymphoblastic leukemia in children. Russ J Pediatric Hematol Oncol. 2016; 3 (4): 60–72. DOI: 10.21682/2311-1267-2016-3-4-60-72.
2. Lee Y, Lin Y, Lima C. Factors Controlling the Role of Zn and Reactivity of Zn-bound Cysteines in Proteins: Application to Drug Target Discovery. J Chin Chem Soc. 2014; 61 (1): 142–50. DOI: 10.1002/jccs.201300392.
3. Chen Z, Ma L, Liu Y, Chen C. Applications of Functionalized Fullerenes in Tumor Theranostics. Theranostics. 2012; 2 (3): 238–50. DOI: 10.7150/thno.3509.
4. Mochalin VN, Shenderova O, Ho D, Gogotsi Y. The properties and applications of nanodiamonds. Nature Nanotechnol. 2011; 7 (1): 11–23. DOI: 10.1038/nnano.2011.209.
5. Meshalkin YP, Bgatova NP. Prospects and problems of using inorganic nanoparticles in oncology. J Siber Fed Univ Biol. 2008; 3 (1): 248–68.
6. Nunes C, Estevez SV, Chantada MP. Inorganic nanoparticles in diagnosis and treatment of breast cancer. J Biol Inorg Chem. 2018; (23): 331–45. DOI: org/10.1007/s00775-018-1542-z.
7. Lasis DD, Papahadjopoulos D, editors. Medical Applications of Liposomes. USA: Elsevier Sci, 2007; 779 p. DOI: 1016/B978-0-444-82917-7.X5000-5.
8. Haidary SM, Corcoles EP, Ali NK. Nanoporous Silicon as Drug Delivery Systems for Cancer Therapies. J Nanomater. 2012; ID 830503:15. DOI: 10.1155/2012/830503.
9. Ferraz MP, Monteiro FJ, Manuel CM. Hydroxyapatite nanoparticles: A review of preparation methodologies. J Appl Biomater Biomechanics. 2004; 2 (2): 74–80.
10. Zhao Y, Alakhova DY, Kim JO, Bronich TK, Kabanov AV. A simple way to enhance Doxil therapy: Drug release from liposomes at the tumor site by amphiphilic block copolymer. J Control Release. 2013; 168 (1): 61–9. DOI: 10.1016/j.jconrel.2013.02.026.
11. Liu JH, Cao L, Luo PG et al. Fullerene-conjugated doxorubicin in cells. Acs Appl Mater Interf. 2010; (2): 1384–9.
12. Buchachenko AL, Kouznetsov DA, Breslavskaya NN, Orlova MA. Magnesium Isotope Effect in Enzymatic Phosphorylation. J Phys Chem. 2008; (112): 2548–56.
13. Orlova MA, Osipova EY, Roumiantsev SA. Effect of 67Zn-Nanoparticles on Leukemic Cells and Normal Lymphocytes. Br J Med Med Res. 2012; 2 (1): 21–30. DOI: 10.9734/BJMMR/2012/783.
14. Sun F, Zhou H, Lee J. Various preparation methods of highly porous hydroxyapatite/polymer nanoscale biocomposites for bone regeneration. Acta Biomaterialia. 2011; 7 (11): 3813–28. DOI: 10.1016/j.actbio.2011.07.002.
15. Hutmacher DW, Schantz JT, Lam CXF, Tan KC, Lim TC. State of the art and future directions of scaffold-based bone engineering from a biomaterials perspective. J Tissue Eng Regenerative Med. 2007; 1 (4): 245–60. DOI: 10.1002/term.24.
16. Orlova MA, Trofimova TP, Aliev RA, Orlov AP, Nikulin SV, Kalmykov SN et al. 69mZn-containing radiopharmaceuticals. A novel approach to molecular design. J Radioanal Nucl Chem. 2017; 311 (2): 1177–83. DOI: 10.1007/s10967-016-5076-y.
17. Орлов А. П., Орлова М. А., Трифонова Т. П., Осипова Е. Ю., Прошин А. Н. Действие салицилатов и солей цинка на лейкемические клетки. Известия АН, Серия химия. 2016; 65 (7): 1879–81. DOI: 10.1007/s11172-016-1525-6.
18. Safronova EV, Putlyaev VI, Sergeeva AI, Kunenkov EV, Tretyakov YD. Synthesis of Nanocrystalline Calcium Hydroxyapatite from Calcium Saccharates and Ammonium Hydrogen Phosphate. Doklady Chem. 2009; 426 (2): 118–23. DOI: 10.1134/S0012500809060020.
19. Thian ES, Konishi T, Kawanobe Y, Lim PN, Choong C, Ho B, Aizawa M. Zinc-substituted hydroxyapatite: a biomaterial with enhanced bioactivity and antibacterial properties. J Mater Sci: Mater Med. 2013; 24 (2): 437–45. DOI: 10.1007/s10856-012-4817-x.
20. Tang Y, Chappell HF, Dove MT, Reeder RJ, Lee YJ. Zinc incorporation into hydroxylapatite. Biomaterials. 2009; 30 (15): 2864–2872. DOI: 10.1016/j.biomaterials.2009.01.043.
21. Severin AV, Pankratov DA. Synthesis of nanohydroxyapatite in the presence of iron (III) ions. Russ J Inorg Chem. 2016; 61 (1): 265–72.
22. Xu Y, Schwartz FW, Traina SJ. Sorption of Zn2+ and Cd2+ on Hydroxyapatite Surfaces. Envir Sci Technol. 1994; 28 (8): 1472–80.
23. Markovic Z, Trajkovic V. Biomedical potential of the reactive oxygen species generation and quenching by fullerenes (C60). Biomaterials, 2008; (29): 3561–73.
24. Fortner JD, Lyon DY, Sayes CM, Boyd AM, Falkner JC, Hotze EM et al. C-60 in water: nanocrystal formation and microbial response. Environ Sci Technol. 2005; (39): 4307–16.
25. Colvin VL. The potential environmental impact of engineered nanomaterials. Nat Biotechnol. 2003; (21): 1166–70.
26. Sayes CM, Gobin AM, Ausman KD, Mendez J, West J, Colvin VL. Nano-C60 cytotoxicity is due to lipid peroxidation. Biomaterials. 2005; (26): 7587–95.
27. Colvin RA, Holmes WR, Fontainea CP, Maret W. Cytosolic zinc buffering and muffling: their role in intracellular zinc homeostasis. Metallomics. 2010; 2 (2): 306–17.
28. Du Y, Guo D, Wu Q, Liu D, Bi H. Zinc Chloride Inhibits Human Lens Epithelial Cell Migration and Proliferation Involved in TGF-β1 and TNF-α Signaling Pathways in HLE B-3 Cells. Biol Trace Elem Res. 2014; 159 (4): 425–43. DOI: 10.1007/s12011-014-9979-6.

ZAIS-BASED COLLOIDAL QDS AS FLUORESCENT LABELS FOR THERANOSTICS: PHYSICAL PROPERTIES, BIODISTRIBUTION AND BIOCOMPATIBILITY

Istomina MS[1,2] ✉, Pechnikova NA[1,3,4], Korolev DV[1], Pochkayeva EI[1], Mazing DS[2], Galagudza MM[1,5], Moshnikov VA[2], Shlyakhto EV[1]

[1] Institute of Experimental Medicine, Almazov National Medical Research Centre, St. Petersburg

[2] Department of Micro- and Nanoelectronics, St. Petersburg State Electrotechnical University "LETI", St. Petersburg

[3] Center of Experimental Pharmacology, St. Petersburg State Chemical Pharmaceutical Academy, St. Petersburg

[4] Laboratory of Parasitic Arthropods, Zoological Institute of Russian Academy of Sciences, St. Petersburg

[5] Department of Pathophysiology, Pavlov First St. Petersburg State Medical University, St. Petersburg

In recent years there has been an increase in interest in the use of colloidal quantum dots (QDs) in biology and medicine. In particular, QDs can be a perspective nanoscale object for theranostics, in which due to the specific accumulation of drug-loaded QDs in the pathological focus, its simultaneous visualization and targeted therapeutic influence occur. One of the serious limitations of the use of QDs in medicine is their potential toxicity, especially when the nanocrystal material contains elements such as cadmium or plumbum. Therefore, it is promising to develop labels based on QDs of relatively less toxic semiconductors of group I-III-VI, such as $CuInS_2$ and $AgInS_2$. In this study, biodistribution and biocompatibility of QDs based on the $AgInS_2$ compound with a ZnS shell (ZAIS) are considered. In the study of biodistribution, the accumulation of QDs in organs such as liver, lungs, heart and kidneys was revealed. It was shown that QDs in the dose range from $2 \cdot 10^{-7}$ to $4 \cdot 10^{-6}$ M/L at intravenous administration in rats does not have a significant effect on body mass dynamics and basic hematological parameters for 30 days. Thus, ZAIS QDs can be used to visualize tissues and organs in various pathological processes, and immobilization of the drugs on their surface will allow to approach their application for theranostics.

Keywords: colloidal quantum dots, QDs, ZnS-$AgInS_2$, ZAIS, theranostics, biodistribution, biocompatibility

✉ **Correspondence should be addressed:** Maria S. Istomina
Parkhomenko 15 B, St. Petersburg, 194156; istominams1993@mail.ru

Received: 28.07.2018 **Accepted:** 23.08.2018

DOI: 10.24075/brsmu.2018.073

ИССЛЕДОВАНИЕ КОЛЛОИДНЫХ КВАНТОВЫХ ТОЧЕК $AGINS_2$/ZNS В КАЧЕСТВЕ ФЛУОРЕСЦЕНТНЫХ МЕТОК ДЛЯ ТЕРАНОСТИКИ: ФИЗИЧЕСКИЕ СВОЙСТВА, БИОРАСПРЕДЕЛЕНИЕ И БИОСОВМЕСТИМОСТЬ

М. С. Истомина[1,2] ✉, Н. А. Печникова[1,3,4], Д. В. Королев[1], Е. И. Почкаева[1], Д. С. Мазинг[2], М. М. Галагудза[1,5], В. А. Мошников[2], Е. В. Шляхто[1]

[1] Институт экспериментальной медицины ФГБУ «НМИЦ имени В. А. Алмазова», Санкт-Петербург

[2] Санкт-Петербургский государственный электротехнический университет «ЛЭТИ» имени В. И. Ульянова (Ленина), Санкт-Петербург

[3] Центр экспериментальной фармакологии, Санкт-Петербургский государственный химико-фармацевтический университет, Санкт-Петербург

[4] Зоологический институт РАН, Санкт-Петербург

[5] Первый Санкт-Петербургский государственный медицинский университет имени И. П. Павлова, Санкт-Петербург

В последние годы отмечается повышение интереса к использованию коллоидных квантовых точек (КТ) в биологии и медицине. В частности, КТ могут представлять собой перспективные наноразмерные объекты для тераностики, при которой за счет специфического накопления нагруженных лекарственным соединением КТ в патологическом очаге происходят одновременно его визуализация и таргетное терапевтическое воздействие. Одним из ограничений использования КТ в медицине является их потенциальная токсичность, особенно если материал нанокристалла содержит такие элементы, как кадмий и свинец. В связи с этим перспективной представляется разработка меток на основе КТ относительно менее токсичных полупроводников группы I-III-VI, таких как $CuInS_2$ и $AgInS_2$. Целью работы было исследование биораспределения и биосовместимости КТ на основе соединения $AgInS_2$ в оболочке ZnS. Для этого проводили синтез КТ инжекционным методом, изучали размеры получаемых КТ, их спектры поглощения и фотолюминисценции. Методом флуоресцентного имиджинга исследовали *in vivo* биораспределение КТ. Биосовместимость образцов определяли *in vivo* по динамике изменения массы тела животных и при помощи гематологических исследований. При изучении биораспределения было выявлено накопление КТ в таких органах, как печень, легкие, сердце и почки. Показано, что КТ в диапазоне доз от $2 \cdot 10^{-7}$ до $4 \cdot 10^{-6}$ моль/л при внутривенном введении крысам не оказывают значимого влияния на динамику массы тела и основные гематологические показатели на протяжении 30 дней. Таким образом, КТ на основе соединения $AgInS_2$ в оболочке ZnS могут быть использованы для визуализации тканей и органов при различных патологических процессах, а возможность иммобилизации на их поверхности лекарственных средств позволит рекомендовать их к применению для тераностики.

Ключевые слова: коллоидные квантовые точки, $AgInS_2$/ZnS, тераностика, биораспределение, биосовместимость

✉ **Для корреспонденции:** Мария Сергеевна Истомина
пр. Пархоменко, д. 15 «Б», г. Санкт-Петербург, 194156; istomina_ms@almazovcentre.ru

Статья получена: 28.07.2018 **Статья принята к печати:** 23.08.2018

DOI: 10.24075/vrgmu.2018.073

Recently, a new approach to the development of pharmaceutical compositions has been actively developed, consisting in the simultaneous resolution of therapeutic and diagnostic problems [1]. For this purpose, various fluorophores can be used as diagnostic markers [2]. However, in world practice only two fluorophore are allowed for clinical use, indocyanine green and various combinations of fluorescein [3]. Besides, fluorescent dyes have a significant disadvantage, the ability to fade with time. A material in which there is no fading out are colloidal quantum dots (QDs) [4]. Besides, many QDs have toxic properties [5]. The main disadvantage of these systems is the toxicity of the crystal core of the material when used in biomedicine. Since in core-shell-like structures, the core is often a compound containing a heavy metal, the shell does not always cover the core or can be destroyed, which leads to the release of heavy metal ions into the body. Also, it was suggested that the toxicity of QDs can be correlated with the physicochemical properties of the shell, the nature of surface "ligands" (providing colloidal stability), the presence of other surface modifications and interactions with various molecules (e.g., proteins) present in biological environments [6–11]. Therefore, an important practical task is the development of non-toxic QDs and the study of their biocompatibility. The results of studies carried out in recent years decisively showed that modifying the surface of QDs or using QDs of a certain composition is accompanied by a significant increase in the biocompatibility of these objects. For example, ZnS-CdSe QDs conjugated with tripeptide arginine-glycine-aspartic acid (RGD) in systemic administration in mice showed no toxic properties in the histological study, and analysis of the tissue samples by mass spectrometry did not reveal Cd^{2+} ions [12]. In [13], a shell of biocompatible copolymers based on 2-(2-methoxyethoxy) ethyl methacrylate and oligo(ethylene glycol) methacrylate was grown on the surface of ZnO QDs by surface-initiated radical polymerization. Analysis of cytotoxicity to human colon cancer cells HT29 has revealed that QDs with polymer coating showed virtually no toxicity at concentrations up to 12.5 μg/mL, whereas when loaded with doxorubicin, high cytotoxicity and decreased viability of HT29 cells occur. In [14], nanocomposites based on silver selenide QDs with an average size of 11.4–12.7 nm, luminescing in the transparency region of biological tissues (705 nm), were obtained and characterized in detail. The absence of toxic properties of materials is achieved using the stabilizing potential of the galactomannan, a natural polysaccharide, as well as a simple, environmentally friendly way of generating highly reactive selenide anions acting as a selenium-containing agent. Carbon QDs and their combinations with various nanoparticles (e.g., based on iron [15]) also are non-toxic.

QDs that do not contain potentially toxic elements in their composition are of specific interest. Such QDs include, in particular, QDs based on the AgInS2 compound in the ZnS shell (ZAIS). In the present work, the physical properties, biodistribution and biocompatibility of ZAIS QDs were studied.

METHODS

Synthesis of colloidal quantum dots

The study objective in this research were ZAIS colloidal quantum dots. Chemical synthesis of QDs was carried out by injection method in an aqueous medium. To achieve a balance of the reactivity of indium and silver cations in the synthesis, ligands such as L-glutathione and sodium citrate were used. Precursors of silver nitrate, $AgNO_3$, (0.005 mM) and indium nitrate, $In(NO_3)_3 \cdot 4.5H_2O$, (0.02 mM) were placed and dissolved in 5 mL of distilled water in a 10 mL flask. Subsequently, 0.01 mM of L-glutathione and 0.08 mM of sodium citrate (200 μL of an aqueous solution) were added to this solution. The anion precursor solution contains of 0.04 mM $Na_2S \cdot 9H_2O$ in 500 μL of distilled water. The precursor solution of sulfur was injected into the initial solution at room temperature, then it was heated to 95 °C for 40 min by the flask heater. To create a shell consisting of zinc sulfide, 0.02 mM of zinc nitrate ($Zn(NO_3)_2 \cdot 6H_2O$) and 0.02 mM of sodium sulfide ($Na_2S \cdot 9H_2O$) were dissolved in 200 μL of distilled water. After cooling of the initial solution of the nanocrystal cores to room temperature, a precursor solution of zinc nitrate and sodium sulfide was simultaneously added into it (drop by drop), then it was heated to 95 °C for 40 min. To isolate the particles from the initial solution, isopropyl alcohol was added followed by centrifugation.

Characterization of colloidal quantum dots

The size of the colloidal quantum dots was estimated by the method of dynamic light scattering, which can also be used to determine the profile of small particle size distribution in suspensions, emulsions, micelles, polymers, proteins, nanoparticles or colloids, by laser particle size analyzer SZ-100 (Horiba Jobin Yvon, Kyoto; Japan) with a range of nanoparticle diameters measuring from 0.3 nm to 8 μm.

The optical absorption spectra of the samples were measured by a spectrophotometer PE-5400UV (ECROSKHIM Co., Ltd.; Russia), and the photoluminescence spectra were obtained by a specially developed spectrofluorometer based on the monochromator MDR-206 (Lomo Fotonika; Russia).

Estimation of QDs biodistribution

Fluorescent imaging of biological samples was carried out on optical imaging system IVIS Lumina LT Series III (PerkinElmer; U.S.A.). After preliminary studies of the absorption and photoluminescence spectra, the filters were optimally matched for ZAIS QDs. The excitation wavelength for these

Table 1. Groups of animals and concentrations of injectants for the study of QDs biocompatibility

Group designation	Injectant	Concentration of injectant, M/L	Dose of the active substance, ml	Time of the experiment, days	Number of animals in the group
QDs-L(15)	QDs	$4 \cdot 10^{-6}$	1	15	5
QDs-M(15)	QDs	$2 \cdot 10^{-6}$	1	15	5
QDs-S(15)	QDs	$2 \cdot 10^{-7}$	1	15	5
Control	NaCl	–	1	30	5
QDs-L(30)	QDs	$4 \cdot 10^{-6}$	1	30	5
QDs-M(30)	QDs	$2 \cdot 10^{-6}$	1	30	5
QDs-S(30)	QDs	$2 \cdot 10^{-7}$	1	30	5

QDs was 535 nm ± 20 nm, the emission wavelength was 655 nm ± 20 nm.

Study of QDs biocompatibility

Biocompatibility assessment was carried out on SPF Wistar male rats (Nursery of laboratory animals "Pushchino"). The body weight of the animals was 235 ± 10%. The tested QDs were injected into the lateral tail vein for 3 min. The formation of groups of animals and their brief characteristics are presented in Table 1. To identify the QDs and their concentrations, the following notations were introduced: the QDs concentration of $3.7 \cdot 10^{-9}$ M/kg — L (large), $1.85 \cdot 10^{-9}$ M/kg — M (medium), $1.85 \cdot 10^{-10}$ M/kg — S (small). At 15 and 30 days after intravenous administration of QDs, hematological parameters, body mass dynamics were recorded in animals, and animal death was also taken into account.

Hematologic studies

Hematologic studies were performed using the hematology analyzer URIT-3000 Vet Plus (URIT Medical Electronic; China). To assess the influence of QDs on the body, the following hematologic parameters were studied: red blood cells (RBC), mean corpuscular volume (MCV), white blood cells (WBC), hemoglobin (HGB), mean corpuscular hemoglobin concentration (MCHC), mean corpuscular hemoglobin (MCH), mean platelet volume (MPV), hematocrit (HCT), platelets (PLT).

Statistical analysis

Testing the hypothesis on the equality of average sample sizes in several dependent samples was carried out by the methods of the variance analysis for repeated measurements; the values in the groups was analyzed by nonparametric statistical methods using median (50^{th} percentile) and interquartile range (IQR; 25^{th} to 75^{th} percentile). Testing the hypothesis on the equality of average sample sizes in independent samples was carried out using the Mann–Whitney test. Differences at a significance level of $p < 0.05$ were considered statistically significant. The calculations were performed using the software GraphPad Prism 7.04 (GraphPad Software Inc.; U.S.A.).

RESULTS

Characteristics of the ZAIS QDs

Study of QDs by the dynamic light scattering method is shown in Fig. 1. According to the study, the largest proportion of QDs had an average radius of 3 to 4.5 nm.

Extinction and photoluminescence spectra of aqueous dispersion of the ZAIS QDs are shown on Fig. 2. The QDs dispersion showed an emission peak at 627 nm.

The photoluminescence spectrum is distinguished by a noticeable asymmetry and a rather large half-width at half-height. Together with a large Stokes shift, this indicates the mechanism of photoluminescence due to defects, internal and, possibly, surface [16–19]. In this case, the half-width of the

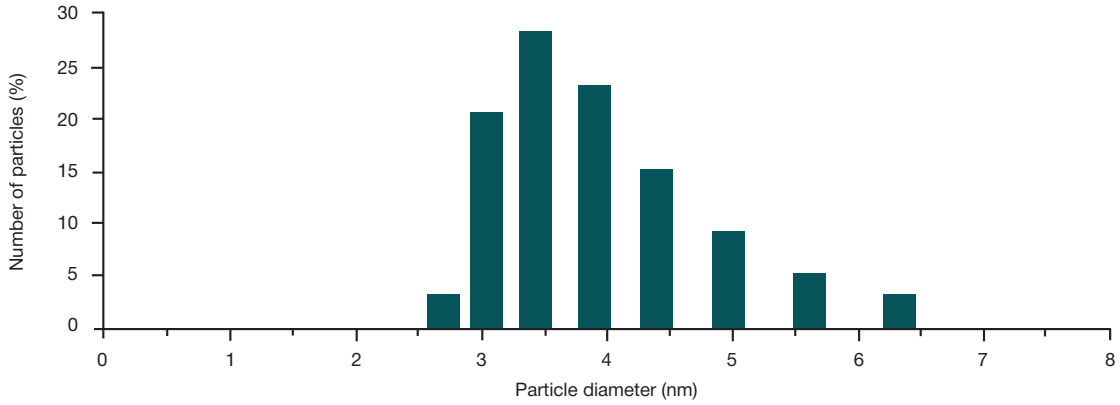

Fig. 1. Histogram of the diameter distribution of the ZAIS QDs obtained in the dynamic light scattering study

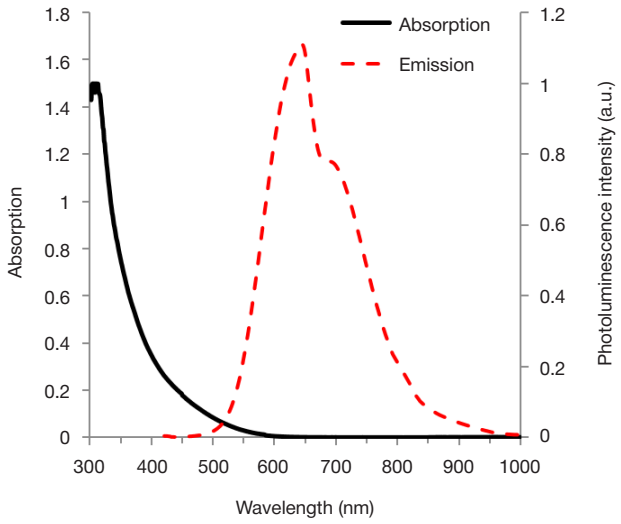

Fig. 2. Absorption and photoluminescence spectra of ZAIS nanocrystals in distilled water

spectrum can depend not only on the particle size distribution, but also on the distribution and nature of the defects in nanocrystals [20]. The absorption spectrum does not contain pronounced inflection points or maxima, which is typical for nanocrystals of triple metal chalcogenides [16, 21].

QDs biodistribution

Preliminary assessment of QDs biodistribution in *ex vivo* organs was performed at 1 and 24 hours after intravenous QDs administration at a dose of $4 \cdot 10^{-6}$ M/L by an optical imaging system IVIS Lumina LT Series III (PerkinElmer; U.S.A.) (Fig. 3).

In the study of biodistribution of ZAIS QDs, an accumulation of nanoparticles in time was noted in such organs as liver, kidneys, lungs and heart. The liver fluorescence intensity at 24 hours after the QDs administration was significantly higher than at 1 hour after administration, which indicates the QDs accumulation in the liver during the first 24 hours after administration, whereas significant differences in fluorescence levels in other organs at 1 hour and 24 hours was not noted.

Body weight of animals

The dynamics of body weight in animals of all experimental groups is shown in Fig. 4.

Statistical analysis of the data showed no significant differences in the body weight of animals in the experimental groups compared with the control throughout the entire experiment ($p > 0.05$).

Hematological parameters

Main hematological parameters, measured on days 15 and 30 after the QDs introduction, are shown in Fig. 5.

Changes in hematological parameters of experimental groups did not show a significant difference in comparison with the control group ($p > 0.05$).

DISCUSSION

QDs are an excellent alternative to traditional organic fluorophores because their size, surface chemistry, spectral properties and stability can be easily adjusted to optimize *in vivo/in vitro* imaging. The colloidal QDs, synthesized by the injection method in an aqueous medium, were used for *ex vivo* imaging. At the moment, QDs are being developed and used in biomedicine for various purposes, such as drug delivery, diagnostic procedures, tumor visualization [21–30]. It should be noted that the problems of QDs biodistribution are currently being studied extensively, in particular, according to the publications of foreign authors, their use shows a positive result as cell markers for imaging tumors of different tissues [31–36]. In this case, the main target organs, in which QDs accumulate, are liver, kidneys and spleen [37–39], as well as lungs [40], skin, gastrointestinal tract and bladder [41], besides these QDs were found in lymph nodes [42]. Our data suggest that ZAIS QDs have a significant tropism to the liver, as evidenced by fluorescence intensity increase within 1 to 24 hours after intravenous administration. In addition, QDs in the dose range from $2 \cdot 10^{-7}$ to $4 \cdot 10^{-6}$ M/L did not have systemic toxicity, which is confirmed by the absence of significant changes in body mass dynamics and significant differences in hematological parameters, absence of animal death within 30 days after administration. Taking into account the fact that in most cases the experimental samples of ZnS-Cd/Se QDs [43] have pronounced systemic toxicity, which affects, in particular, hematological parameters [44], it can be assumed that ZAIS QDs after additional testing on animals can be used as fluorophores in medical practice, and immobilization of the drugs on their surface will allow to approach their application for theranostics.

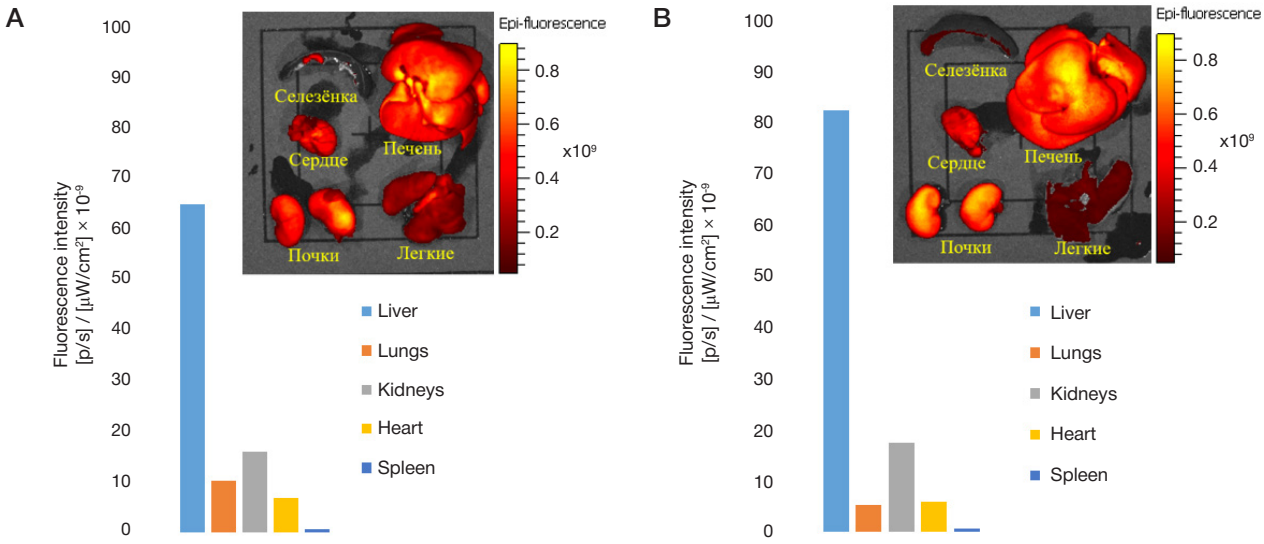

Fig. 3. Visualization of the intensity of fluorescent radiation in the rat organs at 1 hour (**A**) and 24 hours (**B**) after the ZAIS QDs administration

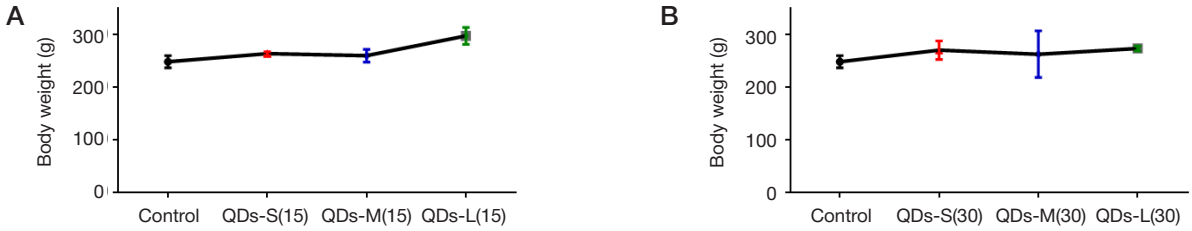

Fig. 4. Animal body weight in the animals 15 days after QDs administration (**A**) and 30 days after QDs administration (**B**)

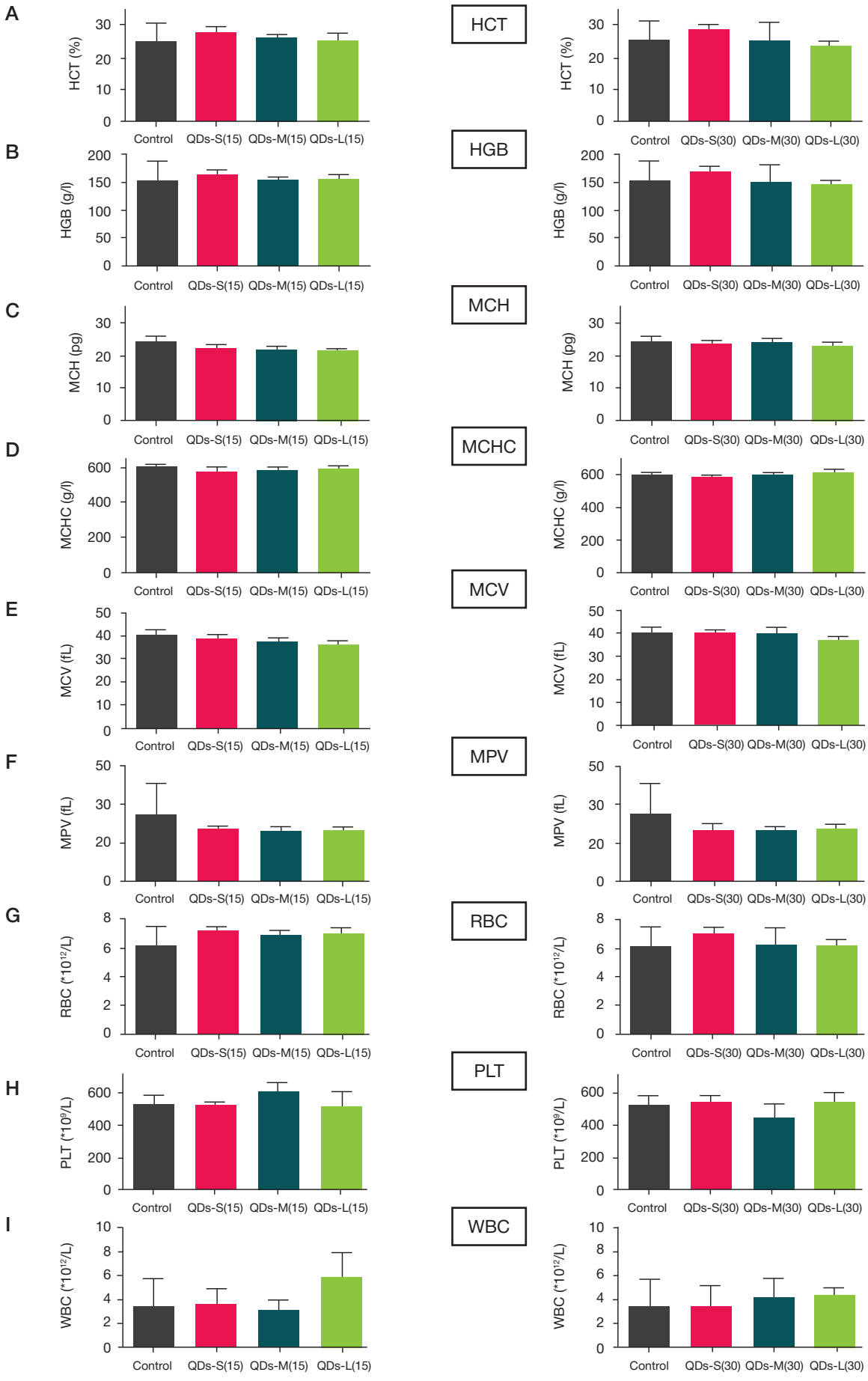

Fig. 5. Results of the research of hematological parameters in the control and at 15 and 30 days after QDs intravenous administration at various doses

CONCLUSIONS

Bioluminescence research of colloidal quantum dots obtained by the injection method in the aqueous medium, demonstrated them as stable agents that can be used in long-term studies. Biodistribution evaluation shows that these ZAIS QDs have a tendency of accumulating in organs such as liver, lungs, heart and kidneys. A study of the toxic effect on hematologic parameters and body mass dynamics showed that these QDs have no pronounced toxicity.

References

1. Melerzanov A, Moskalev A, Zharov V. Precizionnaja medicina i molekuljarnaja teranostika. Vrach. 2016; (12): 11–14.
2. Gareev KG, Babikova KJu, Naumysheva EB, Postnov VN, Korolev DV. Sintez nanomaterialov s fluorescentnoj metkoj dlja medicinskogo naznachenija. Biotehnosfera. 2017; 3 (51): 61–8.
3. Kobayashi H, Ogawa M, Alford R, Choyke PL, Urano Y. New Strategies for Fluorescent Probe Design in Medical Diagnostic Imaging. Chem Rev. 2010; 110 (5): 2620–40.
4. Istomina MS, Korolev DV, Pochkaeva EI, Mazing DS, Moshnikov VA, Gareev KG, Babikova KJu, Postnov VN. issledovanie vozmozhnosti ispol'zovanija kolloidnyh kvantovyh tochek na osnove AgInS2/ZnS dlja fluorescentnogo imidzhinga v sravnenii s fluoroforami, zakreplennymi na poverhnosti nanochastic. Transljacionnaja medicina. 2017; 4 (4): 56–65.
5. Oh E, Liu R, Nel A, Gemill KB, Bilal M, Cohen Y, Medintz IL. Meta-analysis of cellular toxicity for cadmium-containing quantum dots. Nature nanotechnology. 2016; (11): 479–86.
6. Tsoi KM, Dai Q, Alman BA, Chan WCW. Are quantum dots toxic? Exploring the discrepancy between cell culture and animal studies. Acc Chem Res. 2013; (46): 662–71.
7. Ye L, Yong KT, Liu L et al. A pilot study in non-human primates shows no adverse response to intravenous injection of quantum dots. Nature Nanotech. 2012; (7): 453–8.
8. Winnik FM, Maysinger D. Quantum dot cytotoxicity and ways to reduce it. Acc Chem Res. 2013; (46): 672–80.
9. Ding Ya et al. Gold nanoparticles for nucleic acid delivery. Molecular therapy. 2014; 22 (6): 1075–83.
10. Fitzpatrick JA. Andreko SK, Ernst LA, Waggoner AS, Ballou B, Bruchez MP. Long-term persistence and spectral blue shifting of quantum dots in vivo. Nano Lett. 2009; (9): 2736–41.
11. Nel AE, Mädler L, Velegol D, Xia T, Hoek EM, Somasundaran P et al. Understanding biophysicochemical interactions at the nano–bio interface. Nature Mater. 2009; 8 (7): 543–57.
12. Li MM, Cao J, Yang JC, Shen YJ, Cai XL, Chen YW et al. Biodistribution and toxicity assessment of intratumorally injected arginine-glycine-aspartic acid peptide conjugated to CdSe/ZnS quantum dots in mice bearing pancreatic neoplasm. Chem Biol Interact. 2018; (291): 103–10.
13. Dine EJ, Marchal S, Schneider R, Hamie B, Ghanbaja J, Roques-Carmes T et al. A facile approach for doxorubicine delivery in cancer cells by responsive and fluorescent core/shell quantum dots. Bioconjug Chem. 2018; 29 (7): 2248–56.
14. Lesnichaja MV, Suhov BG, Shendrik RJu, Sapozhnikov AN, Trofimov BA. Sintez vodorastvorimyh kvantovyh tochek selenida serebra, ljuminescirujushhih v okne prozrachnosti biologicheskih tkanej. Zhurnal obshhej himii. 2018; 88 (2): 307–10.
15. Huang Y, Gao Y, Zhang Q, Zhang Y, Cao JJ, Ho W et al. Biocompatible FeOOH-Carbon quantum dots nanocomposites for gaseous NOx removal under visible light: Improved charge separation and High selectivity. J Hazard Mater. 2018; (354): 54–62.
16. Drobintseva A, Polyakova V, Matyushkin L, Krylova Y, Masing D, Aleksandrova OA et al. Characterization of ZnSe/ZnS QD Conjugated with Antibody Labeling Kisspeptins. In 3-rd Int. Conf. of BioPhotonics, Florence, Italy. 2015.
17. Alivisatos AP, Gu W, Larabell C. Quantum dots as cellular probes. Annu Rev Biomed Eng. 2005; (7): 55–76.
18. Somers RC, Bawendi MG, Nocera DG. CdSe nanocrystal based chem-/bio-sensors. Chemical Society Reviews. 2007; 36 (4): 579–91.
19. Shamirian A, Appelbe O, Zhang Q, Ganesh B, Kron SJ, Snee PT. A toolkit for bioimaging using near-infrared AgInS2/ZnS quantum dots. Journal of Materials Chemistry B. 2015; 3 (41): 8188–96.
20. Bruchez M, Moronne M, Gin P, Weiss S, Alivisatos AP. Semiconductor nanocrystals as fluorescent biological labels. Science. 1998; 281 (5385): 2013–6.
21. Chan WCW, Nie S. Quantum dot bioconjugates for ultrasensitive nonisotopic detection. Science. 1998; 281 (5385): 2016–8.
22. Tyrakowski CM, Snee PT. A primer on the synthesis, water-solubilization, and functionalization of quantum dots, their use as biological sensing agents, and present status Physical Chemistry Chemical Physics. 2014; 16 (3): 837–55.
23. Yaghini E, Turner HD, Le Marois AM, Suhling K, Naasani I, MacRobert AJ. In vivo biodistribution studies and ex vivo lymph node imaging using heavy metal-free quantum dots. Biomaterials. 2016; (104): 182–91.
24. Matea CT, Mocan T, Tabaran F, et al. Quantum dots in imaging, drug delivery and sensor applications. International Journal of Nanomedicine. 2017; (12): 5421–31.
25. Wang L-W, Peng C-W, Chen C, Li Y. Quantum dots-based tissue and in vivo imaging in breast cancer researches: current status and future perspectives. Breast Cancer Research and Treatment. 2015; 151 (1): 7–17.
26. Wegner KD, Hildebrandt N. Quantum dots: bright and versatile in vitro and in vivo fluorescence imaging biosensors. Chemical Society Reviews. 2015; 44 (14): 4792–834.
27. Walling MA, Novak JA, Shepard JRE. Quantum Dots for live cell and in vivo imaging. International Journal of Molecular Sciences. 2009; 10 (2): 441–91.
28. Kang Yan-Fei et al. Carbon quantum dots for zebrafish fluorescence imaging. Scientific reports. 2005; (5): 11835.
29. Xu G, Lin G, Lin S, Wu N, Deng Y, Feng G et al. The Reproductive Toxicity of CdSe/ZnS Quantum Dots on the in vivo Ovarian Function and in vitro Fertilization. Scientific reports. 2016; (6): 37677.
30. Tang H, Yang ST, Yang YF, Ke DM, Liu JH, Chen X et al. Blood clearance, distribution, transformation, excretion, and toxicity of near-infrared quantum dots Ag2Se in mice. ACS applied materials & interfaces. 2018; 8 (28): 17859–69.
31. Wang C, Gao X, Su X. In vitro and in vivo imaging with quantum dots. Analytical and bioanalytical chemistry. 2010; 397 (4): 1397–415.
32. Gao J, Chen K, Xie R et al. In Vivo Tumor-targeted fluorescence imaging using near-infrared non-cadmium quantum dots. Bioconjugate chemistry. 2010; 21 (4): 604–9.
33. Liu X, Zhou P, Zhan H, Liu H, Zhang J et al. Synthesis and characterization of near–infrared-emitting CdHgTe/CdS/ZnS quantum dots capped by N-acetyl-L-cysteine for in vitro and in vivo imaging. RSC Advances. 2017; 7 (48): 29998–30007.
34. Lin G et al. Passive tumor targeting and imaging by using mercaptosuccinic acid-coated near-infrared quantum dots. International journal of nanomedicine. 2015; (10): 335.
35. Singh SK et al. Drug delivery approaches for breast cancer. International journal of nanomedicine. 2017; (12): 6205.
36. Han X, Wang Y, Shi D. Preparation of QDs@ SiO2/polystyrene composite particles for cancer cells detection. Nano LIFE. 2018.
37. Jain S et al. Applications of Fluorescent Quantum Dots for Reproductive Medicine and Disease Detection. In: Park SB, editor. Rijeka: IntechOpen, 2018; 6.
38. Schipper ML, Iyer G, Koh AL, Cheng Z, Ebenstein Y, Aharoni A et al. Particle size, surface coating, and PEGylation influence the biodistribution of quantum dots in living mice. Small. 2009; 5 (1): 126–34.
39. Yang L, Kuang H, Zhang W, Wei H, Xu H. Quantum dots cause acute systemic toxicity in lactating rats and growth restriction of offspring. Nanoscale. 2018; 10 (24): 11564–77.
40. Roberts JR, Antonini JM, Porter DW et al. Lung toxicity and

biodistribution of Cd/Se-ZnS quantum dots with different surface functional groups after pulmonary exposure in rats. Particle and Fibre Toxicology. 2013; (10): 5.
41. Park Y, Ryu YM, Jung Y et al. Spraying quantum dot conjugates in the colon of live animals enabled rapid and multiplex cancer diagnosis using endoscopy. ACS nano. 2014; 8 (9): 8896–910.
42. Salykina YF, Zherdeva VV, Dezhurov SV et al. Biodistribution and clearance of quantum dots in small animals. Saratov Fall Meeting 2010: Optical Technologies in Biophysics and Medicine. 2011; (12): 7999.
43. Roberts JR, Antonini JM, Porter DW et al. Lung toxicity and biodistribution of Cd/Se-ZnS quantum dots with different surface functional groups after pulmonary exposure in rats. Particle and Fibre Toxicology. 2013; 10 (5).
44. Park Y, Ryu YM, Jung Y et al. Spraying quantum dot conjugates in the colon of live animals enabled rapid and multiplex cancer diagnosis using endoscopy. ACS Nano. 2014; 7 (1): 9309.

Литература

1. Мелерзанов А., Москалев А., Жаров В. Прецизионная медицина и молекулярная тераностика. Врач. 2016; (12): 11–14.
2. Гареев К. Г., Бабикова К. Ю., Наумышева Е. Б., Постнов В. Н., Королев Д. В. Синтез наноматериалов с флуоресцентной меткой для медицинского назначения. Биотехносфера. 2017; 3 (51): 61–8.
3. Kobayashi H, Ogawa M, Alford R, Choyke PL, Urano Y. New Strategies for Fluorescent Probe Design in Medical Diagnostic Imaging. Chem Rev. 2010; 110 (5): 2620–40.
4. Истомина М. С., Королев Д. В., Почкаева Е. И., Мазинг Д. С., Мошников В. А., Гареев К. Г., Бабикова К. Ю., Постнов В. Н. исследование возможности использования коллоидных квантовых точек на основе AgInS2/ZnS для флуоресцентного имиджинга в сравнении с флуорофорами, закрепленными на поверхности наночастиц. Трансляционная медицина. 2017; 4 (4): 56–65.
5. Oh E, Liu R, Nel A, Gemill KB, Bilal M, Cohen Y, Medintz IL. Meta-analysis of cellular toxicity for cadmium-containing quantum dots. Nature nanotechnology. 2016; (11): 479–86.
6. Tsoi KM, Dai Q, Alman BA, Chan WCW. Are quantum dots toxic? Exploring the discrepancy between cell culture and animal studies. Acc Chem Res. 2013; (46): 662–71.
7. Ye L, Yong KT, Liu L et al. A pilot study in non-human primates shows no adverse response to intravenous injection of quantum dots. Nature Nanotech. 2012; (7): 453–8.
8. Winnik FM, Maysinger D. Quantum dot cytotoxicity and ways to reduce it. Acc Chem Res. 2013; (46): 672–80.
9. Ding Ya et al. Gold nanoparticles for nucleic acid delivery. Molecular therapy. 2014; 22 (6): 1075–83.
10. Fitzpatrick JA. Andreko SK, Ernst LA, Waggoner AS, Ballou B, Bruchez MP. Long-term persistence and spectral blue shifting of quantum dots in vivo. Nano Lett. 2009; (9): 2736–41.
11. Nel AE, Mädler L, Velegol D, Xia T, Hoek EM, Somasundaran P et al. Understanding biophysicochemical interactions at the nano–bio interface. Nature Mater. 2009; 8 (7): 543–57.
12. Li MM, Cao J, Yang JC, Shen YJ, Cai XL, Chen YW et al. Biodistribution and toxicity assessment of intratumorally injected arginine-glycine-aspartic acid peptide conjugated to CdSe/ZnS quantum dots in mice bearing pancreatic neoplasm. Chem Biol Interact. 2018; (291): 103–10.
13. Dine EJ, Marchal S, Schneider R, Hamie B, Ghanbaja J, Roques-Carmes T et al. A facile approach for doxorubicine delivery in cancer cells by responsive and fluorescent core/shell quantum dots. Bioconjug Chem. 2018; 29 (7): 2248–56.
14. Лесничая М. В., Сухов Б. Г., Шендрик Р. Ю., Сапожников А. Н., Трофимов Б. А. Синтез водорастворимых квантовых точек селенида серебра, люминесцирующих в окне прозрачности биологических тканей. Журнал общей химии. 2018; 88 (2): 307–10.
15. Huang Y, Gao Y, Zhang Q, Zhang Y, Cao JJ, Ho W et al. Biocompatible FeOOH-Carbon quantum dots nanocomposites for gaseous NOx removal under visible light: Improved charge separation and High selectivity. J Hazard Mater. 2018; (354): 54–62.
16. Drobintseva A, Polyakova V, Matyushkin L, Krylova Y, Masing D, Aleksandrova OA et al. Characterization of ZnSe/ZnS QD Conjugated with Antibody Labeling Kisspeptins. In 3-rd Int. Conf. of BioPhotonics, Florence, Italy. 2015.
17. Alivisatos AP, Gu W, Larabell C. Quantum dots as cellular probes. Annu Rev Biomed Eng. 2005; (7): 55–76.
18. Somers RC, Bawendi MG, Nocera DG. CdSe nanocrystal based chem-/bio-sensors. Chemical Society Reviews. 2007; 36 (4): 579–91.
19. Shamirian A, Appelbe O, Zhang Q, Ganesh B, Kron SJ, Snee PT. A toolkit for bioimaging using near-infrared AgInS2/ZnS quantum dots. Journal of Materials Chemistry B. 2015; 3 (41): 8188–96.
20. Bruchez M, Moronne M, Gin P, Weiss S, Alivisatos AP. Semiconductor nanocrystals as fluorescent biological labels. Science. 1998; 281 (5385): 2013–6.
21. Chan WCW, Nie S. Quantum dot bioconjugates for ultrasensitive nonisotopic detection. Science. 1998; 281 (5385): 2016–8.
22. Tyrakowski CM, Snee PT. A primer on the synthesis, water-solubilization, and functionalization of quantum dots, their use as biological sensing agents, and present status Physical Chemistry Chemical Physics. 2014; 16 (3): 837–55.
23. Yaghini E, Turner HD, Le Marois AM, Suhling K, Naasani I, MacRobert AJ. In vivo biodistribution studies and ex vivo lymph node imaging using heavy metal-free quantum dots. Biomaterials. 2016; (104): 182–91.
24. Matea CT, Mocan T, Tabaran F, et al. Quantum dots in imaging, drug delivery and sensor applications. International Journal of Nanomedicine. 2017; (12): 5421–31.
25. Wang L-W, Peng C-W, Chen C, Li Y. Quantum dots-based tissue and in vivo imaging in breast cancer researches: current status and future perspectives. Breast Cancer Research and Treatment. 2015; 151 (1): 7–17.
26. Wegner KD, Hildebrandt N. Quantum dots: bright and versatile in vitro and in vivo fluorescence imaging biosensors. Chemical Society Reviews. 2015; 44 (14): 4792–834.
27. Walling MA, Novak JA, Shepard JRE. Quantum Dots for live cell and in vivo imaging. International Journal of Molecular Sciences. 2009; 10 (2): 441–91.
28. Kang Yan-Fei et al. Carbon quantum dots for zebrafish fluorescence imaging. Scientific reports. 2005; (5): 11835.
29. Xu G, Lin G, Lin S, Wu N, Deng Y, Feng G et al. The Reproductive Toxicity of CdSe/ZnS Quantum Dots on the in vivo Ovarian Function and in vitro Fertilization. Scientific reports. 2016; (6): 37677.
30. Tang H, Yang ST, Yang YF, Ke DM, Liu JH, Chen X et al. Blood clearance, distribution, transformation, excretion, and toxicity of near-infrared quantum dots Ag2Se in mice. ACS applied materials & interfaces. 2018; 8 (28): 17859–69.
31. Wang C, Gao X, Su X. In vitro and in vivo imaging with quantum dots. Analytical and bioanalytical chemistry. 2010; 397 (4): 1397–415.
32. Gao J, Chen K, Xie R et al. In Vivo Tumor-targeted fluorescence imaging using near-infrared non-cadmium quantum dots. Bioconjugate chemistry. 2010; 21 (4): 604–9.
33. Liu X, Zhou P, Zhan H, Liu H, Zhang J et al. Synthesis and characterization of near–infrared-emitting CdHgTe/CdS/ZnS quantum dots capped by N-acetyl-L-cysteine for in vitro and in vivo imaging. RSC Advances. 2017; 7 (48): 29998–30007.
34. Lin G et al. Passive tumor targeting and imaging by using mercaptosuccinic acid-coated near-infrared quantum dots. International journal of nanomedicine. 2015; (10): 335.

35. Singh SK et al. Drug delivery approaches for breast cancer. International journal of nanomedicine. 2017; (12): 6205.
36. Han X, Wang Y, Shi D. Preparation of QDs@ SiO2/polystyrene composite particles for cancer cells detection. Nano LIFE. 2018.
37. Jain S et al. Applications of Fluorescent Quantum Dots for Reproductive Medicine and Disease Detection. In: Park SB, editor. Rijeka: IntechOpen, 2018; 6.
38. Schipper ML, Iyer G, Koh AL, Cheng Z, Ebenstein Y, Aharoni A et al. Particle size, surface coating, and PEGylation influence the biodistribution of quantum dots in living mice. Small. 2009; 5 (1): 126–34.
39. Yang L, Kuang H, Zhang W, Wei H, Xu H. Quantum dots cause acute systemic toxicity in lactating rats and growth restriction of offspring. Nanoscale. 2018; 10 (24): 11564–77.
40. Roberts JR, Antonini JM, Porter DW et al. Lung toxicity and biodistribution of Cd/Se-ZnS quantum dots with different surface functional groups after pulmonary exposure in rats. Particle and Fibre Toxicology. 2013; (10): 5.
41. Park Y, Ryu YM, Jung Y et al. Spraying quantum dot conjugates in the colon of live animals enabled rapid and multiplex cancer diagnosis using endoscopy. ACS nano. 2014; 8 (9): 8896–910.
42. Salykina YF, Zherdeva VV, Dezhurov SV et al. Biodistribution and clearance of quantum dots in small animals. Saratov Fall Meeting 2010: Optical Technologies in Biophysics and Medicine. 2011; (12): 7999.
43. Roberts JR, Antonini JM, Porter DW et al. Lung toxicity and biodistribution of Cd/Se-ZnS quantum dots with different surface functional groups after pulmonary exposure in rats. Particle and Fibre Toxicology. 2013; 10 (5).
44. Park Y, Ryu YM, Jung Y et al. Spraying quantum dot conjugates in the colon of live animals enabled rapid and multiplex cancer diagnosis using endoscopy. ACS Nano. 2014; 7 (1): 9309.

NANOPRTICLES OF METALS AND THEIR INORGANIC COMPOUNDS OBTAINED THROUGH INTERPHASE AND REDOX-TRANSMETALATION INTERACTION: APPLICATION IN MEDICINE AND PHARMACOLOGY

Vorobyova SA[1]✉, Rzheussky SE[2]

[1] Research Institute for Physical Chemical Problems of the Belarusian State University, Minsk, Belarus

[2] Vitebsk State Order Of Peoples' Friendship Medical University, Vitebsk, Belarus

Synthesis of nanoparticles of metals and their compounds with given morphology and dispersity for use in medicine, pharmacology, microelectronics, as well as subsequent research of their properties, is one of the current problems in the field of preparative inorganic chemistry. Interphase synthesis and redox-transmetalation interaction are as promising as the traditional precipitation from aqueous solutions, but not as researched. This study presents the results of a physicochemical analysis of nanoparticles of metals and their compounds obtained through chemical precipitation from aqueous solutions, interphase and redox-transmetalation interactions. Data describing the influence of phase composition and dispersity of copper and copper oxide (II) nanoparticles on their antimicrobial properties, as well as the results of researching the possibility to use magnetite magnetic fluids for mesenchymal stem cells marking, illustrate the application options synthesized nanoparticles find in pharmacology and medicine.

Keywords: nanomedicine, pharmacology, nanometals, oxides, sulfides, magnetic fluids, stem cells, antimicrobial agents

Funding: experimental stages of the study were supported by the Belarusian Republican Foundation for Fundamental Research (grants X96-157, X04-073, X09-025, X11MS-034).

Acknowledgments: the authors would like to thank N. P. Drazhina and E. A. Petrova for researching the marked mesenchymal stem cells, and fellows of the Laboratory of Condensed Matter Chemistry at the Research Institute for Chemical Physical Problems of the Belarusian State University who participated in the synthesis and research of nanoparticles of metals and their compounds.

✉ **Correspondence should be addressed:** Svetlana A. Vorobyova
Leningradskaya 14, Minsk, Belarus, 220030; vorobyova@bsu.by

Received: 27.06.2018 **Accepted:** 28.07.2018

DOI: 10.24075/brsmu.2018.076

ПРИМЕНЕНИЕ В НАНОМЕДИЦИНЕ И ФАРМАКОЛОГИИ НАНОЧАСТИЦ МЕТАЛЛОВ И ИХ НЕОРГАНИЧЕСКИХ СОЕДИНЕНИЙ, ПОЛУЧЕННЫХ МЕЖФАЗНЫМ И КОНТАКТНЫМ ВЗАИМОДЕЙСТВИЕМ

С. А. Воробьева[1]✉, С. Э. Ржеусский[2]

[1] Научно-исследовательский институт физико-химических проблем Белорусского государственного университета, Минск, Беларусь

[2] Витебский государственный ордена Дружбы народов медицинский университет, Витебск, Беларусь

Одной из актуальных проблем современной препаративной неорганической химии являются получение и исследование наночастиц металлов и их соединений с заданными морфологией и дисперсностью для использования в медицине, фармакологии, микроэлектронике. Наряду с традиционным осаждением из водных растворов перспективны, но менее изучены межфазный синтез и контактное восстановление. В работе представлены результаты физико-химического исследования наночастиц металлов и их соединений, полученных химическим осаждением из водных растворов, межфазным и контактным взаимодействием. Для иллюстрации использования синтезированных наночастиц в фармакологии и медицине приведены данные по влиянию фазового состава и дисперсности наночастиц меди и оксида меди (II) на их противомикробные свойства и результаты исследования возможности применения магнетитовых магнитных жидкостей для маркирования мезенхимальных стволовых клеток.

Ключевые слова: наномедицина, фармакология, нанометаллы, оксиды, сульфиды, магнитные жидкости, стволовые клетки, антимикробные средства

Финансирование: экспериментальные исследования проводились при поддержке Белорусского республиканского фонда фундаментальных исследований (гранты X96-157, X04-073, X09-025, X11MC-034).

Благодарности: авторы благодарят Дражину Н. П и Петрову Е. А. за проведение исследований маркированных мезенхимальных стволовых клеток, а также сотрудников лаборатории химии конденсированных сред НИИ физико-химических проблем Белгосуниверситета, принимавших участие в синтезе и исследовании наноразмерных металлов и их соединений.

✉ **Для корреспонденции:** Светлана Александровна Воробьева
ул. Ленинградская, д. 14, г. Минск, Беларусь, 220030; vorobyova@bsu.by

Статья получена: 27.06.2018 **Статья принята к печати:** 28.07.2018

DOI: 10.24075/vrgmu.2018.076

The problem of synthesizing nanoparticles of metals and their inorganic compounds with defined morphology and dispersity, which largely determine properties and quality of the developed advanced materials, is interesting from the scientific point of view and important from the standpoint of practicality. Therefore, the search for the new and improvement of the already known methods for obtaining nanoparticles of metals and their compounds with required properties is a standing scientific and technological challenge.

To obtain nanoscale metals and their inorganic compounds, chemists often select the traditional and thoroughly researched precipitation technique. However, interphase synthesis

and redox-transmetalation interaction are as promising as precipitation from aqueous solutions, but not as researched. We applied the latter techniques to obtain hydro- and organosols of some metals, oxides and salts.

Data describing the influence of phase composition and dispersity of copper and copper oxide (II) nanoparticles on their antimicrobial properties, as well as the results of researching the possibility to use magnetite magnetic fluids for mesenchymal stem cells labeling, illustrate the application options synthesized nanoparticles find in pharmacology and medicine. These data and results are given below.

Interphase synthesis of nanoscale metals and their inorganic compounds

Interphase synthesis allows obtaining nanoscale metals and their compounds through interaction of reagents dissolved in different phases of aqueous-organic media; as opposed to reactions in microemulsions, the phases are not allowed to mix. These reactions can take place in one of the phases or at the interface between them; the conditions in each phase differ from each other significantly, which allows obtaining inorganic substances with properties different from those received when such substances precipitate in homogeneous media, aqueous solutions in particular [1–8].

The table below and reports [2–8] present the physicochemical properties of the organo- and hydrosols of metals and their compounds we obtained in the context of our study.

Having analyzed the routine and the results of the interphase synthesis, we found that state (sediment, film, colloidal solution) and localization (organic or aqueous phase, their interface) of the reaction products depend on many factors (composition, concentration and ratio of reagents, reaction temperature, volumes of phases, interface area); therefore, it is currently impossible to formulate the patterns of interphase synthesis common to compounds of different classes.

At the same time, the data obtained highlight some features of interphase synthesis. Firstly, it eliminates the need for additional surfactants and stabilizing additives in the composition of colloidal solutions obtained. In the context of interphase synthesis, particles of the dispersed phase of colloidal solutions appear simultaneously with surfactants (oleic acid or sodium oleate) and stabilizing additives (quaternary ammonium compounds); from this viewpoint, the process of obtaining a colloidal solution through interphase interaction can be called self-organizing, with the surfactant's concentration sufficient to synthesize a colloidal solution achieved during the synthesis process and not determined empirically, as is the case for ferromagnetic fluids synthesis.

Secondly, interphase synthesis allows obtaining inorganic substances under conditions that are significantly milder than those seen in chemical precipitation of the same substances from their aqueous solutions. As a result, a change in the composition of a two-phase system — replacing aqueous phase with alcohol phase, for example, and keeping all the other parameters unaltered, — allows synthesizing nanoparticles with different morphology and dispersity, a phenomenon we have demonstrated using zinc oxide as the subject substance [5].

In addition, introduction of a polymeric substance into one of the phases effects a virtually single-stage synthesis of nanocomposites containing nanoscale particles formed directly in the polymer matrix, which prevents their aggregation and, consequently, allows having the obtained nanoparticles highly dispersed.

Interphase synthesis also offers the opportunity to synthesize Fe_3O_4/Au and Fe_3O_4/CdS bifunctional magnetic nanoparticles that feature properties of both a magnetic core (Fe_3O_4) and optically active shells (Au, CdS) [6–8]. Thus, we managed to obtain the Fe_3O_4/Au "core-shell" nanocomposite systems through reduction of the chloroauric acid in a two-phase system with one phase being formed of a magnetite colloidal solution [8].

Synthesis of bi- and trimetallic nanoparticles by redox-transmetalation

We have also applied the redox-transmetalation process to obtain bi- and trimetallic nanoparticles (including those with "core-shell" structure); this method implies reduction of metal

Table. Results of investigation of nanoparticles of metals and their compounds obtained by interphase synthesis in a two-phase system (non-polar solvent / water)

Colloidal dispersity	Reaction products localization phase	Average particle size, nm	UV-vis adsoption maximum λ_{max}, nm	Reference
Au	Organic, water or interface (determined by synthesis conditions)	2.6	514	2
Ag	Organic	10.0	440	3
Pd	Organic	1.4	440	–
Ag/Pd	Organic	2.1	430	–
Ag/Au	Organic, water or interface (determined by synthesis conditions)	4.2	470	–
Cu	Organic or water (determined by synthesis conditions)	10.0	575	–
CuO	Organic	3.2	–	4
ZnO	Organic or water (determined by synthesis conditions)	Particle size and shape depend on the conditions of the synthesis	–	5
CdS	Organic	2.0	311	7
CuS	Organic	Particle size and shape depend on the conditions of the synthesis	–	–
ZnS	Organic	Particle size and shape depend on the conditions of the synthesis	–	–
Fe_3O_4/Au	Organic	12.8	590	6
Fe_3O_4/CdS	Organic	10.3	311	7

salts with metal nanoparticles that form the core [9]. Compared to the "core-shell" composite synthesis methods that involve linkers, redox-transmetalation is relatively simple to apply in the context of experiments and does not require the use of expensive reagents for surface functionalization.

Making use of the redox-transmetalation method, we have obtained and thoroughly researched bi- and trimetallic nanoparticles with metallic copper and magnetic Fe and FeCo nanoparticles as core (reducing agent). According to our findings contact reduction of gold and silver compounds with FeCo nanoparticles produces FeCoAu and FeCoAg magnetic nanoparticles with a "core-shell" structure [10]. The precious metal shells that form on the surface of the easily oxidized magnetic nuclei prevent or reduce the degree of their oxidation; in addition, it makes the resulting nanocomposites more diverse in terms of directed functionalization, thus extending their applicability to cover biomedicine, among other fields.

Effect of dispersity and phase composition on antimicrobial properties of cupriferous antimicrobial agents

In the field of the new antimicrobial drugs, a promising trend is enriching them with low-toxic metal nanoparticles that cause no resistance response and offer pronounced bactericidal, antiviral, fungicidal and immunomodulatory potency.

As a rule, when using nanometals as a pharmaceutical substance, the designers seek to have the particles as disperse as possible and neglect the costs of development and technological adaptation of the superfine particles synthesis methods, which can be considerably greater than the effect form application of those particles. In this connection, we investigated the effect phase composition has on the antimicrobial potency, morphology and dispersity of metallic copper and copper (II) oxide nanoparticles obtained through chemical precipitation from aqueous solutions with polyethylene glycol [11].

The sample preparation technique and the results of the study of antimicrobial potency and range of the nanoparticles obtained were described in detail earlier [12]. Gram-negative (*Escherichia coli*), gram-positive (*Pseudomonas aeruginosa*, *Staphylococcus aureus*), spore-forming (*Bacillus subtilis*) bacteria and microscopic fungi (*Candida albicans*) were used as test cultures. The control treatments were ointments containing chloramphenicol, chlorhexidine and the combination of choline salicylate and cetalconium chloride.

The study revealed that copper nanoparticles can suppress a wide range of gram-positive and gram-negative bacteria, but their antimicrobial effect is less pronounced than that of ointment containing chloramphenicol. At the same time, the antifungal properties of copper nanoparticles are only marginally inferior to those of drugs containing chlorhexidine, choline salicylate and cetalconium chloride.

Having analyzed the dependence of antimicrobial effect on size we learned that the antimicrobial potency of copper nanoparticles, which vary in size from 14 to 37 nm, grows linearly as the size decreases to 14 nm. The findings describe copper-containing suspension the concentration of which does not exceed 0.5 % wt.; when the concentration is 0.75% wt., antimicrobial potency of copper nanoparticles in such a suspension does not increase with the size of particles going down from 37 nm to 14 nm.

Using magnetic nanoparticles for MSC labeling

The options of application of magnetic nanoparticles for mesenchymal stem cells (MSCs) labeling is one of the projects part of the magnetite magnetic fluids research effort undertaken at the Research Institute for Physical Chemical Problems of the Belarusian State University, where such fluids were synthesized. Fellows from the Belarusian State Medical University (Minsk, Belarus) participated in the project. For nanomedicine, the most promising magnetic nanoparticles are nanosized iron (II, III) oxides. They are simple to synthesize and their cytotoxicity level is low [13]. It is known that magnetic nanoparticles can be used for labeling both mesenchymal and neural stem cells with the aim to isolate them in cell suspension [14–16], as well as to concentrate [17] and to enable MRI visualization [18], which is especially valuable when stem cell are transplanted [19].

The synthesis of magnetic nanoparticles, MSC labeling and corresponding research results are detailed in the reports [20, 21]. MSC cultures isolated from the bone marrow of sexually mature white outbred rats were used for the purposes of MSC labeling. Magnetic iron (II, III) oxide nanoparticles were obtained through chemical precipitation from aqueous solutions followed by stabilization by surfactants.

The results of the study prove that the synthesized magnetic nanoparticles, after 24 hours of incubation and at 0.0069% wt., are lowly cytotoxic and can effectively mark MSCs. The findings suggest that magnetic nanoparticles localize in vesicles of the cells' cytoplasm and remain there when replanted; they do not hinder the cells' ability to adhere, spread and proliferate. When the cells divide, magnetic nanoparticles get distributed between daughter cells. It was experimentally confirmed that stem cells labeled with magnetic nanoparticles can be detected *in vivo* by MRI.

It should also be noted that the obtained magnetic nanoparticles, stabilized by oleic acid and triethanolamine, have several advantages over the known materials based on nanoscale iron oxides, which require prolonged incubation with stem cells or additional transporters (e.g., protamine sulfate) and negatively affect the ability of stem cells to differentiate.

CONCLUSION

Despite the significant progress in the development and research of nanoscale metals, oxides and salts synthesis, their application as part of nanocomposite materials designed for various purposes requires joint effort of scientists from various research fields. With regard to nanomedicine and pharmacology, it is crucial to learn to define the morphology, dispersity and phase composition of the nanoparticles used in order to meet the requirements for the developed medical materials and to assess the risks of their practical use.

References

1. Xinkui Yangying, Chen Wang. A new two-phase system for the preparation of nearly monodisperse silver nanoparticles Materials Letters. 2008; (62): 4366–8. DOI: 10.1016/j.matlet.2008.07.034.
2. Vorobyova SA, Sobal NS, Lesnikovich AI. Colloidal gold, prepared by interphase reduction. Colloids and Surfaces A: Physicochem Eng Aspects. 2001; (176): 273–7.
3. Lesnikovich AI, Vorobyova SA, Sobal NS. Preparation of silver

nanoparticles by interphase reduction. Colloids and Surfaces A: Physicochem Eng Aspects. 1999; (152): 375–9.
4. Vorobyova SA, Lesnikovich AI, Mushinskii VV. Interphase synthesis and characterization of CuO in octane. Colloids and Surfaces A: Physicochem Eng Aspects. 1999; (150): 297–300.
5. Vorobyova SA, Lesnikovich AI, Mushinskii VV. Interphase synthesis and characterization of zinc oxide. Materials Letters. 2004; (58): 863–6. DOI: 10.1016/j.matlet.2003.08.008.
6. Semenova EM, Vorobyova SA, Lesnikovich AI, Fedotova JA, Bayev VG. Fabrication and investigation of magnetite nanoparticles with gold shell. Journal of Alloys and Compounds. 2012; (530): 97–101. DOI: 10.1016/j.jallcom.2012.03.090.
7. Semenova EM, Vorobyova SA, Lesnikovich AI. Synthesis of cadmium sulfide coated magnetic nanoparticles. Physics, Chemistry and Application of Nanostructures: Proceeding of the International Conference. Nanomeeting–2011; 2011 May; Minsk, Belarus. 333–336.
8. Semenova EM, Vorobyova SA, Lesnikovich AI. Interphase synthesis of Fe_3O_4/CdS core-shell nanoparticles. Optical Materials. 2011; (34): 99–102. DOI: 10.1016/j.optmat.07.008.
9. Lee W, Kim M, Choi J, Park J. Redox-transmetalation process as a generalized strategy for core-shell magnetic nanoparticles. J Amer Chem Soc. 2005; (127): 16090–7. DOI: 10.1021/ja053659j.
10. Bayev VG, Fedotova JA, Vorobyova SA, Svito IA, Ivashkevich OA, Tyutyunnikov SI, Kolobylina NN, Guryeva PV. Mössbauer spectroscopy and magnetometry of FeCo-Ag and FeCo-Au nanocomposites synthesized by a redox-transmetalation method. Materials Chemistry and Physics. 2018; (216): 349–53. DOI: 10.1016/j.matchemphys.2018.06.031.
11. Auchynnikava AA, Vorobyova SA, Rzheussky SE. Antimicrobial activity of copper nanoparticles depending on the particles size. Physics, Chemistry and Application of Nanostructures: Proceeding of the International Conference. Nanomeeting–2015; 2015 May; Minsk, Belarus. 480–3.
12. Rzheusskij SJe, Avchinnikova EA, Vorobyova SA. Nanodiagnostika i antimikrobnye svojstva nanochastic medi. Vestnik farmacii. 2014; (3): 62–8.
13. Cen L, Neoh KG, Sun J, Hu F et al. Labeling of Adipose Derived Stem Cells by Oleic Acid Modified Magnetic Nanoparticles. Adv Funct Mater. 2009; (8): 1158–66. DOI: 10.1002/adfm.200801670.
14. Wang L, Neoh K-G, Kang E-T et al. Biodegradable magnetic-fluorescent magnetite/poly(DL-lactic acid-co-α, β-malic acid) composite nanoparticles for stem cell labeling. Biomaterials. 2010; (13): 3502–11. DOI: 10.1016/j.biomaterials.2010.01.081.
15. Song M, Moon WK, Kim Y et al. Labeling Efficacy of Superparamagnetic Iron Oxide Nanoparticles to Human Neural Stem Cells: Comparison of Ferumoxides, Monocrystalline Iron Oxide, Cross-linked Iron Oxide (CLIO)-NH_2 and tat-CLIO. Korean J Radiol. 2007; (5): 365–71. DOI: 10.3348/kjr.2007.8.5.365.
16. Odabaş S, Sayar F, Güven G et al. Separation of mesenchymal stem cells with magnetic nanosorbents carrying CD105 and CD73 antibodies in flow-through and batch systems. J Chromatogr B. 2008; 861 (1): 74–80. DOI: 10.1016/j.jchromb.2007.11.017.
17. Ito A, Hibino E, Honda H et al. A new methodology of mesenchymal stem cell expansion using magnetic nanoparticle. Biochem Eng J. 2004; 20 (2–3): 119–25. DOI: 10.1016/j.bej.2003.09.018.
18. Hsiao JK, Tai M-F, Chu H-H et al. Magnetic nanoparticle labeling of mesenchymal stem cells without transfection agent: cellular behavior and capability of detection with clinical 1.5 T magnetic resonance at the single cell level. Magnet Reson Med. 2007: 717–24. DOI: 10.1002/mrm.21377.
19. Zhu J, Wu X, Zhang HL. Adult Neural Stem Cell Therapy: Expansion In Vitro, Tracking In Vivo and Clinical Transplantation. Curr Drug Targets. 2005; 6 (1): 97–110. DOI: 10.2174/1389450053345055.
20. Petrova EA, Drazhina NP, Semenova EM, Vorobyova SA. Primenenie magnitnyh nanochastic dlja markirovanija mezenhimal'nyh stvolovyh kletok. Vestnik BGU. Serija 2. 2012; (3): 54–9.
21. Drazhina NP, Petrova EA, Semenova EM, Vorobyova SA, avtory. Uchrezhdenie obrazovanija «Belorusskij gosudarstvennyj medicinskij universitet», Uchrezhdenie Belorusskogo gosudarstvennogo universiteta «Nauchno-issledovatel'skij institut fiziko-himicheskih problem», patentoobladateli. Koncentrat dlja poluchenija sredstva vital'noj markirovki mezenhimal'nyh stvolovyh kletok. Patent RB 17804. 15.02.2012.

Литература

1. Xinkui Yangying, Chen Wang. A new two-phase system for the preparation of nearly monodisperse silver nanoparticles Materials Letters. 2008; (62): 4366–8. DOI: 10.1016/j.matlet.2008.07.034.
2. Vorobyova SA, Sobal NS, Lesnikovich AI. Colloidal gold, prepared by interphase reduction. Colloids and Surfaces A: Physicochem Eng Aspects. 2001; (176): 273–7.
3. Lesnikovich AI, Vorobyova SA, Sobal NS. Preparation of silver nanoparticles by interphase reduction. Colloids and Surfaces A: Physicochem Eng Aspects. 1999; (152): 375–9.
4. Vorobyova SA, Lesnikovich AI, Mushinskii VV. Interphase synthesis and characterization of CuO in octane. Colloids and Surfaces A: Physicochem Eng Aspects. 1999; (150): 297–300.
5. Vorobyova SA, Lesnikovich AI, Mushinskii VV. Interphase synthesis and characterization of zinc oxide. Materials Letters. 2004; (58): 863–6. DOI: 10.1016/j.matlet.2003.08.008.
6. Semenova EM, Vorobyova SA, Lesnikovich AI, Fedotova JA, Bayev VG. Fabrication and investigation of magnetite nanoparticles with gold shell. Journal of Alloys and Compounds. 2012; (530): 97–101. DOI: 10.1016/j.jallcom.2012.03.090.
7. Semenova EM, Vorobyova SA, Lesnikovich AI. Synthesis of cadmium sulfide coated magnetic nanoparticles. Physics, Chemistry and Application of Nanostructures: Proceeding of the International Conference. Nanomeeting–2011; 2011 May; Minsk, Belarus. 333–336.
8. Semenova EM, Vorobyova SA, Lesnikovich AI. Interphase synthesis of Fe_3O_4/CdS core-shell nanoparticles. Optical Materials. 2011; (34): 99–102. DOI: 10.1016/j.optmat.07.008.
9. Lee W, Kim M, Choi J, Park J. Redox-transmetalation process as a generalized strategy for core-shell magnetic nanoparticles. J Amer Chem Soc. 2005; (127): 16090–7. DOI: 10.1021/ja053659j.
10. Bayev VG, Fedotova JA, Vorobyova SA, Svito IA, Ivashkevich OA, Tyutyunnikov SI, Kolobylina NN, Guryeva PV. Mössbauer spectroscopy and magnetometry of FeCo-Ag and FeCo-Au nanocomposites synthesized by a redox-transmetalation method. Materials Chemistry and Physics 2018; (216): 349–53. DOI: 10.1016/j.matchemphys.2018.06.031.
11. Auchynnikava AA, Vorobyova SA, Rzheussky SE. Antimicrobial activity of copper nanoparticles depending on the particles size. Physics, Chemistry and Application of Nanostructures: Proceeding of the International Conference. Nanomeeting–2015; 2015 May; Minsk, Belarus. 480–3.
12. Ржеусский С. Э., Авчинникова Е. А., Воробьева С. А. Нанодиагностика и антимикробные свойства наночастиц меди. Вестник фармации. 2014; (3): 62–8.
13. Cen L, Neoh KG, Sun J, Hu F et al. Labeling of Adipose Derived Stem Cells by Oleic Acid Modified Magnetic Nanoparticles. Adv Funct Mater. 2009; (8): 1158–66. DOI: 10.1002/adfm.200801670.
14. Wang L, Neoh K-G, Kang E-T et al. Biodegradable magnetic-fluorescent magnetite/poly(DL-lactic acid-co-α, β-malic acid) composite nanoparticles for stem cell labeling. Biomaterials. 2010; (13): 3502–11. DOI: 10.1016/j.biomaterials.2010.01.081.
15. Song M, Moon WK, Kim Y et al. Labeling Efficacy of Superparamagnetic Iron Oxide Nanoparticles to Human Neural Stem Cells: Comparison of Ferumoxides, Monocrystalline Iron Oxide, Cross-linked Iron Oxide (CLIO)-NH_2 and tat-CLIO. Korean J Radiol. 2007; (5): 365–71. DOI: 10.3348/kjr.2007.8.5.365.
16. Odabaş S, Sayar F, Güven G et al. Separation of mesenchymal stem cells with magnetic nanosorbents carrying CD105 and CD73 antibodies in flow-through and batch systems. J Chromatogr B.

2008; 861 (1): 74–80. DOI: 10.1016/j.jchromb.2007.11.017.
17. Ito A, Hibino E, Honda H et al. A new methodology of mesenchymal stem cell expansion using magnetic nanoparticle. Biochem Eng J. 2004; 20 (2–3): 119–25. DOI: 10.1016/j.bej.2003.09.018.
18. Hsiao JK, Tai M-F, Chu H-H et al. Magnetic nanoparticle labeling of mesenchymal stem cells without transfection agent: cellular behavior and capability of detection with clinical 1.5 T magnetic resonance at the single cell level. Magnet Reson Med. 2007: 717–24. DOI: 10.1002/mrm.21377.
19. Zhu J, Wu X, Zhang HL. Adult Neural Stem Cell Therapy: Expansion In Vitro, Tracking In Vivo and Clinical Transplantation. Curr Drug Targets. 2005; 6 (1): 97–110. DOI: 10.2174/1389450053345055.
20. Петрова Е. А., Дражина Н. П., Семенова Е. М., Воробьева С. А. Применение магнитных наночастиц для маркирования мезенхимальных стволовых клеток. Вестник БГУ. Серия 2. 2012; (3): 54–9.
21. Дражина Н. П., Петрова Е. А., Семенова Е. М., Воробьева С. А., авторы. Учреждение образования «Белорусский государственный медицинский университет», Учреждение Белорусского государственного университета «Научно-исследовательский институт физико-химических проблем», патентообладатели. Концентрат для получения средства витальной маркировки мезенхимальных стволовых клеток. Патент РБ 17804. 15.02.2012.

APPLICATION OF NANOSCALE POLYMER COLLOID CARRIERS FOR TARGETED DELIVERY OF THE BRAIN-DERIVED NEUROTROPHIC FACTOR THROUGH THE BLOOD-BRAIN BARRIER IN EXPERIMENTAL PARKINSONISM

Kapitonova MYu[1], Alyautdin RN[2] ✉, Wan-Syazli RWAL[3], Nor-Ashikin MNK[3], Ahmad A[3], Norita S[3], Dydykin SS[4]

[1] Faculty of Medicine and Health Sciences, University Malaysia Sarawak (UNIMAS), Kota Samarahan, Sarawak, Malaysia

[2] Department for Expertise of Medicinal Products safety, Scientific Centre for Expert Evaluation of Medicinal Products, Moscow

[3] Faculty of Medicine, University Teknologi MARA, Sungai Buloh, Selangor, Malaysia

[4] Department of Operative Surgery and Topographic Anatomy, Sechenov First Moscow State Medical University, Moscow

Parkinson disease is one of the common age-related motor neurodegenerative diseases, in which dopamine neurons degeneration is considered to be pathognomic for the development of motor disfunction. Brain-derived neurotrophic factor (BDNF) is a member of the neurotrophin family, which is considered to be a key regulator of neuronal plasticity. BDNF, being a large molecule, does not pass through the blood-brain barrier (BBB). Synthetic polymer nanoparticles (NP), covered by surfactant, provide the phenomenon of "Trojan hoarse" and enable BDNF to penetrate into the brain tissue. For modelling of parkinsonism we used an intraperitoneal (i.p.) injection of neurotoxin 1-methyl-4-phenyl-1,2,3,6-tetrahydropyridine (MPTP) which was injected to the C57BL/6 mice with subsequest treatment with normal saline (group 1), BDNF (group 2), nanoparticulate BDNF (group 3) and surfactant-coated nanoparticulate BDNF (group 4). After 90 min, 24 hours, 72 hours and 7 days manifestations of parkinsonism were evaluated using behavioural tests of open field, rota-rod, assessment of the tremor, length of the body and pace. At the end of experiment the brain was sampled for histological evaluation of changes in the striatum and midbrain and concentration of BDNF in the brain tissues. The results of the experiments demonstrated that nanoparticulate BDNF covered with surfactant significanltly reduced rigidity of the skeletal muscles, oligokinesia and tremor, and also significantly increased BDNF concentration in the brain tissues.

Keywords: brain-derived neurotrophic factor, parkinsonism, nanoparticles, blood-brain barrier, ELISA

Funding: this work was supported by the grant 600-RMI/RAGS 5/3 (92/2013) of the Universiti Teknologi MARA (UiTM), Selangor, Malaysia.

✉ **Correspondence should be addressed:** Renad N. Alayutdin
1 Volokolamskiy Proezd 10, bl. 4, Moscow, 119876; alyautdun@mail.ru

Received: 09.07.18 **Accepted:** 20.08.18

DOI: 10.24075/brsmu.2018.072

ПРИМЕНЕНИЕ ПОЛИМЕРНЫХ КОЛЛОИДНЫХ НОСИТЕЛЕЙ ДЛЯ ТАРГЕТНОЙ ДОСТАВКИ МОЗГОВОГО ТРОФИЧЕСКОГО ФАКТОРА ЧЕРЕЗ ГЕМАТО-ЭНЦЕФАЛИЧЕСКИЙ БАРЬЕР ПРИ ЭКСПЕРИМЕНТАЛЬНОМ ПАРКИНСОНИЗМЕ

М. Ю. Капитонова[1], Р. Н. Аляутдин[2] ✉, Р. В. А. Л. Ван Шазли[3], М. Н. К. Нор-Ашикин[3], А. Ахмад[3], С. Норита[3], С. С. Дыдыкин[4]

[1] Факультет медицины и здравоохранения, Университет Малайзии Саравак (ЮНИМАС), Кота-Самарахан, Саравак, Малайзия

[2] Управление экспертизы безопасности лекарственных средств, Научный центр экспертизы средств медицинского применения, Москва

[3] Медицинский факультет, Университет технологии МАРА, Сунгай Було, Селангор, Малайзия

[4] Кафедра оперативной хирургии и топографической анатомии, Сеченовский Первый Московский государственный медицинский университет, Москва

Болезнь Паркинсона — одно из распространенных возрастных моторных нейродегенеративных заболеваний, при котором дегенерация дофаминергических нейронов считается патогномоничной для развития моторной дисфункции. Мозговой трофический фактор (БДНФ) считается ключевым регулятором нейронной пластичности и, являясь крупной молекулой, не проходит через гемато-энцефалический барьер (ГЭБ). Синтетические полимерные наночастицы (НЧ), покрытые сурфактантом, обеспечивают феномен «троянского коня» и позволяют доставлять БДНФ в ткани головного мозга. Целью работы было оценить нейропротективное действие БДНФ, сорбированного на полилактидных НЧ, в общепринятой модели паркинсонизма, вызванного применением МФТП. Для моделирования синдрома паркинсонизма использовали нейротоксин 1-метил-4-фенил-1,2,3,6-тетрагидропиридин (МФТП), который внутрибрюшинно вводили мышам линии C57BL/6 с последующим внутривенным введением физраствора (1-я группа мышей), раствора БДНФ (2-я группа), БДНФ, сорбированного на полилактидных НЧ (3-я группа), и БДНФ, сорбированного на полилактидных НЧ, покрытых сурфактантом (4-я группа). Через 90 мин, 24 ч, 72 ч и 7 суток оценивали проявления паркинсонизма в поведенческих тестах открытого поля, на рота-роде, по интенсивности тремора, изменению длины тела и шага животных. По окончании эксперимента головной мозг извлекали для гистологической оценки изменений в стриа-паллидарной системе и среднем мозге, а также для определения концентрации БДНФ в тканях головного мозга. Результаты показали, что БДНФ, сорбированный на полилактидных НЧ, покрытых сурфактаном, существенно уменьшал ригидность скелетных мышц, олигокинезию и тремор, а также достоверно повышал концентрацию БДНФ в тканях головного мозга.

Ключевые слова: мозговой трофический фактор, паркинсонизм, наночастицы, гемато-энцефалический барьер, иммуноферментый анализ

Финансирование: исследование выполнено в рамках гранта 600-RMI/RAGS 5/3 (92/2013) Университета технологии МАРА, Селангор, Малайзия.

✉ **Для корреспонденции:** Ренад Николаевич Аляутдин
1-й Волоколамский проезд, д. 10, корп. 4, г. Москва, 119876; e-mail: alyautdun@mail.ru

Статья получена: 09.07.18 **Статья принята к печати:** 20.08.18

DOI: 10.24075/vrgmu.2018.072

The main trend of modern pharmacology is to increase efficacy of the medications with decrease of their toxicity and side effects. Analysis of modern literature revealed two main ways to solve this problem: firstly, to increase selective action of the drugs, and secondly, to provide higher concentration of the medications at the targeted structures, particularly in the central nervous system (CNS) at the expense of directed transport of the drugs using specific carriers [1, 2]. Trying to implement the first direction, we are facing certain limitations, such as presence of the targets with equal sensitivity in different structures of the body which makes the desired selectivity not feasible; persuing the second direction, we come across another limitation, such as toxicity of the carriers for the distant delivery of the drugs, while high selectivity becomes a considerable advantage in this case. Besides, certain potentially important medications were recently identified, such as tumor necrosis factor, which requires both distant and selective delivery to the target organs. Presence of the BBB is an essential obstacle for penetration of many medications into the brain. Tight junctions between the endothelial cells of the brain capillaries interfere with penetration of many high molecular weight and hydrophilic substances into the brain tissues, while presence of the P-glycoprotein hampers penetration of certain lipophilic molecules into the brain [3, 4]. Thus, presence of the BBB is a major limitation for the medicinal correction of the neurodegenerative diseases, tumors and other pathologies of the CNS.

Many peptides and proteins are known as regulators of different functions of the CNS neurons and therefore may potentially be used for treatment of different conditions accompanied by neurodegeneration [5, 6]. Important limitation for clinical application of the peptide medications is their low capacity in penetration through the BBB and their liability to enzymatic inactivation. Polymer colloid systems are capable of providing transport of the medications, including proteins and peptides, into the brain [7].

For modelling of parkinsonism MPTP is a common compound which penetrates through the BBB and forms a metabolite in the brain which blocks thyrosine-hydroxylase, which finally results in deficiency of dopamine in substantia nigra [8]. In our research for the purpose of assessment of BDNF delivery and achievement of the neuroprotective effect in modelled parkinsonism we applied biodegradable surfactant-coated polylactate NP.

The objective of this study is to evaluate neuroprotective effect of nanoparticulate BDNF sorbed on to the polylactic NP in the established model of parkinsonism caused by MPTP.

METHODS

Experiments were conducted using the C57BL/6 male mice weighing 20–25 g (Animal house “LACU”, Institute of the Medical Molecular Biotechnology (IMMB), Universiti Teknologi MARA, Selangor; Malaysia). All animals were given one week to adjust to the laboratory conditions before the experiment started. Each mouse was used only once in the experiment. The animals were having free access to food and water, kept in the temperature of 20–22 °C and humidity 50–60%, with a 12/12 dark/light cycle in the standard steel cages with 4 mice per cage. To minimise circadian fluctuations and avoid chronopharmacological effects, all experiments were conducted starting from 9 o’clock in the morning. Each experimental group contained 6–8 animals.

Parkinsonism was modelled using neurotoxin MPTP injected i. p. [9]. Evaluation of the major extrapyramidal changes were conducted starting from the of MPTP injection continuously for 45 min as described below; thereafter the animals were divided into 4 groups and got an injection into the lateral tail vein of 0.2 ml of one of the medications: 1st group — normal saline, 2nd group — BDNF, 3rd group — nanoparticulate BDNF, 4th group — surfactant-coated (poloxamer 188) nanoparticulate BDNF. All behavioural tests and observations were conducted 90 min, 24 hours, 72 hours and 7 days after injection of neurotoxin.

After the last test was completed on the 8th day of experiment, all the animals were euthanized by decapitation. Brain was sampled, with the right hemisphere fixed in the 10% formalin for subsequent histological examination, while the left hemisphere was frozen by liquid nitrogen in –70° with subsequent determination of level of BDNF in the brain using ELISA.

Chemicals

For parkinsonism modelling we used officinal normal saline (0.9% sodium chloride) (Sigma Aldrich; USA); 1-Methyl-4-phenyl-1,2,3,6-tetra hydropyridine hydrochloride powder (Sigma-Aldrich; USA).

For treatment of parkinsonism the following chemicals were used: officinal normal saline (0.9% sodium chloride) (Sigma-Aldrich; USA); 10% solution of poloxamer 188 (Sigma-Aldrich; USA), recombinant human BDNF (Raybiotech; USA); polylactic NP of medium diameter 200 nm (Degradex TM PLGA (MW 45–75 KD) nanospheres) (Phosphorex, Inc.; USA).

For ELISA we used a set of chemicals for ELISA of BDNF in mice and rats (Total BDNF Immunoassay; Quantikine®ELISA, Catalog Number DBNT00) (R&D Systems, Inc; USA), phosphate buffer (Sigma-Aldrich; USA) and lysis buffer 17 (catalog #895943; R&D system, Abingdon; UK,).

Modelling of parkinsonism

Solution of MPTP was injected i.p. to all animals in a dose of 30 mg/kg.

Preparation of nanoparticulate BDNF

Lyophilized powder of BDNF (50 mkg) was dissolved in 1 ml of normal saline. Solution of BDNF was added to the suspension of NP (40 mg in 1 ml of normal saline) and incubated at low temperature (0–4 °C) for 3 hours with subsequent sonification in the ultrasound disintegrator for 15 min at the power 60 w and stirred by magnetic stirrer at the speed of 300 RPM for 3 hours.

Preparation of the suspension of NP

Lyophilised powder (40 mg) of NP, containing 23.53 mg of polymer, was dispersed in 1 ml of the normal saline until a homogeneous suspension of the lacteous white color is obtained. Sonification was conducted in the ultrasound disintegrator for 15 min with power of 60 w with subsequent stirring by magnetic stirrer at the speed of 300 RPM for 3 hours.

Preparation of the suspension of NP with BDNF and surfactant

Suspension of nanoparticulate BDNF was added to 0.2 ml of 10% poloxamer 188 with subsequest stirring by magnetic stirrer. The final 2 ml of preparation contained 1.18% suspension of NP covered by poloxamer and 50 mcg of BDNF (5 mcg of BDNF per 0.2 ml of the preparation). In this case we used only

0.9 ml of normal saline to dissolve NP and BDNF to maintain total volume of 2 ml of the preparation.

Total of 0.2 ml of normal saline or pure BDNF or nanoparticulate BDNF or nanoparticulate BDNF with poloxamer were injected intravenously (i.v.) to the animals of the 1st, 2nd, 3rd and 4th groups respectively into the lateral tail vein 45 min after the injection of the MPTP.

Efficacy of the preparations was evaluated by its capacity to attenuate the main manifestations of parkinsonism caused by MPTP (oligokinesia, rigidity and tremor). We also considered presence and intensity of such symptoms as salivation, piloerection, retropulsion and respiratory failure.

Methods for evaluation of rigidity

For quantitative evaluation of rigidity we used a symptom of humpback, the extent of which depends on muscular rigidity and may be measured by the shortening of the distance from the tail to the base of the tail. Body length was measured from interauricular line to the base of the tail using videoimages in the open field test. Paws of the animal were marked with a special dye using two different colors for front and rear limbs. Pace was measured between the footprints left by the moving animals on the tape. Rota-rod test was conducted in the Rota-Rod ENV-576 (Med Associates; USA) in accelerated mode N5 (2–20 RPM).

Evaluation of tremor

Tremor was assessed by its intensity in grades and by the number of animals with tremor per group. Based on localization and range, tremor was evaluated as grade 0 — no tremor, grade 1 — low range local tremor of the head, front paws and tail, grade 2 — local middle range tremor, grade 3 — generalized low or middle range tremor of the whole body [10].

Open field test

Parkinsonism induced by neurotoxin causes changes not only of quantity of locomotor activity, but of its quality as well. The term “oligokinesia” refers to reduction of the volume of movements and change of their qualitative features. Open field is a white tetragonal arena with white borders 50 cm high. Its space is divided into 64 equal quadrates 10 × 10 cm each. After each testing the bottom of the arena was wiped with a humid sponge.

For testing in the open field, the animal was placed into the center of arena for 3 minutes immediately after MPTP injection and then 90 min, 24 hours, 72 hours and 7 days after neurotoxin injection. For assessment of the horizontal activity, one crossed quadrate was taken as a unit of distance. Vertical activity included rearing of the animal with the front paws hanging or leaning against the borders of the arena. Both types of locomotor activity were considered as rearing.

ELISA

The following equipment was used for ELISA: microplate reader Victor™ X to measure absorbance at 450 nm (Perkin Elmer; USA), tissue homogenizer Omni-Ruptor 4000 (OMNI International Inc.; US), horizontal orbital shaker with speed of 500+/–50 rpm (VISION Scientific Co. Ltd; Korea).

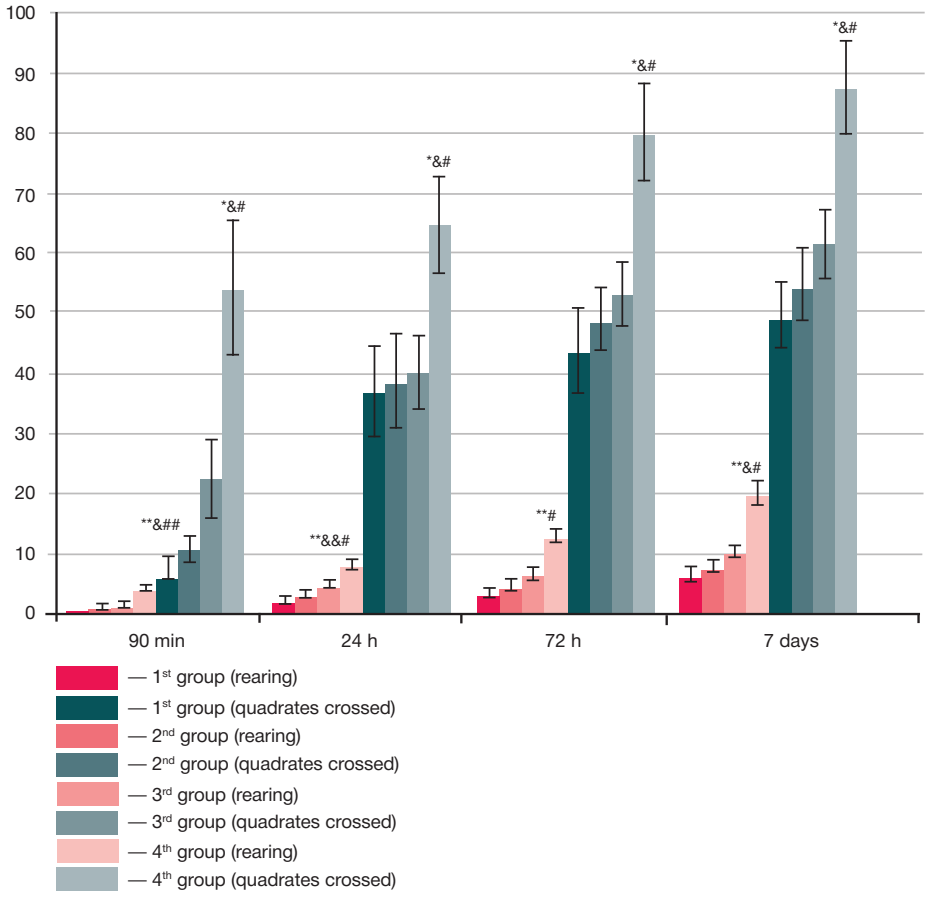

Fig. 1. Open field test results in experimental and control mice with modelled parkinsonism (m ± SEM). * — $p < 0.05$ compared to the 1st group, ** — $p < 0.01$ compared to the 1st group, & — $p < 0.05$ compared to the 2nd group, && — $p < 0.01$ compared to the 2nd group, # — $p < 0.05$ compared to the 3rd group, ## — $p < 0.01$ compared to the 3rd group

Left hemisphere of the brain was rinsed with phosphate buffer and homogenized with a tissue homogenizer in 500 µl of PBS. An equal volume of lysis buffer 17 (R&D Systems, Abingdon, UK) was added and tissues were lysed at room temperature for 30 minutes with gentle agitation. Debris was then removed by centrifugation at 10,000 g, 4 °C, aliquoted and stored at –80 °C before analysis. BDNF level was assesses using ELISA kit (Total BDNF Immunoassay; Quantikine®ELISA) (R&D Systems, Inc.; USA) according to the manufacturer protocol using microplate reader Victor™ X (Perkin Elmer; USA) with

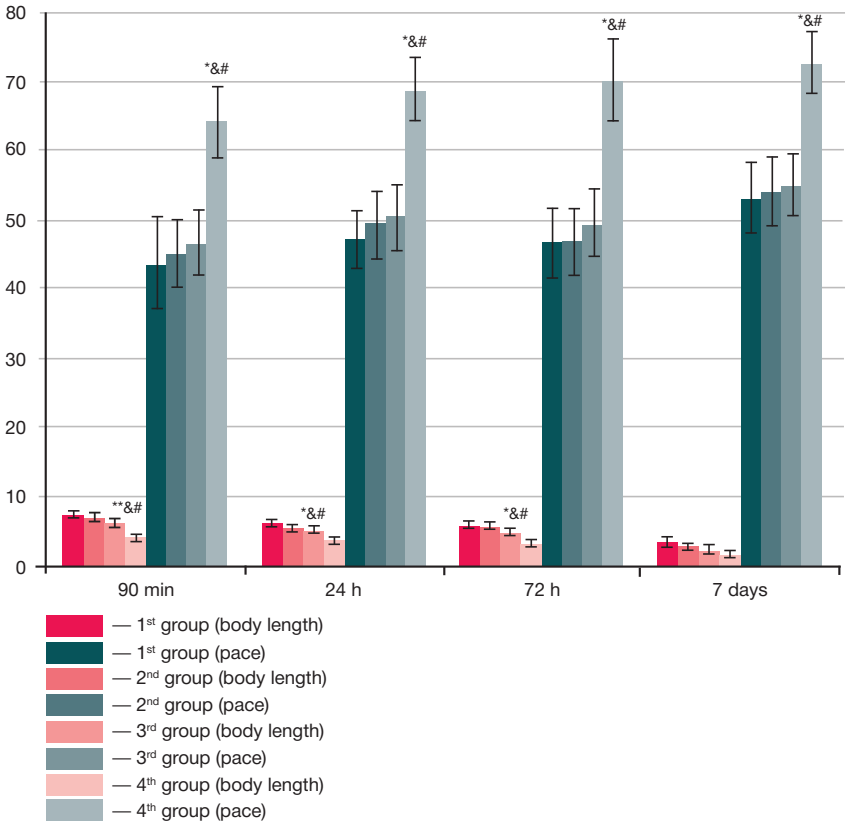

Fig. 2. Body length and pace in the experimental and control mice with modelled parkinsonism, mm (m ± SEM). * — $p < 0.05$ compared to the 1st group, ** — $p < 0.01$ compared to the 1st group, & — $p < 0.05$ compared to the 2nd group, && — $p < 0.01$ compared to the 2nd group, # — $p < 0.05$ compared to the 3rd group, ## — $p < 0.01$ compared to the 3rd group

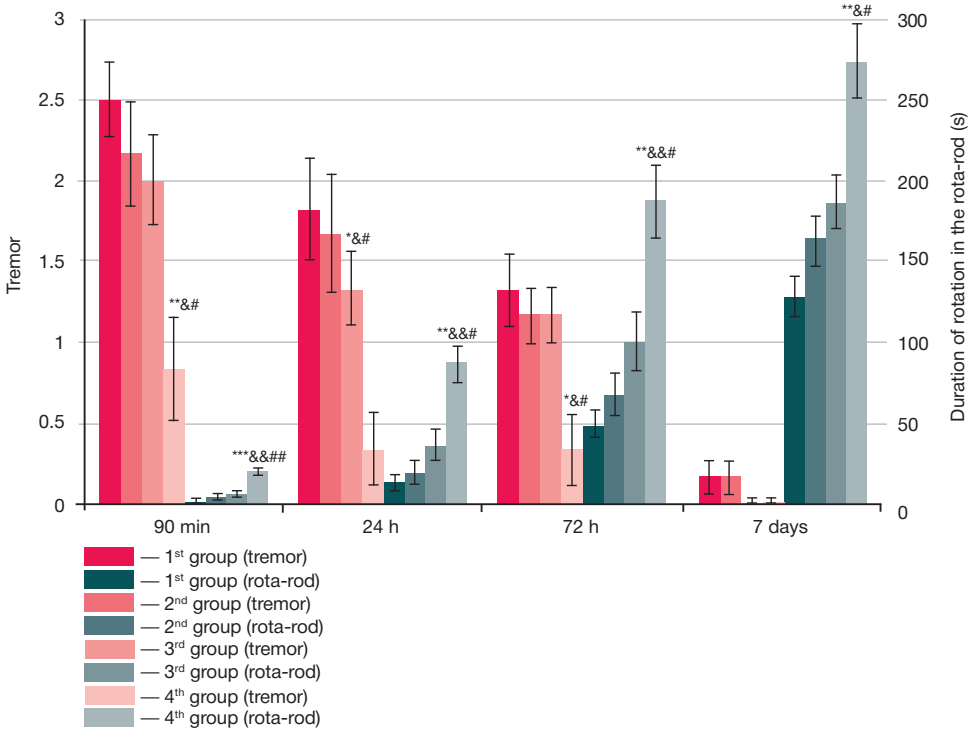

Fig. 3. Tremor and duration of rotation in rota-rod (sec) in experimental and control mice with modelled parkinsonism (m ± SEM). * — $p < 0.05$ compared to the 1st group, ** — $p < 0.01$ compared to the 1st group, & — $p < 0.05$ compared to the 2nd group, && — $p < 0.01$ compared to the 2nd group, # — $p < 0.05$ compared to the 3rd group, ## — $p < 0.01$ compared to the 3rd group

Table 1. Concentration of BDNF in the brain tissue of mice with modelled parkinsonism after treatment with normal saline and BDNF preparations, pg/mg (m+/–SE)

1st group	2nd group	3rd group	4th group
163.91 ± 10.17	184.03 ± 2.28	194.51 ± 1.14*##	204.46 ± 3.71**##&

Note: * — $p < 0.05$ compared to normal saline; ** — $p < 0.01$ compared to normal saline; ## — $p < 0.01$ compared to BDNF; & — $p < 0.05$ compared to nanoparticulate BDNF.

450 nm wavelength. The optical density reading of sample at 450 nm wavelength was subtracted with 570 nm wavelength to avoid imperfection plate. The results of the ELISA as expressed as pg/mg of total protein.

Statistics

The data obtained were processed statistically using Excel software with calculation of the mean, standard deviation, mean error, Student's *t*-test. Difference were considered significant if $p < 0.05$.

RESULTS

As early as 2 minutes past i.p. injection of MPTP the animals of all four groups developed symptoms of parkinsonism: at first generalized tremor, low or middle range, then within the next 3–5 min — retropulsion and piloerection. Piloerection was so prominent, that in many mice white skin was visible between the hair of the black coat, which was especially pronounced at the back of the neck. During next 15 min the symptoms of skeletal muscles rigidity are dominating, namely staggering gait, shortened pace, rotational movements, shortening of the body with appearance of a typical humpback in the thoraco-lumbar region of the vertebral column. After 1.5 hours (45 minutes past injection of BDNF or saline) in mice of the 1st group tremor persisted, rearings were absent, while in groups 2 and 3 tremor was slightly reduced and single rearings might be observed, and in the 4th group tremor almost disappeared and rearings became much more frequent. Animals of the 4th group showed ability to restore the pace and rota-rod rotation, as well as to increase the distance walked in the open field. In animals of the 1st–3rd groups rota-rod test results and the pace almost did not change, while distance walked and body length did not change only in the 1st and 2nd groups, but demonstrated a trend to increase in the 3rd group of mice. Statistical analysis showed that only mice of the 4th group revealed positive dynamics for all the listed parameters compared to all other groups, while in groups 1, 2 and 3 they did not differ significantly (Fig. 1–3).

After 24 and 72 hours since the start of the experiment the trends observed after 90 minutes for distance walked, pace, body length, rota-rod rotation and tremor, persist, though with different level of significance ($p < 0.05$ — $p < 0.01$). After 7 days mice of the 3rd and 4th groups did not show any tremor, while in the 1st and 2nd groups single twitching took place in some animals, but there was no significant difference for this parameter due to considerable variations between the species. Body length continues to restore in all the groups, but the difference between the groups is also not significant. Pace, rota-rod performance, distance walked and rearing remained significantly different in the 4th group compared to all other groups.

As follows from the table 1, injection of BDNF insignificantly (by 11%) increased concentration of BDNF in brain compared to the normal saline ($p > 0.05$), while nanoparticulate BDNF increased it significantly ($p < 0.05$) and surfactant-coated nanoparticulate increased with higher significance ($p < 0.01$) compared to normal saline group. Concentration of BDNF in the brain tissues in animals treated with nanoparticulate BDNF and surfactant-coated nanopaticulate BDNF was significantly higher ($p < 0.01$) than with pure BDNF. Animals treated with nanoparticulate BDNF and nanoparticulate BDNF with surfactant also showed significant difference in BDNF concentration in the brain tissues ($p < 0.05$).

DISCUSSION

Our experiments demonstrated that i.v. injection of poloxamer-coated nanoparticulate BDNF loaded onto PLGA NP significantly increases concentration of neurotrophin in the brain. As a result, BDNF delivered to the brain tissues provides considerable alleviation of the symptoms of MPTP-induced parkinsonism. I. v. injection of pure BDNF did not show any significant antiparkinsonic effect. Significant reduction of rigidity and normalization of locomotor activity was detected only in the group of mice with parkinsonism treated by nanoparticulate BDNF with poloxamer. This effect was observed starting from the 45 minutes after BDNF injection continuously for 7 days. Similar effect on MPTP-related tremor was demonstrated in the group of mice after application of nanoparticulate BDNF with poloxamer. Observed trend of increased BDNF concentration after i. v. injection of pure neurotrophin allows to assume the presence of a transporting system in cells forming BBB. The data obtained correlate with the results regarding directed transport using colloid NP. Experiments with polybutirate NP covered by polysorbate 80 demonstrated that nerve growth factor (NGF) may be delivered into the brain. NGF was shown to be able to reduce intensity of symptoms caused by MPTP in mice [9, 10].

Currently activating effect of BDNF on regeneration of the nerve tissue is under thorough investigation. Thus, Limongi et al. demonstrated that incubation of the nerve tissue in the medium containing BDNF will increase density of the synaptic contacts and neuronal survival rate [11]. Besides, BDNF increases release of acetylcholine and glutamate by the synaptic structures of the central and peripheral nervous system [12, 13]. These mediators form the key mechanisms in functioning of the extrapyramidal system and development of parkinsonism. As it was shown by Bhurtel et al., BDNF stimulates dopaminergic neurons [14]. At the same time direct injection of the BDNF into brain reduced the intensity of symptoms of parkinsonism caused by injection of MPTP [15].

Thus we presume that BDNF delivered to the brain with the aid of NP may decrease intensity of symptoms of parkinsonism caused by MPTP due to direct stimulation of discharge of the mediators and/or stimulation of the regeneratory capacity of the dopaminergic neurons.

CONCLUSIONS

The results obtained demonstrated that poloxamer 188-coated polylactic NP are capable of transporting of the BDNF through the BBB, thus creating its concentration in the brain which is able to cause significant neurotropic effect in the brain.

References

1. Alyautdin RN, Deshmukh R, Petrov VE. Transport lekarstvennykh veshchestv cherez gematoencephalicheskiy barier. Vestnik NII Molekulyarnoy meditsiny. 2003; 11–29.
2. Lockman PR, Mumper RJ, Khan MA, Allen DD. Nanoparticle technology for drug delivery across blood-brain barrier. Drug Dev Ind Pharm. 2002; 28 (1): 1–13.
3. Begley DJ. Understanding and circumventing the blood-brain barrier. Acta Paediatr Suppl. 2003; 92: 83–91.
4. Lefauconneir JM. The blood brain barrier. J Physiological Data. 1998; 140 (1): 3–13.
5. Alyautdin RN, Petrov VE, Kharkevich DA, Kreuter J. Passage of peptides across the blood-brain barrier with nanoparticles. Eur J Pharm Sci. 1994; (3): 91–2.
6. Bibel M, Barde Y. Neurotrophins: key regulator of cell fate and cell shape in the vertebrate nervous system. Genes Dev. 2000; (14): 2919–37.
7. Castellenos-Ortega MR, Cruz-Aguado R, Martinez-Marty L. Nerve growth factor: possibilities and limitations of its clinical application. Rev Neurol. 1999; 29 (5): 439–71.
8. Przedborski S, Jackson-Lewis V, Djaldetti R, Liberatore G, Vila M, Vukosavic S, Almer G. The parkinsonian toxin MPTP: action and mechanism. Restor Neurol Neurosci. 2000; 16 (2): 135–42.
9. Kreuter J. Nanoparticulate systems for brain delivery of drugs. Adv Drug Deliv Rev. 2001; (47): 65–81.
10. Kurakhmaeva K, Djindjikhashvili I, Petrov V, Balabanjan V, Voronina T, Trofimov S et al. Brain targeting of nerve growth factor using poly(butylcyanoacrilate) nanoparticles. J Drug Targ. 2009; (17): 564–74.
11. Limongi T, Rocchi A, Cesca F, Tan H, Miele E, Giugni A. Delivery of Brain-Derived Neurotrophic Factor by 3D Biocompatible Polymeric Scaffolds for Neural Tissue Engineering and Neuronal Regeneration. Mol Neurobiol. 2018 Mar 29. DOI: 10.1007/s12035-018-1022-z.
12. Tyler WJ, Perrett, Pozzo-Miller LD. The role of neurotrophins in neurotransmitter release. Neuroscience. 2002; (8): 524–31.
13. Schindowski K, Belarbi K, Buée L. Neurotrophic factors in Alzheimer's disease: role of axonal transport. Genes Brain Behav. 2008; (7): 43–56.
14. Bhurtel S, Katila N, Neupane S, Srivastav S, Park PH, Choi D. Methyleneblue protects dopaminergic neurons against MPTP-induced neurotoxicity by upregulating brain-derived neurotrophic factor. Ann N Y Acad Sci. 2018.DOI: 10.1111/nyas.13870. Available at: https://www.ncbi.nlm.nih.gov/pubmed/29882218#.
15. Chen JF, Wang M, Zhuang YH, Behnisch T. Intracerebroventricularly-administered 1-methyl-4-phenylpyridinium ion and brain derived neurotrophic factor affect catecholaminergic nerve terminals and neurogenesis in the hippocampus, striatum and substantia nigra. Neural Regen Res. 2018; (13): 717–26. DOI: 10.4103/1673-5374.230300.

Литература

1. Аляутдин Р. Н., Дешмух Р., Петров В. Е. Транспорт лекарственных веществ через гематоэнцефалический барьер. Вестник НИИ Молекулярной медицины. 2003; 11–29.
2. Lockman PR, Mumper RJ, Khan MA, Allen DD. Nanoparticle technology for drug delivery across blood-brain barrier. Drug Dev Ind Pharm. 2002; 28 (1): 1–13.
3. Begley DJ. Understanding and circumventing the blood-brain barrier. Acta Paediatr Suppl. 2003; (92): 83–91.
4. Lefauconneir JM. The blood brain barrier. J Physiological data. 1998; 140 (1): 3–13.
5. Alyautdin RN, Petrov VE, Kharkevich DA, Kreuter J. Passage of peptides across the blood-brain barrier with nanoparticles. Eur J Pharm Sci. 1994; (3): 91–2.
6. Bibel M, Barde Y. Neurotrophins: key regulator of cell fate and cell shape in the vertebrate nervous system. Genes Dev. 2000; (14): 2919–37.
7. Castellenos-Ortega MR, Cruz-Aguado R, Martinez-Marty L. Nerve growth factor: possibilities and limitations of its clinical application. Rev Neurol. 1999; 29 (5): 439–71.
8. Przedborski S, Jackson-Lewis V, Djaldetti R, Liberatore G, Vila M, Vukosavic S, Almer G. The parkinsonian toxin MPTP: action and mechanism. Restor Neurol Neurosci. 2000; 16 (2): 135–42.
9. Kreuter J. Nanoparticulate systems for brain delivery of drugs. Adv Drug Deliv Rev. 2001; (47): 65–81.
10. Kurakhmaeva K, Djindjikhashvili I, Petrov V, Balabanjan V, Voronina T, Trofimov S et al. Brain targeting of nerve growth factor using poly(butylcyanoacrilate) nanoparticles. J Drug Targ. 2009; (17): 564–74.
11. Limongi T, Rocchi A, Cesca F, Tan H, Miele E, Giugni A. Delivery of Brain-Derived Neurotrophic Factor by 3D Biocompatible Polymeric Scaffolds for Neural Tissue Engineering and Neuronal Regeneration. Mol Neurobiol. 2018 Mar 29; DOI: 10.1007/s12035-018-1022-z.
12. Tyler WJ, Perrett, Pozzo-Miller LD. The role of neurotrophins in neurotransmitter release. Neuroscience. 2002; (8): 524–31.
13. Schindowski K, Belarbi K, Buée L. Neurotrophic factors in Alzheimer's disease: role of axonal transport. Genes Brain Behav. 2008; (7): 43–56.
14. Bhurtel S, Katila N, Neupane S, Srivastav S, Park PH, Choi D. Methyleneblue protects dopaminergic neurons against MPTP-induced neurotoxicity by upregulating brain-derived neurotrophic factor. Ann N Y Acad Sci, 2018. DOI: 10.1111/nyas.13870. Доступно по ссылке: https://www.ncbi.nlm.nih.gov/pubmed/29882218#.
15. Chen JF, Wang M, Zhuang YH, Behnisch T. Intracerebroventricularly-administered 1-methyl-4-phenylpyridinium ion and brain derived neurotrophic factor affect catecholaminergic nerve terminals and neurogenesis in the hippocampus, striatum and substantia nigra. Neural Regen Res. 2018; (13): 717–26. DOI: 10.4103/1673-5374.230300.

EXPERIMENTAL STUDY OF DENDRIMER-BASED NANOPARTICLES WITH RGD-PEPTIDE FOR ANTICANCER RADIONUCLIDE THERAPY

Stukalov YuV[1], Grigorieva EYu[1] ✉, Smirnova AV[1,3], Lipengolts AA[1,2], Kubasova IYu[1], Pozdniakova NV[1], Lukashina MI[4]

[1] Blokhin National Medical Research Center of Oncology, Moscow

[2] Burnazyan Federal Medical Biophysical Center, Moscow

[3] Loginov Moscow Clinical Scientific Center, Moscow

[4] Dmitry Rogachev National Research Center of Pediatric Hematology, Oncology and Immunology, Moscow

Radionuclide therapy (RNT) is an effective modality for treating multiple metastases in patients with cancer. The list of malignancies that can be managed with RNT expands with the arrival of novel tumoritropic radiopharmaceuticals (RP). A versatile delivery platform capable of carrying various therapeutic and diagnostic radionuclides, as well as vector molecules needed to achieve sufficient specificity to tumor cells and ensure therapeutic efficacy may hold great promise for radiation therapy. The aim of this work was to assess the performance of a delivery system based on the original dendrimer. The dendrimer demonstrated low toxicity in mice (LD_{50} was 779 ± 111 mg/kg). To study the specificity of the dendrimer to tumor cells and its therapeutic efficacy, we used a nanoplatform (NP) composed of the dendrimer itself, the RGD peptide and ^{188}Re (^{188}Re-NP). Lewis lung carcinoma LLC1 was used as a tumor model. The biodistribution analysis revealed that the compound effectively accumulated in the tumor demonstrating a tumor-to-normal ratio >1 (relative to healthy organs and tissues) and retention time of at least 6 hours. Injections of 185 MBq/kg ^{188}Re-NP caused a statistically significant inhibition of tumor growth ($p < 0.05$) by day 7 following the injection (T/C = 5%), which remained stable for 6 days. Our findings suggest that the proposed dendrimer is a promising platform for RP delivery.

Keywords: dendrimer, RGD peptide, ^{188}Re, radionuclide therapy, biodistribution, research in animals, transplanted tumor model

✉ **Correspondence should be addressed:** Elena Yu. Grigorieva
Kashirskoe shosse 24, Moscow, 115478; grig-elen11@mail.ru

Received: 12.09.2018 **Accepted:** 11.10.2018

DOI: 10.24075/brsmu.2018.089

ЭКСПЕРИМЕНТАЛЬНЫЕ ИССЛЕДОВАНИЯ ДЕНДРИМЕРНОЙ НАНОКОНСТРУКЦИИ С RGD-ПЕПТИДОМ ДЛЯ РАДИОНУКЛИДНОЙ ТЕРАПИИ ОНКОЛОГИЧЕСКИХ ЗАБОЛЕВАНИЙ

Ю. В. Стукалов[1], Е. Ю. Григорьева[1] ✉, А. В. Смирнова[1,3], А. А. Липенгольц[1,2], И. Ю. Кубасова[1], Н. В. Позднякова[1], М. И. Лукашина[4]

[1] Национальный медицинский исследовательский центр онкологии имени Н. Н. Блохина, Москва

[2] Федеральный медицинский биофизический центр имени А. И. Бурназяна, Москва

[3] Московский клинический научно-практический центр имени А. С. Логинова, Москва

[4] Национальный медицинский исследовательский центр детской гематологии, онкологии и иммунологии имени Дмитрия Рогачева, Москва

Радионуклидная терапия (РНТ) является эффективным методом лечения множественных метастазов злокачественных опухолей. Расширение номенклатуры злокачественных новообразований, для которых возможно применение РНТ, происходит за счет создания новых туморотропных радиофармацевтических препаратов (РФП). Перспективно создание РФП на основе универсальной транспортной платформы, которая может быть модифицирована различными терапевтическими и диагностическими радионуклидами, а также векторными молекулами для достижения требуемой специфичности к опухолям и терапевтической эффективности. Целью работы было оценить в качестве такой транспортной платформы конструкцию на основе оригинального дендримера. Исследование на мышах показало его низкую токсичность ($ЛД_{50}$ достигало 779 ± 111 мг/кг). Туморотропность и терапевтическую эффективность дендримера исследовали на примере наноконструкции (НК) из дендримера, RGD-пептида и радионуклида ^{188}Re (^{188}Re-НК). В качестве опухолевой модели использовали мышиную карциному легкого Льюиса LLC1. Данные биораспределения предложенной НК показали ее эффективное накопление в опухоли с коэффициентом дифференциального накопления более 1 по отношению к основным органам и тканям и временем удержания в опухоли не менее 6 ч. Введение ^{188}Re-НК в дозе 185 МБк/кг мышам с подкожно трансплантированной опухолью статистически достоверно ($p < 0,05$) способствовало торможению роста опухоли к 7-м суткам после введения до T/C = 5%, сохраняющемуся в течение 6 суток. Проведенные исследования показали перспективность исследованного дендримера как транспортной платформы для РНТ.

Ключевые слова: дендример, RGD-пептид, ^{188}Re, радионуклидная терапия, биораспределение, исследование на животных, перевивные опухолевые модели

✉ **Для корреспонденции:** Елена Юрьевна Григорьева
Каширское шоссе, д. 24, г. Москва, 115478; grig-elen11@mail.ru

Статья получена: 12.09.2018 **Статья принята к печати:** 11.10.2018

DOI: 10.24075/vrgmu.2018.089

The use of drugs that can effectively and selectively accumulate in malignant tissue is a key to the success of radionuclide, neutron capture and photon activation therapies [1]. Recently, there has been a burgeoning interest in dendrimers [2–6], the spherical molecules sized 2–10 nm that have a large number of functional groups in their outer shell and, therefore, can be conjugated to a wide range of different molecules. This facilitates creation of targeted drug delivery platforms by attaching a tumor-specific agent and a tumoricidal or a diagnostic agent to the dendrimer. Previously, we demonstrated the feasibility and promise of this approach for the therapy and diagnosis of cancer [7–8]. Such platforms can exploit the affinity of cancer cell receptors to a number of low molecular weight compounds. For example, dendrimers functionalized with β-estradiol have been shown to effectively accumulate in transplanted breast adenocarcinoma cells (Ca755) [9]. In the study below, the role of a target-specific component of a tested dendrimer-based platform was played by the RGD-peptide capable of biding to the integrins present on the surface of cancer cells [10–17].

This work aimed to investigate the feasibility of using the original dendrimer-based nanoplatform in radiation therapy and cancer diagnostics in a series of in vivo experiments.

METHODS

The original nanoplatform (NP) consisted of a first-generation dendrimer covalently conjugated to safranin, which binds sodium perrhenate, and a tumor-specific RGD peptide. The dendrimer itself was previously described in [7]. Fig. 1 shows the NP; its structure was confirmed by nuclear magnetic resonance spectroscopy.

The radionuclide ^{188}Re with a half-life of 17 hours was used as a therapeutic agent. Its decay is accompanied by the emission of β-radiation with energies of 2.12 MeV producing the tumoricidal effect and γ-radiation with energies of 155 keV (15.2%) detectable by a γ-camera that records distribution of a radiopharmaceutical agent in a patient's body 18–23]. The GREN-1 ^{188}W/^{188}Re generator (Leipunsky Institute of Physics and Power Engineering, Russia) used in this study was generating ^{188}Re over the course of 4–6 months [24]; therefore, the studied compounds could be labeled with ^{188}Re immediately before use.

Radiolabeling was performed by combining the studied NP and ^{188}Re sodium perrhenate eluted from the generator. The amount of ^{188}RE-NP in the working solution was calculated based on the molarity of the introduced ^{188}Re (1 MBq ^{188}Re — 0.00015 nM). To make sure every ^{188}Re was bound, NP were taken at 100-fold excess. The isotope was added to the studied compounds *ex tempore*. Nuclear magnetic resonance spectra were recorded by the WH-360 spectrometer (Bruker; Germany) operating at 360 MHz. Thin-layer chromatography was performed using Si 60-coated plates (particle size of 5–17 μm) (Fluka; USA). Chromatograms were developed in iodine vapor.

Due to the high costs of the RGD peptide, acute toxicity of ^{188}RE-NP was inferred from the toxicity of the unmodified dendrimer measured in healthy male Balb/c mice weighing 19–21 g. (Stolbovaya nursery of the Research Center for Biomedical Technologies, Russia). The experiments were conducted in full compliance with ethical principles and guidelines for animal research [25].

The animals were kept in the conventional vivarium under natural light conditions. For the experiment, the mice were distributed into 10 groups of 6. Each group consisted of animals of the same age. The dendrimer was dissolved in 0.9% NaCl solution containing 10% of DMSO. The animals received a single intraperitoneal injection of 0.2 ml of the dendrimer solution. In total, ten different dendrimer doses were tested for toxicity: 62.5 mg/kg; 125 mg/kg; 187.5 mg/kg; 250 mg/kg; 375 mg/kg; 500 mg/kg; 750 mg/kg; 1,000 mg/kg; 1,250 mg/kg; and 1,500 mg/kg. The general health of mice and their behavior were monitored for 30 days following the injection. All changes were recorded on a daily basis. The animals who did not survive the experiment were necropsied and their internal organs were examined. Thirty days after the injection, the rest of the mice were euthanized by cervical dislocation. Acute toxicity of the studied compound was assessed based on the number of animals who died during the experiment, the day of their death, clinical manifestations of the intoxication, changes in behavior, and macroscopic examination of the organs and tissues conducted post-mortem [26–28]. Toxic doses were calculated in BioStat Pro 2008 5.0.1 (AnalystSoft; USA).

Biodistribution of the synthesized ^{188}RE-NP was compared to that of ^{188}Re sodium perrhenate in animals with subcutaneously transplanted LLC1 cells from the collection of cancer cell lines of Blokhin National Medical Research Center of Oncology, Russia. The choice of the cell line was dictated by the fact that the αvβ3 receptor, which is an RGD-binding integrin, has been reported to homogenously distribute in the LLC1 tumor [29]. Male C57Bl/6 mice weighing 19–21 g were divided into groups of 6. The suspension of cancer cells (4, 000, 000 cells per animal) was transplanted subcutaneously in the right thigh of each mouse. On day 10 following the inoculation, the mice received 0.2 ml of ^{188}RE-NP (1.85 MBq per mouse, or 92.5 MBq/kg) injected intravenously. The mice were decapitated 1, 3, 6, 9, 13, and 24 h after the ^{188}RE-NP injection. Tissue and arterial blood samples were collected during autopsy. Radioactivity of the injected doses was determined using the dose calibrator ISOMED 2010 (MED Nuklear-Medizintechnik Dresden GmbH; Germany). Distribution of ^{188}RE-NP in the biological tissue of mice was studied by direct radiometric measurements. The emitted radiation was measured by WIZARD 2480 scintillation

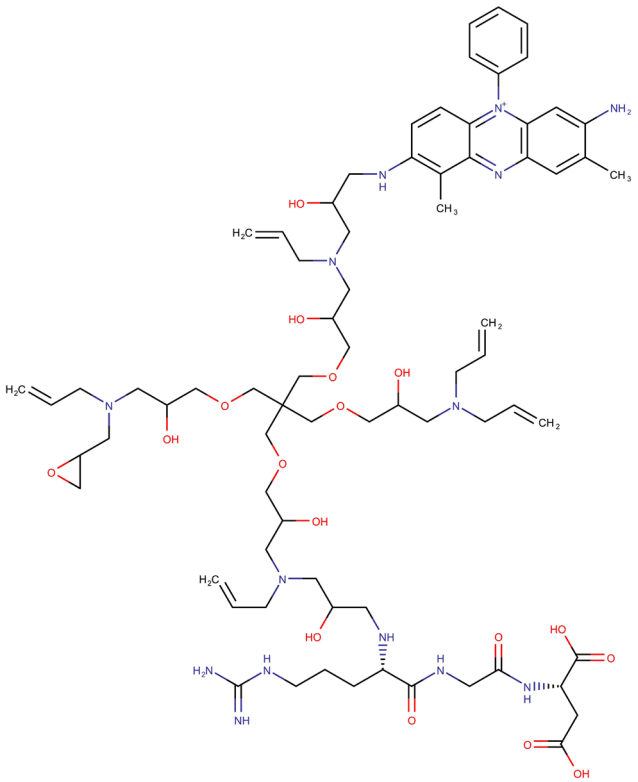

Fig. 1. The nanoplatform based on the dendrimer conjugated to the RGD peptide

gamma-counter (Perkin Elmer; USA). ^{188}RE-NP accumulation was evaluated based on the amount of ^{188}Re in 1 g of the tissue/organ relative to its injected amount.

The therapeutic efficacy of ^{188}RE-NP was tested in male C57Bl/6 mice weighing 20–22 g. The mice were distributed into groups of 8. Two days after the subcutaneous transplantation of the LLC1 cells, the mice received single 0.2 ml doses of ^{188}Re sodium perrhenate and ^{188}RE-NP in 0.9% NaCl solution. The following ^{188}Re doses were studied for their therapeutic effect: 15 MBq/kg, 92.5 MBq/kg, and 185 MBq/kg (0.3 MBq, 1.85 MBq, and 3.7 MBq per animal, respectively). The control group received 0.2 ml of 0.9% NaCl solution. The size and volume of tumors were measured on a daily basis throughout the experiment. The T/C value (a standard indicator of a tumoricidal effect) was calculated for the control and experimental groups using the equation [30]:

$$T/C = 100 \cdot V_{exper} / V_{contr},$$

where V_{exper} is an average tumor volume in the experimental group and V_{contr} is an average tumor volume in the control group.

The data were analyzed in OriginPro 8.0 (OriginLab; USA) and Excel 2003 (Microsoft; USA). Statistical significance of the obtained results was tested using the nonparametric Mann-Whitney U test; differences were considered significant at $p \leq 0.05$.

RESULTS

The acute toxicity of the studied compound was assessed based on the number of animals who did not survive the experiment and the day of their death following the dendrimer injection. We found that the lowest lethal dose of the dendrimer was 500 mg/kg; it killed 2 of 6 animals. Four of six mice died at a dose of 1,000 mg/kg. A dose of 1,500 mg/kg was lethal

Table 1. Dynamics of ^{188}Re-NP and ^{188}Re accumulation in the organs and tissues of mice with subcutaneously transplanted LLC1 cells (expressed as % from the injected amount per 1 g of the organ/tissue)

Tissue/organ	Compound	Time elapsed from the injection					
		1 h	3 h	6 h	9 h	12 h	24 h
Blood	^{188}Re-NP	14.90 ± 0.20	10.40 ± 0.51	7.76 ± 0.25	4.42 ± 0.24	2.31 ± 0.20	1.32 ± 0.12
	^{188}Re	15.04 ± 0.12	9.40 ± 0.80	7.36 ± 0.20	5.00 ± 0.34	2.64 ± 0.48	0.94 ± 0.24
		p >0 .2	p > 0.2	p > 0.1	p > 0.1	p > 0.2	p > 0.1
Liver	^{188}Re-NP	5.22 ± 0.36	4.09 ± 0.13	3.69 ± 0.23	3.06 ± 0.25	1.02 ± 0.07	0.07 ± 0.01
	^{188}Re	5.44 ± 0.29	4.66 ± 0.42	3.53 ± 0.18	1.98 ± 0.51	1.36 ± 0.24	0.15 ± 0.05
		p > 0.2	p > 0.2	p > 0.2	p > 0.1	p > 0.1	p > 0.1
Kidneys	^{188}Re-NP	7.27 ± 0.42	5.04 ± 0.21	4.47 ± 0.29	3.32 ± 0.35	1.84 ± 0.19	0.35 ± 0.07
	^{188}Re	7.34 ± 0.46	5.35 ± 0.56	3.67 ± 0.35	2.08 ± 0.41	1.44 ± 0.25	0.35 ± 0.07
		p > 0.8	p > 0.5	p > 0.1	p > 0.1	p > 0.1	p > 0.6
Lungs	^{188}Re-NP	10.01 ± 0.50	7.46 ± 0.31	5.68 ± 0.16	4.61 ± 0.32	2.75 ± 0.23	0.34 ± 0.06
	^{188}Re	10.09 ± 0.50	7.79 ± 0.52	5.52 ± 0.26	3.31 ± 0.38	1.99 ± 0.33	0.30 ± 0.05
		p > 0.5	p > 0.2	p > 0.3	p > 0.1	p > 0.1	p > 0.2
Spleen	^{188}Re-NP	9.77 ± 1.17	7.66 ± 0.43	4.74 ± 0.35	4.15 ± 0.30	2.16 ± 0.06	0.29 ± 0.05
	^{188}Re	9.52 ± 0.40	6.90 ± 0.37	4.72 ± 0.47	3.01 ± 0.20	1.95 ± 0.33	0.31 ± 0.11
		p > 0.8	p > 0.1	p > 0.8	p > 0.1	p > 0.2	p > 0.8
Femoral bone	^{188}Re-NP	5.61 ± 5.61	3.77 ± 3.77	3.14 ± 3.14	2.13 ± 2.13	1.45 ± 1.45	0.44 ± 0.44
	^{188}Re	5.02 ± 0.29	3.98 ± 0.38	2.77 ± 0.21	1.58 ± 0.06	1.11 ± 0.09	0.44 ± 0.05
		p > 0.1	p > 0.5	p > 0.1	p > 0.1	p > 0.1	p > 0.8
Tumor	^{188}Re-NP	8.16 ± 0.26	8.20 ± 0.14	8.24 ± 0.06	6.54 ± 0.35	3.15 ± 0.35	1.17 ± 0.07
	^{188}Re	6.06 ± 0.17	3.82 ± 0.26	2.32 ± 0.42	1.90 ± 0.16	1.14 ± 0.09	0.66 ± 0.07
		p < 0.03	p < 0.01	p < 0.01	p < 0.01	p < 0.05	p < 0.05

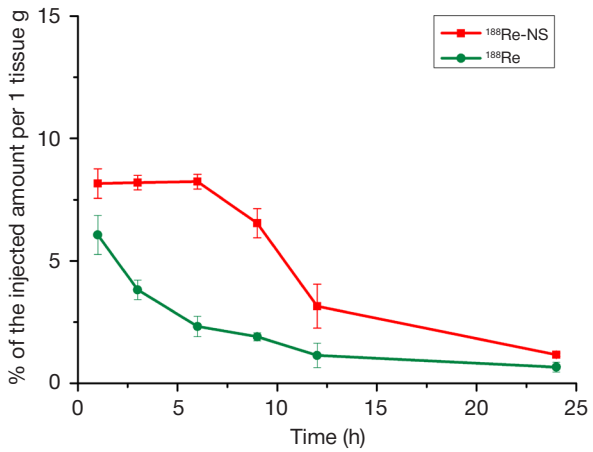

Fig. 2. Dynamics of ^{188}Re-NP and ^{188}Re accumulation (% of the injected amount per 1 g of tissue) in the subcutaneously transplanted LLC1male in male C57Bl/6 mice

for the entire group. Lethal dendrimer doses caused transient motor excitation for the first 30 min that subsequently turned into sopor. The mice died within 144 hours after the injection depending on the dose of the dendrimer. A transient loss of weight (5–8%) and increased motor activity were observed in the surviving mice during the first 5 days following the injection. Necropsy revealed no visible signs of pathology in the heart, kidneys, spleen, and lungs of the animals; no visible pathology or hyperthermia were observed in the peritoneum; the liver was enlarged and its edges were blunt. The sublethal doses of the dendrimer did not induce any visible changes in the behavior or general health of mice: no ataxia or local paresis were observed. The mice were gaining weight at the rate of the control group. Their skin condition was normal. No macroscopic changes were noticed in the internal organs during autopsy. Based on the number of dead animals in each of 10 experimental groups, toxic dendrimer doses were calculated for mice: LD_{10} = 270 ± 92 mg/kg; LD_{16} = 382 ± 94 mg/kg; LD_{50} = 779 ± 111 mg/kg; LD_{84} = 1177 ± 196 mg/kg; LD_{90} = 1289 ± 260 mg/kg; LD_{100} = 1376 ± 367 mg/kg.

Table 1 compares the dynamics of ^{188}RE-NP and ^{188}Re-sodium perrhenate accumulation over time in mice with subcutaneously transplanted LLC1 carcinoma. The only significant difference was revealed for drug accumulation in the tumor, in contrast to healthy tissue. The dynamics of ^{188}Re-NP and ^{188}Re-sodium perrhenate accumulation in LLC1 are presented in Fig. 2

Because ^{188}Re-NP is intended for anticancer radiation therapy, its tumor-to-normal uptake is an important pharmacokinetic characteristic. Calculated tumor-to-normal ratio (T/N) values for the most important organs are shown in Table 2. In the case of ^{188}Re-NP, the T/N value was > 1 for almost all organs and tissues 3 h after the injection. This indicates more vigorous clearance of the substance from healthy organs than from the tumor. The rate of ^{188}Re clearance from the tumor was comparable to that measured for the liver and the femoral bone.

The therapeutic efficacy of ^{188}Re-NP was being studied for 30 days following tumor transplantation. A single injection of the compound produced a marked tumoricidal effect ($p < 0.05$) throughout the entire observation period only at doses of 185 MBq/kg (Table 3, Fig. 3). Single doses of ^{188}Re-sodium perrhenate taken at 185 MBq/kg had no therapeutic effect at all (Fig. 4). The T/C values for the studied ^{188}Re doses are presented in Table 3.

The observed tumoricidal effect was dose-dependent. It was significant at a ^{188}Re-NP dose of 185 MBq/kg, weak at 92.5 MBq/kg, and insignificant at 15 MBq/kg. The minimal effective therapeutic concentration of ^{188}Re-NP was determined based on the curves demonstrating the dynamics of tumor growth.

DISCUSSION

This study shows that the toxicity of the proposed dendrimer is comparable to the toxicity of its analogs from the same class of compounds [31].

Our findings suggest that ^{188}Re-NP taken up by the tumor is retained there for up to 6 hours following the injection. During this time period, the amount of ^{188}Re-NP in the tumor remains high, making 8.2% of the injected amount. This may indicate the stability of the bonds between ^{188}Re-NP and the tumor tissue. The dynamics of ^{188}Re sodium perrhenate accumulation does not follow the same pattern. The maximum ratio of ^{188}Re-NP to ^{188}Re sodium perrhenate uptake by the tumor was 3.55 ± 0.660 6 hours after the injection.

The ^{188}Re-NP dose of 185 MBq/kg at which the most significant tumoricidal effect was observed in mice was converted to a human dose equivalent of 15.42 MBq/kg. This is lower than the standard doses of radiopharmaceutical agents used in radiation therapy (44–47 MBq/kg) [32]. Consequently, the effective radiation dose can be reduced if ^{188}Re-NP is used as a radiopharmaceutical agent. Another advantage of the proposed platform is its low toxicity. The studied substance was taken at 100-fold excess to ensure the complete binding of ^{188}Re; the concentration of NP at 185 MBq/kg was

Table 2. Comparison of tumor-to-normal uptake ratio of ^{188}Re-NP and ^{188}Re by the organs and tissues of experimental mice

Tissue/organ	Compound	Time elapsed from the injection					
		1 h	3 h	6 h	9 h	12 h	24 h
Tumor/blood	^{188}Re-NP	0.55 ± 0.02	0.79 ± 0.04	1.06 ± 0.04	1.48 ± 0.04	1.36 ± 0.06	0.89 ± 0.11
	^{188}Re	0.40 ± 0.01	0.41 ± 0.06	0.32 ± 0.07	0.38 ± 0.05	0.45 ± 0.11	0.72 ± 0.18
		$p > 0.1$	$p < 0.05$	$p < 0.004$	$p < 0.004$	$p < 0.004$	$p > 0.1$
Tumor/liver	^{188}Re-NP	1.57 ± 0.14	2.01 ± 0.09	2.24 ± 0.13	2.15 ± 0.24	3.09 ± 0.29	16.55 ± 2.7
	^{188}Re	1.11 ± 0.04	0.82 ± 0.02	0.66 ± 0.14	1.02 ± 0.37	0.86 ± 0.19	4.65 ± 1.25
		$p < 0.05$	$p < 0.004$	$p < 0.001$	$p < 0.004$	$p < 0.001$	$p < 0.001$
Tumor/kidneys	^{188}Re-NP	1.12 ± 0.07	1.63 ± 0.04	1.85 ± 0.11	1.99 ± 0.22	1.73 ± 0.30	3.42 ± 0.85
	^{188}Re	0.83 ± 0.07	0.72 ± 0.08	0.63 ± 0.09	0.95 ± 0.27	0.81 ± 0.19	1.91 ± 0.15
		$p < 0.004$	$p < 0.004$	$p < 0.004$	$p < 0.004$	$p < 0.05$	$p < 0.05$
Tumor/lungs	^{188}Re-NP	0.82 ± 0.06	1.10 ± 0.06	1.45 ± 0.05	1.43 ± 0.17	3.86 ± 0.80	13.92 ± 2.56
	^{188}Re	0.60 ± 0.04	0.49 ± 0.05	0.42 ± 0.09	0.58 ± 0.10	0.59 ± 0.14	2.18 ± 0.17
		$p < 0.05$	$p < 0 . 004$	$p < 0.004$	$p < 0.004$	$p < 0.02$	$p < 0.002$
Tumor/spleen	^{188}Re-NP	0.84 ± 0.11	1.07 ± 0.04	1.75 ± 0.12	1.58 ± 0.05	1.46 ± 0.12	4.09 ± 0.80
	^{188}Re	0.64 ± 0.04	0.55 ± 0.02	0.49 ± 0.04	0.63 ± 0.08	0.60 ± 0.14	2.26 ± 0.64
		$p < 0.05$	$p < 0.004$	$p < 0.004$	$p < 0.004$	$p < 0.004$	$p < 0.004$
Tumor/femoral bone	^{188}Re-NP	1.46 ± 0.10	2.17 ± 0.01	2.64 ± 0.23	3.08 ± 0.22	2.18 ± 0.32	2.67 ± 0.15
	^{188}Re	1.21 ± 0.10	0.97 ± 0.13	0.85 ± 0.21	1.20 ± 0.14	1.04 ± 0.14	1.51 ± 0.31
		$p < 0.05$	$p < 0.004$	$p < 0.004$	$p < 0.004$	$p < 0.05$	$p < 0.004$
Tumor ^{188}Re-NP/Tumor ^{188}Re		1.35 ± 0.05	2.15 ± 0.19	3.55 ± 0.66	3.45 ± 0.32	2.76 ± 0.51	1.79 ± 0.24

Table 3. The therapeutic effect of the ^{188}Re-NP against the LLC1 carcinoma

Time elapsed from the injection, days	7 days			14 days			18 days		
The dose of ^{188}Re, MBq/kg	15	92.5	185	15	92.5	185	15	92.5	185
T/C, %	100	41	5	74	55	13	87	75	20

Note: The table shows the results of therapeutic efficacy assessment on days 7, 14 and 18 after drug administration.

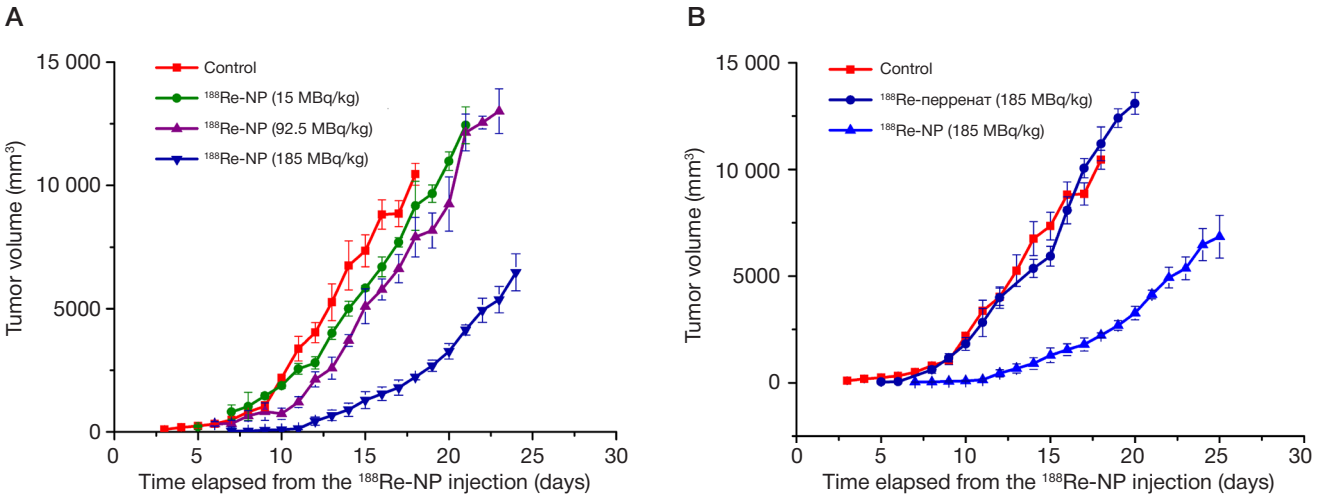

Fig. 3. The growth dynamics of the subcutaneously transplanted LLC1 tumor in C57Bl/6 mice following a single injection of ^{188}Re-NP taken at different ^{188}Re doses (**A**) and a single injection of ^{188}Re sodium perrhenate and ^{188}Re -NP (^{188}Re dose = 185 MBq/kg) (**B**)

4.05 • 10^{-3} mg/kg (or 2.16 • 10^{-3} mg/kg of the dendrimer), which is lower than LD_{10} by 5 orders of magnitude. Our findings suggest that the proposed NP may hold promise as a potent radiopharmaceutical.

CONCLUSIONS

This study demonstrates the feasibility of the proposed dendrimer-based platform for targeted drug delivery of tumoricidal agents. We have established the minimally effective therapeutic dose of ^{188}Re in the studied compound and revealed that the synthesized dendrimer exhibits dose-dependent activity against tumor cells. Acute toxicity tests conducted in mice have shown that the ^{188}Re-NP platform is lowly toxic and ensures a considerable tumoricidal effect at doses much lower than LD_{10}. The levels of ^{188}Re-NP accumulation in the tumor, as well as the value of the T/N ratio, lead us to conclude that the compound can be safely used to enhance the therapeutic dose of β-radiation in the tumor. The ^{188}Re component of the ^{188}Re-NP composition taken at a dose of 185 Mbq/kg induces a marked tumoricidal effect 18 days following its administration.

Литература

1. Kulakov VN, Lipengolts AA, Grigorieva EY, Shimanovskii NL. Pharmaceuticals for Binary Radiotherapy and Their Use for Treatment of Malignancies (A Review). Pharm Chem J. 2016 Sep 8; 50 (6): 388–93.
2. Rakesh Kumar Tekade, Palanirajan Vijayaraj Kumar, Narendra Kumar Jain. Dendrimers in Oncology: An Expanding Horizon. Chem Rev. 2009; 109: 49–87.
3. Wu L-P, Ficker M, Christensen JB. Dendrimers in Medicine: Therapeutic Concepts and Pharmaceutical Challenges. Bioconjugate Chem. 2015; 26: 1198–211.
4. Olson ES, Jiang T, Aguilera T, Nguyen QT, Ellies LG, Scadeng M, et al. Activatable cell penetrating peptides linked to nanoparticles as dual probes for in vivo fluorescence and MR imaging of proteases. Proc Natl Acad Sci. 2010; 107 (9): 4311–6.
5. Palmerston Mendes L, Pan J, Torchilin V. Dendrimers as Nanocarriers for Nucleic Acid and Drug Delivery in Cancer Therapy. Molecules. 2017; 22 (9): 1401.
6. Xu L, Yeudall WA, Yang H. Folic acid-decorated polyamidoamine dendrimer exhibits high tumor uptake and sustained highly localized retention in solid tumors: Its utility for local siRNA delivery. Acta Biomater. 2017; (57): 251–61.
7. Stukalov YuV, Grigorieva EYu, Kulakov VN, Baryshnikov AYu. Transport platform synthesis for drug development. Pharmaceutical chemistry journal. 2017; 51 (6): 480–1.
8. Григорьева Е. Ю., Стукалов Ю. В., Смирнова А. В., Колдаева Е. Ю., Калыгина Н. С., Кулаков В. Н. и др. Цитотоксическое действие конструкций на основе дендримеров с 188Re с моноклональными антителами анти-ICO-25 (MUC1) и анти-ICO-80 (CD5) На моделях клеточных линий SKOV-3 (рак яичника) и Jurkat (Т-лимфобластная лимфома). Химико-фармацевтический журнал. 2018; 52 (8): 3–6.
9. Григорьева Е. Ю., Стукалов Ю. В., Колдаева Е. Ю. Конструкции на основе дендримеров нового класса для таргетной радиотерапии онкологических заболеваний. Российский биотерапевтический журнал. 2009; 8 (1): 5–6.
10. Domingo-Espín J, Petegnief V, de Vera N. RGD-based cell ligands for cell-targeted drug delivery act as potent trophic factors. Nanomedicine: Nanotechnology, Biology, and Medicine. 2012; (8): 1263–6.
11. Берман А. Е., Козлова Н. И., Морозевич Г. Е. Интегрины как потенциальная мишень для целевой терапии рака. Биомедицинская химия. 2013; 59 (3): 239–48.
12. Miller LM, Pritchard JM, Macdonald SJF, Jamieson C, Watson AJB. The Emergence of Small Molecule Non-RGD-mimetic Inhibitors for RGD Integrins Journal of Medicinal Chemistry. 2017; 60 (8): 3241–51.
13. Hwang R, Varner J. The role of integrins in tumor angiogenesis. Hematol Oncol Clin North Am. 2004; 18 (5): 991–1006.

14. Koistinen P, Ahonen M, Kähäri VM, Heino J. AlphaV integrin promotes in vitro and in vivo survival of cells in metastatic melanoma. Int J Cancer. 2004; 112 (1): 61–70.
15. Kuphal S, Bauer R, Bosserhoff AK. Integrin signaling in malignant melanoma. Cancer Metastasis Rev. 2005; 24 (2): 195–222.
16. Veeravagu A, Liu Z, Niu G, Chen K, Jia B, Cai W et al. Integrin alphavbeta3-targeted radioimmunotherapy of glioblastoma multiforme. Clin Cancer Res. 2008; (14): 7330–9.
17. Landen CN, Kim TJ, Lin YG, Merritt WM, Kamat AA, Han LY et al. Tumour-selective response to antibody-mediated targeting of alphavbeta3 integrin in ovarian cancer. Neoplasia. 2008; 10 (11): 1259–67.
18. Beiki D, Tajik M, Haddad P, Fallahi B, Arefpour AM, Mirzaei H et. al. Effectiveness and complications of 188Re-HEDP in palliative treatment of diffuse skeletal metastases. Iran J Nucl Med. 2015; 23 (1): 44–8.
19. Erfani M, Doroudi A, Dinari MA, Shirmardi SP. Preparation of a rhenium-188 labeled bisphosphonate for bone pain palliation therapy. Journal of Radioanalytical and Nuclear Chemistry. 2015; 303 (3): 2027–32.
20. Zamora PO, Gulhke S, Bender H. Experimental radiotherapy of receptor-positive human prostate adenocarcinoma with 188Re-RC-160, a directly-radiolabeled somatostatin analogue. Int J Cancer. 1999; (6): 214–20.
21. Molina-Trinidad EM, Arteaga de Murphy C, Ferro-Flores G. Radiopharmacokinetic and dosimetric parameters of 188Re-lanreotide in athymic mice with induced human cancer tumors. Int J Pharm. 2006; (310): 125–30.
22. Krylov V, Kochetova T, Smolyarchuk M, Petriev V, Kanygin V, Alexandrova A et al. Evaluation of 188Re-khedp (phosphoren) for palliative treatment in patients with bone metastases., World Journal of Nuclear Medicine. 2013; 12 (2): 255–6.
23. Kochetova T, Smolyarchuk M, Krylov V, Voloznev V, Lunev A, Petriev VM. 188Re-zoledronic acid: first in man study. World Journal of Nuclear Medicine. 2013; 12 (2): 228–9.
24. Konior M, Iller E. Classic Radionuclide 188W/188Re Generator (Experiments, Design and Construction). Mod Chem appl. 2014; (2): 143.
25. Европейская конвенция по защите позвоночных животных, используемых для экспериментальных и других научных целей, ЕЭС, Страсбург, 1985 г. Ланималогия. 1993; (1): 29 с.
26. Беленький М. Л. Элементы количественной оценки фармакологического эффекта: Л.: Изд-во «МедГиз», 1968; 151 с.
27. Гуськова Т. А. Токсикология лекарственных средств: М.: Изд-во «Русский врач», 2003; 154 с.
28. Трахтенберг И. А., Сова А. Е., Шефтель В. О., Оникиенко Ф. А. Проблема нормы в токсикологии. М.: Изд-во «Медицина», 1992; 208 с.
29. Seguin J, Nicolazzi C, Mignet N, Scherman D, Chabot GG. Vascular density and endothelial cell expression of integrin alpha v beta 3 and E-selectin in murine tumours. Tumour Biol. 2012; 33 (5): 1709–17.
30. Трещалина Е. М., Жукова О. С., Герасимова Г. К., Андронова Н. В. и др. Методические рекомендации по доклиническому изучению противоопухолевой активности лекарственных средств. В книге: Миронов А. Н., Бунатян Н. Д. и др., редакторы. Руководство по проведению доклинических исследований лекарственных средств. М.: Гриф и К., 2012; с. 642–657.
31. Колдаева Е. Ю., Григорьева Е. Ю., Стукалов Ю. В. Сравнительная токсикология наноконструкций на основе дендримеров для таргетной радиотерапии в онкологии. Российский биотерапевтический журнал. 2010; 9 (3): 13–14.
32. Argyrou M, Valassi A, Andreou M, Lyra M. Rhenium-188 Production in Hospitals, by W-188/Re-188 Generator, for Easy Use in Radionuclide Therapy. Int J Mol Imaging. 2013; (2013): 1–7.

References

1. Kulakov VN, Lipengolts AA, Grigorieva EYu, Shimanovskii NL. Pharmaceuticals for Binary Radiotherapy and Their Use for Treatment of Malignancies (A Review). Pharm Chem J. 2016 Sep 8; 50 (6): 388–93.
2. Rakesh Kumar Tekade, Palanirajan Vijayaraj Kumar, Narendra Kumar Jain. Dendrimers in Oncology: An Expanding Horizon. Chem Rev. 2009; 109: 49–87.
3. Wu L-R, Ficker M, Christensen JB. Dendrimers in Medicine: Therapeutic Concepts and Pharmaceutical Challenges. Bioconjugate Chem. 2015; 26: 1198–211.
4. Olson ES, Jiang T, Aguilera T, Nguyen QT, Ellies LG, Scadeng M, et al. Activatable cell penetrating peptides linked to nanoparticles as dual probes for in vivo fluorescence and MR imaging of proteases. Proc Natl Acad Sci. 2010; 107 (9): 4311–6.
5. Palmerston Mendes L, Pan J, Torchilin V. Dendrimers as Nanocarriers for Nucleic Acid and Drug Delivery in Cancer Therapy. Molecules. 2017; 22 (9): 1401.
6. Xu L, Yeudall WA, Yang H. Folic acid-decorated polyamidoamine dendrimer exhibits high tumor uptake and sustained highly localized retention in solid tumors: Its utility for local siRNA delivery. Acta Biomater. 2017; (57): 251–61.
7. Stukalov YuV, Grigorieva EYu, Kulakov VN, Baryshnikov AYu. Transport platform synthesis for drug development. Pharmaceutical chemistry journal. 2017; 51 (6): 480–1.
8. Grigorieva EYu, Stukalov YV, Smirnova AV, Koldaeva EY, Kalygina NS, Kulakov VN et al. Cytotoxicity of Conjugates of 188Re-Labeled Dendrimers and Monoclonal Antibodies Anti-ICO-25 (MUC1) and Anti-ICO-80 (CD5) Against SKOV-3 (Ovary Cancer) and Jurkat Tumor Cell Lines (T-Lymphoblstic Lymphoma). Pharm Chem J. 2018; 52 (8): 681–4.
9. Grigorieva EYu, Stukalov YuV, Koldaeva EYu. Konstruktsii na osnove dendrimerov novogo klassa dlya targetnoy radioterapii onkologicheskikh zabolevaniy. Rossiyskiy bioterapevticheskiy zhurnal. 2009; 8 (1): 5–6. Russian.
10. Domingo-Espín J, Petegnief V, de Vera N. RGD-based cell ligands for cell-targeted drug delivery act as potent trophic factors. Nanomedicine: Nanotechnology, Biology, and Medicine. 2012; (8): 1263–6.
11. Berman AE, Kozlova, NI, Morozevich GE. Integrins as a potential target for targeted anticancer therapy. Biochem. Moscow Suppl Ser B. 2012; 6 (3): 205–10.
12. Miller LM, Pritchard JM, Macdonald SJF, Jamieson C, Watson AJB. The Emergence of Small Molecule Non-RGD-mimetic Inhibitors for RGD Integrins Journal of Medicinal Chemistry. 2017; 60 (8): 3241–51.
13. Hwang R, Varner J. The role of integrins in tumor angiogenesis. Hematol Oncol Clin North Am. 2004; 18 (5): 991–1006.
14. Koistinen P, Ahonen M, Kähäri VM, Heino J. AlphaV integrin promotes in vitro and in vivo survival of cells in metastatic melanoma. Int J Cancer. 2004; 112 (1): 61–70.
15. Kuphal S, Bauer R, Bosserhoff AK. Integrin signaling in malignant melanoma. Cancer Metastasis Rev. 2005; 24 (2): 195–222.
16. Veeravagu A, Liu Z, Niu G, Chen K, Jia B, Cai W et al. Integrin alphavbeta3-targeted radioimmunotherapy of glioblastoma multiforme. Clin Cancer Res. 2008; (14): 7330–9.
17. Landen CN, Kim TJ, Lin YG, Merritt WM, Kamat AA, Han LY et al. Tumour-selective response to antibody-mediated targeting of alphavbeta3 integrin in ovarian cancer. Neoplasia. 2008; 10 (11): 1259–67.
18. Beiki D, Tajik M, Haddad P, Fallahi B, Arefpour AM, Mirzaei H et. al. Effectiveness and complications of 188Re-HEDP in palliative treatment of diffuse skeletal metastases. Iran J Nucl Med. 2015; 23 (1): 44–8.
19. Erfani M, Doroudi A, Dinari MA, Shirmardi SP. Preparation of a rhenium-188 labeled bisphosphonate for bone pain palliation therapy. Journal of Radioanalytical and Nuclear Chemistry. 2015; 303 (3): 2027–32.
20. Zamora PO, Gulhke S, Bender H. Experimental radiotherapy of

receptor-positive human prostate adenocarcinoma with 188Re-RC-160, a directly-radiolabeled somatostatin analogue. Int J Cancer. 1999; (6): 214–20.
21. Molina-Trinidad EM, Arteaga de Murphy C, Ferro-Flores G. Radiopharmacokinetic and dosimetric parameters of 188Re-lanreotide in athymic mice with induced human cancer tumors. Int J Pharm. 2006; (310): 125–30.
22. Krylov V, Kochetova T, Smolyarchuk M, Petriev V, Kanygin V, Alexandrova A et al. Evaluation of 188Re-khedp (phosphoren) for palliative treatment in patients with bone metastases., World Journal of Nuclear Medicine. 2013; 12 (2): 255–6.
23. Kochetova T, Smolyarchuk M, Krylov V, Voloznev V, Lunev A, Petriev VM. 188Re-zoledronic acid: first in man study. World Journal of Nuclear Medicine. 2013; 12 (2): 228–9.
24. Konior M, Iller E. Classic Radionuclide 188W/188Re Generator (Experiments, Design and Construction). Mod Chem appl. 2014; (2): 143.
25. Evropejskaja konvencija po zashhite pozvonochnyh zhivotnyh, ispol'zuemyh dlja jeksperimental'nyh i drugih nauchnyh celej, EJeS, Strasburg, 1985 g. Lanimalogija. 1993; (1): 29 s.
26. Belenkiy ML. Jelementy kolichestvennoj ocenki farmakologicheskogo jeffekta: L.: Izd-vo «MedGiz», 1968; 151 s.
27. Guskova TA. Toksikologiya lekarstvennyh sredstv: M.: Izd-vo «Russkij vrach», 2003; 154 s.
28. Trahtenberg IA, Sova AE, Sheftel VO, Onikienko FA. Problema normy v toksikologii. M.: Izd-vo «Medicina», 1992; 208 s.
29. Seguin J, Nicolazzi C, Mignet N, Scherman D, Chabot GG. Vascular density and endothelial cell expression of integrin alpha v beta 3 and E-selectin in murine tumours. Tumour Biol. 2012; 33 (5): 1709–17.
30. Treshhalina EM, Zhukova OS, Gerasimova GK, Andronova NV i dr. Metodicheskie rekomendacii po doklinicheskomu izucheniju protivoopuholevoj aktivnosti lekarstvennyh sredstv. V knige: Mironov AN, Bunatjan ND i dr., redaktory. Rukovodstvo po provedeniju doklinicheskih issledovanij lekarstvennyh sredstv. M.: Grif i K., 2012; S. 642–657.
31. Koldaeva EYu, Grigorieva EYu, Stukalov YuV. Sravnitel'naja toksikologija nanokonstrukcij na osnove dendrimerov dlja targetnoj radioterapii v onkologii. Rossijskij Bioterapevticheskij Zhurnal. 2010; 9 (3): 13–14.
32. Argyrou M, Valassi A, Andreou M, Lyra M. Rhenium-188 Production in Hospitals, by W-188/Re-188 Generator, for Easy Use in Radionuclide Therapy. Int J Mol Imaging. 2013; (2013): 1–7.

POLY(3-HYDROXYALKANOATE)-BASED DRUG FORMULATIONS: THE MICRO- AND NANOSTRUCTURE

Bonartsev AP[1,2] ✉, Bonartseva GA[2], Voinova VV[1], Kirpichnikov MP[1], Shaitan KV[1]

[1] Faculty of Biology, Lomonosov Moscow State University, Moscow

[2] A. N. Bach Institute of Biochemistry, Research Center of Biotechnology, RAS, Moscow

Biodegradable and biocompatible polymers referred to as polyhydroxyalkanoates (PHAs) are extensively used in the production of pharmaceutical drugs to ensure sustained release, targeted delivery, reduced toxicity, and increased stability of the drug substance. Although the pharmaceutical industry ordinarily exploits chemically synthesized PHAs, bioengineered polymers are also starting to enjoy growing interest. This article focuses on the research and development of drug formulations based on natural PHAs that act as auxiliary substances for antibacterial, anti-inflammatory, anticancer, and hormonal medications, as well as pain killers, and discusses the association between their properties and the micro/nano structure of the synthetic drug. The problems associated with the poor performance of active components in traditional dosage forms can be overcome in PHAs-based formulations.

Keywords: poly(3-hydroxyalkanoates), poly(3-hydroxybutyrate), microparticles, nanoparticles, nanostructure, sustained release

Funding: this work was supported by the grant of the Russian Science Foundation (project 17-74-20104, section 1) and the grant of the Russian Foundation for Basic Research (project 15-29-04856, section 2).

✉ **Correspondence should be addressed:** Anton P. Bonartsev
Leninskie gory 1, str. 12, Moscow, 119234; ant_bonar@mail.ru

Received: 26.08.2018 **Accepted:** 22.09.2018

DOI: 10.24075/brsmu.2018.083

ЛЕКАРСТВЕННЫЕ СИСТЕМЫ НА ОСНОВЕ ПОЛИ-3-ОКСИАЛКАНОАТОВ: МИКРО- И НАНОСТРУКТУРА

А. П. Бонарцев[1,2] ✉, Г. А. Бонарцева[2], В. В. Воинова[1], М. П. Кирпичников[1], К. В. Шайтан[1]

[1] Биологический факультет, Московский государственный университет имени М. В. Ломоносова, Москва

[2] Институт биохимии имени А. Н. Баха, Федеральный исследовательский центр «Фундаментальные основы биотехнологии» РАН, Москва

Биоразлагаемые и биосовместимые полимеры, полиоксиалканоаты (ПОА), активно используют для изготовления широкого спектра лекарственных форм, придающих лекарственным средствам такие свойства, как пролонгированное действие, направленная доставка, сниженная токсичность, увеличенная стабильность. В основном в медицинской промышленности используют ПОА, полученные химическим синтезом, но растет интерес к использованию в фармацевтике природных ПОА, полученных биотехнологическим путем. В статье обсуждаются разработка и исследование разнообразных лекарственных форм, полученных на основе природных ПОА как вспомогательных веществ для антибактериальных, противовоспалительных, противоопухолевых, обезболивающих, гормональных и других средств, и связь их свойств с микро- и наноструктурой изделий. Лекарственные системы на основе ПОА позволят устранить недостатки активных действующих веществ, связанных с особенностями их физико-химических характеристик в традиционных лекарственных формах.

Ключевые слова: поли-3-оксиалканоаты, поли-3-оксибутират, микрочастицы, наночастицы, наноструктура, пролонгированное высвобождение

Финансирование: работа поддержана грантом РНФ, проект № 17-74-20104 в рамках раздела 1 и грантом РФФИ офи-м, проект № 15-29-04856 в рамках раздела 2.

✉ **Для корреспонденции:** Антон Павлович Бонарцев
Ленинские горы, д. 1, стр. 12, г. Москва, 119234; ant_bonar@mail.ru

Статья получена: 26.08.2018 **Статья принята к печати:** 22.09.2018

DOI: 10.24075/vrgmu.2018.083

The use of poly(3-hydroxyalkanoates) in the design of pharmaceutical drugs

The use of micro- and nanoparticles (NP) derived from the biodegradable polymers known as poly(hydroxyalkanoates) (PHAs) holds great promise for the design of injectable systems for sustained drug release. Immobilization of drug substances (DS) in polymer matrices composed of micro- or nanoparticles facilitates extended release of a drug and helps to maintain its optimal concentrations in a target organ or tissue for up to several months, ensuring the desired pharmacological response. Maintaining constant therapeutic yet nontoxic DS concentrations over a long period is one of the ways to overcome the adverse effects typically associated with conventional drugs, including increased toxicity, poor stability, unsteady rates of release, and the inefficient use of active ingredients in the manufacturing process. Polymer drug delivery platforms enable drug release at a target site at a predetermined rate, which is essential in treating chronic diseases. At present, the following PHAs polymers are used both in clinical practice and scientific research: a group of synthetic polymers including poly(2-hydroxypropanoic) acid (polylactic acid, PLA, or polylactide), poly(2-hydroxyacetic) acid also known as polyglycolic acid (PGA) or polyglycolide, and poly(6-

hydroxycaprolactone) (PCL); and a group of naturally occurring polymers consisting of poly(3-hydroxybutyric) acid referred to as poly(3-hydroxybutyrate) (PHB), poly(4-hydroxybutyric) acid (P4HB), poly(3-hydroxyvaleric) acid (poly(3-hydroxyvalerate)), poly(3-hydroxyhexanoate), poly(3-hydroxyoctanoate), their copolymers, and polymers with a similar structure, such as poly(p-dioxanone) (PDO). The diversity of currently available PHA-based drugs is enormous; more are underway. PHAs ensure targeted delivery, extended release, reduced toxicity, and increased stability of a drug substance. Since 1981, PHA-based medications have been permeating the pharmaceutical market. Among them are poly(lactic-co-glycolic acid)-based prolonged-release dosage forms of peptide hormones for the treatment of prostate cancer (Zoladex, Lupron Depot, Trelstar, Eligard), acromegaly (Sandostatin LAR, Somatuline), and dwarfism (Nutropin depot); prolonged-release dosage forms of antibiotics encapsulated in microparticles (Atridox, Arestin); a prolonged-release antitumor medication against glioblastoma multiforme produced in the form of an implantable membrane (Gliadel); prolonged-release anti-inflammatory agents encapsulated in microparticles used for treating macular edema (Ozurdex); prolonged-release DS to fight alcoholism and drug abuse (Vivitrol); prolonged-release atypic antipsychotic DS encapsulated in microparticles for patients with schizophrenia (Risperdal Consta), and many others [1].

All PHAs possess a unique combination of properties paving the way for their application in clinical practice. PHA polymers are biodegradable: they decompose safely in the human body without producing any toxic agents. PHAs are biocompatible with human organs and tissues. They are also characterized by good thermoplasticity and have specific diffusion properties. The process of PHA production is advantageously efficient. Nevertheless, not every PHA enjoys wide use in the pharmaceutical industry. The greatest share of the pharmaceutical market belongs to synthetic PHAs, including polylactic and polyglycolic acids and their copolymers (poly(lactic-co-glycolic) acids). These copolymers are synthetic analogs of naturally occurring poly(3-hydroxyalkanoates), polyesters of 3-hydroxyalkane acids; accordingly, PHB is a linear polyester of 3-hydroxybutyric acid. Depending on the side radical, a few different P3HA types are distinguished: PHB, poly(3-hydroxyvalerate), poly(3-hydroxyhexanoate), poly(3-hydroxyoctanoate), etc. They all differ considerably in their physicochemical properties, specifically in crystallinity, melting and glass transition temperatures, hydrophobicity, plasticity, elastic modulus, etc. [2].

Naturally occurring PHAs hold promise as polymer platforms for controlled-release drugs. PHB and its copolymers can be loaded with a wide range of drug substances: model DS (2,7- dichlorofluorescein, FITC-dextran, methyl red, 7-hydroxyethyltheophylline, calcein, Sudan Red 5B (Oil Red O), rhodamine B isothiocyanate, thymoquinone), antibiotics and antibacterial DS (rifampicin, tetracycline, cefoperazone, gentamycin, sulperazone, duocid, sulbactam, cefoperazone, fusidic acid, nitrofural, norfloxacin, azithromycin, ceftiofur), anticancer drugs (5-fluorouracil, 2',3'-diacyl-5-fluoro-2'-deoxyuridine, paclitaxel, docetaxel, rubidomycin, tacrolimus, chlorambucil, etoposide, doxorubicin), anti-inflammatory drugs (indocid, flurbiprofen, ibuprofen, triamcinolone acetate), pain relievers (morphine, hydroxymorphine, codeine, bupivacaine, tramadol), antiplatelet agents (dipyridamole, nitric oxide donors, nimodipine, felodipine), antihypertensive drugs (manidipine hydrochloride), immunosuppressants (fingolimod), birth control (levonorgestrel), model and therapeutic proteins

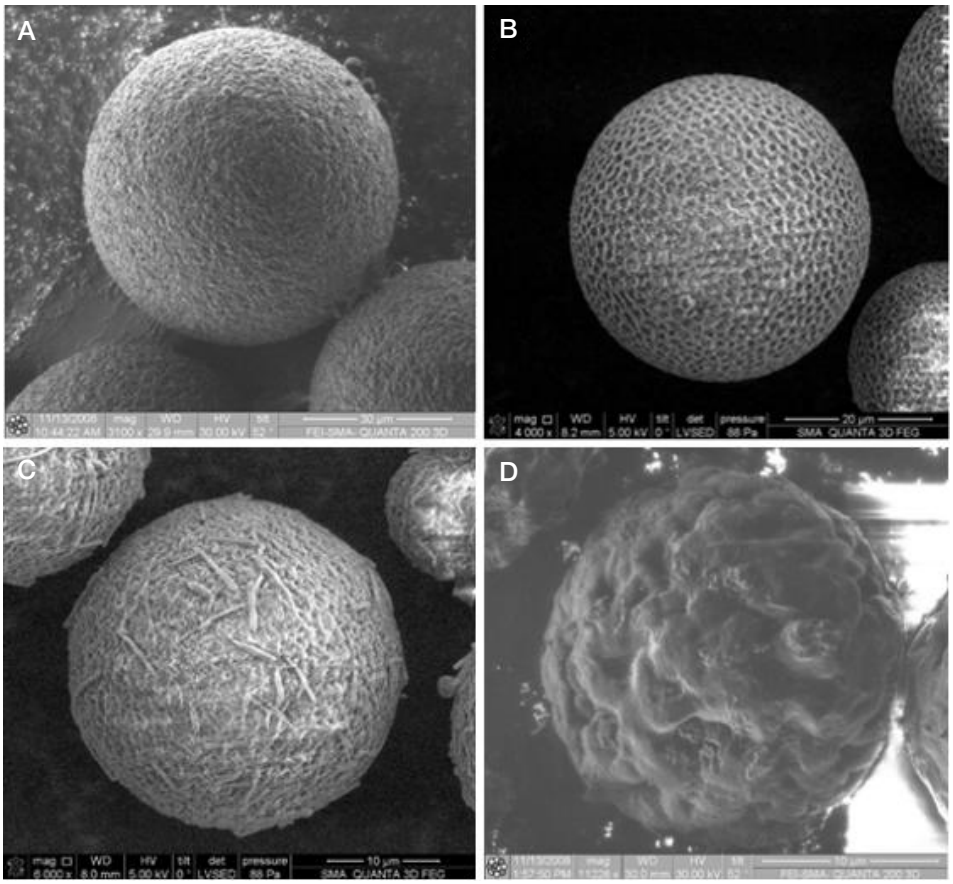

Fig. 1. PHB-derived microparticles with encapsulated DS: microparticles loaded with paclitaxel (**A**); microparticles loaded with doxorubicin (**B**); coumarin crystals on the surface of a microparticle loaded with this substance (**C**); microparticles loaded with methotrexate (**D**)

and peptides (bovine serum albumin, hepatocyte growth factor, mycobacterial proteins for vaccine production, bone morphogenetic protein, nafarelin, and insulin) [1].

PHA-based micro- and nanoparticles for DS loading can be obtained using a variety of different methods: precipitation, one-, two-, or multiple-step emulsification, spray-drying, layer-by-layer self-assembly in a solution, dialysis, precipitation in the presence of supercritical carbon dioxide, and electrospraying. There have been successful attempts to use PHB homopolymers, copolymers and composites as components of medicinal products loaded with active pharmaceutical ingredients; the list of such products comprises experimental films, prototypes of medical devices, micro- and nanoparticles, and pharmaceutical formulations [1].

A number of such PHA-based medicinal products have been tested both *in vitro* and *in vivo* for their pharmacological activity, specifically their antibacterial and antitumor effects and cytotoxicity in mammalian cancer cells; their safety and therapeutic efficacy has been studied in laboratory rats and mice [1].

Micro- and nanostructure of PHA-based drug systems

The inner structure and surface morphology of biopolymer microparticles are determined by a number of factors, including the method of their synthesis and the physiochemical properties of the encapsulated DS and the polymer itself. Biopolymer microparticles will be homogenous and nonporous only if the encapsulated drug substance is well soluble in a solvent used to dissolve the polymer. Fig. 1A shows homogenous PHB-based microspheres, which were synthesized during one of our experiments, loaded with paclitaxel. Unlike the spheres doped with doxorubicin (Fig. 1B), paclitaxel-loaded microparticles have a smooth surface.

If a loaded DS is not well soluble in the solvent, it can organize into crystals inside the polymer matrix of a microparticle, as well as on its surface (Fig. 1C) [3].

Poor solubility of a loaded DS in the solvent may stimulate formation of defective microparticles with lamellar structure, undesired porosity and irregular shape regardless of the synthesis technique applied (Fig. 1D).

Doping PHA-derived microparticles with high molecular weight bioactive agents (therapeutic proteins) yields a composite consisting of polymers with very different physical and chemical properties. In fact, doping leads to the formation of complex supramolecular structures characterized by unintended porosity, roughness, and irregular shape.

Synthesis of NP from PHA is another important area of nanotechnology [4]. Nanoparticles are particles with a diameter of less than 1 μm. The small size of polymer NP determines their biological and physiochemical properties, such as the ability to overcome physical barriers, to be taken up by the mucosa of the bronchi, nasal pharynx, oral cavity, and stomach, and to permeate the cell membrane via endocytosis. The lack of interaction with immune cells, such as macrophages and lymphocytes, ensures increased bioavailability of DS encapsulated in polymer NP [5, 6]. As a rule, amphiphilic PHA copolymers are used for NP synthesis so as to extend the time of NP circulation in the blood stream; they also allow covalent conjugation of NP to the ligands capable of producing a target effect [7, 8].

The kinetics of DS release from microparticles derived from PHB or its copolymers is largely affected by a partially crystalline structure of the polymer. As a rule, PHB can organize into lamellar crystals of 0.3–2 μm and 5–10 μm in dimensions for the short and long axis, respectively (Fig. 2A).

The thickness of PHB crystals varies from 4 to 10 nm depending on the molecular weight, the solvent used, and crystallization temperature [9]. Fig. 2B shows a stack of parallel lamellae of 11–40 nm in width. According to some reports, the lamellar thickness of similar films measured by small-angle X-ray scattering is 6.4 nm [10]. Such difference in the lamellar thickness can be explained by the fact that lamellar planes can be spatially positioned at different angles to the film surface (Fig. 2B).

The diversity of crystalline structures that PHB can assemble into has been demonstrated using PHB-based ultrathin films and encompasses crystals resembling seaweeds in morphology and two-dimensional spherulites (Fig. 2C). On average, these structures rise 4.5 nm above the substrate and take different growth directions from the crystal core. Unlike "seaweeds", 2D spherulites are uniform in their growth direction.

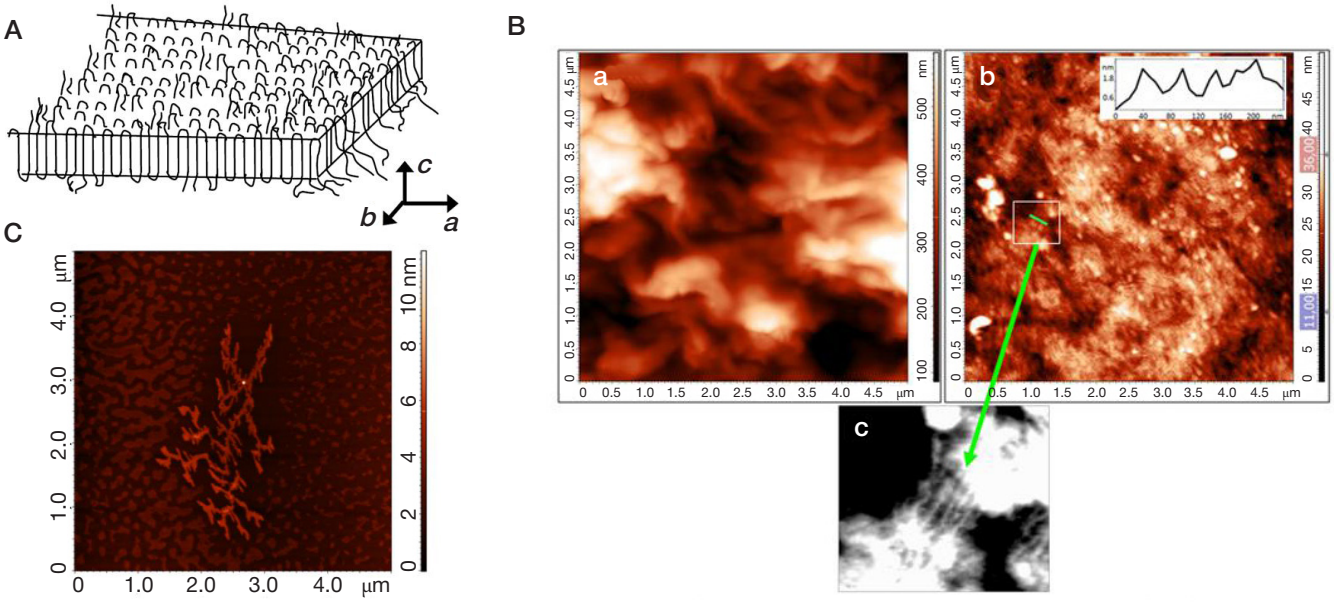

Fig. 2. A. A schematic representation of chain packing in single PHB crystals (Iwata T. et al. [9]). **B**. The rough (**a**) and smooth (**b**) surfaces of a macroscopic PHB film and the cross-section of a lamellar stack (marked with a green arrow) (**c**). **C**. A topographic image of an ultrathin PHB film; the crystalline structure of the polymer can be clearly seen [19]

The observed partially crystalline PHB structures are analogous to the structures occurring in ultrathin films of other polymers, such as polyethylene oxide, polylactide, and polystyrene [11].

Controlled release of DS from a polymer matrix derived from PHB or its copolymers indirectly depends on the natural properties of this biopolymer. In nature, PHB is synthesized in PHA granules or carbonosomes of a bacterial cell where it exists in a mobile amorphous state [12]. It is hypothesized that water that constitutes a small part (5–10%) of native PHB granules plays the role of a plasticizer that allows the biopolymer to maintain its amorphous state [12, 13]. Once water is removed from native granules, the polymer chains organize into a lamellar-crystalline structure. An assumption was made that water molecules promote formation of cross-linking hydrogen bonds between the carbonyl groups of polyether chains. Such molecular structure can explain the mobile amorphous state that PHB has *in vivo* [14]. The nanostructure of PHB samples precipitated from a solution promotes diffusion of water deep into the polymer matrix once the polymer is again submerged into an aqueous medium; this stimulates plasticization (to a very small degree, though) similar to that occurring in the PHA granules of bacteria. At the same time, even if PHB is in its mobile amorphous state, its specific structure protects it against hydrolytic destruction by water that plasticizes it in the granules [15–18]. Water that plasticizes PHB also promotes diffusion of DS encapsulated in the medicinal products based on PHB-derived micro- or nanoparticles: PHB polymer chains are actively synthesized and cleaved in carbonosomes; this process is accompanied by the intense diffusion of PHB monomer precursors, ATP, NADP/NADPH, and other low molecular weight compounds in the matrix of the amorphous polymer. This means that the mechanism of synthesis and degradation of PHB in the bacterial cell involves diffusion of low molecular weight compounds in the polymer matrix and that the interactions between the biopolymer and proteins occurring in the polymer granule (carbonosome) of the bacterial cell render immobilization of proteins and other biomolecules in polymer micro- and nanoparticles possible.

CONCLUSIONS

The functional properties of PHA-based drug systems may depend on the biomimetic nano- and microstructure of PHA that, in turn, is dictated by the natural function the polymer exerts in bacterial cells. New biomimetic PHA-based drugs will help to overcome the drawbacks of traditional drug formulations that often exhibit unsatisfactory physiochemical performance.

References

1. Bonartsev AP. Poly(3-hydroxybutyrate): applications. In: Mishra M, editor. Encyclopedia of Polymer Applications. Boca Raton: CRC Press, Taylor and Francis Group, 2019; 5250 p. DOI: 10.1201/9781351019422-140000085.
2. Bonartsev AP, Voinova VV, Bonartseva GA. Poly(3-hydroxybutyrate) and human microbiota. Applied biochemistry and microbiology. 2018; 54 (6): 547–68. DOI: 10.1134/S0003683818060066.
3. Lee TH, Wang J, Wang CH. Double-walled microspheres for the sustained release of a highly water soluble drug: characterization and irradiation studies. J Control Release. 2002; (83): 437–52.
4. Dong Y, Feng SS. Poly(D,L-lactide-co-glycolide)/montmorillonite nanoparticles for oral delivery of anticancer drugs. Biomaterials. 2005; (26): 6068–76.
5. Gu FX, Karnik R, Wang AZ, Alexis F, Levy-Nissenbaum E, Hong S et al. Targeted nanoparticles for cancer therapy. Nano Today. 2007; (2): 14–21.
6. Brigger I, Dubernet C, Couvreur P. Nanoparticles in cancer therapy and diagnosis Adv Drug Deliv Rev. 2002; (54): 631–51.
7. Blanco E, Bey EA, Dong Y, Weinberg BD, Sutton DM, Boothman DA, Gao J. β-Lapachone-containing PEG–PLA polymer micelles as novel nanotherapeutics against NQO1-overexpressing tumor cells. J Control Release. 2007; (122): 365–74.
8. Nguyen A, Marsaud V, Bouclier C, Top S, Vessieres A, Pigeon P, Gref R, Legrand P, Jaouen G, Renoir JM. Nanoparticles loaded with ferrocenyl tamoxifen derivatives for breast cancer treatment. Int J Pharm. 2008; (347): 128–35.
9. Iwata T et al. Enzymatic Degradation and Adsorption on Poly[(R)-3-hydroxybutyrate] Single Crystals with Two Types of Extracellular PHB Depolymerases from Comamonas acidovorans YM1609 and Alcaligenes faecalis T1. Macromolecules. 1997; 97 (30): 5290–6.
10. Capitán MJ, Rueda DR, Ezquerra TA. Inhibition of the crystallization in nanofilms of poly(3-hydroxybutyrate). Macromolecules. 2004; 15 (37): 5653–9.
11. Liu YX, Chen EQ. Polymer crystallization of ultrathin films on solid substrates. Coordination Chemistry Reviews. 2010; 254 (9–10): 1011–37.
12. Barnard GN, Sanders JK. J Biol Chem. 1989; 264 (6): 3286–91.
13. Harrison ST, Chase HA, Amor SR, Bonthrone KM, Sanders JK. Plasticization of poly(hydroxybutyrate) in vivo. Int J Biol Macromol. 1992; 14 (1): 50–6.
14. Lauzier C, Revol JF, Marchessault RH. FEMS Microbiol Rev. 1992; (103): 299–310.
15. Sudesh K, Abe H, Doi Y. Synthesis, structure and properties of polyhydroxyalkanoates: biological polyesters. Prog Polym Sci. 2000; (25): 1503–55.
16. Abe H, Doi Y. Structural effects on enzymatic degradability for poly[(R)-3-hydroxybutyric acid] and its copolymers: mini-review. Int J Biol Macromol. 1999; (25): 185–92.
17. Schliecker G, Schmidt C, Fuchs S, Wombacher R, Kissel T. Hydrolytic degradation of poly(lactide-co-glycolide) films: effect of oligomers on degradation rate and crystallinity. Int J Pharm. 2003; 266 (1–2): 39-49.
18. Kunze C, Edgar Bernd H, Androsch R, Nischan C, Freier T, Kramer S, Kramp B, Schmitz KP. In vitro and in vivo studies on blends of isotactic and atactic poly (3-hydroxybutyrate) for development of a dura substitute material. Biomaterials. 2006; 27 (2): 192–201.
19. Zhujkov VA. Issledovanie izmenenij fiziko-himicheskih svojstv poli-3-oksibutirata i ego sopolimerov v processe biodegradacii in vitro [dissertacija]. M.: 2018.

Литература

1. Bonartsev AP. Poly(3-hydroxybutyrate): applications. In: Mishra M, editor. Encyclopedia of Polymer Applications. Boca Raton: CRC Press, Taylor and Francis Group, 2019; 5250 p. DOI: 10.1201/9781351019422-140000085.
2. Bonartsev AP, Voinova VV, Bonartseva GA. Poly(3-hydroxybutyrate) and human microbiota. Applied biochemistry and microbiology. 2018; 54 (6): 547–68. DOI: 10.1134/S0003683818060066.
3. Lee TH, Wang J, Wang CH. Double-walled microspheres for the sustained release of a highly water soluble drug: characterization and irradiation studies. J Control Release. 2002; (83): 437–52.

4. Dong Y, Feng SS. Poly(D,L-lactide-co-glycolide)/montmorillonite nanoparticles for oral delivery of anticancer drugs. Biomaterials. 2005; (26): 6068–76.
5. Gu FX, Karnik R, Wang AZ, Alexis F, Levy-Nissenbaum E, Hong S et al. Targeted nanoparticles for cancer therapy. Nano Today. 2007; (2): 14–21.
6. Brigger I, Dubernet C, Couvreur P. Nanoparticles in cancer therapy and diagnosis Adv Drug Deliv Rev. 2002; (54): 631–51.
7. Blanco E, Bey EA, Dong Y, Weinberg BD, Sutton DM, Boothman DA, Gao J. β-Lapachone-containing PEG–PLA polymer micelles as novel nanotherapeutics against NQO1-overexpressing tumor cells. J Control Release. 2007; (122): 365–74.
8. Nguyen A, Marsaud V, Bouclier C, Top S, Vessieres A, Pigeon P, Gref R, Legrand P, Jaouen G, Renoir JM. Nanoparticles loaded with ferrocenyl tamoxifen derivatives for breast cancer treatment. Int J Pharm. 2008; (347): 128–35.
9. Iwata T et al. Enzymatic Degradation and Adsorption on Poly[(R)-3-hydroxybutyrate] Single Crystals with Two Types of Extracellular PHB Depolymerases from Comamonas acidovorans YM1609 and Alcaligenes faecalis T1. Macromolecules. 1997; 97 (30): 5290–6.
10. Capitán MJ, Rueda DR, Ezquerra TA. Inhibition of the crystallization in nanofilms of poly(3-hydroxybutyrate). Macromolecules. 2004; 15 (37): 5653–9.
11. Liu YX, Chen EQ. Polymer crystallization of ultrathin films on solid substrates. Coordination Chemistry Reviews. 2010; 254 (9–10): 1011–37.
12. Barnard GN, Sanders JK. J Biol Chem. 1989; 264 (6): 3286–91.
13. Harrison ST, Chase HA, Amor SR, Bonthrone KM, Sanders JK. Plasticization of poly(hydroxybutyrate) in vivo. Int J Biol Macromol. 1992; 14 (1): 50–6.
14. Lauzier C, Revol JF, Marchessault RH. FEMS Microbiol Rev. 1992; (103): 299–310.
15. Sudesh K, Abe H, Doi Y. Synthesis, structure and properties of polyhydroxyalkanoates: biological polyesters. Prog Polym Sci. 2000; (25): 1503–55.
16. Abe H, Doi Y. Structural effects on enzymatic degradability for poly[(R)-3-hydroxybutyric acid] and its copolymers: mini-review. Int J Biol Macromol. 1999; (25): 185–92.
17. Schliecker G, Schmidt C, Fuchs S, Wombacher R, Kissel T. Hydrolytic degradation of poly(lactide-co-glycolide) films: effect of oligomers on degradation rate and crystallinity. Int J Pharm. 2003; 266 (1–2): 39-49.
18. Kunze C, Edgar Bernd H, Androsch R, Nischan C, Freier T, Kramer S, Kramp B, Schmitz KP. In vitro and in vivo studies on blends of isotactic and atactic poly (3-hydroxybutyrate) for development of a dura substitute material. Biomaterials. 2006; 27 (2): 192–201.
19. Жуйков В. А. Исследование изменений физико-химических свойств поли-3-оксибутирата и его сополимеров в процессе биодеградации in vitro [диссертация]. М.: 2018.

THE USE OF IRON OXIDE MAGNETIC NANOSPHERES AND NANOCUBES FOR TARGETED DOXORUBICIN DELIVERY INTO 4T1 MOUSE BREAST CARCINOMA CELLS

Nizamov TR[1] ✉, Garanina AS[1,2], Uvarova VI[1,2], Naumenko VA[1], Schetinin IV[3], Savchenko AG[1]

[1] Laboratory of Biomedical Nanomaterials, National University of Science and Technology "MISiS", Moscow

[2] Laboratory of Tissue-Specific Ligands, Faculty of Chemistry, Lomonosov Moscow State University, Moscow

[3] Department of Physical Materials Science, National University of Science and Technology "MISiS", Moscow

[4] D. Mendeleev University of Chemical Technology of Russia, Moscow

Magnetic nanoparticles (MNP) are attracting increasing attention as promising materials for the treatment and diagnosis of cancer. The aim of this work was to explore the effect of the magnetic core shape of iron oxide nanoparticles (NP) on the efficiency of doxorubicin delivery into 4T1 cells. Nanospheres (NS) and nanocubes (NC) were synthesized by thermal decomposition of iron (III) oleate. This method of synthesis enables control over the NP shape and size. The NP were hydrophilized using Pluronic F-127. The obtained particles were doped with doxorubicin in a sodium phosphate buffer. The weight fractions of doxorubicin in the NS and NC were 15.22% and 15.44%, respectively. The IC50 of free doxorubicin was 1 μM. The IC_{50} of doxorubicin-loaded NS and NC were 6.4 μM and 5.5 μM, respectively. Unloaded NP did not exhibit any toxicity towards the cells at a studied range of concentrations between 1.77 mg/l and 227.2 mg/l. Free doxorubicin demonstrated more vigorous accumulation dynamics in 4T1 cells with a tendency to localize in the cell nucleus, whereas doxorubicin loaded onto iron oxide NP was mainly accumulated in the vesicles surrounding the nucleus and was able to enter it only after being incubated with the cells for 2 h. We conclude that doxorubicin loaded onto cubic-shaped NP is delivered into the cell nucleus a little bit more efficiently at early incubation stages in comparison with nanospheres, but the difference is insignificant.

Keywords: iron oxide nanoparticles, nanoparticle shape, cytotoxicity, drug delivery, doxorubicin

Funding: this work was supported by the Project 14.578.21.0201 (ID RFMEFI57816X0201).

✉ **Correspondence should be addressed:** Timur R. Nizamov
Leninsky prospect 4, Moscow, 119049; nizamov.timur@gmail.com

Received: 28.08.2018 **Accepted:** 20.09.2018

DOI: 10.24075/brsmu.2018.085

ИСПОЛЬЗОВАНИЕ МАГНИТНЫХ НАНОЧАСТИЦ ОКСИДА ЖЕЛЕЗА СФЕРИЧЕСКОЙ И КУБИЧЕСКОЙ ФОРМ ДЛЯ ДОСТАВКИ ДОКСОРУБИЦИНА В КЛЕТКИ ЛИНИИ КАРЦИНОМЫ МОЛОЧНОЙ ЖЕЛЕЗЫ МЫШИ 4T1

Т. Р. Низамов[1] ✉, А. С. Гаранина[1,2], В. И. Уварова[1,2], В. А. Науменко[1], И. В. Щетинин[3], А. Г. Савченко[1]

[1] Лаборатория биомедицинских наноматериалов, Национальный исследовательский технологический университет «МИСиС», Москва

[2] Лаборатория тканеспецифических лигандов, Московский государственный университет имени М. В. Ломоносова, Москва

[3] Кафедра физического материаловедения, Национальный исследовательский технологический университет «МИСиС», Москва

[4] Российский химико-технологический университет имени Д. И. Менделеева, Москва

Магнитные наночастицы (МНЧ) все больше привлекают внимание в качестве перспективного материала для разработки эффективных систем противоопухолевой терапии и диагностики. Целью работы было исследование влияния формы магнитного ядра наночастиц (НЧ) оксида железа на эффективность доставки доксорубицина в клетки линии 4T1. Наночастицы сферической (СНЧ) и кубической (КНЧ) форм синтезировали методом термического разложения олеата железа (III), что позволило эффективно контролировать их форму и размер. Затем НЧ гидрофилизировали посредством использования Pluronic F-127. В полученные средства доставки загружали доксорубицин в среде натрий-фосфатного буфера. Загрузка составила 15,22% для СНЧ и 15,44% для КНЧ. IC_{50} для незагруженного доксорубицина оказалась равной 1 мкМ, в то время как для СНЧ и КНЧ с препаратом — 6,4 мкМ и 5,5 мкМ соответственно. В протестированном диапазоне концентраций от 1,77 мг/л до 227,2 мг/л цитотоксичность у НЧ без препарата не выявлена. Согласно данным динамики накопления доксорубицина, в клетках 4T1 активнее всего идет накопление свободного препарата — он локализуется в клеточном ядре. В то же время доксорубицин, загруженный в НЧ, накапливается менее интенсивно и первоначально локализуется в везикулах вокруг ядра, обнаруживаясь в самом ядре лишь после 2 ч совместной инкубации. Противоопухолевый препарат, загруженный в КНЧ, несколько более активно доставляется на ранних сроках инкубации с клетками по сравнению со СНЧ, однако данная разница не существенна.

Ключевые слова: наночастицы оксида железа, форма наночастиц, цитотоксичность, адресная доставка, доксорубицин

Финансирование: работа выполнена при поддержке Министерства образования и науки РФ, соглашение № 14.578.21.0201 (уникальный идентификатор RFMEFI57816X0201).

✉ **Для корреспонденции:** Тимур Радикович Низамов
Ленинский пр-т, д. 4, г. Москва, 119049; nizamov.timur@gmail.com

Статья получена: 28.08.2018 **Статья принята к печати:** 20.09.2018

DOI: 10.24075/vrgmu.2018.085

Magnetic nanoparticles (MNP) including those derived from iron oxide are increasingly seen as holding promise for the design of efficient diagnostic platforms and therapeutic anticancer agents. State-of-the-art technologies provide tools for the synthesis of MNP with programmed properties and chemical modification of their surface for targeted drug delivery and MR imaging [1–5]. Because MNP have remarkable contrast-enhancing properties, MNP-based drug delivery platforms can be employed to study the distribution of therapeutic agents in the target in real time and to assess the efficacy of treatment [6]. Other carriers, such as polymer NP, liposomes, micelles, etc., do not meet the requirements for contrast enhancement and, therefore, cannot be used to monitor drug distribution *in vivo*. That said, MNP have a number of drawbacks: they are toxic, tend to aggregate, and typically lack the ability to form stable covalent bonds with surface modifiers. These drawbacks can be overcome, though, by coating the NP surface with biocompatible polymers, thereby reducing NP toxicity and minimizing the risk of their aggregation. This approach is instrumental in achieving good contrast-enhancing properties, improved resistance to aggregation, and low toxicity; it also prepares the surface for further functionalization with ligands, therapeutic agents, vectors, etc. One approach to the design of MNP-based targeted drug delivery platforms stands out as innovative and promising. It consists of two steps. First, iron oxide nanoparticles are fabricated from iron (III) oleate by thermal decomposition in the presence of a stabilizing agent (oleic acid). Then, the obtained NP are transferred to an aqueous phase using Pluronic F-127, the poly(ethylene glycol)-block-poly(propylene glycol)-block-poly(ethylene glycol) copolymer with surfactant properties. The hydrophobic sites in the polymeric coating covering the NP facilitate delivery of hydrophobic drugs to the target [7–9].

There are a few factors driving the interactions between a drug delivery platform and biological molecules, including the chemical composition of an NP core and surface, as well as their geometry. The data describing how the shape of NP affects their cytotoxicity and cellular uptake is conflicting, suggesting that it is difficult to predict the behavior of nanoparticles in a living organism based on their geometry. For example, one of the studies demonstrated that carbon nanotubes induced more DNA damage in primary mouse embryo fibroblasts than less toxic carbon black nanocubes [10]. The authors of the study hypothesized that the effect was caused by the elongated shape of nanotubes with an aspect (length to width) ratio of 625. Another research work reported that zinc oxide nanorods with an aspect ratio of 3 were less toxic against MG-63 human osteosarcoma cells than nanospheres derived from the same material [11]. A group of researchers revealed that an increase in the aspect ratio of silica NP resulted in a slightly more pronounced cytotoxicity and better uptake by A375 human melanoma cells [12]. Another group investigated the impact of Ag NP geometry on the growth of *S. cerevisiae* and the intensity of cellular uptake [13]. Ag nanoplates proved to be less toxic than nanospheres, nanocubes and nanorods. The authors linked the described phenomenon to the chemically active {111} facets dominating the surface of nanoplates that enhanced NP cytotoxicity against yeast. In a study carried out by different authors, Au nanospheres were more vigorously accumulated in MDCK II epithelial cells than Au nanorods and exhibited higher cytotoxicity [14]. At the same time, no data is available on the role of an MNP shape in targeted drug delivery and cytotoxicity.

Doxorubicin is a well-known and widely used chemotherapy drug with antiproliferative activity. It was introduced in clinical practice 40 years ago. However, poor selectivity and high toxicity against healthy cells impose certain limitations on its use. The most dangerous side effects of doxorubicin include cardiomyopathy and cardiac failure [15]. They dictate a need for innovative targeted drug delivery systems that can overcome the drawbacks of doxorubicin therapy. The solution is offered by Pluronic F-127-based carriers [9]. Doxorubicin is capable of binding to the hydrophobic sites of surfactants that stabilize the NP surface. The release of the drug is induced either by Brownian relaxation after applying an external magnetic field or by the acid environment of lysosomes once the particle is taken up by the cell [16].

The aim of the present study was to investigate the effect of spherical and cubic shapes of iron oxide NP modified with Pluronic F-127 and doped with doxorubicin on the cytotoxicity of the particles against 4TI mouse mammary carcinoma cells, the efficacy of their targeted delivery into the cells and distribution of the drug inside the cells.

METHODS

The following reagents were used: Pluronic F-127 (Sigma Aldrich; USA); deionized water; chemically pure toluene (Komponent-reaktiv, Russia); iron (III) chloride, 97% (Sigma Aldrich; USA); oleic acid, ≥99% (Roth; Germany); sodium oleate, 95% (Roth; Germany); chemically pure hydrochloric acid (SigmaTek; Russia); ferrozine, ≥ 97% (Sigma Aldrich; USA); ammonium acetate, ≥ 98% (Sigma Aldrich; USA); ascorbic acid, ≥99% (Sigma Aldrich; USA); doxorubicin hydrochloride, ≥ 98% (Glentham; UK); sodium phosphate buffer tablets, biotechnology grade (Amresco; USA); chemically pure isopropanol (SigmaTek; Russia); 1-octadecene, ≥ 95% (Sigma Aldrich; USA); ethanol, ≥ 95% (Sigma Aldrich; USA); chemically pure hexane (SigmaTek; Russia); MTS (Promega; USA); dimethyl sulfoxide, ≥ 99% (Sigma Aldrich; USA); iron standard for ICP (Sigma Aldrich; USA).

Synthesis of carriers and doxorubicin loading

Synthesis of nanospheres and nanocubes

Nanospheres were synthesized by thermal decomposition of iron oleate following the original yet slightly modified technique described in [17, 18]. Briefly, sodium oleate (100 mmol) and anhydrous iron (III) chloride (33 mmol) were dissolved in a mixture of ethanol (66.7 ml), water (50 ml) and hexane (116 ml) under vigorous stirring. The resulting solution was heated to 70 °C and stirred at that temperature for 4 hours. Then, the organic phase was separated and the solvent was gradually evaporated using a rotovap until a brown waxy complex of iron (III) oleate was formed. After that, 2.2 mmol of the obtained iron oleate and 12 mmol of oleic acid were dissolved in 10 ml of 1-octadecene. The mixture was heated to 320 °C at a rate of 3.3 °C/min under vigorous stirring under argon flow and then incubated at 320 °C for 60 min. Following incubation, the mixture was cooled down to room temperature and diluted fivefold with isopropanol. Nanoparticles were collected using a neodymium magnet and washed in isopropanol 3 times. The precipitate was re-dispersed by sonication in toluene.

Nanocubes were synthesized by thermal decomposition of iron (III) oleate [19]. The original protocol was slightly modified. Briefly, 33 ml of a solution containing the iron oleate complex (4 mmol), sodium oleate (1.3 mmol) and oleic acid (1.3. mmol) were poured into a three-necked flask equipped with a 100 ml

reflux condenser. The mixture was heated to 140°C and kept at that temperature for 60 min to remove residual water. Then, the mixture was brought to the boiling point at a rate of 4 °C/ min and was allowed to boil for 30 min. All manipulations were performed under argon flow. The obtained solution was cooled down to room temperature. The obtained NP were isolated by adding 320 ml of isopropanol solution followed by magnetic decantation. The final product was washed in isopropanol 3 times and re-dispersed in toluene.

Ferrozine assay

Ammonium acetate (385.4 mg), ferrozine (3.2 mg) and ascorbic acid (352.2 mg) were weighed and dissolved in 1 ml of deionized water. The obtained solution was later used to spectrophotometrically measure iron concentrations.

Phase transfer of nanoparticles assisted by Pluronic F-127

Phase transfer of the synthesized NP to an aqueous phase was aided by the nonionic surfactant Pluronic F-127 using the technique described in [20, 21], which we slightly modified. Briefly, 15 ml of the NP solution in toluene with an iron oxide concentration of 1 mg/ml were combined with the same volume of Pluronic F-127 solution in water (Pluronic concentration C = 25 mg/ml). The mixture was incubated overnight under vigorous stirring. The emulsion was separated by centrifugation at 1,000 g and the aqueous phase was collected. Then, the aqueous phase was again centrifuged at 12,000 g to stimulate precipitation of magnetite NP. Finally, the precipitate was re-dispersed under sonication in deionized water. The solution was diluted to achieve an iron oxide concentration of 0.32 mg/ml.

Loading of doxorubicin onto iron oxide nanoparticles coated with Pluronic F-127

The aqueous solution of 5 mg/ml doxorubicin (0.2 ml) and the phosphate buffered saline (0.2 ml) concentrated fivefold relative to the isotonic solution (pH = 7.4) were added to 10 ml of the obtained aqueous solution of NP and stirred on the magnetic stirrer at room temperature for 24 h. The total doxorubicin concentration in the NP solution C_{total}(dox) was 96.0 mg/ml. Then the solution was centrifuged to precipitate all NP. The collected NP were re-dispersed in the sodium phosphate buffer under vigorous stirring using a shaker.

Characteristics of synthesized magnetic nanoparticles

Transmission electron microscopy (TEM)

The morphology and size of the nanoparticles were examined under the 200 kV FE transmission electron microscope JEOL JEM-2100F (JEOL; Japan) operated at a beam current of 0.8 A. The samples for TEM were prepared by applying 1–2 µl of the NP solution onto a formvar-coated copper mesh (*d* = 3.05 mm) and allowing them to air-dry.

Dynamic light scattering

The hydrodynamic size of the nanoparticles and their zeta-potential were measured in the volumes ranging from 1 to 2 ml using the Zetasizer Nano ZS analyzer (Malvern; Germany).

Vibrating-sample magnetometry

Magnetic properties of the particles were evaluated using the Quantum Design Physical Property Measurement System (PPMS; Germany) equipped with a vibrating sample magnetometer (oscillation amplitude of 2 mm, frequency of 40 Hz, sensitivity of 10^{-6} emu).

X-ray diffraction analysis (XRD)

The crystalline structure of the synthesized MNP was characterized using the DRON-4 diffractometer (Burevestnik; Russia) with the following parameters: cobalt X-ray source with λ = 0.179 nm, voltage of 40 kV, current of 30 mA. The samples were scanned through a range of diffraction angles 2θ from 20° to 120° by increments of 0.1°. Exposure time was 3 seconds per frame.

Spectrophotometry

1. *Doxorubicin concentration measurement and loading efficiency*. 600 mµ of doxorubicin solutions were introduced into two wells of a 96-well plate (300 mµ per well). Absorption

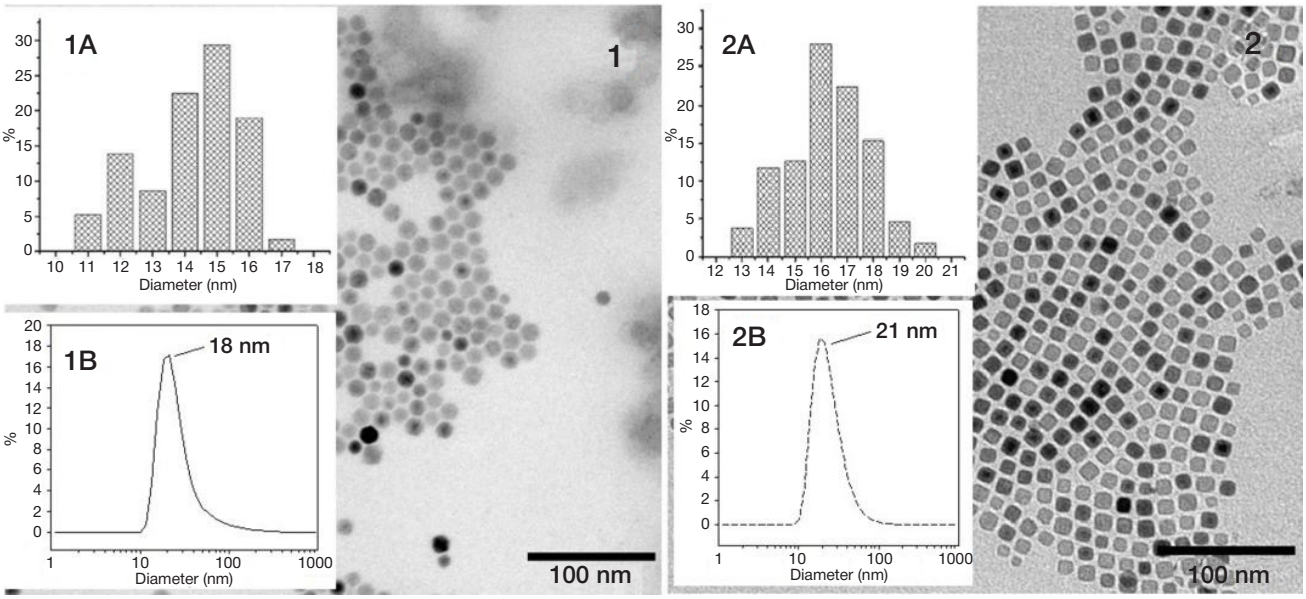

Fig. 1. Microimages of iron oxide NS (**1**) and NC (**2**), histograms of size distribution and average hydrodynamic size of the particles

was measured at λ = 495 nm by the Multiskan GO spectrophotometer (Thermo Scientific; USA). The concentration of doxorubicin was calculated based on a 6-point calibration curve (1,0; 2,5; 5,0; 10,0; 25,0; and 50 μkg/ml). The amount of loaded doxorubicin (C_{load}(dox)) was calculated by measuring the residual concentration of the drug in the supernatant (C_{res}(dox)) yielded by centrifugation, which was subtracted from the initial concentration of the drug C_{total}(dox) in the solution. Encapsulation efficiency was calculated by the formula: ω = 100% • C_{load}(dox)/(C_{load}(dox) + C(NP)), where C_{load}(dox) is a concentration of the loaded doxorubicin expressed as mg/l and C(NP) is a concentration of NP = 308 mg/l.

2. Iron concentration. A series of iron ICP standard solutions were prepared with concentrations of 0.1, 0.25, 0.5, 0.75, 1, 1.5, and 2 mg/ml. Briefly, 100 mμ of a sample with known iron concentrations were incubated with 400 mμ of concentrated hydrochloric acid for 2 h. Then, the solution was diluted 100-fold with deionized water, and 400 mμ of the obtained mixture were combined with 200 mμ of deionized water and 40 mμ of the ferrozine assay prepared in advance. Five minutes later, the resulting product was transferred to two wells of a 96-well plate (300 mμ per well), and its absorption was measured at λ = 560 nm by Multiskan GO in the photometry mode. Iron concentration was inferred from the absorption data.

Cell culture

4T1 mouse mammary carcinoma cells (ATCC® CRL-2539™, USA) were cultured in the RPMI-1640 medium (Gibco) supplemented with 2 mM L-glutamine (Gibco) and 10% fetal bovine serum (Gibco) at 37 °C and 5% CO_2.

MTS cytotoxicity assay

The cells were seeded in a 96-well plate (12,000–15,000 cells per well) and left there for 24 h before introducing the particles. Free doxorubicin, doxorubicin-loaded nanoparticles and nanoparticles without the drug were dissolved in the sodium phosphate buffer and added to the cells at various concentrations. Cell cultures supplemented with the buffer were used as a negative control. Cell cultures supplemented with dimethyl sulfoxide (20 mμ of the reagent per 100 mμ of the medium) were used as a positive control. The cells were incubated with the NP and the controls in the incubator at 37 °C and 5% CO_2 for 48 h. Upon incubation, the number of viable cells in each well was determined by the MTS assay. Briefly, the culture medium was replaced with an MTS solution in the fresh medium (20 mμ of MTS per 100 mμ medium) and incubated for 4 h in the dark at 37 °C and 5% CO_2. Then, the plates were mounted on a permanent magnet and left to sit there for 5 min to separate the nanoparticles. After that, samples were carefully collected from each well and transferred to another plate to avoid contamination with NP. The optical density of the samples was measured spectrophotometrically at λ = 490 nm. Histograms of cell survival were constructed and standard deviation was calculated in Microsoft Office Excel 2007.

Accumulation dynamics of free and NP-loaded doxorubicin

The cells were seeded onto Petri dishes at 120,000–150,000 cells per dish. Free doxorubicin and doxorubicin loaded onto NC and NS (drug concentrations of 50 μkg/ml) were introduced into culture samples 24 hours later. The cells incubated with the drug- or NP-free medium were used as a control. The cultures were incubated with the studied samples for 15, 30, 45 min and 1h, 2h, 4h, 6h, 24 h. Upon incubation, the cells were fixed in 3.7% formalin solution in the sodium phosphate buffer (pH 7.2–7.4; Gibco) for 15 min. The obtained samples were examined under the fluorescence microscope EVOS equipped with the LplanFL PH2 ×60 lens (Life technologies; USA). The images were processed and fluorescence intensity was measured in ImageJ 1.52a (Wayne Rasband (NIH); USA). A single factor ANOVA test was applied to carry out statistical analysis. Differences were considered significant at $p < 0.05$.

RESULTS

Iron oxide NP synthesized by thermal decomposition were studied using TEM (Fig. 1). The histogram of size distribution shows that the technique for the synthesis of nanospheres yielded magnetite particles with an average size of 15 nm (Fig. 1–1A). As we expected, the fabricated NP had a spherical shape. The average hydrodynamic size of the nanospheres in toluene was about 18 nm (Fig. 1–1B).

The samples synthesized according to the protocol for the fabrication of nanocubes were also characterized using TEM (Fig. 1–2). As we expected, the resulting NP with an

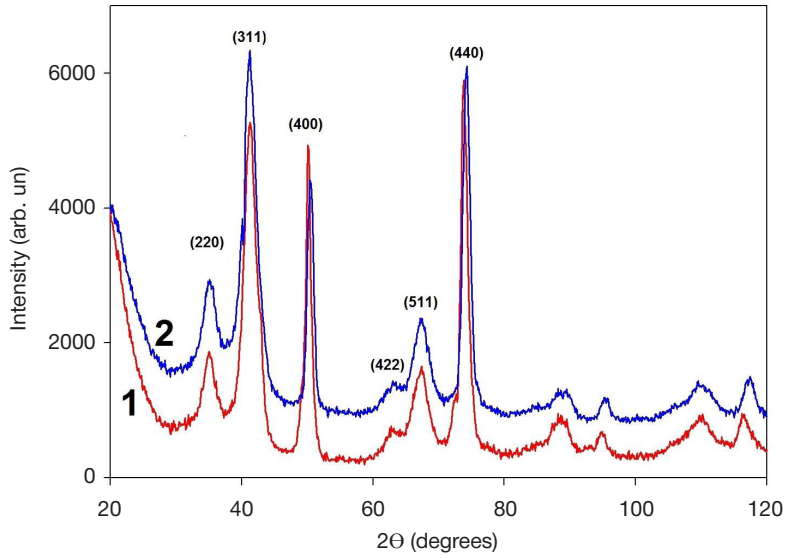

Fig. 2. Data yielded by the XRD analysis for NS (**1**) and NC (**2**)

average size of 16 nm had a cubic shape (Fig. 1–2A). The average hydrodynamic size of nanocubes was about 21 nm (Fig. 1–2B).

The X-ray diffraction analysis of the nanospheres revealed that the position of the diffraction peaks and their intensity were indicative of the inverse spinel structure typical of magnetite (Fig. 2–1). Nanocubes had a similar structure (Fig. 2–2). More information is available in the Table below.

Measurements of magnetic properties revealed that the magnetic saturation Ms of the nanospheres was 50.5 emu/g, and coercivity Hc was 20.5 Oe (Fig. 3–1). Magnetic properties of the nanocubes were comparable: magnetic saturation was 60.5 emu/g and coercivity was 20.0 Oe (Fig. 3–2).

The average hydrodynamic size of NP after the phase transfer from toluene to water and stabilization with Pluronic F-127 increased to 43 nm for NS (Fig. 4–1) and to 50 nm for NC (Fig. 4–2), whereas their zeta-potentials were –10 mV and –15.1 mV, respectively. After the particles were loaded with doxorubicin, the average size of NS reached 68 nm (Fig. 4–3), whereas their zeta-potential became positive (+21.1 mV). A similar tendency was observed for NC: their hydrodynamic size increased to 78 nm (Fig. 4–4), and their zeta-potential was now +22.0 mV. The amount of doxorubicin loaded onto the NS was calculated as follows: the concentration of the drug in the supernatant C_{res}(dox) was 40.7 mg/l; therefore, C_{load}(dox) = C_{total}(dox) – C_{res}(dox) = 96.0 – 40.7 = 55.3 mg/ml. The mass percentage of the drug in the NS ω(NS) = 100% • C_{load}(dox)/(C_{load}(dox) + C(NP)) = 100% • 55.3/(55.3 + 308) = 15.22%. The amount of doxorubicin loaded onto the NC was calculated as follows: C_{load}(dox) = 39.2 mg/l; then C_{load}(dox) = C_{total}(dox) – C_{res}(dox) = 96.0 – 39.2 = 56.2 mg/l. In the case of the NC, ω(NC) = 100% • C_{load}(dox)/(C_{load}(dox) + C(NP)) = 100% • 56.2/(56.2 + 308) = 15.44%.

It was established that all studied concentrations of NC and NS were not toxic against 4T1 cells (Fig. 5A). However, after the cells were incubated with the same concentrations of doxorubicin-loaded NS and NC, the number of viable cells in the cultures decreased. IC_{50} (the half maximal inhibitory concentration) of the NC doped with doxorubicin (NC-Dox) was 21 mg/l iron oxide and 5.5 μM doxorubicin. For the NS doped with doxorubicin (NS-Dox), IC_{50} was 25 mg/l and 6.4 μM for iron oxide and the drug, respectively. IC_{50} of free doxorubicin was about 1 μM (Fig. 5B). It means that NC-Dox had a slightly more pronounced tumoricidal effect than NS-Dox. However, this difference was insignificant. Free doxorubicin was the most effective of all drug variations in killing the cells.

The analysis of the accumulation dynamics of free and NP-bound doxorubicin in the cells demonstrated than after 15 min of incubation with the cells, a weak fluorescence signal was recorded coming from doxorubicin. After 30 min of incubation, the intensity of the signal emitted from free doxorubicin was comparable to that of doxorubicin delivered to the cells by NC. However, free doxorubicin tended to accumulate mostly in the nuclei, whereas doxorubicin loaded onto NC was visualized in the vesicles near the nucleus (Fig. 6A, D, L). The fluorescence signal emitted from NS-Dox was significantly less intense than

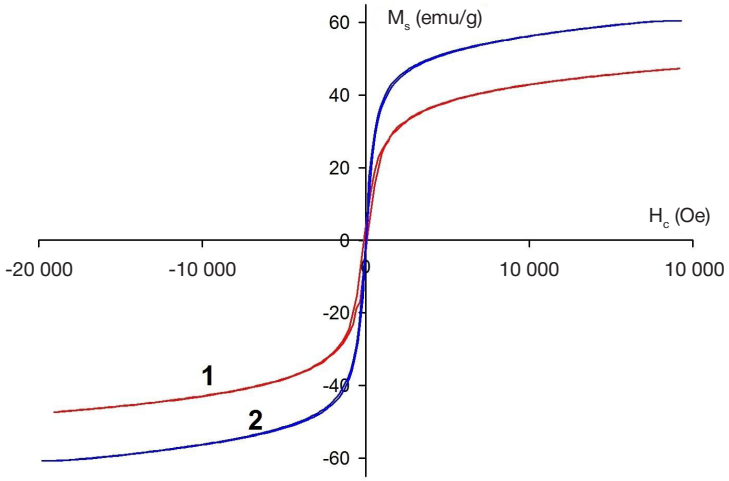

Fig. 3. Magnetization curves for NS (**1**) and NC (**2**)

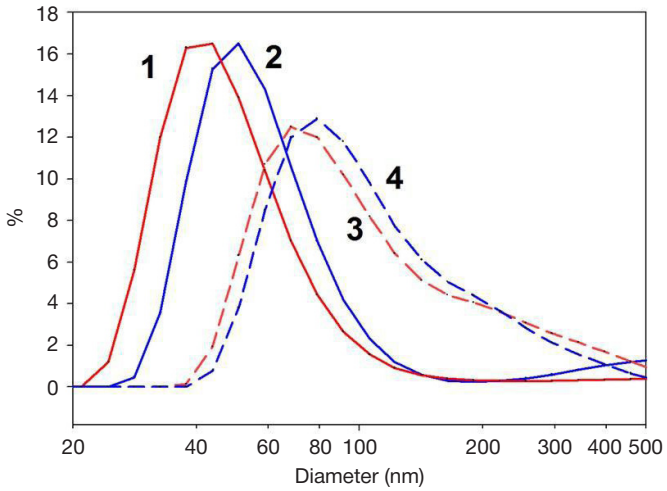

Fig. 4. The hydrodynamic size of NP after transfer to an aqueous phase: NS before (**1**) and after (**3**) doxorubicin loading; NC before (**2**) and after (**4**) doxorubicin loading.

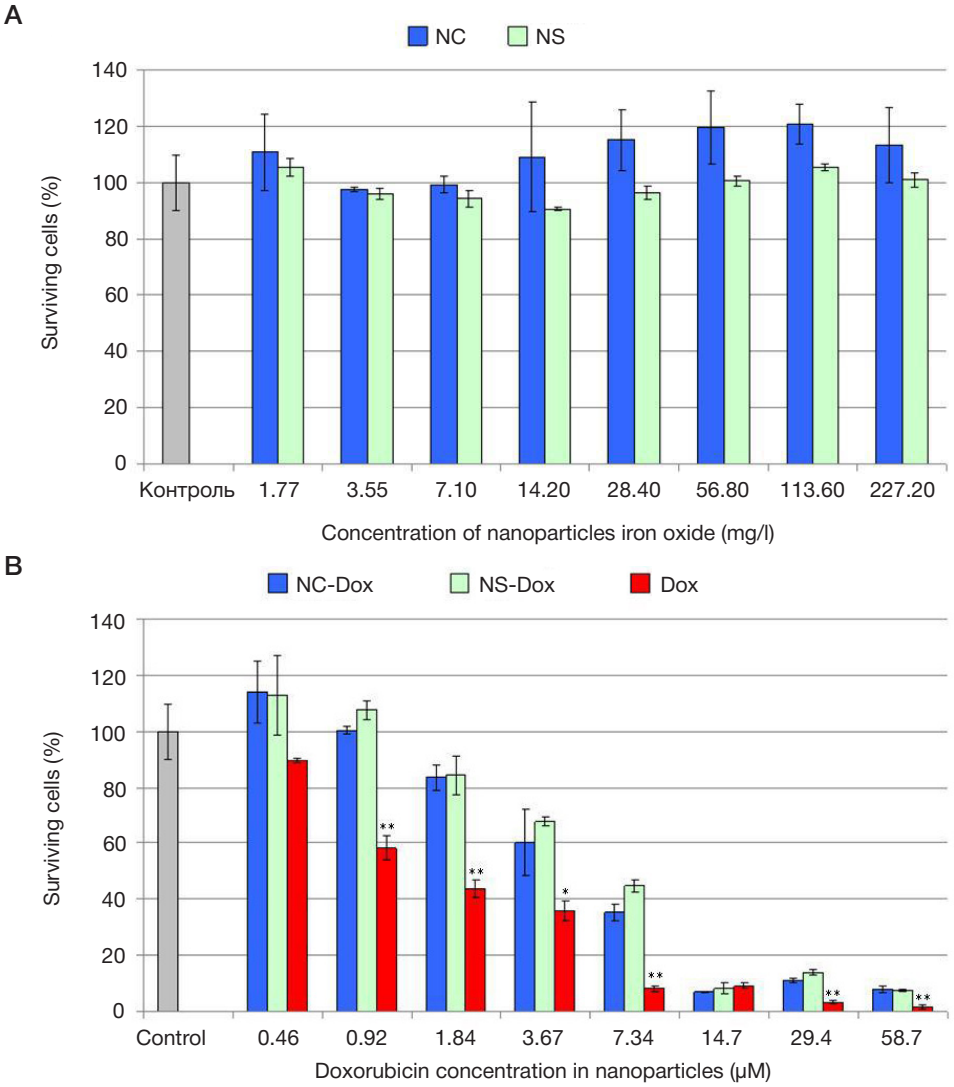

Fig. 5. Toxicity of NP against the 4T1 cell line. The histogram shows cell survival after 48 h incubation with NC and NS (**A**); after 48-h incubation with NC-Dox, NS-Dox and free doxorubicin (**B**). The MTS assay. Results are presented as mean values ±SD. * $p < 0.05$; ** $p < 0.01$. Percentage of living cells incubated with the sodium phosphate buffer was taken as 100%

that of NC-Dox and free doxorubicin (Fig. 6G). This tendency was also observed after 45 min-long incubation of the cells with the free and NP-loaded drug. In later periods, the fluorescence intensity of the drug did not differ significantly between the types of its carriers. However, accumulation of free doxorubicin was more pronounced than that of the loaded drug. It should be noted that the drug was visualized mainly in cell nuclei only after the cells were incubated with NC-Dox and NS-Dox for 2 h. Thus, the efficiency of drug delivery is higher for free doxorubicin than for the drug carried by NP. It was also established that NC penetrate cells more readily than NS, but this difference levels out over time.

DISCUSSION

Thermal decomposition of iron (III) oleate is a method for fabricating stable sols of monodisperse iron oxide NP with programmed sizes and shapes: spherical [17, 18], cubic [19], and some other. [22]. The initial iron (III) oleate complex decomposes at high temperatures and can be partially reduced to Fe (II) by the components of the reaction mixture producing magnetite (Fe_3O_4) or maghemite (γ-Fe_2O_3) nanoparticles. Both oxides have ferrimagnetic properties. The final size and shape of NP are determined by the presence of stabilizing agents in the reaction mixture, such as oleic acid and sodium oleate. They are capable to selectively adsorb to the {111} facets of growing NP and shape their geometry. By adsorbing to the surface of NP, stabilizing agents confer hydrophobicity critical for the design of platforms for the targeted delivery of hydrophobic drugs, including doxorubicin.

During the experiment, we fabricated nanocubes and nanospheres and stabilized them with Pluronic F-127 (Fig. 1). The analysis of their structure (Fig. 2) and magnetic properties (Fig. 3) revealed that the synthesized particles were iron oxide compositions with the inverse spinel structure. Because the NP size identified by TEM did not coincide with the size of the coherent scattering region, we concluded that the samples were polycrystalline (Table). The coercivity of both samples was >0, meaning the latter were ferrimagnetic.

The samples were stable both in hydrophobic media (Fig. 1–1B, Fig. 1–2B) and in an aqueous phase containing Pluronic F-127 (Fig. 4–1, Fig. 4–2). This polymer has a hydrophobic site of polypropylene glycol allowing it to adsorb onto the NP surface and two hydrophilic terminal regions of polyethylene glycol pointing towards the outside. Transferred to an aqueous phase, NP acquire hydrophobic sites, which can bind hydrophobic drugs, and a hydrophilic shell, which considerably improves the solubility of NP in aqueous media.

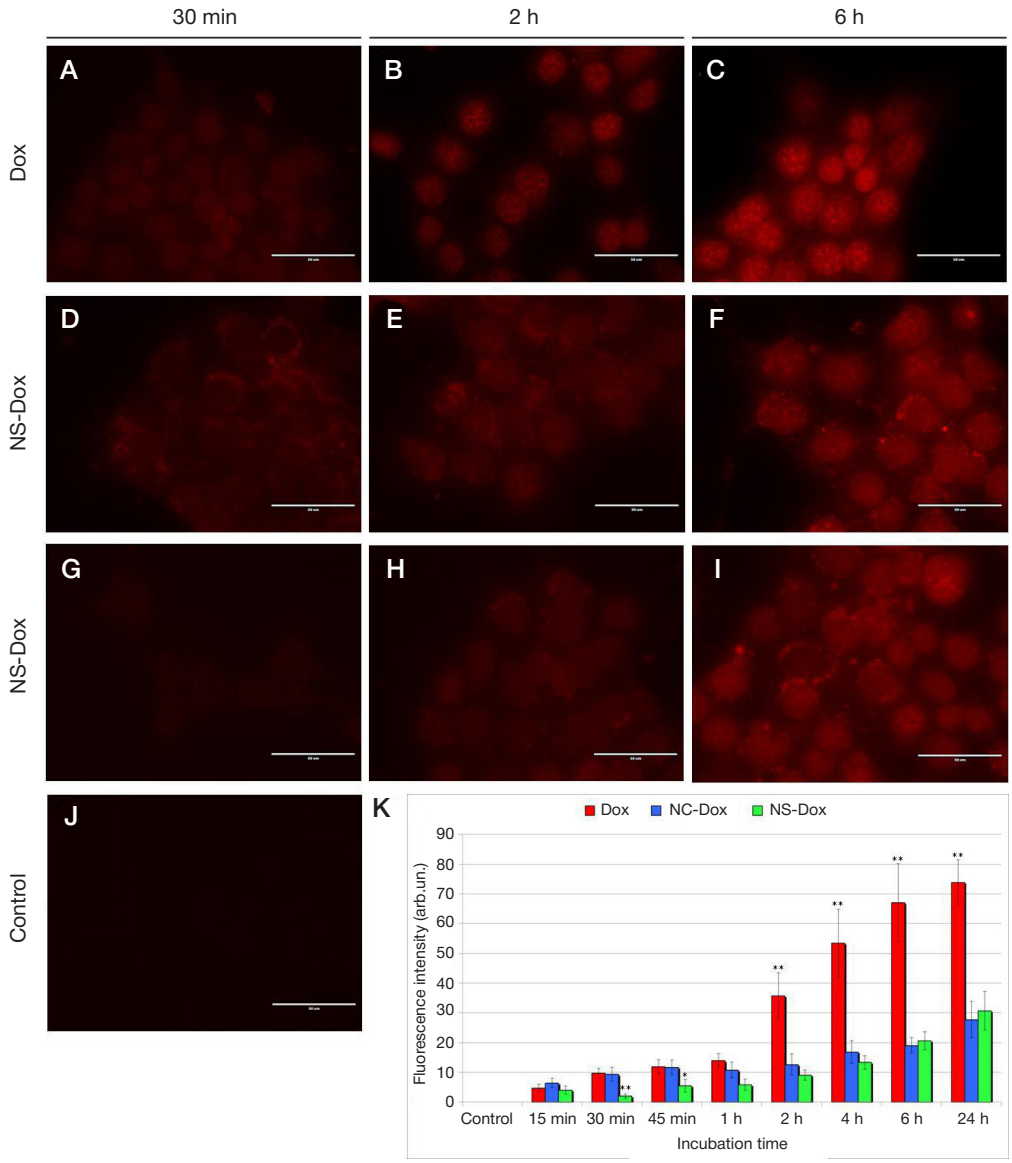

Fig. 6. Accumulation dynamics of free and entrapped doxorubicin in 4T1 cells. Fluorescence microscopy (**A–J**); a histogram showing the relationship between the intensity of doxorubicin fluorescence in the cells and the time of cell incubation with Dox, NC-Dox and NS-Dox (**K**). Results are presented as mean values ±SD. * $p < 0.05$; ** $p < 0.01$

The increase in the hydrodynamic size of NP in the aqueous solution is also associated with the adsorption of a stabilizing agent.

Doxorubicin is poorly soluble in water; therefore, in clinical practice its hydrochloride derivative is used instead. The polymer shell of nanoparticles is loaded with the drug in a sodium phosphate buffer where doxorubicin hydrochloride molecules are deprotonated and crystals start to form from its poorly soluble base. If the medium contains NP with hydrophobic sites, deprotonated doxorubicin can adsorb onto them. This also leads to an increase in the hydrodynamic size of NP doped with the drug and surface recharge (Fig. 4–3, Fig. 4–4). The entrapped drug can be protonated in a more acidic environment of cellular lysosomes (pH 4.5–5) and released from the polymer shell of the particles [16].

Recently a number of publications have demonstrated the advantages of nonspheric NP for hyperthermia therapy and MR imaging. There are reports that nanocubes [23, 24] and octopods [25] have higher SAR in comparison with nanospheres and therefore are suitable for magnetic hyperthermia. Besides, magnetic nanocubes have higher T2 relaxation values than their spherical counterparts [26]. Considering the above said, we decided to conduct the comparative analysis of the impact of NS and NC on mouse mammary carcinoma cells and on the efficiency of drug delivery to the cells.

Table. Results of the XRD analysis of NS and NC

	Phase	DTEM, nm	CSR, nm	Lattice constant, nm
NS	Fe_3O_4 (100%)	11–17	6 ± 1	0.8373 ± 0.0004
NC	Fe_3O_4 (100%)	13–20	6 ± 1	0.8378 ± 0.0004

We established that at concentrations of up to 227 mg/l both shapes do not exhibit cytotoxicity. NC loaded with doxorubicin induced a slightly more significant cell death than NS. A possible explanation here is that NC penetrate the cell faster than NS. But this difference was insignificant in our experiment. Free doxorubicin has a significantly more powerful tumoricidal effect and more readily accumulates in cell nuclei, perhaps due to the fact that free doxorubicin enters the cell by diffusion, whereas the drug carried by NP is endocytosed, which takes longer. Importantly, the particles loaded with doxorubicin are first visualized in intracellular vesicles (probably, lysosomes) where it is later protonated. Only after that the drug can be released from its carrier and transported into the nucleus

[27]. Summing up, doxorubicin carried to the cell by NP has a weaker tumoricidal effect but the platform can be modified by attaching specific ligands to the NP surface in order to achieve improved cytotoxicity [28].

CONCLUSIONS

Our study revealed that the efficiency of free doxorubicin delivery to 4T1 mouse mammary carcinoma cells is higher than that of the drug loaded onto NS and NC. Free doxorubicin enters the cell by diffusion and accumulates in the cell nucleus. If the drug is carried to the cell by iron oxide nanoparticles, it is endocytosed and then accumulates in the vesicles. Then it is gradually released into the intracellular environment. Partial release results in lower IC_{50} of the loaded drug in comparison with free doxorubicin. Although NC were more efficient than NS in delivering the drug into the cells, this difference was insignificant.

Литература

1. Ling D, Hyeon T. Chemical design of biocompatible iron oxide nanoparticles for medical applications. Small. 2013; 9 (9–10): 1450–66. DOI:10.1002/smll.201202111.
2. Majewski P, Thierry B. Functionalized Magnetite Nanoparticles — Synthesis, Properties, and Bio-Applications. Crit Rev Solid State Mater Sci. 2007; 32 (3–4): 203–15.DOI:10.1080/10408430701776680.
3. Xie J, Huang J, Li X, Sun S, Chen X. Iron oxide nanoparticle platform for biomedical applications. Curr Med Chem. 2009; 16 (10): 1278–94. DOI:10.2174/092986709787846604.
4. Oh JK, Park JM. Iron oxide-based superparamagnetic polymeric nanomaterials: Design, preparation, and biomedical application. Prog Polym Sci. 2011; 36 (1): 168–89. DOI:10.1016/j.progpolymsci.2010.08.005.
5. Laurent S, Forge D, Port M, Roch A, Robic C, Vander Elst L et al. Magnetic iron oxide nanoparticles: Synthesis, stabilization, vectorization, physicochemical characterizations and biological applications. Chem Rev. 2008; 108 (6): 2064–110. DOI:10.1021/cr068445e.
6. Lin JJ, Chen JS, Huang SJ, Ko JH, Wang YM, Chen TL et al. Folic acid-Pluronic F127 magnetic nanoparticle clusters for combined targeting, diagnosis, and therapy applications. Biomaterials. 2009; 30 (28): 5114–24. DOI:10.1016/j.biomaterials.2009.06.004.
7. Andhariya N, Chudasama B, Mehta RV, Upadhyay RV. Biodegradable thermoresponsive polymeric magnetic nanoparticles: A new drug delivery platform for doxorubicin. J Nanoparticle Res. 2011; 13 (4): 1677–88. DOI:10.1007/s11051-010-9921-6.
8. Tavano L, Vivacqua M, Carito V, Muzzalupo R, Caroleo MC, Nicoletta F. Doxorubicin loaded magneto-niosomes for targeted drug delivery. Colloids Surfaces B Biointerfaces. 2013; (102): 803–7. DOI:10.1016/j.colsurfb.2012.09.019.
9. Jain TK, Foy SP, Erokwu B, Dimitrijevic S, Flask CA, Labhasetwar V. Magnetic resonance imaging of multifunctional pluronic stabilized iron-oxide nanoparticles in tumor-bearing mice. Biomaterials. 2009; 30 (35): 6748–56. DOI:10.1016/j.biomaterials.2009.08.042.
10. Yang H, Liu C, Yang D, Zhang H, Xi Z. Comparative study of cytotoxicity, oxidative stress and genotoxicity induced by four typical nanomaterials: The role of particle size, shape and composition. J Appl Toxicol. 2009; 29 (1): 69–78. DOI:10.1002/jat.1385.
11. Nair S, Sasidharan A, Divya Rani VV, Menon D, Nair S, Manzoor K et al. Role of size scale of ZnO nanoparticles and microparticles on toxicity toward bacteria and osteoblast cancer cells. J Mater Sci Mater Med. 2009; 20 (1): 235–41. DOI:10.1007/s10856-008-3548-5.
12. Huang X, Teng X, Chen D, Tang F, He J. The effect of the shape of mesoporous silica nanoparticles on cellular uptake and cell function. Biomaterials. 2010; 31 (3):438–48. DOI:10.1016/j.biomaterials.2009.09.060.
13. Xiong Y, Brunson M, Huh J, Huang A, Coster A, Wendt K et al. The role of surface chemistry on the toxicity of Ag nanoparticles. Small. 2013; 9 (15): 2628–38. DOI:10.1002/smll.201202476.
14. Tarantola M, Pietuch A, Schneider D, Rother J, Sunnick E, Rosman C et al. Toxicity of gold-nanoparticles: Synergistic effects of shape and surface functionalization on micromotility of epithelial cells. Nanotoxicology. 2011; 5 (2): 254–68. DOI:10.3109/17435390.2010.528847.
15. Tacar O, Sriamornsak P, Dass CR. Doxorubicin: An update on anticancer molecular action, toxicity and novel drug delivery systems. J Pharm Pharmacol. 2013; 65 (2): 157–70. DOI:10.1111/j.2042-7158.2012.01567.x.
16. Gautier J, Munnier E, Paillard A, Hervé K, Douziech-Eyrolles L, Soucé M et al. A pharmaceutical study of doxorubicin-loaded PEGylated nanoparticles for magnetic drug targeting. Int J Pharm. 2012; 423 (1): 16–25. DOI:10.1016/j.ijpharm.2011.06.010.
17. Yu WW, Falkner JC, Yavuz CT, Colvin VL. Synthesis of monodisperse iron oxide nanocrystals by thermal decomposition of iron carboxylate salts. Chem Commun. 2004; (20): 2306–7. DOI:10.1039/b409601k.
18. Park J, An K, Hwang Y, Park JG, Noh HJ, Kim JY et al. Ultra-large-scale syntheses of monodisperse nanocrystals. Nat Mater. 2004; 3 (12): 891–5. DOI:10.1038/nmat1251.
19. Hai HT, Yang HT, Kura H, Hasegawa D, Ogata Y, Takahashi M et al. Size control and characterization of wustite (core)/spinel (shell) nanocubes obtained by decomposition of iron oleate complex. J Colloid Interface Sci. 2010; 346 (1): 37–42. DOI:10.1016/j.jcis.2010.02.025.
20. Simon T, Boca S, Biro D, Baldeck P, Astilean S. Gold-Pluronic core-shell nanoparticles: Synthesis, characterization and biological evaluation. J Nanoparticle Res. 2013; 15 (4): 1578. DOI:10.1007/s11051-013-1578-5.
21. Gonzales M, Krishnan KM. Phase transfer of highly monodisperse iron oxide nanocrystals with Pluronic F127 for biomedical applications. J Magn Magn Mater. 2007; 311 (1): 59–62. DOI:10.1016/j.jmmm.2006.10.1150.
22. Zhou Z, Zhu X, Wu D, Chen Q, Huang D, Sun C et al. Anisotropic shaped iron oxide nanostructures: Controlled synthesis and proton relaxation shortening effects. Chem Mater. 2015; 27 (9): 3505–15. DOI:10.1021/acs.chemmater.5b00944.
23. Kolosnjaj-Tabi J, Di Corato R, Lartigue L, Marangon I, Guardia P, Silva AKA et al. Heat-Generating Iron Oxide Nanocubes: Subtle "Destructurators" of the Tumoral Microenvironment. ACS Nano. 2014; 8 (5): 4268–83. DOI:10.1021/nn405356r.
24. Guardia P, Di Corato R, Lartigue L, Wilhelm C, Espinosa A, Garcia-Hernandez M et al. Water Soluble Iron Oxide Nanocubes with High Values of Specific Absorption Rate for Cancer Cell Hyperthermia Treatment. ACS nano. 2012; 6 (4): 3080–91. DOI:10.1021/nn2048137.
25. Nemati Z, Alonso J, Martinez LM, Khurshid H, Garaio E, Garcia JA et al. Enhanced Magnetic Hyperthermia in Iron Oxide Nano-Octopods: Size and Anisotropy Effects. J Phys Chem C. 2016; 120 (15): 8370–9. DOI:10.1021/acs.jpcc.6b01426.
26. Lee N, Kim H, Choi SH, Park M, Kim D, Kim H-C et al. Magnetosome-like ferrimagnetic iron oxide nanocubes for highly sensitive MRI of single cells and transplanted pancreatic islets. Proc Natl Acad Sci. 2011; 108 (7): 2662–7. DOI:10.1073/pnas.1016409108.
27. Nizamov TR, Garanina AS, Grebennikov IS, Zhironkina OA, Strelkova OS, Alieva IB et al. Effect of Iron Oxide Nanoparticle Shape on Doxorubicin Drug Delivery Toward LNCaP and PC-3 Cell Lines. BioNanoScience. 2018; 8 (1): 394–406. DOI:10.1007/s12668-018-0502-y.
28. Kievit FM, Wang FY, Fang C, Mok H, Wang K, Silber JR et al. Doxorubicin loaded iron oxide nanoparticles overcome multidrug resistance in cancer in vitro. J Control Release. 2011; 152 (1): 76–83. DOI:10.1016/j.jconrel.2011.01.024.

References

1. Ling D, Hyeon T. Chemical design of biocompatible iron oxide nanoparticles for medical applications. Small. 2013; 9 (9–10): 1450–66. DOI:10.1002/smll.201202111.
2. Majewski P, Thierry B. Functionalized Magnetite Nanoparticles — Synthesis, Properties, and Bio-Applications. Crit Rev Solid State Mater Sci. 2007; 32 (3–4): 203–15.DOI:10.1080/10408430701776680.
3. Xie J, Huang J, Li X, Sun S, Chen X. Iron oxide nanoparticle platform for biomedical applications. Curr Med Chem. 2009; 16 (10): 1278–94. DOI:10.2174/092986709787846604.
4. Oh JK, Park JM. Iron oxide-based superparamagnetic polymeric nanomaterials: Design, preparation, and biomedical application. Prog Polym Sci. 2011; 36 (1): 168–89. DOI:10.1016/j.progpolymsci.2010.08.005.
5. Laurent S, Forge D, Port M, Roch A, Robic C, Vander Elst L et al. Magnetic iron oxide nanoparticles: Synthesis, stabilization, vectorization, physicochemical characterizations and biological applications. Chem Rev. 2008; 108 (6): 2064–110. DOI:10.1021/cr068445e.
6. Lin JJ, Chen JS, Huang SJ, Ko JH, Wang YM, Chen TL et al. Folic acid-Pluronic F127 magnetic nanoparticle clusters for combined targeting, diagnosis, and therapy applications. Biomaterials. 2009; 30 (28): 5114–24. DOI:10.1016/j.biomaterials.2009.06.004.
7. Andhariya N, Chudasama B, Mehta RV, Upadhyay RV. Biodegradable thermoresponsive polymeric magnetic nanoparticles: A new drug delivery platform for doxorubicin. J Nanoparticle Res. 2011; 13 (4): 1677–88. DOI:10.1007/s11051-010-9921-6.
8. Tavano L, Vivacqua M, Carito V, Muzzalupo R, Caroleo MC, Nicoletta F. Doxorubicin loaded magneto-niosomes for targeted drug delivery. Colloids Surfaces B Biointerfaces. 2013; (102): 803–7. DOI:10.1016/j.colsurfb.2012.09.019.
9. Jain TK, Foy SP, Erokwu B, Dimitrijevic S, Flask CA, Labhasetwar V. Magnetic resonance imaging of multifunctional pluronic stabilized iron-oxide nanoparticles in tumor-bearing mice. Biomaterials. 2009; 30 (35): 6748–56. DOI:10.1016/j.biomaterials.2009.08.042.
10. Yang H, Liu C, Yang D, Zhang H, Xi Z. Comparative study of cytotoxicity, oxidative stress and genotoxicity induced by four typical nanomaterials: The role of particle size, shape and composition. J Appl Toxicol. 2009; 29 (1): 69–78. DOI:10.1002/jat.1385.
11. Nair S, Sasidharan A, Divya Rani VV, Menon D, Nair S, Manzoor K et al. Role of size scale of ZnO nanoparticles and microparticles on toxicity toward bacteria and osteoblast cancer cells. J Mater Sci Mater Med. 2009; 20 (1): 235–41. DOI:10.1007/s10856-008-3548-5.
12. Huang X, Teng X, Chen D, Tang F, He J. The effect of the shape of mesoporous silica nanoparticles on cellular uptake and cell function. Biomaterials. 2010; 31 (3):438–48. DOI:10.1016/j.biomaterials.2009.09.060.
13. Xiong Y, Brunson M, Huh J, Huang A, Coster A, Wendt K et al. The role of surface chemistry on the toxicity of Ag nanoparticles. Small. 2013; 9 (15): 2628–38. DOI:10.1002/smll.201202476.
14. Tarantola M, Pietuch A, Schneider D, Rother J, Sunnick E, Rosman C et al. Toxicity of gold-nanoparticles: Synergistic effects of shape and surface functionalization on micromotility of epithelial cells. Nanotoxicology. 2011; 5 (2): 254–68. DOI:10.3109/17435390.2010.528847.
15. Tacar O, Sriamornsak P, Dass CR. Doxorubicin: An update on anticancer molecular action, toxicity and novel drug delivery systems. J Pharm Pharmacol. 2013; 65 (2): 157–70. DOI:10.1111/j.2042-7158.2012.01567.x.
16. Gautier J, Munnier E, Paillard A, Hervé K, Douziech-Eyrolles L, Soucé M et al. A pharmaceutical study of doxorubicin-loaded PEGylated nanoparticles for magnetic drug targeting. Int J Pharm. 2012; 423 (1): 16–25. DOI:10.1016/j.ijpharm.2011.06.010.
17. Yu WW, Falkner JC, Yavuz CT, Colvin VL. Synthesis of monodisperse iron oxide nanocrystals by thermal decomposition of iron carboxylate salts. Chem Commun. 2004; (20): 2306–7. DOI:10.1039/b409601k.
18. Park J, An K, Hwang Y, Park JG, Noh HJ, Kim JY et al. Ultra-large-scale syntheses of monodisperse nanocrystals. Nat Mater. 2004; 3 (12): 891–5. DOI:10.1038/nmat1251.
19. Hai HT, Yang HT, Kura H, Hasegawa D, Ogata Y, Takahashi M et al. Size control and characterization of wustite (core)/spinel (shell) nanocubes obtained by decomposition of iron oleate complex. J Colloid Interface Sci. 2010; 346 (1): 37–42. DOI:10.1016/j.jcis.2010.02.025.
20. Simon T, Boca S, Biro D, Baldeck P, Astilean S. Gold-Pluronic core-shell nanoparticles: Synthesis, characterization and biological evaluation. J Nanoparticle Res. 2013; 15 (4): 1578. DOI:10.1007/s11051-013-1578-5.
21. Gonzales M, Krishnan KM. Phase transfer of highly monodisperse iron oxide nanocrystals with Pluronic F127 for biomedical applications. J Magn Magn Mater. 2007; 311 (1): 59–62. DOI:10.1016/j.jmmm.2006.10.1150.
22. Zhou Z, Zhu X, Wu D, Chen Q, Huang D, Sun C et al. Anisotropic shaped iron oxide nanostructures: Controlled synthesis and proton relaxation shortening effects. Chem Mater. 2015; 27 (9): 3505–15. DOI:10.1021/acs.chemmater.5b00944.
23. Kolosnjaj-Tabi J, Di Corato R, Lartigue L, Marangon I, Guardia P, Silva AKA et al. Heat-Generating Iron Oxide Nanocubes: Subtle "Destructurators" of the Tumoral Microenvironment. ACS Nano. 2014; 8 (5): 4268–83. DOI:10.1021/nn405356r.
24. Guardia P, Di Corato R, Lartigue L, Wilhelm C, Espinosa A, Garcia-Hernandez M et al. Water Soluble Iron Oxide Nanocubes with High Values of Specific Absorption Rate for Cancer Cell Hyperthermia Treatment. ACS nano. 2012; 6 (4): 3080–91. DOI:10.1021/nn2048137.
25. Nemati Z, Alonso J, Martinez LM, Khurshid H, Garaio E, Garcia JA et al. Enhanced Magnetic Hyperthermia in Iron Oxide Nano-Octopods: Size and Anisotropy Effects. J Phys Chem C. 2016; 120 (15): 8370–9. DOI:10.1021/acs.jpcc.6b01426.
26. Lee N, Kim H, Choi SH, Park M, Kim D, Kim H-C et al. Magnetosome-like ferrimagnetic iron oxide nanocubes for highly sensitive MRI of single cells and transplanted pancreatic islets. Proc Natl Acad Sci. 2011; 108 (7): 2662–7. DOI:10.1073/pnas.1016409108.
27. Nizamov TR, Garanina AS, Grebennikov IS, Zhironkina OA, Strelkova OS, Alieva IB et al. Effect of Iron Oxide Nanoparticle Shape on Doxorubicin Drug Delivery Toward LNCaP and PC-3 Cell Lines. BioNanoScience. 2018; 8 (1): 394–406. DOI:10.1007/s12668-018-0502-y.
28. Kievit FM, Wang FY, Fang C, Mok H, Wang K, Silber JR et al. Doxorubicin loaded iron oxide nanoparticles overcome multidrug resistance in cancer in vitro. J Control Release. 2011; 152 (1): 76–83. DOI:10.1016/j.jconrel.2011.01.024.

ENABLING TECHNOLOGIES FOR THE PREPARATION OF MULTIFUNCTIONAL “BULLETS” FOR NANOMEDICINE

Martina K, Serpe L, Cavalli R, Cravotto G✉

Department of Drug Science & Technology,
Centre for Nanostructured Interfaces and Surfaces (NIS), University of Turin, Turin, Italy

Recent advances in nanotechnology, including modern enabling techniques that can improve synthetic preparation and drug formulations, have opened up new frontiers in nanomedicine with the development of nanoscale carriers and assemblies. The use of delivery platforms has attracted attention over the past decade as researchers shift their focus away from the development of new drug candidates, and toward new means with which to deliver therapeutic and/or diagnostic agents. This work will explore a transdisciplinary approach for the production of a number of nanomaterials, nanocomplexes and nanobubbles and their application in a variety of potential biological and theranostic protocols. Particular attention will be paid to nanobubbles, stimuli responsive nanoparticles and cyclodextrin grafted nanosystems produced under non-conventional conditions, such as microwave and ultrasound irradiation. Besides nanoparticles preparation, ultrasound can also act as an enabling technology when activating sensitive nanobubbles and nanoparticles.

Keywords: nanoparticles, nanobubbles, stimuli responsive, ultrasound, microwave

Funding: the University of Turin is warmly acknowledged for their financial support (Ricerca Locale 2017).

✉ **Correspondence should be addressed:** Giancarlo Cravotto
Via P. Giuria 9, Turin, Italy, 10125; giancarlo.cravotto@unito.it

Received: 26.06.2018 **Accepted:** 30.08.2018

DOI: 10.24075/brsmu.2018.082

ИСПОЛЬЗОВАНИЕ ПЕРЕДОВЫХ ТЕХНОЛОГИЙ ДЛЯ НАНОМЕДИЦИНЫ: ПОЛУЧЕНИЕ МНОГОФУНКЦИОНАЛЬНЫХ «ВОЛШЕБНЫХ ПУЛЬ»

К. Мартина, Л. Серпе, Р. Кавалли, Д. Кравотто ✉

Кафедра фармацевтических технологий,
Центр наноструктурированных интерфейсов и поверхностей, Туринский университет, Турин, Италия

Недавние достижения в области нанотехнологии, в том числе современные методы, позволяющие усовершенствовать способы приготовления лекарственных средств, открыли новые горизонты в наномедицине, связанные с разработкой наноразмерных средств доставки лекарственных препаратов и целых комплексов. Последнее десятилетие большое внимание уделяется использованию нанопереносчиков — усилия исследователей направлены не столько на разработку новых препаратов, сколько на поиск способов целевой доставки терапевтических и/или диагностических агентов. В работе рассмотрены трансдисциплинарный подход к получению наноматериалов, нанокомплексов, нановезикул и перспективы их применения в биологии и тераностике. Особое внимание уделено получению нанопузырьков, стимулчувствительных наночастиц (НЧ) и наносистем с привитым циклодекстрином при нестандартных условиях, таких как действие ультразвука (УЗ) и микроволнового излучения. Помимо использования в процессе приготовления НЧ, УЗ можно так же эффективно применять для активации чувствительных нановезикул и НЧ.

Ключевые слова: наночастицы, нанопузырьки, стимулчувствительный, ультразвук, микроволновое излучение

Финансирование: авторы признательны администрации Туринского университета за их финансовую поддержку (Ricerca Locale 2017).

✉ **Для корреспонденции:** Джанкарло Кравотто
ул. P. Giuria, д. 9, Турин, Италия, 10125; giancarlo.cravotto@unito.it

Статья получена: 26.06.2018 **Статья принята к печати:** 30.08.2018

DOI: 10.24075/vrgmu.2018.082

Engineered nanomaterials can be made from nearly any substance; carbon based nanomaterials, natural and synthetic polymers, silica, metal and metal oxides can all be used, just as lipophilic colloidal nanoparticles (NP) can be made from solid lipids and phospholipids. In the field of bionanotechnologies, nanomaterials are used for biomedical applications, including as drug carriers, contrast agents and biosensors. Many of the properties that make nanomaterials useful may also be responsible for toxicity to cells and organisms. Their high surface area, in fact, allows them to be more readily reactive and easily transported through environmental barriers, cellular membranes and throughout the body. Attention must be paid to safety issues and a rational, science-based approach to nanotoxicology must be undertaken if the full potential of nanotechnologies is to be realised.

A number of different approaches to NP preparation have been attempted over the years, with both conventional and non-conventional methodologies being used in the solid and liquid phases [1]. Producing NPs that are homogeneous in their size and shape distributions is paramount and a number of techniques have been tested for their ability to accomplish this task; mechanochemistry has been used in solvent-free, solid-phase protocols, while microwave (MW) and ultrasound (US) irradiation have mostly seen use in aqueous solution syntheses. MW radiation can produce high quality NPs in short time periods because it is an efficient heating source. Moreover,

sonochemical irradiation produces high mixing uniformity and a reduction in crystal growth, which can also lead to an acceleration in chemical dynamics effects and reaction rates. It can therefore be considered one of the most powerful tools in nanostructured material synthesis [2, 3].

Experience in sonochemistry and MW-assisted syntheses has been beneficial to the derivatization of carbon-based nanomaterials as well as to the production of nanostructured cyclodextrin (CD) oligomers and CD-grafted nanomaterials for biomedical applications. CD derivatives have been shown to host drugs and contrast agents and can thus act as versatile and efficient carriers and contrast agent for MRI. Furthermore, the grafting of CDs onto NPs increases their water solubility, surface accessibility and hosting capability. Nanobubbles (NBs) are spherical core/shell structures and innovative nanoplatforms upon which to develop multifunctional nanocarriers for targeted imaging and therapeutic applications. In the field of cancer medicine, nanosystems with stimuli-responsive features have attracted a great deal of attention because of their enhanced cancer drug targeting.

Interestingly, these nanodelivery strategies can all have a key role to play in the success of a therapy as they can provide “on demand release” and “personalized treatment”. These ideas can be exploited even further by applying the concept of “the right drug for the right person in the right moment”. This review highlights the current state and future prospects of smart drug delivery systems that benefit from their responses to specific internal (*e.g.*, variation in redox gradient) and external (*e.g.*, light, US and magnetic field) triggers.

Cyclodextrin-based or grafted nanomaterials

The use of nanotechnology for drug delivery applications provides new opportunities and may change the landscape of the pharmaceutical and biotechnology industries as the goal of targeted drug delivery, the delivery of drugs to intracellular targets and the monitoring of drug delivery sites (theranostics), comes ever closer. CDs can play a crucial role in the achievement of such challenging goals as they are biocompatible and are well-known to improve the physicochemical properties of drugs (stability, solubility and bioavailability) [4]. Non-conventional US and MW irradiation have seen widespread use, besides a variety of other synthetic methods, in the production of novel and known CD-based structures and have done so with high efficiency and in short reaction times.

A water-soluble oligo CD heterononamer has been synthesized under US irradiation for use as a dendrimeric multicarrier with high hosting ability. Its applicability as an MRI contrast agent was demonstrated via the relaxometric titration of Gd complexes placed within the dendrimeric platforms, as well as by cell viability and binding affinity experiments, which all gave excellent results [5].

CD can be efficiently grafted onto silica under conventional and non-conventional conditions [6, 7] (Fig. 1), while this hybrid system's ability to absorb organic molecules has been extensively studied and applied. An interesting example of dual-pore silica NPs has been investigated by J.-H. Lee *et al*. as efficient therapy for gene–chemo cancer. The positively charged larger pore was loaded with negatively charged siRNA and the smaller pore was loaded with doxorubicin, capped by 1-adamantanthiol and a CD complex [8].

A one-shot approach to the derivatization of carbon nanotubes (SWCNT) with CDs and contrast agents has been successfully performed under MW irradiation [9]. The efficiency of MW has also been exploited for the preparation of porphine grafted graphene oxide [10].

The capacity of CDs to include/release drugs in the field of magnetic NPs has been studied. Iron oxide NPs and Au nanoroots were modified with CD-conjugated ethylenediamine-functionalized poly(glycidyl methacrylate) with the aim of obtaining a multifunctional theranostic nanoplatform [11]. Magnetic NPs were efficiently coated with β-CD under US irradiation to provide an increase in magnetization, which was likely due to the high crystallinity of the system produced [12].

Nanobubbles: a versatile tool for biomedical applications

NBs are another valuable platform, one of the nanotechnology-based “bullets”, that is sensitive to physical external triggers and that has been proposed for imaging and therapeutic applications.

NBs derive from microbubbles, which are currently used in clinical practice as US contrast agents, but have nanoscale sizes. This feature offers some advantages, such as their extravasation from blood vessels into surrounding tissues, which improves imaging and delivery efficiency. In particular, this capability allows tumour tissues to be passively targeted via the Enhanced Permeability and Retention (EPR) effect that favours their local accumulation over long time periods. In addition, they can be triggered by US to enhance their acoustic and targeting properties. Indeed, NBs can be used as therapeutic cavitation nuclei for US-induced sonoporation, leading to the formation of transient pores in plasma membranes and the modification of cell permeability [13].

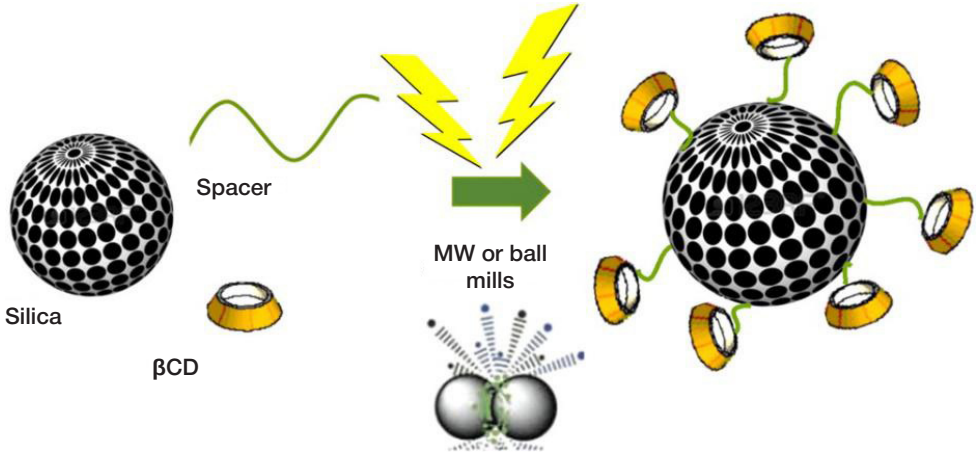

Fig. 1. Schematic representation of cyclodextrin grafted silica prepared under unconventional conditions [6]. Reprinted (adapted) with permission from (Martina K, Baricco F, Berlier G, Caporaso M, Cravotto G. ACS Sustainable Chem. Eng. 2014;2(11):2595-603). Copyright (2018) American Chemical Society)

They can be described as spherical core/shell structures that are filled with gases or vaporizable compounds, such as perfluorocarbons, sulfur hexafluoride, air or carbon dioxide [14]. The core is a single inner chamber that makes up the largest part of a particle's volume. The use of suitable core components is crucial since composition can affect both structural and functional behaviour. The use of gases that are insoluble in water for the core (e.g. perfluorocarbons) reduces the dissolution rate of the gas from the core into the external environment, enhancing the shelf life of the systems. The compressibility characteristics of the gas core can have a significant effect on system volumetric oscillations due to the compression and rarefaction cycles of US. The bubble volumetric oscillation can facilitate backscatter echoes and drug release, which can be useful for diagnostic imaging and therapeutic applications, respectively.

The composition of the shell determines the stiffness of the bubbles, their resistance to rupture in the US pressure field, recognition by the reticuloendothelial system and their biodistribution [15]. The shell generally consists of lipids (phospholipids, cholesterol), polymers (Pluronic, polysaccharides, PLGA) or proteins (albumin).

A great deal of research has been focused on a number of NB architectures and related compositions, among these we can find polysaccharide-shelled perfluorocarbon-cored NB that have provided some interesting results [16]. They are polymer/lipid hybrid systems that have been purposely tuned to overcome NB stability issues and to improve drug-loading capability. Moreover, the presence of the polysaccharide shell means that functionalization with specific target ligands is possible.

These hybrid systems contain a phospholipid monolayer at the NB interface that can interact with polyelectrolytes. The formulation design of the hybrid lipid/polymer system was based on the knowledge that phospholipid monolayers can adsorb charged polymers, such as polysaccharides, via various types of attraction, including both electrostatic and hydrophobic interactions.

A number of manufacturing approaches have attempted to reduce bubble size. Most of these involve post-formulation microbubble manipulation, such as gradient separation by gravitational forces, physical filtration or floatation. Another approach to achieving this aim, however, is the *ab initio* formulation of nanoscaled systems. In this approach, NBs are mainly prepared by sonication, high shear emulsification, thin-layer evaporation and mechanical agitation; procedures that have also been used in microbubble preparation [13].

NB technology is a versatile tool for the development of externally-triggered nanocarriers that provide controlled payload release with imaging properties.

Interestingly, NBs show good drug-encapsulation efficiency and prolonged-drug release kinetics. Table 1 reports a list of bioactive molecules that have been loaded into polysaccharide-shelled, perfluorocarbon-cored NB formulations using various loading methods.

Stimuli-responsive nanosystems

The efficiency of pharmacological treatment is strongly dependent on the success rate with which the active compound reaches the target site. Indeed, there are numerous challenges that a drug has to tackle before achieving its objective; enzyme attack, difficulty in accessing the target area and target-cell selectivity in competition with other sites. NP-based drug delivery systems (DDS) are therefore a promising strategy with which to face these issues, as nanotechnology has shown great improvements in target-specific drug delivery thanks to advances in passive and active targeted-drug delivery. Moreover, new additional properties that can be included within the NP-based DDS and that can enhance drug bioavailability at the disease site are very promising.

Conventional NP-based DDS ensures that the drug will not freely extravasate during blood circulation, but only be released at the target where the NPs accumulate, via either a passive or active targeting strategy. The passive strategy relies on the enhanced permeability and retention (EPR) effect that is observed in some pathological tissues. For instance, the accumulation of NPs in tumour tissue is much faster than in other tissues and is characterized by uneven distributions and particle-size dependency. On the other hand, active drug targeting takes advantages of specific target area features by decorating a NP-based DDS with monoclonal antibodies or bioconjugates [17].

However, these conventional NP-based DDSs are often accompanied by systemic side effects that are related to their non-specific biodistribution and uncontrollable drug release characteristics. There are already several NP-formulations of anticancer drugs on the market, including Doxil® and Abraxane®, which have shown improved safety profiles as compared to free-drug formulations. However, drug bioavailability at the tumour is still quite low which leads to insufficient improvements in therapeutic activity [18].

Advanced controlled NP-based DDSs are being developed to achieve drug release at target sites in a spatio-temporally controlled manner, and thus overcome these limitations. The fusion of engineered nanomaterials and pharmaceutical research is paving the way for the development of innovative nanoplatforms, especially for cancer treatment, where nanomaterials can add further functionality to the loaded drug and play a crucial therapeutic role. Well-defined nanosystems can increase drug-targeting efficacy and reduce side effects by taking advantage of responses to specific internal or external triggers, giving rise to so-called "smart" or stimuli-responsive nanosystems [19].

Table 1. Examples of bioactive molecules loaded into NB formulations

Therapeutic Applications	Loaded Drugs	Administration Routes
Anticancer	Doxorubicin, paclitaxel, docetaxel, cisplatin	Parenteral
Antibacterial	Vancomycin, erithromycin	Topical
Antifungal	Itraconazole	Topical
Antiviral	Acyclovir, valacyclovir	Topical
Anti-Inflammatory	Prednisolone	Parenteral
Gene Therapy	DNA, si RNA	Parenteral
Hypoxia-Associated Pathology	Oxygen	Parenteral/Topical
Theranostic System	Gd Complexes	Parenteral
Others	Curcumin, melatonin	Parenteral/Topical

There are a number of stimuli-responsive nanosystems that we can primarily distinguish; i) those that recognize changes in the biological milieu and thus modulate the drug-release rate as closed-loop systems related to disease features (internal triggers, such as variations in pH, redox gradient, temperature and substance concentrations), and ii) those that switch drug release on as a function of specific external triggers and thus operate as open-loop systems that can provide pulsed drug release when externally activated (external triggers such as light, US, temperature, magnetic field and high energy radiation).

Sensitiveness to internal or external stimuli can be achieved using nanomaterials (mostly polymers) that bear functional groups that are able to modify their properties as a function of the intensity of the signal, which results in changes in DDS features, such as the ability to release the drug. These changes can have different levels of complexity, but only when these structural changes are reversible and proportional to the stimulus intensity can the NP-based DDS be considered "smart". When the target cells are those of a tumour, these requirements can be summarised in the 2R2S features, *i.e*. drug retention in blood circulations *versus* release in tumour (2R) and stealthy in blood *versus* sticky in tumour (2S) [18].

1. Nanosystems that are responsive to internal stimuli

1.1. pH responsive NPs

One typical example of internal-stimuli responsive nanosystems can be found in pH-responsive nanocarriers for solid tumour targeting. The low pH that exists in the tumour extracellular matrix, caused by a high rate of glycolysis, can be used as a specific stimulus. Surface charge switchable polymeric nanosystems have been designed to enhance tumour drug delivery, as surface charge is pivotal for cell uptake. Indeed, positively charged NPs display significant cellular uptake thanks to electrostatic interactions with cell membranes. Moreover, positively charged NPs are capable of acting as "proton sponges" that disrupt lysosomes, enhance cytoplasmic delivery and induce cancer-cell death [20].

A new tetraglucose-based biomaterial, made up of cyclic nigerosyl-1-6-nigerose (CNN), has been produced by Caldera *et al*. A cross-linking reaction with pyromellitic dianhydride formed solid NPs, called nanosponges (NS). This new nanomaterial is biocompatible and able to swell in response to the pH value. Doxorubicin was incorporated to a good extent and released with very slow and constant kinetics. Interestingly, local pH plays a role in controlling the release profile of the drug. The pH-dependent and prolonged-release kinetics of doxorubicin from CNN-NS and their enhanced anticancer activity mean that doxorubicin-loaded CNN-NS acted as a nanomedicine tool for local tumour treatment and did so with a favourable toxicology profile [21].

Interestingly, fluorescent CD derivatives have been used as acid-sensitive gatekeepers to block silica mesopores and have undergone successful doxorubicin release studies. This system presents the significant advantage of operators being able to trace the NP pathways using the green fluorescence and thus monitor therapy process [22].

1.2. Redox responsive NPs

The design and fabrication of redox responsive NPs is another promising means of targeting specific tumour intracellular sites. Glutathione (GSH) reduction is a well-known redox system that operates within cancer cells, which has led to GSH-responsive nanocarriers being proposed for targeted intracellular anticancer drug release. Indeed, GSH levels within cancer cells are 100 to 500 times higher than normal ranges [23]. It is well known that intracellular GSH can trigger thiol-disulfide bond exchange. Polymers with disulfide bonds can make use of this property to facilitate rapid release from carriers when stimulated by GSH. In general, there are two ways that disulfide bonds can be used in polymer systems; a) via modification of the disulfide bond on the backbone, and b) via the use of disulfide bonds as cross-linkers within the polymeric network.

Daga *et al*. have tuned nanosponge-based drug delivery systems to be bioresponsive to GSH for rapid nanosystem destabilization inside cells. The disulfide bridge remains stable in extracellular fluids for long periods before being reduced upon internalization within the cytosol. This improves drug bioavailability and the efficiency of the reduction-sensitive nanosystem as depleting endogenous antioxidants, such as GSH, makes cancer cells more chemosensitive. A new class of GSH-responsive CD nanosponges (GSH-NS) was then designed to preferentially release doxorubicin in cells with high GSH content. Doxorubicin-loaded GSH-NS inhibited clonogenic growth, cell viability, topoisomerase II activity and induced DNA damage with higher effectiveness than the free drug in various cancer cell lines. It is worth noting that GSH-NS were able to reduce human prostatic tumour development more than the free drug, without evidence of significant organ toxicity in a xenograft model [24]. Doxorubicin-GSH-NS can affect cell proliferation at doses lower than the free-form drug, which allows effective drug doses and, therefore, systemic adverse effects to be reduced.

2. Nanosystems that are responsive to external stimuli

2.1. Light responsive NPs

Light-responsive nanosystems are a way to trigger drug release at a desired target using external light at appropriate wavelengths. However, the poor penetration depth of light into tissues currently limits its applications. Light-triggered release can be achieved by conjugating drugs to the nanosystems via photo-cleavable bonds or by developing photosensitive carriers that are able to provide on/off drug release via changes in their nanostructure under light exposure. For example, NIR-triggered release has been observed in poly(lactic-co-glycolic acid) matrix particles containing doxorubicin and covered with a gold over-layer [25]. Gold-containing DDSs have attracted a great deal of attention in recent years due to their enhanced and tunable optical properties, easy production and functionalization as well as good biocompatibility. Moreover, gold NPs set themselves apart from other nanoplatforms thanks to their unique localized surface plasmon resonance (SPR), which can be used in the multimodal treatment of cancer, an example of which is photothermal therapy [26]. Under NIR irradiation, the SPR of the gold NPs causes the local temperature to increase above body temperature by several degrees. For example, this feature is being used in AuroShells, which are gold nanoshells that are already in clinical trials for the treatment of solid tumours. After intravenous injection, these nanosystems are irradiated with a fibre-optic laser to provide high temperatures to the tumour area for the photothermal therapy of cancer [27]. Moreover, the surface of gold NPs is suitable for the conjugation of drugs, oligonucleotides and peptides making gold NPs appropriate platforms for DDS that can be activated by external stimuli.

2.2. Temperature –responsive and US responsive NPs and NBs

Temperature is one of the most convenient and effective factors that can be used to control drug release. In pathophysiological conditions, such as tumours, tissue temperatures are higher than those in healthy tissues. This temperature difference allows functionalized nanosystems to be triggered and enhances drug release in tumours. Thermo-sensitive nanocarriers are usually designed to retain the drug at physiological temperature (37 °C), and rapidly release it when the temperature is higher than 40–45 °C. This is commonly the reason for NB release, but a number of different nanosystems have been designed with the aim of maintaining safety without losing sensitivity to slight temperature differences.

Tumour-specific drug accumulation can be achieved by combining hyperthermia and temperature-sensitive liposomes. ThermoDox, which is a temperature-sensitive doxorubicin liposome formulation, is probably the closest to clinical use at the moment. This nanosystem was designed to simultaneously achieve the passive targeting of doxorubicin towards tumour tissues and enhanced drug delivery in tumour microvasculature by applying an external source of heating, such as US. Dipalmitoyl phosphatidylcholine's lipid-crystallization melting temperature of 41.5 °C means that doxorubicin is released from the nanosystem at this temperature. Moreover, radiofrequency ablation was also used to trigger drug release from ThermoDox. Liver-cancer targeted ThermoDox displayed an improved safety profile compared to free doxorubicin in a Phase I clinical trial. Although the life span after ThermoDox treatment failed to reach the 33% threshold in Phase III clinical trials, the treatment strategy has a promising future as a stimuli-responsive DDS [19].

2.3. US responsive NPs and NBs

US has been extensively used in clinics for diagnosis and therapy because of its intrinsic tissue penetration and high safety; low-frequency US can penetrate several centimetres into the body with very low scattering [18].

US can affect tissues via a variety of mechanisms, thermal and non-thermal, and by tuning frequency, power intensity and exposure time. The heat generation produced by US is a well-known mechanism and is used in so-called high intensity focused ultrasound (HIFU) for the treatment of prostatic cancer [28], whereas the therapeutic uses of non-thermal US have been investigated less thoroughly. Besides the direct thermal effect, the effects of US on tissues include: a) alterations in biobarrier permeability (namely sonoporation), b) drug delivery and c) sonodynamic activity. The last of these effects has opened up new perspectives for cancer treatment, including sonodynamic therapy (SDT), in which a nontoxic molecule or system (chemical actuator, sonosensitizer) is activated by US (physical activator) and yields oxidative damage and consequent cancer cell death. SDT is thus achieved by an external physical stimulus that activates molecules or colloidal systems providing, in turn, a biological effect only when the two are combined together. Briefly, acoustic cavitation is defined as the formation or activity of gas- or vapour-filled cavities (bubbles) in a medium exposed to an US field. Specifically, bubbles in a stable cavitation state oscillate, which causes the surrounding liquid to stream, resulting in the mixing of the surrounding media, whereas gas bubbles in an inertial cavitation state grow to near-resonance size and expand to a maximum before collapsing violently. In this latter case, the extreme temperatures, up to 10,000 K, and pressures, up to 81 MPa, that are produced in the surrounding microenvironment by the energy released during implosion are viewed as constituting a “sonochemical reactor” [29]. In anticancer sonodynamic activity, NPs may not only act as a sonosensitiser vehicle capable of improved and spatio-temporal controlled anticancer activity upon external US stimulus, but also as a sonosensitiser *per se* if appropriately designed [30].

In the field of US-responsive drug delivery systems, the use of NB in combination with US is also attractive for the targeted delivery of nucleic acids [31]. This could be achieved using various loading methods, such as the direct physical incorporation of DNA into the shell during fabrication, the use of cationic lipids or polymers in the shell to bind DNA by electrostatic interaction, and the covalent linking of DNA-NPs.

The authors of the present manuscript have exploited the capabilities of various nanosystems and used them as delivery systems for US-responsive chemical compounds (sonosensitisers), and as US-responsive systems themselves for the sonodynamic treatment of cancer. We demonstrated the significant anticancer activity of poly-methyl methacrylate core-shell NPs loaded with meso-tetrakis (4-sulfonatophenyl) porphyrin (TPPS-PMMANP) under US exposure at the target site in an *in vitro* neuroblastoma model [32]. These porphyrin-loaded core-shell NPs were then engineered for use as *in vivo* sonosensitizing systems, radiotracers and magnetic resonance (MR) imaging agents, which may be suitable for the selective treatment of solid tumours and imaging analyses. Indeed, PMMANP were either loaded with TPPS for sonodynamic anticancer treatment, with ^{64}Cu-TPPS for positron emission tomography biodistribution studies or with Mn(III)-TPPS for MR tumour accumulation evaluation. TPPS-PMMANP demonstrated US responsiveness, as measured by MR analyses of pre- and post-treatment tumour volumes, in a syngeneic breast cancer model, proving that this multimodal system can efficiently induce selective and externally guided anticancer activity [33].

The properties of inorganic NPs, in this case gold NPs, have been investigated to harness their unique SPR phenomenon. Folate-PEG decorated gold NPs (FA-PEG-GNP) were tested as sonosensitizers for the treatment of cancer. Their US responsiveness in human cancer cell lines that expressed varying amounts of folate receptors was tested, and FA-PEG-GNP was found to selectively target folate-receptor overexpressing cancer cells providing a significant reduction in cell growth upon US exposure, along with impressive reactive oxygen species generation and an increase in necrotic cells [34]. The simultaneous exploitation of the gold NP targeting capacity and the sensitizing effect afforded by localized external stimuli make these nanosystems promising candidates for the site-specific treatment of cancer. This *in vitro* study can be considered proof of concept for gold NP use as nanosonosensitizers in the US-based treatment of cancer.

Formulations that are referred to as “NBs”, prior to the application of external stimuli such as US, should be considered “nanodroplets” when the core is constituted of perfluoropentane, which is a perfluorocarbon that is found in the liquid state at room temperature (boiling point 29 °C). Release can be activated in the presence of US via the Acoustic Droplet Vaporization (ADV) mechanism [35].

The feasibility of combining NB with US as a topical treatment for skin disease has been investigated in the design of a therapeutic tool to topically treat hypoxia-associated dermal pathologies and promote the wound-healing process [36].

Dextran- and chitosan-shelled NBs loaded with decafluoropentane (called nanodroplets) or dodecafluoropentane (called NBs) have been developed as oxygen delivery systems

thanks to the ability of perfluorocarbons to solubilize and store oxygen in the core and release it with prolonged kinetics [36–39]. Decafluoropentane systems have shown marked effectiveness, both *in vitro* and *in vivo*, in releasing oxygen to hypoxic environments, as demonstrated by complementary analysis that made use of oxymetry and photoacoustic imaging. Chitosan-shelled and oxygen-loaded nanodroplets were proposed [36, 40] as an innovative tool for the adjuvant treatment of infected chronic wounds by exploiting chitosan's antimicrobial properties.

Oxygen-loaded nanodroplets have shown significant cytostatic activity against methicillin-resistant Staphylococcus aureus (MRSA) and Candida Albicans, and no toxicity in human keratinocytes (HaCaT cells). Moreover, complementary US treatment promoted oxygen transdermal delivery from the nanodroplets to hypoxic tissues. Much research has been devoted in recent years to the study of NB formulations to carry oxygen as exogenous oxygen is difficult to deliver into tumours that are distant from blood vessels. The high oxygen solubility of bubbles is beneficial for hypoxic tissue oxygenation.

New vancomycin-loaded dextran sulfate-shelled NBs have been designed [41] for local drug delivery for the treatment of cutaneous infectious disease. The combination of vancomycin-loaded NB and US enhanced the drug's penetration through the skin by sonophoresis and triggered local drug release at the site of infection.

Diethylaminoethyl-dextran (DEAE)-shelled NBs have been found to incorporate and protect DNA from the action of proteases and transfect plasmid DNA across the cell membrane without any resulting cytotoxic effects [42]. Another NB formulation, consisting of a chitosan-based shell, has also been designed for DNA delivery. DNA-loaded chitosan NBs with a mean diameter of less than 300 nm and a good DNA payload were obtained [43]. *In vitro* transfection experiments were performed by exposing adherent COS7 cells to US (2.5 MHz) in the presence of varying concentrations of plasmid DNA-loaded NBs. NBs failed to trigger transfection in the absence of US at all concentrations tested. By contrast, 30 seconds of US promoted a moderate degree of transfection. Cell viability experiments demonstrated that neither US nor NB affected cell viability under these experimental conditions.

Continuous efforts in the field of cancer immunotherapy in recent years have led to the development of several vaccination strategies that are based on tumour-associated-antigens, such as the HER2 oncogene.

Cancer vaccination offers distinct advantages over standard therapies. These advantages include higher specificity, lower toxicity and reduced long-term effects, which are all due to immunologic memory. Nanotechnology has great potential to make immune therapy more efficient. Indeed, in order to correctly expand the immune response against tumours, a vaccine needs to effectively reach the dendritic cells, which play a critical role in inducing a proper immune activation.

A novel immunotherapeutic tool, which is based on chitosan-shelled NBs loaded with a DNA vaccine and functionalized with anti-CD11c antibodies to target DCs, has recently been developed for the treatment of HER2+ breast cancer [44]. The intradermal injection of pHER2-loaded CD11c-NBs led to the migration of dermal DCs to draining lymph nodes and the delayed growth of HER2+ tumours, thus promoted cellular and humoral immune responses were observed in the mouse model.

Various NB formulations have been investigated as theranostic platforms with the intention of exploiting their echogenic properties. In fact, polymer-shelled NBs have been widely proposed as multifunctional agents with the aim of providing cancer cell targeting, US imaging and US-triggered cancer therapy.

The authors of the present review have tuned a chitosan-based NB formulation to act as a theranostic system that can provide the double imaging detection of NBs [45]. The formulation was designed for the co-delivery of prednisolone phosphate, located at the interface with the perfluoropentane core, and a negatively charged GD-DOTP complex, which was electrostatically bound to the cationic chitosan NB shell. The NBs were echogenic, meaning that it may be possible to visualize them by means of real-time echography imaging, while the ability to generate positive MRI contrast was demonstrated.

Extracorporeal Shock Waves (ESWs) have also been studied as another physical external stimulus with which to trigger drug release from NBs, besides US. ESWs are short-duration (<10 μs) focused acoustic waves that are widely used in urology for lithotripsy and for the treatment of several musculoskeletal diseases. The effectiveness of using drug-loaded NBs together with Extracorporeal Shock Waves (ESW) was thoroughly investigated. Interestingly, the effects of combining chemotherapeutic drug-loaded NBs and ESWs have recently been demonstrated in two different types of aggressive cancers, anaplastic thyroid cancer (ATC) and castration resistant prostate cancer (CRPC) [46–49]. Moreover, Marano *et al*. have reported that combined treatment with either paclitaxel- or docetaxel-loaded NBs and ESW enhanced the cytotoxicity of both the drugs in two different cell lines (PC3 and DU145) of CRPC, resulting in a paclitaxel GI50 reduction of about 55% and in a docetaxel GI50 reduction of about 45% (Fig. 2) [48].

2.4. Magnetic responsive NPs

Magnetic stimuli may provide a non-invasive approach to the temporal and spatial control of carrier targeting and drug release under the programmable exposure of an external magnetic field. The most commonly-used core/shell magnetic NPs (MNP) exhibit a variety of unique magnetic properties. The large surface-to-volume ratio of MNPs provides abundant active sites for biomolecule conjugation and thus facilitates their precise design and engineering, which should ensure that their intended smart capabilities, such as long-lasting circulation in the blood stream, target specificity to lesion tissues, and therapeutic delivery, operate efficiently under the action of a localized external magnetic field. Temperature increases can be obtained using a variety of energy sources, with the most commonly used being electromagnetic (EM) energy. Hyperthermia (HT) is typically performed at high frequencies (13 MHz to 430 MHz according to tumour depth) with phased-array antennas being placed outside the body, while MWs (915 MHz or 2.45 GHz) are applied in thermal ablation (MTA) through interstitial antennas placed in the tumour centre. Both HT and MTA have proven their safety and efficacy in several clinical trials [50]. However, both techniques suffer from poor reproducibility and difficulties in controlling the temperature distribution inside the tumour over the various clinical conditions. Research is thus currently being devoted to the improvement of heating uniformity and target specificity, while aiming to minimise invasiveness. A promising route to this aim can be found in MNP-mediated thermotherapies, which are used as sources of local heating after their injection into the tissue and successive exposure to external magnetic fields. The main limitation of magnetic thermotherapy is the poor heating efficiency of most magnetic nanomaterials, so that therapeutic effects are only observed when large amounts of MNP are

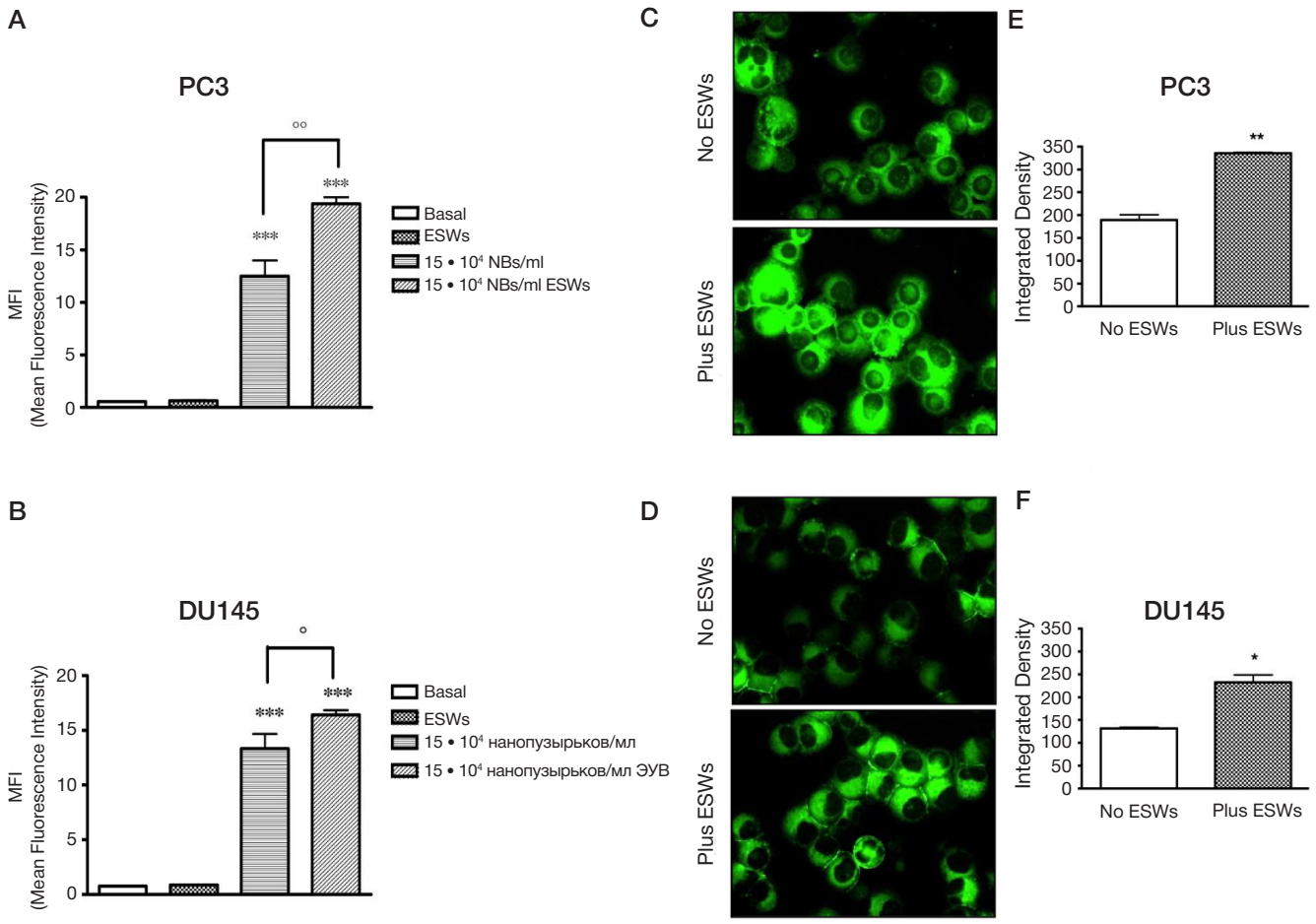

Fig. 2. Nanobubble entrance. Cytofluorimetric analysis of PC3 (**A**) and DU145 (**B**) cells treated for 24 hours with 6-coumarin-labelled glycol chitosan NBs (15 • 10^4 NBs/ml), either in the absence and in the presence of ESWs, expressed as Mean Fluorescence Intensity (MFI). Significance vs untreated cells (Basal): $p < 0.001$ (***); significance vs ESWs: $p < 0.05$ (°); $p < 0.01$ (°°). Photos by fluorescence microscope of PC3 (**C**) and DU145 (**D**) cells treated with 6-coumarin-labelled glycol chitosan NBs at 15 • 10^4 NBs/ml, either in the absence and in the presence of ESWs. Pictures were taken at ×200 final magnification (scale bar: 100 μm). The images are representative of three independent experiments; for each experiment, 10 fields were quantified. Image-based quantification of 6-coumarin-labelled glycol chitosan NBs in PC3 (**E**) and DU145 (**F**) cells. Significance vs no ESWs: $p < 0.05$ (*); $p < 0.01$ (**). [ref 48]

injected into the tumour. Significant work is accordingly being performed on the optimization of heating efficiency and biocompatibility by tuning MNP size and physical properties, as well as considering several different coating materials. Magnetic nanodisks (MND) and nanorings have recently emerged as a valid alternative to MNPs, as they are characterized by negligible remnant magnetization and the consequent advantageous reduction of the long-range magnetostatic forces responsible for particle agglomeration. Preliminary studies demonstrated the potential of these nanostructures as effective nanomediators for cancer thermotherapy as they show improved HT properties with respect to isotropic MNPs. Magnetic Ni80Fe20 NPs with a disc shape have been obtained by nanolithography and were directly coated with a gold layer [51]. Functionalization of the gold surface of coated MNDs was performed with a cysteine-fluorescein isothiocyanate (FITC) derivative, by the authors of the present manuscript, in order to induce random fluorescence for use as a means to evaluate intracellular uptake. The magnetization process of all the MNDs was characterized by the presence of a vortex which pointing to a possible exploitation in drug delivery process and also in magnetic hyperthermia. It is worth noting that cytotoxicity tests confirmed that gold-coated MNDs displayed higher biocompatibility than the bare nanodisks despite not being completely coated. The intracellular uptake of the MNDs was confirmed by cytofluorimetric analysis using the FITC conjugate on the surface of the gold-coated MNDs [52].

CONCLUSIONS

Smart DDSs have proven themselves to be highly efficient in biomedical applications. However, their potential druggability still requires extensive evaluation before clinical use is feasible. Indeed, there are a number of stimuli-responsive nanosystems are currently undergoing clinical evaluation, but only a few have been approved for clinical use, such as NanoTherms®, and most of them are commercialized for research use only [18]. Future work on smart DDSs should therefore be focused on more feasible and homogeneous preparation methods and on clinical translation to ensure that more stimulus-sensitive nanomedicines can see use in clinics. Indeed, improving the preclinical research of advanced DDSs to make them more reproducible and then translate that to success into clinical trials will be an enormous challenge for researchers.

References

1. Portehault D, Delacroix S, Gouget G, Grosjean R, Chan-Chang T-H-C. Beyond the Compositional Threshold of Nanoparticle-Based Materials. Accounts of Chemical Research. 2018; 51 (4): 930–9.
2. Cravotto G, Boffa L. Preparation of nanomaterials under combined ultrasound/microwave irradiation. Pan Stanford Publishing Pte. Ltd.: 2014; p. 203–26.
3. Martina K, Tagliapietra S, Barge A, Cravotto G. Combined Microwaves/Ultrasound, a Hybrid Technology. Top Curr Chem. 2016; 374 (6): 1–27.
4. Davis ME, Brewster ME. Cyclodextrin-based pharmaceutics: past, present and future. Nat Rev Drug Discov. 2004; (3): 1023–35.
5. Barge A, Caporaso M, Cravotto G, Martina K, Tosco P, Aime S et al. Design and Synthesis of a γ1β8-Cyclodextrin Oligomer: A New Platform with Potential Application as a Dendrimeric Multicarrier. Chem Eur J. 2013; 19 (36): 12086–92.
6. Martina K, Baricco F, Berlier G, Caporaso M, Cravotto G. Efficient Green Protocols for Preparation of Highly Functionalized β-Cyclodextrin-Grafted Silica. ACS Sustainable Chem Eng. 2014; 2 (11): 2595–603.
7. Huq R, Mercier L, Kooyman PJ. Incorporation of Cyclodextrin into Mesostructured Silica. Chem Mater. 2001; 13 (12): 4512–9.
8. Lee J-H, Kang S, Ahn M, Jang H, Min D-H. Development of dual-pore coexisting branched silica nanoparticles for efficient gene-chemo cancer therapy. Small. 2018; 14 (7): 1702564.
9. Calcio Gaudino E, Tagliapietra S, Martina K, et al. Novel SWCNT platform bearing DOTA and β-cyclodextrin units. "One shot" multidecoration under microwave irradiation. Org Biomol Chem. 2014; (12): 4708–15.
10. Bosca F, Orio L, Tagliapietra S, Corazzari I, Turci F, Martina K, Pastero L, Cravotto G et al. Microwave-Assisted Synthesis and Physicochemical Characterization of Tetrafuranylporphyrin-Grafted Reduced-Graphene Oxide. Chem Eur J. 2016; (22): 1608–13.
11. Duan S, Li J, Zhao N, Xu F-J. Multifunctional hybrids with versatile types of nanoparticles via self-assembly for complementary tumor therapy. Nanoscale. 2018; (10): 7649–57.
12. Bolden NW, Rangari VK, Jeelani S, Boyoglu S, Singh SR. Synthesis and evaluation of magnetic nanoparticles for biomedical applications. J Nanopart. 2013: 1–9; DOI:10.1155/2013/370812.
13. Güvener N, Appold L, de Lorenzi F, Golombek SK, Rizzo LY, Lammers T, Kiessling F. Recent advances in ultrasound-based diagnosis and therapy with micro-and nanometer-sized formulations. Methods. 2017; (130): 4–13.
14. Cavalli R, Soster M, Argenziano M. Nanobubbles: a promising efficient tool for therapeutic delivery. Ther Deliv. 2016; 7 (2): 117–38.
15. Delalande A, Postema M, Mignet N, Midoux P, Pichon C. Ultrasound and microbubble-assisted gene delivery: recent advances and ongoing challenges. Ther Deliv. 2012; 3 (10): 1199–215.
16. Cavalli R, Bisazza A, Giustetto P, Civra A, Lembo D, Trotta G et al. Preparation and characterization of dextran nanobubbles for oxygen delivery. Int J Pharm. 2009; 381 (2): 160–5.
17. Malam Y, Loizidou M, Seifalian AM. Liposomes and nanoparticles: nanosized vehicles for drug delivery in cancer. Trends Pharmacol Sci. 2009 Nov; 30 (11): 592–9.
18. Alvarez-Lorenzo C1, Concheiro A. Smart drug delivery systems: from fundamentals to the clinic. Chem Commun. 2014; 50 (58): 7743–65.
19. Liu D, Yang F, Xiong F, Gu N. The Smart Drug Delivery System and Its Clinical Potential. Theranostics. 2016 Jun 7; 6 (9): 1306–23.
20. Sharifi S, Behzadi S, Laurent S, Forrest ML, Stroeve P, Mahmoudi M. Toxicity of nanomaterials. Chem Soc Rev. 2012 Mar 21; 41 (6): 2323–43.
21. Caldera F, Argenziano M, Trotta F, Dianzani C, Gigliotti L, Tannous M et al. Cyclic nigerosyl-1,6-nigerose-based nanosponges: An innovative pH and time-controlled nanocarrier for improving cancer treatment. Carbohydr Polym. 2018; (194): 111–21.
22. Chen X, Yao X, Wang C, Chen L, Chen X. Mesoporous silica nanoparticles capped with fluorescence-conjugated cyclodextrin for pH-activated controlled drug delivery and imaging. Microporous Mesoporous Mater. 2015; (217): 46–53.
23. Torchilin VP. Multifunctional, stimuli-sensitive nanoparticulate systems for drug delivery. Nat Rev Drug Discov. 2014 Nov; 13 (11): 813–27.
24. Daga M, Ullio C, Argenziano M, Dianzani C, Cavalli R, Trotta F et al. GSH-targeted nanosponges increase doxorubicin-induced toxicity "in vitro" and "in vivo" in cancer cells with high antioxidant defenses. Free Radic Biol Med. 2016; (97): 24–37.
25. Yang J, Lee J, Kang J, Oh SJ, Ko HJ, Son JH et al. Smart drug-loaded polymer gold nanoshells for systemic and localized therapy of human epithelial cancer. Adv Mater. 2009 Nov 20; 21 (43): 4339–42.
26. Shukla R, Bansal V, Chaudhary M, Basu A, Bhonde RR, Sastry M. Biocompatibility of gold nanoparticles and their endocytotic fate inside the cellular compartment: a microscopic overview. Langmuir. 2005 Nov 8; 21 (23): 10644–54.
27. Schwartz JA, Shetty AM, Price RE, Stafford RJ, Wang JC, Uthamanthil RK et al. Feasibility study of particle-assisted laser ablation of brain tumors in orthotopic canine model. Cancer Res. 2009 Feb 15; 69 (4): 1659–67.
28. Maloney E, Hwang JH. Emerging HIFU applications in cancer therapy. Int J Hyperthermia. 2015; 31 (3): 302–9.
29. Giuntini F, Foglietta F, Marucco AM, Troia A, Dezhkunov NV, Pozzoli A et al. Insight into ultrasound-mediated reactive oxygen species generation by various metal-porphyrin complexes. Free Radic Biol Med. 2018; (121): 190–201.
30. Serpe L, Foglietta F, Canaparo R. Nanosonotechnology: The next challenge in cancer sonodynamic therapy. Nanotechnology Reviews. 2012; 1 (2): 173–82.
31. Cavalli R, Bisazza A, Lembo D. Micro-and nanobubbles: a versatile non-viral platform for gene delivery. Int J Pharm. 2013; 456 (2): 437–45.
32. Canaparo R, Varchi G, Ballestri M, Foglietta F, Sotgiu G, Guerrini A et al. Polymeric nanoparticles enhance the sonodynamic activity of meso-tetrakis (4-sulfonatophenyl) porphyrin in an in vitro neuroblastoma model. Int J Nanomedicine. 2013; (8): 4247–63.
33. Varchi G, Foglietta F, Canaparo R, Ballestri M, Arena F, Sotgiu G et al. Engineered porphyrin loaded core-shell nanoparticles for selective sonodynamic anticancer treatment. Nanomedicine 2015; 10 (23): 3483–94.
34. Brazzale C, Canaparo R, Racca L, Foglietta F, Durando G, Fantozzi R et al. Enhanced selective sonosensitizing efficacy of ultrasound-based anticancer treatment by targeted gold nanoparticles. Nanomedicine. 2016; 11 (23): 3053–70.
35. Kripfgans OD, Fowlkes JB, Miller DL Eldevik OP, Carson PL. Acoustic droplet vaporization for therapeutic and diagnostic applications. Ultrasound Med Biol. 2000; 6 (7): 1177–89.
36. Prato M, Magnetto C, Jose J, Khadjavi A, Cavallo F, Quaglino E et al. 2H, 3H-decafluoropentane-based nanodroplets: new perspectives for oxygen delivery to hypoxic cutaneous tissues. PLoS One. 2015; 10 (3): e0119769.
37. Basilico N, Magnetto C, D'Alessandro S, Panariti A, Rivolta I, Genova T et al. Dextran-shelled oxygen-loaded nanodroplets reestablish a normoxia-like pro-angiogenic phenotype and behavior in hypoxic human dermal microvascular endothelium, Toxicol Appl Pharmacol. 2015; 288 (3): 330–8.
38. Cavalli R, Bisazza A, Rolfo A, Balbis S, Madonnaripa D, Caniggia I et al. Ultrasound-mediated oxygen delivery from chitosan nanobubbles. Int J Pharm. 2009; 378 (1–2): 215–7.
39. Khadjavi A, Magnetto C, Panariti A, Argenziano M, Gulino GR, Rivolta I et al. Chitosan-shelled oxygen-loaded nanodroplets abrogate hypoxia dysregulation of human keratinocyte gelatinases and inhibitors: new insights for chronic wound healing. Toxicol Appl Pharmacol. 2015; 286 (3): 198–206.
40. Banche G, Prato M, Magnetto C, Allizond V, Giribaldi G, Argenziano M et al. Antimicrobial chitosan nanodroplets: new insights for ultrasound-mediated adjuvant treatment of skin infection. Future Microbiol. 2015; 10 (6): 929–39.
41. Argenziano M, Banche G, Luganini A, Finesso N, Allizond V, Gulino GR et al. Vancomycin-loaded nanobubbles: A new platform for controlled antibiotic delivery against methicillin-resistant Staphylococcus aureus infections. Int J Pharm. 2017;

523 (1): 176–88.
42. Bisazza A, Civra A, Donalisio M, Lembo D, Cavalli R. The in vitro characterization of dextran-based nanobubbles as possible DNA transfection agents. Soft Matter. 2011; 7 (22): 10590–3.
43. Cavalli R, Bisazza A, Trotta M, Argenziano M, Civra A, Donalisio M et al. New chitosan nanobubbles for ultrasound-mediated gene delivery: preparation and in vitro characterization. Int J Nanomedicine. 2012; (7): 3309–18.
44. Cavalli R, Occhipinti S, Argenziano M, Bessone F, Guiot C, Giovarelli M. Nanobubble technology-based HER2 immunotherapy through dendritic cells targeting. Presented at "CRS Annual Meeting & Exposition", July 16–19 2017; Boston, Massachusetts, USA.
45. Cavalli R, Argenziano M, Vigna E, Giustetto P, Torres E, Aime S et al. Preparation and in vitro characterization of chitosan nanobubbles as theranostic agents. Colloids Surf B Biointerfaces. 2015; (129): 39–46.
46. Marano F, Argenziano M, Frairia R, Adamini A, Bosco O, Rinella L et al. Doxorubicin-loaded nanobubbles combined with extracorporeal shock waves: basis for a new drug delivery tool in anaplastic thyroid cancer. Thyroid. 2016; 26 (5): 705–16.
47. Marano F, Frairia R, Rinella L, Argenziano M, Bussolati B, Grange C et al. Combining doxorubicin-nanobubbles and shockwaves for anaplastic thyroid cancer treatment: preclinical study in a xenograft mouse model. Endocr Relat Cancer. 2017; 24 (6): 275–86.
48. Marano F, Rinella L, Argenziano M, Cavalli R, Sassi F, D'Amelio P et al. Targeting Taxanes to Castration-Resistant Prostate Cancer Cells by Nanobubbles and Extracorporeal Shock Waves. PloS One. 2016; 11 (12): e0168553.
49. Roberta C, Francesca M, Monica A, Alessandra V, Roberto F, Maria Graziella C. Combining Drug-Loaded Nanobubbles and Extracorporeal Shock Waves for Difficult-to-Treat Cancers. Current Drug Delivery. 2017; (14): 1–3.
50. Glazer ES, Curley SA. The ongoing history of thermal therapy for cancer. Surg Oncol Clin N Am. 2011; 20 (2): 229–35.
51. Kosiorek A, Kandulski W, Glaczynska H, Giersig M. Fabrication of nanoscale rings, dots, and rods by combining shadow nanosphere lithography and annealed polystyrene nanosphere masks. Small. 2005; (1): 439–44.
52. Barrera G, Serpe L, Celegato F, Coïsson M, Martina K, Canaparo R et al. Surface modification and cellular uptake evaluation of Au-coated Ni80Fe20 nanodiscs for biomedical applications. Interface Focus. 2016; 6 (6). DOI: 10.1098/rsfs.2016.0052.

Литература

1. Portehault D, Delacroix S, Gouget G, Grosjean R, Chan-Chang T-H-C. Beyond the Compositional Threshold of Nanoparticle-Based Materials. Accounts of Chemical Research. 2018; 51 (4): 930–9.
2. Cravotto G, Boffa L. Preparation of nanomaterials under combined ultrasound/microwave irradiation. Pan Stanford Publishing Pte. Ltd.: 2014; p. 203–26.
3. Martina K, Tagliapietra S, Barge A, Cravotto G. Combined Microwaves/Ultrasound, a Hybrid Technology. Top Curr Chem. 2016; 374 (6): 1–27.
4. Davis ME, Brewster ME. Cyclodextrin-based pharmaceutics: past, present and future. Nat Rev Drug Discov. 2004; (3): 1023–35.
5. Barge A, Caporaso M, Cravotto G, Martina K, Tosco P, Aime S et al. Design and Synthesis of a γ1β8-Cyclodextrin Oligomer: A New Platform with Potential Application as a Dendrimeric Multicarrier. Chem Eur J. 2013; 19 (36): 12086–92.
6. Martina K, Baricco F, Berlier G, Caporaso M, Cravotto G. Efficient Green Protocols for Preparation of Highly Functionalized β-Cyclodextrin-Grafted Silica. ACS Sustainable Chem Eng. 2014; 2 (11): 2595–603.
7. Huq R, Mercier L, Kooyman PJ. Incorporation of Cyclodextrin into Mesostructured Silica. Chem Mater. 2001; 13 (12): 4512–9.
8. Lee J-H, Kang S, Ahn M, Jang H, Min D-H. Development of dual-pore coexisting branched silica nanoparticles for efficient gene-chemo cancer therapy. Small. 2018; 14 (7): 1702564.
9. Calcio Gaudino E, Tagliapietra S, Martina K, et al. Novel SWCNT platform bearing DOTA and β-cyclodextrin units. "One shot" multidecoration under microwave irradiation. Org Biomol Chem. 2014; (12): 4708–15.
10. Bosca F, Orio L, Tagliapietra S, Corazzari I, Turci F, Martina K, Pastero L, Cravotto G et al. Microwave-Assisted Synthesis and Physicochemical Characterization of Tetrafuranylporphyrin-Grafted Reduced-Graphene Oxide. Chem Eur J. 2016; (22): 1608–13.
11. Duan S, Li J, Zhao N, Xu F-J. Multifunctional hybrids with versatile types of nanoparticles via self-assembly for complementary tumor therapy. Nanoscale. 2018; (10): 7649–57.
12. Bolden NW, Rangari VK, Jeelani S, Boyoglu S, Singh SR. Synthesis and evaluation of magnetic nanoparticles for biomedical applications. J Nanopart. 2013: 1–9; DOI:10.1155/2013/370812.
13. Güvener N, Appold L, de Lorenzi F, Golombek SK, Rizzo LY, Lammers T, Kiessling F. Recent advances in ultrasound-based diagnosis and therapy with micro-and nanometer-sized formulations. Methods. 2017; (130): 4–13.
14. Cavalli R, Soster M, Argenziano M. Nanobubbles: a promising efficient tool for therapeutic delivery. Ther Deliv. 2016; 7 (2): 117–38.
15. Delalande A, Postema M, Mignet N, Midoux P, Pichon C. Ultrasound and microbubble-assisted gene delivery: recent advances and ongoing challenges. Ther Deliv. 2012; 3 (10): 1199–215.
16. Cavalli R, Bisazza A, Giustetto P, Civra A, Lembo D, Trotta G et al. Preparation and characterization of dextran nanobubbles for oxygen delivery. Int J Pharm. 2009; 381 (2): 160–5.
17. Malam Y, Loizidou M, Seifalian AM. Liposomes and nanoparticles: nanosized vehicles for drug delivery in cancer. Trends Pharmacol Sci. 2009 Nov; 30 (11): 592–9.
18. Alvarez-Lorenzo C1, Concheiro A. Smart drug delivery systems: from fundamentals to the clinic. Chem Commun. 2014; 50 (58): 7743–65.
19. Liu D, Yang F, Xiong F, Gu N. The Smart Drug Delivery System and Its Clinical Potential. Theranostics. 2016 Jun 7; 6 (9): 1306–23.
20. Sharifi S, Behzadi S, Laurent S, Forrest ML, Stroeve P, Mahmoudi M. Toxicity of nanomaterials. Chem Soc Rev. 2012 Mar 21; 41 (6): 2323–43.
21. Caldera F, Argenziano M, Trotta F, Dianzani C, Gigliotti L, Tannous M et al. Cyclic nigerosyl-1,6-nigerose-based nanosponges: An innovative pH and time-controlled nanocarrier for improving cancer treatment. Carbohydr Polym. 2018; (194): 111–21.
22. Chen X, Yao X, Wang C, Chen L, Chen X. Mesoporous silica nanoparticles capped with fluorescence-conjugated cyclodextrin for pH-activated controlled drug delivery and imaging. Microporous Mesoporous Mater. 2015; (217): 46–53.
23. Torchilin VP. Multifunctional, stimuli-sensitive nanoparticulate systems for drug delivery. Nat Rev Drug Discov. 2014 Nov; 13 (11): 813–27.
24. Daga M, Ullio C, Argenziano M, Dianzani C, Cavalli R, Trotta F et al. GSH-targeted nanosponges increase doxorubicin-induced toxicity "in vitro" and "in vivo" in cancer cells with high antioxidant defenses. Free Radic Biol Med. 2016; (97): 24–37.
25. Yang J, Lee J, Kang J, Oh SJ, Ko HJ, Son JH et al. Smart drug-loaded polymer gold nanoshells for systemic and localized therapy of human epithelial cancer. Adv Mater. 2009 Nov 20; 21 (43): 4339–42.
26. Shukla R, Bansal V, Chaudhary M, Basu A, Bhonde RR, Sastry M. Biocompatibility of gold nanoparticles and their endocytotic fate inside the cellular compartment: a microscopic overview. Langmuir. 2005 Nov 8; 21 (23): 10644–54.
27. Schwartz JA, Shetty AM, Price RE, Stafford RJ, Wang JC, Uthamanthil RK et al. Feasibility study of particle-assisted laser ablation of brain tumors in orthotopic canine model. Cancer Res. 2009 Feb 15; 69 (4): 1659–67.
28. Maloney E, Hwang JH. Emerging HIFU applications in cancer therapy. Int J Hyperthermia. 2015; 31 (3): 302–9.

29. Giuntini F, Foglietta F, Marucco AM, Troia A, Dezhkunov NV, Pozzoli A et al. Insight into ultrasound-mediated reactive oxygen species generation by various metal-porphyrin complexes. Free Radic Biol Med. 2018; (121): 190–201.
30. Serpe L, Foglietta F, Canaparo R. Nanosonotechnology: The next challenge in cancer sonodynamic therapy. Nanotechnology Reviews. 2012; 1 (2): 173–82.
31. Cavalli R, Bisazza A, Lembo D. Micro-and nanobubbles: a versatile non-viral platform for gene delivery. Int J Pharm. 2013; 456 (2): 437–45.
32. Canaparo R, Varchi G, Ballestri M, Foglietta F, Sotgiu G, Guerrini A et al. Polymeric nanoparticles enhance the sonodynamic activity of meso-tetrakis (4-sulfonatophenyl) porphyrin in an in vitro neuroblastoma model. Int J Nanomedicine. 2013; (8): 4247–63.
33. Varchi G, Foglietta F, Canaparo R, Ballestri M, Arena F, Sotgiu G et al. Engineered porphyrin loaded core-shell nanoparticles for selective sonodynamic anticancer treatment. Nanomedicine 2015; 10 (23): 3483–94.
34. Brazzale C, Canaparo R, Racca L, Foglietta F, Durando G, Fantozzi R et al. Enhanced selective sonosensitizing efficacy of ultrasound-based anticancer treatment by targeted gold nanoparticles. Nanomedicine. 2016; 11 (23): 3053–70.
35. Kripfgans OD, Fowlkes JB, Miller DL Eldevik OP, Carson PL. Acoustic droplet vaporization for therapeutic and diagnostic applications. Ultrasound Med Biol. 2000; 6 (7): 1177–89.
36. Prato M, Magnetto C, Jose J, Khadjavi A, Cavallo F, Quaglino E et al. 2H, 3H-decafluoropentane-based nanodroplets: new perspectives for oxygen delivery to hypoxic cutaneous tissues. PLoS One. 2015; 10 (3): e0119769.
37. Basilico N, Magnetto C, D'Alessandro S, Panariti A, Rivolta I, Genova T et al. Dextran-shelled oxygen-loaded nanodroplets reestablish a normoxia-like pro-angiogenic phenotype and behavior in hypoxic human dermal microvascular endothelium, Toxicol Appl Pharmacol. 2015; 288 (3): 330–8.
38. Cavalli R, Bisazza A, Rolfo A, Balbis S, Madonnaripa D, Caniggia I et al. Ultrasound-mediated oxygen delivery from chitosan nanobubbles. Int J Pharm. 2009; 378 (1–2): 215–7.
39. Khadjavi A, Magnetto C, Panariti A, Argenziano M, Gulino GR, Rivolta I et al. Chitosan-shelled oxygen-loaded nanodroplets abrogate hypoxia dysregulation of human keratinocyte gelatinases and inhibitors: new insights for chronic wound healing. Toxicol Appl Pharmacol. 2015; 286 (3): 198–206.
40. Banche G, Prato M, Magnetto C, Allizond V, Giribaldi G, Argenziano M et al. Antimicrobial chitosan nanodroplets: new insights for ultrasound-mediated adjuvant treatment of skin infection. Future Microbiol. 2015; 10 (6): 929–39.
41. Argenziano M, Banche G, Luganini A, Finesso N, Allizond V, Gulino GR et al. Vancomycin-loaded nanobubbles: A new platform for controlled antibiotic delivery against methicillin-resistant Staphylococcus aureus infections. Int J Pharm. 2017; 523 (1): 176–88.
42. Bisazza A, Civra A, Donalisio M, Lembo D, Cavalli R. The in vitro characterization of dextran-based nanobubbles as possible DNA transfection agents. Soft Matter. 2011; 7 (22): 10590–3.
43. Cavalli R, Bisazza A, Trotta M, Argenziano M, Civra A, Donalisio M et al. New chitosan nanobubbles for ultrasound-mediated gene delivery: preparation and in vitro characterization. Int J Nanomedicine. 2012; (7): 3309–18.
44. Cavalli R, Occhipinti S, Argenziano M, Bessone F, Guiot C, Giovarelli M. Nanobubble technology-based HER2 immunotherapy through dendritic cells targeting. Presented at "CRS Annual Meeting & Exposition", July 16–19 2017; Boston, Massachusetts, USA.
45. Cavalli R, Argenziano M, Vigna E, Giustetto P, Torres E, Aime S et al. Preparation and in vitro characterization of chitosan nanobubbles as theranostic agents. Colloids Surf B Biointerfaces. 2015; (129): 39–46.
46. Marano F, Argenziano M, Frairia R, Adamini A, Bosco O, Rinella L et al. Doxorubicin-loaded nanobubbles combined with extracorporeal shock waves: basis for a new drug delivery tool in anaplastic thyroid cancer. Thyroid. 2016; 26 (5): 705–16.
47. Marano F, Frairia R, Rinella L, Argenziano M, Bussolati B, Grange C et al. Combining doxorubicin-nanobubbles and shockwaves for anaplastic thyroid cancer treatment: preclinical study in a xenograft mouse model. Endocr Relat Cancer. 2017; 24 (6): 275–86.
48. Marano F, Rinella L, Argenziano M, Cavalli R, Sassi F, D'Amelio P et al. Targeting Taxanes to Castration-Resistant Prostate Cancer Cells by Nanobubbles and Extracorporeal Shock Waves. PloS One. 2016; 11 (12): e0168553.
49. Roberta C, Francesca M, Monica A, Alessandra V, Roberto F, Maria Graziella C. Combining Drug-Loaded Nanobubbles and Extracorporeal Shock Waves for Difficult-to-Treat Cancers. Current Drug Delivery. 2017; (14): 1–3.
50. Glazer ES, Curley SA. The ongoing history of thermal therapy for cancer. Surg Oncol Clin N Am. 2011; 20 (2): 229–35.
51. Kosiorek A, Kandulski W, Glaczynska H, Giersig M. Fabrication of nanoscale rings, dots, and rods by combining shadow nanosphere lithography and annealed polystyrene nanosphere masks. Small. 2005; (1): 439–44.
52. Barrera G, Serpe L, Celegato F, Coïsson M, Martina K, Canaparo R et al. Surface modification and cellular uptake evaluation of Au-coated Ni80Fe20 nanodiscs for biomedical applications. Interface Focus. 2016; 6 (6). DOI: 10.1098/rsfs.2016.0052.

DETECTING REACTIVE OXYGEN SPECIES IN BIOLOGICAL FLUIDS BY PLATINUM NANOELECTRODE APPLYING AMPEROMETRIC METHOD

Vaneev AN[1] ✉, Alova AV[1], Erofeev AS[1,2], Gorelkin PV[3], Aleksashkin AD[1], Beznos OV[4], Chesnokova NB[4], Kost OA[1], Majouga AM[1,2,5], Korchev Y[6,7], Klyachko NL[1]

[1] Lomonosov Moscow State University, Moscow, Russia
[2] National University of Science and Technology «MISIS», Moscow, Russia
[3] Medical Nanotechnology LLC, Moscow, Russia
[4] Helmholtz Institute of Ophthalmology, Moscow, Russia
[5] Dmitry Mendeleev University of Chemical Technology of Russia, Moscow, Russia
[6] Department of Medicine, Imperial College London, London, United Kingdom
[7] WPI Nano Life Science Institute (WPI-NanoLSI), Kanazawa University, Kanazawa, Japan

Reactive oxygen species (ROS) are vital metabolites in numerous biological functions. Disorders of cellular mechanisms can cause overproduction of ROS and, subsequently, oxidative damage to DNA, proteins, cells and tissues, which is associated with the pathogenesis of a number of neurodegenerative and inflammatory diseases. Development of highly sensitive, relatively simple and fast-to-implement innovative methods to detect oxidative stress requires understanding of how such disorders relate to the level of ROS. This research aimed to apply the biological fluids' ROS detection method we have developed (using the stable platinum nanoelectrode that allows assessing the level of hydrogen peroxide (H_2O_2) down to 1 μM) and determine the level of H_2O_2 in lacrimal and intraocular fluids of rabbits, as well as to investigate how the level of H_2O_2 changes under the influence of antioxidant therapy. The effect superoxide dismutase (SOD) nanoparticles produce on biological fluids' ROS level was shown. The level of H_2O_2 in lacrimal fluid increased 10 and 30 min after instillation of SOD nanoparticles. As for the intraocular fluid, H_2O_2 concentration starts to grow only 30 min after instillation of SOD nanoparticles, which suggests that the they penetrate the internal structures of the eye gradually. The method seems to be of value in the context of eye diseases diagnosing and treatment.

Keywords: antioxidant activity, platinum nanoelectrode, reactive oxygen species, nanosensor, superoxide dismutase nanoparticles, oxidative stress

Funding: the study was supported by the Ministry of Education and Science of the Russian Federation in the context of the Agreement #14.575.21.0147 (project code RFMEFI57517X0147).

✉ **Correspondence should be addressed:** Alexander N. Vaneev
Leninskie Gory 1, bl. 11B, Moscow, 119991; vaneev.aleksandr@gmail.com

Received: 28.06.2018 **Accepted:** 25.07.2018

DOI: 10.24075/brsmu.2018.045

ОПРЕДЕЛЕНИЕ АКТИВНЫХ ФОРМ КИСЛОРОДА В БИОЛОГИЧЕСКИХ ЖИДКОСТЯХ С ПОМОЩЬЮ ПЛАТИНОВОГО НАНОЭЛЕКТРОДА АМПЕРОМЕТРИЧЕСКИМ МЕТОДОМ

А. Н. Ванеев[1] ✉, А. В. Алова[1], А. С. Ерофеев[1,2], П. В. Горелкин[3], А. Д. Алексашкин[1], О. В. Безнос[4], Н. Б. Чеснокова[4], О. А. Кост[1], А. Г. Мажуга[1,2,5], Ю. Е. Корчев[6,7], Н. Л. Клячко[1]

[1] Московский государственный университет имени М. В. Ломоносова, Москва
[2] Национальный исследовательский технологический университет «МИСИС», Москва
[3] ООО «Медицинские нанотехнологии», Москва
[4] Научно-исследовательский институт глазных болезней, Москва
[5] Российский химико-технологический университет имени Д. И. Менделеева, Москва
[6] Департамент медицины, Имперский колледж Лондона, Лондон
[7] Институт наноиндустрии WPI (WPI-NanoLSI), Университет Канадзава, Канадзава

Активные формы кислорода (АФК) являются жизненно необходимыми метаболитами в многочисленных биологических функциях. Нарушение клеточных механизмов может привести к перепроизводству АФК и вызвать окислительное повреждение ДНК, белков, клеток и тканей, которое связано с патогенезом ряда нейродегенеративных и воспалительных заболеваний. Понимание взаимосвязи между уровнем АФК и этими нарушениями важно при разработке методов лечения для борьбы с окислительным стрессом. Целью работы было использование разработанного нами метода определения АФК в биологических жидкостях, а именно в слезе и внутриглазной жидкости, с помощью стабильного платинового наноэлектрода, позволяющего оценивать уровень пероксида водорода (H_2O_2) вплоть до 1 мкМ, а также изучение динамики изменения уровня H_2O_2 при антиоксидантной терапии. Показано влияние наночастиц супероксиддисмутазы (СОД) на уровень АФК в биологических жидкостях. После закапывания наночастиц СОД происходило увеличение уровня H_2O_2 в слезе через 10 и 30 мин. В случае с внутриглазной жидкостью рост концентрации H_2O_2 начинается только спустя 30 мин после закапывания, что свидетельствует о постепенном проникновении наночастиц во внутренние структуры глаза. Использование метода представляется эффективным для диагностики и контроля лечения глазных заболеваний.

Ключевые слова: антиоксидантная активность, платиновый наноэлектрод, активные формы кислорода, наносенсор, наночастицы супероксиддисмутазы, окислительный стресс

Финансирование: работа выполнена при поддержке Министерства образования и науки Российской Федерации в рамках Соглашения №14.575.21.0147 (Уникальный идентификатор проекта RFMEFI57517X0147).

✉ **Для корреспонденции:** Александр Николаевич Ванеев
Ленинские горы, д. 1, стр. 11Б, г. Москва, 119991; vaneev.aleksandr@gmail.com

Статья получена: 28.06.2018 **Статья принята к печати:** 25.07.2018

DOI: 10.24075/vrgmu.2018.045

Oxidative stress in tissues is accompanied by excessive generation of reactive oxygen species (ROS) and depletion of the endogenous antioxidants reserves [1]. Entering endogenous metabolic reactions, aerobic cells produce ROS, such as superoxide anion ($\bullet O_2^-$), hydrogen peroxide (H_2O_2), hydroxyl radical (•OH) [2]. Organs of vision are some of the most vulnerable parts of the body [3]. Tissues of the eye are exposed to light for a considerably long time to have radical processes constantly photoinitiated and cells damaged, membrane lipids peroxidized, protein modified through oxidization, DNA damaged through the same process [4]. Many eye pathologies are associated with oxidative stress: cataracts [5], uveitis [6], retinopathy [7], corneal inflammation [8]. All ROS oxidize cellular components, which mostly results in irreversible damage to cells. In the body, antioxidant enzymes (superoxide dismutase (SOD), catalase) and low-molecular antioxidants (vitamins A, C, E, etc.) control concentration of ROS [9].

Thus, learning antioxidant profiles of lacrimal and intraocular fluids is an important task. Modern methods of ROS levels detection are flawed: their sensitivity is low, and, in most cases, the measurements are indirect [10]. The volume of lacrimal fluid a laboratory animal can provide is also limited, which makes the majority of analytical methods inapplicable [11, 12].

Thus, detecting and describing the antioxidant component of lacrimal and intraocular fluids requires special, highly effective and sensitive methods that allow determining ROS level with only a minor volume and concentration of fluids, which is important for ophthalmic diseases diagnosing and prevention [13].

It is common to apply chemiluminescent and spectrophotometric methods [14, 15] to determine the antioxidant activity of lacrimal fluid. These methods imply modeling that allows generating ROS and then assessing the level of antioxidants in the sample based on the model reactions inhibition or stopping. The drawbacks of such modeling systems are the medium's pH, which is different from the physiological conditions, and indirect nature of ROS level measurement process peculiar to the majority of methods available, which imposes a number of limitations and reduces reliability of the data obtained.

Activation of free radicals is one of the causes of vessel neoplasms forming in the context of inflammatory processes. Therefore, oxidative stress is an important constituent of inflammation pathogenesis. Some of the major triggers of inflammation are infections, systemic autoimmune diseases, traumatic eye injuries, burns, hormonal imbalance and metabolic disorders [16, 17]. For example, choroid inflammation, or uveitis, often affects other structures of this organ and translates into various vision disorders [18]. Such disorders result from sensitization of the eye tissues with infection or other antigens and neutrophils penetrating to the nidus. Neutrophils destroy microorganisms and produce ROS by NADPH•H oxidase. Another major source of ROS accompanying inflammation (regardless of the disease etiology) is macrophages [19]. Therefore, antioxidants are a feasible addition to anti-inflammatory drugs in the context of an anti-inflammatory therapy. Complications associated with the inflammatory processes in the eyes mainly result from the activation of free radicals oxidation reactions and accumulation of ROS [3].

In this case, nanoparticles as carries show promise, since they can significantly increase the bioavailability of the drug [20]. SOD nanoparticles of block-ionomer complexes, for example, are non-toxic, non-immunogenic and biocompatible. Due to the repeated reaction with the substrate, antioxidant enzymes are more effective than low-molecular antioxidants. The major advantage of SOD nanoparticles is their ability to circulate in the eye's tissues longer than the native enzymes. *In vivo* experiments have shown that SOD nanoparticles are quite effective in the context of immunogenic uveitis and chemical eye burn therapies [21].

The goal of this research was to detect ROS in lacrimal and intraocular fluids of rabbits by means of amperometry using a platinum nanoelectrode, as well as to study the effect SOD nanoparticles have on the dynamics of ROS concentration in lacrimal and intraocular fluids of intact rabbits.

METHODS

We obtained SOD nanoparticles following the protocol described in paper [22]. The method implies spontaneous layer-by-layer self-assembly of oppositely charged polyions, which brings stoichiometric complexes with 100% efficiency of loading. To that effect, protamine (Sigma; USA), positively charged at pH = 7.4, was added to a SOD solution in a 0.01 M phosphate buffer PBS (pH = 7.4) (Fermentniye tekhnologii, Russia) mostly negatively charged under physiological conditions; next, a negatively charged block copolymer of polyethylene glycol and poly-L-glutamic acid (Alamanda Polymers; USA) was added, followed by cross-linking with glutaraldehyde (Sigma; USA).

The test subjects were samples of lacrimal and intraocular fluids of rabbits provided by the Helmholtz Institute of Ophthalmology. All in all, 25 chinchilla rabbits (weight 2.0–2.5 kg each) donated the fluids. They were taken care of in compliance with "Experimental Biological Clinics (Vivaria) Sanitary Management Rules" approved by the Ministry of Health of the USSR on 06.07.73, and order #755 of 12.08.77 issued by the same ministry. Routine care followed the laboratory's SOP. Keeping conditions: indoors, rooms with a 12-hour lighting cycle, temperature range — 18–26 °C, relative humidity of 30–70%, 100% ventilation without recirculation, air exchange rate — 7–12 room volumes per hour, one animal per cage equipped with drinking bowls and feeders. The rabbits were fed «Universal Granulated Compound Feed for Rabbits» (Provimi-Volosovo, Leningrad region).

The pre-tests adaptation period for the animals was 14 days. During that time, their health was monitored for any deviations from the norm. The animals underwent thorough examination before being split into groups. Each animal was given an individual number. Experimental groups consisted of rabbits exhibiting no visible deviations from the normal state of health (randomized selection).

In this study, rabbits of the gray chinchilla line were used as a test system. This line is a regular choice in the context of pharmacological research studying the impact of medicines on the eye tissues.

Gray chinchilla has big eyes, which simplifies evaluation of clinical manifestations of the disease and allows collecting sufficient volumes of fluids from the anterior chamber of the eye.

All operations and activities that involved experimental animals complied with provisions of the order #755 of 12.08.77 issued by the Ministry of Health and the Helsinki declaration. All procedures the animals were part of received approval of the Helmholtz Institute of Ophthalmology ethics committee.

All rabbits were simultaneously instilled 30 µl of the nanoparticles solution (2 mg/ml) into one eye, while the other eye served as control. Then, lacrimal and intraocular fluids were taken 10, 30, 60, 120 min after the instillation.

We used a number of filter paper circle patches (diameter 5 mm) to obtain lacrimal fluid samples. The patches were put into the posterior fornix of conjunctiva for 5 min, then taken out and dipped into 300 µl PBS solution for 20 min. The eluate was centrifuged for 10 min at 4000 rpm in a centrifuge

(Labsystems; Finland) and the resulting supernatant was used for measurement purposes.

To take the intraocular fluid, we punctured cornea near the sulcus (paracentesis). Once all samples were taken, the animal was euthanized by air embolism.

We applied the amperometric method to determine the level of ROS. To this effect, we used platinum-coated carbon nanoelectrodes in the fluids and a silver chloride reference electrode.

Patch-clamp amplifier Model 2400 (AM Systems; USA) allowed registering the potential difference between platinum microelectrode and reference electrode. USB-6211 ADC-DAC converter (National instruments; USA) and WinWCP software allowed data transfer and recording. PatchStar micromanipulator (Scientifica; UK) helped position the nanosensor. The desk for all manipulations was the table of an inverted microscope (Nikon; Japan).

ROS concentration, namely that of H_2O_2, was evaluated at the potential of +800 mV to the silver chloride electrode [23]. These are the conditions allowing $2H_2O_2 \leftrightarrow 2H_2O + O_2$ reaction, which is catalyzed by platinum; since superoxide radical rapidly converts into hydrogen peroxide in the solution, the total concentration of H_2O_2 determines the general background of the oxidative processes [24]. The level of oxygen was evaluated at the potential of –800 mV.

Quartz capillaries (inner and outer diameters 0.9 mm and 1.2 mm, respectively; Fig. 1) were used to make platinum electrodes. The capillaries were pulled by a laser puller (Sutter; USA) to make two nanocapillaries that had a hole with the diameter of 100–500 nm. Pyrolytic carbon was deposited on the nanocapillaries through thermal decomposition of butane in an oxygen-free environment.

Nanocapillary was filled with butane through a rubber tube that fit tightly around the wide end of the quartz nanocapillary. Then, sharp end of the nanocapillary was pushed into a similar quartz capillary of the appropriate size. This capillary carried the laminar flow of argon. Next, starting with the sharp end of the nanocapillary we subjected it to thermal treatment with the help of a butane-propane, distance — 1 cm, duration — 15 s.

We applied the electrochemical cavitation method with subsequent deposition of platinum [25–27]. The electrode was etched in a solution containing 0.1 mM NaOH and 10 mM KCl. Both the nanoelectrode and the reference electrode

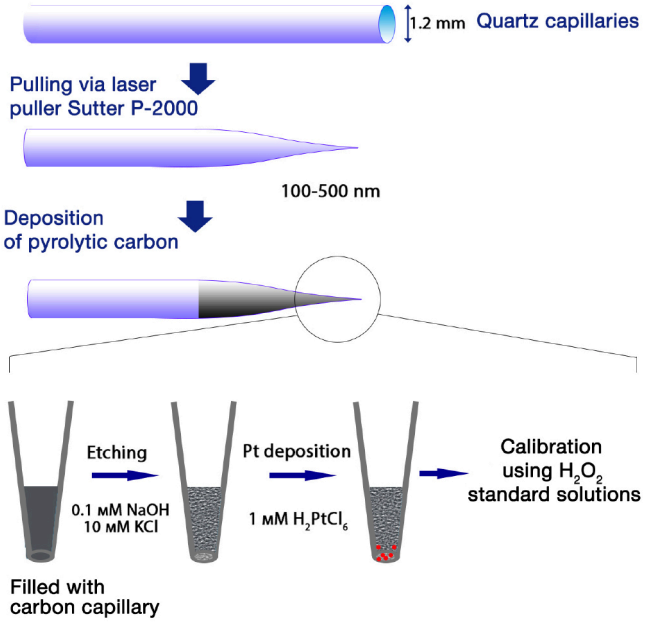

Fig. 1. Platinum electrodes production pattern

were immersed in the solution; reference electrode received a symmetrical V-shaped alternating current with an amplitude of 1.5–2 V. Increasing amplitude signaled of the growing current running through the nanoelectrode and, accordingly, of the increasing area of carbon on the quartz tube's tip. When the signal's amplitude was sufficient, the etching was stopped.

After etching in the 0.1 M KCl/10 mM NaOH solution, the treated billets were put into the 2 mM hexachloroplatinic acid (H_2PtCl_6) solution to electrochemically deposit platinum

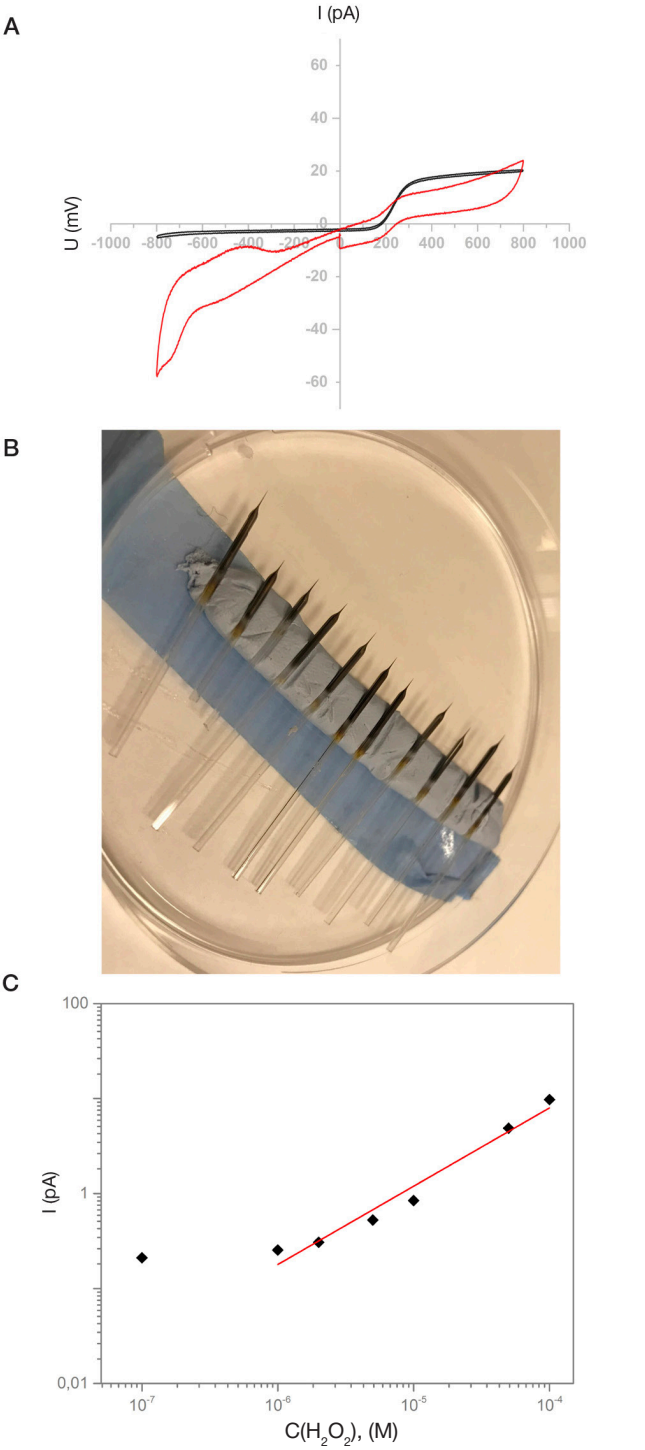

Fig. 2. A. Volt-ampere characteristics for a nanoelectrode against Ag / AgCl (1 V/s). Cyclic volt-amper-grams measured in a 1 mM solution of ferrocene methanol. Black shows the current-voltage characteristic for a carbon nanoelectrode, red — after deposition of platinum. **B**. Photograph of the manufactured nanoelectrodes. **C**. Calibration line of the platinum electrode used to determine the concentration of H_2O_2 in lacrimal and intraocular fluids

onto the tip of the capillary, delivering a 0.8 V symmetrical sawtooth-shaped potential to the reference electrode. The differences in cyclic volt-ampere-grams of the nanoelectrode in ferrocenemethanol in the region of negative potentials before and after deposition of platinum indicated the success of the operation, i.e. that we had platinum deposited on the electrode (Fig. 2A)

OriginPro 8 software (OriginLab, 2018) was used to process the obtained volt-ampere characteristics. We registered the average current values at +800 mV (pro rata to the H_2O_2 concentration) relative to the current level at zero potential.

The platinum electrode and the reference electrode, dipped into the samples, allowed measuring H_2O_2 level in lacrimal and intraocular fluids taken from the test animals. See fig. 2B for the picture of nanoelectrodes.

RESULTS

Prior to measuring the levels in the samples, we calibrated each platinum electrode using several standard H_2O_2 solutions and plotted a calibration curve that consequently allowed determining the level of H_2O_2 in the samples (Fig. 2C)

According to the calibration, the higher the current value, the greater the concentration of H_2O_2 in the sample. Left eye of the test animals was instilled with SOD nanoparticles; right eye, the control, received 0.01 M PBS buffer (pH = 7.4). The data describes each rabbit at 5 different time points: before the instillation (control) and after 10, 30, 60 and 120 min after that. Seemingly due to the individual characteristics of each test animal, the results vary to a certain extent at each time point. In all animals we have seen the H_2O_2 level decreasing as the time elapsed from instillation increased.

Because of the considerable variability of the results, we have calculated the difference between H_2O_2 levels in test and control eyes of each animal (lacrimal fluid) with the aim to visualize the dynamics of the process as it developed in time. The data obtained were averaged out and presented for 5 rabbits as mean values with standard errors (Fig. 3). The values indicate that, compared to the control eye (PBS instillation), the H_2O_2 level in the test eye (nanoparticles instillation) was growing for 30 min after instillation. Then, the level of ROS in both eyes became approximately equal.

Next, we measured the ion currents in the intraocular fluid samples. Left eye of the test animals was instilled with SOD nanoparticles; right eye, the control, received 0.01 M PBS buffer (pH = 7.4). After instillation, the H_2O_2 level in the intraocular fluid of experimental animals was increasing. As time went by, the values registered were growing increasingly varied at each time point. The data obtained were averaged out and presented for 5 rabbits as mean values with standard errors (Fig. 4). Ten min after the instillation was over, the values describing test and control eyes showed no significant differences, but after 30 min the level of H_2O_2 in the test eye (nanoparticles instillation) began to grow compared to the control.

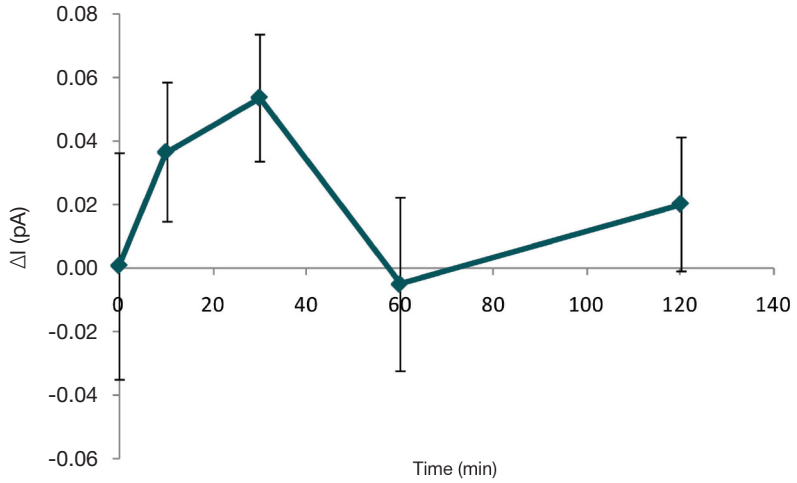

Fig. 3. Kinetics of the ROS changes in rabbit tear samples after instillation with SOD nanoparticles. Averaged data for 5 rabbits with standard errors. Difference between ROS levels in test and control eyes of each animal (lacrimal fluid)

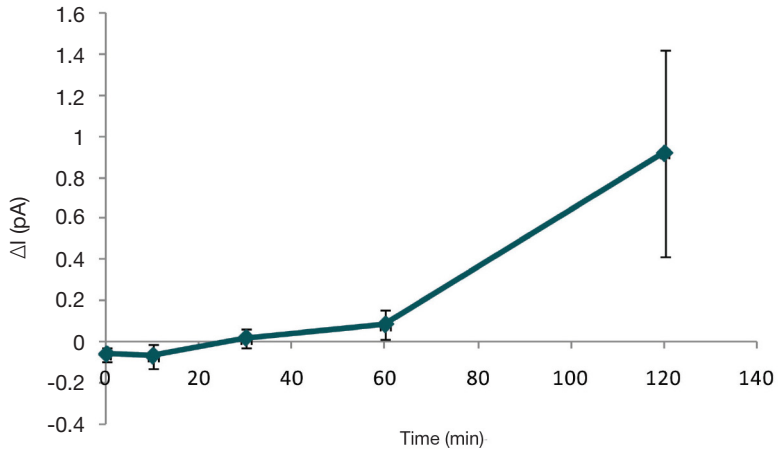

Fig. 4. Kinetics of the ROS changes in rabbit intraocular fluid samples after instillation with SOD nanoparticles. Averaged data for 5 rabbits with standard errors. Difference between ROS levels in test and control eyes of each animal (lacrimal fluid)

DISCUSSION

SOD nanoparticles catalyze reaction $2O_2^- + 2H_3O^+ \leftrightarrow O_2 + H_2O_2 + 2H_2O$, which translates into the growing levels of H_2O_2 in the samples of lacrimal and intraocular fluids.

In the lacrimal fluid, the level of H_2O_2 increased 10 and 30 min after the beginning of instillation and returned to baseline an hour after (dome-shaped graph). This is different from the ROS level dynamics seen in the intraocular samples, where the concentration of H_2O_2 starts growing only 30 min after instillation. It is difficult for SOD to penetrate to the intraocular fluid, which explains the latent period of about 30 min.

When the SOD concentration in the lacrimal fluid grows, that of superoxide radicals decreases significantly, while the concentration of H_2O_2 increases (Fig. 3). The H_2O_2 concentration reaches the maximum level in 30 min, which indicates a shift in the equilibrium of superoxide radical dismutation reaction towards generation of H_2O_2. In 1 hour, the H_2O_2 concentration returns to baseline because of the two related processes seen in lacrimal fluid: firstly, in 1 hour the concentration of SOD nanoparticles decreases significantly due to leaching from the eye surface, which means the rate of H_2O_2 generation also slows down; secondly, the antioxidant system found in lacrimal fluid decomposes H_2O_2 to water and oxygen.

It should be noted once again that the lifetime of superoxide radicals is only about 10^{-6} s because of their reactivity. Being a nucleophilic compound, O_2^- is capable of oxidizing lipoproteins and phospholipids of the membranes, which results in the destruction of cells [28]. In addition to the dismutation reaction that results in H_2O_2 generation, superoxide radical is also part of the Haber-Weiss reaction ($O_2^- + H_2O_2 \leftrightarrow OH^- + OH\bullet + {}^1O_2$). Therefore, it is impossible to have superoxide radicals in the lacrimal fluid samples right after they are taken, so all the measurements are based on the concentration dynamics of H_2O_2 relatively stable under physiological conditions.

The concentration in the lacrimal fluid reaches the sufficient level immediately after instillation, but penetrating the intraocular fluid takes some time, which is why the concentration of H_2O_2 increases after a slight delay.

Physiological barriers in the eye greatly hinder topical application of conventional drugs; the barriers effectively reduce the concentration of the drug at the site of its administration [29]. Stability of the enzyme absorbed by the cells in the form of nanoparticles increases significantly; presumably, it is the result of stabilization of the enzyme molecule against metabolic degradation and/or lysosomal destruction, which prolongs the time of circulation in the eye tissues compared to the native enzyme [30].

In the future, it is possible to measure the level of H_2O_2 directly in the eye tissues with the help of nanoelectrodes. Since nanoelectrodes are extremely small (100–500 nm), they can be used to penetrate both isolated cells and live eye tissues for real-time measurements.

CONCLUSIONS

Test making use of platinum nanoelectrode may be of diagnostic value in assessing the course of eye pathologies associated with inflammatory processes. Evaluation of the level of H_2O_2 by means of the method suggested allows justified application of the antioxidant drugs in the context of eye inflammation therapy. The technology is simple and sufficiently sensitive, and its effectiveness makes it very promising for biomedical applications. In the context of our research we have shown a method to make sensitive platinum nanoelectrodes that can be used to detect ROS in biological fluids. We have come to the conclusion that this direct method is more sensitive and promising in biological applied research.

References

1. Zenkov NK, Lankin VZ, Men'shchikova EB. Okislitel'nyy stress: Biokhimicheskiy i patofiziologicheskiy aspekty. Moskva: Nauka/ Interperiodika, 2001; 343 p.
2. Fridovich I. The biology of oxygen radicals. Science. 1978; 201 (4359): 875–80.
3. Kravchuk EL. Rol' svobodnoradikal'nogo okisleniya v patogeneze zabolevaniy glaz. Vestnik oftal'mologii. 2004; 120 (5): 48–51.
4. Catala A. Lipid peroxidation of membrane phospholipids in the vertebrate retina. Front Biosci (Schol Ed). 2011; (3): 52–60.
5. Spector A. Oxidative stress-induced cataract: mechanism of action. The FASEB Journal. 1995; 9 (12): 1173–82.
6. Chesnokova NB, Neroev VV, Beznos OV, Beyshenova GA, Nikol'skaya II, Kost OA, et al. Okislitel'nyy stress pri uveite i ego korrektsiya antioksidantnym fermentom superoksiddismutazoy (eksperimental'noe issledovanie). Vestnik oftal'mologii. 2014; 130 (5): 30–5.
7. Niesman MR, Johnson KA, Penn JS. Therapeutic effect of liposomal superoxide dismutase in an animal model of retinopathy of prematurity. Neurochemical research. 1997; 22 (5): 597–605.
8. Alio JL, Ayala MJ, Mulet ME, Artola A, Ruiz JM, Bellot J. Antioxidant therapy in the treatment of experimental acute corneal inflammation. Ophthalmic research. 1995; 27 (3): 136–43.
9. Rodriguez C, Mayo JC, Sainz RM, Antolin I, Herrera F, Martin V, et al. Regulation of antioxidant enzymes: a significant role for melatonin. Journal of pineal research. 2004; 36 (1): 1–9.
10. Gulidova OV, Lyubitskiy OB, Klebanov GI, Chesnokova NB. Izmenenie antiokislitel'noy aktivnosti sleznoy zhidkosti pri eksperimental'noy ozhogovoy bolezni glaz. Byulleten' eksperimental'noy biologii i meditsiny. 1999; 128 (11): 571–4.
11. Choy CKM, Benzie IFF, Cho P. Ascorbic acid concentration and total antioxidant activity of human tear fluid measured using the FRASC assay. Investigative ophthalmology & visual science. 2000; 41 (11): 3293–8.
12. Koracevic D, Koracevic G, Djordjevic V, Andrejevic S, Cosic V. Method for the measurement of antioxidant activity in human fluids. Journal of clinical pathology. 2001; 54 (5): 356–61.
13. Crouch RK, Goletz P, Snyder A, Coles WH. Antioxidant enzymes in human tears. Journal of Ocular Pharmacology and Therapeutics. 1991; 7 (3): 253–8.
14. Gritsuk AI, Sirota TV, Dravitsa LV, Kreddok EA. Otsenka sostoyaniya antioksidantnoy aktivnosti sleznoy zhidkosti. Biomeditsinskaya khimiya. 2006; 52 (6): 601–7.
15. Marklund S, Marklund G. Involvement of the superoxide anion radical in the autoxidation of pyrogallol and a convenient assay for superoxide dismutase. The FEBS Journal. 1974; 47 (3): 469–74.
16. Fernández-Sánchez A, Madrigal-Santillán E, Bautista M, Esquivel-Soto J, Morales-González Á, Esquivel-Chirino C, et al. Inflammation, oxidative stress, and obesity. International journal of molecular sciences. 2011; 12 (5): 3117–32.
17. Reuter S, Gupta SC, Chaturvedi MM, Aggarwal BB. Oxidative stress, inflammation, and cancer: how are they linked? Free Radical Biology and Medicine. 2010; 49 (11): 1603–16.
18. Yamada M, Shichi H, Yuasa T, Tanouchi Y, Mimura Y. Superoxide in ocular inflammation: human and experimental uveitis. Journal of free radicals in biology & medicine. 1986; 2 (2): 111–7.
19. Ishimoto S, Wu G-S, Hayashi S, Zhang J, Rao NA. Free radical tissue damages in the anterior segment of the eye in experimental autoimmune uveitis. Investigative ophthalmology & visual science.

1996; 37 (4): 630–6.
20. Sahoo SK, Dilnawaz F, Krishnakumar S. Nanotechnology in ocular drug delivery. Drug discovery today. 2008; 13 (3–4): 144–51.
21. Kost OA, Beznos O V, Davydova NG, Manickam DS, Nikolskaya II, Guller AE, et al. Superoxide dismutase 1 nanozyme for treatment of eye inflammation. Oxidative medicine and cellular longevity. 2016; 2016 (1): 1–13.
22. Nukolova NV, Aleksashkin AD, Abakumova TO, Morozova AY, Gubskiy IL, Kirzhanova EA, et al. Multilayer polyion complex nanoformulations of superoxide dismutase 1 for acute spinal cord injury. Journal of Controlled Release. 2018; (270): 226–36.
23. Amatore C, Arbault S, Bouton C, Coffi K, Drapier J, Ghandour H, et al. Monitoring in real time with a microelectrode the release of reactive oxygen and nitrogen species by a single macrophage stimulated by its membrane mechanical depolarization. ChemBioChem. 2006; 7 (4): 653–61.
24. Fridovich I. Superoxide radical: an endogenous toxicant. Annual review of pharmacology and toxicology. 1983; 23 (1): 239–57.
25. Clausmeyer J, Actis P, Córdoba AL, Korchev Y, Schuhmann W. Nanosensors for the detection of hydrogen peroxide. Electrochemistry Communications. 2014; (40): 28–30.
26. Actis P, Tokar S, Clausmeyer J, Babakinejad B, Mikhaleva S, Cornut R, et al. Electrochemical nanoprobes for single-cell analysis. Acs Nano. 2014; 8 (1): 875–84.
27. Erofeev A, Gorelkin P, Garanina A, Alova A, Efremova M, Vorobyeva N, et al. Novel method for rapid toxicity screening of magnetic nanoparticles. Scientific reports. 2018; 8 (1): 7462.
28. Deby C, Boes M, Pincemail J, Bourdon-Neuray J, Deby-Dupont G. Degradation of membrane phospholipids by a direct nucleophilic action of superoxide anion. In: Free Radicals, Lipoproteins, and Membrane Lipids. Springer, 1990; p. 105–13.
29. Prausnitz MR, Noonan JS. Permeability of cornea, sclera, and conjunctiva: a literature analysis for drug delivery to the eye. Journal of pharmaceutical sciences. 1998; 87 (12): 1479–88.
30. Manickam DS, Brynskikh AM, Kopanic JL, Sorgen PL, Klyachko NL, Batrakova EV, et al. Well-defined cross-linked antioxidant nanozymes for treatment of ischemic brain injury. Journal of controlled release. 2012; 162 (3): 636–45.

Литература

1. Зенков Н. К, Ланкин В. З, Меньщикова Е. Б. Окислительный стресс: Биохимический и патофизиологический аспекты. М.: Наука/Интерпериодика, 2001; 343 с.
2. Fridovich I. The biology of oxygen radicals. Science. 1978; 201 (4359): 875–80.
3. Кравчук Е. Л. Роль свободнорадикального окисления в патогенезе заболеваний глаз. Вестник офтальмологии. 2004; 120 (5): 48–51.
4. Catala A. Lipid peroxidation of membrane phospholipids in the vertebrate retina. Front Biosci (Schol Ed). 2011; (3): 52–60.
5. Spector A. Oxidative stress-induced cataract: mechanism of action. The FASEB Journal. 1995; 9 (12): 1173–82.
6. Чеснокова Н. Б., Нероев В. В., Безнос О. В. , Бейшенова Г.А., Никольская И. И., Кост О. А., и др. Окислительный стресс при увеите и его коррекция антиоксидантным ферментом супероксиддисмутазой (экспериментальное исследование). Вестник офтальмологии. 2014; 130 (5): 30–5.
7. Niesman MR, Johnson KA, Penn JS. Therapeutic effect of liposomal superoxide dismutase in an animal model of retinopathy of prematurity. Neurochemical research. 1997; 22 (5): 597–605.
8. Alio JL, Ayala MJ, Mulet ME, Artola A, Ruiz JM, Bellot J. Antioxidant therapy in the treatment of experimental acute corneal inflammation. Ophthalmic research. 1995; 27 (3): 136–43.
9. Rodriguez C, Mayo JC, Sainz RM, Antolin I, Herrera F, Martin V, et al. Regulation of antioxidant enzymes: a significant role for melatonin. Journal of pineal research. 2004; 36 (1): 1–9.
10. Гулидова О. В., Любицкий О. Б., Клебанов Г. И., Чеснокова Н. Б. Изменение антиокислительной активности слезной жидкости при экспериментальной ожоговой болезни глаз. Бюллетень экспериментальной биологии и медицины. 1999; 128 (11): 571–4.
11. Choy CKM, Benzie IFF, Cho P. Ascorbic acid concentration and total antioxidant activity of human tear fluid measured using the FRASC assay. Investigative ophthalmology & visual science. 2000; 41 (11): 3293–8.
12. Koracevic D, Koracevic G, Djordjevic V, Andrejevic S, Cosic V. Method for the measurement of antioxidant activity in human fluids. Journal of clinical pathology. 2001; 54 (5): 356–61.
13. Crouch RK, Goletz P, Snyder A, Coles WH. Antioxidant enzymes in human tears. Journal of Ocular Pharmacology and Therapeutics. 1991; 7 (3): 253–8.
14. Грицук А. И. , Сирота Т. В. , Дравица Л. В. , Крэддок Е. А.. Оценка состояния антиоксидантной активности слезной жидкости. Биомедицинская химия. 2006; 52 (6): 601–7.
15. Marklund S, Marklund G. Involvement of the superoxide anion radical in the autoxidation of pyrogallol and a convenient assay for superoxide dismutase. The FEBS Journal. 1974; 47 (3): 469–74.
16. Fernández-Sánchez A, Madrigal-Santillán E, Bautista M, Esquivel-Soto J, Morales-González Á, Esquivel-Chirino C, et al. Inflammation, oxidative stress, and obesity. International journal of molecular sciences. 2011; 12 (5): 3117–32.
17. Reuter S, Gupta SC, Chaturvedi MM, Aggarwal BB. Oxidative stress, inflammation, and cancer: how are they linked? Free Radical Biology and Medicine. 2010; 49 (11): 1603–16.
18. Yamada M, Shichi H, Yuasa T, Tanouchi Y, Mimura Y. Superoxide in ocular inflammation: human and experimental uveitis. Journal of free radicals in biology & medicine. 1986; 2 (2): 111–7.
19. Ishimoto S, Wu G-S, Hayashi S, Zhang J, Rao NA. Free radical tissue damages in the anterior segment of the eye in experimental autoimmune uveitis. Investigative ophthalmology & visual science. 1996; 37 (4): 630–6.
20. Sahoo SK, Dilnawaz F, Krishnakumar S. Nanotechnology in ocular drug delivery. Drug discovery today. 2008; 13 (3–4): 144–51.
21. Kost OA, Beznos O V, Davydova NG, Manickam DS, Nikolskaya II, Guller AE, et al. Superoxide dismutase 1 nanozyme for treatment of eye inflammation. Oxidative medicine and cellular longevity. 2016; 2016 (1): 1–13.
22. Nukolova NV, Aleksashkin AD, Abakumova TO, Morozova AY, Gubskiy IL, Kirzhanova EA, et al. Multilayer polyion complex nanoformulations of superoxide dismutase 1 for acute spinal cord injury. Journal of Controlled Release. 2018; (270): 226–36.
23. Amatore C, Arbault S, Bouton C, Coffi K, Drapier J, Ghandour H, et al. Monitoring in real time with a microelectrode the release of reactive oxygen and nitrogen species by a single macrophage stimulated by its membrane mechanical depolarization. ChemBioChem. 2006; 7 (4): 653–61.
24. Fridovich I. Superoxide radical: an endogenous toxicant. Annual review of pharmacology and toxicology. 1983; 23 (1): 239–57.
25. Clausmeyer J, Actis P, Córdoba AL, Korchev Y, Schuhmann W. Nanosensors for the detection of hydrogen peroxide. Electrochemistry Communications. 2014; (40): 28–30.
26. Actis P, Tokar S, Clausmeyer J, Babakinejad B, Mikhaleva S, Cornut R, et al. Electrochemical nanoprobes for single-cell analysis. Acs Nano. 2014; 8 (1): 875–84.
27. Erofeev A, Gorelkin P, Garanina A, Alova A, Efremova M, Vorobyeva N, et al. Novel method for rapid toxicity screening of magnetic nanoparticles. Scientific reports. 2018; 8 (1): 7462.
28. Deby C, Boes M, Pincemail J, Bourdon-Neuray J, Deby-Dupont G. Degradation of membrane phospholipids by a direct nucleophilic action of superoxide anion. In: Free Radicals, Lipoproteins, and Membrane Lipids. Springer, 1990; p. 105–13.
29. Prausnitz MR, Noonan JS. Permeability of cornea, sclera, and conjunctiva: a literature analysis for drug delivery to the eye. Journal of pharmaceutical sciences. 1998; 87 (12): 1479–88.
30. Manickam DS, Brynskikh AM, Kopanic JL, Sorgen PL, Klyachko NL, Batrakova EV, et al. Well-defined cross-linked antioxidant nanozymes for treatment of ischemic brain injury. Journal of controlled release. 2012; 162 (3): 636–45.

THE USE OF MONOCLONAL ANTIBODIES IN AUTOIMMUNITY TREATMENT

Merzlyak EM[1,2] ✉, Syrko DS[2], Musatkina EA[2], Israelson MA[1,2]

[1]Shemyakin–Ovchinnikov Institute of Bioorganic Chemistry, RAS, Moscow

[2] Research Institute of Translational Medicine,
Pirogov Russian National Research Medical University, Moscow

Recently, monoclonal antibodies (MA) have gained popularity as therapeutic agents for the treatment of autoimmune disorders. These antibodies target proinflammatory cytokines, as well as T and B cells potentially involved in the pathogenesis of such conditions. In the present work we attempt to give a systematic description of available therapeutic MA, highlight their key mechanisms of action and pinpoint their adverse effects. We believe that MA that are capable of recognizing and eliminating pathogenic T- and B-cell clones hold the most promise for medical application as biologics. Detection and identification of autoreactive lymphocyte clones is one of the most serious challenges of contemporary medicine.

Keywords: autoimmune disorders, biologics, therapeutic antibodies for autoimmunity treatment, mechanism of action of monoclonal antibodies

Funding: this work was supported by the Ministry of Science and Higher Education of the Russian Federation (ID RFMEFI60716X0158).

✉ **Correspondence should be addressed:** Ekaterina M. Merzlyak
Miklouho-Maclay, 16/10, Moscow, 117997; ekaterin99@mail.ru

Received: 06.12.2018 **Accepted:** 20.12.2018

DOI: 10.24075/brsmu.2018.094

ИСПОЛЬЗОВАНИЕ МОНОКЛОНАЛЬНЫХ АНТИТЕЛ ДЛЯ ТЕРАПИИ АУТОИММУННЫХ ЗАБОЛЕВАНИЙ

Е. М. Мерзляк[1,2] ✉, Д. С. Сырко[2], Е. А. Мусаткина[2], М. Израельсон[1,2]

[1] Институт биоорганической химии имени М. М. Шемякина и Ю. А. Овчинникова Российской академии наук, Москва

[2] Научно-исследовательский институт трансляционной медицины,
Российский национальный исследовательский медицинский университет имени Н. И. Пирогова, Москва

В последнее время в терапии аутоиммунных заболеваний стали активно применять моноклональные антитела (МА). Мишенью этих антител служат провоспалительные цитокины и собственно Т- и В-клетки, потенциально участвующие в патогенезе заболевания. В данной статье сделана попытка систематизировать используемые препараты и привести основные механизмы, лежащие в основе такого рода терапии, описаны нежелательные побочные действия. Потенциальными путями и перспективами развития биологиксов в лечении аутоиммунных заболеваний, по нашему мнению, являются МА, которые узнают и элиминируют клоны Т- и В-клеток, обусловливающие патогенез аутоиммунного заболевания. Поиск аутореактивных клонов является одной из сложных и актуальных задач современной биомедицины.

Ключевые слова: аутоиммунные заболевания, биологиксы, терапевтические антитела для лечения аутоиммунных заболеваний, механизм действия моноклональных антител

Финансирование: работа выполнена при поддержке Минобрнауки России (идентификатор соглашения RFMEFI60716X0158).

✉ **Для корреспонденции:** Екатерина Марковна Мерзляк
ул. Миклухо-Маклая, д. 16/10, г. Москва, 117997; ekaterin99@mail.ru

Статья получена: 06.12.2018 **Статья принята к печати:** 20.12.2018

DOI: 10.24075/vrgmu.2018.094

As we broaden our knowledge of the mechanisms underlying the adaptive immunity, we learn to identify its malfunctioning elements posing a risk of autoimmune disorders. The latter encompass an extensive array of pathologies affecting almost all body tissues. The pathogenesis of these disorders is linked to the production of autoimmune antibodies and proliferation of effector T-cell clones that recognize self-antigens and therefore provoke inflammation both locally and systemically. In their anergic (self-tolerant) state, autoreactive T-cells have also been found in the bloodstream of healthy donors [1] where they are controlled by regulatory T cells (Tregs). The aberrant concentrations and abnormal functional activity of Tregs are among the possible causes of inflammation accompanying autoimmune disorders.

Current approaches to treating autoimmunity are based on the suppression of the immune system by therapeutic agents that directly or indirectly mitigate inflammation (see the Figure). This article looks at therapies for autoimmune diseases that involve the use of monoclonal antibodies (MA). Such MA, as well as other genetically engineered pharmaceutical agents, are referred to as biologics in the literature published in English. Some MA have already been proved effective in managing autoimmune conditions; some are currently undergoing clinical trials.

Therapeutic MA considerably vary in terms of their mechanism of action. They can bind a soluble ligand or a receptor on the membrane of a target cell thereby blocking the interaction between the receptor and the ligand, modulating the signal from the receptor or triggering apoptosis (Fig).

The mechanisms underlying the depletion of a target cell population by MA are diverse. Depletion mediated by the Fc fragment can induce apoptosis of the target cell, lead to cell

death via antibody- or complementary-dependent cellular cytotoxicity (ADCC/CDC) pathways, and provoke antigen-dependent phagocytosis. The mechanisms activated by the blockade of surface costimulatory receptors are fundamentally different. They suppress the signal produced in response to antigen-induced stimulation or reprogram effector T cells into Tregs.

Therapeutic antibodies causing a decline in the levels of anti-inflammatory cytokines (IFNɣ, TNF, IL17, and others) or blocking cytokine receptors can only bring temporary remission depending on their clearance rate. We think that approaches based on the depletion of lymphocyte subpopulations enriched in autoreactive T cells are the most promising because they allow us to eliminate the cause of an autoimmune disease. Another interesting therapeutic strategy is based on the functional activation of regulatory T cells in order to boost the expression of inhibitory cytokines, such as IL10.

An overview of the structure of therapeutic antibodies and their application

In the past few years, the list of therapeutic antibodies has been expanded considerably to comprise drugs with selective mechanisms of action used in disease modifying therapies (DMT). The US Food and Drug Administration (FDA) has approved about 40 MA for treating various diseases including those of autoimmune nature.

As a rule, the primary products of MA synthesis require further optimization. The optimization strategies include modification of the Fc fragment aimed to extend the half-life of the obtained antibody; humanization by altering the amino acid sequence (this ensures the similarity of the synthetic structure to human antibodies and therefore reduces the immunogenicity of the drug); the use of special cell lines for antibody synthesis deficient in glycosylation enzymes, which helps to enhance the cytotoxicity of the end product. The cytotoxicity of nonfucosylated therapeutic antibodies is 500–1,000 times higher than that of the same antibodies with a high degree of glycosylation [2]. Recently, there have been proposals to introduce modifications to the Fc-fragment to avoid a wide range of adverse effects caused by inflammatory cytokines that are released in response to the massive death of effector cells that accompanies the use of therapeutic antibodies against surface markers found in many cell types.

Monoclonal antibodies against cytokines and inflammatory factors

The first MA approved in 2002 by FDA for the treatment of inflammatory diseases (mostly autoimmune) were anti-TNF (tumor necrosis factor) antibodies. Recently, the list of therapeutic targets has been upgraded with a number of cytokines, including IL1, IL6, IL12, IL15, IL17, IL18, and IL23, associated with autoimmune pathology. The efficacy of the MA designed to fight various autoimmune disorders has been discussed in a few review articles [3, 4].

TNF is one of the primary inducers of inflammation in the cytokine cascade; therefore, its inhibitors can cause nonspecific inflammation in patients suffering from autoimmune disorders, such as rheumatoid arthritis or RA, ankylosing spondylitis, psoriasis, Crohn's disease, etc. Today, 4 MA against TNF are available clinically: infliximab, golimumab, certolizumab, and adalimumab. They are different in their humanization degree and the site they target. These drugs are widely used to manage rheumatoid disorders of autoimmune nature, including ankylosing spondylitis. TNF inhibitors slow down the progression of this disease but cannot prevent it from happening. However, not every patient responds to anti-TNF therapy. For example, one-third of patients with RA do not show any improvement when treated with TNF inhibitors. No therapeutic effect is also observed in patients with multiple sclerosis.

Unfortunately, the use of anti-TNF MA contributes to the risk of cancer and infection. In addition, TNF blockade does not cause any decline in IL1 implicated in cartilage degradation and joint erosion, which was demonstrated in mice with experimental RA [5].

Proinflammatory IL1 is another therapeutic target. We still think, though, that unlike anakinra (the antagonist of the IL1 receptor), MA against IL1 may not find wide application in clinical practice. For example, an anti-IL1β drug gevokizumab has proved ineffective against noninfectious uveitis (the symptom of Behcet's disease). Another fully human anti-IL1β antibody (IgG1, canakinumab) has recently completed a phase III clinical trial [6]. Although it was able to induce therapeutic response in

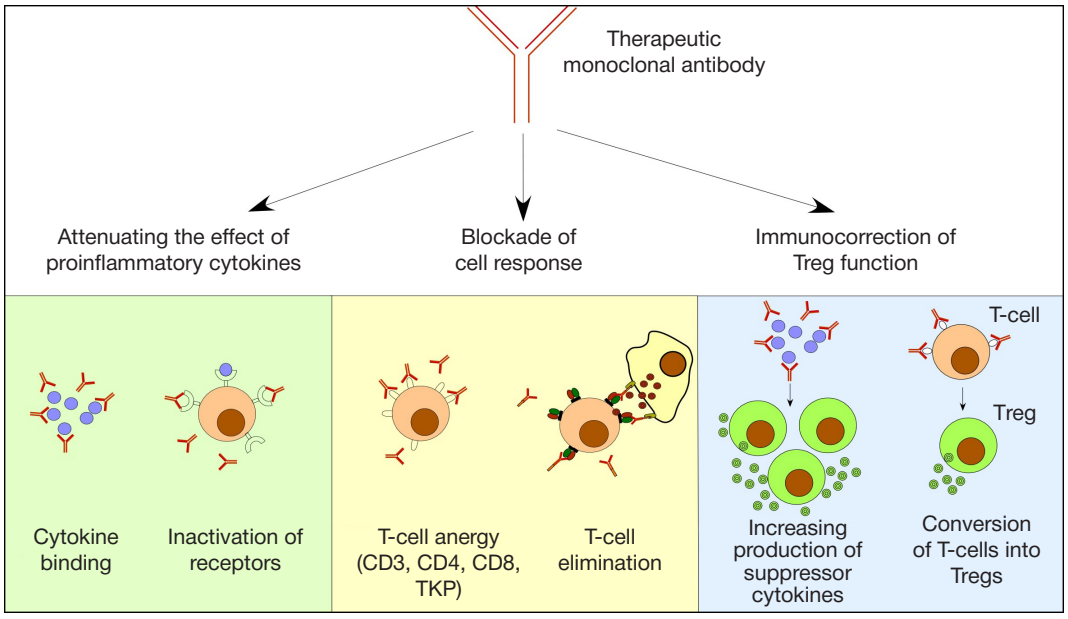

Monoclonal antibody treatment approaches for autoimmune disorders

less than half of patients with RA and juvenile idiopathic arthritis (JIA) [7], it was still approved by FDA for the treatment of JIA and the cryopyrin-associated periodic syndrome (CAPS). Sustained remission was observed in 97% of patients with CAPS after a single dose of the drug; the adverse reactions were very mild [8, 9].

Another effective strategy for treating autoimmune disorders relies on the blockade of cytokines involved in the activation or differentiation of Th1- and Th17-cell populations associated with the pathogenesis of many autoimmune diseases. IL6 is an example of such proinflammatory factors that together with IL23 and TGFβ triggers differentiation of naïve $CD4^+$-lymphocytes into Th17 cells [10]. Normally, Th17 cells participate in the immune response to bacterial and fungal infections. Hyperactive Th17 excessively produce IL17, GM-CSF, and IL21, promoting inflammation. The Th17/Tregs imbalance is observed in systemic lupus erythematosus (SLE), in the peripheral blood of patients with RA, at inflammation sites in patients with JIA, type 1 diabetes and Crohn's disease [11, 12].

One of the most effective drugs capable of inhibiting IL6 is tocilizumab (IgG1). It is a monoclonal antibody against the β-chain of the IL6 receptor that competes for this receptor preventing its binding to IL6. The drug has been proved safe and highly effective for the treatment of RA and JIA. The same level of efficacy has been demonstrated by olokizumab (a humanized antibody against IL6) that successfully completed a phase II clinical trial in 2017.

IL6 blockade by tocilizumab leads to an increase in the proportion of Tregs in the population of $CD4^+$-cells both in mice with experimental EAE and patients with RA. This correlates with marked remission observed in such patients [13]. The therapeutic effect of these MA against IL6 relies on the methylation of the Foxp3 promoter induced by IL6, which leads to a decline in the functional activity of Tregs [14]. IL6 plays an important role in the immune response to bacterial infection in healthy individuals. It also exhibits protective properties in patients with liver/neural tissue injuries. It should be born in mind, though, that the prolonged intake of MA against IL6 can increase sensitivity to bacterial and viral infections and poses a risk of death in people with liver cirrhosis and strokes.

The blockade of interleukins or their receptors by MA can have a better therapeutic effect than methotrexate-based treatment or the use of other immunosuppressive drugs. Sadly, it is associated with a number of adverse effects (infections, pharyngitis, etc.). The drugs described above alleviate the symptoms of autoimmune diseases and sometimes slow down their progression, but cannot eliminate their cause ensuring only temporary remission.

Blockade of cell response

At the cell level, autoimmunity can be suppressed by the MA that specifically recognize unique receptors marking certain cell populations (CD2, CD3, CD4, CD8, CD19, CD20, and CD22). This treatment strategy, however, leads to the inhibition of the entire subpopulation of lymphocytes, affects healthy cells and causes serious immune suppression.

CD3

The MA against CD3 perform well in the mouse models of autoimmune diseases, including autoimmune encephalitis, TNP-KLH-induced colitis, and collagen-induced arthritis. The therapeutic effect of these antibodies can be explained by a few different yet noncontradictory mechanisms. Anti-CD3 MA bind to the ξ-subunit of CD3, and the entire CD3-complex is then internalized or blocked. As a result, the T cell temporarily stops to respond to antigens presented to it. Anti-CD3 antibodies are also reported to cause apoptosis of activated T cells [15].

Teplizumab and otelixizumab (ChAglyCD3) are another pair of antibodies against CD3. They are capable of halting (not permanently, though) the death of insulin-producing β-cells in patients with type I diabetes [16]. Currently, teplizumab is undergoing a phase III clinical trial (TrialNet) that has recruited over 500 patients with stage 2 of diabetes.

Nondepleting antibodies against CD4 and CD8

A few research works have been published recently on the use of nondepleting monoclonal antibodies against the coreceptors CD4 and CD8. The efficacy of the drugs has been demonstrated in mice with experimentally induced type 1 diabetes [17]. The mechanism of their action is based on the specific interaction with surface receptors of lymphocytes that prevents activation of the immune response. Cell depletion does not occur because the Fc-fragment of MA is unable to bind the Fc-receptor of the recipient and, therefore, does not cause cell death. The mice who received nondepleting MA went into long-term remission (over 20 days) characterized by the reduction in the hyperproduction of IL2 and IFNγ.

Anti-CD20

An anti-CD20 MA known as rituximab (Mabthera) has turned to be highly effective against some autoimmune diseases, such as autoimmune vasculitis, antiphospholipid syndrome, myasthenia gravis, RA, SLE, and multiple sclerosis. The therapeutic effect of the drug is based on the depletion of B cells and lasts for 6 months. In many patients, the response to rituximab is delayed: it is often registered a few months after the intravenous infusion of the drug. A few possible explanations have been proposed: 1) the rate of B-cell clearance from the body varies from patient to patient; 2) the half-life of a plasma cell can affect the rate of response because the cell does not carry CD20 on its surface and keeps secreting antibodies; 3) in some patients even low concentrations of autoimmune antibodies can trigger pathology, delaying response to therapy until the antibodies are cleared from the body. The efficacy of rituximab is comparable or higher than that of immunosuppressants, such as cyclophosphamide, azathioprine, etc. However, rituximab ensures long term remission in as few as 20% of patients. Among the adverse reactions accompanying the rituximab-based regimens are sensitivity to infection, hypogammaglobulinemia and neutropenia [18, 19]. In the studies mentioned above rituximab was prescribed to patients with severe RA whose conventional treatment with glucocorticoids and cytotoxic agents had failed. It is likely that rituximab not only induces depletion of B lymphocytes, but also leads to the elimination of $CD20^+$-Th17-effector cells whose proportion is quite high in the blood of patients with RA, which explains the therapeutic effect of the drug [20]. Another possible mechanism exploited by the anti-CD20 therapy is associated with active production of IL6 by B cells: IL6 stimulates the differentiation of T-cell precursors into Th17 and inhibits their conversion into Tregs [21, 22]. Another humanized anti-CD20 antibody known by the name of ocrelizumab has successfully completed its clinical trials and is now approved by FDA for the treatment of multiple sclerosis; it reduces the number of lesions and slows down the progression of the disease [23].

Immune therapy: reprogramming T cells into Tregs

Tregs ensure immune tolerance in the peripheral organs by attenuating the immune response and bringing autoimmune reactions to a halt [24]. Tregs secrete anti-inflammatory cytokines IL10, TGFβ, and IL35, activate granzyme/perforin pathways mediating the apoptosis of effector cells, and inhibit dendritic cell functions. On the one hand, attempts to intentionally elevate the blood levels of Tregs or stimulate hyperproduction of suppressor cytokines can be regarded as an approach to treating autoimmune diseases. On the other hand, hyperactivity of Tregs leads to the suppression of the immune response and promotes malignancy. A new drug tregalizumab based on nondepleting MA was tested in 2016; it binds the unique epitope on the CD4 molecule, causing $CD4^+$-lymphocytes to differentiate into Treg cells.

We believe that combination therapy should be a preferred treatment modality in patients with autoimmune disorders. Such therapy should include the targeted elimination of T- or B-cell clones associated with autoimmunity. The treatment regimen can be based on the consecutive administration of several biologics that target different components of the immune response. For example, cytokine inhibitors and depleting MA can be used as a first-line therapy, as proposed recently. The second-line therapy could include inhibitors of CD28 co-stimulation mediators or of homeostatic cytokines [25]. Recent studies have demonstrated that inhibition of homeostatic cytokines such as IL15 or IL7 can be a promising approach to the therapy of autoimmune diseases [26].

So far, identification of unique markers of autoimmune inflammation remains an unsolved problem. T- and B-cell receptors (TCR, BCR) present on the surface of autoreactive lymphocytes can serve as such markers. The search for pathology-associated receptors can start from the sequencing of TCR and BCR repertoires of peripheral blood lymphocytes, as well as of lymphocytes isolated from the sites of inflammation, followed by the comparative analysis of TCR and BCR repertoires of healthy donors and disease-stricken individuals. Today, we know the structure of TCR potentially implicated in the celiac disease and ankylosing spondylitis [27–29]. Our team has established the structure of TCR associated with ankylosing spondylitis [28]; our findings were independently confirmed by our British colleagues [29]. We showed that the pathological T-cell clone carries a variable gene segment TRBV9 and synthesized MA that specifically bind and deplete T cells carrying the TCR associated with ankylosing spondylitis *in vitro* [30]. The described approach to designing novel therapeutic agents and the MA we synthesized may be a good platform for the development of drugs against autoimmune disorders in general and ankylosing spondilitis in particular.

CONCLUSIONS

Massive sequencing of immune repertoires of healthy donors and patients with severe autoimmune disorders, including multiple sclerosis and type 1 diabetes, followed by HLA-typing paves the way to the identification of new targets for immune therapies.

References

1. Danke NA, Koelle DM, Yee C, Beheray S, Kwok WW. Autoreactive T cells in healthy individuals. J Immunol. 2004; (172): 5967–2.
2. Konno Y, Kobayashi Y, Takahashi K, Takahashi E, Sakae S, Wakitani M, et al. Fucose content of monoclonal antibodies can be controlled by culture medium osmolality for high antibody-dependent cellular cytotoxicity. Cytotechnology. 2012; (64): 249–65.
3. Lai Y, Dong C. Therapeutic antibodies that target inflammatory cytokines in autoimmune diseases. Int Immunol. 2016; (28): 181–8.
4. Nasonov EL, Denisov LN, Stanislav ML. Interleukin-17 is a new target for anti-cytokine therapy of immune inflammatory rheumatic diseases. Rheumatology Science and Practice. 2013; (51): 545.
5. van den Berg WB, Joosten LA, Kollias G, van De Loo FA. Role of tumour necrosis factor alpha in experimental arthritis: separate activity of interleukin 1beta in chronicity and cartilage destruction. Ann Rheum Dis. 1999; 58 (Suppl 1): I40–8.
6. Dinarello CA, Simon A, van der Meer JWM. Treating inflammation by blocking interleukin-1 in a broad spectrum of diseases. Nat Rev Drug Discov. 2012; (11): 633–52.
7. Ruperto N, Brunner HI, Quartier P, Constantin T, Wulffraat NM, Horneff G, et al. Canakinumab in patients with systemic juvenile idiopathic arthritis and active systemic features: results from the 5-year long-term extension of the phase III pivotal trials. Ann Rheum Dis. 2018; (77): 1710–9.
8. Georgiev K, Georgieva M. Pharmacological properties of monoclonal antibodies directed against interleukins. In: Metodiev K, editor. Immunopathology and Immunomodulation. IntechOpen; 2015; p. 261–86. DOI: 10.5772/61774.
9. Goh AXH, Bertin-Maghit S, Ping Yeo S, Ho AWS, Derks H, Mortellaro A, et al. A novel human anti-interleukin-1β neutralizing monoclonal antibody showing in vivo efficacy. MAbs. 2014; (6): 765–73.
10. Gaffen SL, Jain R, Garg AV, Cua DJ. The IL23-IL17 immune axis: from mechanisms to therapeutic testing. Nat Rev Immunol. 2014; (14): 585–600.
11. Tabarkiewicz J, Pogoda K, Karczmarczyk A, Pozarowski P, Giannopoulos K. The role of IL17 and Th17 lymphocytes in autoimmune diseases. Arch Immunol Ther Exp. 2015; (63): 435–49.
12. Lee GR. The Balance of Th17 versus Treg Cells in Autoimmunity. Int J Mol Sci. 2018; 19 (3): 730. DOI:10.3390/ijms19030730.
13. Kikuchi J, Hashizume M, Kaneko Y, Yoshimoto K, Nishina N, Takeuchi T. Peripheral blood CD4(+)CD25(+)CD127(low) regulatory T cells are significantly increased by tocilizumab treatment in patients with rheumatoid arthritis: increase in regulatory T cells correlates with clinical response. Arthritis Res Ther. 2015; (17): 10.
14. Lal G, Zhang N, van der Touw W, Ding Y, Ju W, Bottinger EP, et al. Epigenetic regulation of Foxp3 expression in regulatory T cells by DNA methylation. J Immunol. 2009; (182): 259–73.
15. Kuhn C, Weiner HL. Therapeutic anti-CD3 monoclonal antibodies: from bench to bedside. Immunotherapy. 2016; (8): 889–906.
16. Guglielmi C, Williams SR, Del Toro R, Pozzilli P. Efficacy and safety of otelixizumab use in new-onset type 1 diabetes mellitus. Expert Opin Biol Ther. 2016; (16): 841–6.
17. Yi Z, Diz R, Martin AJ, Morillon YM, Kline DE, Li L et al. Long-term remission of diabetes in NOD mice is induced by nondepleting anti-CD4 and anti-CD8 antibodies. Diabetes. 2012; (61): 2871–80.
18. Randall KL. Rituximab in autoimmune diseases. Aust Prescr. 2016; (39): 131–4.
19. Looney RJ. B cells as a therapeutic target in autoimmune diseases other than rheumatoid arthritis. Rheumatology. 2005; 44 (Suppl 2): ii13–ii17.
20. Mélet J, Mulleman D, Goupille P, Ribourtout B, Watier H, Thibault G. Rituximab-induced T cell depletion in patients with rheumatoid arthritis: association with clinical response. Arthritis Rheum. 2013; (65): 2783–90.
21. Barr TA, Shen P, Brown S, Lampropoulou V. B cell depletion therapy ameliorates autoimmune disease through ablation of IL-6–producing B cells. J Exp Med. 2012; 209 (5): 1001–10. DOI: 10.1084/jem.20111675.
22. Korn T, Mitsdoerffer M, Croxford AL, Awasthi A, Dardalhon VA, Galileos G et al. IL6 controls Th17 immunity in vivo by inhibiting the conversion of conventional T cells into Foxp3+ regulatory T cells. Proc Natl Acad Sci USA. 2008; (105): 18460–5.
23. Mulero P, Midaglia L, Montalban X. Ocrelizumab: a new milestone

in multiple sclerosis therapy. Ther Adv Neurol Disord. 2018; (11): 1756286418773025. DOI: 10.1177/1756286418773025.
24. König M, Rharbaoui F, Aigner S, Dälken B, Schüttrumpf J. Tregalizumab — A Monoclonal Antibody to Target Regulatory T Cells. Front Immunol. 2016; (7): 11.
25. Smilek DE, Ehlers MR, Nepom GT. Restoring the balance: immunotherapeutic combinations for autoimmune disease. Dis Model Mech. 2014; (7): 503–13.
26. Chen Y, Chauhan SK, Tan X, Dana R. Interleukin-7 and -15 maintain pathogenic memory Th17 cells in autoimmunity. J Autoimmun. 2017; (77): 96–103.
27. Yohannes DA, Freitag TL, de Kauwe A, Kaukinen K, Kurppa K, Wacklin P et al. Deep sequencing of blood and gut T-cell receptor β-chains reveals gluten-induced immune signatures in celiac disease. Sci Rep. 2017; (7): 17977.
28. Komech EA, Pogorelyy MV, Egorov ES, Britanova OV, Rebrikov DV, Bochkova AG et al. CD8+ T cells with characteristic T cell receptor beta motif are detected in blood and expanded in synovial fluid of ankylosing spondylitis patients. Rheumatology. 2018; (57): 1097–104.
29. Faham M, Carlton V, Moorhead M, Zheng J, Klinger M, Pepin F et al. Discovery of T Cell Receptor β Motifs Specific to HLA--B27--Positive Ankylosing Spondylitis by Deep Repertoire Sequence Analysis. Arthritis & Rheumatology. Wiley Online Library; 2017; (69): 774–84.
30. Israelson MA, Stepanov AV, Staroverov DB, Shagina IA, Misorin AK, Evstratieva AV, Merzlyak EM, Bogdanova EA, Britanova OV, Lukyanov SA. Testing of monoclonal antibodies against the T-cell receptor associated with ankylosing spondylitis. Bulletin of RSMU. 2018; (5): 71–9. DOI: 10.24075/brsmu.2018.064.

Литература

1. Danke NA, Koelle DM, Yee C, Beheray S, Kwok WW. Autoreactive T cells in healthy individuals. J Immunol. 2004; (172): 5967–2.
2. Konno Y, Kobayashi Y, Takahashi K, Takahashi E, Sakae S, Wakitani M, et al. Fucose content of monoclonal antibodies can be controlled by culture medium osmolality for high antibody-dependent cellular cytotoxicity. Cytotechnology. 2012; (64): 249–65.
3. Lai Y, Dong C. Therapeutic antibodies that target inflammatory cytokines in autoimmune diseases. Int Immunol. 2016; (28): 181–8.
4. Nasonov EL, Denisov LN, Stanislav ML. Interleukin-17 is a new target for anti-cytokine therapy of immune inflammatory rheumatic diseases. Rheumatology Science and Practice. 2013; (51): 545.
5. van den Berg WB, Joosten LA, Kollias G, van De Loo FA. Role of tumour necrosis factor alpha in experimental arthritis: separate activity of interleukin 1beta in chronicity and cartilage destruction. Ann Rheum Dis. 1999; 58 (Suppl 1): I40–8.
6. Dinarello CA, Simon A, van der Meer JWM. Treating inflammation by blocking interleukin-1 in a broad spectrum of diseases. Nat Rev Drug Discov. 2012; (11): 633–52.
7. Ruperto N, Brunner HI, Quartier P, Constantin T, Wulffraat NM, Horneff G, et al. Canakinumab in patients with systemic juvenile idiopathic arthritis and active systemic features: results from the 5-year long-term extension of the phase III pivotal trials. Ann Rheum Dis. 2018; (77): 1710–9.
8. Georgiev K, Georgieva M. Pharmacological properties of monoclonal antibodies directed against interleukins. In: Metodiev K, editor. Immunopathology and Immunomodulation. IntechOpen; 2015; p. 261–86. DOI: 10.5772/61774.
9. Goh AXH, Bertin-Maghit S, Ping Yeo S, Ho AWS, Derks H, Mortellaro A, et al. A novel human anti-interleukin-1β neutralizing monoclonal antibody showing in vivo efficacy. MAbs. 2014; (6): 765–73.
10. Gaffen SL, Jain R, Garg AV, Cua DJ. The IL23-IL17 immune axis: from mechanisms to therapeutic testing. Nat Rev Immunol. 2014; (14): 585–600.
11. Tabarkiewicz J, Pogoda K, Karczmarczyk A, Pozarowski P, Giannopoulos K. The role of IL17 and Th17 lymphocytes in autoimmune diseases. Arch Immunol Ther Exp. 2015; (63): 435–49.
12. Lee GR. The Balance of Th17 versus Treg Cells in Autoimmunity. Int J Mol Sci. 2018; 19 (3): 730. DOI:10.3390/ijms19030730.
13. Kikuchi J, Hashizume M, Kaneko Y, Yoshimoto K, Nishina N, Takeuchi T. Peripheral blood CD4(+)CD25(+)CD127(low) regulatory T cells are significantly increased by tocilizumab treatment in patients with rheumatoid arthritis: increase in regulatory T cells correlates with clinical response. Arthritis Res Ther. 2015; (17): 10.
14. Lal G, Zhang N, van der Touw W, Ding Y, Ju W, Bottinger EP, et al. Epigenetic regulation of Foxp3 expression in regulatory T cells by DNA methylation. J Immunol. 2009; (182): 259–73.
15. Kuhn C, Weiner HL. Therapeutic anti-CD3 monoclonal antibodies: from bench to bedside. Immunotherapy. 2016; (8): 889–906.
16. Guglielmi C, Williams SR, Del Toro R, Pozzilli P. Efficacy and safety of otelixizumab use in new-onset type 1 diabetes mellitus. Expert Opin Biol Ther. 2016; (16): 841–6.
17. Yi Z, Diz R, Martin AJ, Morillon YM, Kline DE, Li L et al. Long-term remission of diabetes in NOD mice is induced by nondepleting anti-CD4 and anti-CD8 antibodies. Diabetes. 2012; (61): 2871–80.
18. Randall KL. Rituximab in autoimmune diseases. Aust Prescr. 2016; (39): 131–4.
19. Looney RJ. B cells as a therapeutic target in autoimmune diseases other than rheumatoid arthritis. Rheumatology. 2005; 44 (Suppl 2): ii13–ii17.
20. Mélet J, Mulleman D, Goupille P, Ribourtout B, Watier H, Thibault G. Rituximab-induced T cell depletion in patients with rheumatoid arthritis: association with clinical response. Arthritis Rheum. 2013; (65): 2783–90.
21. Barr TA, Shen P, Brown S, Lampropoulou V. B cell depletion therapy ameliorates autoimmune disease through ablation of IL-6–producing B cells. J Exp Med. 2012; 209 (5): 1001–10. DOI: 10.1084/jem.20111675.
22. Korn T, Mitsdoerffer M, Croxford AL, Awasthi A, Dardalhon VA, Galileos G et al. IL6 controls Th17 immunity in vivo by inhibiting the conversion of conventional T cells into Foxp3+ regulatory T cells. Proc Natl Acad Sci USA. 2008; (105): 18460–5.
23. Mulero P, Midaglia L, Montalban X. Ocrelizumab: a new milestone in multiple sclerosis therapy. Ther Adv Neurol Disord. 2018; (11): 1756286418773025. DOI: 10.1177/1756286418773025.
24. König M, Rharbaoui F, Aigner S, Dälken B, Schüttrumpf J. Tregalizumab — A Monoclonal Antibody to Target Regulatory T Cells. Front Immunol. 2016; (7): 11.
25. Smilek DE, Ehlers MR, Nepom GT. Restoring the balance: immunotherapeutic combinations for autoimmune disease. Dis Model Mech. 2014; (7): 503–13.
26. Chen Y, Chauhan SK, Tan X, Dana R. Interleukin-7 and -15 maintain pathogenic memory Th17 cells in autoimmunity. J Autoimmun. 2017; (77): 96–103.
27. Yohannes DA, Freitag TL, de Kauwe A, Kaukinen K, Kurppa K, Wacklin P et al. Deep sequencing of blood and gut T-cell receptor β-chains reveals gluten-induced immune signatures in celiac disease. Sci Rep. 2017; (7): 17977.
28. Komech EA, Pogorelyy MV, Egorov ES, Britanova OV, Rebrikov DV, Bochkova AG et al. CD8+ T cells with characteristic T cell receptor beta motif are detected in blood and expanded in synovial fluid of ankylosing spondylitis patients. Rheumatology. 2018; (57): 1097–104.
29. Faham M, Carlton V, Moorhead M, Zheng J, Klinger M, Pepin F et al. Discovery of T Cell Receptor β Motifs Specific to HLA--B27--Positive Ankylosing Spondylitis by Deep Repertoire Sequence Analysis. Arthritis & Rheumatology. Wiley Online Library; 2017; (69): 774–84.
30. Израельсон М. А., Степанов А. В., Староверов Д. Б., Шагина И. А., Мисорин А. К., Евстратьева А. В. и др. Тестирование моноклональных антител к Т-клеточному рецептору, ассоциированному с анкилозирующим спондилитом. Вестник РГМУ. 2018; (5): 83–92. DOI: 10.24075/vrgmu.2018.064.

CHIMERIC ANTIGEN RECEPTOR EXPRESSION IN NATURAL KILLER CELL LINE NK-92 BY TRANSDUCTION WITH LENTIVIRAL PARTICLES PSEUDOTYPED WITH THE SURFACE GLYCOPROTEINS OF THE MEASLES VIRUS VACCINE STRAIN

Kravchenko YE, Gagarinskaya DI, Frolova EI, Chumakov SP ✉

Shemyakin-Ovchinnikov Institute of Bioorganic Chemistry of the Russian Academy of Sciences, Moscow

Cancer immunotherapy with T-cells that carry chimeric antigen receptors is currently on cutting edge of modern oncology. Autotransplantation of T-lymphocytes with chimeric receptor specific for certain tumor antigen proves to be clinically effective, but costly. Linear carriers of chimeric antigen receptors based on natural killer NK-92 cell culture may be an affordable alternative, however, this culture is resistant to lentiviral transduction. Recently, lentiviral vectors, pseudotyped with surface glycoproteins of the measles virus vaccine strain, have recently been successfully applied for transduction of primary immune cells. The aim of the work was to assess the efficiency of transduction of NK-92 cells with lentivirus vectors, pseudotyped with measles F and H surface glycoproteins, as well as to establish optimal conditions for selection of NK-92 transduced with the chimeric receptor against CD20 and to evaluate the culture's cytotoxic potential. The results showed that the maximum infectious titer is achieved using the HΔ18 variant in combination with FΔ30, and the use of the TBK1/IKKε inhibitor BX795 results in additional 3-fold increase in the infectious titer. CAR-expressing NK-92 were able to suppress the proliferation of $CD20^+$ cell line Raji in lower effector-to-target ratios than unmodified NK-92.

Keywords: cellular immunotherapy, chimeric antigen receptors, CAR, lentiviral vectors, natural killer cells, linear cellular carriers, pseudotyping with measles glycoproteins

Funding: this work was funded by MESR (project code RFMEFI60716X0156).

✉ **Correspondence should be addressed:** Stepan P. Chumakov
Miklukho-Maklaya 16/10, Moscow, 117997; hathkul@gmail.com

Received: 27.11.2018 **Accepted:** 20.12.2018

DOI: 10.24075/brsmu.2018.091

ЭКСПРЕССИЯ ХИМЕРНОГО АНТИГЕННОГО РЕЦЕПТОРА В НАТУРАЛЬНЫХ КИЛЛЕРАХ ЛИНИИ NK-92 ПУТЕМ ТРАНСДУКЦИИ ЛЕНТИВИРУСНЫМИ ЧАСТИЦАМИ, ПСЕВДОТИПИРОВАННЫМИ ПОВЕРХНОСТНЫМИ ГЛИКОПРОТЕИНАМИ ВАКЦИННОГО ШТАММА ВИРУСА КОРИ

Ю. Е. Кравченко, Д. И. Гагаринская, Е. И. Фролова, С. П. Чумаков ✉

Институт биоорганической химии имени М. М. Шемякина и Ю. А. Овчинникова РАН, Москва

Клеточная иммунотерапия с использованием химерных антигенных рецепторов (ХАР) является одним из перспективных направлений развития современной онкологии. Собственные Т-лимфоциты пациента с приданной специфичностью в отношении неоантигенов опухолей за счет экспрессии ХАР демонстрируют клиническую эффективность, однако стоимость такой терапии чрезвычайно высока. В качестве более доступной альтернативы могут быть использованы унифицированные носители ХАР на основе линии клеток натуральных киллеров NK-92. Эта культура отличается устойчивостью к лентивирусной трансдукции; однако для трансдукции первичных иммунных клеток недавно начали успешно применять лентивирусные векторы, псевдотипированные поверхностными гликопротеинами вакцинного штамма вируса кори. Целью работы было определить эффективность трансдукции клеток NK-92 лентивирусами, псевдотипированными гликопротеинами F и H вируса кори, а также условия селекции NK-92, трансдуцированных химерным рецептором против CD20, и оценить их цитотоксическое действие. Результаты исследования показали, что максимальный трансфекционный титр достигается при использовании варианта белка H (HΔ18) в сочетании с вариантом белка F (FΔ30), а применение BX795 (ингибитора TBK1/IKKε) дополнительно позволяет добиться трехкратного увеличения инфекционного титра. ХАР-экспрессирующие клетки NK-92 оказались способными подавлять пролиферацию $CD20^+$-клеток линии Raji в меньшей дозе, по сравнению с немодифицированными клетками NK-92.

Ключевые слова: клеточная иммунотерапия, химерные антигенные рецепторы, ХАР, лентивирусные векторы, натуральные киллеры, линейные клеточные носители, псевдотипирование, гликопротеины кори

Финансирование: работа выполнена при финансовой поддержке Министерства образования и науки РФ, уникальный код проекта RFMEFI60716X0156.

✉ **Для корреспонденции:** Степан Петрович Чумаков
ул. Миклухо-Маклая, 16/10, г. Москва, 117997; hathkul@gmail.com

Статья получена: 27.11.2018 **Статья принята к печати:** 20.12.2018

DOI: 10.24075/vrgmu.2018.091

Cellular immunotherapy is one of the key areas of development of modern oncology. By introducing into the patient's bloodstream the immune cells that target tumor antigens it may be possible to achieve high specificity of action and treatment efficacy, with a low incidence of undesirable effects [1]. In research and clinical trials, the most frequent vehicle is the patient's own cytotoxic T-lymphocytes with induced specificity for a particular tumor antigen or their combination. These modifications are performed by expressing a chimeric antigen receptor (CAR), consisting of several intracellular signaling domains for T-lymphocyte activation and an extracellular region that recognizes a tumor antigen [2]. For the introduction of constructs expressing CAR, chemical transfection of cells [3], electroporation [4], or transduction with viral vectors [5] is used most frequently. After transduction, the cell population can be expanded in culture to obtain the required number of cells. Treatment regimens based on CAR-T cells demonstrate good clinical efficacy, but the cost of therapy is often extremely high, which is due to the requirement for production of a personalized T-cell population for each patient. Another factor which constrains the prospects for the massive adoption of CAR-T cells in clinical practice is the limited availability of the patient's own T-lymphocytes in patients with late stages of cancer. It is possible to overcome these drawbacks, but this will require a significant improvement in the field of cell culturing and production.

Natural killer cell lines that carry chimeric antigen receptors may be considered as a less expensive, universal and more affordable alternative than CAR-T cell preparations. Out of 11 established and widely available natural killer lines that were obtained from patients with various lymphoproliferative diseases, only two — KHYG-1 [6] and NK-92 [7] — have a pronounced ability to suppress the growth of tumor cells due to intrinsic cytotoxic activity, in the absence of expression of Fc receptors [8]. Both cell lines are able to proliferate in the presence of IL2 in the culture medium, NK-92, in particular, was shown to be able to selectively destroy K-562 lymphoma cells cultured in a mixture with normal peripheral mononuclear cells. NK-92 cells were also able to maintain cytotoxicity after gamma irradiation with a dose of 10 Gray, without being proliferatively active, which allows them to be used for the treatment of cancer [9].

To enhance the cytotoxic properties of NK-92, genetically modified variants have been created that express either their own IL2, IL15 [10]; or additional receptors — CD16, for targeting tumor cells with antibodies, or CAR, for direct recognition of tumor antigens [11]. Functionally, CAR-expressing NK-92 are similar to CAR-T cells, while the cost of therapy may be substantially reduced — the cell line can be expanded in bulk quantities; and preliminary procedures for treating a patient will consist only in defrosting the ready-to-use aliquot [12]. In addition to being used for therapy, NK-92 cells can serve as a platform for testing and development of various types of chimeric receptors *in vitro* and *in vivo*. The main obstacle while manipulating with cells of this line is its sensitivity to cultivation conditions, as well as high resistance to lentiviral transduction: viral vectors pseudotyped with VSV G-protein do not efficiently transduce NK-92 cells, and as the amount of viral particles in the medium increases, the cells quickly lose viability [13]. For lentiviral transduction of peripheral T-lymphocytes and immune cells of myeloid lineage, lentiviral vector particles pseudotyped with surface glycoproteins of the measles virus vaccine strain have been recently developed [14]. Compared to conventional lentiviral vectors pseudotyped with VSV G-protein, they have shown to posess much higher ability to transduce immune cells without either stimulating cell division, or changing their phenotype or the profile of secreted cytokines [15]. The aim of this work was to determine the efficicacy of transduction of NK-92 cells with lentiviruses, pseudotyped F and H glycoproteins of the measles virus, as well as to determine the conditions for isolation and purification of NK-92 cells transduced with a chimeric receptor directed against the CD20 antigen, and to assess their cytotoxic potential.

METHODS

Plasmids and constructs

For packaging of lentiviral vectors, pseudotyped with VSV-G, packaging plasmids psPAX2 (contains lentiviral structural proteins) and pMD2-G (encodes VSV G-protein) were used. Both plasmids were kindly provided by Didier Trono (Addgene plasmid # 12260; http://n2t.net/addgene:12260; RRID: Addgene_12260 and Addgene plasmid # 12259; http://n2t.net/addgene:12259; RRID: Addgene_12259). For pseudotyping with measles glycoproteins, instead of pMD2-G, the plasmid pMD2-FΔ30 was used, which encodes a fragment of the F protein of the measles virus of the ESC vaccine strain with a cytoplasmic domain truncated by 30 amino acids. For preparation of measles virus cDNA and subsequent amplification of target genome fragment by PCR, were used primers *Fdelta30 dir EcoRI* (AGAGGAATTCACCACCATGTCC ATCATGGGTCTCAAGGTGAACGTCTCTG) and *Fdelta30 rev EcoRI* (AGAGAGAATTCTCAACGCCCCCTGCAGCAACATA TTAAAGCG), cloning was performed to the vector pMD2-G by EcoRI sites. In combination with pMD2-FΔ30, the plasmid pCG-HcΔ18 was used, provided by Jacob Reiser (Addgene plasmid # 84817; http://n2t.net/addgene:84817; RRID: Addgene_84817), as well as its variants, with truncation of 24 N-terminal amino acids of the H protein (pCG-HcΔ24), or with addition of 4 alanine residues (pCG-4AHcΔ24). The plasmids were produced by cloning the original H protein fragment amplified with primers *Hd24 BamHI dir* (AGAGAGGGATCCAG GGTGCAAGATCATCCACAATGAACCGGGAGCACCTGATG) and *H rev* (CTGATGTCTATTTCACACTAGTACAAAC), or with primers Hd24 4a BamHI dir (AGAGAGGGATCCAGGGTGCA AGATCATCCACAATGGCCGCTGCAGCCAACCGGGAGCAC CTGATG) and *H rev*, respectively, by restriction sites BamHI and SpeI. Lentiviral vectors pLCMV-tagRFP-puro (containing sequence of red fluorescent protein tagRFP (Evrogen; Russia) under the control of a cytomegalovirus promoter) and pLSF-@ CD20-229-tagRFP containing the sequence of 3-rd gen chimeric receptor against the surface antigen CD20 (CD8 leader peptide, ScFv from HB-9645 hybridoma clone, DYKDDDDK epitope, 229 amino acid linker region, CD28 transmembrane domain, and CD28, CD137, and CD3z signaling domains) and tagRFP, with polycistronic expression using the T2A signal sequence under the control of the SFFV promoter.

Cell cultures

For lentivirus packaging, the HEK-293T cell line was used, cells were cultured in DMEM-F12 (PAA; Austrian) medium with addition of fetal calf serum up to 10%, 2 mM alanyl-glutamine (PanEco; Russia), 20 mM HEPES and 100 μg/ml penicillin and streptomycin.

Cultivation of NK-92 was carried out in RPMI-1640 medium (PAA; Austrian) with the addition of fetal calf serum and horse serum up to 20% in equal proportions, 2 mM alanyl-glutamine (PanEco; Russia), 20 mM HEPES, 0.2 mM inositol, 0.1 mM

2-mercaptoethanol, 1 μM water-soluble hydrocortisone (Sigma; USA), 20 μM folic acid and recombinant IL2 at a final concentration of 100 μg/ml.

Raji cells (Burkitt's lymphoma) (ATCC; USA) expressing GFP fluorescent protein were used as targets for CAR-expressing NK-92 cells. The cells were cultivated in RPMI-1640 medium (PanEco; Russia) with the addition of fetal calf serum up to 10%, 2 mM alanyl-glutamine (PanEco; Russia), 20 mM HEPES and 100 μg/ml penicillin and streptomycin. All cells were cultured in 5% CO_2 conditions at 37 °C.

Transfection and viral transduction

Transfection was carried out on 6-well plates in OptiMEM medium (Invitrogen; USA) using polyethyleneimine 25kDA (PEI-25, Polysciences; USA) on HEK-293T cells at 40–60% confluence seeded the day before the procedure.

For lentiviral vectors pseudotyped with VSV-G, a mixture of the following plasmids was prepared: pLCMV-tagRFP-puro containing marker protein (1.5 μg), psPAX2 (0.9 μg) and pMD2-G (0.6 μg) in the ratio of 5 : 3 : 2, respectively. For pseudotyping with measles glycoproteins, plasmids pLCMV-tagRFP-puro or pLSF-@CD20-229-tagRFP (0.9 μg), psPAX2 (0.9 μg), pMD2-FΔ30 (0.79 μg), pCG-HcΔ18 (0.11 μg) or its variations pCG-HcΔ24 (0.11 μg) and pCG-4AHcΔ24 (0.11 μg) were used in a ratio of 8 : 8 : 7 : 1. After a three-hour incubation of the cells with the transfection mixture, the medium was replaced with RPMI-1640 containing the serum replacement (Serum Replacement Solution, PeproTech; USA), 2 mM alanyl-glutamine (PanEco; Russia), 20 mM HEPES and 4 mM caffeine, in which HEK-293T were incubated for 24 hours for the production of viral particles. Viral transduction was performed for 8–12 hours on NK-92 cells in the concentration of at least $5 \cdot 10^5$ per ml. Polybrene at a concentration of

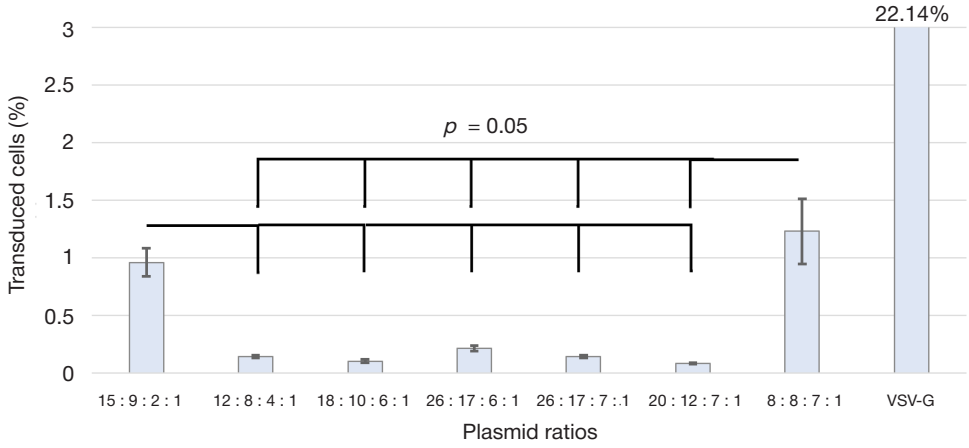

Fig. 1. The share of fluorescent HEK-293 cells, measured 48 hours post transduction by H/F-pseudotyped or VSV-G-pseudotyped lentiviral vectors. Axis X — plasmid ratios for vector:psPAX2:pMD2-FΔ30:pCG-H

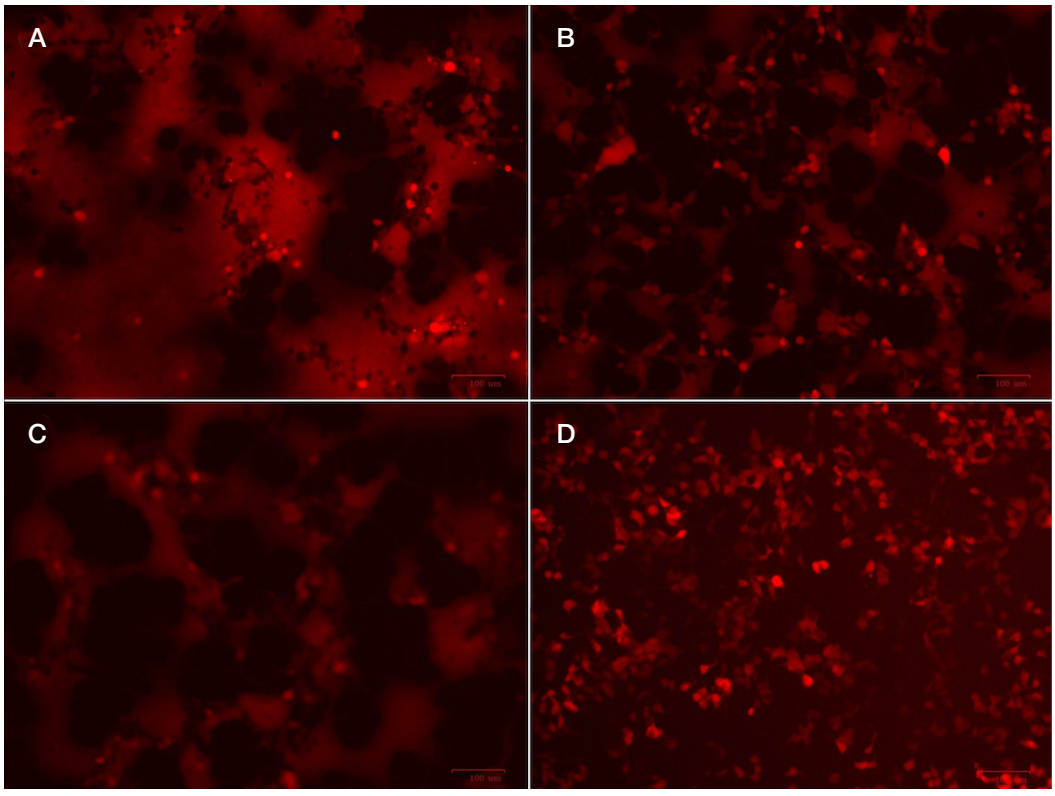

Fig. 2. Syncytia formed by HEK-293T cells after transfection with plasmid mixture for production of H/F-pseudotyped lentivirus particles. **A**. pCG-HcΔ18 + pMD2-FΔ30. **B**. pCG-HcΔ24 + pMD2-FΔ30. **C**. pCG-4A-HcΔ24 + pMD2-FΔ30. D. pMD2-G

8 μg/ml and all required supplements for the cultivation of NK-92 cells, as well as BX795 at a concentration of 3 μM, were added to the medium containing the virus upon infection. After transduction, the medium was replaced with complete NK-92 culture medium. The result of the transduction was assesed after 48 hours. Infectious viral titers and transduction efficiency were determined using a flow cytometer by evaluating the tagRFP positive fraction.

Cytotoxicity assay

To assess cytotoxicity, NK-92 cells were mixed with Raji cells expressing GFP in different ratios. After co-cultivation for 48 hours, the proportion and number of GFP positive cells were assessed on a flow cytometer.

RESULTS

Determination of the optimal ratio of packaging plasmids

To assess the efficiency of transduction of NK-92 cells, preparations of lentiviral vector particles pseudotyped with VSV G-protein or three different variants of measles virus H protein in combination with F protein (H/F pseudotyped) were used. Several authors reported controversial information on the optimal ratio of packaging plasmids, required to obtain highest viral titers [15–19]. The known ratios as well as the ratios extrapolated from the VSV-G pseudotyped lentiviral vectors used for packaging (5 : 3 : 2 for the vector : psPAX2: pMD2-G) were used to repare lentiviral stocks and then determine infectious titers (Fig. 1). Results showed that plasmid ratios of 8 : 8 : 7 : 1 and 15 : 9 : 2 : 1 for the pLCMV-tagRFP-puro : psPAX2 : pMD2-Fd30 : pCG-HΔ18 vectors showed the most efficient packaging of lentiviral particles for the H protein variant Δ18. For all further experiments, the ratio 8 : 8 : 7 : 1 was used.

Table. Infectious viral titers of viral stocks, producев with different variants of H protein. All values were calculated per 10^6 packaging cells

	HEK-293	NK-92
HΔ18/FΔ30	~6.15 • 10^4	~2.1 • 10^4
HΔ24/FΔ30	<2 • 10^2	<2 • 10^2
4A-HΔ24/FΔ30	~4.3 • 10^4	~1.6 • 10^4
VSV-G	~1.1 • 10^6	~3.5 • 10^3

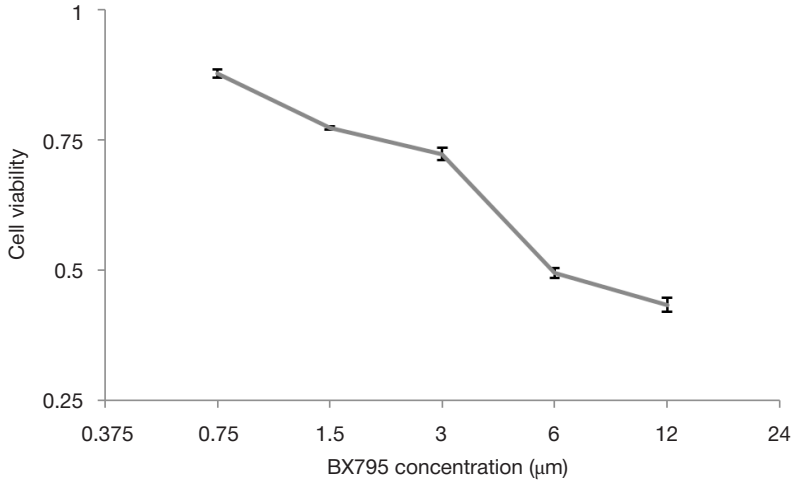

Fig. 3. Proliferative activity of NK-92 cells, measured 48 hours post addition of different amounts of BX795 to the cultivation media. All values were normalized relative to control (untreated culture). Values below 0.5 are characteristic to the culture that wasn't proliferating after addition of BX795

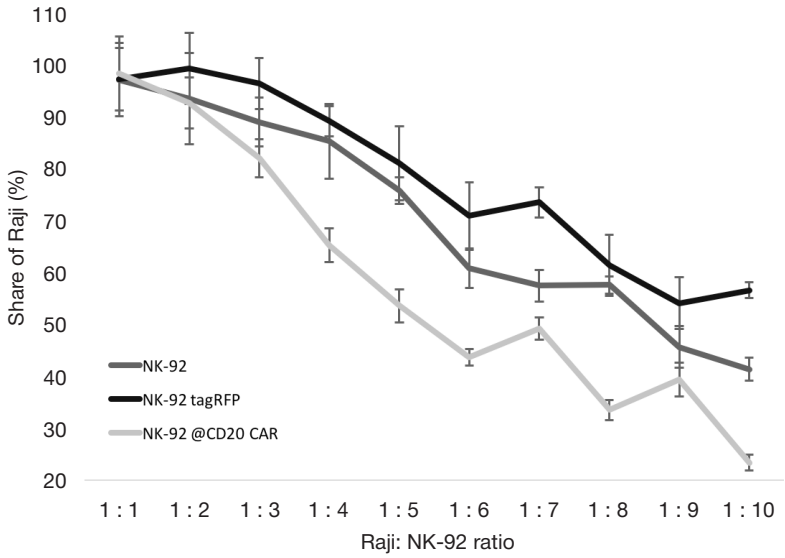

Fig. 4. Suppression of proliferation of Raji cells upon co-culturing with NK-92 cells. Axis Y — % of Raji with normal phenotype (FSC/SSC) after 2 days of co-culturing, compared to control sample (no NK-92 addition). Series: non-transduced NK-92; NK-92, transduced by tagRFP expressor (non-selected); NK-92, transduced by CAR @CD20 after selection on magnetic microspheres

Comparison of variants of protein H

A characteristic feature of pseudotyping with H/F proteins is the formation of syncytia in the culture of packaging cells. The length of the cytoplasmic tails of proteins H and F directly affects the intensity of this process, and the lesser syncytia is formed, the longer the packaging cells may be used to collect lentiviral supernatants. Excessive truncation of the cytoplasmic tails leads to a sharp drop in the infectious titers. The founding work on this topic reports that the variant of the HΔ18 protein in combination with the FΔ30 protein produces lentiviral vector stocks with highest transfection titer, while shortening to HΔ24 almost completely suppresses the production of the infectious virus, and the addition of four alanine residues at the N-terminus of a HΔ24 mutant restores viral titers to maximum values [16]. In another work, researchers used the HΔ24 protein variant to produce highly concentrated lentiviral stocks [15]. The results of our comparison of three variants of protein H showed that the size and rate of syncytium formation is maximum for the variant of protein HΔ18, significantly lower for variant 4A-HΔ24, and is minimal for HΔ24 (Fig. 2); the transfection titer was also maximal for the HΔ18 variant; however, for the 4A-HΔ24 variant, the resulting transfection titer was only slightly inferior to the HΔ18 variant, and for the HΔ24 variant it was at least 2 orders of magnitude lower than the HΔ18 variant. In further experiments, lentiviral particles pseudotyped by HΔ18/FΔ30 proteins were used. When measured on HEK-293 cells, the average viral titer of H/F pseudotyped lentiviral stocks was 15–20 times lower than for lentiviruses, pseudotyped with VSV G-protein (Table).

Optimization of NK-92 cell transduction conditions

The use of VSV-G-pseudotyped lentivirus vectors for transduction of NK-92 cells showed that addition of over ~ 10^5 i.u. per ml of medium for 8 hours leads to a significant drop in the viability of the culture. In addition, NK-92 cells were much less efficiently transduced by VSV-G-pseudotyped lentiviruses, the difference in transfection titer compared to HEK-293 was more than 3 orders of magnitude. To increase the efficiency of natural killer transduction, the use of the TBK1/IKKε inhibitor BX795 at a concentration of 6–8 μM has been described [20]. Evaluation of the effect of BX795 on the viability of NK-92 cells showed that they retain their viability at concentrations up to 3 μM (Fig. 3). BX795 allowed to reduce the difference in the transduction efficiency of VSV-G-pseudotyped viral particles up to 300-fold. Under the same transduction conditions, H/F pseudotyped lentiviral vectors were able to transduce NK-92 cells with three times less efficacy than HEK-293 cells.

Evaluation of the cytotoxic effect of CAR-expressing NK-92 cells

Since NK-92 cells require to be cultivated in high densities in order to maintain proliferative activity, the tolerable cell:i.u. ratios did not allow to obtain sufficiently high percentage of transduced cells. Isolation of the tagRFP-expressing populations by FASC made it possible to obtain small fractions of CAR-expressing cells, however, the stress incurred by the sorting procedure led to significant loss of viability. To circumvent this problem, we performed sorting of CAR-expressing cells on magnetic particles coated with monoclonal antibodies to DYKDDDDK epitope. This approach turned out to be more gentle and did not lead to suppression of proliferation of NK-92 cells. CAR-expressing cells obtained with this method were tested for their ability to inhibit growth of $CD20^+$ GFP-expressing Raji cells (Burkitt's lymphoma). Compared to unmodified cells, @CD20-NK-92 were able to suppress proliferation of Raji cells in lower dosages (Fig. 4).

DISCUSSION

When comparing different variants of H glycoproteins, we found that shortening the cytoplasmic tail by more than 20 amino acids is impractical because of the strong decrease in transfection titers. H/F pseudotyped lentiviral particles showed significantly lower packing efficiency compared to lentiviral particles pseudotyped with VSV G-protein, but this factor was compensated by greater efficiency of transduction of NK-92 cells. We noted that infection with H/F pseudotyped viral vectors leads to less significant suppression of proliferation of NK-92 cells, which allows to use of higher concentrations of viral particles for transduction, leading to an additional increase in efficiency. It is also noteworthy that with respect to NK-92 cells, BX795 was found to be active in lower concenrations than during transduction of primary cultures. In general, the use of a combination of H/F-pseudotyped lentiviral vectors, BX795 and subsequent sorting of transduced cells on magnetic microspheres allowed us to consistently obtain populations of CAR-expressing NK-92, that demonstrated high levels of cytotoxicity against antigen-expressing target cells.

NK-92 cells are distinguished by their sensitivity for cultivation conditions and, as the experiments have shown, they are more resistant to transduction with lentiviral vectors. However, these difficulties associated with the production of NK-92 CAR-expressing cells can later be compensated by the greater versatility of their applications for cellular immunotherapy, or as components of complex therapeutic approaches, for example, as carrier cells for the delivery of oncolytic viruses.

CONCLUSIONS

The results of the study showed that the optimal variant of the H protein of the measles virus for producing of H/F-pseudotyped lentivirus vectors is HΔ18 (in terms of transfection titer) and 4A-HΔ24 (in terms of the duration of production of viral particles), the largest transfection titers were achieved using a plasmid ratio of 8 : 8 : 7 : 1. The resulting preparations of H/F-pseudotyped lentiviral particles had 15–20 times lower transfection titer, compared with VSV-G-pseudotyped, while in the transduction of NK-92 cells the difference in titers was ~ 5 : 1 towards for H/F-pseudotyped virus vectors. The optimal concentration of the inhibitor TBK1/IKKε BX795 was 3 μM, the use of BX795 allowed to increase the transduction efficiency by ~ 3 times. Transduced CAR-NK-92 cells were successfully isolated by magnetic separation and were highly capable of inhibiting the proliferation of CD20-positive Raji cells.

References

1. Restifo NP, Dudley ME, Rosenberg SA. Adoptive immunotherapy for cancer: harnessing the T cell response. Nat Rev Immunol. 2012; 12 (4): 269–81. DOI: 10.1038/nri3191. PubMed PMID: 22437939.
2. Zah E, Lin MY, Silva-Benedict A, Jensen MC, Chen YY. T Cells Expressing CD19/CD20 Bispecific Chimeric Antigen Receptors Prevent Antigen Escape by Malignant B Cells. Cancer immunology research. 2016; 4 (6): 498–508. DOI: 10.1158/2326-6066.CIR-15-0231. PubMed PMID: 27059623.
3. Olden BR, Cheng Y, Yu JL, Pun SH. Cationic polymers for non-viral gene delivery to human T cells. J Control Release. 2018; (282): 140–7. DOI: 10.1016/j.jconrel.2018.02.043. PubMed PMID: 29518467.
4. Zhang Z, Qiu S, Zhang X, Chen W. Optimized DNA electroporation for primary human T cell engineering. BMC Biotechnol. 2018; 18 (1): 4. DOI: 10.1186/s12896-018-0419-0. PubMed PMID: 29378552.
5. Tumaini B, Lee DW, Lin T, Castiello L, Stroncek DF, Mackall C et al. Simplified process for the production of anti-CD19-CAR-engineered T cells. Cytotherapy. 2013; 15 (11): 1406–15. DOI: 10.1016/j.jcyt.2013.06.003. PubMed PMID: 23992830.
6. Yagita M, Huang CL, Umehara H, Matsuo Y, Tabata R, Miyake M et al. A novel natural killer cell line (KHYG-1) from a patient with aggressive natural killer cell leukemia carrying a p53 point mutation. Leukemia. 2000; 14 (5): 922–30. PubMed PMID: 10803526.
7. Gong JH, Maki G, Klingemann HG. Characterization of a human cell line (NK-92) with phenotypical and functional characteristics of activated natural killer cells. Leukemia. 1994; 8 (4): 652–8. PubMed PMID: 8152260.
8. Matsuo Y, Drexler HG. Immunoprofiling of cell lines derived from natural killer-cell and natural killer-like T-cell leukemia-lymphoma. Leuk Res. 2003; 27 (10): 935–45. PubMed PMID: 12860014.
9. Klingemann HG, Wong E, Maki G. A cytotoxic NK-cell line (NK-92) for ex vivo purging of leukemia from blood. Biol Blood Marrow Transplant. 1996; 2 (2): 68–75. PubMed PMID: 9118301.
10. Zhang J, Sun R, Wei H, Zhang J, Tian Z. Characterization of interleukin-15 gene-modified human natural killer cells: implications for adoptive cellular immunotherapy. Haematologica. 2004; 89 (3): 338–47. PubMed PMID: 15020274.
11. Chen Y, You F, Jiang L, Li J, Zhu X, Bao Y et al. Gene-modified NK-92MI cells expressing a chimeric CD16-BB-zeta or CD64-BB-zeta receptor exhibit enhanced cancer-killing ability in combination with therapeutic antibody. Oncotarget. 2017; 8 (23): 37128–39. DOI: 10.18632/oncotarget.16201. PubMed PMID: 28415754.
12. Suck G, Odendahl M, Nowakowska P, Seidl C, Wels WS, Klingemann HG et al. NK-92: an 'off-the-shelf therapeutic' for adoptive natural killer cell-based cancer immunotherapy. Cancer Immunol Immunother. 2016; 65 (4): 485–92. DOI: 10.1007/s00262-015-1761-x. PubMed PMID: 26559813.
13. Boissel L, Betancur M, Lu W, Wels WS, Marino T, Van Etten RA et al. Comparison of mRNA and lentiviral based transfection of natural killer cells with chimeric antigen receptors recognizing lymphoid antigens. Leuk Lymphoma. 2012; 53 (5): 958–65. DOI: 10.3109/10428194.2011.634048. PubMed PMID: 22023526.
14. Humbert JM, Frecha C, Amirache Bouafia F, N'Guyen TH, Boni S, Cosset FL et al. Measles virus glycoprotein-pseudotyped lentiviral vectors are highly superior to vesicular stomatitis virus G pseudotypes for genetic modification of monocyte-derived dendritic cells. J Virol. 2012; 86 (9): 5192–203. DOI: 10.1128/JVI.06283-11. PubMed PMID: 22345444.
15. Frecha C, Costa C, Negre D, Gauthier E, Russell SJ, Cosset FL et al. Stable transduction of quiescent T cells without induction of cycle progression by a novel lentiviral vector pseudotyped with measles virus glycoproteins. Blood. 2008; 112 (13): 4843–52. DOI: 10.1182/blood-2008-05-155945. PubMed PMID: 18812471.
16. Funke S, Maisner A, Muhlebach MD, Koehl U, Grez M, Cattaneo R et al. Targeted cell entry of lentiviral vectors. Mol Ther. 2008; 16 (8): 1427–36. DOI: 10.1038/mt.2008.128. PubMed PMID: 18578012.
17. Kneissl S, Abel T, Rasbach A, Brynza J, Schneider-Schaulies J, Buchholz CJ. Measles virus glycoprotein-based lentiviral targeting vectors that avoid neutralizing antibodies. PLoS ONE. 2012; 7 (10): e46667. DOI: 10.1371/journal.pone.0046667. PubMed PMID: 23071609.
18. Ou W, Marino MP, Suzuki A, Joshi B, Husain SR, Maisner A et al. Specific targeting of human interleukin (IL)-13 receptor alpha2-positive cells with lentiviral vectors displaying IL13. Human gene therapy methods. 2012; 23 (2): 137–47. DOI: 10.1089/hgtb.2012.054. PubMed PMID: 22612657.
19. Marino MP, Panigaj M, Ou W, Manirarora J, Wei CH, Reiser J. A scalable method to concentrate lentiviral vectors pseudotyped with measles virus glycoproteins. Gene Ther. 2015; 22 (3): 280–5. DOI: 10.1038/gt.2014.125. PubMed PMID: 25608718.
20. Sutlu T, Nystrom S, Gilljam M, Stellan B, Applequist SE, Alici E. Inhibition of intracellular antiviral defense mechanisms augments lentiviral transduction of human natural killer cells: implications for gene therapy. Hum Gene Ther. 2012; 23 (10): 1090–100. DOI: 10.1089/hum.2012.080. PubMed PMID: 22779406.

Литература

1. Restifo NP, Dudley ME, Rosenberg SA. Adoptive immunotherapy for cancer: harnessing the T cell response. Nat Rev Immunol. 2012; 12 (4): 269–81. DOI: 10.1038/nri3191. PubMed PMID: 22437939.
2. Zah E, Lin MY, Silva-Benedict A, Jensen MC, Chen YY. T Cells Expressing CD19/CD20 Bispecific Chimeric Antigen Receptors Prevent Antigen Escape by Malignant B Cells. Cancer immunology research. 2016; 4 (6): 498–508. DOI: 10.1158/2326-6066.CIR-15-0231. PubMed PMID: 27059623.
3. Olden BR, Cheng Y, Yu JL, Pun SH. Cationic polymers for non-viral gene delivery to human T cells. J Control Release. 2018; (282): 140–7. DOI: 10.1016/j.jconrel.2018.02.043. PubMed PMID: 29518467.
4. Zhang Z, Qiu S, Zhang X, Chen W. Optimized DNA electroporation for primary human T cell engineering. BMC Biotechnol. 2018; 18 (1): 4. DOI: 10.1186/s12896-018-0419-0. PubMed PMID: 29378552.
5. Tumaini B, Lee DW, Lin T, Castiello L, Stroncek DF, Mackall C et al. Simplified process for the production of anti-CD19-CAR-engineered T cells. Cytotherapy. 2013; 15 (11): 1406–15. DOI: 10.1016/j.jcyt.2013.06.003. PubMed PMID: 23992830.
6. Yagita M, Huang CL, Umehara H, Matsuo Y, Tabata R, Miyake M et al. A novel natural killer cell line (KHYG-1) from a patient with aggressive natural killer cell leukemia carrying a p53 point mutation. Leukemia. 2000; 14 (5): 922–30. PubMed PMID: 10803526.
7. Gong JH, Maki G, Klingemann HG. Characterization of a human cell line (NK-92) with phenotypical and functional characteristics of activated natural killer cells. Leukemia. 1994; 8 (4): 652–8. PubMed PMID: 8152260.
8. Matsuo Y, Drexler HG. Immunoprofiling of cell lines derived from natural killer-cell and natural killer-like T-cell leukemia-lymphoma. Leuk Res. 2003; 27 (10): 935–45. PubMed PMID: 12860014.
9. Klingemann HG, Wong E, Maki G. A cytotoxic NK-cell line (NK-92) for ex vivo purging of leukemia from blood. Biol Blood Marrow Transplant. 1996; 2 (2): 68–75. PubMed PMID: 9118301.
10. Zhang J, Sun R, Wei H, Zhang J, Tian Z. Characterization of interleukin-15 gene-modified human natural killer cells: implications

for adoptive cellular immunotherapy. Haematologica. 2004; 89 (3): 338–47. PubMed PMID: 15020274.
11. Chen Y, You F, Jiang L, Li J, Zhu X, Bao Y et al. Gene-modified NK-92MI cells expressing a chimeric CD16-BB-zeta or CD64-BB-zeta receptor exhibit enhanced cancer-killing ability in combination with therapeutic antibody. Oncotarget. 2017; 8 (23): 37128–39. DOI: 10.18632/oncotarget.16201. PubMed PMID: 28415754.
12. Suck G, Odendahl M, Nowakowska P, Seidl C, Wels WS, Klingemann HG et al. NK-92: an 'off-the-shelf therapeutic' for adoptive natural killer cell-based cancer immunotherapy. Cancer Immunol Immunother. 2016; 65 (4): 485–92. DOI: 10.1007/s00262-015-1761-x. PubMed PMID: 26559813.
13. Boissel L, Betancur M, Lu W, Wels WS, Marino T, Van Etten RA et al. Comparison of mRNA and lentiviral based transfection of natural killer cells with chimeric antigen receptors recognizing lymphoid antigens. Leuk Lymphoma. 2012; 53 (5): 958–65. DOI: 10.3109/10428194.2011.634048. PubMed PMID: 22023526.
14. Humbert JM, Frecha C, Amirache Bouafia F, N'Guyen TH, Boni S, Cosset FL et al. Measles virus glycoprotein-pseudotyped lentiviral vectors are highly superior to vesicular stomatitis virus G pseudotypes for genetic modification of monocyte-derived dendritic cells. J Virol. 2012; 86 (9): 5192–203. DOI: 10.1128/JVI.06283-11. PubMed PMID: 22345444.
15. Frecha C, Costa C, Negre D, Gauthier E, Russell SJ, Cosset FL et al. Stable transduction of quiescent T cells without induction of cycle progression by a novel lentiviral vector pseudotyped with measles virus glycoproteins. Blood. 2008; 112 (13): 4843–52. DOI: 10.1182/blood-2008-05-155945. PubMed PMID: 18812471.
16. Funke S, Maisner A, Muhlebach MD, Koehl U, Grez M, Cattaneo R et al. Targeted cell entry of lentiviral vectors. Mol Ther. 2008; 16 (8): 1427–36. DOI: 10.1038/mt.2008.128. PubMed PMID: 18578012.
17. Kneissl S, Abel T, Rasbach A, Brynza J, Schneider-Schaulies J, Buchholz CJ. Measles virus glycoprotein-based lentiviral targeting vectors that avoid neutralizing antibodies. PLoS ONE. 2012; 7 (10): e46667. DOI: 10.1371/journal.pone.0046667. PubMed PMID: 23071609.
18. Ou W, Marino MP, Suzuki A, Joshi B, Husain SR, Maisner A et al. Specific targeting of human interleukin (IL)-13 receptor alpha2-positive cells with lentiviral vectors displaying IL13. Human gene therapy methods. 2012; 23 (2): 137–47. DOI: 10.1089/hgtb.2012.054. PubMed PMID: 22612657.
19. Marino MP, Panigaj M, Ou W, Manirarora J, Wei CH, Reiser J. A scalable method to concentrate lentiviral vectors pseudotyped with measles virus glycoproteins. Gene Ther. 2015; 22 (3): 280–5. DOI: 10.1038/gt.2014.125. PubMed PMID: 25608718.
20. Sutlu T, Nystrom S, Gilljam M, Stellan B, Applequist SE, Alici E. Inhibition of intracellular antiviral defense mechanisms augments lentiviral transduction of human natural killer cells: implications for gene therapy. Hum Gene Ther. 2012; 23 (10): 1090–100. DOI: 10.1089/hum.2012.080. PubMed PMID: 22779406.

MODERN ANEURYSM SURGERY: A PRO-OPEN SURGERY VIEW

Dubovoy AV[1], Bervitskiy AV[2], Spallone A[3] ✉

[1] Federal Neurosurgical Center, Novosibirsk, Novosibirsk

[2] Yevdokimov Moscow State University of Medicine and Dentistry, Moscow

[3] NCL-Neuromed Institute of Neurological Sciences, Rome, Italy

Modern management of intracranial aneurysms is matter of great debate between supporters of "traditional" microsurgical treatment and those of relatively new endovascular management. This paper briefly reports the experience of two experienced microvascular "traditional" neurosurgeons who shares the same management philosophy favouring open microsurgery in the modern era in which endovascular management is becoming fashionable. Difficult posterior circulation aneurysms are nowadays as a rule managed endovascularly, whilst anterior circulation aneurysms can be treated with both techniques, and MCA as well as distal ACA aneurysms are better treated microsurgically. Technical refinement and — hopefully- lower cost of endovascular devices will favour a trend of prevailing use of endovascular method in the future. However the need for well-prepared microvascular surgeon will always be there, and proper training of future generations of microvascular surgeons in a setting of decreasing number of patients and open surgical casuistics represents a big challenge for the neurosurgical community, to which an answer should be given.

Keywords: Intracranial aneurysms, microsurgery, cerebral revascularization, endovascular treatment, flow diverters, management guidelines, training

✉ **Correspondence should be addressed:** Aldo Spallone
Via Patrica 15, Rome, Italy, 00178; segreteria1@nclroma.it

Received: 28.06.2018 **Accepted:** 21.09.2018

DOI: 10.24075/brsmu.2018.093

СОВРЕМЕННОЕ СОСТОЯНИЕ ХИРУРГИИ АНЕВРИЗМ: «ПРОМИКРОХИРУРГИЧЕСКИЙ» ВЗГЛЯД

А. В. Дубовой[1], А. В. Бервицкий[1,2], А. Спаллоне[3] ✉

[1] Федеральный центр нейрохирургии, Новосибирск

[2] Московский медико-стоматологический университет имени Е. И. Евдокимова, Москва

[3] NCL- Neuromed, Институт нейрологии, Рим, Италия

Современные способы лечения пациентов с внутричерепными аневризмами являются предметом дискуссий между сторонниками традиционной микрохирургической техники и относительно нового эндоваскулярного лечения. В статье представлен опыт нейрохирургов — сторонников открытой микрохирургии. Сложные аневризмы задней циркуляции в настоящее время, как правило, оперируются эндоваскулярно, в то время как аневризмы переднего бассейна могут быть вылечены обоими методами, а для аневризм средней мозговой артерии и дистальных аневризм передней мозговой артерии лучше подходит микрохирургия. Техническое усовершенствование и, вероятно, снижение стоимости эндоваскулярных устройств будут способствовать тенденции к использованию эндоваскулярного метода. Однако потребность в хорошо подготовленных микрососудистых хирургах, на наш взгляд, останется, и надлежащая подготовка будущих поколений таких специалистов в условиях снижения числа пациентов и случаев открытых хирургических вмешательств представляет собой серьезную проблему для нейрохирургического сообщества, решение которой предстоит найти.

Ключевые слова: внутричерепные аневризмы, микрохирургия, реваскуляризация головного мозга, эндоваскулярное лечение

✉ **Для корреспонденции:** Альдо Спаллоне
ул. Патрика, д. 15, г. Рим, Италия, 00178; segreteria1@nclroma.it

Статья получена: 28.06.2018 **Статья принята к печати:** 21.09.2018

DOI: 10.24075/vrgmu.2018.093

Optimal management of intracranial aneurysm is still matter of debate. The introduction in the clinical practice of endovascular techniques following the pioneer work of Serbinenko [1] and his group [2–5] has stimulated both researchers and industry to develop increasingly sophisticated technological items, coils [6] and more recently flow diverters [7–9] with the aim of excluding the aneurysm from the circulation and/or promoting its thrombosis while potentially reducing the stress to the patient and the invasiveness of the procedure.

However, debate is still going on and despite several large clinical trials no definitive conclusion has been reached [6, 10–18]. As a matter of fact the experience of the treating surgeon, whether "classical" neurovascular surgeon or endovascular surgeon, seems to be the best discriminating factor for choosing the management strategy in each individual case nowadays.

Actually personal "traditional, hands-on" experience with difficult neurovascular surgery appears to be the prerequisite for competing with the "rising endovascular stars". This scenario may change in the future if the number of openly operated patients will decrease stepwise and consequently it would become difficult to give adequate training to future "open" neurovascular surgeons, and this will create a vicious circle following which open aneurysms surgery will progressively come to the end.

However this would be not necessary so. The senior author (AS) has been fellow of Cooperative Study on aneurysm surgery in the 80's [19] and continued to believe that open surgery should keep a role in the management of aneurysm patients. He met recently an extremely interesting and highly qualified neurosurgical realty in Novosibirsk, Russia. In this setting he could verify and analyse the results of a management protocol which privileges open surgery for aneurysm patients, quite similar to the one used in Rome.

This paper reports the results of this management philosophy in a large series of aneurysms treated during a 3,5-year period.

Results of the philosophy of treatment of a large series of aneurysms

In 3,5-year time span starting in January 2014, 925 patients were managed by the authors. Due to the different referral characteristics, the overwhelming majority of the studied patients were treated in Novosibirsk. All surgeries were performed by either the first (AD) or the senior (AS) authors. Table 1 presents the main demographic data of patients.

The management protocol was quite similar in both Institutions and privileged open surgery. Ruptured aneurysms were operated on in the early stage whenever possible. Endovascular treatment, either by balloon or stent assisted coiling and, most recently, flow diverters was performed by experienced endovascular specialists who has been routinely involved in the management planning, on a-consultant ship base (in Rome) or as a staff member (in Novosibirsk).

Endovascular treatment was basically reserved to almost all posterior fossa aneurysms. As exception of this rule PICA aneurysms were operated microsurgically, although occasionally (6 cases) they were treated endovascularly. Anterior circulation aneurysms were as a rule treated with craniotomy unless the general clinical conditions of the patient contraindicated open surgery. Fusiform and giant aneurysms were subjected to wise case-by-case evaluation, and treated with flow diverters if trapping preceded by selective blood flow augmentation via a bypass, as well as direct clipping, were considered unfeasible. In particular giant cavernous ICA aneurysms were treated with carotid occlusion and ECIC bypass if there were signs of a intracavernous nerves compression (in order to avoid the risk of functional worsening due to aneurysm compaction and/or enlargement) and by flow diverters if they were asymptomatic, and CoA aneurysms were treated endovascularly only if close anatomical relationships with optic nerves were not the case. As far the bypasses, if the STA was of adequate size, a STA-to-M3 bypass in the deep of the sylvian fissure was performed. Otherwise a high-flow bypass using a radial artery graft to either the MCA (28 cases) or the PCA (1 case) was performed. In four patients a A2 cross-link was performed, and in one patient a PICA-to-PICA anastomosis was confectioned. As a rule bypasses were performed prior to either main artery occlusion, aneurysm trapping or for blood augmentation in case of expected prolonged temporary clamping.

The use of flow diverters in the cases of difficult lesions of the basilar artery was indicated after a thoughtful discussion of all alternative management possibilities, due to the well-known risk of perforators compromise with using this technique in arteries which give off several, functionally very important, perforating branches. Figure 1 summarizes the management algorithm used in the present patient.

As a rule endovascular treatment was considered feasible only if the dome-to-neck ratio was less than 2 : 1. Otherwise, open treatment was considered mandatory. Obviously other hemodynamic and geometric factors were thoughtfully taken into consideration when deciding which type of management was the best for the patient.

Patient characteristics and final outcome

Among the patients there were 312 (33.7%) men and 613 (66.3%) women. Age ranged from 1 to 84 years and averaged 58 years. 286 patients (30.9%) presented with SAH 64 of which (6.9%) were operated in the acute stage. 184 patients (19.9%) had multiple aneurysms, thus a total of 1162 aneurysms were operated. 119 (12.8%) of them were large and giant. Aneurysms were localized on the internal carotid artery (ICA) in 480 cases (41.3%), on the anterior cerebral-anterior communicating complex (ACA–AcoA) in 231 cases (19.8%), on middle cerebral artery (MCA) in 290 cases (24.9%), on the posterior cerebral artery (PCA) in 20 cases (1.7%), on the basilar artery (BA) in 95 cases (8.1%), on the superior cerebellar artery (SCA) in 23 cases (2%), on the anterior inferior cerebellar artery (AICA) in 4 cases (0.5%), and on the posterior inferior cerebellar artery (PICA) in 19 cases (1.7%). 417 aneurysms (36%) were operated by the endovascular method, 740 (63.6%) microsurgically, 5 (0.4%) had a combined therapy (endovascular occlusion + revascularization). Exclusion of the aneurysm in 99 (10.7%) cases was supplemented by revascularization via 106 different anastomoses: in 15 cases intracranial micro anastomoses were performed, in 60 cases a STA-to-M3 by-passes, was confectioned, 2 patients had a bypass between maxillary artery and MCA with radial graft and 29 had a high-flow bypass using an interposed arterial segment

The results of surgery were evaluated 1 year after the operation. Among the 861 patients without SAH 842 (97.8%) patients retained independent status, 17 (2%) patients had severe disability, 2 (0.2%) patient died. Out of the 64 patients operated in the acute period of SAH, a good outcome was achieved in 51 (79.6%) cases, 9 patients (14%) were left disabled and 4 (6.4%) patients died.

Main aneurysms characteristics, data of treatment modalities and results are summarized in Table 2.

Disussion

The debate between endovascular and open surgery as which would be the best method for treating intracranial aneurysms has characterized the last decade of neurovascular surgery. Refinement of technology together with increased experience [7–9] has shifted significantly the opinion of the general neurosurgical audience towards the idea that open aneurysms surgery would be close to its end. This brings two obvious consequences: increasing shortage of craniotomy-operated cases; consequent reduced capacity for adequately training the new generations in open neurovascular surgery. On the other hand careful evaluation of the results of endovascular surgery, even when using the most updated technology shows that this is not the panacea, and that other alternative methods

Table 1. Summarizes the main demographic data of the treated series

Age (years)	58.1 (1–84 years)
Sex (male/female)	312 (33.7%) / 613 (66.3%)
History of SAH	286 (30.9%)
No history of SAH	640 (69.1%)
Acute SAH patients	64 (6.9%)

Note: SAH — subarachnoid hemorrhage.

for treating aneurysms, in particular difficult aneurysms, are possibly still to be considered.

The main authors of this paper (AD and AS) met by chance and shared completely their personal opinion on this controversial issue. Both are aware that endovascular management can be in the future the management of choice for this pathology but this will require further technological advancement in the construction of the devices as well as, a very critical issue, significant lowering of the costs.

On the other hand in the nowadays scenario, open surgery still seems to play a significant, possibly a leading, role at least for treating anterior circulation aneurysms [20–23] and consequently adequate training of future generations, possibly uniformation of training criteria between different countries together with proper selection of the trainees who should be enough gifted and versed to difficult microsurgery, is an obligation for the present neurosurgical community.

It is out of the scope of the present paper to discuss in detail the specific aspects of the management protocol used in the present patients. Simply, we want to stress that it is based on the available clinical incidence and guidelines, whilst giving conceptual priority to microsurgery and all its available technical resources — including different methods of revascularization — however utilising properly endovascular technique when considered more indicated on the basis of a thoughtful team-based discussion.

Present results

The present results were quite comparable to the largest series of intracranial aneurysm, reported in the recent literature, in which both methods, either microsurgical or endovascular approach, had been used, and match well with the results of a large series of intracranial aneurysm treated microsurgically, a significant number of which were also of large to giant size [24], reported less than a decade ago, in which surgical revascularization was considered a milestone in the management of technically demanding aneurysms. A main point is a sort of "cultural" integration between microsurgery experts and endovascular fellows which recognizes the proper, main role of direct surgery in the management of such a demanding lesions. In our environments there was an agreement on the fact that endovascular treatment was reserved to patients with unfavourable geometry, in which the placement of a by-pass could not guarantee from the later occurrence of ischemic complications should a major artery had to be closed for obliterating the aneurysm, and to technically formidable lesions of the posterior circulation.

One may argue that the particular type of referral of patients led to treating a relative minority of ruptured aneurysms, particularly in the acute stage. However, if this group of patients is analysed separately, the results are still very good. Again, we cannot under-consider the major role of properly used revascularisation techniques in the management of complex aneurysm, a fact already stressed by Cantore et al. [24] and reworked also very recently [25]. This in our view allowed us concretely to obtain good results in some very demanding cases. Again, the crucial importance of a proper hands-on training of microsurgical specialists cannot be overemphasized.

In a recently published critical review of modern aneurysms treatment, Rahal and Malek [26] suggested — wisely — that "a balance (should) be maintained between technical virtuosity and procedural safety of either (open or endovascular treatment modalities)". The problem remains has how to offer good quality training with enough large case material in order to prepare well a new generation of specialists if the significant stepwise decrease of patients managed with microsurgery observed in the last years will continue. The present experience suggests that well-prepared neurovascular surgeons can achieve good results, comparable to the published series of aneurysms patients, even if privileging open "traditional" neurovascular approach. In this respect an age–related limitation is maybe to be considered in order to keep the required technical standard for performing these demanding procedures.

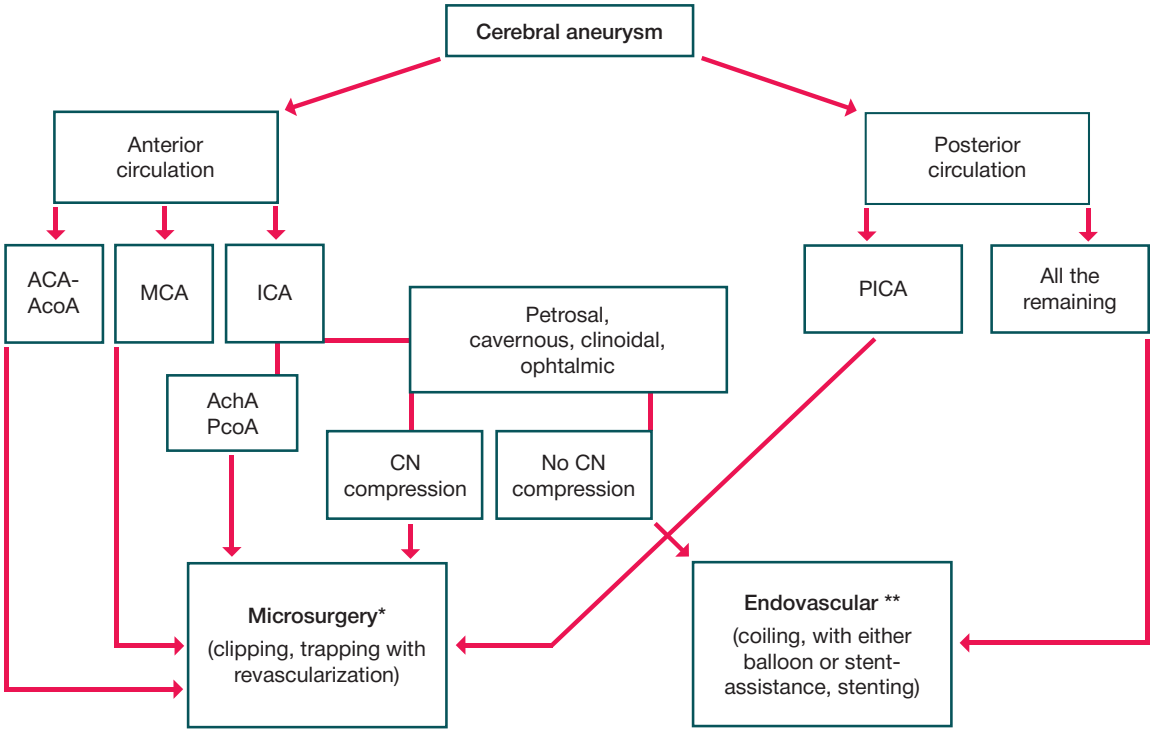

Fig. 1. Decision-making algorithm based on aneurysm location. * — except cases of general contraindications to open surgery, or patient individual choice; ** — except cases of allergic reactions for contrast

Table 2. Aneurysms and treatment characteristics. Results

Total number of aneurysms	1162			
Large and Giant	119 (12.8%)			
Localization	Total	Endovascular	Microsurgery	Combined
ICA	480 (41.3%)	251	228	1
ACA-AcomA	231 (19.8%)	16	215	
MCA	290 (24.9%)	23	264	3
PCA	20 (1.7%)	18	2	
BA	95 (8.1%)	84	10	1
SCA	23 (2%)	15	8	
AICA	4 (0.4%)	4		
PICA	19 (1.7%)	6	13	
Revascularization				
Intracranial	15			
STA-to-M3	60			
Maxillary to MCA with graft	2			
High-flow bypass	29			
Results	Total	Unruptured (n = 861)	Acute SAH (n = 64)	
Independent	893	842	51	
Dependent	26	17	9	
Death	6	2	4	

Future guidelines

Age-related changes affecting manual ability are physiological but also individual ones, so technical ability with demanding microsurgery can be maintained until different age in different individuals. The senior author (AS,) born 1952, decided himself to stop doing microsurgical by-passes a couple of years ago. Maybe a sort of "self-controlling tremor evaluation" using available sophisticated technology could be considered for objectively checking the technical capacity of each individual surgeon to perform safely delicate microvascular procedures, but this suggestion would not achieve easily wide acceptance. Also, as far as training in general, it should be noted that the first author achieved an objectively high degree of technical skill by long exercising with animal models and cadaver dissections even without making a specific clinical neurovascular fellowship in reputed institutions. In the selection of possible candidates for this difficult job, the individual characteristics (firm hand, calmness, strong emotional control — of fundamental importance in managing emergent situation during surgery) should be considered very carefully before let him/her spending long time in a difficult training program, and this concepts should have possibly serious consideration by the Committees in charge for establishing trainings guidelines. Also, the possibility to introduce a dual figure of both open and endovascular surgeon as the neurovascular expert in the future must also be considered, with its pros and contras. But again, sufficient case material of open neurovascular surgery would still be necessary, also because, apart from microvascular laboratory exercises with animal models, no other model possibly simulating the real clinical scenario of aneurysm surgery appears to be available nowadays.

CONCLUSIONS

In conclusion, open "traditional" neurovascular surgery, if performed with wise indications and management strategy by well-prepared neurovascular surgeons is still far from its end. The training of future generation is a challenge. Whether the future, in which significant technical improvement of endovascular devices is to be expected, will still give space to open neurovascular surgeons, or a dual figure of both open — and endo–vascular expert will be the recommended solution, is likely to be matter of debate to be addressed to high- ranked training Committees. A strong recommendation to lower devices costs should come from the neurosurgical community.

References

1. Serbinenko FA. Balloon catheterization and occlusion of major cerebral vessels. J Neurosurg. 1974 Aug; 41 (2): 125–45.
2. Serbinenko FA. Balloon occlusion of saccular aneurysms of the cerebral arteries. [Article in Russian] Vopr Neirokhir. 1974 Jul-Aug; (4): 8–15.
3. Serbinenko FA. 7-year experience in endovascular surgery [Article in German]. Zentralbl Neurochir. 1977; 38 (2): 141–4.
4. Serbinenko FA. Six hundred endovascular neurosurgical procedures in vascular pathology. A ten-year experience. Acta Neurochir Suppl (Wien). 1979; 28 (1): 310–1.
5. Serbinenko FA, Filatov JM, Spallone A, Tchurilov MV, Lazarev VA. Management of giant intracranial ICA aneurysms with combined extracranial-intracranial anastomosis and endovascular occlusion. J Neurosurg. 1990 Jul; 73 (1): 57–63.
6. Li H, Pan R, Wang H, Rong X, Yin Z, Milgrom DP et al. Clipping versus coiling for ruptured intracranial aneurysms: a systematic review and meta-analysis. Stroke. 2013 Jan; 44 (1): 29–37.
7. Kabbasch C, Mpotsaris A, Behme D, Dorn F, Stavrinou P, Liebig T. Pipeline Embolization Device for Treatment of Intracranial Aneurysms-The More, the Better? A Single-center Retrospective Observational Study. J Vasc Interv Neurol. 2016 Oct; 9 (2): 14–20.
8. Raymond J, Gentric JC, Darsaut TE, Iancu D, Chagnon M, Weill A

et al. Flow diversion in the treatment of aneurysms: a randomized care trial and registry. J Neurosurg. 2017 Sep; 127 (3): 454–62. DOI: 10.3171/2016.4.JNS152662. Epub 2016 Nov 4.
9. Brinjikji W, Lanzino G, Cloft HJ, Siddiqui AH, Kallmes DF. Risk Factors for Hemorrhagic Complications following Pipeline Embolization Device Treatment of Intracranial Aneurysms: Results from the International Retrospective Study of the Pipeline Embolization Device. AJNR Am J Neuroradiol. 2015 Dec; 36 (12): 2308–13.
10. Zhang X, Li L, Hong B, Xu Y1, Liu Y, Huang Q et al. A Systematic Review and Meta-analysis on Economic Comparison between Endovascular Coiling versus Neurosurgical Clipping for Ruptured Intracranial Aneurysms. World Neurosurg. 2018 Feb 21; pii: S1878-8750(18)30349-8.
11. Alreshidi M, Cote DJ, Dasenbrock HH, Acosta M, Can A, Doucette J et al. Coiling Versus Microsurgical Clipping in the Treatment of Unruptured Middle Cerebral Artery Aneurysms: A Meta-Analysis. Neurosurgery. 2018 Feb 9. DOI: 10.1093/neuros/nyx623. [Epub ahead of print]
12. Fotakopoulos G, Tsianaka E, Fountas K, Makris D, Spyrou M, Hernesniemi J. Clipping Versus Coiling in Anterior Circulation Ruptured Intracranial Aneurysms: A Meta-Analysis. World Neurosurg. 2017 Aug; (104): 482–8.
13. Xia ZW, Liu XM, Wang JY, Cao H, Chen FH, Huang J et al. Coiling Is Not Superior to Clipping in Patients with High-Grade Aneurysmal Subarachnoid Hemorrhage: Systematic Review and Meta-Analysis. World Neurosurg. 2017 Feb; (98): 411–20.
14. Ruan C, Long H, Sun H, He M, Yang K, Zhang H et al. Endovascular coiling vs. surgical clipping for unruptured intracranial aneurysm: A meta-analysis. Br J Neurosurg. 2015; 29 (4): 485–92.
15. Suzuki M, Yoneda H, Ishihara H, Shirao S, Nomura S, Koizumi H et al. Adverse events after unruptured cerebral aneurysm treatment: a single-center experience with clipping/coil embolization combined units. J Stroke Cerebrovasc Dis. 2015 Jan; 24 (1): 223–31.
16. Hwang US, Shin HS, Lee SH, Koh JS. Decompressive Surgery in Patients with Poor-grade Aneurysmal Subarachnoid Hemorrhage: Clipping with Simultaneous Decompression Versus Coil Embolization Followed by Decompression. J Cerebrovasc Endovasc Neurosurg. 2014 Sep; 16 (3): 254–61.
17. Frontera JA, Moatti J, de los Reyes KM, McCullough S, Moyle H, Bederson JB et al. Safety and cost of stent-assisted coiling of unruptured intracranial aneurysms compared with coiling or clipping. J Neurointerv Surg. 2014 Jan; 6 (1): 65–71.
18. Brunken M, Kehler U, Fiehler J, Leppien A, Eckert B. Coiling vs. clipping: hospital stay and procedure time in intracranial aneurysm treatment. [Article in German] Rofo. 2009 Oct; 181 (10): 989–95.
19. Pasqualin A, Kassel NF, Torner JC, Benedetti A, Da Pian R, Guidetti B et al. Results of treatment (Article). Journal of Neurosurgical Sciences. 1988; 32 (1): 25–38.
20. McDougall CG, Spetzler RF, Zabramski JM, Partovi S, Hills NK, Nakaji P et al. The Barrow Ruptured Aneurysm Trial. J Neurosurg. 2012 Jan; 116 (1): 135–44.
21. Spetzler RF1, McDougall CG, Albuquerque FC, Zabramski JM, Hills NK, Partovi S et al. The Barrow Ruptured Aneurysm Trial: 3-year results. J Neurosurg. 2013 Jul; 119 (1): 146–57.
22. Spetzler RF, McDougall CG, Zabramski JM, Albuquerque FC, Hills NK et al. The Barrow Ruptured Aneurysm Trial: 6-year results. J Neurosurg. 2015 Sep; 123 (3): 609–17.
23. Spetzler RF, Zabramski JM, McDougall CG, Albuquerque FC, Hills NK, Wallace RC et al. Analysis of saccular aneurysms in the Barrow Ruptured Aneurysm Trial. J Neurosurg. 2018 Jan; 128 (1): 120–12.
24. Cantore G, Santoro A, Guidetti G, Delfinis CP, Colonnese C, Passacantilli E. Surgical treatment of giant intracranial aneurysms: current viewpoint. Neurosurgery. 2008 Oct; 63 (4) (Suppl 2): 279–90.
25. Tayebi Meybodi A, Huang W, Benet A, Kola O, Lawton MT. Bypass surgery for complex middle cerebral artery aneurysms: an algorithmic approach to revascularization. J Neurosurg. 2017 Sep; 127 (3): 463–79.
26. Rahal JP, Malek AM. Clip occlusion versus coil embolization for the treatment of cerebral aneurysms. J Neurosurg Sci. 2012 Sep; 56 (3): 175–90.

Литература

1. Serbinenko FA. Balloon catheterization and occlusion of major cerebral vessels. J Neurosurg. 1974 Aug; 41 (2): 125–45.
2. Serbinenko FA. Balloon occlusion of saccular aneurysms of the cerebral arteries. [Article in Russian] Vopr Neirokhir. 1974 Jul-Aug; (4): 8–15.
3. Serbinenko FA. 7-year experience in endovascular surgery [Article in German]. Zentralbl Neurochir. 1977; 38 (2): 141–4.
4. Serbinenko FA. Six hundred endovascular neurosurgical procedures in vascular pathology. A ten-year experience. Acta Neurochir Suppl (Wien). 1979; 28 (1): 310–1.
5. Serbinenko FA, Filatov JM, Spallone A, Tchurilov MV, Lazarev VA. Management of giant intracranial ICA aneurysms with combined extracranial-intracranial anastomosis and endovascular occlusion. J Neurosurg. 1990 Jul; 73 (1): 57–63.
6. Li H, Pan R, Wang H, Rong X, Yin Z, Milgrom DP et al. Clipping versus coiling for ruptured intracranial aneurysms: a systematic review and meta-analysis. Stroke. 2013 Jan; 44 (1): 29–37.
7. Kabbasch C, Mpotsaris A, Behme D, Dorn F, Stavrinou P, Liebig T. Pipeline Embolization Device for Treatment of Intracranial Aneurysms-The More, the Better? A Single-center Retrospective Observational Study. J Vasc Interv Neurol. 2016 Oct; 9 (2): 14–20.
8. Raymond J, Gentric JC, Darsaut TE, Iancu D, Chagnon M, Weill A et al. Flow diversion in the treatment of aneurysms: a randomized care trial and registry. J Neurosurg. 2017 Sep; 127 (3): 454–62. DOI: 10.3171/2016.4.JNS152662. Epub 2016 Nov 4.
9. Brinjikji W, Lanzino G, Cloft HJ, Siddiqui AH, Kallmes DF. Risk Factors for Hemorrhagic Complications following Pipeline Embolization Device Treatment of Intracranial Aneurysms: Results from the International Retrospective Study of the Pipeline Embolization Device. AJNR Am J Neuroradiol. 2015 Dec; 36 (12): 2308–13.
10. Zhang X, Li L, Hong B, Xu Y1, Liu Y, Huang Q et al. A Systematic Review and Meta-analysis on Economic Comparison between Endovascular Coiling versus Neurosurgical Clipping for Ruptured Intracranial Aneurysms. World Neurosurg. 2018 Feb 21; pii: S1878-8750(18)30349-8.
11. Alreshidi M, Cote DJ, Dasenbrock HH, Acosta M, Can A, Doucette J et al. Coiling Versus Microsurgical Clipping in the Treatment of Unruptured Middle Cerebral Artery Aneurysms: A Meta-Analysis. Neurosurgery. 2018 Feb 9. DOI: 10.1093/neuros/nyx623. [Epub ahead of print]
12. Fotakopoulos G, Tsianaka E, Fountas K, Makris D, Spyrou M, Hernesniemi J. Clipping Versus Coiling in Anterior Circulation Ruptured Intracranial Aneurysms: A Meta-Analysis. World Neurosurg. 2017 Aug; (104): 482–8.
13. Xia ZW, Liu XM, Wang JY, Cao H, Chen FH, Huang J et al. Coiling Is Not Superior to Clipping in Patients with High-Grade Aneurysmal Subarachnoid Hemorrhage: Systematic Review and Meta-Analysis. World Neurosurg. 2017 Feb; (98): 411–20.
14. Ruan C, Long H, Sun H, He M, Yang K, Zhang H et al. Endovascular coiling vs. surgical clipping for unruptured intracranial aneurysm: A meta-analysis. Br J Neurosurg. 2015; 29 (4): 485–92.
15. Suzuki M, Yoneda H, Ishihara H, Shirao S, Nomura S, Koizumi H et al. Adverse events after unruptured cerebral aneurysm treatment: a single-center experience with clipping/coil embolization combined units. J Stroke Cerebrovasc Dis. 2015 Jan; 24 (1): 223–31.
16. Hwang US, Shin HS, Lee SH, Koh JS. Decompressive Surgery in Patients with Poor-grade Aneurysmal Subarachnoid Hemorrhage: Clipping with Simultaneous Decompression Versus Coil Embolization Followed by Decompression. J Cerebrovasc Endovasc Neurosurg. 2014 Sep; 16 (3): 254–61.

17. Frontera JA, Moatti J, de los Reyes KM, McCullough S, Moyle H, Bederson JB et al. Safety and cost of stent-assisted coiling of unruptured intracranial aneurysms compared with coiling or clipping. J Neurointerv Surg. 2014 Jan; 6 (1): 65–71.
18. Brunken M, Kehler U, Fiehler J, Leppien A, Eckert B. Coiling vs. clipping: hospital stay and procedure time in intracranial aneurysm treatment. [Article in German] Rofo. 2009 Oct; 181 (10): 989–95.
19. Pasqualin A, Kassel NF, Torner JC, Benedetti A, Da Pian R, Guidetti B et al. Results of treatment (Article). Journal of Neurosurgical Sciences. 1988; 32 (1): 25–38.
20. McDougall CG, Spetzler RF, Zabramski JM, Partovi S, Hills NK, Nakaji P et al. The Barrow Ruptured Aneurysm Trial. J Neurosurg. 2012 Jan; 116 (1): 135–44.
21. Spetzler RF1, McDougall CG, Albuquerque FC, Zabramski JM, Hills NK, Partovi S et al. The Barrow Ruptured Aneurysm Trial: 3-year results J Neurosurg. 2013 Jul; 119 (1): 146–57.
22. Spetzler RF, McDougall CG, Zabramski JM, Albuquerque FC, Hills NK et al. The Barrow Ruptured Aneurysm Trial: 6-year results. J Neurosurg. 2015 Sep; 123 (3): 609–17.
23. Spetzler RF, Zabramski JM, McDougall CG, Albuquerque FC, Hills NK, Wallace RC et al. Analysis of saccular aneurysms in the Barrow Ruptured Aneurysm Trial. J Neurosurg. 2018 Jan; 128 (1): 120–12.
24. Cantore G, Santoro A, Guidetti G, Delfinis CP, Colonnese C, Passacantilli E. Surgical treatment of giant intracranial aneurysms: current viewpoint. Neurosurgery. 2008 Oct; 63 (4) (Suppl 2): 279–90.
25. Tayebi Meybodi A, Huang W, Benet A, Kola O, Lawton MT. Bypass surgery for complex middle cerebral artery aneurysms: an algorithmic approach to revascularization. J Neurosurg. 2017 Sep; 127 (3): 463–79.
26. Rahal JP, Malek AM. Clip occlusion versus coil embolization for the treatment of cerebral aneurysms. J Neurosurg Sci. 2012 Sep; 56 (3): 175–90.

IDENTIFICATION OF BRCA1/2 MUTATIONS IN BREAST CANCER PATIENTS BY NEXT-GENERATION SEQUENCING

Stetsenko IF[1], Krasnenko AYu[1,2], Stanoevich US[3], Mescheryakov AA[4], Vorotnikov IK[4], Druzhilovskaya OS[1], Belova VA[1], Churov AV[1,5] ✉

[1] Vavilov Institute of General Genetics of the Russian Academy of Sciences, Moscow
[2] Genotek Ltd., Moscow
[3] Russian Scientific Center for X-ray Radiology of the Ministry of Health of the Russian Federation, Moscow
[4] Blokhin Russian Cancer Research Centre, Moscow
[5] IB KarRC RAS, Petrozavodsk

Breast cancer is one of the most widespread forms of solid tumors. By analyzing the traits of breast cancer pathogenesis at the molecular level using modern genetic analysis techniques and at different stages of the disease new data can be obtained to be further utilized in clinical practice. Molecular profiling based on next-generation sequencing is being increasingly applied as a clinical test to select target drugs for treating breast cancer patients with tumors highly resistant to therapy. In this study, we performed targeted sequencing of *BRCA1* and *BRCA2* oncogenes. In the total of 66 DNA samples from patients with breast tumors, BRCA1/2 mutations were found in 39 patients. There were 78 unique genetic variants, including 30 mutations in *BRCA1* and 48 mutations in *BRCA2*. We identified 33 mutations affecting the sites of post-translational modification in proteins (PMT mutations).

Keywords: *BRCA1*, *BRCA2*, breast cancer, NGS, DNA-sequencing, mutation, personalized medicine

Funding: this work was supported by the Ministry of Education and Science of the Russian Federation (Project ID RFMEFI60716X0152).

✉ **Correspondence should be addressed:** Alexey V. Churov
Pushkinskaya 11, Petrozavodsk,185910; achurou@yandex.ru

Received: 03.12.2018 **Accepted:** 14.12.2018

DOI: 10.24075/brsmu.2018.074

ИДЕНТИФИКАЦИЯ BRCA1/2-МУТАЦИЙ ПРИ РАКЕ МОЛОЧНОЙ ЖЕЛЕЗЫ С ПРИМЕНЕНИЕМ ТЕХНОЛОГИИ ВЫСОКОПРОИЗВОДИТЕЛЬНОГО СЕКВЕНИРОВАНИЯ

И. Ф. Стеценко[1], А. Ю. Красненко[1,2], У. С. Станоевич[3], А. А. Мещеряков[4], И. К. Воротников[4], О. С. Дружиловская[1], В. А. Белова[1], А. В. Чуров[1,5] ✉

[1] Институт общей генетики имени Н. И. Вавилова РАН, Москва
[2] ООО «Генотек», Москва
[3] Российский научный центр рентгенорадиологии МЗ РФ, Москва
[4] Национальный медицинский исследовательский центр онкологии имени Н. Н. Блохина, Москва
[5] Институт биологии, Карельский научный центр (ИБ КарНЦ РАН), Петрозаводск

Рак молочной железы (РМЖ) является одной из наиболее распространенных форм солидных опухолей. Анализ особенностей патогенеза РМЖ на молекулярном уровне с применением современных методов генетического анализа и на разных стадиях заболевания позволяет получить новые данные для их дальнейшего применения в клинической практике. Молекулярное профилирование с применением технологий высокопроизводительного секвенирования все чаще применяют в качестве клинического теста при подборе таргетных препаратов для лечения пациентов с высокорезистентными к терапии опухолями при РМЖ. Целью работы было провести таргетное секвенирование генов *BRCA1* и *BRCA2* в составе панели онкогенов. Из 66 образцов ДНК пациентов с опухолями молочной железы, мутации BRCA1/2 обнаружены у 39 пацентов. Найдено 78 уникальных генетических вариантов, из них 30 мутаций в гене *BRCA1* и 48 мутаций в гене *BRCA2*. Идентифицировано 33 мутации, оказывающие влияние на сайты посттрансляционной модификации белков (PMT-мутации).

Ключевые слова: *BRCA1*, *BRCA2*, рак молочной железы, NGS, ДНК-секвенирование, мутация, персонализированная медицина

Финансирование: работа выполнена при финансовой поддержке государства в лице Минобрнауки России (идентификатор соглашения RFMEFI60716X0152).

✉ **Для корреспонденции:** Алексей Викторович Чуров
ул. Пушкинская, д. 11, г. Петрозаводск, 185035; achurou@yandex.ru

Статья получена: 03.12.2018 **Статья принята к печати:** 14.12.2018

DOI: 10.24075/vrgmu.2018.074

Breast cancer (BC) is one of the most widespread forms of malignant neoplasms, next only to lung cancer and colorectal cancer. BC incidence has been growing in many parts of the world [1–4]. Early detection of the pathology and screening for BC is therefore a key task.

Suppressor genes *BRCA1* and *BRCA2* are important actors in regulating the signaling pathways associated with the functioning of DNA repair systems. Mutations in these genes entail an elevated risk of developing BC and some other forms of malignant tumors.

A substantial proportion of the mutations in tumors are somatic mutations, playing an important role both in the pathogenesis of sporadic BC and in the development of *de novo* resistance to anticancer drugs. Sporadic forms of cancer constitute, on average, 70–80% of BC cases, whereas only 10% of all the patients carry inherited mutations in the *BRCA1* and *BRCA2* genes [5].

The actual task of oncogenetics today is the development and improvement of approaches to the effective selection of anticancer drugs, taking into account the molecular-genetic features of tumor development.

The aim of this study was to identify the spectrum of mutations in the *BRCA1* and *BRCA2* genes in patients with BC by Illumina next-generation sequencing.

METHODS

Material for the study. Clinical characteristics of the patients

The collection of tumor samples for the study was taken from 66 patients with malignant breast neoplasms in hospital care at NN Blokhin National Medical Research Centre of Oncology of the Russian Health Ministry and Russian Scientific Center for X-ray Radiology of the Ministry of Health of the Russian Federation, (Moscow). The average age of the patients was 52.5 ± 9.7 years. The criteria for being included in the study were: age of 18 to 70, female, clinically verified BC diagnosis. Exclusion criteria: history of other forms of neoplasms, pregnancy. BC was staged according to TNM classification [6]. The study involved patients with stages T1–3N0–3M0–1. The study adhered to the principles of voluntariness and confidentiality. All patients provided informed consent to the study. The principal clinical characteristics of the patients are given in Table 1.

DNA isolation and quality control. Oncogene panel sequencing

Genomic DNA was isolated from tumor tissue samples by using DNeasy Blood and Tissue Kit (Qiagen; USA) as instructed by the manufacturer. The concentration of the extracted DNA specimens was measured with a Qubit 3.0 fluorometer (Thermo Fisher Scientific; USA). The quality of the DNA samples was additionally tested by electorphoresis in 1% agarose gel with ethidium bromide.

DNA fragment libraries were prepared using NEBNext Ultra DNA Library Prep Kit for Illumina (New England Biolabs; USA). The libraries were barcoded by PCR using two reagent kits: NEBNext Ultra DNA Library Prep Kit for Illumina and NEBNext Multiplex Oligos for Illumina (Dual Index Primers Set 1, New England Biolabs; USA). DNA library quality control was done by measurements with Agilent Bioanalyzer 2100 (Agilent Technologies; USA) using High Sensitivity Kit as instructed by the manufacturer.

Coding regions of the tumor genome were enriched using MYbaits Onconome KL v1.5 Panel (Mycroarray; USA). The analysis was performed with a high-throughput genome sequencing system HiSeq 2500 (Illumina; USA) using paired 100-nucleotide reads. The samples were prepared and initiated according to Illumina protocols.

Bioinformatic processing of NGS data

Bioinformatic processing of the resultant NGS data was carried out using a previously developed algorithm [7, 8]. At first, the quality of the reads from DNA sequencing was assessed by Cutadapt software, and they were mapped to the reference genome hg19 (GRCh37.p13) by using the BWA tool (Burrows-

Table 1. Clinical characteristics of women with breast cancer (*n* = 66)

Parameter	Value, abs. no (%)
Age (years)	52.5 ± 9.7
Principal diagnosis:	
Left breast cancer	32 (48.5)
Right breast cancer	32 (48.5)
Bilateral cancer	2 (3)
Tumor T-stage (TNM classification):	
T1	36 (54.5)
T2	29 (43.9)
T3	1 (1.5)
Metastases in lymph nodes:	
without metastases, M0	56 (84.8)
with metastases, M1	10 (15.2)
Expression of estrogen receptors (ER):	
ER+	53 (80.3)
ER–	13(19.7)
Expression of progesterone receptors (PR):	
PR+	50 (75.8)
PR–	16 (24.2)
Expression of HER2/neu (Cerb-B2):	
Her2+	38 (57.6)
Her2–	28 (42.4)

Note: the values are in M ± SD or % form; T 1–3 — tumor stages according to TNM classification; ER — estrogen receptor expression; PR — progesterone receptor expression; HER2/neu (Cerb-B2) — expression of the human epidermal growth factor receptor *2*.

Wheeler Aligner). Paired reads were removed by running the specialized rmdup command in the SAMtools software package. Mutations in the NGS dataset were detected by MuTect, and DNA sequences covered by at least 12 readswere considered the most significant.

The mutation abundance was defined as the proportion (%) of mutation-supporing reads at a position. The functional effect of the mutations was assessed relying on ActiveDriverDB database [9]. The mutations affecting the coded protein were visualized using the ProteinPaint application [10].

RESULTS

We analyzed DNA samples from breast tumors (*n* = 66) for the presence of mutations in the *BRCA1* and *BRCA2* genes by Illumina next-generation sequencing. Bioinformatic processing of the NGS data revealed mutations in the *BRCA1* and *BRCA2* genes in 39 (59.1%) out of the 66 BC patients. Altogether 78 unique genetic variants were detected in the study, including 30 mutations in *BRCA1* and 48 mutations in *BRCA2*. Among all these mutations, 70 of the detected variants were identified as new mutations (89.7%). All the detected genetic variants are listed in the Table 2.

The highest frequency in the analysis was demonstrated by the mutations 17:41246746:T>C in *BRCA1* gene (52%) and 13:32914688:G>T in *BRCA2* gene (47%). The mutation 13:32910800:A>C in *BRCA2* gene occurred the most frequently among all samples, being identified in 10.7% (*n* = 3/28) of tumors with *BRCA2* mutations. Mutations in both *BRCA1* and *BRCA2* were found in 11 patients with BC (16.7%; *n* = 66).

Annotation against databases revealed 33 mutations (42.3%) influencing the sequence of the coded protein, including 16 in *BRCA1* gene and 17 in *BRCA2* gene. The

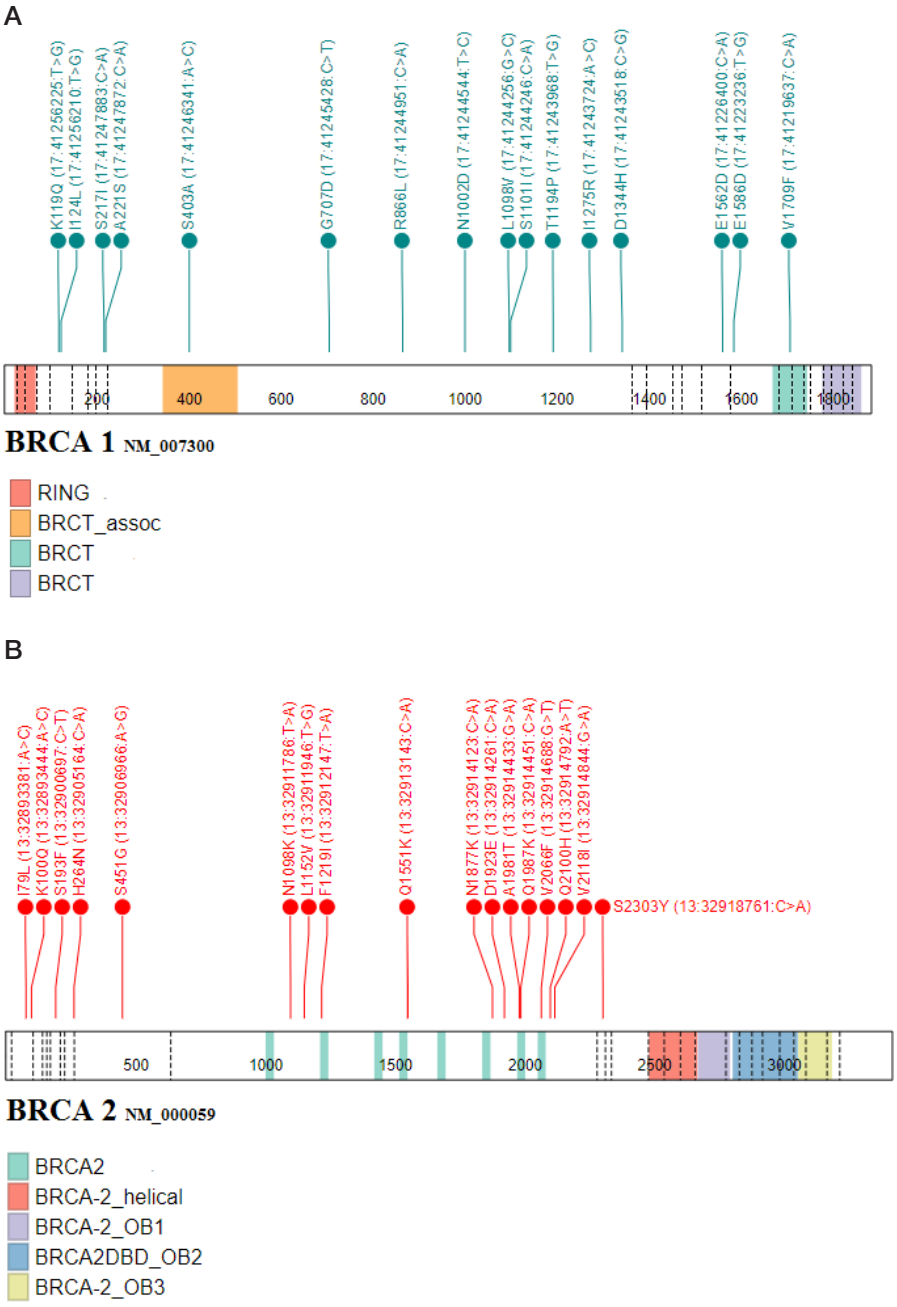

Fig. 1. The spectrum of mutations* affecting post-translational modification sites of proteins (PMT-mutations) in the genes *BRCA1* (**A**) and *BRCA2* (**B**), in patients with breast cancer (*n* = 39). * — based on mutation effect prediction according to ActiveDriverDB

Table 2. *BRCA1* and *BRCA2* mutations identified in patients with BC

Gene	Sample ID	BC Stage	The proportion of cancer cells in the sample[1], %	Variant allele frequency, %	Coverage at the point	PTM-mutation	Effect[2]	Reference number[2]	Canonical designation
BRCA1	1	IIIA	20	52	235	No	None	Novel	17:41246746:T>C
	2	IIA	9	30	117	No	None	rs1800744	17:41226488:C>A
	3	IA	70	4	106	No	None	Novel	17:41251858:T>G
				3	115	Yes	distal	Novel	17:41223236:T>G
				2	267	Yes	proximal	Novel	17:41243968:T>G
				1	439	No	None	Novel	17:41245560:C>A
	4	I	30	4	116	Yes	proximal	rs80357088 (dbSNP)	17:41247872:C>A
				1	685	Yes	proximal	rs80357192 (dbSNP)	17:41245428:C>T
	5	IIA	8	4	230	Yes	network-rewiring - motif loss	Novel	17:41244256:G>C
	6	I	90	2	169	Yes	direct	Novel	17:41244246:C>A
	7	IIA	21	2	250	No	None	Novel	17:41244207:T>C
	8	IA	8	2	306	No	None	Novel	17:41246576:A>C
	9	IA	6	2	270	Yes	distal	Novel	17:41243724:A>C
	10	IA	32	2	142	Yes	proximal	Novel	17:41256210:T>G
				2	142	Yes	distal	Novel	17:41256225:T>G
				1	333	Yes	direct	Novel	17:41246341:A>C
	11	IIB	95	2	166	Yes	proximal	BRCA (TCGA MC3)	17:41243518:C>G
				1	467	No	None	Novel	17:41245516:C>A
	12	IA	98	1	202	Yes	distal	Novel	17:41247883:C>A
	13	IA	15	1	660	Yes	network-rewiring - motif loss	Novel	17:41244951:C>A
	14	IIB	35	1	444	No	None	Novel	17:41245785:C>A
	15	I	12	1	569	No	None	Novel	17:41245228:C>T
	16	IIB	12	1	351	No	None	Novel	17:41245832:T>G
	17	IIA	57	1	413	No	None	Novel	17:41245859:C>A
	18	IA	12	1	211	Yes	proximal	Novel	17:41226400:C>A
	19	IIA	38	1	342	Yes	distal	rs786202665 (dbSNP)	17:41244544:T>C
	20	IIA	32	1	307	No	None	Novel	17:41246752:C>A
	21	IA	35	1	336	Yes	distal	Novel	17:41219637:C>A
				1	379	No	None	Novel	17:41246125:T>A
	22	IIA	10	1	390	No	None	Novel	17:41245026:C>A
BRCA2	9	IA	6	47	189	Yes	distal	Novel	13:32914688:G>T
				2	210	Yes	distal	Novel	13:32905164:C>A
	12	IA	98	6	471	No	None	rs28897716 (dbSNP)	13:32911295:G>A
				1	434	Yes	proximal	Novel	13:32893381:A>C
	23	IA	15	4	100	No	None	Novel	13:32906550:T>C
	24	I	50	3	63	No	None	rs55924966 (dbSNP)	13:32929408:G>A
	19	IIA	38	3	152	No	None	Novel	13:32912843:G>T
				2	276	No	None	Novel	13:32912258:C>A
	25	IA	65	2	319	No	None	Novel	13:32910800:A>C
	14	IIB	35	2	316	Yes	direct	rs864622305 (dbSNP)	13:32900697:C>T
	7	IIA	21	2	251	No	None	Novel	13:32944694:G>T
	26	IA	10	2	255	No	None	Novel	13:32911260:A>T
				1	537	No	None	Novel	13:32910800:A>C
	27	IIA	11	2	87	Yes	proximal	Novel	13:32918761:C>A
				2	238	No	None	Novel	13:32930703:C>A
	28	IIA	70	2	130	No	None	Novel	13:32931930:G>T
				1	307	Yes	distal	Novel	13:32914451:C>A
	29	I	1	2	262	No	None	Novel	13:32910800:A>C

End of Table 2

	30	IIA	55	2	200	No	None	Novel	13:32911499:C>A
				2	237	No	None	Novel	13:32913030:A>C
				1	274	Yes	distal	Novel	13:32914261:C>A
	10	IA	32	2	99	Yes	distal	Novel	13:32893444:A>C
				2	179	No	None	Novel	13:32907009:T>G
				2	188	Yes	proximal	Novel	13:32911946:T>G
	4	I	30	2	807	No	None	Novel	13:32914484:C>A
				1	323	No	None	Novel	13:32899216:G>A
				1	747	No	None	Novel	13:32915036:A>T
				1	279	No	None	Novel	13:32930596:T>A
				1	285	No	None	Novel	13:32930604:A>G
	21	IA	35	2	332	No	None	Novel	13:32914234:C>A
				1	440	No	None	Novel	13:32907309:C>A
	22	IIA	10	2	164	No	None	Novel	13:32912375:C>A
				1	298	No	None	Novel	13:32907051:A>T
				1	358	Yes	distal	Novel	13:32914844:G>A
	2	IIA	9	2	165	No	None	Novel	13:32968849:T>C
	31	IIIC	18	1	405	No	None	Novel	13:32913099:A>C
				1	266	No	None	Novel	13:32929173:C>A
	32	IIA	9	1	526	Yes	proximal	Novel	13:32913143:C>A
				1	399	No	None	Novel	13:32968988:C>A
	33	IIIA	10	1	233	Yes	distal	Novel	13:32911786:T>A
	14	IA	15	1	362	No	None	Novel	13:32936764:C>A
	34	IIA	14	1	371	Yes	distal	Novel	13:32912147:T>A
	35	IB	5	1	246	No	None	Novel	13:32913558:C>T
				1	434	Yes	distal	Novel	13:32914792:A>T
	36	IIB	25	1	344	Yes	distal	Novel	13:32914433:G>A
	37	IIB	80	1	569	Yes	distal	rs374326934 (dbSNP)	13:32914123:C>A
				1	275	No	None	Novel	13:32937605:G>A
	1	IIIA	20	1	320	Yes	distal	Novel	13:32906966:A>G
	38	I	10	1	439	No	None	Novel	13:32913444:C>A
	39	IIA	18	1	262	No	None	Novel	13:32930600:C>A
				1	363	No	None	Novel	13:32936793:C>A

Note: [1] — based on histological data; [2] — based on ActiveDriverDB data (https://www.activedriverdb.org/).

mutations affecting the sites of post-translational modification in proteins (PMT mutations) are shown in the Fig. 1.

DISCUSSION

Personalized targeted therapy is gaining ground in modern oncology. The development of a highly sensitive and cost-efficient approach to affordable routine diagnosis of tumors is therefore a priority task.

The “gold standard” for mutation detection today is Sanger sequencing, but its diagnostic capabilities are limited compared to next-generation genetic analysis systems. Tumor cells are histologically and genetically heterogeneous, contributing to the advantage of NGS-based techniques, which allow developing efficient bioinformatics pipelines for detecting genetic variants both in pairs of tumor and normal tissues samples and within individual biopsies containing a fraction of normal cell DNA.

Mutations in the key BC oncogenes *BRCA1* and *BRCA2* are among the most frequent and significant molecular aberrations, whose analysis can help in assessing the risk of tumor development, clinical prediction for BC patients, and in predicting the effectivenesss of anticancer drug therapy.

The *BRCA1* gene was identified by Y. Miki et al. in 1994 by positional cloning on the long arm of chromosome 17. The second gene — *BRCA2*, was mapped and isolated on chromosome 13q. *BRCA1* and *BRCA2* are suppressor genes, characterized by the autosomal dominant inheritance pattern and high penetrance. Recent molecular studies of *BRCA1* and *BRCA2* have demonstrated a wide spectrum of mutations present in these genes [5].

The international COSMIC database [11] contains over 900 somatic coding mutations of the *BRCA1* gene and over 1400 coding mutations of the *BRCA2* gene. A substantial part of these mutations result in structural transformations modifying

the function of protein products, thus undermining the capacity of repair systems to effectively fix DNA lesions. Many of the mutations in *BRCA1/BRCA2* are missence mutations, where the coding sequence is altered and one functional codon is changed to another.

Having analyzed the NGS data for the BC tumors in our study by bioinformatics techniques, we identified 78 unique mutations in the genes *BRCA1* and *BRCA2.* A majority of the mutations were found in *BRCA2*. According to the literature, the frequency of mutations differs notably between the genes *BRCA1* and *BRCA2* [5].

Further analysis using ActiveDriverDB showed that a large part of the genetic variants produce a functional effect on post-translational modification sites of the coded proteins (Fig. 1). Our study revealed 33 PMT-mutations, many of them previously unannotated. To confirm the pathogenic variants detected in the study and the status of the mutations, the research results need to be verified by Sanger sequencing using normal tissue samples.

CONCLUSIONS

Targeted next-generation sequencing appears to be the most promising approach for molecular profiling of tumors for clinical application. An integrated NGS-based analysis of mutations in the genes *BRCA1* and *BRCA2* in BC patients enables the identification of a greater number of mutations, including low mutant allele frequency variants, as well as genetic variants in biopsy samples with low tumor cell content. NGS-based approaches revealing mutations in the entire *BRCA1* and *BRCA2* coding sequence will enable a more effective identification of the patients to whom an adequate therapy with targeted anticancer drugs can be administered.

References

1. Bejsebaev EN. Sovremennye sravnitel'nye aspekty jepidemiologii raka molochnoj zhelezy. Vestnik KazNMU. 2014; (1): 78–83.
2. Ferlay J, Soerjomataram I, Dikshit R, Eser S, Mathers C, Rebelo M et al. Cancer incidence and mortality worldwide: sources, methods and major patterns in GLOBOCAN 2012. Int J Cancer. 2015; (136): E359–86.
3. Tao Z, Shi A, Lu C, Song T, Zhang Z, Zhao J. Breast Cancer: Epidemiology and Etiology. Cell Biochem Biophys. 2015; (72): 333–8.
4. Ghoncheh M, Pournamdar Z, Salehiniya H. Incidence and Mortality and Epidemiology of Breast Cancer in the World. Asian Pac J Cancer Prev. 2016; (17): 43–6.
5. Bykova AV, Vorotnikov IK, Vishnevskaja JaV, Denchik DA, Ljubchenko LN. Rol' mutacii genov BRCA 1 i BRCA 2 v vozniknovenii raka molochnoj zhelezy u muzhchin. Opuholi zhenskoj reproduktivnoj sistemy. 2011; (1): 29–31.
6. Giuliano AE, Connolly JL, Edge SB, Mittendorf EA, Rugo HS, Solin LJ et al. Breast Cancer-Major changes in the American Joint Committee on Cancer eighth edition cancer staging manual. CA Cancer J Clin. 2017; 67 (4): 290–303.
7. Cukanov KJu, Krasnenko AJu, Korostin DO, Churov AV, Stecenko IF, Plotnikov NA i dr. Rak molochnoj zhelezy: analiz spektra somaticheskih drajvernyh mutacij s primeneniem vysokoproizvoditel'nogo sekvenirovanija. Vestnik RGMU. 2017; (6): 52–8.
8. Cukanov KJu, Krasnenko AJu, Plahina DA, Korostin DO, Churov AV, Druzhilovskaja O. S. i dr. Bioinformaticheskij protokol dlja obrabotki NGS-dannyh i identifikacii mutacij v solidnyh opuholjah cheloveka. Biomedicinskaja himija. 2017; 63 (5): 413–7.
9. Krassowski M, Paczkowska M, Cullion K, Huang T, Dzneladze I, Ouellette BFF et al. ActiveDriverDB: human disease mutations and genome variation in post-translational modification sites of proteins. Nucleic Acids Res. 2018; 46: D901–D910.
10. Zhou X, Edmonson MN, Wilkinson MR, Patel A, Wu G, Liu Y et al. Exploring genomic alteration in pediatric cancer using protein paint. Nat Genet. 2015; (48): 4–6.
11. Forbes SA, Beare D, Bindal N, Bamford S, Ward S, Cole CG et al. COSMIC: High-Resolution Cancer Genetics Using the Catalogue of Somatic Mutations in Cancer. Curr Protoc Hum Genet. 2016; (91): 10.11.1–10.11.37.

Литература

1. Бейсебаев Е. Н. Современные сравнительные аспекты эпидемиологии рака молочной железы. Вестник КазНМУ. 2014; (1): 78–83.
2. Ferlay J, Soerjomataram I, Dikshit R, Eser S, Mathers C, Rebelo M et al. Cancer incidence and mortality worldwide: sources, methods and major patterns in GLOBOCAN 2012. Int J Cancer. 2015; (136): E359–86.
3. Tao Z, Shi A, Lu C, Song T, Zhang Z, Zhao J. Breast Cancer: Epidemiology and Etiology. Cell Biochem Biophys. 2015; (72): 333–8.
4. Ghoncheh M, Pournamdar Z, Salehiniya H. Incidence and Mortality and Epidemiology of Breast Cancer in the World. Asian Pac J Cancer Prev. 2016; (17): 43–6.
5. Быкова А. В., Воротников И. К., Вишневская Я. В., Денчик Д. А., Любченко Л. Н. Роль мутации генов BRCA 1 и BRCA 2 в возникновении рака молочной железы у мужчин. Опухоли женской репродуктивной системы. 2011; (1): 29–31.
6. Giuliano AE, Connolly JL, Edge SB, Mittendorf EA, Rugo HS, Solin LJ et al. Breast Cancer-Major changes in the American Joint Committee on Cancer eighth edition cancer staging manual. CA Cancer J Clin. 2017; 67 (4): 290–303.
7. Цуканов К. Ю., Красненко А. Ю., Коростин Д. О., Чуров А. В., Стеценко И. Ф., Плотников Н. А. и др. Рак молочной железы: анализ спектра соматических драйверных мутаций с применением высокопроизводительного секвенирования. Вестник РГМУ. 2017; (6): 52–8.
8. Цуканов К. Ю., Красненко А. Ю., Плахина Д. А., Коростин Д. О., Чуров А. В., Дружиловская О. С. и др. Биоинформатический протокол для обработки NGS-данных и идентификации мутаций в солидных опухолях человека. Биомедицинская химия. 2017; 63 (5): 413–7.
9. Krassowski M, Paczkowska M, Cullion K, Huang T, Dzneladze I, Ouellette BFF et al. ActiveDriverDB: human disease mutations and genome variation in post-translational modification sites of proteins. Nucleic Acids Res. 2018; 46: D901–D910.
10. Zhou X, Edmonson MN, Wilkinson MR, Patel A, Wu G, Liu Y et al. Exploring genomic alteration in pediatric cancer using protein paint. Nat Genet. 2015; (48): 4–6.
11. Forbes SA, Beare D, Bindal N, Bamford S, Ward S, Cole CG et al. COSMIC: High-Resolution Cancer Genetics Using the Catalogue of Somatic Mutations in Cancer. Curr Protoc Hum Genet. 2016; (91): 10.11.1–10.11.37.